Thermodynamic and Transport Property Modeling in Supercritical Water

by
Michael C. Kutney

B.S. Chemical Engineering
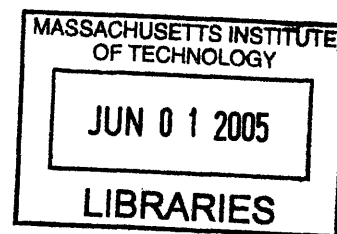University of California, San Diego (1993)

Submitted to the Department of Chemical Engineering in partial fulfillment of the requirements
for the degree of

DOCTOR OF SCIENCE IN CHEMICAL ENGINEERING
at the
MASSACHUSETTS INSTITUTE OF TECHNOLOGY
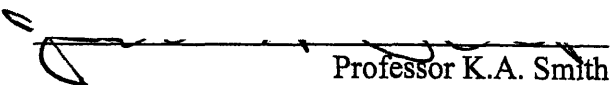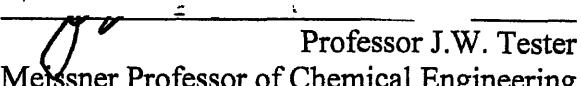
February 7th, 2005

[June 2005]

Signature of Author: _____
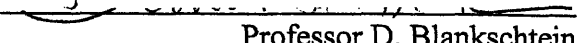Department of Chemical Engineering
February 7th, 2005

Certified by: _____
Professor K.A. Smith
Edwin R. Gilliland Professor of Chemical Engineering
Thesis Supervisor

Certified by: _____
Professor J.W. Tester
Herman P. Meissner Professor of Chemical Engineering
Thesis Supervisor

Accepted by: _____
Professor D. Blankschtein
Professor of Chemical Engineering
Chairman, Committee for Graduate Students

1

Thermodynamic and Transport Property Modeling in Supercritical Water
by
Michael C. Kutney

ABSTRACT

Supercritical water oxidation (SCWO) is a thermally-based, remediation and waste-treatment process that relies on unique property changes of water when water is heated and pressurized above its critical point. Above its critical point (374.1°C and 220.9 bar), water becomes gas-like and somewhat non-polar due to the decrease in density and disruption of the hydrogen-bond network. When oxidants and organic compounds are combined with supercritical water (SCW), they rapidly form a single phase, and these organics are quickly and completely oxidized to simple molecules including water and carbon dioxide. Laboratory research is currently being conducted in order to increase the level of understanding of key SCWO areas including reaction kinetics, corrosion, and salt-related phenomena and in order to develop realistic SCWO process and fluid-dynamic simulators. Understanding the phenomena in each of these areas requires accurate thermodynamic- and transport-property predictions. However, these often do not exist. Furthermore, available correlations are often used in operating regimes where they were not originally validated, thereby potentially reducing their accuracy.

This thesis focuses on the development of accurate thermodynamic-property and diffusivity-transport-property models for use at typical SCWO operating conditions, namely $25°C \leq T \leq 650°C$ and $1 \text{ bar} \leq P \leq 300 \text{ bar}$, along with the measurement of molecular diffusivity, an important transport-phenomena property. These models can be incorporated into simulation tools which are used to model SCWO processes or physically simulate the flow, kinetics, corrosion, salt nucleation, and salt precipitation inside SCWO reactors. These large-scale SCWO simulations should ultimately lead to improved reactor designs which have less operating risk, appropriately sized reactors, optimized residence times, lower costs, fewer technical limitations, and increased destruction efficiencies.

Thermodynamic-property research:
Hard-sphere, volume-translated van der Waals equation of state (EOS)

The hard-sphere, volume-translated van der Waals EOS is comprised of the semi-theoretical Carnahan-Starling expression that properly represents the molecular interactions between hard spheres and a simple van der Waals attraction term. It also utilizes volume translation to further improve high density predictions. The translation constant is determined by a fit to liquid and vapor coexistence density data while the Carnahan-Starling and van der Waals parameters are determined from widely available critical-point data. An analysis of several important thermodynamic properties (*e.g.*, density, vapor pressure, and enthalpy) has been shown to fit within average deviations of 1–30% over a wide range of conditions for the selected components: ammonia, carbon dioxide, ethylene, methane, nitrogen, oxygen, and water.

Thermodynamic-property research:
An analysis of EOS Zeno behavior

The behavior of the "Zeno" ($Z = PV/RT = 1$) line has been examined in a collaborative project in order to investigate this recently rediscovered empirical regularity of fluids and to determine if such a regularity can be utilized to improve EOSs and their predictions. For a wide range of pure fluids, this contour of unit compressibility factor in the temperature-density plane has been empirically observed to be nearly linear (and arrow-like, thus "Zeno") from the Boyle temperature of the low density vapor to near the triple point in the liquid region. Although quantitative agreement between Zeno EOS predictions and experimental data is not exact, the general trends suggest that these EOS models adequately capture the dynamic balance that exists between repulsive and attractive forces along the Zeno line. In addition, molecular simulation of Zeno behavior showed good agreement with experimental data.

Transport-property research:
Measurement and modeling of molecular diffusivities

The transport-property research consists of measuring molecular diffusivities at SCWO operating conditions using nuclear magnetic resonance (NMR) and validating diffusivity models with these experimental and previously published results. Self-diffusivities of pure supercritical water have been previously measured and published for a limited range of conditions, but accurate SCW binary-diffusivity data are extremely limited. For this reason, diffusivities of aqueous acetone mixtures have been measured at SCWO conditions using a novel, first-of-a-kind SCW/NMR flow system and the NMR spin-echo technique. Experimental results are compared with predictions from kinetic-gas-theory models and hydrodynamic-theory correlations. For SCWO operating conditions, the Tracer Liu-Silva-Macedo (TLSM) and Mathur-Thodos correlations were found to provide the most accurate diffusivity predictions. The Mathur-Thodos correlation requires only critical constants and molecular weights and has an average absolute deviation (AAD) of 18% for supercritical-water self-diffusivities and supercritical tracer & infinitely dilute mutual diffusivities above 400°C. Similar results were obtained with the TLSM model (23% AAD for data above 400°C) which requires only molecular weights and two Lennard-Jones (LJ) 6-12 parameters for each pure component. Further improvement was made when mole-fraction-weighted experimental solute and LSM-provided water LJ parameters were used (20% AAD).

As a result of the improved thermodynamic- and transport-property modeling capabilities along with the collection of additional aqueous supercritical diffusivities contained in this thesis, the SCWO community now has additional thermodynamic- and transport-property knowledge that leads to a greater understanding of key issues that impact the design and operation of SCWO technology.

Thesis supervisors: Professor K.A. Smith
                                 Edwin R. Gilliland Professor of Chemical Engineering

                                 Professor J.W. Tester
                                 Herman P. Meissner Professor of Chemical Engineering

ACKNOWLEDGEMENTS

There are so many individuals to thank, especially those that have inspired me, contributed to, and kept the faith during this work. First, to my wife Laura, to my children, and to my parents: this dissertation could never have been completed without your support. Thank you! To my advisors Prof. Ken Smith and Prof. Jeff Tester: thank you for working with me and improving important skills ranging from performing basic research to strengthening my scientific resolve.

I am indebted to my thesis committee consisting of Prof. David Cory, Prof. Karen Gleason, and Dr. Howard Herzog. Your guidance, candor, and involvement are greatly appreciated. Special thanks are owed to Prof. Cory for providing the resources required to complete the experimental measurements in this dissertation and include the laboratory, NMR equipment, and access to his group and himself. This group, whom I am also indebted, includes Dr. Werner Maas, Dr. Ross Mair, Dr. Aaron Sodickson, and Dr. John Zhang.

I am also grateful and am honored to have worked with a wonderfully talented supercritical-fluids group. These group members include Ms. Bonnie Caputo, Dr. Jason Cline, Dr. Joanna DiNaro, Dr. Matt Dipippo, Dr. Marc Hodes, Mr. Yuji Kubo, Future Dr. Russ Lachance, Dr. Phil Marrone, Dr. Brian Phenix, Dr. Matt Reagan, Dr. Josh Taylor, and Dr. Randy Weinstein. We learned so much while at MIT and so much about each other.

Individuals who have contributed to this work are also acknowledged and are also appreciated. They have provided assistance or have reviewed components of the dissertation. They include:

Equations of state

Henry D. Cochran (Oak Ridge National Laboratory),

Bobby Dodd (formerly at Massachusetts Institute of Technology)

E.U. Franck (University of Karlsruhe),

Jonathan Harris (formerly at Massachusetts Institute of Technology),

Keith P. Johnston (University of Texas, Austin),

Paul M. Mathias (Aspen Technology, Inc.),

Michael Modell (Massachusetts Institute of Technology),

John M. Prausnitz (University of California, Berkeley),

Robert C. Reid (emeritus professor at Massachusetts Institute of Technology) and

Robert W. Shaw (Army Research Office)

Zeno Line

Tomas Arias (Cornell University)

James Ely (Colorado School of Mines)

Dudley R. Herschbach (Harvard University)

Matt T. Reagan (formerly at Massachusetts Institute of Technology)

NMR

Mark S. Conradi (George Washington University)

Karen Gleason (Massachusetts Institute of Technology)

Werner E. Maas (Bruker Instruments)

Ross Mair (Harvard University)

Ron DeRocher (Massachusetts Institute of Technology)

TABLE OF CONTENTS

11

LIST OF FIGURES

13

14

16

19

22

.

LIST OF TABLES

27

LIST OF NOMENCLATURE

a	interaction energy parameter
a_c	value of a at the critical temperature
A	hard-sphere roughness factor
b	molecular size parameter
b^{HS}	hard-sphere excluded volume (often written as $b = 2\pi\sigma^3 N_a/3$)
b_o	hard-sphere molecular volume (equals $\pi\sigma^3 N_a/6$)
c	Part II: kinetic-gas-theory molecular root-mean-square speed Part II: SR-POLAR-EOS volume-translation parameter
d	volume-translation scaling parameter
D_i	tracer diffusivity for the species i
D_{ii}	self-diffusivity for the species i
D_{ij}	mutual diffusivity for the solute i and solvent j
g	radial-distribution function
$\mathbf{G}$	magnetic-field gradient vector
G	magnetic-field gradient
f	friction factor
f_i	fugacity for pure component i
$f_n(T)$	temperature dependent virial coefficient (Eq. (46))
$f_n^{rep}(T)$	repulsive contribution to pressure (Eq. (47))
$f_n^{att}(T)$	attractive contribution to pressure (Eq. (47))
H	enthalpy
$\mathbf{J}$	molar flux
k	Boltzmann's constant
k_{ii}	parameter or expression for component i
$\mathbf{k}$	spin-magnetization wave vector
K_w	water ion product
m, n	parameters in Soave's polar α equation
n	number density
M	Part I: number of data points or contributions in pressure series Part II: molecular weight
$\langle n_{HB}\rangle$	average numbers of hydrogen bonds per molecule
N	number of moles, molecules or components

N_a	Avogadro's number
P	pressure for a fluid at a given T and V
q	SR-POLAR-EOS used to fit α as a function of T_r
r	site-site interatomic separation distance
R	gas constant
q_i	point charge
S	entropy
t	volume-translation parameter
T	absolute temperature
T_2	NMR spin-spin relaxation time
V	specific volume
V^{UT}	untranslated specific volume
$\underline{V}$	total volume
x_i	mole fraction for component i
y	hard-sphere excluded-volume ratio ($y = b^{HS}/4V$)
Z	compressibility factor ($Z = PV/RT$)

Greek letters

α	Part I: interaction energy parameter
	Part II: thermodynamic correction factor
α_A, α_B	HSVTvdW-EOS parameters used to fit α as a function of T_r
β	sliding frictional coefficient
χ	diffusivity correction factor
δ	Part I: volume-translation scaling parameter
	Part II: Brokaw polar collision-integral correction term
Ω_D	collision diameter
ε	static dielectric constant
ε_{ij}	Lennard-Jones energy well-depth parameter
ε_o	vacuum permittivity
ϕ_i	Part I and Part II: fugacity coefficient for pure component i
ϕ_2	Part II: Wilke-Chang solvent association factor
$\Phi(r)$	interatomic potential energy of interaction

γ	activity coefficient
η	Part I: fitted volume-translation constant Part II: viscosity
κ_T	isothermal compressibility $\equiv -\dfrac{1}{V}\left(\dfrac{\partial V}{\partial P}\right)_T$
μ	dipole moment
π	NMR pulse width
ρ	density or mixture density
σ	hard-sphere molecular diameter
σ_{ij}	Lennard-Jones soft-sphere diameter
ς	Takahashi correction term
ω	NMR resonance frequency

Subscripts

b	normal-boiling-point value
c	critical value
$calc$	calculated value
$expt$	published experimental or smoothed data value
g	glass-transition value
ii	pure component i pair-interaction parameter
i, j	component i or j
max	maximum
min	minimum
r	reduced value $(e.g.,\ T_r = T/T_c)$
sat	saturation value
0	solvent close-packed hard-sphere value
1	solute value
12	mixture value
2	solvent value

Superscripts

calc	calculated value
data	published experimental or smoothed data value
EOS	equation-of-state value
HS	hard-sphere value or contribution
ID	ideal-gas-state value
L	liquid-phase value
o	ideal gas ideal-gas reference state value
r	residual- or departure-function value
T	translated value
UT	untranslated value
vap	vaporization value (*e.g.*, ΔH^{vap})
V	vapor-phase value
∞	infinitely dilute value
'	Onsager coefficients

DISSERTATION BACKGROUND, MOTIVATION, AND OBJECTIVES
FOR PART I AND II

PART I – THERMODYNAMIC-PROPERTY RESEARCH
PART II – TRANSPORT-PROPERTY RESEARCH

1. Background and Motivation

1.1 Supercritical Water (SCW)

Water is one of the most important and unique molecules on this planet. The presence of water is a key factor which makes Earth inhabitable. Water structure and interactions between water molecules influence numerous water properties and the properties of solutes dissolved in water.

Water (H_2O) is simply two hydrogen atoms covalently bonded to an oxygen atom. According to valence-shell electron-pair-repulsion theory, it should form a tetrahedron (four sp^3 orbitals) with two orbitals filled with unbonded pairs of unshielded valence electrons, have an oxygen atom in the center, and have a H–O–H bond angle of $109.5°$. Since the lone electron pairs are not held in as close to the oxygen atom as the bonded pairs, the corresponding orbital lobes occupy more space and force the hydrogen atoms closer towards each other until the observed bond angle of $104.5°$ is reached (Levine, 1988). Furthermore, because there is an unequal electron distribution in a water molecule, the lone pairs attain a negative charge, while the hydrogen atoms become positively charged. These structural and electronic maneuvers create a permanent dipole moment and turn water into a polar molecule which is shown in Figure 1a (Campbell, 1987).

The unbalanced charge is also the basis for a coulombic attraction between a positively charged hydrogen atom and a negatively charged oxygen atom of a neighboring water molecule. This low-strength dipole–dipole interaction is called a *hydrogen bond* (HB) and has an approximate bond energy of 25 kJ/mol (about a twentieth of the covalent bond strength) (Chang, 1988; Kalinichev and Bass, 1997). Although HBs only last for approximately 1 picosecond (10^{-12} s), at any instant a substantial percentage of water molecules are bonded (Campbell, 1987). At ambient conditions (temperature (T) = 25°C, pressure (P) = 1 bar, and density (ρ) = 0.997 g/cm^3) the average number of hydrogen bonds per water molecule, $<n_{HB}>$, has been shown to equal 3.2 (Kalinichev and Bass, 1997). When water is frozen, the average number of hydrogen bonds per water molecule reaches its maximum of 4.0 since every tetrahedral lobe can bond with another molecule as shown in Figure 1b. Additionally, there are dipole–induced-dipole van der Waals interaction forces between neighboring oxygen atoms induced by a temporary additional
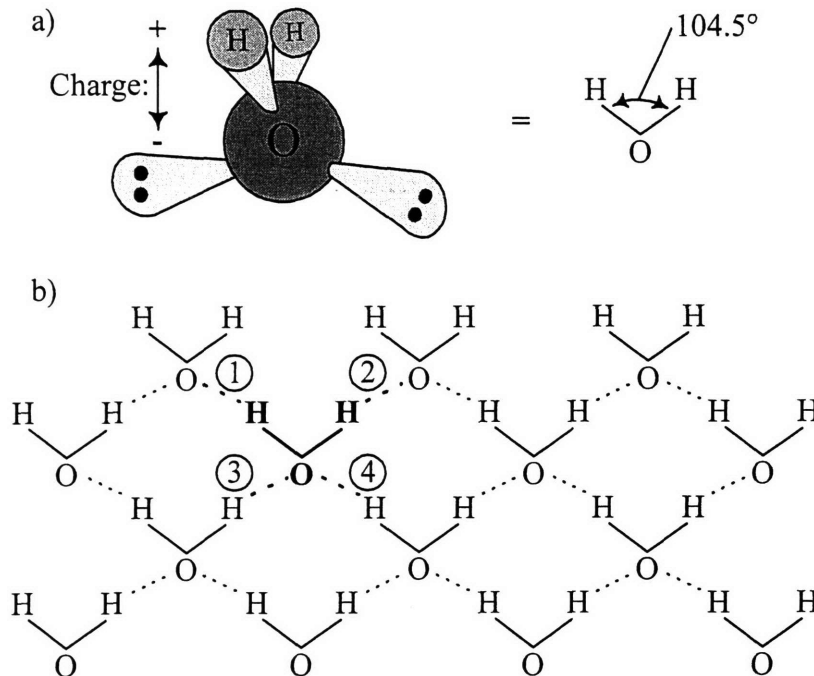
Figure 1. a) Illustration of tetrahedral shape of water shown along with its bond angle and b) a two-dimensional representation of a hydrogen-bonded water network with $<n_{HB}> = 4.0$ (one water molecule is bolded and shown with all 4 HBs).

accumulation of negative charge in one atom and positive in the other, but these are very weak (Campbell, 1987).

     If water did not form such a strong hydrogen-bonded network, then it would behave more like many non-polar compounds with atmospheric boiling temperatures below 100°C. Because water is hydrogen bonded, most water properties are atypical compared to a similarly sized molecule. Water has a rather large specific heat value (ambient: $C_p = 4.18$ J g^{-1} °C^{-1}) partly due to the energy required to break up the hydrogen-bond network, and its large heat of vaporization can be similarly explained since the heat of vaporization is roughly twice as much as that of ethanol (Campbell, 1987). Water is a good solvent for other polar species such as alcohols, and it dissociates into a hydronium (H_3O^+) and hydroxide (OH^-) ion when a shared hydrogen atom shifts to the other water molecule. Ionic molecules (*e.g.*, salts) are also soluble after they are dissociated, *i.e.*, the ions are isolated between water molecules in what is described as the solvent cage effect. This solvation strength is often correlated with the static dielectric constant (ambient: $\varepsilon = 79.3$) and the ion product (ambient: $K_w = [H^+][OH^-] = 10^{-14}$ with pH $= -\log([H^+] = 10^{-7}) = 7$). The dielectric constant of a material represents the change in force between electronic

charges when that material is and is not present and is dependent on polarization and dipole moments of that material (Levine, 1988). The ion product characterizes the degree of dissociation and contributes to the overall solubility product constant which determines solubility. There are many other water properties that are affected by hydrogen bonding, *e.g.*, surface tension, but the focus will now be shifted to temperature, pressure, and density effects and the resulting property changes in water.

When water is heated, the energy of the system increases, the hydrogen-bond network is disrupted, and the density decreases. At the boiling temperature (100°C at 1 bar), liquid water vaporizes, and the density drops to $\sim 5 \times 10^{-4}$ g/cm^3.

When water is heated and pressurized above its critical point ($T \geq T_c = 314.1$°C and $P \geq P_c = 220.9$ bar where $\rho_c = 0.326$ g/cm^3), the hydrogen bond network is further destabilized as documented in Table 1, and the water solvation strength decreases. At these elevated temperatures and pressures, water is supercritical, a term used to describe the fluid when there is no longer a distinction between liquid and vapor and any further pressure increase can never compress the fluid into a liquid state. A generic *PT* diagram of a pure material illustrating locations of the liquid, solid, vapor, and supercritical regions is contained in Figure 2, while critical parameters of several materials are listed in Table 2.

Other thermodynamic and transport properties also change when water becomes supercritical, and property changes are more easily understood if compared along a supercritical isobar. The density of water at 250 bar is shown as a function of temperature in Figure 3 through Figure 10 along with enthalpy, entropy, heat capacity, ion product, speed of sound, static dielectric constant, thermal conductivity, and viscosity in order to illustrate these dramatic changes (Bandura and Lvov, 2000; Marshall and Franck, 1981; NIST, 1996). In addition to the order of magnitude changes shown, some properties exhibit critical-point anomalies which either approach zero or infinity. For example, the heat capacity at constant pressure approaches infinity and the speed of sound approaches zero at the critical point (Bejan, 1988). It is worth noting that critical phenomena effects are visible in Figure 5 and Figure 7 even though 250 bars is 13% higher than the critical pressure (note that in this case the anomaly occurs at 385°C, the pseudo-critical temperature where $(\partial^2 T/\partial V^2)_P = 0$).

Table 1. Representative hydrogen-bonding levels for pure water

State	T (°C)	ρ (g/cm³)	P (bar)	$<n_{HB}>$ [a]	Source
Ice	0	0.92	1	4.0	Kalinichev and Bass, 1997
Ambient	25	1.00	1	3.2	Kalinichev and Bass, 1997
Near critical	374	0.45	226	0.5	Walrafen et al., 1999
Supercritical	400	0.20	264	0.4	Ikushima et al., 1998
Supercritical	500	0.08	229	0.3	Ikushima et al., 1998
Steam	>500	0.001	<<1	~0	Hoffmann and Conradi, 1997

[a] $<n_{HB}> \equiv$ average number of hydrogen bonds per molecule

Table 2. Critical parameters for several materials

Material	T_c [a] (°C)	P_c [a] (bar)	V_c [a] (m³/kmol)	$Z_c = P_c V_c / R T_c$
Ammonia	132.40	112.775	0.0724	0.2422
Benzene	288.95	48.940	0.2590	0.2710
Carbon dioxide	31.06	73.821	0.0939	0.2741
Ethanol	239.35	80.959	0.1180	0.2240
Ethylene	9.19	50.404	0.1290	0.2770
Methane	−82.62	45.979	0.0990	0.2874
Nitrogen	−146.89	33.980	0.0896	0.2900
Oxygen	−118.57	50.430	0.0734	0.2886
Water	374.14	220.899	0.0559	0.2295

[a] Obtained from Reid et al., 1977; Braker and Mossman, 1980; Walas 1985; Sato et al., 1991.
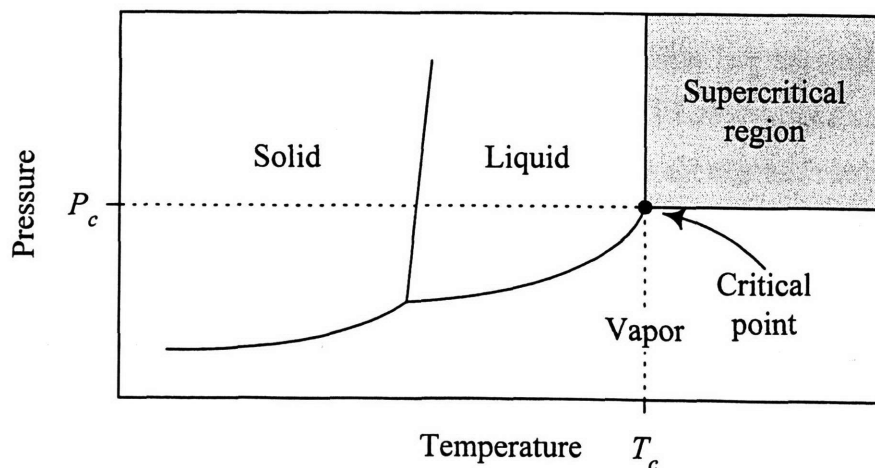
Figure 2. Pressure-temperature PT diagram for a pure material illustrating the location of the critical point and supercritical region.
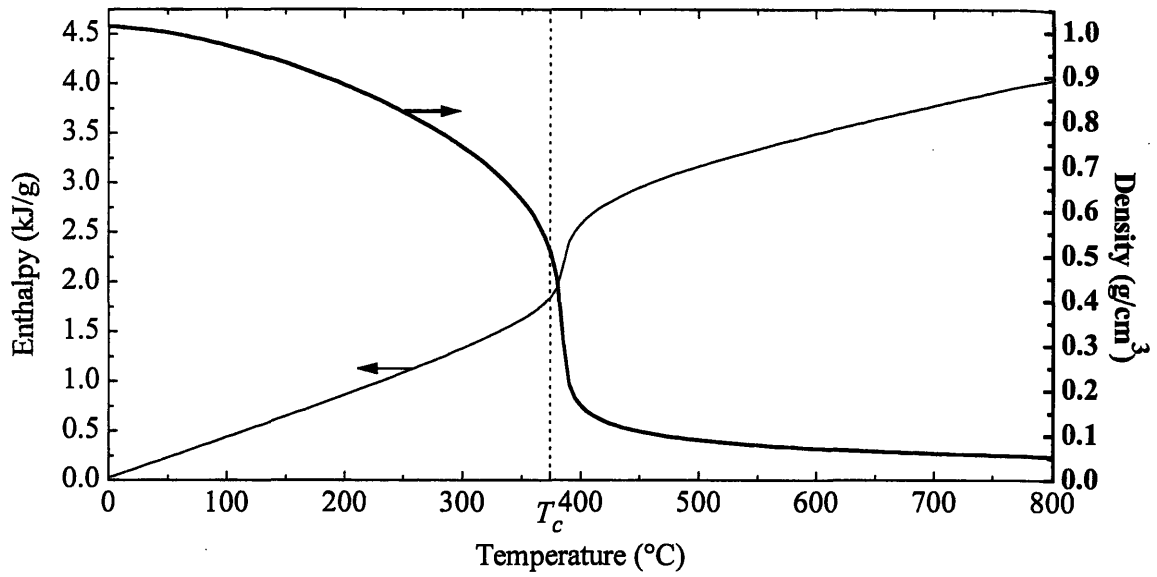
Figure 3. Enthalpy and density comparisons for pure water at P = 250 bar (NIST, 1996).
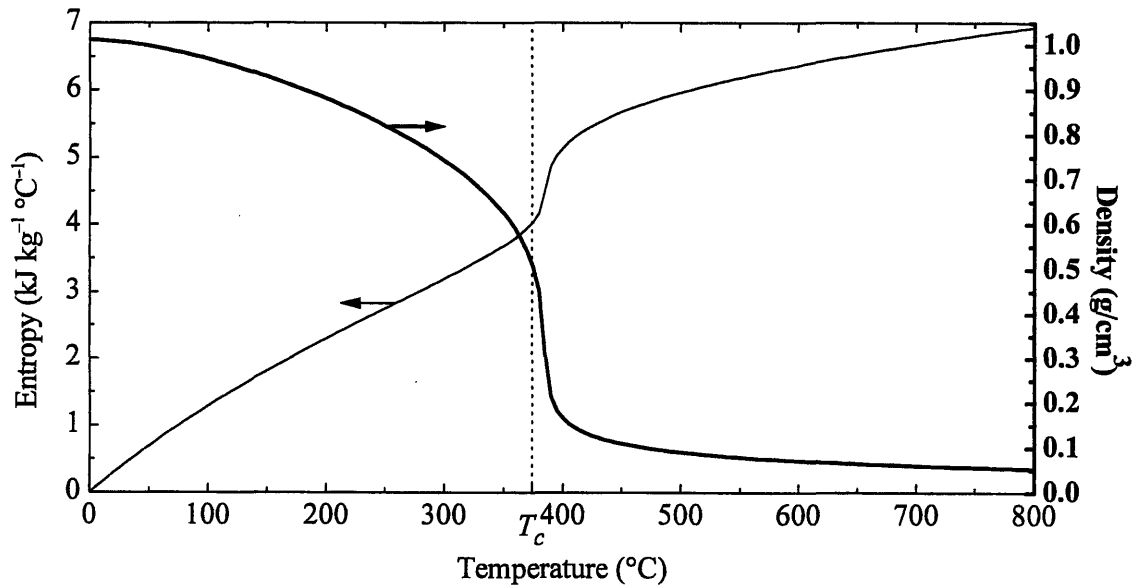
Figure 4. Entropy and density comparisons for pure water at P = 250 bar (NIST, 1996).

41
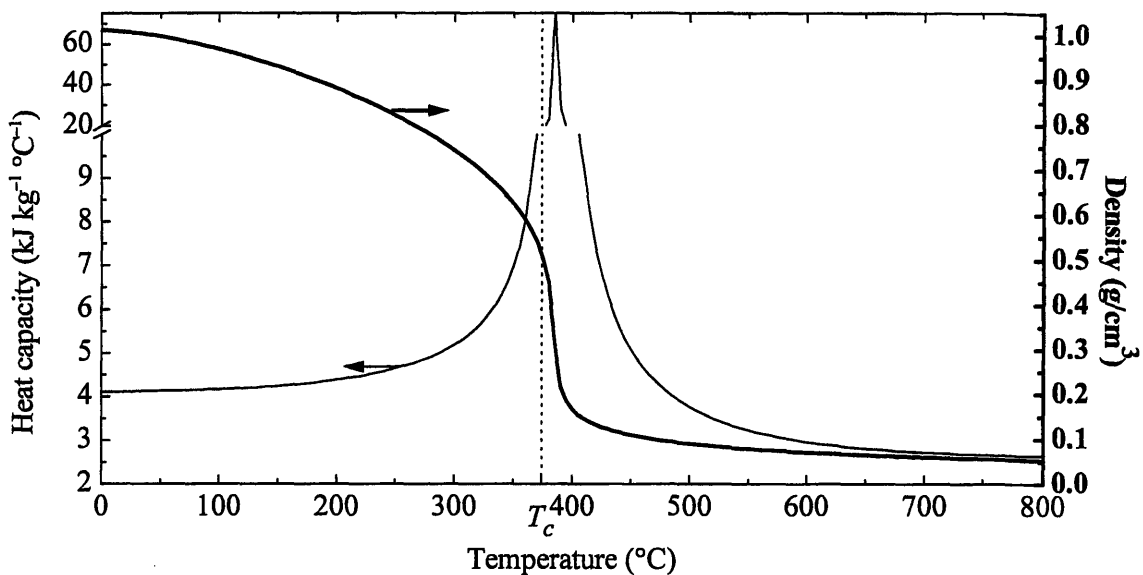
Figure 5. Heat capacity and density comparisons for pure water at $P = 250$ bar (NIST, 1996).
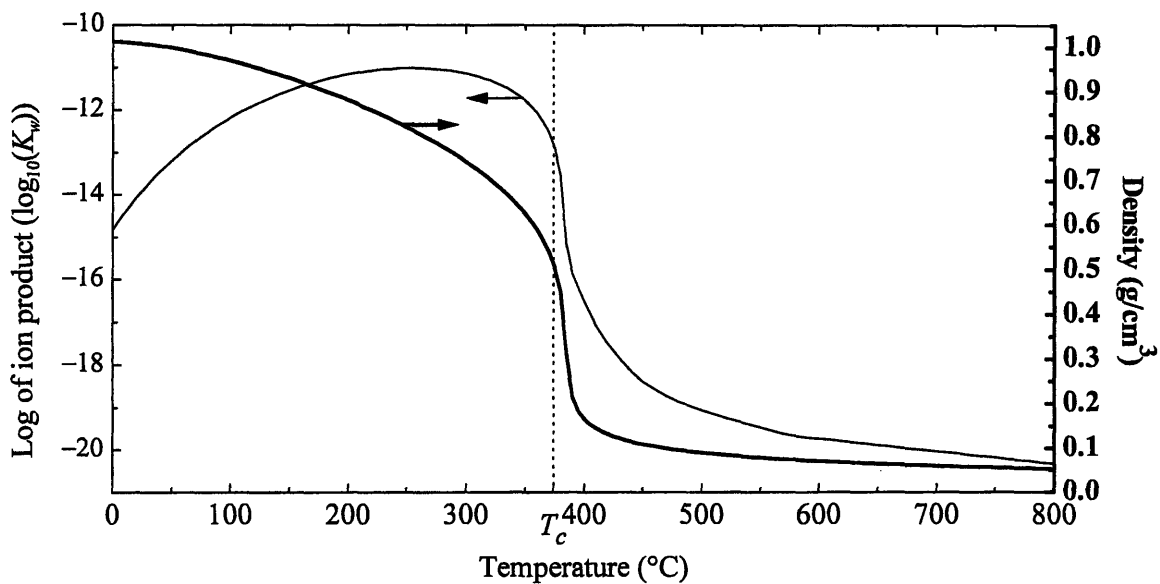
Figure 6. Ion product and density comparisons for pure water at $P = 250$ bar (Bandura and Lvov, 2000 for densities less than 0.4 g/cm^3; Marshall and Franck, 1981 for densities greater than 0.4 g/cm^3; NIST, 1996).
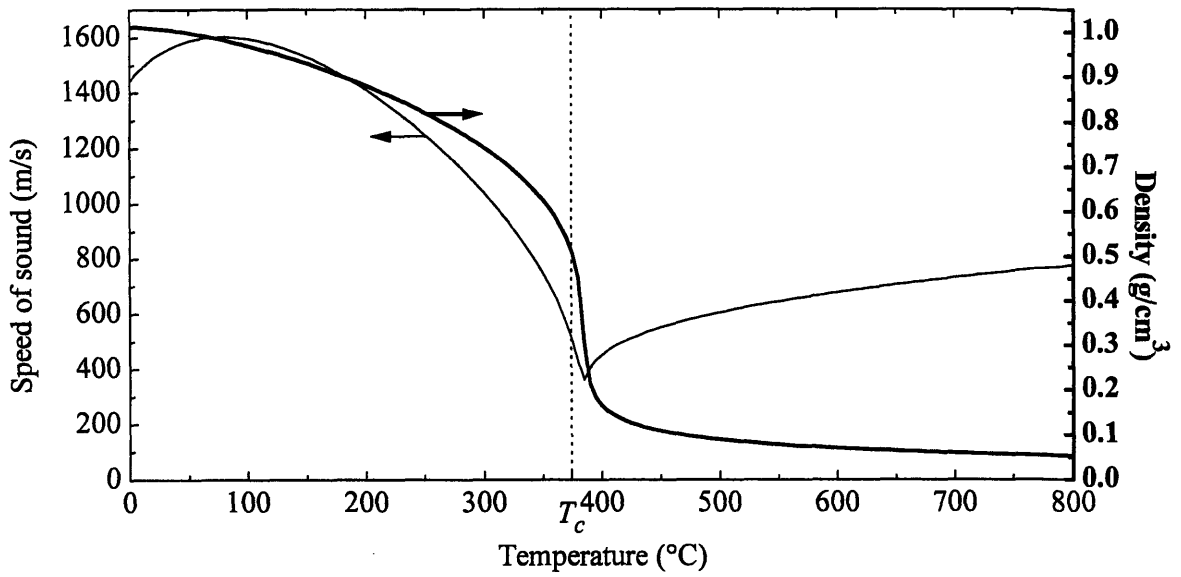
Figure 7. Isentropic speed of sound and density comparisons for pure water at $P = 250$ bar (NIST, 1996).
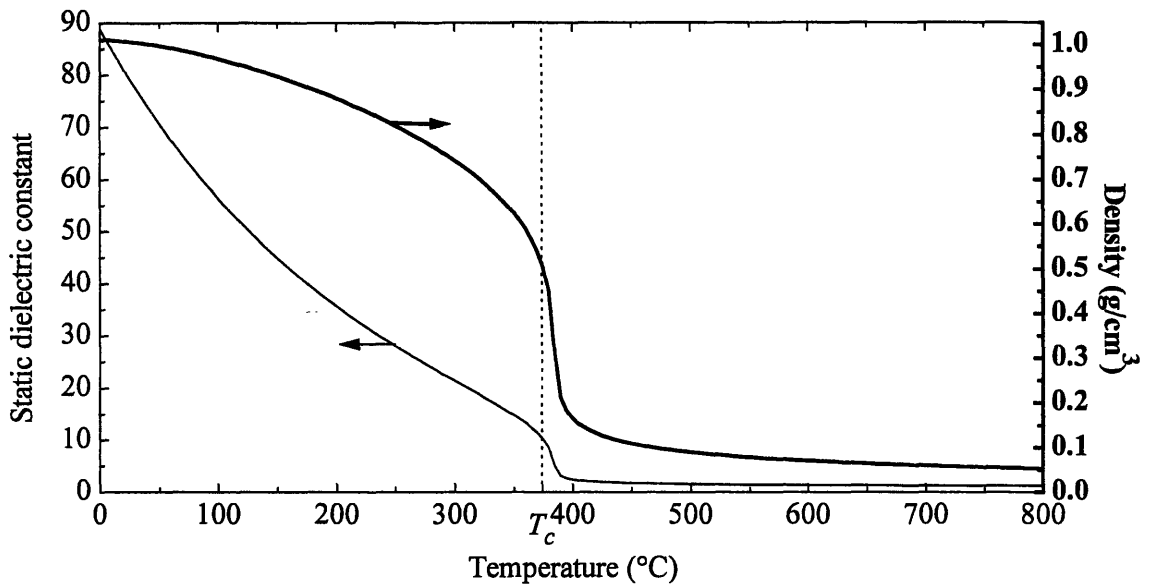
Figure 8. Static dielectric constant and density comparisons for pure water at $P = 250$ bar (NIST, 1996).

43
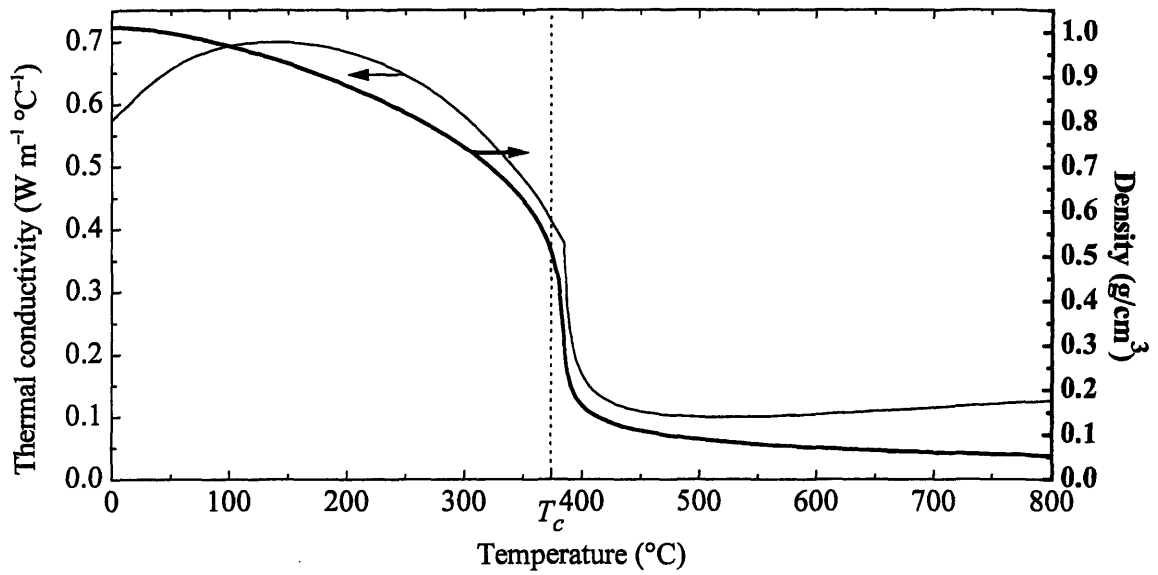
Figure 9. Thermal conductivity and density comparisons for pure water at $P = 250$ bar (NIST, 1996).
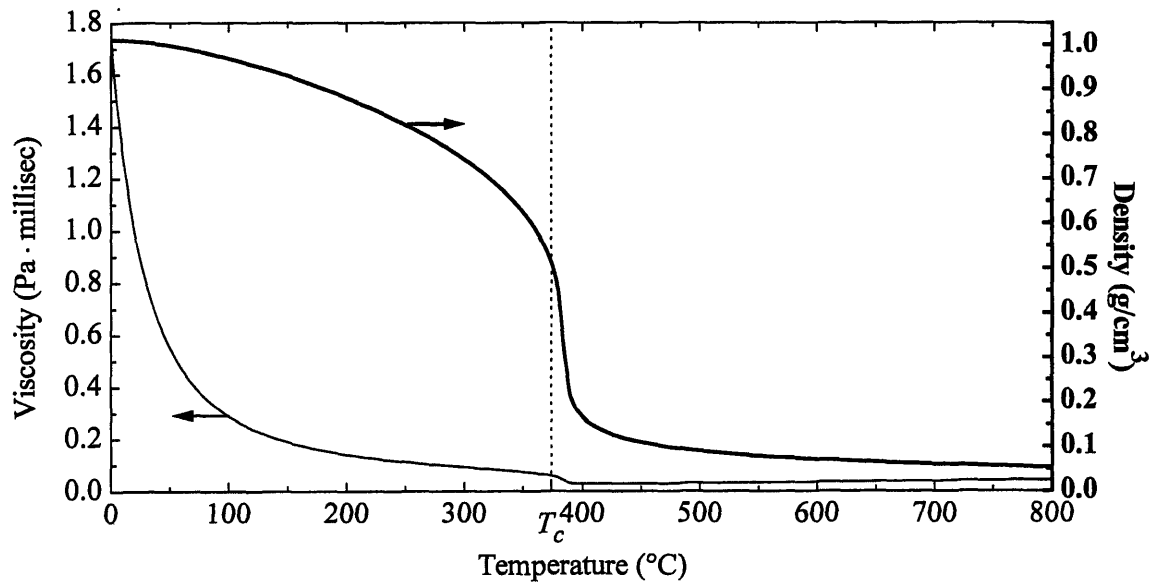
Figure 10. Viscosity and density comparisons for pure water at $P = 250$ bar (NIST, 1996).

Solvation strength is dependent on the ion product and static dielectric constant and decreases significantly at high temperatures above the critical pressure. Thus, supercritical water has the features of a non-polar solvent, *i.e.*, ionic and polar compounds are sparingly or no longer soluble, while non-polar organic compounds and inorganic gases such as carbon dioxide, hydrogen, nitrogen, and oxygen are highly soluble! Sodium sulfate (Na_2SO_4) solubility, for example, is roughly 50 wt.% in ambient liquid water, but it drops to 3 wt.% at 362.8°C and 250 bar (Perry *et al.*, 1984; Hodes, 1998). Benzene is sparingly soluble at ambient conditions (0.18 wt.% = 1800 wppm), yet it is completely miscible above 300°C and 250 bar (DiNaro, 1999; Marrone, 1998).

If an organic compound and an oxidant such as oxygen are combined in supercritical water, then a single homogenous phase will form that is primed for organic oxidation, a process aptly named *Supercritical Water Oxidation (SCWO)*.

1.2 Supercritical Water Oxidation (SCWO)

Supercritical water oxidation (SCWO) is a thermally-based, remediation and waste-treatment process that has emerged as a viable technology for the destruction of aqueous organic wastes in a fully contained system. The SCWO process brings together an oxidant and organic compounds (compounds containing carbon, hydrogen, oxygen, and nitrogen and heteroatoms such as chlorine, phosphorous, and sulfur) in an aqueous environment to achieve complete oxidation, with water, carbon dioxide and molecular nitrogen as the primary products (Modell, 1989; Tester *et al.*, 1993). Heteroatoms form their corresponding mineral acids (HCl, H_2PO_4, and H_2SO_4), but can be neutralized with base, thereby forming salts which can precipitate out of the aqueous SCW phase.

Feed conditions are usually ambient whereas oxidation occurs above the critical point of pure water at moderate temperatures (450°C–650°C) and high pressures (250–300 bar). At these elevated conditions oxygen and organics are completely soluble, and oxidation is essentially complete in less than 60 seconds with destruction efficiencies consistently reaching >99.99%. Detailed review articles are available and contain a wealth of information ranging from chemical reactions (Subramaniam and McHugh, 1986; Savage *et al.*, 1995; Hauthal, 2001; Akiya and Savage, 2002) to salt formation in supercritical fluids and the current state of the SCWO technology (Modell, 1989; Thomason *et al.*, 1990; Barner *et al.*, 1992; Tester *et al.*, 1993; Shaw and Dahmen, 2000; Hodes *et al.*, 2004).

1.2.1 SCWO Applications

As previously stated, one of the most promising applications of the SCWO process is the destruction of organic waste. As it turns out, extraction and chemical synthesis with SCW are not generally considered practible due to the relatively difficult operating conditions and the high energy levels of SCW which are more favorable for oxidation. The phase, type, and concentration of waste are key factors in determining whether the SCWO process is economical and practical. The first waste discussed is hazardous non-military organic waste.

Conventionally, this type of hazardous waste is either disposed in landfills or destroyed in incinerators. Since landfills are no longer abundant, are for the most part more expensive, are subject to tightening regulations, and do not even treat the waste, this disposal technique is not ideal. Although incineration resembles the SCWO process, actually treats the waste, and is for

the most part more economical, it nonetheless has encountered significant public resistance in the United States which haunts current incinerators and hinders new ones from being built. Furthermore, incinerator operational costs are sometimes high since auxiliary fuel may be needed to heat and vaporize the water component (as previously shown, liquid water requires an unusually large energy input to heat and vaporize). On the emissions front, SCWO does not by design release NO_xs and SO_xs, but incineration can. For the last two decades, industrial and academic researchers have studied SCWO as an alternative waste-treatment technology since toxic products are not formed and it destroys waste in a closed system, which the Environmental Protection Agency (EPA) favors. Numerous organic wastes have been destroyed with SCWO, and many are listed in Table 3. Multiple companies have been involved with commercializing SCWO technology and are summarized in Table 4, and several have had operating pilot-plant facilities including MODAR, MODEC, and EcoWaste Technologies, Inc. (Marrone et al., 2004). Companies in Europe, Japan, and the United States are using SCWO for the destruction of municipal sludge and pulp mills wastes and in semiconductor processing (Shaw, 2000 and Marrone et al., 2004).

The United States military has also been involved in SCWO technology development. As required by law, they have searched for alternative treatment technologies for the destruction of their chemical weapons stockpile and have tested SCWO along with other technologies (NRC, 1993). An estimated 30,000 tons require treatment. They are located at eight domestic sites and at one in the Pacific Ocean, as shown in Table 5 (Shaw and Cullinane, 1997). The US stockpile consists of the nerve agents sarin/GB ($C_4H_{10}FO_2P$) and VX ($C_{11}H_{26}NO_2PS$) and H, HD, and HT vesicant mustards ($C_4H_8Cl_2S$, distilled $C_4H_8Cl_2S$, and $C_8H_{16}Cl_2OS_2$). The nerve agents disrupt nerve-cell activity, making muscle response uncontrollable, and lead to death usually by suffocation. In addition, a second inventory for research and testing and a third inventory of recovered munitions and similar non-stockpile items amount to approximately 10 tons and are stored at an estimated 65 sites.

Testing has shown that SCWO is capable of destroying chemical weapon agent (Downey et al., 1995; Sprizter et al., 1995; Snow et al., 1996) along with other military waste including energetics, propellants (Buelow, 1990; Buelow, 1992, Harradine et al., 1993; Spritzer et al., 1995), smokes, and dyes (Robinson, 1992; Rice et al., 1994; LaJeunesse and Rice, 1997). As a result, contracts were awarded to build SCWO units at Newport, Indiana (General

Table 3. Hazardous organic waste treated with SCWO

Waste treated with SCWO	Reference
Bacteria	Thomason et al., 1990
Biopharmaceutical waste	Johnston et al., 1988
Contaminated sludge	Shanableh, 1995
Dioxins	Thomason et al., 1990;
	Thomason and Modell, 1984
Flame retardant tetrabromobisphenol	Hirth et al., 1998
Hexachlorobenzene	Hirth et al., 1998
γ-Hexachlorobenzene	Hirth et al., 1998
Human waste	Hong et al., 1987;
	Hong et al., 1988
Manned-space-mission waste	Takahashi et al., 1988
Mixed sludge (bleach plant effluent, pond sludge, and primary clarifier sludge)	Cooper et al., 1997
Municipal sludge	Shanableh and Gloyna, 1991;
	Tongdhamachart and Gloyna, 1991;
	Goto et al., 1997
Perchlorinated dibenzofurans in fly ash	Sako et al., 1997
Perchlorinated dibenzo-p-dioxines in fly ash	Sako et al., 1997
Pesticide DDT	Modell et al., 1992
Pharmaceutical waste	Johnston et al., 1988
Polychlorinated biphenyls (PCBs)	Staszak et al., 1987
Polyvinyl chloride (PVC)	Hirth et al., 1998
Process waste water	Li et al., 1993;
	Sawicki and Casas, 1993
Pulp and paper industry sludge	Modell, 1990;
	Modell et al., 1992;
	Modell et al., 1995
Urea	Timberlake et al., 1982

Table 4. Companies involved in SCWO commercialization (Marrone *et al.*, 2004)

Company	Years of operation
MODAR, Inc. (now part of General Atomics)	1980–1996
MODEC (Modell Environmental Corp.)	1986–~1990
Oxidyne	1986–1991
EcoWaste Technologies, Inc. (now part of Chematur Engineering)	1990–1999
Abitibi-Price, Inc. (sold technology to Connor Pacific Environmental Technologies)	1991–1997
General Atomics	1991–Present
Foster Wheeler Development Corp.	1993–Present
SRI International	1993–Present
KemShredder, Ltd. (now part of HydroProcessing)	1993–1996
Chematur Engineering AB	1995–Present
HydroProcessing, L.L.C.	1996–Present

Table 5. Location of US chemical weapons stockpiles

Location
Johnston Atoll in the Pacific Ocean
Edgewood, Maryland
Anniston, Alabama
Blue Grass, Kentucky
Newport, Indiana
Pine Bluff, Arkansas
Pueblo, Colorado
Tooele, Utah
Umatilla, Oregon

Atomics), Pine Bluff, Arkansas (Foster Wheeler Development Corporation) (Haroldsen *et al.*, 1996a; Haroldsen *et al.*, 1996b), Blue Grass, Kentucky (G.E. Parsons with the subcontractor General Atomics) and on US Navy ships (General Atomics) (Kirts, 1995; Elliot *et al.*, 2000; and Parsons, 2003). The Newport, Indiana contract has since been canceled. The US Air Force is also using SCWO to destroy aircraft maintenance wastes, and the US Department of Energy is using SCWO to treat radioactive waste and explosives (Shaw, 2000). Other technologies being evaluated or used at other chemical-weapons-stockpile locations include hydrolysis followed by bioremediation (Pueblo, Colorado) and incineration.

SCWO treatment of other wastes is limited by the waste type and economic constraints, although SCWO treatment is ideal for aqueous solutions containing 1 to 20 wt.% organic waste (Thomason and Modell, 1984; Modell, 1989; Modell *et al.*, 1995). Bioremediation and activated carbon techniques are better suited for less than 1 wt.% solutions, but also have limitations. In the case of bioremediation, any change in waste composition may kill the bacteria, stopping the treatment process. Solutions with greater than 20 wt.% waste are better treated with conventional incineration. Solids can be treated as long as they can be dissolved, so pretreatment and dilution is usually necessary. Other supercritical fluids besides water are impractical to use since they are not environmentally benign solvents, are expensive, or are not good solvents.

1.2.2 SCWO Process Description

SCWO processing occurs above the critical point of pure water at moderate temperatures (450°C–600°C) and high pressures (between 250 and 300 bar). As shown in two simple process flow diagrams (Figure 11 and Figure 12), several feed streams are used to introduce water, an oxidant (oxygen, air, or hydrogen peroxide), waste, and if applicable, a basic solution for acidic product neutralization. Each stream is pressurized to the SCWO process pressure. At a specific location, the streams are combined either before preheating, during preheating, or inside the SCWO reaction chamber depending on the vendor and system. The preheated, mixed stream, which is usually a single phase, is further heated to the final operating temperature in the SCWO reactor. The typical residence time is under 60 seconds, a sufficient time for nearly complete oxidation. If any salts are present, customized techniques are used to isolate or re-dissolve the salt products (Hodes *et al.*, 2004). With the oxidation complete, the effluent is cooled using standard heat-recovery techniques and then is depressurized, resulting in gas and liquid streams.
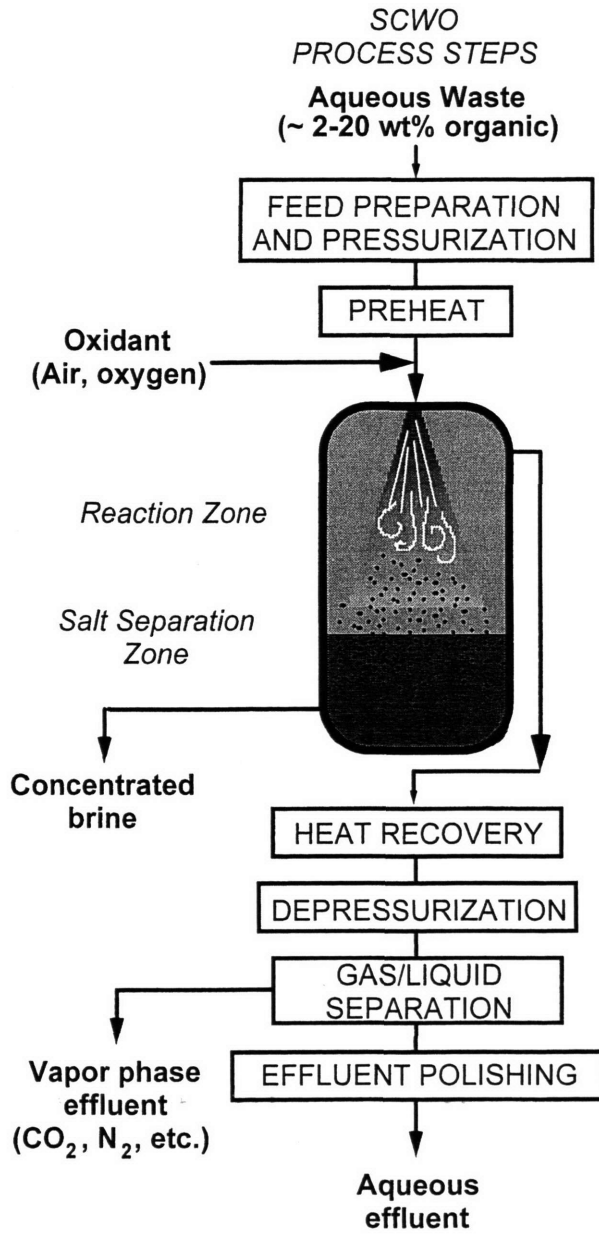
Figure 11. Generic schematic of the SCWO process.
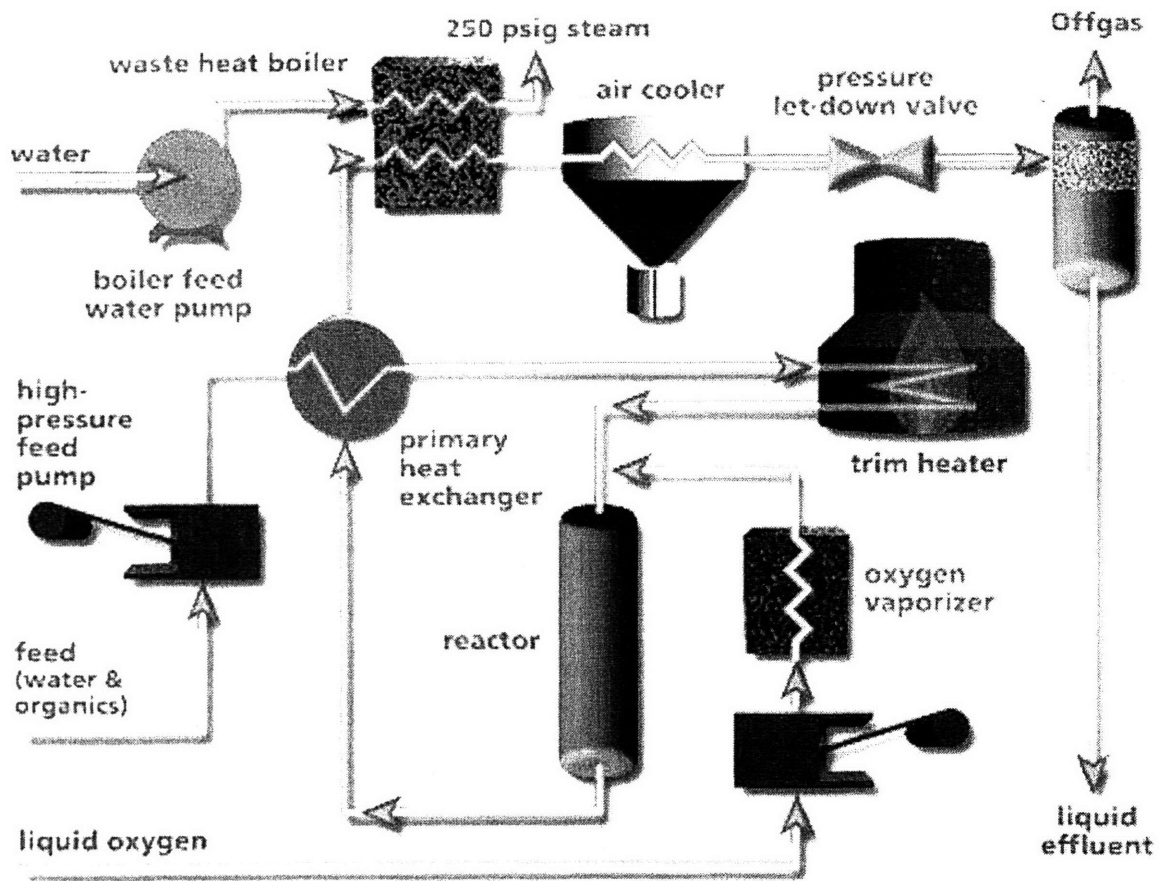
Figure 12. Simplified process flow diagram of Eco Waste Technology SCWO process (Eco Waste Technology, 1999).

The liquid stream may be further processed or polished to remove any solids, salts, or byproducts while gases are released after any required separation or treatment.

The components used in the SCWO apparatus must be able to tolerate long-term exposure to the chemicals, high pressure, and moderate temperature. Nickel alloys such as Hastelloy C276 and Inconel 625 are often used since they have high tensile strengths which are capable of withstanding these conditions. These alloys are also used because they have been found to have good corrosion resistance (Downey et al., 1995). Platinum-lined surfaces have also been employed and show improvement over alloy surfaces when exposed to some SCWO wastes (Downey et al., 1995).

Corrosion, salt fouling, and erosion are the three major technical challenges still facing SCWO system designers and limit the commercial acceptance and widespread use of SCWO technology. Supercritical water is corrosive and some aqueous species are extremely aggressive (e.g., chlorides). System failures have occurred due to corrosion-weakened pressure-bearing walls. The reader is referred to J. Cline's MIT Ph.D. dissertation for more information about corrosion in SCWO systems (Cline, 2000).

Salt fouling is another serious SCWO issue (Armellini, 1993; Dipippo, 1998; Hodes, 1998; Hodes et al., 2004). In extreme cases, tubes or the reactor will plug, disable the reactor, and force a system shutdown until the salt is redissolved in water or the salt can be physically removed with mechanical force. Even partial salt restriction can force a shutdown since there will be pressure and flow disruptions. On the other hand, salt nucleation and precipitation could be used as an advantage if salt is to be deliberately isolated and collected in a SCWO system. This design feature was incorporated into the MODAR system with some success, but their system design has since been shelved by General Atomics, the new owners of MODAR.

Erosion is another issue that has often been dismissed or neglected. It is not uncommon to have solid particles suspended, or even generated, in feed and product streams and the reactor. Erosion is of greatest concern if there are large pressure drops where particle velocity is dramatically increased and particles can collide with surfaces and wear away surfaces. Valves and pressure relief devices bear the burden and, as a result, have experienced severely shortened service lives. Due to all of these technical challenges, scale-up of bench-scale systems to pilot and full-sized plant is difficult and requires alternative approaches in order to control erosion (Barner et al., 1992; Lee, 1997).

1.3 SCWO Research

Laboratory research is currently being conducted in order to increase the level of understanding of key SCWO areas including reaction kinetics, corrosion, and salt-related phenomena. Past MIT research includes work by R. Helling (1986), P. Webley (1990), R. Holgate (1993), J. Meyers (1993), F. Armellini (1993), R. Lachance (1995), M. Dipippo (1998), M. Hodes (1998), P. Marrone (1998), B. Phenix (1998), J. DiNaro (1999), J. Cline (2000), Y. Kubo (2000), M. Reagan (2000), J. Taylor (2001), and P. Sullivan (2002). Other institutions have SCWO research programs including the Los Alamos National Laboratory, Sandia National Laboratory, Rutgers University (M. Klein was previously at the University of Delaware), University of Illinois, University of Michigan, University of Texas at Austin, and Western Michigan University (Tester *et al.*, 1993; Savage *et al.*, 1995; Shaw and Dahmen, 2000, Akiya and Savage, 2002). Research usually includes experimental work along with predictions and modeling of laboratory results. This modeling effort, whether it is for reaction kinetics or salt-related phenomena, requires knowledge of supercritical-water or supercritical-water mixture properties. These values can be categorized into thermodynamic and transport properties.

1.3.1 Key Thermodynamic Properties

Thermodynamic properties are usually calculated with empirical or semi-empirical models called equations of state (EOSs) or with statistical-mechanics techniques based on rigorous theoretical principles which often account for intermolecular interactions. Both models have parameters that are regressed directly to experimental data. The predictions usually needed for SCWO modeling are density, enthalpy, heat capacity, and fugacities for vapor-liquid equilibrium. As will be discussed in detail in a forthcoming chapter, some EOSs are very accurate for predicting pure component properties, though they cannot be used for all SCWO mixture modeling. Others can be used for mixtures, but have other deficiencies. Most often, liquid-density predictions are poor, yet density is a key property in SCWO modeling. Without accurate properties, process simulations will inaccurately model key components in a SCWO system, *e.g.*, reactors and heat exchangers. Accurate equations of state are needed.

1.3.2 Key Transport Properties

Transport properties are also predicted by using empirical or semi-empirical models. Whether they are correlations strictly based on experimental data or are partially based on

fundamental thermodynamic or transport theory, both types have parameters which are regressed directly to experimental data. The transport properties used in SCWO modeling are viscosity, thermal conductivity, and molecular diffusivity. Transport modeling typically covers a wide range of topics including heat transfer, temperature profiles, salt deposition, corrosion, fluid-dynamics simulation, species diffusion and overall SCWO process and equipment simulations. Pure water properties are available for all three transport properties at typical SCWO conditions, yet binary diffusivity data are scarce. Although most SCWO reactors are designed to avoid mass-transfer limitations, they nonetheless can occur. For this reason, molecular-diffusivity data are valued and needed. At SCWO conditions, the ratio between pure water self-diffusivities and aqueous-salt binary diffusivities ranges from a factor of 5 to 50 (Lamb *et al.*, 1981; Butenhoff *et al.*, 1996)! Self-diffusivity values are not necessarily accurate for binary predictions.

To further complicate matters, transport correlations are developed on the basis of either data for pure water at SCWO conditions or on binary data at non-SCWO conditions. These two approaches circumvent the ideal scenario which is to measure and develop correlations based on data collected at SCWO process conditions (mixtures at moderate temperatures and high pressures). As it turns out, collecting such data is difficult, although several have tried with limited success and questionable accuracy (Lamb *et al.*, 1981; Butenhoff *et al.*, 1996). Accurate binary diffusivity data and models are needed.

Nuclear magnetic resonance (NMR) is one technique that has been used to measure molecular diffusivities at SCWO operating conditions and will be discussed shortly (Lamb *et al.*, 1981).

1.4 References

Armellini, F.J. (1993) "Phase equilibria and precipitation phenomena of sodium chloride and sodium sulfate in sub- and supercritical water." MIT Dept. of Chem. Eng., Doctoral dissertation, Cambridge, MA.

Akiya, N. and Savage, P.E. (2002) "Roles of water for chemical reactions in high-temperature water." *Chem. Rev.*, **102**, 2725–2750.

Bandura, A.V. and Lvov, S.N. (2000) "The ionization constants of water over a wide range of temperatures and densities." Steam, water, and hydrothermal systems: Physics and chemistry meeting the needs of industry, Procs. 13th Int. Conf. Props. Water Steam, NRC Press, Ed. by P.R. Tremaine, P.G. Hill, D.E. Irish, P.V. Balakrishnan, Ottawa, Canada.

Barner, H.E., Huang, C.Y., Johnson, T., Jacobs, G., Martch, M.A. and Killilea, W.R. (1992) "Supercritical water oxidation: an emerging technology." *J. Haz. Mats.*, **31 (1)**, 17.

Bejan, A. (1988) *Advanced Engineering Thermodynamics*, John Wiley & Sons, Inc., New York, NY.

Braker, W. and Mossman, A.L. (1980) *Matheson Gas Data Book*, 6th ed., Lyndurst, NJ.

Buelow, S.J. (1990) "Destruction of propellant components in supercritical water." Los Alamos National Laboratory, LA-UR-90-1338, Los Alamos, NM.

Buelow, S.J. (1992) "Chemical reactions of nitrogen containing compounds in supercritical water." *Proc. Work. Fed. Prog. Involving Supercritical Water Oxid.*, July 6–7, Gaithersburg, MD, 7.

Butenhoff, T.J., Goemans, M.G.E. and Buelow, S.J. (1996) "Mass diffusion coefficients and thermal diffusivity in concentrated hydrothermal $NaNO_3$." *J. Phys. Chem.*, **100**, 5982–5992.

Campbell, N.A. (1987) *Biology*, Benjamin/Cummings, Reading, MA.

Chang, R. (1988) *Chemistry*, Random House, 3rd ed., New York, NY.

Cline, J.A. (2000) "Experimental and ab initio investigations into the fundamentals of corrosion, in the context of supercritical water oxidation systems." MIT Dept. of Chem. Eng., Doctoral dissertation, Cambridge, MA.

Cooper, S.P., Folster, H.G., Gairns, S.A. and Hauptmann, E.G. (1997) "Treatment of lagoon sludge, primary clarifier sludge, and bleach plant effluent by superciritical water oxidation." *Pulp Pap. Can.*, **98 (10)**, 37–41.

DiNaro, J.L. (1999) "Oxidation of benzene in supercritical water: experimental measurements and development of an elementary reaction mechanism." MIT Dept. of Chem. Eng., Doctoral dissertation, Cambridge, MA.

Dipippo, M.M. (1998) "Phase behavior of inorganic salts in sub- and supercritical water." MIT Dept. of Chem. Eng., Doctoral dissertation, Cambridge, MA.

Downey, K.W., Snow, R.H., Hazlebeck, D.A. and Roberts, A.J. (1995) "Corrosion and chemical agent destruction. Research on supercritical water oxidation of hazardous military wastes." *ACS Symp. Ser., No. 608*, **30 (5)**, 313.

Eco Waste Technologies (1999) http://www.jump.net/~ewt, Austin, TX.

Elliott, J.P., Hazlebeck, D.A., Ordway, D.W., Roberts, A.J., Spritzer, M.H., Hurley, J.A., and Rising S.A. (2000) "Update on hydrothermal oxidation developments on DARPA/ONR and Air Force projects at General Atomics." *Proceedings of the International Conference on Incineration and Thermal Treatment Technologies*, Portland, OR, 25.

Goto, M., Nada, T., Kawajiri, S., Kodama, A. and Hirose, T. (1997) "Decomposition of municipal sludge by supercritical water oxidation." *J. Chem. Eng. Jpn.*, **30 (5)**, 813–818.

Haroldsen, B.L., Ariizumi, D.Y., Mills, B.E., Brown, B.G. and Greisen, D. (1996a) "Transpiring wall supercritical water oxidation reactor salt deposition studies." Sandia National Laboratories, SAND96-8213 UC-702, Livermore, CA.

Haroldsen, B.L., Ariizumi, D.Y., Mills, B.E., Brown, B.G. and Rousar, D.C. (1996b) "Transpiring wall supercritical water oxidation reactor test reactor design report." Sandia National Laboratories, SAND96-8213 UC-402, Livermore, CA.

Harradine, D.M., Buelow, S.J., Dell'Orco, P.C., Dyer, R.B., Foy, B.R., Robinson, J.M., Sanchez, J.A., Sportarelli, T. and Wander, J.D. (1993) "Oxidation chemistry of energetic materials in supercritical water." *Haz. Waste Haz. Mats.*, **10**, 233.

Hauthal, W.H. (2001) "Advances with supercritical fluids [review]." *Chemosphere*, **43**, 123–135.

Helling, R.K. (1986) "Oxidation kinetics of simple compounds in supercritical water: carbon monoxide, ammonia and ethanol." MIT Dept. of Chem. Eng., Doctoral dissertation, Cambridge, MA.

Hirth, T., Heck, L., Jahnke, S., Michelfelder, B. and Schweppe, R. (1998) "Supercritical water oxidation-waste destruction and synthesis." *Koatsuryoku no Kagaku to Gijutsu*, Procs.Int. Conf.-AIRAPT-16 and HPCJ-38 on High Pres. Sci. Tech., 1997, **7**, 1375.

Hodes, M.S. (1998) "Measurement and modeling of deposition rates from near-supercritical, aqueous, sodium sulfate and potassium sulfate solutions to a heated cylinder." MIT Dept. of Mech. Eng., Doctoral dissertation, Cambridge, MA.

Hodes, M., Marrone, P.A., Hong, G.T., Smith, K.A., and Tester, J.W. (2004) "Salt precipitation and scale control in supercritical water oxidation-part a: fundamentals and research." *J. Supercritical Fluids*, **29 (3)**, 265–288.

Hoffman, M.M. and Conradi, M.S. (1997) "Are there hydrogen bonds in supercritical water?." *J. Am. Chem. Soc.*, **119**, 3811–3817.

Holgate, H.R. (1993) "Oxidation chemistry and kinetics in supercritical water : hydrogen, carbon monoxide, and glucose." MIT Dept. of Chem. Eng., Doctoral dissertation, Cambridge, MA.

Hong, G.T., Fowler, P.K., Killilea, W.R. and Swallow, K.C. (1987) "Supercritical water oxidation: treatment of human waste and system configuration tradeoff study." *Procs. 17th Intersoc. Conf. Environ. Sys.*, July 13-15, Seattle, WA.

Hong, G.T., Killilea, W.R. and Thomason, T.B. (1988) "Supercritical water oxidation: space applications." *Procs.ASCE Space*, August 29-31, Albuquerque, NM.

Ikushima, Y., Hatakeda, K., Saito, N. and Arai, M. (1998) "An in-situ Raman spectroscopy study of subcritical and supercritical water: the peculiarity of hydrogen bonding near the critical point." *J. Chem. Phys.*, **108 (14)**, 5855–5860.

Johnston, J.B., Hannah, R.E., Cunningham,V.L., Daggy, B.P., Sturm, F.J. and Kelley, R.M. (1988) "Destruction of pharmaceutical and biopharmaceutical wastes by the MODAR supercritical water oxidation process." *Biotechnology*, **6 (12)**, 1423–1427.

Kalinichev, A.G. and Bass, J.D. (1997) "Hydrogen bonding in supercritical water. 2. computer simulations." *J. Phys. Chem. A*, **101**, 9720–9727.

Kirts, R.E. (1995) "Destruction of navy hazardous wastes by supercritical water oxidation." *Procs. Ann. Meeting-Air Waste Management Assoc.*, **9**.

Kubo, Y. (2000) "Molecular dynamics and self-diffusion in supercritical water." MIT Dept. of Chem. Eng., Masters dissertation, Cambridge, MA.

Lachance, R.S. (1995) "Oxidation and hydrolysis reactions in supercritical water: chlorinated hydrocarbons and organosulfur compounds." MIT Dept. of Chem. Eng., Masters dissertation, Cambridge, MA.

LaJeunesse, C.A. and Rice, S.F. (1997) "Case study on the destruction of organic dyes in supercritical water." *Chem. Oxid.*, **5**, 13.

Lamb, W.J., Hoffman, G.A. and Jonas, J. (1981) "Self-diffusion in compressed supercritical water." *J. Chem. Phys.*, **74 (12)**, 6875–6880.

Lee, A. (1997) "Effect of shape and orientation on the performance of supercritical water oxidation reactors." *ASME Procs. 32nd Nat. Heat Trans. Conf.*, **12**, 99–106.

Levine, I.N. (1988) *Physical Chemistry*, McGraw-Hill, 3rd ed., New York, NY.

Li, L., Gloyna, E.F. and Sawicki, J.E. (1993) "Treatability of DNT process wastewater by supercritical water oxidation." *Water Environ. Res.*, **65**, 250.

Marrone, P.A. (1998) "Hydrolysis and oxidation of model organic compounds in sub- and supercritical water : reactor design, kinetics, measurements, and modeling." MIT Dept. of Chem. Eng., Doctoral dissertation, Cambridge, MA.

Marrone, P.A., Hodes, M., Smith, K.A., and Tester, J.W. (2004) "Salt precipitation and scale control in supercritical water oxidation-part b: commercial/full-scale applications." *J. Supercritical Fluids.*, **29** (3), 289–312.

Marshall, W.L. and Franck, E.U. (1981) "Ion product of water substance, 0-1,000°C, 1-10,000 bars. New international formulation and its background." *J. Phys. Chem. Ref. Data*, **10** (2), 295.

Meyers, J.C. (1993) "Oxidation chemistry and kinetics of model compounds in supercritical water : glucose, acetic acid, and methylene chloride." MIT Dept. of Chem. Eng., Doctoral dissertation, Cambridge, MA.

Modell, M. (1989) "Supercritical water oxidation." *Standard Handbook of Hazardous Waste Treatment and Disposal*, McGraw-Hill, New York, NY.

Modell, M. (1990) "Treatment of pulp mill sludges by supercritical water oxidation." DOE Contract No. FG05-90CE40914.

Modell, M., Larson, J. and Sobczynski, S.F. (1992) "Supercritical water oxidation of pulp mill sludges." *Tappi J.*, **75** (6), 195–202.

Modell, M., Mayr, S. and Kemna, A. (1995) "Supercritical water oxidation of aqueous wastes." *Proc. 56th Ann. Int. Water Conf.*, October 31, Pittsburgh, PA, 478.

NIST (1996) NIST standard reference database 10–steam tables, Boulder, CO.

NRC (1993) "Alternative technologies for the destruction of chemical agents and munitions." National Research Council, Washington, DC.

Parsons (2003) "Bechtel/Parsons joint venture selected for multibillion dollar blue grass contract." http://www.parsons.com/about/press_rm/projects/pr0306b.asp, Pasadena, CA.

Perry, R.H., Green, D.W. and Maloney, J.O. (1984) *Perry's chemical engineering handbook*, McGraw-Hill, 6th ed., New York, NY.

Phenix, B.D. (1998) "Hydrothermal oxidation of simple organic compounds." MIT Dept. of Chem. Eng., Doctoral dissertation, Cambridge, MA.

Reagan, M.T. (2000) "Multiscale molecular modeling of aqueous systems from ambient to supercritical conditions." MIT Dept. of Chem. Eng., Doctoral dissertation, Cambridge, MA.

Reid, R., Prausnitz, J.M. and Sherwood, T.K. (1977) *The Properties of Gases and Liquids*, McGraw-Hill, 3rd ed., New York, NY.

Rice, S.F., LaJeunesse, C.A., Hanush, R.G., Aiken, J.D. and Johnston, S.C. (1994) "Supercritical water oxidation of colored smoke, dye, and pyrotechnic compositions." Sandia National Laboratory, SAND-94-8209, Livermore, CA.

Robinson, C. (1992) "Demilitarization R&D technology for conventional munitions via SCWO of colored smokes, dyes, and pyrotechnics." *Proc. Work. Fed. Prog. Involving Supercritical Water Oxid.*, July 6–7, Gaithersburg, MD, 160.

Sako T., Sugeta T., Otake K., Sato M., Tsugumi M., Hiaki T. and Hongo M. (1997) "Decomposition of dioxins in fly ash with supercritical water oxidation." *J.Chem. Eng. Jpn.*, **30 (4)**, 744–747.

Sato, H., Watanabe, K., Levelt-Sengers, J.M.H., Gallagher, J.S., Hill, P.G., Straub, J. and Wagner, W. (1991) "Sixteen thousand evaluated experimental thermodynamic property data for water and steam." *J. Phy. Chem. Ref. Data*, **20**, 1023–1044.

Savage, P.E., Gopalan, S., Mizan, T.I., Martino, C.J. and Brock, E.E. (1995) "Reactions at supercritical conditions: applications and fundamentals." *AIChE J.*, **41 (7)**, 1723–1778.

Sawicki, J.E. and Casas, B. (1993) "Wet oxidation systems-process concept to design." *Environ. Prog.*, **12**, 275.

Shanableh, A. (1995) "Destruction of sludge in supercritical water." *Water*, **22 (3)**, 16.

Shanableh, A. and Gloyna, E.F. (1991) "Supercritical water oxidation-wastewater and sludges." *Water Sci. Tech.*, **23**, 389.

Shaw, R.W. (2000) "New technologies for chemical weapons demilitarization: tools for reactor design and operation." *Symp. Destruction Chemical Weapons-Technologies and Practical Aspects*, July 30-August 3, Munster, Germany.

Shaw, R.W. and Cullinane, M. J. (1997) "Destruction of military toxic material." *Encyclopedia Environmental Analysis and Remediation*, John Wiley & Sons, Inc., New York, NY.

Shaw, R.W. and Dahmen, N. (2000) "Destruction of toxic organic materials using supercritical water oxidation: current state of the technology." *Supercritical Fluids*, Kluwer Academic Publishers, July 12-24, 1998, Kemer, Antalya, Turkey, 425–437.

Snow, R.H., Sabato, W., Taylor, K., Sresty, G.C., Downey, K., Hazlebeck, D. and Jensen, D. (1996) "Demilitarization of chemical agents by hydrolysis and supercritical water oxidation." *Proc. ERDEC Sci. Conf. Chem. Bio. Def. Res.*, 359.

Spritzer, M.H., Hazlebeck, D.A. and Downey, K.W. (1995) "Supercritical water oxidation of chemical agents and solid propellants." *J. Energetic Mats.*, **13 (3&4)**, 185.

Staszak, C.N., Malinowski, K.C. and Killilea, W.R. (1987) "The pilot-scale demonstration of the MODAR oxidation process for the destruction of hazardous waste materials." *Environ. Prog.*, **6 (1)**, 39–43.

Subramaniam, B. and McHugh, M.A. (1986) "Reactions in supercritical fluids-a review." *Ind. Eng. Chem. Proc. Des. Dev.*, **25 (1)**, 1–12.

Sullivan, P. (2002) MIT Dept. of Chem. Eng., Doctoral dissertation, Cambridge, MA.

Takahashi, Y.T., Koo, T. and Koo, C. (1988) "Subcritical and supercritical water oxidation of CELSS model wastes." *Adv. Space Res.*, **9**, 99.

Taylor, J. (2001) "Hydrothermal chemistry of methylene chloride and MTBE: experimental kinetics and reaction pathways." MIT Dept. of Chem. Eng., Doctoral dissertation, Cambridge, MA.

Tester, J.W., Holgate, H.R., Armellini, F.J., Webley, P.A., Killilea, W.R., Hong, G.T. and Barner, H.B. (1993) "Supercritical water oxidation technology–process development and fundamental research. emerging technologies in waste management III." *ACS Symp. Ser., No. 518*, 35–76.

Thomason, T.B. and Modell, M. (1984) "Supercritical water destruction of aqueous wastes." *Haz. Waste Haz. Mats.*, **1 (4)**, 453–467.

Thomason, T.B., Hong, G.T., Swallow, K.C. and Killilea, W.R. (1990) "The MODAR supercritical water oxidation process." *Innovative Haz. Waste Treatment Series, Volume 1: Thermal Processes*, Technomic Publishing, Ed. by H.M. Freeman, Lancaster, PA, 31.

Timberlake, S.H., Hong, G.T., Simson, M. and Modell, M. (1982) "Supercritical water oxidation for wastewater treatment: preliminary study of urea destruction." *Procs. 12th InterSoc. Conf. Environ. Sys.*, July 19-21, San Diego, CA.

Tongdhamachart, C. and Gloyna, E.F. (1991) "Supercriticwater oxidation of anaerobically digested municipal sludge." Univ. of Texas at Austin, CRWR Tech. Report 229, Austin, TX.

Walas, S.M. (1985) *Phase Equilibria in Chemical Engineering*, Butterworth-Heinemann, Stoneham, MA.

Walrafen, G.E., Yang, W.-H. and Chu, Y.C. (1999) "Raman spectra from saturated water vapor to the supercritical fluid." *J. Phys. Chem. B*, **103**, 1332–1338.

Webley, P.A. (1990) "Fundamental oxidation kinetics of simple compounds in supercritical water." MIT Dept. of Chem. Eng., Doctoral dissertation, Cambridge, MA.

2. Dissertation Objectives

The objectives of this dissertation are to develop accurate thermodynamic and transport-property models for use at typical SCWO operating conditions. The dissertation is divided into two sections and further subdivided into appropriate chapters. These sections are introduced and summarized below.

2.1 Thermodynamic-property research

2.1.1 Thermodynamic-property research: a hard-sphere, volume-translated van der Waals equation of state for pure components

The first objective is to develop an accurate equation of state for use in SCWO *PVT* modeling. A hard-sphere, volume-translated van der Waals EOS has been developed and is comprised of the semi-theoretical Carnahan-Starling expression that properly represents the molecular interactions between hard spheres and a simple van der Waals attraction term. It also utilizes volume translation to further improve high density predictions. The translation constant is determined by a fit to liquid and vapor coexistence density data, while the Carnahan-Starling and van der Waals parameters are determined from widely available critical point data. An analysis of several important pure component thermodynamic properties (*e.g.*, density, vapor pressure, and enthalpy) has been conducted in order to determine the accuracy of this EOS. Background on EOS development and comparisons with other widely used EOSs is also provided.

2.1.2 Thermodynamic-property research: a hard-sphere, volume-translated van der Waals equation of state for mixtures

The volume-translated EOS has also been extended to model mixtures by using a theoretically correct mixture form for hard-sphere interactions. Simple mixing and combining rules and a simple binary parameter are also employed. Binary phase diagrams for several mixtures have been calculated using this model.

2.1.3 Thermodynamic-property research: an analysis of EOS Zeno behavior

The behavior of the "Zeno" ($Z = PV/RT = 1$) line has been examined in an attempt to investigate this recently rediscovered empirical regularity of fluids and to determine if such a regularity can be utilized to improve EOSs and their predictions. For a wide range of pure fluids,

this contour of unit compressibility factor in the temperature-density plane has been empirically observed to be nearly linear (and arrow-like, thus "Zeno") from the Boyle temperature of the low density vapor to near the triple point in the liquid region (Ben-Amotz and Herschbach, 1990a; Ben-Amotz and Herschbach, 1990b). An analysis which compares several EOSs and experimental values has been performed. Comparisons between volume-translated EOSs, variations of Peng-Robinson EOS models, and other species (methane and carbon dioxide) are shown and discussed in detail.

2.2 Transport-property research

2.2.1 Transport-property research: molecular-diffusivity measurement

Molecular diffusivities of pure supercritical water and supercritical-water mixtures have been measured by using nuclear magnetic resonance (NMR). Diffusivities of aqueous organic mixtures were measured at typical SCWO operating conditions with a novel, first-of-a-kind SCW/NMR flow system and the NMR spin-echo technique. Self-diffusivity measurements of supercritical water were also made and are compared with values previously measured and published.

2.2.2 Transport-property research: molecular-diffusivity modeling

Binary diffusivity models used for SCWO diffusivity predictions have only recently been evaluated. Due to the lack of experimental data, such evaluations have not been performed in great detail. With newly available data measured in this dissertation, several established models were reexamined. Comparisons, new expressions, and a discussion of recommended models for SCWO transport-property modeling are presented.

With these more accurate thermodynamic- and transport-property models, users of simulation tools can increase their confidence in these tools. These simulation tools are used to model SCWO processes and physically simulate the flow, kinetics, corrosion, salt nucleation, and salt precipitation inside SCWO reactors. Improvements in large-scale SCWO simulations should ultimately lead to improved reactor designs which will have less operating risk, appropriately sized reactors, optimized residence times, lower costs, fewer technical limitations, and increased destruction efficiencies.

2.3 References

Ben-Amotz, D. and Herschbach, D.R. (1990a) "Estimation of effective diameters for molecular fluids." *J. Phys. Chem.*, **94 (3)**, 1038–1047.

Ben-Amotz, D. and Herschbach, D.R. (1990b) "Correlation of Zeno ($Z = 1$) line for supercritical fluids with vapor liquid rectilinear diameters." *Israel J. Chem.*, **30**, 59–68.

PART I – THERMODYNAMIC-PROPERTY RESEARCH

I.1. Hard-Sphere, Volume-Translated van der Waals Equation of State for Pure Components

I.1.1 Introduction

For simulating a SCWO system, an equation of state (EOS) that relates the pressure (P), specific volume (V) or density (ρ), absolute temperature (T) and composition or mole fraction (x_i) of the reacting fluid mixture is required. The objectives of this chapter are twofold: (1) to review the applicability of available EOS models and (2) to propose a formulation that is accurate for modeling properties from ambient to SCWO process conditions (P from 1 to 300 bar; T from 25°C to 600°C; ρ from gas-like (10^{-3} g/cm^3) to liquid-like (1 g/cm^3) conditions). A suitable EOS should:

1) give accurate density predictions for pure components from ambient to supercritical temperatures and pressures;

2) be explicit in either pressure or volume to facilitate analytical expressions for derived thermodynamic properties;

3) give accurate predictions of density and phase compositions when extended to mixtures of water, hydrocarbons and gases using a set of simple mixing and combining rules (see Section I.2 on page 109); and

4) have a relatively small number of adjustable parameters.

In general, there have been two main approaches for formulating an EOS. One approach, pioneered by physicists and physical chemists, is to build models based on rigorous theoretical principles taking into account intermolecular interactions. The model results are then related to observable macroscopic properties. Statistical mechanical techniques are used to solve this problem, frequently with deterministic molecular simulations utilizing Monte Carlo or molecular dynamics methods. Typically, intermolecular parameters are estimated by comparing predicted theoretical results with experimental data.

The second approach, traditionally led by chemical engineers, is to propose empirical expressions that are fit to experimental data. Two general empirical formulations have seen sustained success. The first relies on the robust characteristics of the van der Waals formulation which uses a cubic equation in volume to predict both volumetric and residual $PVTx_i$-dependent

properties with two to three fitted parameters. The second uses a truncated virial format with modifications and numerous adjustable parameters to provide accurate $PVTx_i$ property prediction. For supercritical-fluid properties, both semi-theoretical and empirical approaches have been extensively used to model real systems (Brennecke and Eckert, 1989; Bruno and Ely, 1991).

Both theoretical and empirical approaches are discussed in detail along with the presentation of the developed empirical EOS.

I.1.2 Theoretical Approach

I.1.2.1 Classical Statistical Mechanics

From classical statistical mechanics, a PVT EOS may be developed by using the thermodynamic relationship between pressure and the configurational part of the partition function (Hirschfelder *et al.*, 1964):

$$P = -\left(\frac{\partial \underline{A}}{\partial \underline{V}}\right)_{T,N} = kT\left(\frac{\partial \ln Z_N}{\partial \underline{V}}\right)_{T,N}. \tag{1}$$

Here, Z_N is the classical configurational integral for a system containing N identical spherically symmetric molecules and is defined by a spatial integral over all possible arrangements in a defined volume $\underline{V}$:

$$Z_N = \frac{1}{N!\Lambda^{3N}} \iiint\limits_{\underline{V}} \exp\left(\frac{-\Phi(\underline{r}^N)}{kT}\right) d\underline{r}^N \tag{2}$$

where Λ is the deBroglie wavelength defined as

$$\Lambda \equiv \sqrt{\frac{h^2}{2\pi m'kT}}, \tag{3}$$

$\underline{r}^N$ are the position vectors for each molecule ($\underline{r}_j = [x_j, y_j, z_j]$) and $\Phi(\underline{r}^N)$ is the total potential energy due to the interactions between the N molecules of mass m' in a given volume.

Thus, the relationship between the three macroscopic properties of the system, *i.e.* pressure, volume and temperature, can be defined rigorously. This set of equations can be solved

in a closed form for only the simplest cases. For instance, for an ideal gas $(^{\text{ID}})$ where $\Phi(\underline{r}^N) = 0$, it can be shown that:

$$P = P^{\text{ID}} = kT\left(\frac{\partial N \ln \underline{V}}{\partial \underline{V}}\right)_{T,N} = \frac{NkT}{\underline{V}} = \frac{kT}{V}.$$

(4)

A second approach is one used by van der Waals (1873) where the configurational integral is approximated as follows (Vera and Prausnitz, 1972):

$$Z_N \cong \frac{1}{N! \Lambda^{3N}}\left\{\underline{V}_f \exp\left(\frac{|\Phi_{ij}|}{2kT}\right)\right\}^N$$

(5)

while the mean potential energy $|\Phi_{ij}|$ is averaged over the pairwise-additive potential energy and the radial distance:

$$|\Phi_{ij}| = \frac{N}{\underline{V}} \int_0^\infty \Phi_{ij}(r_{ij}) \cdot g(r_{ij}) \cdot 4\pi r_{ij}^2 \, dr_{ij} \cong \frac{-2aN}{\underline{V}N_a^2}.$$

(6)

Note that a captures the intermolecular interactions between the N molecules as defined above, but is often empirically adjusted in an EOS model. The free volume $\underline{V}_f$ was also approximated by assuming that N hard spheres of excluded volume b^{HS} were placed in a volume $\underline{V}$:

$$\underline{V}_f = \underline{V} - \frac{N}{N_a} b^{HS} = \underline{V} - \frac{2\pi N \sigma^3}{3}.$$

(7)

When Eqs. (1), (5), (6) and (7) are combined, the result is the van der Waals (vdW) EOS:

$$P = \frac{RT}{V - b} - \frac{a}{V^2}.$$

(8)

The vdW EOS is inaccurate for most real, highly compressible gases and liquids but nonetheless provides a basis for the development of many other practical EOSs which usually simulate van der Waals behavior in one form or another.

I.1.2.2 Statistical Mechanics Simulations

To treat real gases and liquids via statistical mechanics, one must resort either to deterministic numerical techniques, asymptotic expansions or integral approximation methods. An example of these numerical techniques is Monte Carlo simulation, where average properties

are evaluated by generating a series of random configurations of the molecules comprising the system. The total energy of the system in these states can be calculated if the intermolecular forces and the positions of the molecules are known. The contributions from these configurations can then be numerically integrated or averaged to approximate Z_N. The computer simulations themselves are quite tedious and repetitive, but with modern computers this is not a major limitation. Such simulations have been carried out for several model fluids (Alder, 1964; Henderson, 1979). The central problem is that the calculation of the potential energy of the system in a given configuration requires detailed knowledge of the forces between the molecules, for example their dependence on spatial position and orientation. This problem is made more tractable by first approximating the total energy of the system by the sum of the energies of all possible pairs, *i.e.* assuming pairwise additivity and then by adopting simple models to represent the potential function between two molecules. Lennard-Jones 6-12 or other intermolecular potential functions (Hirschfelder *et al.*, 1964) that depend explicitly on the separation distance and on the relative orientation are typically used for this purpose. A few commonly used intermolecular potential models are listed in Table 6.

The second method to estimate Z_N employs an integral equation or density functional theory along with approximations that include only certain significant terms in Eq. (2). Again as in Eqs. (5) and (6), a pairwise-additive mean potential energy function is employed. In addition, one needs to know the pair or radial distribution function $g(r^N)$ of the molecules in the system.

Although $g(r^N)$ can be obtained experimentally, *e.g.*, using x-ray scattering methods, it is not possible to obtain its explicit dependence on V and T in analytic form directly from experiment. Theoretical expressions of the radial distribution function depend on the potential function model used and have been estimated only for some simple models such as hard spheres (Thiele, 1963; Wertheim, 1964).

Even with these theoretical constraints, knowledge of molecular interactions can help in developing the general form of the EOS. In particular, the expression for the pressure of a fluid consisting of hard spheres with an uniform diameter σ has been obtained by applying the Percus-Yevick approximation (Wertheim, 1964) to Eq. (2):

$$P^{HS} = \frac{RT}{V}\left(\frac{1+y+y^2}{(1-y)^3}\right) \tag{9}$$

where y is the hard-sphere excluded-volume ratio defined as

$$y = \frac{b^{HS}}{4V} = \frac{b_o}{V} = \frac{\pi\sigma^3 N_a}{6}\frac{1}{V}.$$ (10)

Carnahan and Starling (1969) have proposed the following approximate expression for a hard-sphere fluid which is quite accurate:

$$P^{HS} = \frac{RT}{V}\left(\frac{1+y+y^2-y^3}{(1-y)^3}\right).$$ (11)

Expansions for the compressibility factor Z are given in Table 7. For comparison, the virial-expansion result obtained by Ree and Hoover (1967) is also included. In Figure 13 these results are compared to the Monte Carlo simulation results of Henderson (1979). In the low density limit ($y < 0.05$ where $y = \rho/\rho_c^{HS}$), the repulsive vdW term rigorously matches the simulation results because it is correct to first order in y (see Table 7). But at moderate densities ($0.05 < y < 0.125$), the values from the vdW term deviate and finally become meaningless at higher densities. The agreement between the simulation results and the Carnahan-Starling result is excellent and is the reason the Carnahan-Starling result is often used in the development of semi-theoretical hard-sphere EOSs.

In short, attempts to relate properties of fluids to intermolecular interactions using rigorous fundamental analysis do not yield exact expressions except for the case of an ideal gas. The approximate methods used to solve these problems provide only partially satisfactory PVT predictions for real fluids, especially in the dense fluid region ($\rho_r > 0.35$) which is of importance in SCWO processes.

71

Table 6. Intermolecular potential energy models
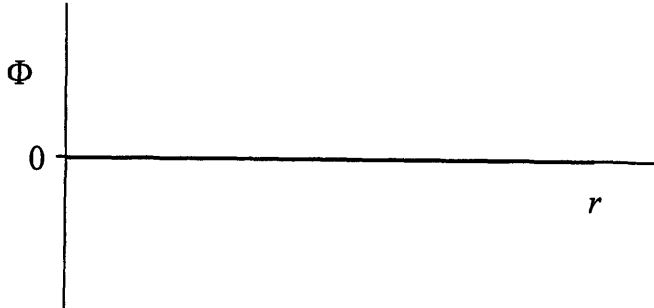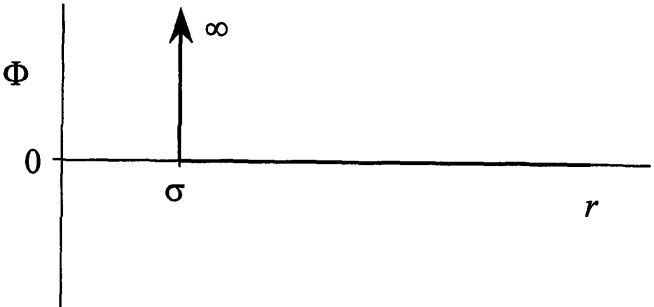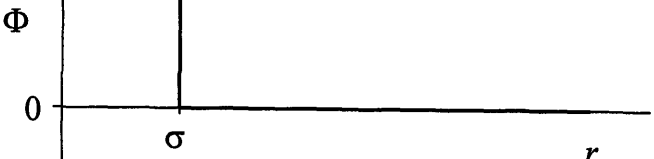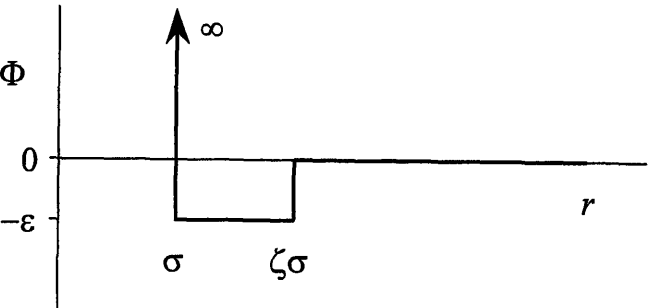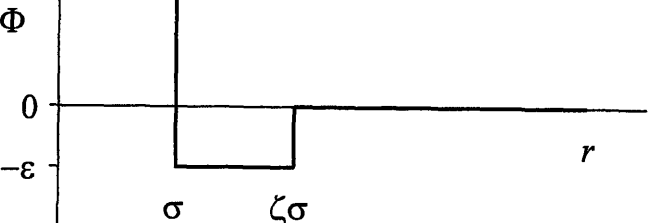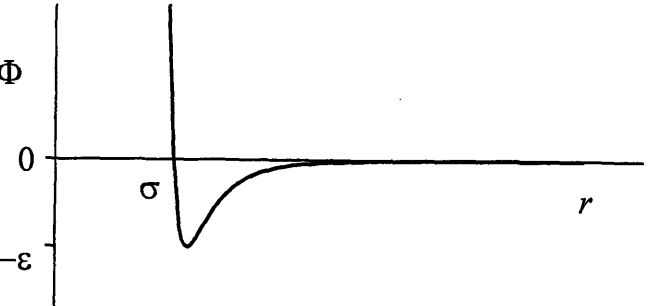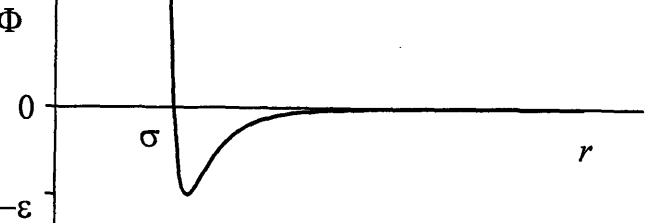
Model	Plot
Ideal Gas $\Phi = 0$	
Hard Spheres $\Phi = \begin{cases} \infty \\ 0 \end{cases}$ if $\begin{array}{c} r \le \sigma \\ r > \sigma \end{array}$	
Square Well $\Phi = \begin{cases} \infty & r \le \sigma \\ -\varepsilon & \text{if} \quad \sigma < r \le \zeta\sigma \\ 0 & r > \zeta\sigma \end{cases}$	
Lennard-Jones 6-12 $\Phi = 4\varepsilon\left(\left(\dfrac{\sigma}{r}\right)^{12} - \left(\dfrac{\sigma}{r}\right)^{6}\right)$	

Table 7. Compressibility-factor expansion of several hard-sphere expressions [a]

	Equation	$Z^{HS} = \dfrac{P^{HS}V}{RT} =$	Expansion of $Z^{HS} = \dfrac{P^{HS}V}{RT} =$
van der Waals (excluded-volume term only)	(8)	$\dfrac{1}{(1-4y)}$	$1+4y+16y^2+64y^3+256y^4+1024y^5+4096y^6$
Percus-Yevick	(9)	$\dfrac{\left(1+y+y^2\right)}{(1-y)^3}$	$1+4y+10y^2+19y^3+31y^4+46y^5+64y^6$
Carnahan-Starling	(11)	$\dfrac{\left(1+y+y^2-y^3\right)}{(1-y)^3}$	$1+4y+10y^2+18y^3+28y^4+40y^5+54y^6$
Virial Expansion (Ree and Hoover, 1967)	—	—	$1+4y+10y^2+18.3648y^3+28.2368y^4+39.5264y^5+56.5248y^6$

[a] $y = \dfrac{b^{HS}}{4V} = \dfrac{b_o}{V}$ and for the vdW EOS, $b = b^{HS}$.

73
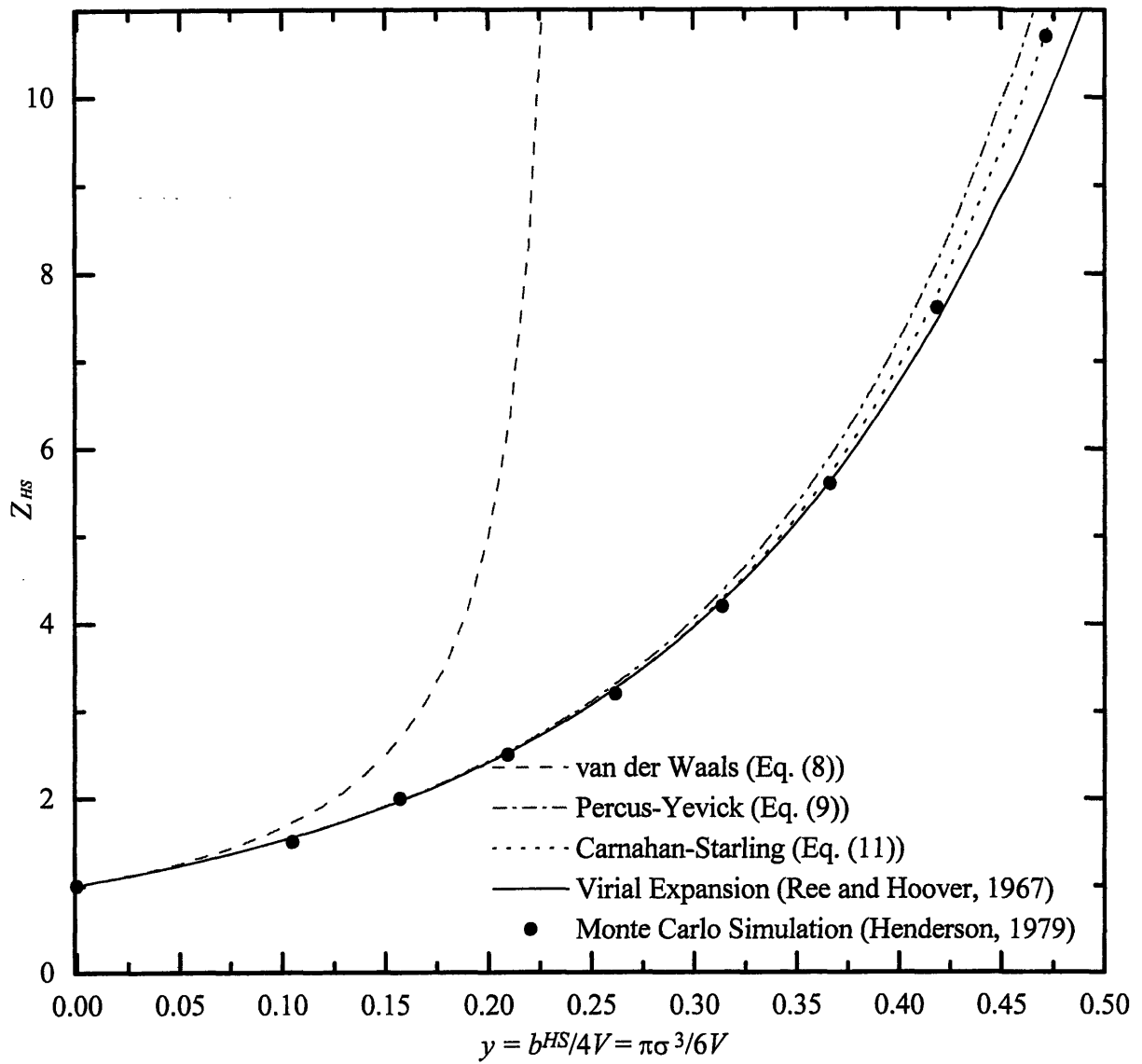
Figure 13. Comparison of the predicted hard-sphere compressibility factor.

I.1.3 Empirical Approach

As a rigorous theoretical approach to the formulation of an EOS is intractable except for the simplest cases, one must resort to the use of an empirical EOS for engineering calculations. At best, these EOSs represent average behavior and are not based on the exact nature of molecular interactions. Therefore, one should not expect them to give accurate predictions over the entire $PVTx_i$ space. A judicious choice of the parameters could extend the range of utility of the EOS — usually, the greater the number of fitted parameters used, the more accurate the EOS is. However, given the limited amount of reliable experimental data (particularly for supercritical mixtures) to fit the parameters used in the EOS, it is wise to use as few adjustable parameters as possible.

I.1.3.1 Phase Stability Criteria

The empirical approach can yield reasonably accurate PVT predictions by the use of creatively placed, although somewhat arbitrary, parameters that correlate the observed behavior of the fluid (Reid *et al.*, 1987). Typically, these empirical EOSs use fundamental phase stability criteria at the critical point in an attempt to specify pure-component parameters. At this point the spinodal stability locus and the vapor–liquid equilibrium binodal coexistence locus osculate, requiring that

$$\left(\frac{\partial P}{\partial \underline{V}}\right)_{T_c,N} = 0 \tag{12}$$

$$\left(\frac{\partial^2 P}{\partial \underline{V}^2}\right)_{T_c,N} = 0 \tag{13}$$

Evaluation of Eqs. (12) and (13) specifies two parameters contained in the EOS. Typically, these parameters are a molecular volume term b and an attraction interaction term a. The critical temperature T_c and pressure P_c are the properties most accurately known and, therefore, are most commonly used for the evaluation of a and b. As a result, the critical volume V_c and critical compressibility Z_c are determined by the form of the EOS using specified values of T_c and P_c. More complicated equations of state with additional parameters typically use

experimental *PVT* data, in conjunction with the stability criteria, to determine the additional constants.

Simple and straightforward mixing rules for mixtures are also advantageous. Again, one wants to minimize the number of fitted parameters used to account for binary interactions, as binary data in the supercritical region for many of the hydrocarbon–gas–water mixtures of importance in SCWO are quite limited.

I.1.3.2 Empirical Equations of State

The ideal gas law, which has both an empirical and theoretical basis, works well for fluids at low reduced densities ($\rho_r < 0.01$):

$$P = P^{ID} = \frac{NRT}{\underline{V}} = \frac{RT}{V} \tag{14}$$

and was not improved upon until about 125 years ago when van der Waals (1873) proposed his cubic equation of state:

$$P = \frac{RT}{V-b} - \frac{a}{V^2} \tag{15}$$

The van der Waals (vdW) EOS can predict vapor–liquid equilibrium for pure compounds and reduces to the ideal gas equation at low densities. However, its volumetric *PVT* predictions get considerably worse as the density of the fluid increases.

As this equation has only two parameters, both of which are fit to the stability criteria at the critical point, it predicts a universal value of the critical compressibility factor ($Z_c = 0.375$) for all fluids. Introducing a third physical constant, analogous to the acentric factor in the application of corresponding states concepts, would alleviate the constraint of a fixed Z_c. Moreover, the vdW EOS does not give accurate estimates of derived thermodynamic properties, *e.g.*, enthalpies and entropies, although this failing may be diminished if *a* is allowed to vary with temperature and/or other properties such as density.

Numerous modifications of vdW EOS have been proposed (Walas, 1985). Popular pressure-explicit, cubic forms for chemical-engineering applications are due to Redlich and Kwong (1949) (RK EOS),

76

$$P = \frac{RT}{V-b} - \frac{a}{\sqrt{T}V(V+b)}$$ (16)

Soave (1972) (RKS EOS)

$$P = \frac{RT}{V-b} - \frac{a}{V(V+b)}$$ (17)

where

$$a = a_c \alpha(\omega, T_r)$$ (18)

and ω is the acentric factor, and Peng and Robinson (1976) (PR EOS)

$$P = \frac{RT}{V-b} - \frac{a}{V(V+b)+b(V-b)}$$ (19)

where a is again defined by Eq. (18). All of these EOSs give far better predictions than the original vdW EOS over a wide range of densities. Figure 14 presents density predictions for several EOSs for pure water along the vapor (V)–liquid (L) coexistence curve, which is obtained by equating the pure-component fugacities:

$$f_i^V = f_i^L$$ (20)

or the corresponding fugacity coefficients ϕ_i, where for the liquid phase

$$\ln \phi_i^L \equiv \ln \frac{f_i^L}{P} = -\int_\infty^{V^L} \left[\frac{P}{RT} - \frac{1}{V} \right] dV - \ln Z^L + Z^L - 1$$ (21)

and a similar expression can be written for the vapor phase. Figure 14 clearly illustrates the inadequacy of these two-parameter cubic EOSs in providing accurate liquid density predictions for water.

The RK, RKS and PR EOSs predict universal values of critical compressibility like the vdW EOS, but ones that are closer to actual values for most substances (*i.e.*, $Z_c = 0.333$ for the RK and RKS EOSs and $Z_c = 0.307$ for the PR EOS; typical experimental values are between 0.22 and 0.29). Further, the RKS and PR EOSs treat the attractive interaction parameter a as a function of temperature and, therefore, predict more accurate vapor pressures, fugacities, residual enthalpies and residual entropies than the vdW EOS. A residual or departure function is defined as the difference between the actual property value and that which would pertain for a hypothetical ideal-gas at the same P and T. Residual enthalpies and entropies can be calculated with the following formulas:

$$\Delta H^r \equiv H(T,V) - H^{ID}(T,V^o = \frac{RT}{P}) = PV - RT - \int_\infty^V \left[P - T\left(\frac{\partial P}{\partial T}\right)_V \right] dV \tag{22}$$
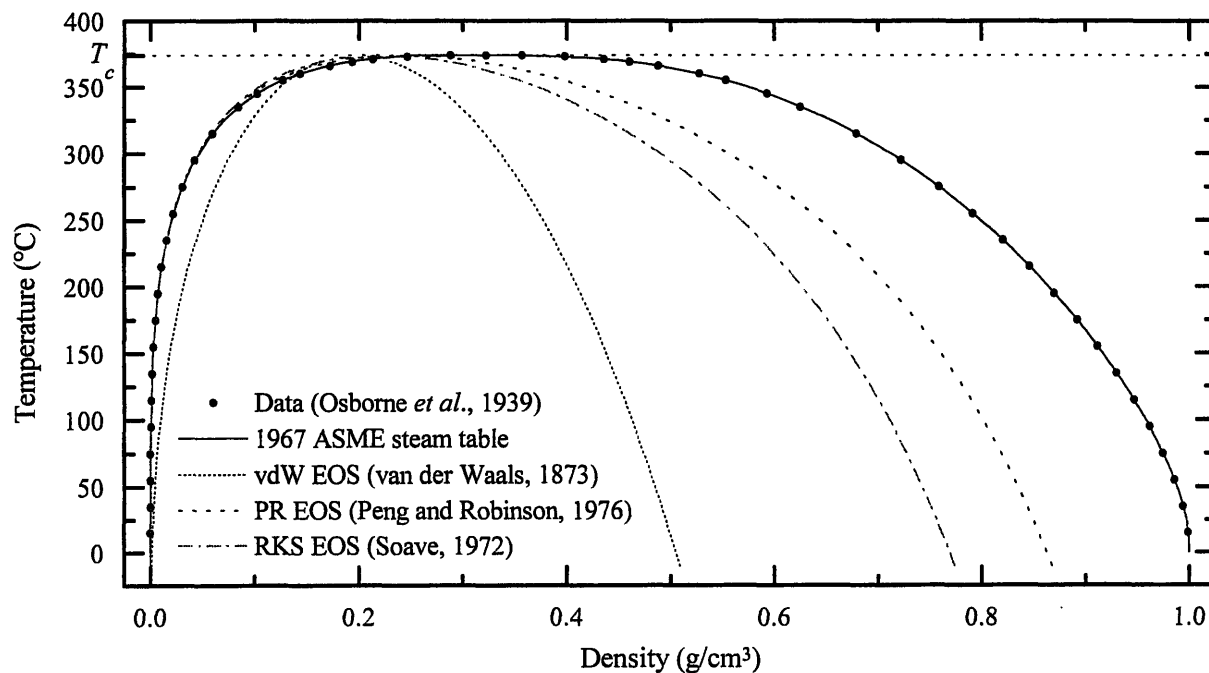
Figure 14. Density predictions for the vdW EOS (Eq. (15)), PR EOS (Eq. (19)) and RKS EOS (Eq. (17)) for pure water along the *V–L* coexistence curve.

$$\Delta S^r \equiv S(T,V) - S^{ID}(T,V^o = \frac{RT}{P}) = R \ln Z - \int_{\infty}^{V}\left[\frac{R}{V} - \left(\frac{\partial P}{\partial T}\right)_V\right]dV \qquad (23)$$

Another class of EOSs incorporates knowledge of specific molecular interactions with additional fitted parameters. A good example of these is vdW-type EOSs that model the repulsive contribution with the accurate hard-sphere relation proposed by Carnahan and Starling (1969):

$$P^{HS} = \frac{RT}{V}\left[\frac{1+y+y^2-y^3}{(1-y)^3}\right] \qquad (24)$$

where y is the hard-sphere excluded-volume ratio defined as

$$y = \frac{b^{HS}}{4V} = \frac{b_o}{V} = \frac{\pi\sigma^3 N_a}{6}\frac{1}{V} \qquad (25)$$

and σ is the molecular hard-sphere diameter. Thereafter, empirical perturbation terms are added to model real gases and fluids. For example, Vera and Prausnitz (1972) developed an EOS using the Carnahan–Starling result for repulsive effects and the empirical Strobridge–Gosman EOS for attractive effects. Johnston and Eckert (1981) used a simple first-order perturbation term in their Carnahan–Starling van der Waals (CSvdW) EOS in an attempt to model the dense supercritical region:

$$P = \frac{RT}{V}\left[\frac{V^3 + b_oV^2 + b_o^2V - b_o^3}{(V-b_o)^3}\right] - \frac{a}{V^2} \qquad (26)$$

However, the CSvdW EOS did not accurately model the highly compressible critical region. As a result, Johnston et al. (1982) introduced an Augmented van der Waals (AvdW) EOS which had a second-order perturbation term for more accurate modeling of the critical region. Recently, Heilig and Franck (1989) have proposed an EOS for supercritical mixtures involving water and hydrocarbons that works well for predicting the critical curves of such mixtures, but it does not give accurate values of density for liquids or supercritical fluids.

The molecular volume term b used in most EOSs is qualitatively similar to the hard-sphere excluded volume b^{HS} described in Eq. (25). For hard spheres, the values of b and b^{HS} are equal:

$$b = b^{HS} = \frac{2\pi\sigma^3 N_a}{3} = 4b_o \tag{27}$$

However, for molecules of different structures and interactions, it is difficult to estimate the correct value of b *a priori*. By using stability criteria instead, a fitted b can be obtained from the critical data (T_c and P_c), avoiding the difficult calculation of a geometrically correct excluded volume. A more realistic molecular-volume term was obtained by Shah *et al.* (1994) in their twenty-three constant quartic EOS for pure non-polar fluids, as their molecular-volume term uses the experimental critical volume V_c instead of P_c. Consequently, their EOS does not specify the critical compressibility Z_c, but relies on the assumption that V_c is accurately known, which is often not the case.

As the true nature of the intermolecular interactions is unknown, the vdW-type terms used to account for these interactions are merely closed-form approximations of a more complex function. To achieve higher accuracy, some researchers have proposed equations with different functional forms and/or additional adjustable parameters. Among these are the equations proposed by Benedict *et al.* (1940), Starling and Han (1972), Starling (1973), Martin and Stanford (1974) and Lee and Kesler (1975). These equations typically combine a virial format with exponential terms for high-density behavior and, consequently, have many more parameters than cubic EOSs. These parameters have typically been evaluated only for the specific classes of compounds for which these EOSs were originally developed.

Higher precision is usually achieved in an EOS by fitting more parameters, *e.g.* in the modeling of water, the Haar *et al.* (1984) EOS with eighty parameters is frequently used to achieve high levels of accuracy. Errors of less than 0.1% are obtained by using multiple parameter, non-linear regression methods to fit a comprehensive set of data. Such EOSs can be used to generate smoothed "data" for important pure compounds, *e.g.*, the 1967 American Society of Mechanical Engineers (ASME) and the 1987 National Institute of Standards and Technology (NIST) steam tables (Haar *et al.*, 1984; Aspen Technology, 1994). Although these

equations are highly accurate for certain pure compounds, they cannot, in general, be used for mixtures.

In short, attempts to relate properties of fluids to intermolecular interactions using rigorous fundamental analysis do not yield exact expressions, except for the case of an ideal gas. Simple cubic-type EOSs provide only partially satisfactory PVT predictions for real fluids, especially in the dense fluid region ($\rho_r > 0.35$) which is of importance in SCWO processes. To preserve simplicity and achieve higher accuracy, an alternative approach is needed.

I.1.3.3 Volume-Translated Equations of State

Cubic vdW-type models can be improved significantly by translating the volume to provide a more satisfactory match to liquid density data (see Figure 14). Martin (1967) was the first to propose this concept, using a fixed volume translation t to arrive at a best-fit EOS that gave substantially better density predictions than other cubic EOSs (Martin, 1979). In his formulation:

$$V = V^{UT} + t \tag{28}$$

where V is the final predicted volume with translation and the superscript ^{UT} denotes the untranslated volume V^{UT} to emphasize the fact that V^{UT} is the estimated volume from the untranslated EOS. Consequently, two equations, in general, are needed to obtain the final volume or density prediction at a given P and T: the untranslated EOS

$$V^{UT} = V^{UT}(P, T) \tag{29}$$

and the equation that performs the translation

$$V = f(V^{UT}, t). \tag{30}$$

For pure water and aqueous supercritical mixtures, Martin's constant translation formulation gives large positive errors (up to 25%) for $\rho_c < \rho < 1.5\rho_c$ and negative errors for $\rho > 2\rho_c$ (Martin, 1979). To improve the fit for such systems, the volume translation can be correlated to changes in density.

Subsequently, Peneloux *et al.* (1982), Soave (1984), Chou and Prausnitz (1989) and Mathias *et al.* (1989) have refined the use of translation to improve density predictions. Peneloux *et al.* (1982) and Soave (1984) corrected the predictions for liquid volumes far away from the critical point by using a fixed translation (see Eq. (28)):

$$t = 0.40768 \frac{RT_c}{P_c} \left(0.29441 - \frac{P_c V_c}{RT_c} \right). \tag{31}$$

Chou and Prausnitz improved these previous methods for the volume-translated RKS (VTRKS) EOS by adding a "distance" variable d in order to account for the increasing difference between the predicted and experimental state as one approaches the critical point and to match the experimental critical volume V_c at the critical point:

$$V = V^{UT} - t - (V_c^{UT} - V_c - t)\left(\frac{\eta}{\eta + d} \right) \tag{32}$$

where

$$d = \frac{\left(V_{satL}^{UT} \right)^2}{RT_c} \left(\frac{\partial P}{\partial V^{UT}} \right) \bigg|_{T, V^{UT} = V_{satL}^{UT}} \qquad T_r < 1 \tag{33}$$

$$d = 0 \qquad\qquad\qquad\qquad T_r = 1 \tag{34}$$

$$d = \frac{\left(V_c^{UT} \right)^2}{RT_c} \left(\frac{\partial P}{\partial V^{UT}} \right) \bigg|_{V^{UT} = V_c^{UT}} \qquad T_r > 1. \tag{35}$$

The terms V_c^{UT} and V_{satL}^{UT} are the critical volume and saturated liquid volume predicted by the untranslated EOS, respectively, V_c is the experimental critical volume and η is a fitted universal constant. The volume-translation parameter for the VTRKS EOS was calculated with Eq. (31). Note that at any particular temperature in the coexistence region, the volume translation given by Eqs. (32) and (33) is a constant since Eq. (33) is always evaluated at the saturated liquid volume. For this reason, it can be shown that the Chou and Prausnitz volume translation is thermodynamically consistent for phase-equilibrium calculations where equivalence of the fugacities or fugacity coefficients is required (see Eq. (20)).

In an attempt to match the experimental critical volume V_c at the critical point and to improve the liquid-density predictions elsewhere, Mathias and coworkers (1989) applied a continuously variable translation to the PR EOS (VTPR EOS):

$$V = V^{UT} + t + (V_c - V_c^{UT} - t)\left(\frac{\eta}{\eta + \delta}\right)$$ (36)

where

$$\delta = \frac{\left(V^{UT}\right)^2}{RT}\left(\frac{\partial P}{\partial V^{UT}}\right)_T.$$ (37)

Translation values reported by Mathias *et al.* (1989) were used for the evaluation of the VTPR EOS in this paper. Figure 15 shows how these volume translations improve the predictions of the vapor–liquid coexistence curve of water. Note that for a polar compound such as water, Chou and Prausnitz used a modified α as suggested by Soave (1979):

$$\alpha = 1 + (1 - T_r)\left(m + \frac{n}{T_r}\right)$$ (38)

where the constants m and n were regressed to vapor-pressure data and determined to be 0.5075 and 0.0261, respectively, for water. Further, Mathias and coworkers (1989) have found that by fitting a temperature dependent t to data, they obtain more accurate coexistence densities, *e.g.*, for water:

$$t = -5.26 + \frac{1801}{1.8T}$$ (39)
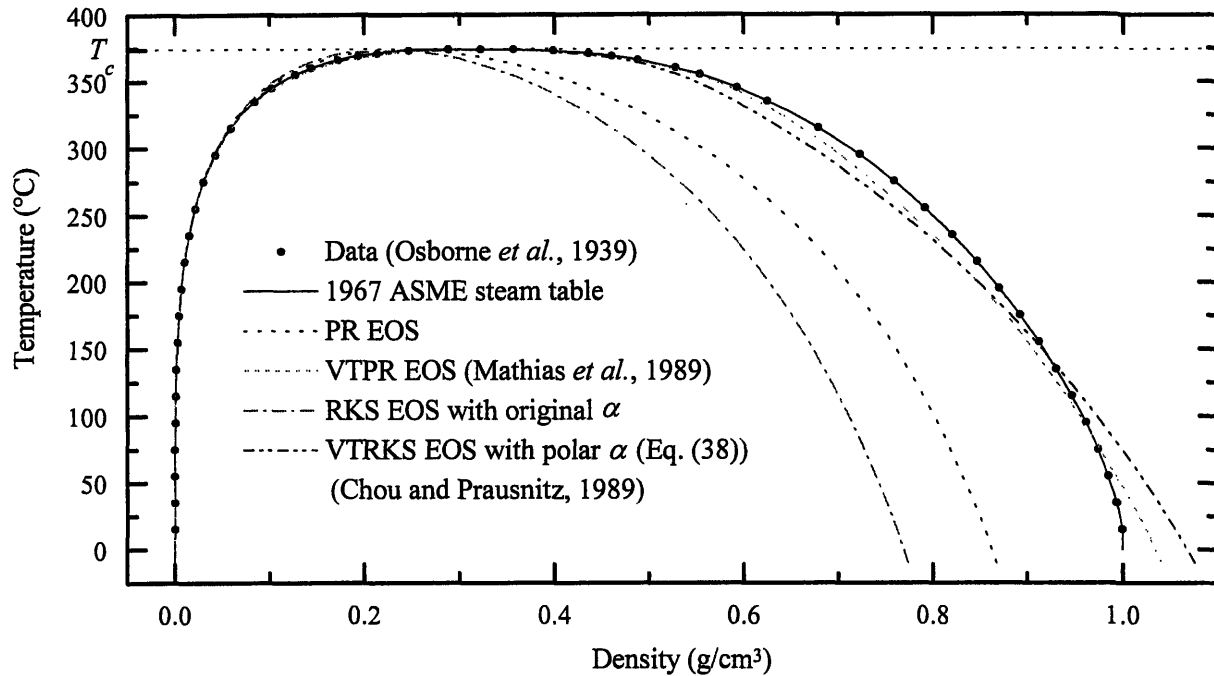
Figure 15. Comparison of untranslated and volume-translated EOSs for pure water along its vapor–liquid coexistence curve.

where the average error for saturated liquid densities is reduced to 0.2% (Mathias and Klotz, 1994). In the above equation, the volume-translation parameter t is given in cubic centimeters per mole and the temperature is in Kelvin.

More recently, investigators have decided to use volume translations that are independent of temperature and volume as part of their effort to develop universal volume-translation parameters. For example, Polishuk and coworkers (2000) developed a four-parameter vdW-like EOS where volume-translation constants c and d are determined from the experimental critical compressibility and liquid-phase triple-point volume for each pure species (a and b are still determined from stability criteria). Another approach suggested by several researchers is to use a constant translation calculated from the difference between the experimental and calculated volumes at a reduced temperature of 0.7 (Ahler and Gmehling, 2002; Wang et al., 2003).

One limitation of using temperature-dependent volume translations is the potential for isotherm crossing (Yelash and Kraska, 2003). When Pfohl (1999) examined the volume translation evaluated by de Sant' Ana and Ungerer (1999),

$$c = c_0 + (c_c - c_0)\exp(\beta[1 - T_r])$$ (40)

84

he found that isotherms will cross at low volumes since low temperature isotherms with a small translation will intersect higher (or critical) temperature isotherms which have a larger translation. As a result, inconsistent volumes can be calculated during isobaric heating when the liquid volume decreases. Therefore, the use of solely temperature-dependent volume translations is not recommended, especially when used outside the *PVT* region that the empirically-based volume translation was developed for.

Another volume-translation concern is whether derived thermodynamic properties are properly determined. To obtain derived thermodynamic properties such as the fugacity, residual enthalpy and residual entropy in a thermodynamically consistent manner, one must correctly account for the volume translation. Thus, when volume translation is used, Eqs. (21)–(23) assume more complicated forms:

$$\ln \phi_i \equiv \ln \frac{f_i}{P} = -\int_{\infty}^{V^{UT}} \left[\frac{P}{RT} - \frac{1}{V} \right] \left(\frac{\partial V}{\partial V^{UT}} \right)_T dV^{UT} - \ln Z + Z - 1 \tag{41}$$

$$\Delta H^r = PV - RT - \int_{\infty}^{V^{UT}} \left[P - T \left(\frac{\partial P}{\partial T} \right)_V \right] \left(\frac{\partial V}{\partial V^{UT}} \right)_T dV^{UT} \tag{42}$$

$$\Delta S^r = R \ln Z - \int_{\infty}^{V^{UT}} \left[\frac{R}{V} - \left(\frac{\partial P}{\partial T} \right)_V \right] \left(\frac{\partial V}{\partial V^{UT}} \right)_T dV^{UT} \tag{43}$$

where V in all equations refers to the volume-translated value from Eq. (30). In addition,

$$\left(\frac{\partial P}{\partial T} \right)_V = \left(\frac{\partial P}{\partial T} \right)_{V^{UT}} - \left(\frac{\partial V}{\partial T} \right)_{V^{UT}} \cdot \left(\frac{\partial P}{\partial V^{UT}} \right)_T \cdot \left(\frac{\partial V^{UT}}{\partial V} \right)_T \tag{44}$$

which quantifies the contributions to $(\partial P / \partial T)_V$ from the untranslated EOS and from the volume-translation equation. After substitution of Eq. (44) into Eqs. (42) and (43), all of the integrands are in terms of V^{UT} and constants. Mathias and coworkers did not use the volume-translated derived property equations and, as a result, report thermodynamically inconsistent coexistence curves. In their earlier treatment, the untranslated fugacity equation (Eq. (21) with $V = V^{UT}$) was used and not the volume-translated equation (Eq. (41)). Likewise, Chou and Prausnitz would be required to use Eqs. (41)–(44) if they wanted specific fugacity values or any other derived thermodynamic properties. However, as they only utilized the equivalence of fugacity in their

85

phase-equilibrium calculations for constant volume translation (Eq. (20)), they were able to use the untranslated fugacity-coefficient equation (Eq. (21)). In principle, any EOS can be used with volume translation as long as a thermodynamically consistent set of equations is applied (*e.g.*, Eqs. (41)–(44) for a pressure-explicit EOS).

I.1.4 Hard-Sphere Volume-Translated van der Waals (HSVTvdW) Equation of State

In this section the development of a new, thermodynamically consistent, volume-translated EOS is presented. First, the untranslated portion of this EOS is introduced, followed by stability criteria analysis. The translation is then developed to provide accurate density predictions.

I.1.4.1 Approach

As the state of a single-phase, one-component system is fully specified by any two intensive properties, the pressure can be explicitly written as a function of the temperature and the untranslated specific volume:

$$P = f(T, V^{UT}).$$ (45)

Using a virial-type expansion, one can rewrite a pressure-explicit EOS in the form of a finite series:

$$P = \sum_{n=1}^{M} \frac{f_n(T)}{\left(V^{UT}\right)^n} = \sum_{n=1}^{M} f_n(T)\left(\rho^{UT}\right)^n .$$ (46)

The lowest index on V^{UT} in this series is unity which corresponds to the ideal gas state. To simplify this expression further, the repulsive and attractive components of the intermolecular forces between molecules are separated to give

$$P = \sum_{n=1}^{M^{rep}} \frac{f_n^{rep}(T)}{\left(V^{UT}\right)^n} - \sum_{n=1}^{M^{att}} \frac{f_n^{att}(T)}{\left(V^{UT}\right)^n} .$$ (47)

An empirical EOS can be obtained by truncating either series after a certain number of terms or by proposing a closed form that approximates the series to some order. For example, the vdW EOS is obtained by proposing a certain closed form for the first series and truncating the second

series after the second term with $f_1^{att}(T) = 0$. Most modifications of the vdW EOS, *e.g.* the RK EOS, use a closed form for both series, and this may account for their better performance. However, the repulsive term in these cubic EOSs is inherently inaccurate at higher densities (Henderson, 1979). The Carnahan–Starling hard-sphere approximation given by Eq. (24) provides an excellent choice for the repulsive part. Thus, a form similar to that originally proposed by Carnahan and Starling is used here with $y = b/V^{UT}$ and b calculated from stability criteria at the critical point:

$$P = P^{HS} - \sum_{n=1}^{M^{att}} \frac{f_n^{att}(T)}{\left(V^{UT}\right)^n} = \frac{RT}{V^{UT}} \left[\frac{\left(V^{UT}\right)^3 + b\left(V^{UT}\right)^2 + b^2 V^{UT} - b^3}{(V^{UT} - b)^3} \right] - \sum_{n=1}^{M^{att}} \frac{f_n^{att}(T)}{\left(V^{UT}\right)^n} . \tag{48}$$

Since the repulsive term models only the hard-sphere contribution, the first-order perturbation attraction term must incorporate the unknown soft-sphere contribution in addition to the attractive contribution. For the second series, a simple (but somewhat arbitrary) closed form was selected. Thus, the modified equation of state, which is called a Hard-Sphere van der Waals (HSvdW) EOS, is written as

$$P = \frac{RT}{V^{UT}} \left[\frac{\left(V^{UT}\right)^3 + b\left(V^{UT}\right)^2 + b^2 V^{UT} - b^3}{(V^{UT} - b)^3} \right] - \frac{a}{(V^{UT} + 2b)^2} \tag{49}$$

where

$$a = a_c \alpha . \tag{50}$$

Note that Eq. (49) represents an EOS without volume translation, hence the introduction of the untranslated ^{UT} superscript for V. The integer multiplier of 2 in the $(V^{UT} + 2b)^2$ term was determined by duplicating the PV slope along the critical isotherm for several compounds and is shown for water in Figure 16.

I.1.4.2 Stability Criteria

Equations (12), (13) and (49) form a system of three equations and five unknowns (a_c, b, P_c, T_c and V_c^{UT}) at the critical point. Note that even though two equations are necessary to predict fluid density, *i.e.*, the untranslated EOS given by Eq. (49) and a volume-translation

87
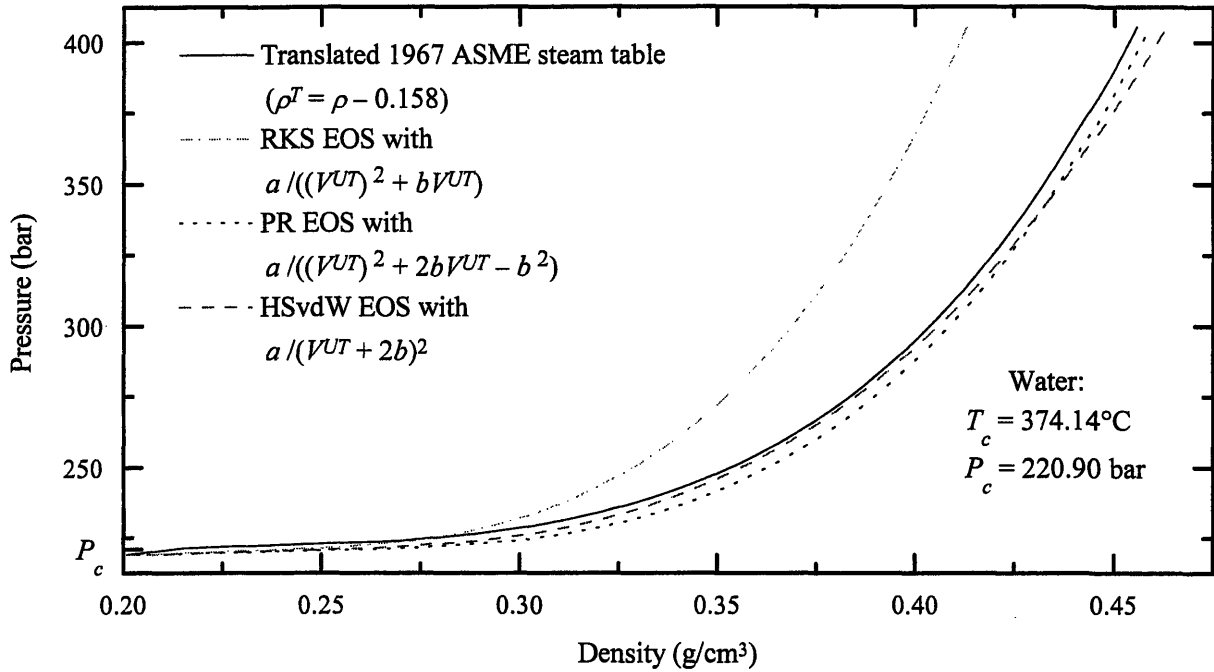
Figure 16. Comparison of the vdW attraction terms for several EOSs along the critical isotherm of water.

equation, the stability criteria at the critical point (Eqs. (12) and (13)) may be expressed solely as untranslated variables; this is easily shown using implicit derivatives, provided that the volume-translation equation has finite partial derivatives with respect to V^{UT} at the critical point, i.e.

$$\left(\frac{\partial P}{\partial \underline{V}}\right)_{T_c,N} = \left(\frac{\partial P}{\partial \underline{V}^{UT}}\right)_{T_c,N} \bigg/ \left(\frac{\partial \underline{V}}{\partial \underline{V}^{UT}}\right)_{T_c,N} = 0 \tag{12}$$

The solution to this equation set is

$$a_c = 0.4496088\frac{R^2 T_c^2}{P_c} \tag{51}$$

$$b = 0.0245878\frac{RT_c}{P_c} \tag{52}$$

$$Z_c^{UT} = \frac{V_c^{UT} P_c}{RT_c} = 0.3183919. \tag{53}$$

1.1.4.3 Volume Translation

A volume translation is used to improve the density predictions given by Eq. (49). By examining *PVT* data for pure carbon dioxide, nitrogen and oxygen along their respective vapor–

liquid coexistence curves and PVT and H data for pure water along its vapor–liquid coexistence curve, its critical isotherm ($T_r = 1.0$ for $1.0 < P_r < 1.8$), and selected isobars ($P_r = 1.1$ for $0.42 < T_r < 1.0$ and $P_r = 1.8$ for $1.0 < T_r < 1.66$), errors in the predicted density were significantly reduced by use of the following expression:

$$V = V^{UT} + t + (V_c - V_c^{UT} - t) \left[\frac{(8.0 \pm 0.7)V_r^{UT} T_r^{-4.5 \pm 0.4}}{\left(V_r^{UT}\right)^3 + (6.5 \pm 0.7)T_r^{-6.5 \pm 0.3} + 0.5} \right] \tag{54}$$

where V^{UT} is given by Eq. (49), t is the volume-translation constant and V_c is the experimental critical volume. The exponents given in Eq. (54) are universal constants, independent of the compound being modeled, while the volume-translation parameter t is obtained by regression of liquid or vapor–liquid coexistence density data for each pure compound (see Table 8). The exponents on V_r^{UT} (1 and 3) were previously determined and fixed during the optimization of the other four universal constants. The constant, 0.5, in the denominator was adjusted during the optimization of the universal constants in order for $V = V_c$ at the critical point since the rightmost-bracketed term in Eq. (54) should be unity at the critical point. In this paper, vapor–liquid coexistence data were used for the t regression. The form of Eq. (54) insures that the EOS predicts the experimental critical volume exactly. Note that thermodynamically consistent, derived-property equations (Eqs. (41) through (44)) must be invoked, because a variable volume translation has been employed. Also note that in the ideal-gas region (for large V^{UT} and T), the volume-translation equation correctly reduces to $V = V^{UT}$ as seen in Figure 17 for the critical isotherm. The improvement of volume-translation predictions is clearly seen at higher densities in Figure 17 and also demonstrates the validity of differentiating the stability criteria with untranslated and volume-translated terms as shown in Eq. (12) on page 88. In all cases, the volume-translated EOSs and their associated untranslated forms emulate $(\partial P / \partial V)_{Tc} = 0$ with a zero slope at the critical point.

Table 8. Pure-component parameters for the HSVTvdW EOS

Compound	T_c (°C)	P_c (bar)	V_c (m³/kgmol)	b (m³/kgmol)	t (m³/kgmol)	a_c (m⁶bar/kgmol²)	α_A	α_B
CH_4	−82.62	45.979	0.0990	0.0085	0.0140	2.45	0.037	0.501
CO_2	31.06	73.821	0.0939	0.0084	0.0129	3.90	0.000	0.913
C_2H_4	9.19	50.404	0.1290	0.0115	0.0180	4.92	0.081	0.578
H_2O	374.14	220.900	0.0559	0.0060	0.0048	5.89	0.105	1.038
NH_3	132.40	112.775	0.0724	0.0074	0.0069	4.53	0.114	0.844
N_2	−146.89	33.980	0.0896	0.0076	0.0127	1.46	0.059	0.504
O_2	−118.57	50.430	0.0734	0.0063	0.0104	1.47	0.049	0.500
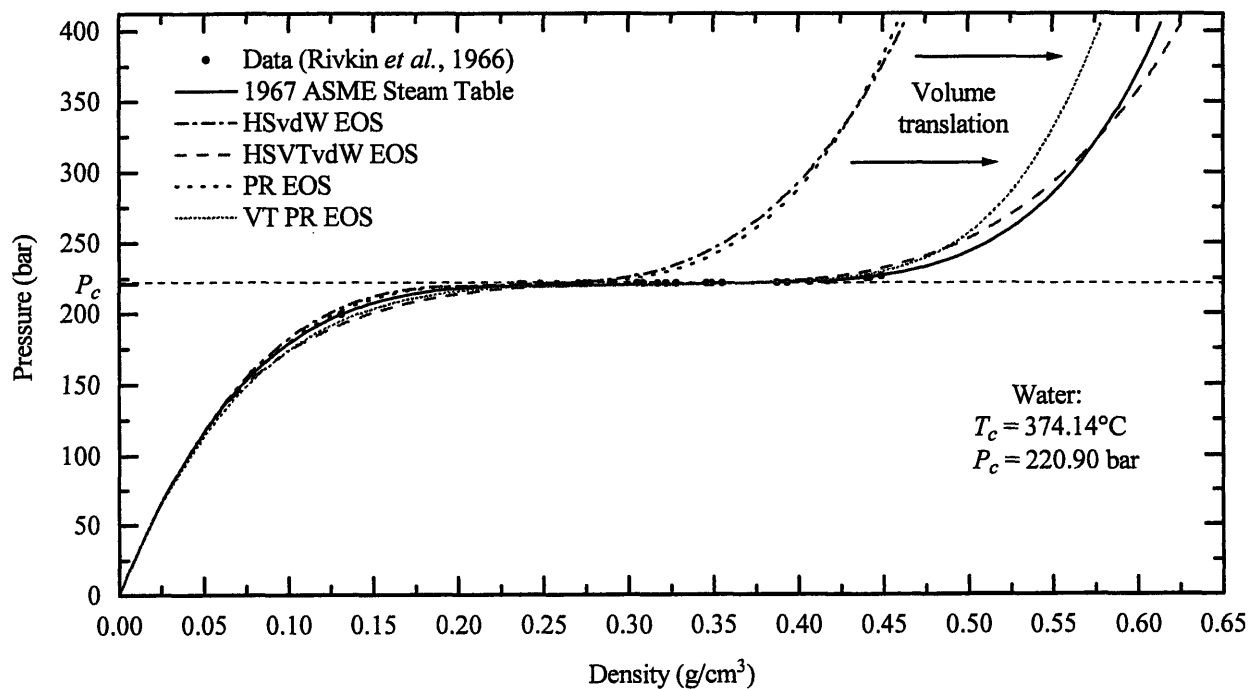
Figure 17. Comparison of untranslated and volume-translated EOSs for pure water along the critical isotherm.

I.1.4.4 α Determination

The functional form of α (or α_i for the pure component i) must be selected carefully because coexistence curve predictions are very sensitive to the values of α. Soave (1972) suggested that the value of α be evaluated using the equilibrium condition given by Eq. (20) for each V–L tie line. This fitting ensures thermodynamic consistency along the coexistence curve, and for this reason the EOS gives accurate predictions of thermodynamic properties. Soave (1972) also proposed the following form for fitting α_i as a function of T_r:

$$\alpha_i = \left[1 + k_{ii}\left(1 - \sqrt{T_r}\right)\right]^2 \tag{55}$$

where k_{ii} is a pure-component expression or constant. To increase prediction accuracy further, other forms of α_i have been proposed, e.g., Twu et al. (1996). In the case of Eq. (49), it was found that the plot of α_i versus T_r (obtained using Eq. (20) and saturation vapor-pressure data) is nearly the same curve for non-polar as well as polar substances. Therefore, α_i can be regarded as a universal correlation that represents all pure components i, and the subscript i can be dropped. In addition to using saturation vapor-pressure data for α regression, saturation enthalpy data were used for the fitting since the residual enthalpy is a function of the temperature derivative of α, an expression that is extremely sensitive to temperature:

$$\Delta H^r = PV - RT - a_c\left[T_r\left(\frac{d\alpha}{dT_r}\right) - \alpha\right]\int_{\infty}^{V^{UT}} \frac{1}{\left(V^{UT} + 2b\right)^2}\left(\frac{\partial V}{\partial V^{UT}}\right)_T dV^{UT} \tag{56}$$

$$-T_r\int_{\infty}^{V^{UT}}\left(\frac{\partial P}{\partial V^{UT}}\right)_T \cdot \left(\frac{\partial V}{\partial T_r}\right)_{V^{UT}} dV^{UT}.$$

As a result, the following expression was developed for α as a function of T_r:

$$\alpha = \exp\left[\left(1 - T_r\right)\left(\frac{\alpha_A}{T_r^{0.93\pm0.04}} + \alpha_B T_r^{0.75\pm0.04}\right)\right]. \tag{57}$$

The use of an exponential function prevents calculations of negative α, as would occur if a linear variation of α with T_r were used. The use of $\left(1 - T_r\right)$ ensures thermodynamic consistency, i.e. at

the critical temperature $a = a_c$. The exponents -0.93 and 0.75 are universal, are crucial for calculating accurate saturated residual properties, and were simultaneously optimized with the other four universal constants given in Eq. (54). Finally, it is argued that the value of α should never increase with temperature, *i.e.*

$$\frac{d\alpha}{dT_r} \leq 0.$$ (58)

so that as temperature is increased, numerical inconsistencies, as seen with several α formulations, are never experienced (Polishuk *et al.*, 2002). Therefore, it can be shown that the pre-component constants α_A and α_B must not be negative. As α_A, α_B and t are coupled through the volume-translated fugacity equation (Eq. (41)), they were simultaneously regressed with *PVT* vapor–liquid coexistence data once all eight universal constants were determined. Table 8 contains α_A and α_B for several compounds. It has been determined that the use of Eq. (57) in the $T_r > 1$ region is sometimes inaccurate for properties other than density, *e.g.*, residual enthalpy errors may reach 30%. Rather than develop an even more complicated expression for α, it was decided to accept these deficiencies.

ASPEN PLUS™ (Release 8.5-3, Aspen Technology, MA) was employed for the regression of all universal constants and pure-component parameters in the HSVTvdW EOS and the property predictions of all EOSs evaluated in this study. The generalized least-squares and maximum-likelihood methods were used for the regression of all parameters. Regression data and results are stored and are available (Kutney *et al.*, 1996).

In summary, the HSVTvdW EOS is specified by three operating equations:

$$P = \frac{RT}{V^{UT}} \left[\frac{\left(V^{UT}\right)^3 + b\left(V^{UT}\right)^2 + b^2 V^{UT} - b^3}{(V^{UT} - b)^3} \right] - \frac{a}{(V^{UT} + 2b)^2}$$ (49)

$$a = a_c \alpha = a_c \exp\left[(1 - T_r)\left(\frac{\alpha_A}{T_r^{0.93}} + \alpha_B T_r^{0.75} \right) \right]$$ (59)

$$V = V^{UT} + t + (V_c - V_c^{UT} - t) \left[\frac{8 V_r^{UT} T_r^{-4.5}}{\left(V_r^{UT}\right)^3 + 6.5 T_r^{-6.5} + 0.5} \right] \tag{54}$$

where a_c and b are fit to pure-component stability criteria at the critical point (Eqs. (12) and (13)) and α_A, α_B and t are simultaneously regressed from PVT vapor–liquid coexistence data.

I.1.5 Results

The success of the α equation given by Eq. (57) is illustrated in Figure 18, where the vapor-pressure percentage deviations of several EOSs are plotted for saturated water as a function of temperature. Table 9 compares the average absolute error of the vapor-pressure predictions for pure components, while Table 10 through Table 12 compare the average absolute errors for other saturation properties. The average absolute error for the parameter of interest is defined in the first footnote to Table 9. The effectiveness of using the translation given by Eq. (54) for the coexistence curve of water is illustrated in Figure 19. Figure 20 and Figure 21 compare saturation residual enthalpies and entropies for water as predicted by the HSVTvdW, RKS and PR EOSs, while Figure 22 and Figure 23 provide similar comparisons for saturated carbon dioxide and methane, respectively. (Note that the residual entropy in Figure 21 is calculated using the definition given in Eq. (43), whereas ASPEN PLUS™ uses a different basis.) In all cases, the HSVTvdW EOS improved the untranslated density predictions significantly.

In addition, improvements were observed for other thermodynamic property predictions. Figure 24 and Figure 25 compare the predicted densities and residual enthalpies for water at 253.31 bar (250 atm) from ambient to 500°C, which is of interest for SCWO processing. Figure 26 and Figure 27 present the results for water at 400°C from 1 to 400 bar. Isobar and isotherm results are summarized in Table 14 and Table 15 and show that the proposed HSVTvdW EOS is reasonably accurate for pure compounds in both the supercritical and subcritical regions of water. In some regions residual-property predictions may exhibit inaccuracies as large as 30%.

Figure 28 and Figure 29 present several pure water isotherms and demonstrate that the HSVTvdW EOS is accurate for density and residual enthalpy, respectively, even though the pure-component parameters (α_A, α_B and t) were regressed only to vapor–liquid coexistence data. However, there is an improvement in high-pressure predictions when high-pressure data are used

in the determination of pure-component parameters. This improvement may outweigh the decrease in accuracy of coexistence-curve predictions. However, for a number of species including carbon dioxide, methane and nitrogen, this decrease may be acceptable since their coexistence-curve temperatures and pressures may not correspond to the temperatures and pressures of interest. So if the pure-component parameters that are regressed to coexistence data result in unsatisfactory predictions, it is recommended that these parameters be re-regressed using available data in an attempt to improve the EOS accuracy in the region of interest.

The constants used in this analysis are given in Table 8. For an in depth examination of the HSVTvdW EOS, including the regression data and a sensitivity analysis of the pure-component parameters, see Kutney *et al.* (1996).

Table 9. Comparison of saturated vapor-pressure predictions for several EOSs

Compound	Range	EOS average absolute percentage deviation[a]				
		HSVTvdW	PR	VTPR[b]	RKS	VTRKS
CH_4	$0.48 < T_r < 0.99$	0.1 ± 0.1	1.5 ± 0.7	–	1.9 ± 1.9	1.9 ± 2.0
CO_2	$0.71 < T_r < 1.00$	1.5 ± 1.5	0.7 ± 0.5	–	0.4 ± 0.2	0.4 ± 0.2
C_2H_4	$0.37 < T_r < 0.99$	1.0 ± 2.0	4.8 ± 7.5	–	1.0 ± 0.5	1.0 ± 0.5
H_2O	$0.42 < T_r < 1.00$	0.3 ± 0.3	4.2 ± 5.3	–	7.1 ± 8.7	0.5 ± 0.4^c
NH_3	$0.54 < T_r < 0.96$	0.5 ± 0.3	0.2 ± 0.1	–	1.3 ± 1.1	1.3 ± 1.1
N_2	$0.50 < T_r < 0.98$	0.3 ± 0.2	1.3 ± 0.6	–	1.9 ± 1.3	1.9 ± 1.3
O_2	$0.35 < T_r < 0.98$	0.4 ± 0.4	4.1 ± 3.3	–	3.3 ± 3.0	3.3 ± 3.7
	Average	0.6 ± 0.4	2.4 ± 1.4	–	2.4 ± 1.4	1.5 ± 0.7

[a] Defined as $\bar{f} = \dfrac{100}{M} \sum_{i=1}^{M} \dfrac{\left| f^{calc} - f^{data} \right|}{f^{data}}$, where f is the parameter of interest, in this case the

vapor pressure, M is the number of data points and $\pm x$ indicates the root-mean-square uncertainty.

[b] Not calculated due to thermodynamic inconsistency.

[c] For water, the VTRKS EOS used the polar α equation given by Eq. (38).
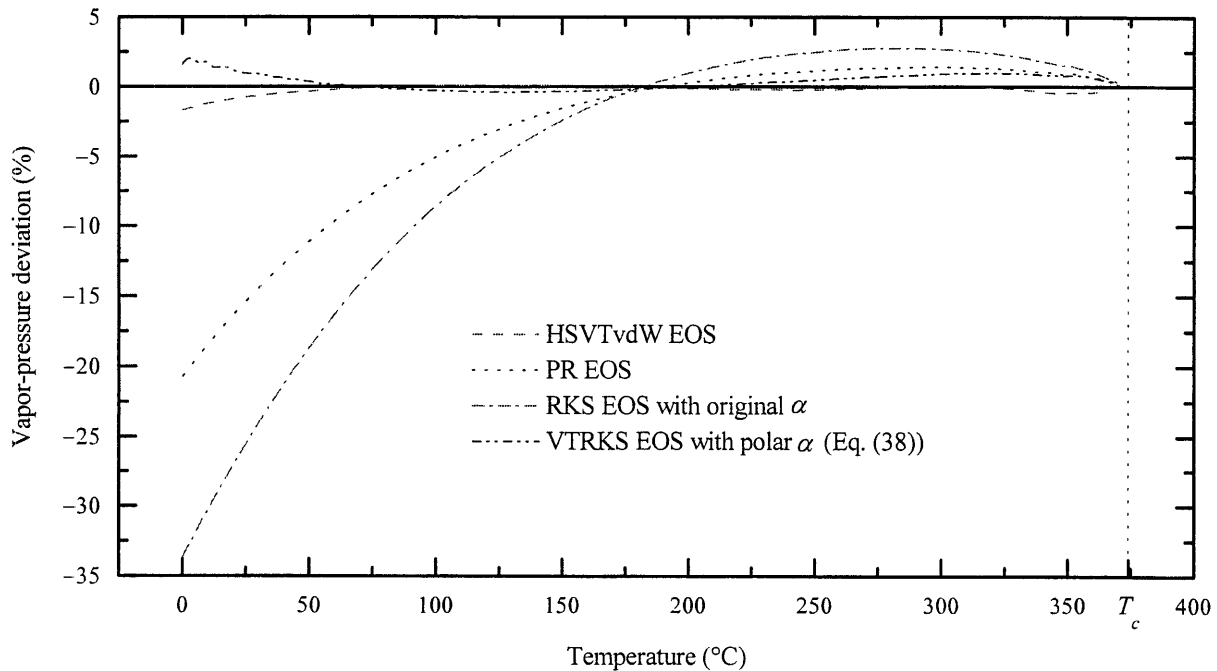
Figure 18. Deviations of the predicted vapor pressure for pure water using the 1967 ASME steam table as the reference.

Table 10. Comparison of vaporization enthalpy predictions for several EOSs[a]

Compound	Range	EOS average absolute percentage deviation				
		HSVTvdW	PR	VTPR[b]	RKS	VTRKS[b]
CH_4	$0.48 < T_r < 0.99$	1.7 ± 2.7	2.0 ± 3.5	–	2.9 ± 3.0	–
CO_2	$0.71 < T_r < 1.00$	3.4 ± 4.2	2.9 ± 4.5	–	3.5 ± 4.6	–
C_2H_4	$0.37 < T_r < 0.99$	1.9 ± 2.3	2.2 ± 2.5	–	1.6 ± 2.4	–
H_2O	$0.42 < T_r < 1.00$	2.3 ± 3.1	3.7 ± 2.8	–	5.1 ± 3.0	–
NH_3	$0.54 < T_r < 0.96$	3.0 ± 2.0	2.9 ± 2.0	–	4.0 ± 1.8	–
N_2	$0.50 < T_r < 0.98$	2.0 ± 3.0	1.8 ± 3.3	–	3.0 ± 2.8	–
O_2	$0.35 < T_r < 0.98$	1.7 ± 2.6	1.7 ± 3.1	–	2.8 ± 2.6	–
	Average	2.3 ± 1.1	2.5 ± 1.2	–	3.3 ± 1.1	–

[a] Defined as $\Delta H^{vap} = H^r_{satV} - H^r_{satL}$.

[b] Not calculated due to thermodynamic inconsistency.

Table 11. Comparison of saturated vapor density ρ_{satv} predictions for several EOSs

Compound	Range	EOS average absolute percentage deviation				
		HSVTvdW	PR	VTPR[a]	RKS	VTRKS
CH_4	$0.48 < T_r < 0.99$	1.6 ± 2.2	3.5 ± 0.8	3.8 ± 1.4	2.0 ± 1.7	2.8 ± 2.0
CO_2	$0.71 < T_r < 1.00$	2.8 ± 2.4	1.5 ± 0.8	2.6 ± 2.0	2.0 ± 1.3	1.9 ± 1.6
C_2H_4	$0.37 < T_r < 0.99$	2.7 ± 3.7	4.6 ± 5.9	–[b]	1.3 ± 1.6	1.9 ± 1.8
H_2O	$0.42 < T_r < 1.00$	2.8 ± 5.5	5.7 ± 4.9	4.9 ± 5.2	8.5 ± 8.4	1.9 ± 1.0
NH_3	$0.54 < T_r < 0.96$	2.5 ± 1.7	3.6 ± 3.0	–	4.9 ± 3.7	2.9 ± 1.0
N_2	$0.50 < T_r < 0.98$	1.4 ± 2.2	1.4 ± 1.5	1.6 ± 2.0	2.4 ± 2.4	2.9 ± 2.1
O_2	$0.35 < T_r < 0.98$	3.0 ± 5.3	3.4 ± 3.2	–	4.8 ± 7.6	5.2 ± 7.3
	Average	2.4 ± 1.4	3.4 ± 1.3	3.2 ± 1.5	3.7 ± 1.8	2.8 ± 0.6

[a] Calculated for comparison, although not thermodynamically consistent since the untranslated fugacity relation was used for the determination of the saturation pressure and density.

[b] Not calculated because no translation parameter was provided by Mathias et al. (1989).

Table 12. Comparison of saturated liquid density ρ_{satL} predictions for several EOSs

Compound	Range	EOS average absolute percentage deviation				
		HSVTvdW	PR	VTPR[a]	RKS	VTRKS
CH_4	$0.48 < T_r < 0.99$	0.8 ± 0.8	8.9 ± 3.8	0.7 ± 0.8	4.6 ± 5.0	2.7 ± 1.3
CO_2	$0.71 < T_r < 1.00$	1.2 ± 1.1	4.6 ± 4.0	1.7 ± 0.8	12.8 ± 4.6	1.4 ± 1.0
C_2H_4	$0.37 < T_r < 0.99$	1.5 ± 0.8	6.8 ± 2.4	$-$[b]	6.4 ± 3.9	3.6 ± 1.6
H_2O	$0.42 < T_r < 1.00$	1.2 ± 1.6	19.0 ± 4.1	1.8 ± 1.0	28.2 ± 3.7	3.3 ± 1.9
NH_3	$0.54 < T_r < 0.96$	2.1 ± 1.2	13.6 ± 3.8	$-$	23.5 ± 3.0	1.2 ± 1.0
N_2	$0.50 < T_r < 0.98$	0.9 ± 0.8	9.7 ± 3.9	0.9 ± 0.6	3.8 ± 4.7	2.5 ± 1.1
O_2	$0.35 < T_r < 0.98$	0.8 ± 0.7	9.8 ± 3.7	$-$	3.4 ± 4.6	2.8 ± 1.2
	Average	1.2 ± 0.4	10.3 ± 1.4	1.3 ± 0.4	11.8 ± 1.6	2.5 ± 0.5

[a] Calculated for comparison, although not thermodynamically consistent since the untranslated fugacity relation was used for the determination of the saturation pressure and density.

[b] Not calculated because no translation parameter was provided by Mathias et al. (1989).
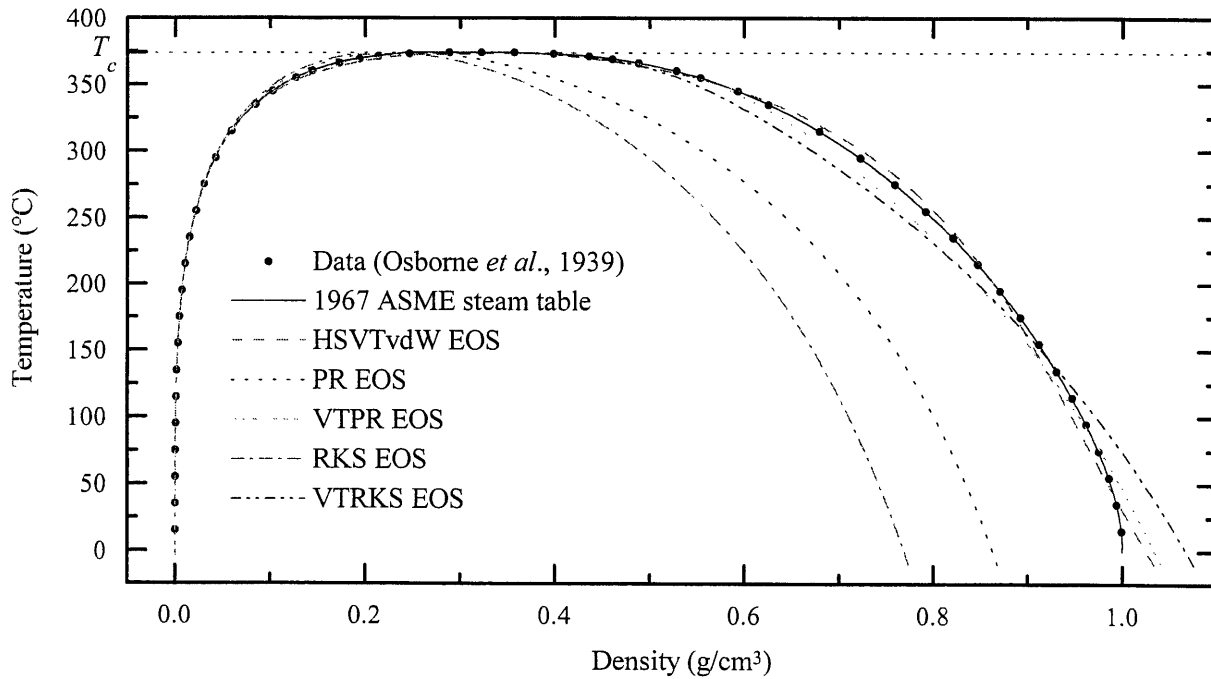
Figure 19. Saturated density comparisons for pure water.
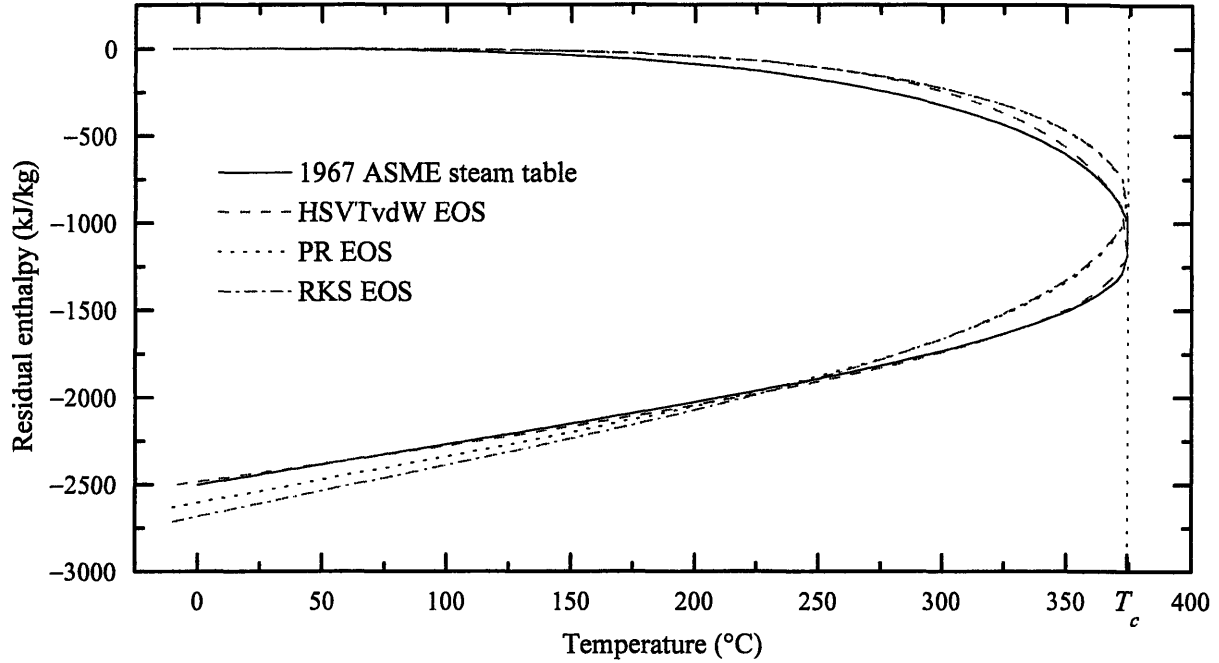
Figure 20. Residual enthalpy comparisons for saturated pure water.
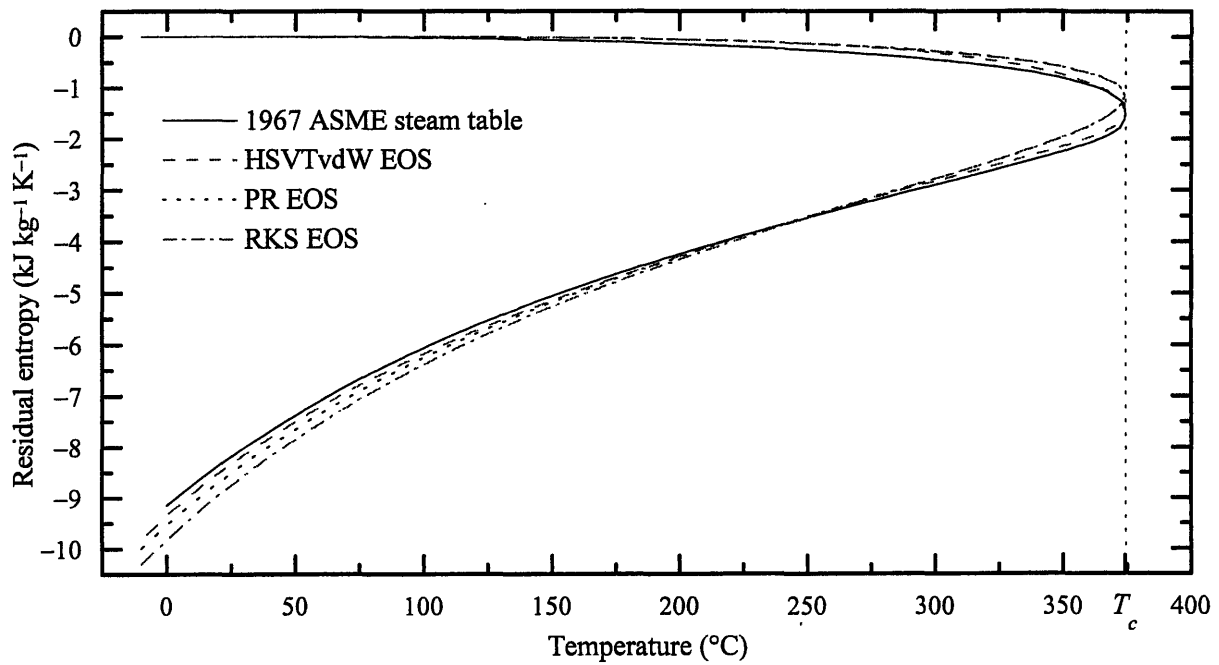
Figure 21. Residual entropy comparisons for saturated pure water.
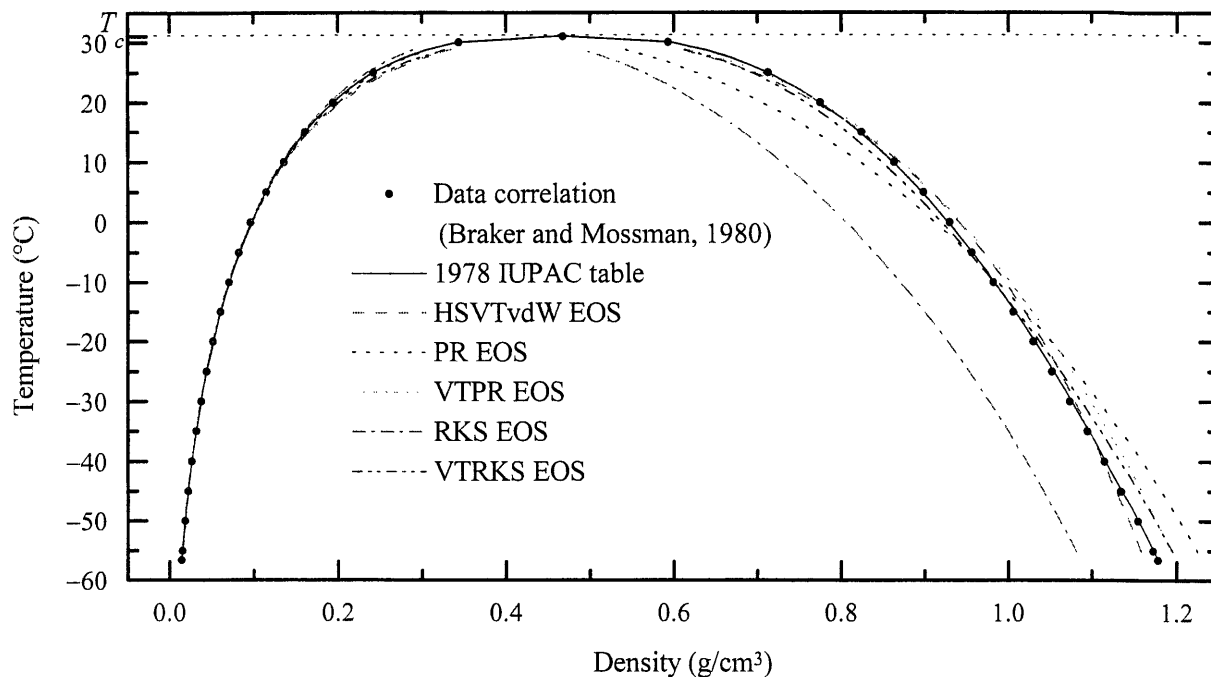
Figure 22. Saturated density comparisons for pure carbon dioxide (IUPAC, 1978; Braker and Mossman, 1980).
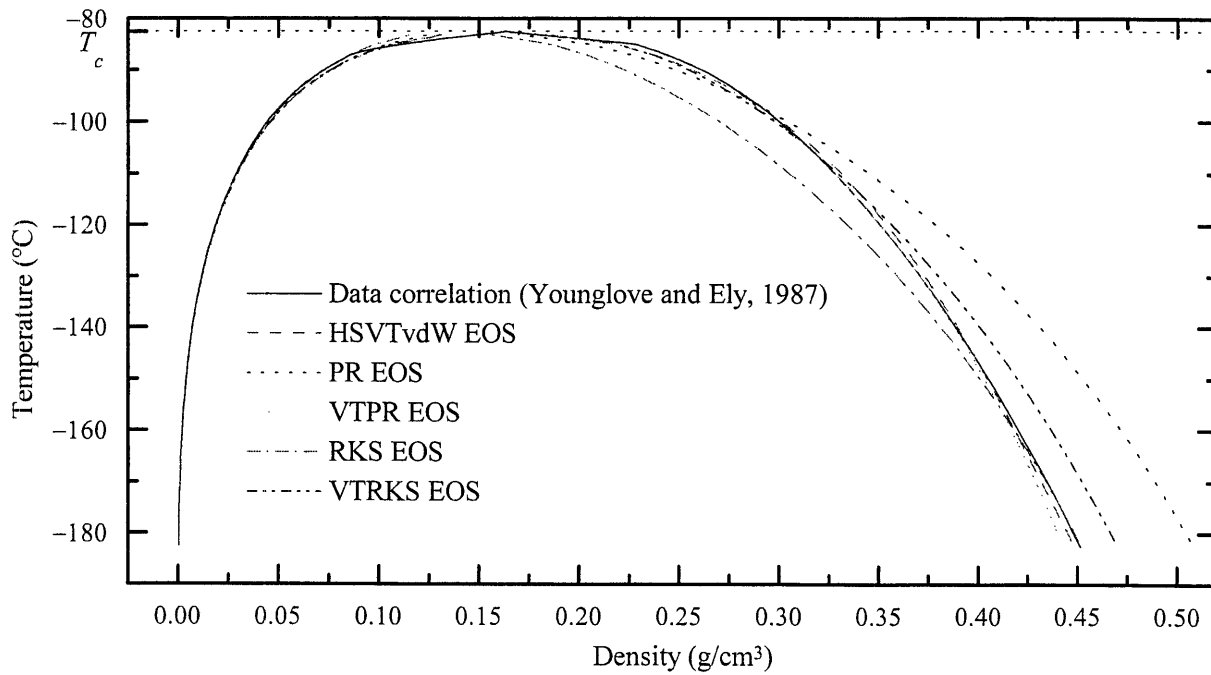
Figure 23. Saturated density comparisons for pure methane (Younglove and Ely, 1987).

Table 13. Comparison of density predictions for several EOSs at high pressures

Compound	Range	EOS average absolute percentage deviation				
		HSVTvdW	PR	VTPR	RKS	VTRKS
CH_4 (250 bar)	$1.15 < T_r < 3.25$	12.6 ± 4.2	0.9 ± 1.0	0.7 ± 0.2	4.3 ± 1.0	15.6 ± 3.4
CO_2 (250 bar)	$0.76 < T_r < 2.53$	10.2 ± 4.8	3.0 ± 1.2	1.7 ± 0.6	7.3 ± 2.3	3.3 ± 6.6
C_2H_4 (300 bar)	$0.89 < T_r < 1.42$	9.2 ± 3.0	5.2 ± 3.2	$-$[a]	4.5 ± 1.7	11.8 ± 11.7
H_2O (253 bar)	$0.42 < T_r < 1.19$	2.4 ± 3.3	15.2 ± 8.1	3.8 ± 3.0	22.9 ± 10.2	4.1 ± 2.5
N_2 (300 bar)	$1.74 < T_r < 6.02$	10.9 ± 3.7	1.7 ± 0.6	0.4 ± 0.3	1.8 ± 1.4	0.5 ± 0.4
Average		9.1 ± 1.8	5.2 ± 1.8	1.6 ± 0.8	8.2 ± 2.1	7.1 ± 2.8

[a] Not calculated because a translation parameter is not provided by Mathias *et al.* (1989).

Table 14. Comparison of isobaric enthalpy difference predictions for several EOSs at high pressures[a]

Compound	EOS average absolute percentage deviation				
	HSVTvdW	PR	VTPR[b]	RKS	VTRKS[b]
CH_4 (250 bar)	15.05	1.59	$-$	2.58	$-$
CO_2 (250 bar)	5.83	1.06	$-$	2.05	$-$
C_2H_4 (300 bar)	31.77	0.51	$-$	2.32	$-$
H_2O (253 bar)	2.13	2.09	$-$	4.83	$-$
N_2 (300 bar)	2.11	1.50	$-$	0.95	$-$
Average	11.38 ± 12.57	1.35 ± 0.60	$-$	2.55 ± 1.28	$-$

[a] Defined as $\Delta H = H(500°C, \sim 250 \text{ bar}) - H(25°C, \sim 250 \text{ bar})$.

[b] Not calculated due to thermodynamic inconsistency.
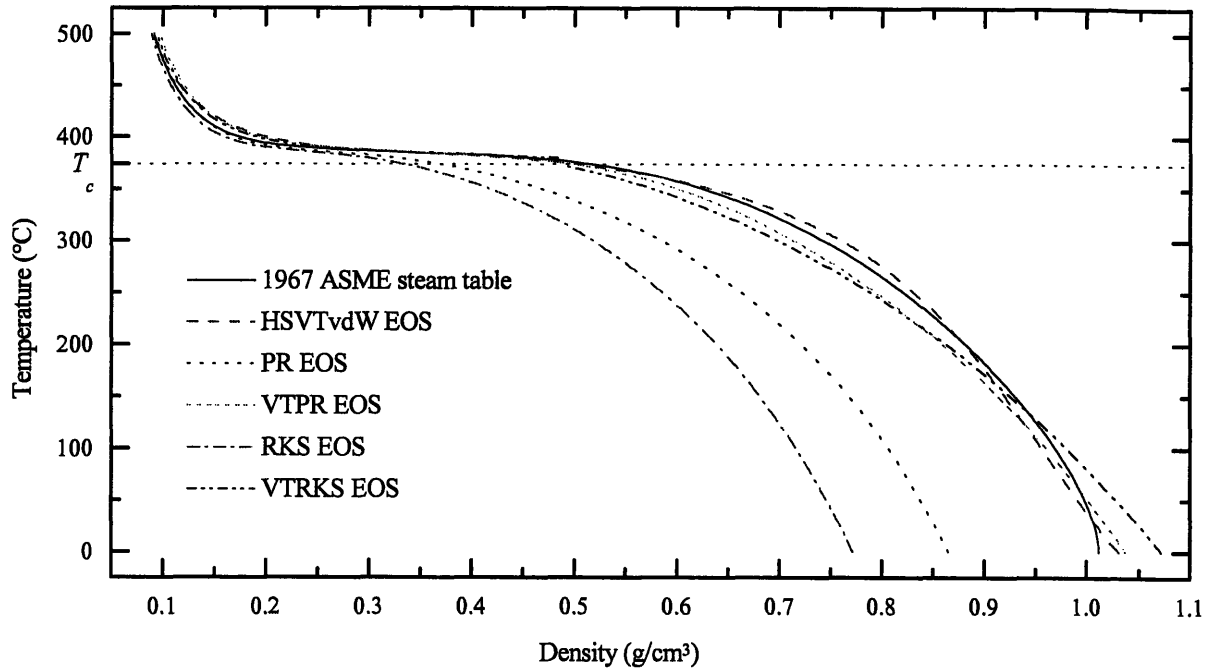
Figure 24. Isobaric density comparisons for pure water at P = 253.31 bar.
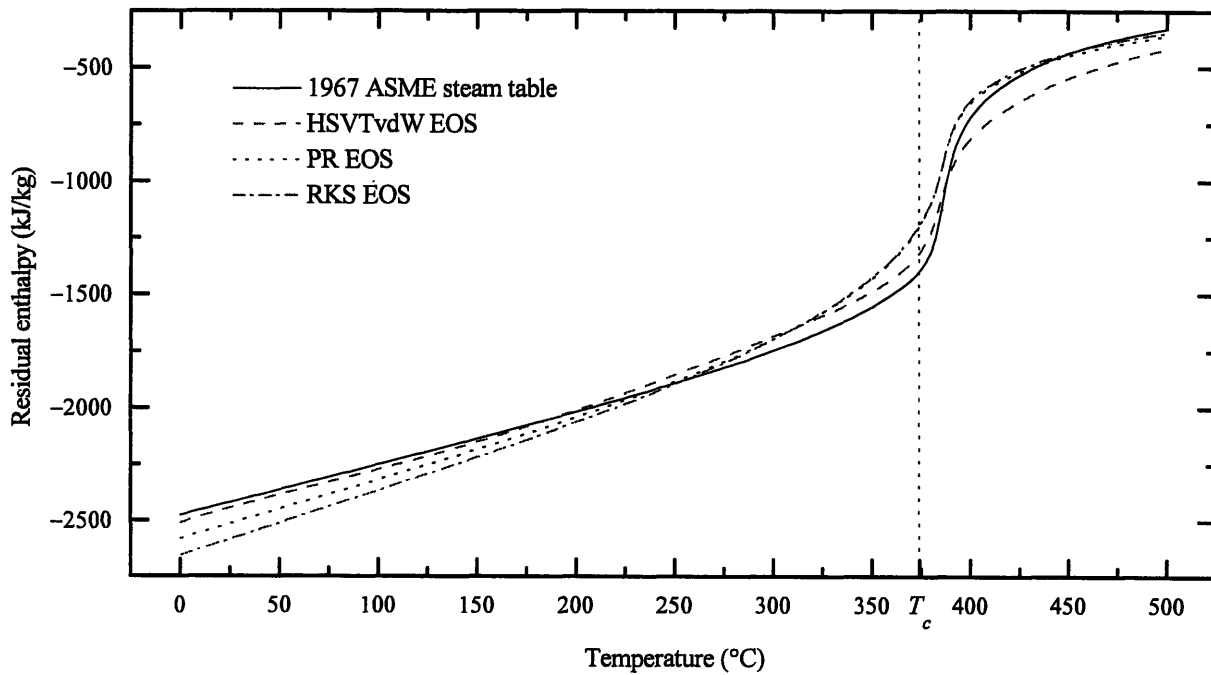
Figure 25. Residual enthalpy comparisons for pure water at P = 253.31 bar.
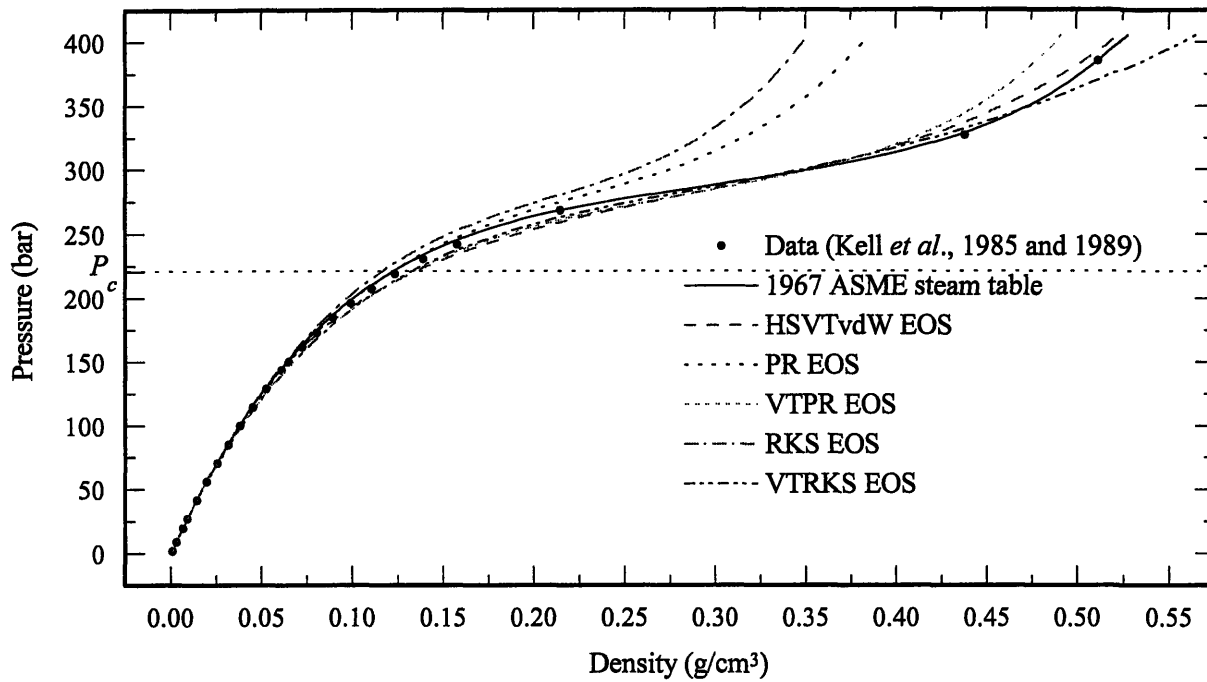
Figure 26. Isothermal density comparisons for pure water at $T = 400°C$.
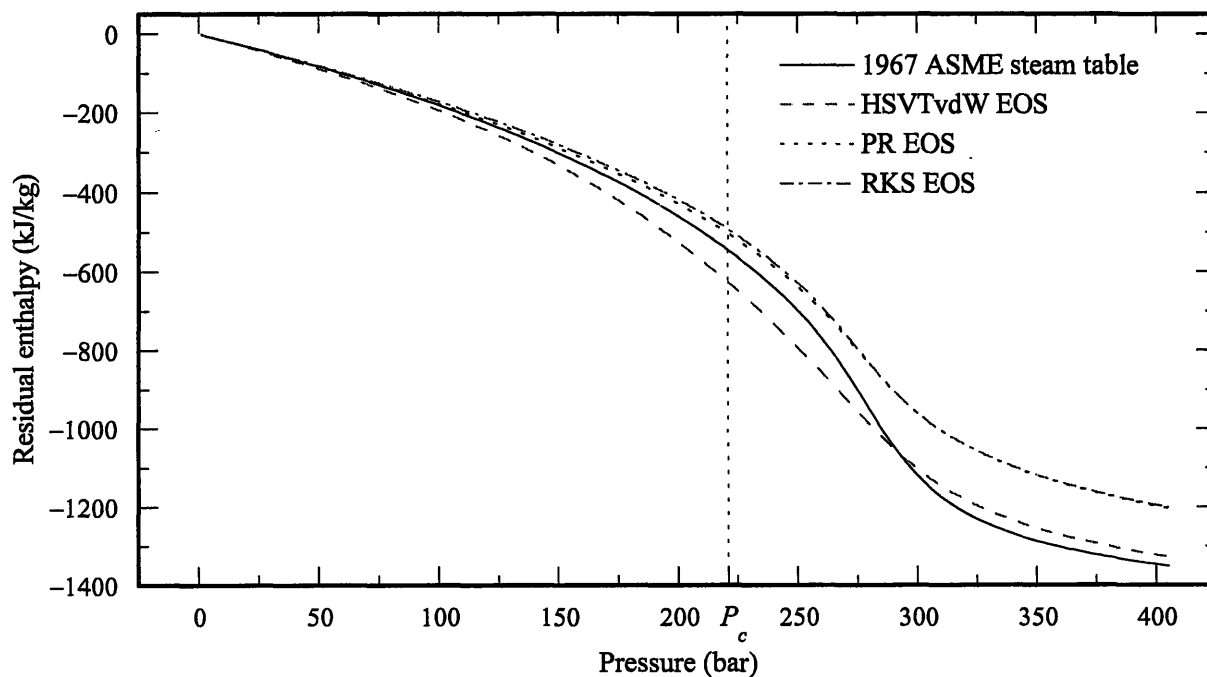
Figure 27. Residual enthalpy comparisons for pure water at $T = 400°C$.
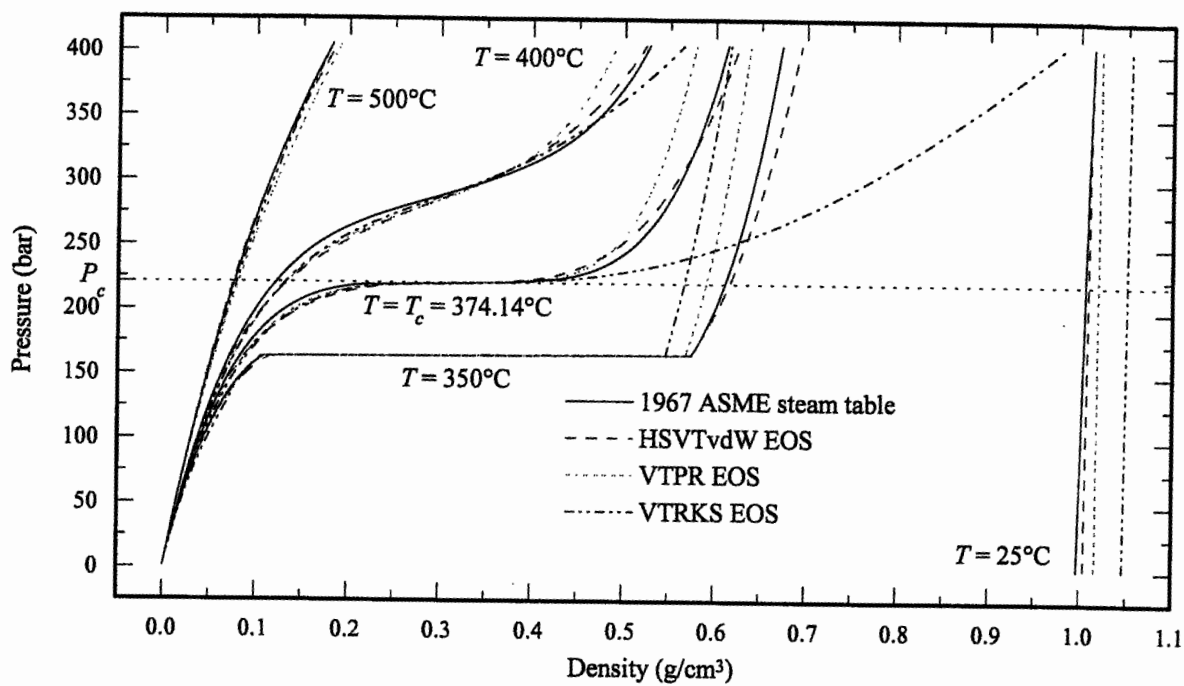
Figure 28. Volume-translated density comparisons for pure water along several isotherms.
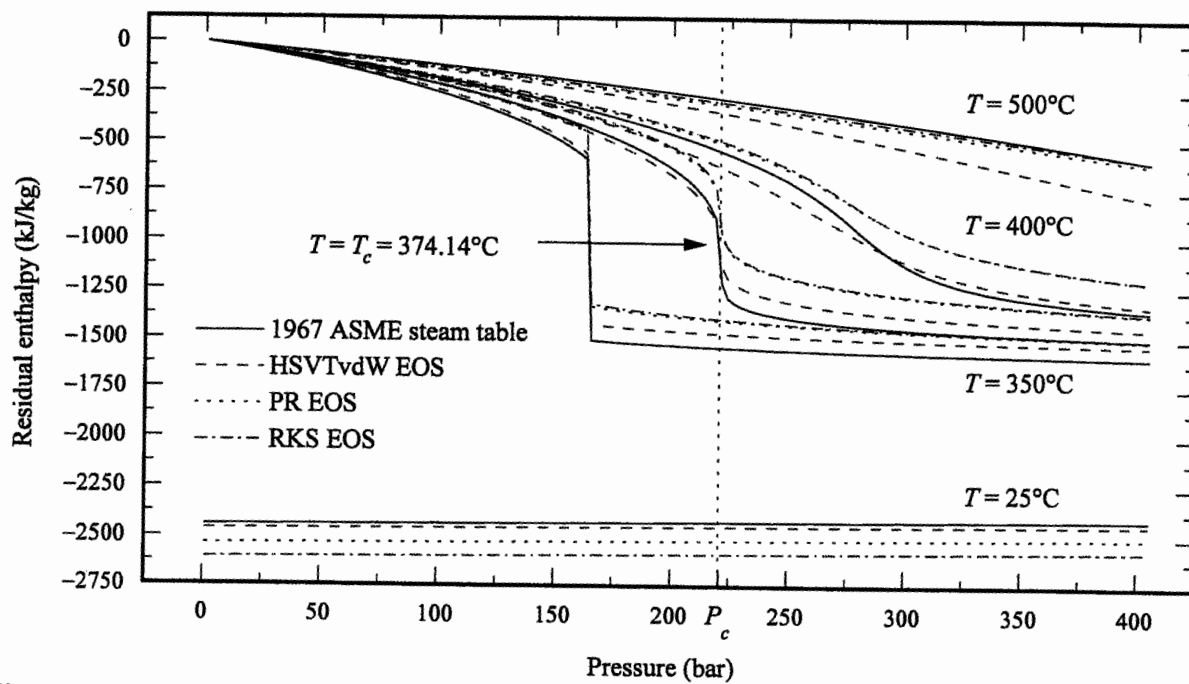
Figure 29. Residual enthalpy comparisons for pure water along several isotherms.

I.1.6 Conclusions

The analysis indicates that the new hard-sphere volume-translated equation of state (HSVTvdW EOS) can be used for accurate predictions of densities and thermodynamic properties over a wide range of temperatures and pressures for pure materials such as carbon dioxide, methane and water. Ammonia, ethylene, nitrogen and oxygen have also been accurately modeled with the HSVTvdW EOS (Kutney *et al.*, 1996). Densities and residual properties are predicted in a thermodynamically consistent manner with average errors of 5% and 7%, respectively, and within 13% and 32%, respectively, over temperatures and pressures ranging from ambient to 500°C and 400 bar. For each pure component i, the critical temperature T_{ci} and pressure P_{ci} are required for determining a_{ci} and b_i. The volume translation requires the experimental critical volume V_{ci} and a parameter t_i which is correlated with the liquid or vapor-liquid coexistence density. Two more parameters (α_{Ai} and α_{Bi}) are used to provide temperature dependence and are fit to coexistence vapor-pressure data.

In addition to requiring accurate predictions for pure materials, another important feature of a successful equation of state is its ability to simulate thermodynamic properties of mixtures. For supercritical-water systems, these mixtures would most likely contain low concentrations of gases and hydrocarbons. With the pure species analysis complete, the analysis of thermodynamic properties can now begin for supercritical-water systems with additional components such as these.

1.1.7 References

Ahlers, J., and Gmehling, J. (2002) "Development of a universal group contribution equation of state iii. prediction of vapor-liquid equilibria, excess enthalpies, and activity coefficients at infinite dilution with the VTPR model." *Ind. Eng. Chem. Res.*, **41**, 5890–5899.

Alder, B.J. (1964) "Studies in molecular dynamics. iii. a mixture of hard spheres." *J. Chem. Phys.*, **40**, 2724–2730.

Aspen Technology (1994) Physical Properties Methods and Models – Reference Manual, Volume 2, Cambridge, MA.

Benedict, M., Webb, G.B. and Rubin, L.C. (1940) "An empirical equation for thermodynamic properties of light hydrocarbons and their mixtures." *J. Chem. Phys.*, **8**, 334–345.

Braker, W. and Mossman, A.L. (1980) *Matheson Gas Data Book*, 6th ed., Lyndurst, NJ.

Brennecke, J.F. and Eckert, C.A. (1989) "Phase equilibria for supercritical process design." *AIChE J.*, **35**, 1409–1427.

Bruno, T.J. and Ely, J.F. (1991) *Supercritical Fluid Technology: Review in Modern Theory and Applications*, CRC Press, Boca Ratan, FL.

Carnahan, N.F. and Starling, K.E. (1969) "Intermolecular repulsions and the equation of state for fluids." *J. Chem. Phys.*, **51**, 635–636.

Chou, G.F. and Prausnitz, J.M. (1989) "A phenomenological correction to an equation of state for the critical region." *AIChE J.*, **35**, 1487–1496.

de Sant' Ana, H.B. and Ungerer, P. (1999) "Evaluation of an improved volume translation for the prediction of hydrocarbon volumetric properties." *Fluid Phase Equilibria*, **154**, 193–204.

Haar, L., Gallagher, J.S. and Kell, G.S. (1984) *NIST standard reference database 10–steam tables*, Hemisphere Pub. Corp., New York, NY.

Heilig, M. and Franck, E.U. (1989) "Calculation of thermodynamic properties of binary fluid mixtures to high temperatures and high pressures." *Ber. Busenges. Phys. Chem.*, **93**, 898–905.

Henderson, D.J. (1979) "Practical calculations of the equation of state of fluids and fluid mixtures using perturbation theory and related theories." *ACS Adv. Chem. Ser., No. 182*, **1–30**.

Hirschfelder, J.O., Curtiss, C.F. and Bird, R.B. (1964) *Molecular Theory of Gases and Liquids*, 2nd ed., Wiley, New York, NY.

IUPAC thermodynamic table project (1978) "International thermodynamic tables of the fluid state 3: carbon dioxide." Pergamon, Oxford.

Johnston, K.P. and Eckert, C.A. (1981) "An analytical Carnahan-Starling-van der Waals model for solubility of hydrocarbon solids in supercritical fluids." *AIChE J.*, **27**, 773–779.

Johnston, K.P., Ziger, D.H. and Eckert, C.A. (1982) "Solubilities of hydrocarbon solids in supercritical fluids: the augmented van der Waals treatment." *Ind. Eng. Chem. Fund.*, **21**, 191–197.

Kell, G.S., McLaurin, G.E. and Whalley, E. (1985) "The PVT properties of water v: the fluid to 1 kbar at 350–500°C and along the saturation line from 150 to 350°C." *Phil. Trans. R. Soc. Lond. A*, **315**, 235–246.

Kell, G.S., McLaurin, G.E. and Whalley, E. (1989) "PVT properties of water VII: vapour densities of light and heavy water from 150 to 500°C." *Proc. R. Soc. Lond. A*, **425**, 49–71.

Kutney, M.C., Dodd, V.S., Smith, K.A., Herzog, H.J. and Tester, J.W. (1996) "Equations of state for supercritical process modeling." MIT Energy Laboratory, Cambridge, MA, MIT–EL 94–003 (revised).

Lee, B.I. and Kesler, M.G. (1975) "A generalized thermodynamic correlation based on three-parameter corresponding states." *AIChE J.*, **21**, 510–527.

Martin, J.J. (1967) "Equations of state." *Ind. Eng. Chem.*, **59**, 34–56.

Martin, J.J. and Stanford, T.G. (1974) "Development of high precision equations of state for wide ranges of density utilizing a minimum of input information: example argon." *AIChE Symp. Ser.*, **70**, 1–13.

Martin, J.J. (1979) "Cubic equation of state–which?" *Ind. Eng. Chem. Fund.*, **18**, 81–97.

Mathias, P.M., Naheiri, T. and Oh, E.M. (1989) "A density correction for the Peng-Robinson equation of state." *Fluid Phase Equilibria*, **47**, 77–87.

Mathias, P.M. and Klotz, H.C. (1994) "Take a closer look at thermodynamic property models." *Chem. Eng. Prog.*, **90**, 67–75.

Osborne, N.S., Stimson, H.F. and Ginnings, D.C. (1939) "Thermal properties of saturated water and steam." *J. Res. NBS*, **23**, 261–270.

Peneloux, A., Rauzy, E. and Freze, R. (1982) "A consistent correction for Redlich-Kwong-Soave volumes." *Fluid Phase Equilibria*, **8**, 7–23.

Peng, D.-Y. and Robinson, D.B. (1976) "New two-constant equation of state." *Ind. Eng. Chem. Fund.*, **15**, 59–64.

Pfohl, O. (1999) "Evaluation of an improved volume translation for the prediction of hydrocarbon volumetric properties." *Fluid Phase Equilibria*, **163**, 157–159.

Polishuk, I., Wisniak, J., and Segura, H. (2000) "A novel approach for defining parameters in a four-parameter EOS." *Chem. Eng. Sci.*, **55**, 5705–5720.

Polishuk, I., Wisniak, J., Segura, H., and Kraska, T. (2002) "About the relation between the empirical and the theoretically based parts of van der Waals-like equations of state." *Ind. Eng. Chem. Res.*, **41**, 4414–4421.

Redlich, O. and Kwong, J.N.S. (1949) "On the thermodynamics of solutions." *Chem. Rev.*, **44**, 233–244.

Ree, F.H. and Hoover, W.G. (1967) "Seventh virial coefficients for hard spheres and hard disks. *J. Chem. Phys.*, **46**, 4181–4197.

Reid, R.C., Prausnitz, J.M. and Poling, B.E. (1987) *The Properties of Liquids and Gases*, McGraw-Hill, 4th ed., New York, NY.

Rivkin, S.L., Akhundov, T.S., Kremenevskaya, E.A., and Asadullaeva, N.N. (1966) *Teploenergetika*, **13**, 59–76.

Shah, V.M., Bienkowski, P.R., and Cochran, H.D, (1994) "Generalized quartic equation of state for pure nonpolar fluids." *AIChE J.*, **40**, 152–159.

Soave, G.S. (1972) "Equilibrium constants from a modified Redlich-Kwong equation of state." *Chem. Eng. Sci.*, **27**, 1197–1203.

Soave, G.S. (1979) "Application of a cubic equation of state to vapor-liquid equilibria of systems containing polar compounds." *Int. Chem. E. Symp. Ser., No. 56*, **12**, 1–16.

Soave, G.S. (1984) "Improvement of the van der Waals equation of state." *Chem. Eng. Sci.*, **39**, 357–369.

Starling, K.E. and Han, M.S. (1972) "Thermo data refined for LPG." *Hydrocarbon Processing*, **51**, 129–132.

Starling, K.E. (1973) *Fluid Thermodynamic Properties for Light Petroleum Systems*, Gulf Publishing, Houston, TX.

Thiele, E. (1963) "Equation of state for hard spheres." *J. Chem. Phys.*, **39**, 474–479.

Twu, C.H., Coon, J.E., Harvey, A.H. and Cunningham, J.R.. (1996) "An approach for the application of a cubic equation of state to hydrogen–hydrocarbon systems." *Ind. Eng. Chem. Res.*, **35**, 905–910.

van der Waals, J.D. (1873) "Over de continuiteit van den gas-en vloeistoftoestand." Doctoral dissertation, Leiden, Holland.

Vera, J.H. and Prausnitz, J.M. (1972) "Interpretive review–generalized van der Waals theory for dense fluids." *Chem. Eng. J.*, **3**, 1–13.

Walas, S.M. (1985) *Phase Equilibria in Chemical Engineering*, Butterworth-Heinemann, Stoneham, MA.

Wang, L.S., Ahlers, J., and Gmehling, J. (2003) "Development of a universal group contribution equation of state. 4. prediction of vapor-liquid equilibria of polymer solutions with the volume translated group contribution equation of state." *Ind. Eng. Chem. Res.*, **42**, 6205–6211.

Wertheim, M.S. (1964) "Exact solution of the Percus-Yevick integral equation for hard spheres." *Phys. Rev. Letters*, **110**, 321–323.

Yelash, L.V. and Kraska, T. (2003) "Volume-translated equations of state: empirical approach and physical relevance." *AIChE J.*, **49**, 1569–1579.

Younglove, B.A. and Ely, J.F. (1987) "Thermophysical properties of fluids. ii. methane, ethane, propane, isobutane, and normal butane." *J. Phy. Chem. Ref. Data*, **116**: 577.

I.2. Hard-Sphere, Volume-Translated van der Waals Equation of State for Mixtures

I.2.1 Introduction

Although equations of state are often used to predict pure component properties, a majority of EOSs are developed in order to model a mixture of components and to generate accurate thermodynamic properties and equilibria. For SCWO process modeling, typical mixtures include water, hydrocarbons and gases, and EOSs used for SCWO process modeling must make reliable predictions of these mixtures. At SCWO process conditions, the typical water content of these mixtures is approximately 90 wt.%.

The HSVTvdW EOS can be extended to mixtures using simple mixing and combining rules. Other groups (Huron and Vidal, 1979; Wong and Sandler, 1992; Novenario *et al.*, 1996) have recently derived theoretically correct mixing rules which try to reproduce the statistical-mechanics result, *i.e.*, a second virial coefficient with quadratic dependence on composition. These mixing rules require estimation of the excess Helmholtz free energy in an infinite pressure state using models such as the non-random, two-liquid (NRTL) model (Renon and Prausnitz, 1968). However, the use of simple mixing and combining rules has been chosen as a first step in order to determine the accuracy of the mixture HSVTvdW EOS.

I.2.2 Mixture Hard-Sphere Volume-Translated van der Waals (HSVTvdW) Equation of State

In engineering practice, it is common to use unweighted Lorentz-Berthelot combining rules to formulate mixing rules, for example:

$$a_{ij} = \sqrt{a_i a_j}\,(1 - k_{ij}) \tag{60}$$

$$b_{ij} = \frac{b_i + b_j}{2} \tag{61}$$

where b_i, b_j, a_i and a_j are pure component parameters, k_{ij} is a constant binary interaction parameter. The proposed mixing rule for the HSVTvdW EOS follows from the classical van der Waals weighted mixing rule used to represent a mixture as a pseudo single component:

$$f = \sum_{i=1}^{N} \sum_{j=1}^{N} x_i x_j f_{ij} \tag{62}$$

where f is the EOS mixture parameter of interest and f_{ij} represents the binary i-j interaction which is often based on the Lorentz-Berthelot combining rule. Although not consistent with rigorous statistical mechanics in the low density limit and not successful for all simple mixtures, the van der Waals rule has been successfully used in the modeling of non-ideal mixtures and is still widely used today (Shibata and Sandler, 1989). When Eqs. (60) and (61) are substituted into Eq. (62), the mixture is effectively reduced to a pseudo single component with

$$a = a_{mixture} = \sum_{i=1}^{N}\sum_{j=1}^{N} x_i x_j a_{ij}(1 - k_{ij}) \tag{63}$$

$$b = b_{mixture} = \sum_{i=1}^{N} x_i b_i . \tag{64}$$

For the translation parameter, the Lorentz combining rule and vdW mixing rule are adopted as suggested by Martin (1979):

$$t = t_{mixture} = \sum_{i=1}^{N} x_i t_i . \tag{65}$$

The pseudocritical mixture volume for the volume-translation equation (Eq. (54)) was obtained using the usual combining and vdW mixing rule for binaries:

$$V_{cij} = \left(\frac{\left(V_{ci}^{1/3} + V_{cj}^{1/3} \right)}{2} \right)^3 \tag{66}$$

$$V_c = V_{cmixture} = \sum_{i=1}^{N}\sum_{j=1}^{N} x_i x_j V_{cij} . \tag{67}$$

These pseudo parameters are then used in the EOS and property equations to predict mixture densities and thermodynamic properties. These combining and mixing rules are reasonably accurate provided that the ratio of the component diameters is not too large. At this time, preliminary results indicate that mixture property predictions are not sensitive to the value of the constant k_{ij}.

To be theoretically consistent with respect to hard spheres, one cannot simply substitute Eqs. (63) and (64) into the HSVTvdW EOS (Eq. (49)) since the Carnahan-Starling result (Eq. (11) or (24)) used in the EOS was developed for mixtures of hard spheres with uniform diameter

σ. For mixtures of fluids with varying sizes of hard spheres, the theoretical mixture result, which was developed independently by Boublik (1970) and by Mansoori *et al.* (1971), should be used (Dimitrelis and Prausnitz, 1986):

$$P^{HS} = \frac{RT}{V} \left(\frac{1 + \left(\frac{3DE}{F} - 2 \right)y + \left(\frac{3E^3}{F^2} - \frac{3DE}{F} + 1 \right)y^2 - \left(\frac{E^3}{F^2} \right)y^3}{(1-y)^3} \right) \tag{68}$$

when the following pseudo volume parameter and mixing rules obtained with Eq. (62) are employed:

$$b^{HS} = \frac{2\pi N_a}{3} F \tag{69}$$

$$D = \sum_{i=1}^{N} x_i \sigma_i \tag{70}$$

$$E = \sum_{i=1}^{N} x_i \sigma_i^2 \tag{71}$$

$$F = \sum_{i=1}^{N} x_i \sigma_i^3 . \tag{72}$$

A comparison of the Boublik-Mansoori (Eq. (68)), Carnahan-Starling (Eq. (11) or (24)) and the vdW repulsive term results (Eq. (15)) and the Molecular Dynamic simulations of Alder (1964) for an equimolar binary hard-sphere mixture with $\sigma_j / \sigma_i = 3.0$ is presented in Figure 30. Note that the ratio of $\sigma_j / \sigma_i = 3.0$ is unusually large for real mixtures and was used to exaggerate the differences. For $\sigma_j / \sigma_i = 1.0$, the Boublik-Mansoori result reduces to the Carnahan-Starling
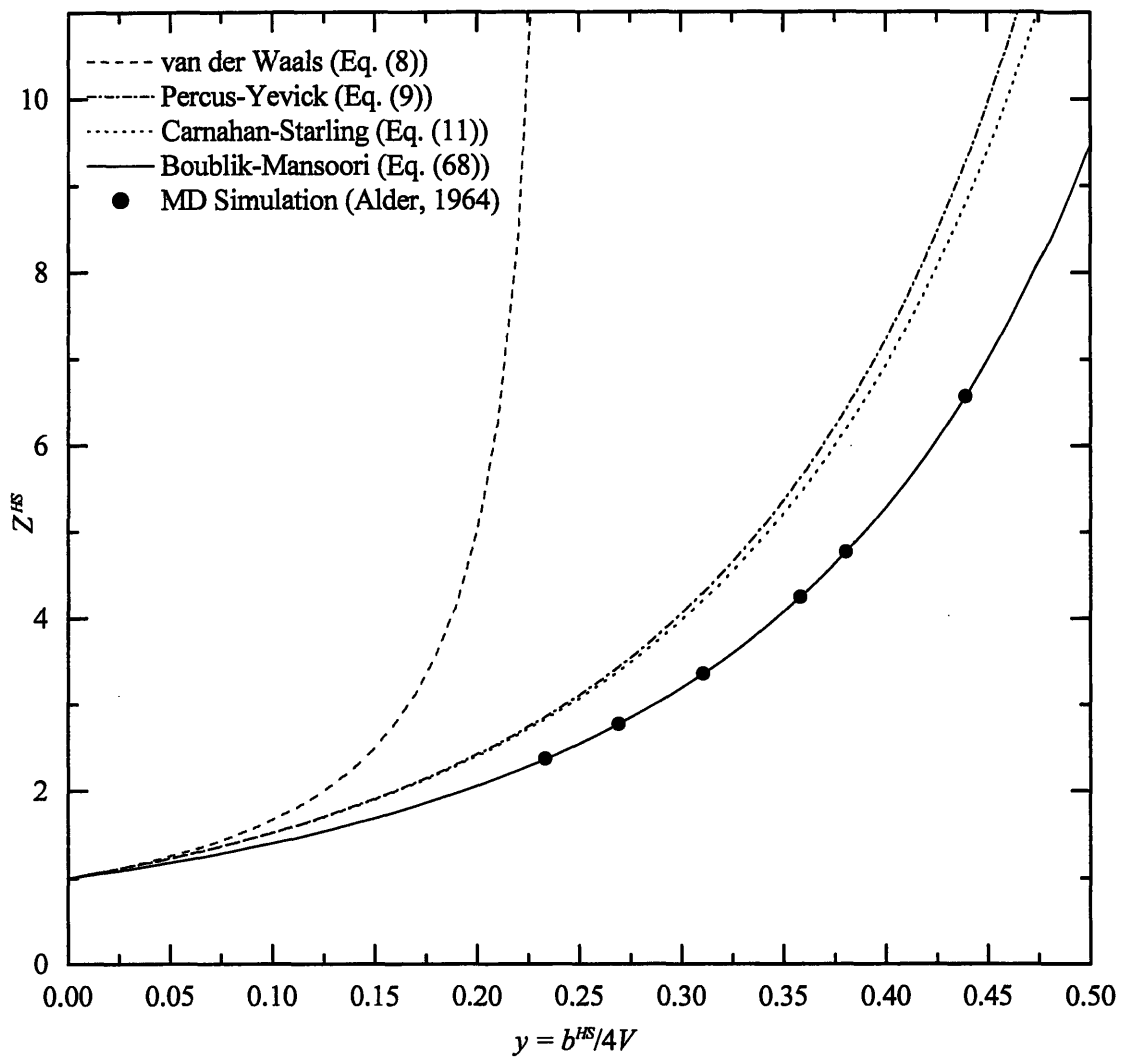
Figure 30. Comparison of the predicted hard-sphere compressibility factor for an equimolar binary mixture with $\sigma_j/\sigma_i = 3.0$.

result, as expected. So, to be consistent and more accurate for mixtures, the repulsive term of the newly developed EOS should use the Boublik-Mansoori result:

$$P = \frac{RT}{V}\left(\frac{V^3 + b_A V^2 + b_B^2 V - b_C^3}{(V-b)^3}\right) - \frac{a}{(V+2b)^2} \tag{73}$$

where

$$b_A = 3b_D b_E - 2b \tag{74}$$

$$b_B^2 = 3b_E^3 - 3b_D b_E b + b^2 \tag{75}$$

$$b_C^3 = b_E^3 b \tag{76}$$

$$b_D = \sum_{i=1}^{N} x_i b_i^{1/3} \tag{77}$$

$$b_E = \sum_{i=1}^{N} x_i b_i^{2/3} \tag{78}$$

$$b = \sum_{i=1}^{N} x_i b_i \; . \tag{64}$$

When these mixing and combining rules are used in conjunction with the HSVTvdW EOS, a complete mixture EOS is formed.

I.2.3 Results

Only a few mixtures have been examined, but the ones studied are in fact relevant to SCWO process modeling. Furthermore, experimental data are required in order to regress binary interaction parameters, and these data are not always available. The two mixtures modeled are carbon dioxide and methane followed by carbon dioxide and water. For all EOSs considered here, the binary interaction parameters were fit to all of the available experimental data. Unfortunately, this method does not allow EOSs and non-regressed experimental data to be compared at other *PVT* conditions where one can judge how accurate the EOSs are. Ideally, parameters are regressed to only a single *PVT* region.

Though there are many performance tests which could be used to judge the performance of the HSVTvdW EOS for mixtures, only vapor-liquid equilibria results are shown. In addition,

one could look at other thermodynamic mixture property including mixture enthalpy and density, however, finding experimental data for comparisons is difficult if not impossible. Three carbon dioxide and methane P–x–y phase diagrams at incremented temperatures are shown in Figure 31 through Figure 33. At $-43.15°C$, there is no surprise that the PR and RKS EOS perform superbly since these EOSs are well known to accurately model this type of binary system. As for the HSVTvdW EOS, there is relatively good agreement, but the upper critical solution pressure is clearly underestimated. Without comparing experimental solution densities, it is premature to conclude that the HSVTvdW EOS performs poorly. Density differences would cause a change in the predicted critical solution temperature. At the other two temperatures ($-23.15°C$ and $-3.15°C$) compared, similar trends are seen.

Carbon dioxide and water equilibria at 200 bar are shown in Figure 34. Since ASPEN PLUS™ was unable to generate error-free PR and RKS EOS results, the HSVTvdW EOS was the only EOS compared with zeroed and regressed binary interaction parameters. The HSVTvdW EOS also had ASPEN PLUS™ flash errors and for this reason, only limited composition results are available. Little difference is seen between the two ($k = -0.035$ and $k = 0.000$) model predictions, but this may be due to the limited number of experimental data near these predictions where the regression occurred. A general fit is shown, but probably with the same accuracy as in the carbon dioxide-methane case.

I.2.4 Conclusions

While the HSVTvdW EOS has not been thoroughly tested with a wide variety of mixtures, these limited results nonetheless confirm that the HSVTvdW EOS can be used for mixture modeling with sufficient accuracy. It also offers some advantages over other EOSs currently used in SCWO thermodynamic modeling. Pure component liquid-density HSVTvdW EOS predictions have been shown to be more accurate, along with other water properties including enthalpy and entropy. Since a majority of SCWO process modeling streams typically have more than 85% water content, the HSVTvdW EOS, which has been developed for SCWO process modeling, provides thermodynamic properties with sufficient accuracy for use in stream and property modeling. Although simple mixing and combining rules have been employed,
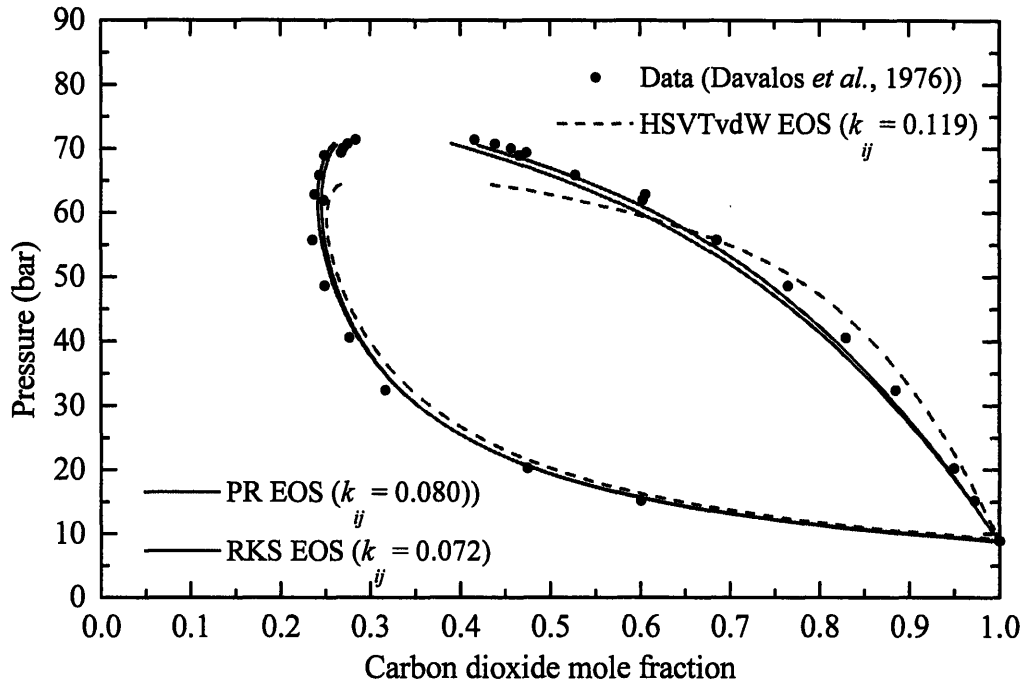
Figure 31. Binary phase diagram for a carbon dioxide and methane mixture at –43.15°C, comparing experimental data (Davalos *et al.*, 1976) and the HSVTvdW EOS, PR EOS, and RKS EOSs.
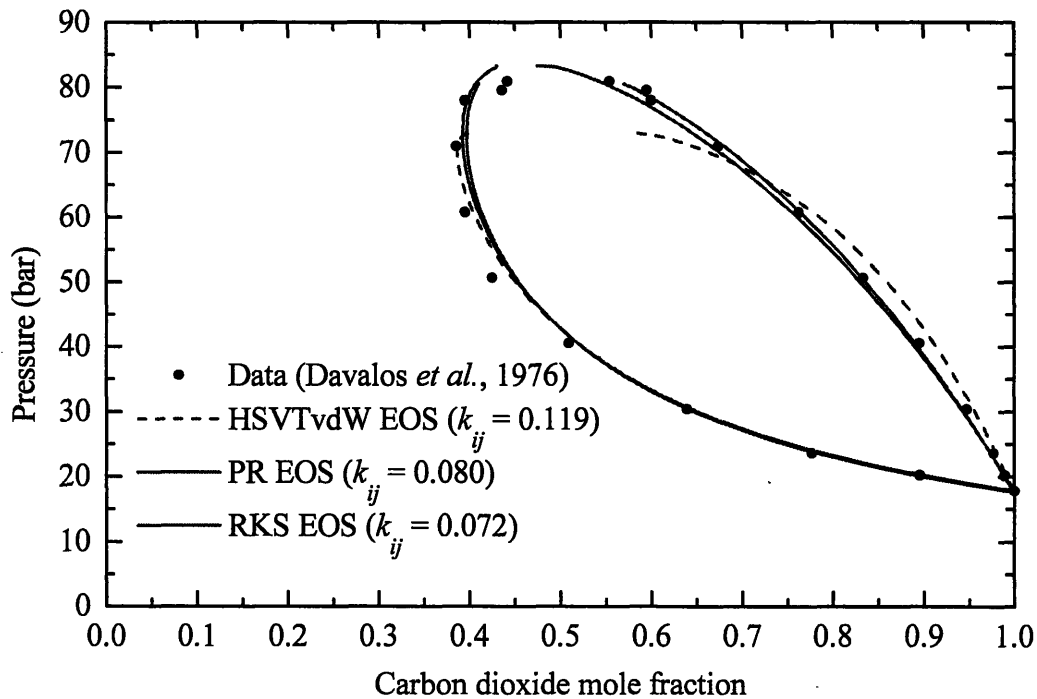
Figure 32. Binary phase diagram for a carbon dioxide and methane mixture at –23.15°C, comparing experimental data (Davalos *et al.*, 1976) and the HSVTvdW EOS, PR EOS, and RKS EOSs.
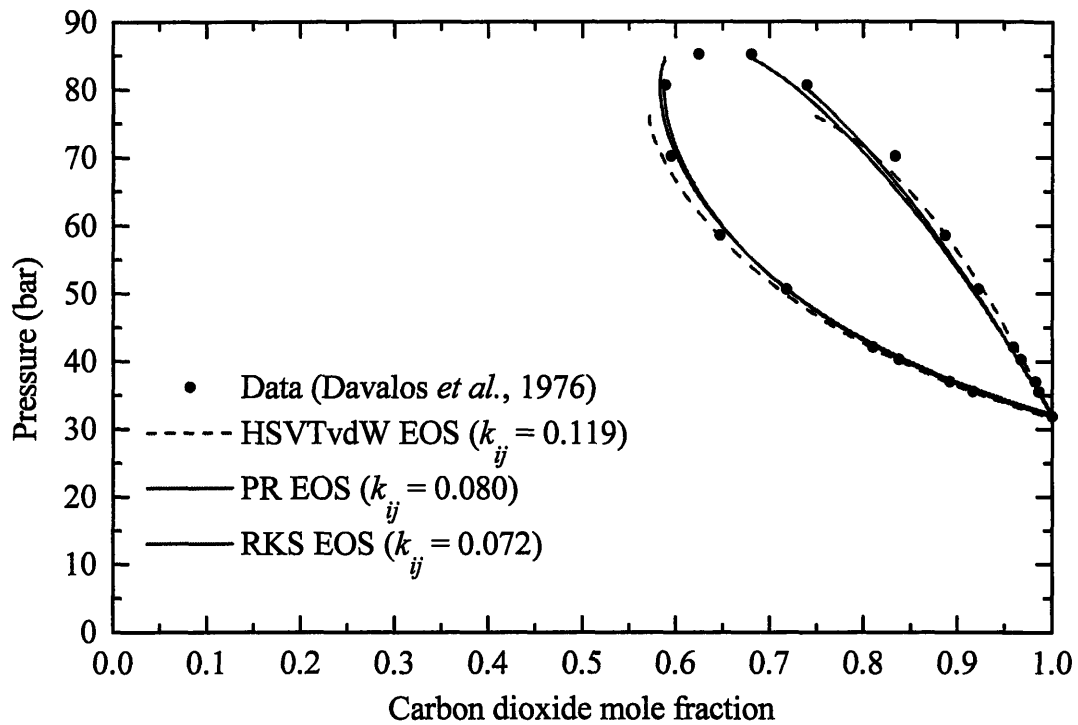
Figure 33. Binary phase diagram for a carbon dioxide and methane mixture at –3.15°C, comparing experimental data (Davalos *et al.*, 1976) and the HSVTvdW EOS, PR EOS, and RKS EOSs.
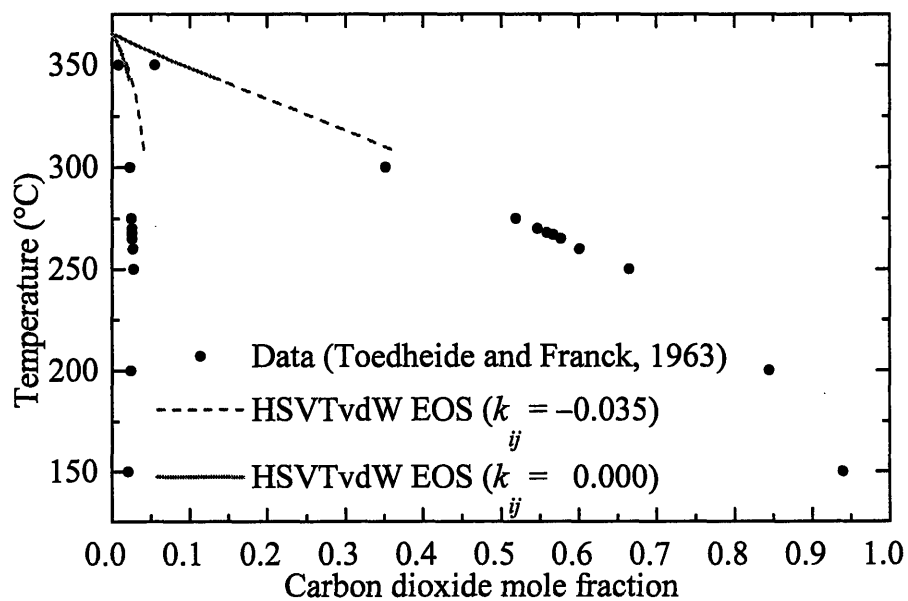
Figure 34. Binary phase diagram for a carbon dioxide and water mixture at 200 bar, comparing experimental data (Toedheide and Franck, 1963) and the HSVTvdW EOS with zeroed and regressed binary interaction parameters.

there are no significant obstacles to using more complex rules, except the time and effort required to examine their usage.

I.2.5 Recommendations

Since the HSVTvdW EOS has been originally formulated for more accurate density predictions, a complete analysis including density comparisons of the mixture phases should be completed. As already stated, an investigation of additional mixtures relevant to SCWO process modeling should be also performed. Those systems studied should include ones that are well characterized such as aqueous mixtures of:

simple feed waste, *e.g.*, methanol, ethanol, ammonia,

oxidant, *e.g.*, oxygen,

simple products, *e.g.*, nitrogen.

Once more systems are studied and compared and the performance of the HSVTvdW EOS is completely analyzed, it can then be determined if the HSVTvdW EOS is a worthwhile addition to a SCWO process modeler's simulation toolbox.

I.2.6 References

Alder, B.J. (1964) "Studies in molecular dynamics.III. a mixture of hard spheres." *J. Chem. Phys.*, **40**, 2724–2730.

Boublik, T. (1970) "Hard-sphere equation of state." *J. Chem. Phys.*, **53**, 471–472.

Davalos, J., Anderson, W.R., Phelps, R.E. and Kidnay, A.J. (1976) "Liquid-vapor equilibria at 250.00K for systems containing methane, ethane, and carbon dioxide." *J. Chem. Eng. Data*, **21 (1)**, 81–84.

Dimitrelis, D. and Prausnitz, J.M. (1986) "Comparison of two hard-sphere reference systems for perturbation theories for mixtures." *Fluid Phase Equilibria*, **31**, 1–21.

Huron, M.J. and Vidal, J. (1979) "New mixing rules in simple equations of state for representing vapor-liquid equilibria of strongly non-ideal mixtures." *Fluid Phase Equilibria*, **3**, 255–271.

Mansoori, G.A., Carnahan N.F., Starling, K.E. and Leland, T.W. (1971) "Equilibrium thermodynamic properties of the mixture of hard spheres." *J. Chem. Phys.*, **54**, 1523–1525.

Martin, J.J. (1979) "Cubic equation of state–which?." *Ind. Eng. Chem. Fund.*, **18**, 81–97.

Novenario, C.R., Caruthers, J.M. and Chao, K.C. (1996) "A mixing rule to incorporate solution model into equation of state." *Ind. Eng. Chem. Res.*, **35**, 269–277.

Renon H. and Prausnitz, J.M. (1968) "Local compositions in thermodynamic excess functions for liquid mixtures." *AIChE J.*, **14**, 135–144.

Shibata, S.K. and Sandler, S.I. (1989) "Critical evaluation of equation of state mixing rules for the prediction of high pressure phase equilibria." *Ind. Eng. Chem. Res.*, **28**, 1893–1898.

Toedheide, K. and Franck, E.U. (1963) "Two-phase range and the critical curve in the system carbon dioxide-water." *Z Physik. Chem.*, **37 (5/6)**, 387–401.

Wong, D.S.H. and Sandler, S.I. (1992) "A theoretically correct mixing rule for cubic equations of state." *AIChE J.*, **38**, 671–680.

I.3. An Analysis of Equation of State Zeno Behavior

This section documents the results of collaborative work with M. Reagan who performed Zeno molecular simulations. This joint work is documented in this dissertation, in the dissertation by Reagan (2000), and is also published in Kutney *et al.* (2000).

I.3.1 Introduction

For more than a century, researchers have recognized that fluids exhibit several regular and scalable volumetric features including the following characteristics:

- *The Theorem of Corresponding States* which states that the volumetric properties of a fluid are comparable when scaled by their critical-point values. For example, in the two-parameter corresponding states model, the compressibility factor (Z), defined in terms of the temperature (T), pressure (P), molar volume (V) or density $(\rho \equiv 1/V)$, is functionally represented by:

$$Z \equiv \frac{PV}{RT} = \frac{P}{\rho RT} = f(T_r, V_r) \quad \text{or} \quad f(T_r, \rho_r) \tag{79}$$

  where $P_r \equiv P/P_c$, $V_r \equiv V/V_c$, $\rho_r \equiv \rho/\rho_c$, and $T_r = T/T_c$ represent reduced properties.

- *The Law of Rectilinear Diameters* which states that for any species the average of vapor and liquid density is a linear function of temperature in the vapor-liquid coexistence region (Ben-Amotz and Herschbach, 1990a; Ben-Amotz and Herschbach, 1990b; Boushehri *et al.*, 1993).

- *The Tait-Murnaghan Relation* which states that the bulk modulus κ_T^{-1} of a liquid is a linear function of pressure (Boushehri *et al.*, 1993; Parsafar and Mason, 1993; Parsafar and Mason, 1994).

Another less well known empirical regularity of fluids is known as the *Zeno line* (Ben-Amotz and Herschbach, 1990a; Ben-Amotz and Herschbach, 1990b). Along the contour defined by $Z = 1$, where the compressibility factor is the same as for an ideal gas, the density of many fluids has been found to be nearly a linear function of temperature. For example, Zeno contours for water, carbon dioxide and methane are shown in Figure 35 (see Table 15 for the data that are generated from correlations which are regressed from experimental data and which are described

119
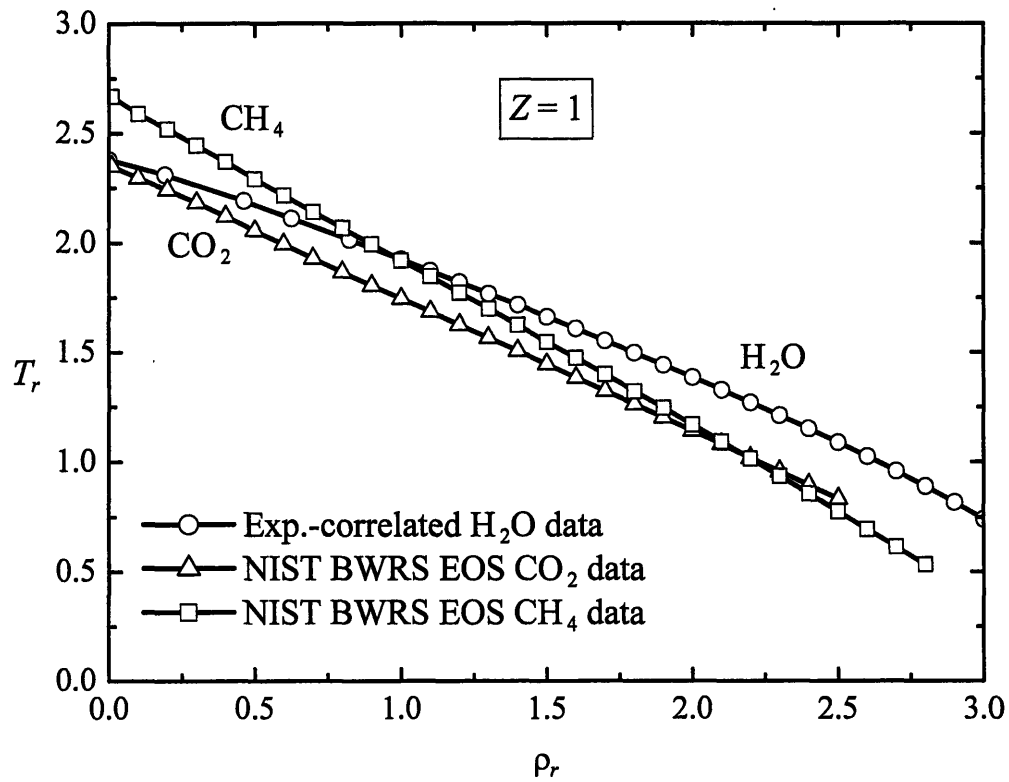
Figure 35. Experimental Zeno lines for pure H_2O, CO_2, and CH_4. Data tabulated in Table 15 from the following sources: H_2O (Haar *et al.*, 1984; ChemicaLogic, 1999), CH_4 and CO_2 (McCarty and Arp, 1992).

Table 15. Experimentally-correlated data calculated from correlations based on experimental data (Reduced properties are calculated with critical-point values given in Table 18)

ρ (g/cm³)	ρ_r	T (°C)	T_r	P (bar)	P_r	T (°C)	T_r	P (bar)	P_r	T (°C)	T_r	P (bar)	P_r	Ref
H₂O		Z = 0.75				Z = 0.90				Z = 1.00				
0.0003	0.001									1267.3	2.38	1.4	0.006	A
0.062	0.19									1222.1	2.31	366	1.66	A
0.149	0.46									1144.4	2.19	933	4.22	A
0.201	0.63									1092.6	2.11	1228	5.56	A
0.233	0.72									1060.3	2.06	1397	6.32	A
0.266	0.83									1031.1	2.02	1540	6.97	A
0.016	0.05	230.3	0.78	28.1	0.13	308.8	0.90	38.9	0.18					B
0.032	0.10	277.1	0.85	61.4	0.28	460.6	1.13	98.2	0.44					B
0.048	0.15	340.4	0.95	102.7	0.46	562.8	1.29	167.8	0.76					B
0.064	0.20	396.9	1.04	149.5	0.68	635.1	1.40	243.2	1.10					B
0.081	0.25	444.1	1.11	200.0	0.91	688.3	1.49	321.7	1.46					B
0.097	0.30	483.6	1.17	253.3	1.15	728.8	1.55	402.4	1.82					B
0.113	0.35	517.1	1.22	308.5	1.40	760.4	1.60	484.2	2.19					B
0.129	0.40	545.5	1.26	365.3	1.65	784.7	1.63	566.4	2.56					B
0.145	0.45	569.4	1.30	422.9	1.91	803.3	1.66	648.4	2.94					B
0.161	0.50	589.8	1.33	481.3	2.18	817.5	1.69	730.0	3.30					B
0.177	0.55	607.0	1.36	540.0	2.44	827.9	1.70	810.6	3.67					B
0.193	0.60	621.3	1.38	598.6	2.71	835.3	1.71	890.2	4.03					B
0.209	0.65	633.2	1.40	657.2	2.98	839.8	1.72	968.4	4.38					B
0.225	0.70	642.9	1.42	715.2	3.24	842.1	1.72	1045.0	4.73					B
0.242	0.75	650.5	1.43	772.7	3.50	842.3	1.72	1119.9	5.07					B
0.258	0.80	656.5	1.44	829.6	3.76	840.9	1.72	1193.0	5.40					B
0.274	0.85	660.8	1.44	885.6	4.01	838.0	1.72	1264.2	5.72					B
0.290	0.90	663.8	1.45	940.6	4.26	833.6	1.71	1333.3	6.04					B
0.306	0.95	665.5	1.45	994.7	4.50	829.0	1.70	1401.5	6.34					B
0.322	1.00	665.9	1.45	1047.5	4.74	822.7	1.69	1466.9	6.64	972.5	1.92	1853	8.39	B
0.338	1.05	665.4	1.45	1099.3	4.98	813.8	1.68	1527.8	6.92	955.9	1.90	1919	8.69	B
0.354	1.10	663.8	1.45	1149.7	5.20	805.6	1.67	1588.3	7.19	938.5	1.87	1982	8.97	B
0.370	1.15	661.2	1.44	1198.6	5.43	798.1	1.66	1649.1	7.47	922.2	1.85	2045	9.26	B
0.386	1.20	657.9	1.44	1246.3	5.64	788.9	1.64	1706.0	7.72	905.8	1.82	2104	9.52	B
0.403	1.25	653.7	1.43	1292.3	5.85	778.6	1.62	1759.7	7.97	888.5	1.79	2160	9.78	B
0.419	1.30	648.7	1.42	1336.8	6.05	766.7	1.61	1809.4	8.19	870.9	1.77	2212	10.01	B
0.435	1.35	643.1	1.42	1379.8	6.25	755.5	1.59	1858.8	8.41	854.0	1.74	2263	10.24	B
0.451	1.40	636.8	1.41	1421.0	6.43	744.1	1.57	1906.3	8.63	837.8	1.72	2313	10.47	B
0.467	1.45	629.8	1.39	1460.5	6.61	732.5	1.55	1951.8	8.84	819.3	1.69	2356	10.67	B
0.483	1.50	622.2	1.38	1498.2	6.78	720.6	1.54	1995.3	9.03	802.3	1.66	2399	10.86	B
0.499	1.55	614.1	1.37	1534.0	6.94	707.1	1.51	2033.8	9.21	785.0	1.63	2439	11.04	B
0.515	1.60	605.4	1.36	1568.1	7.10	693.7	1.49	2070.7	9.37	767.3	1.61	2476	11.21	B
0.531	1.65	596.2	1.34	1600.1	7.24	680.9	1.47	2107.3	9.54	749.6	1.58	2510	11.36	B
0.547	1.70	586.5	1.33	1630.2	7.38	667.2	1.45	2140.0	9.69	731.6	1.55	2540	11.50	B
0.564	1.75	576.1	1.31	1657.8	7.50	652.4	1.43	2168.1	9.81	713.9	1.52	2569	11.63	B
0.580	1.80	565.7	1.30	1684.2	7.62	637.8	1.41	2194.9	9.94	695.9	1.50	2594	11.74	B
0.596	1.85	554.3	1.28	1707.6	7.73	623.7	1.39	2221.1	10.05	677.9	1.47	2617	11.85	B
0.612	1.90	542.8	1.26	1729.3	7.83	608.1	1.36	2241.3	10.15	659.8	1.44	2636	11.93	B
0.628	1.95	531.0	1.24	1749.1	7.92	593.4	1.34	2261.9	10.24	641.4	1.41	2652	12.01	B
0.644	2.00	518.3	1.22	1765.6	7.99	577.2	1.31	2276.4	10.31	623.4	1.39	2667	12.07	B
0.660	2.05	505.5	1.20	1780.5	8.06	562.0	1.29	2291.6	10.37	605.0	1.36	2677	12.12	B
0.676	2.10	492.3	1.18	1793.0	8.12	545.9	1.27	2302.2	10.42	586.1	1.33	2684	12.15	B
0.692	2.15	479.0	1.16	1803.8	8.17	529.4	1.24	2309.8	10.46	567.8	1.30	2689	12.17	B
0.708	2.20	464.8	1.14	1811.0	8.20	512.7	1.21	2314.1	10.48	548.7	1.27	2689	12.17	B
0.725	2.25	450.6	1.12	1816.4	8.22	495.7	1.19	2315.6	10.48	529.8	1.24	2687	12.16	B
0.741	2.30	435.8	1.10	1818.9	8.23	478.4	1.16	2313.9	10.47	510.5	1.21	2681	12.14	B
0.757	2.35	420.4	1.07	1818.0	8.23	460.8	1.13	2308.7	10.45	491.4	1.18	2672	12.10	B
0.773	2.40	404.7	1.05	1814.7	8.22	443.2	1.11	2301.4	10.42	471.9	1.15	2659	12.04	B

ρ (g/cm³)	ρ_r	Z = 0.75				Z = 0.90				Z = 1.00				
		T (°C)	T_r	P (bar)	P_r	T (°C)	T_r	P (bar)	P_r	T (°C)	T_r	P (bar)	P_r	Ref
0.789	2.45	388.8	1.02	1809.0	8.19	425.1	1.08	2290.0	10.37	451.8	1.12	2642	11.96	B
0.805	250	372.2	1.00	1799.8	8.15	406.7	1.05	2275.1	10.30	431.7	1.09	2621	11.87	B
0.821	2.55	355.1	0.97	1787.0	8.09	387.5	1.02	2255.0	10.21	411.2	1.06	2596	11.75	B
0.837	2.60	337.6	0.94	1771.2	8.02	368.1	0.99	2231.7	10.10	390.7	1.03	2567	11.62	B
0.853	2.65	319.7	0.92	1752.4	7.93	348.6	0.96	2205.4	9.98	369.6	0.99	2533	11.47	B
0.869	2.70	301.0	0.89	1729.3	7.83	328.1	0.93	2173.0	9.84	347.9	0.96	2494	11.29	B
0.886	2.75	281.8	0.86	1702.2	7.71	307.5	0.90	2137.2	9.67	326.1	0.93	2451	11.10	B
0.902	2.80	261.7	0.83	1670.6	7.56	285.8	0.86	2095.1	9.48	303.6	0.89	2402	10.87	B
0.918	2.85	241.0	0.79	1634.6	7.40	263.8	0.83	2048.3	9.27	280.3	0.86	2346	10.62	B
0.934	2.90	219.6	0.76	1594.1	7.22	241.0	0.79	1995.9	9.04	256.5	0.82	2284	10.34	B
0.950	2.95	197.0	0.73	1547.1	7.00	217.6	0.76	1937.7	8.77	232.0	0.78	2216	10.03	B
0.966	3.00	173.5	0.69	1494.8	6.77	193.0	0.72	1871.8	8.47	206.6	0.74	2140	9.69	B

ρ (g/cm³)	ρ_r	Z = 1.10				Z = 1.25				Z = 2.00				
		T (°C)	T_r	P (bar)	P_r	T (°C)	T_r	P (bar)	P_r	T (°C)	T_r	P (bar)	P_r	Ref
0.435	1.35	984.1	1.94	2776.8	1.59									B
0.451	1.40	957.3	1.90	2818.4	1.57									B
0.467	1.45	931.9	1.86	2858.7	1.55									B
0.483	1.50	904.9	1.82	2891.0	1.54									B
0.499	1.55	881.8	1.78	2928.8	1.51									B
0.515	1.60	857.5	1.75	2959.6	1.49									B
0.531	1.65	833.8	1.71	2988.2	1.47									B
0.547	1.70	810.5	1.67	3013.8	1.45	967.8	1.92	3922.0	17.75					B
0.564	1.75	787.8	1.64	3037.5	1.43	932.6	1.86	3922.9	17.76					B
0.580	1.80	764.8	1.60	3056.6	1.41	898.1	1.81	3919.4	17.74					B
0.596	1.85	742.2	1.57	3073.3	1.39	865.2	1.76	3915.3	17.72					B
0.612	1.90	720.0	1.53	3087.2	1.36	833.8	1.71	3910.1	17.70					B
0.628	1.95	698.0	1.50	3098.4	1.34	803.2	1.66	3902.0	17.66					B
0.644	2.00	676.1	1.47	3106.0	1.31	773.8	1.62	3892.7	17.62					B
0.660	2.05	654.4	1.43	3110.8	1.29	744.8	1.57	3879.6	17.56					B
0.676	2.10	632.8	1.40	3112.4	1.27	716.6	1.53	3864.1	17.49					B
0.692	2.15	611.1	1.37	3110.3	1.24	689.1	1.49	3846.2	17.41					B
0.708	2.20	589.6	1.33	3105.2	1.21	662.3	1.45	3826	17.32					B
0.725	2.25	568.3	1.30	3097.5	1.19	635.5	1.40	3801.1	17.21					B
0.741	2.30	546.8	1.27	3085.3	1.16	609.2	1.36	3773.0	17.08					B
0.757	2.35	525.3	1.23	3069.6	1.13	583.3	1.32	3741.9	16.94					B
0.773	2.40	503.5	1.20	3049.4	1.11	558.0	1.28	3708.4	16.79					B
0.789	2.45	481.7	1.17	3025.5	1.08	388.8	1.02	2412	10.92					B
0.805	2.50	459.6	1.13	2997.2	1.05	372.2	1.00	2400	10.86					B
0.821	2.55	437.5	1.10	2964.7	1.02	355.1	0.97	2383	10.79	987.0	1.95	9558.4	43.27	B
0.837	2.60	415.1	1.06	2927.6	0.99	337.6	0.94	2362	10.69	890.3	1.80	8998.3	40.73	B
0.853	2.65	392.5	1.03	2885.7	0.96	319.7	0.92	2336	10.57	809.5	1.67	8534.0	38.63	B
0.869	2.70	369.4	0.99	2838.3	0.93	301.0	0.89	2306	10.44	736.6	1.56	8109.8	36.71	B
0.886	2.75	346.0	0.96	2785.6	0.90	281.8	0.86	2270	10.28	674.9	1.46	7754.8	35.11	B
0.902	2.80	322.2	0.92	2726.9	0.86	261.7	0.83	2227	10.08	615.5	1.37	7401.3	33.51	B
0.918	2.85	298.0	0.88	2662.8	0.83	241.0	0.79	2179	9.86	561.7	1.29	7077.6	32.04	B
0.934	2.90	273.0	0.84	2590.9	0.79	219.6	0.76	2125	9.62	510.5	1.21	6759.9	30.60	B
0.950	2.95	247.4	0.80	2512.3	0.76	197.0	0.73	2063	9.34	461.5	1.14	6446.5	29.18	B
0.966	3.00	221.1	0.76	2425.5	0.72	173.5	0.69	1993	9.02	414.9	1.06	6140.1	27.80	B

[A] Source: ChemicaLogic (1999).

[B] Source: Haar *et al.* (1984).

122

CH$_4$		$Z = 1.00$				
ρ (g/cm^3)	ρ_r	T (°C)	T_r	P (bar)	P_r	Ref
0.002	0.01	234.7	2.67	4.3	0.09	C
0.016	0.1	221.4	2.59	41.4	0.90	C
0.032	0.2	207.1	2.52	80.5	1.75	C
0.049	0.3	192.8	2.45	117.2	2.55	C
0.065	0.4	178.5	2.37	151.5	3.29	C
0.081	0.5	163.2	2.29	182.9	3.98	C
0.097	0.6	148.9	2.21	212.2	4.62	C
0.113	0.7	134.7	2.14	239.2	5.20	C
0.129	0.8	120.8	2.07	264.2	5.74	C
0.146	0.9	107.0	2.00	286.9	6.24	C
0.162	1.0	92.7	1.92	306.6	6.67	C
0.178	1.1	78.9	1.85	324.7	7.06	C
0.194	1.2	64.6	1.77	339.6	7.39	C
0.210	1.3	50.6	1.70	352.8	7.67	C
0.226	1.4	36.3	1.62	363.2	7.90	C
0.243	1.5	21.7	1.55	370.5	8.06	C
0.259	1.6	7.5	1.47	376.2	8.18	C
0.275	1.7	−6.8	1.40	379.6	8.26	C
0.291	1.8	−21.4	1.32	379.6	8.26	C
0.307	1.9	−35.8	1.25	378.0	8.22	C
0.323	2.0	−50.3	1.17	373.6	8.12	C
0.340	2.1	−65.0	1.09	366.6	7.97	C
0.356	2.2	−79.8	1.01	356.4	7.75	C
0.372	2.3	−94.8	0.94	343.6	7.47	C
0.388	2.4	−109.9	0.86	328.6	7.15	C
0.404	2.5	−125.3	0.78	309.7	6.74	C
0.420	2.6	−140.6	0.70	288.8	6.28	C
0.437	2.7	−156.0	0.61	265.4	5.77	C
0.453	2.8	−171.3	0.53	238.7	5.19	C
CO$_2$		$Z = 1.00$				
ρ (g/cm^3)	ρ_r	T (°C)	T_r	P (bar)	P_r	Ref
0.005	0.01	441.7	2.35	6.32	0.09	C
0.047	0.1	425.6	2.30	61.8	0.84	C
0.094	0.2	408.9	2.24	120.7	1.63	C
0.141	0.3	390.9	2.18	176.1	2.39	C
0.187	0.4	371.8	2.12	228.2	3.09	C
0.234	0.5	352.0	2.06	276.4	3.74	C
0.281	0.6	333.1	1.99	321.7	4.36	C
0.328	0.7	313.4	1.93	362.9	4.92	C
0.375	0.8	294.5	1.87	401.6	5.44	C
0.422	0.9	275.9	1.81	436.9	5.92	C
0.469	1.0	257.7	1.75	469.4	6.36	C
0.516	1.1	239.4	1.69	498.6	6.75	C
0.562	1.2	221.2	1.63	524.6	7.11	C
0.609	1.3	202.9	1.57	547.5	7.42	C
0.656	1.4	184.7	1.51	567.4	7.69	C
0.703	1.5	166.1	1.44	582.8	7.89	C
0.750	1.6	147.3	1.38	594.7	8.06	C
0.797	1.7	129.0	1.32	604.7	8.19	C
0.844	1.8	110.8	1.26	612.0	8.29	C
0.891	1.9	92.2	1.20	613.5	8.31	C
0.937	2.0	74.0	1.14	614.4	8.32	C
0.984	2.1	55.4	1.08	610.5	8.27	C
1.031	2.2	36.5	1.02	602.7	8.16	C
1.078	2.3	18.0	0.96	592.0	8.02	C
1.125	2.4	−0.9	0.90	578.1	7.83	C
1.172	2.5	−19.7	0.83	560.5	7.59	C

^{C} Source: McCarty and Arp (1992).

later in the text). Although the linearity of the $Z = 1$ contour was discovered by Batschinski in 1906 (Batschinski, 1906), it appears to have been forgotten until nearly six decades later.

Beginning in the early 1960's, researchers at the University of Karlsruhe, Odessa Institute of Marine Engineering, and several Russian institutes discussed the Zeno line extensively (Morsy, 1963; Vasserman, 1964; Schaber, 1965), related it to other thermodynamic properties (Nedostup, 1970; Burshtein, 1974; Nedostup and Gal'kevich, 1976) and incorporated it in the development of various thermodynamic models (Nedostup and Gal'kevich, 1980; Nedostup and Bekker, 1980). Independently, during the late 1960's Holleran and coworkers (Holleran and Sinka, 1971; Holleran and Jacobs, 1972; Holleran and Hammes, 1975; Holleran, 1967-1990) proposed several useful applications for the $Z = 1$ contour. Diverse names were used including orthometric condition, ideal-gas curve, and unit compressibility line, but the term Zeno line (Ben-Amotz and Herschbach, 1990a; Ben-Amotz and Herschbach, 1990b) has been adopted to "emphasize the paradoxical character of its arrow-like linearity."

At low density, the $Z = 1$ contour is readily shown to be linear (Ben-Amotz and Herschbach, 1990a). The $\rho \to 0$ intercept of the supercritical vapor corresponds to the Boyle temperature (T_B) where the second virial coefficient vanishes and the slope at T_B is given by $-B_3/(dB_2/dT)$, the ratio of the third virial coefficient to the derivative of the second. Remarkably, the $Z = 1$ contour retains its linearity even in the dense fluid region, as it nears the triple point. Near the triple point, intermolecular interactions are important, but as has been shown, attractive and repulsive contributions are in dynamic balance along the entire Zeno contour (Ben-Amotz and Herschbach, 1990a).

For a wide range of normal fluids, extending well beyond the regime of Corresponding States, the Zeno line is found to be strongly correlated with the line of rectilinear diameters (Ben-Amotz and Herschbach, 1990a), even though the latter pertains to the subcritical region and a portion of the Zeno contour lies in the supercritical region. This enables the critical density, which is relatively difficult to measure, to be estimated to about 1% accuracy from the Zeno line (Ben-Amotz and Herschbach, 1990a; Xu and Herschbach, 1992). Furthermore, the Zeno line intercepts on the T and ρ axes are strongly correlated with the acentric factor of normal fluids (Xu and Herschbach, 1992).

Because this Zeno behavior appears to be a generic property of pure fluids, it is advantageous to incorporate it in equation of state (EOS) model conception, development, and parameter regression. In recent work of this kind, Nedostup and coworkers (1988) proposed equations of state based on Helmholtz free energy and that are dependent on second virial coefficients which are derived from $Z = 1$ contour properties. In addition, Serovskii (1990) modified the van der Waals EOS to include Zeno-line dependent parameters in an attempt to match experimental properties and provide the basis for new models of real and unknown substances. Further, Marracho and Ely (1998) used the Zeno condition to refine and interpret shape factors in applying their Extended Corresponding States Theory (ECST) to both polar and non-polar fluids. Unfortunately, other EOS models that are commonly employed for estimating $PVTx_i$ behavior do not take advantage of Zeno behavior to generalize their parameters.

Water (H_2O), methane (CH_4), and carbon dioxide (CO_2) are ideal candidates for analysis because they have very different polarities and have widely accepted databases. For H_2O, the National Institute of Standards and Technology (NIST) correlation of Haar, Gallagher, and Kell (1984) was used for reduced temperatures T_r less than 2.0, and the International Association for the Properties of Water and Steam (IAPWS) correlation used by ChemicaLogic (1999) was used from $T_r > 2.0$ to the Boyle temperature, $T_{B,r} = 2.38$. For CH_4 and CO_2, the Benedict-Webb-Rubin-Starling EOS correlations given by McCarty and Arp was used (McCarty and Arp, 1992). Accurate data for these substances are available over a wide range of densities from ambient to very high pressures (>1 kbar). Figure 36 and Table 15 provide additional data for pure water for constant values of Z ranging from 0.75 to 2.00.

Practical EOSs used in process engineering calculations are semi-empirical or fully empirical expressions that are fit to experimental data. Popular, simple models frequently used for pure fluids extend the cubic form of the van der Waals (vdW) EOS (van der Waals, 1873):

$$Z = \left(\frac{RT}{V-b} - \frac{a_c}{V^2} \right) \left(\frac{V}{RT} \right) \tag{80}$$

where a_c and b are parameters that are commonly fit to critical point stability criteria and are normally expressed as explicit functions of T_c and P_c. Examples of such extended models include the Peng-Robinson (PR) EOS (Peng and Robinson, 1976)

$$Z = \left(\frac{RT}{V-b} - \frac{a_c \alpha}{V^2 + 2bV - b^2} \right) \left(\frac{V}{RT} \right) \tag{81}$$

and the Redlich-Kwong-Soave (RKS) EOS (Soave, 1972)

$$Z = \left(\frac{RT}{V-b} - \frac{a_c \alpha}{V(V+b)} \right) \left(\frac{V}{RT} \right) \tag{82}$$

where $\alpha = f(T_r, \omega)$ and ω is the Pitzer acentric factor. Researchers have regressed and proposed other α models in an attempt to increase EOS accuracy for other species, to extend predictions to other density regions, or to predict other properties. A few representative α models for the PR EOS are summarized in Table 16.

The accuracy of cubic-type EOSs has been improved by translating the volume to provide a better match to liquid density data. Martin (1967), who was the first to propose this concept, used a fixed volume translation t. In this case:

$$V = V^{UT} + t \tag{83}$$

where V^{UT} is the untranslated volume obtained from the EOS and V is the predicted specific volume. It is important to note that the volume translation will have a substantial effect at small specific volumes (*i.e.*, high densities) under which conditions the magnitude of t approaches or even exceeds V^{UT}. The volume-translated EOSs evaluated in this investigation are the VTPR EOS (Mathias *et al.*, 1989) and HSVTvdW EOS (Kutney *et al.*, 1996 and 1997) and are summarized in Table 17.

The Zeno condition was used to examine whether cubic and hard sphere vdW EOSs can be fundamentally improved. Given that EOSs typically have parameters which are regressed from experimental data in specific pressure, volume, and temperature regimes, accurate Zeno-line predictions at higher densities can test the robustness of the EOS model. Alternatively, Zeno-point data can, themselves, be included in refining EOS parameter regressions. Zeno behavior using molecular-simulation methods were also studied in order to test the hypothesis of balanced repulsive and attractive interactions and to search for structural insights at a molecular level.
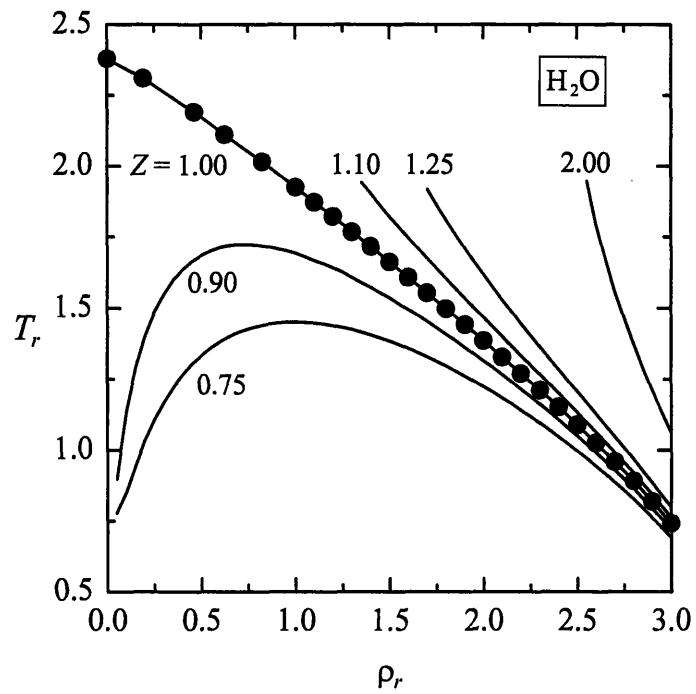
Figure 36. Water phase diagram showing the Zeno line ($Z = 1$) along with other contours of constant compressibility factor produced using the experimentally-correlated water properties from Haar *et al.* (1984) and ChemicaLogic (1999).

Table 16. Published α models for use with the PR EOS

Name	$\alpha = f(T_r)$ Model
Peng-Robinson (PR) (Peng and Robinson, 1976)	$\alpha = \left(1 + \kappa\left(1 - \sqrt{T_r}\right)\right)^2$ $\kappa = 0.37464 + 1.54226\omega - 0.26992\omega^2$
Stryjek-Vera (PRSV2) (Stryjek and Vera, 1986)	$\alpha = \left(1 + \kappa''\left(1 - \sqrt{T_r}\right)\right)^2$ $\kappa'' = \kappa_0 + \left(\kappa_1 + \kappa_2\left(\kappa_3 - T_r\right)\left(1 - \sqrt{T_r}\right)\right)\left(1 + \sqrt{T_r}\right)\left(0.7 - T_r\right)$ $\kappa_0 = 0.378893 + 1.4897153\omega - 0.17131848\omega^2 + 0.0196554\omega^3$
Twu et al. (1995)	$\alpha = \alpha_2 + \omega\left(\alpha_3 - \alpha_2\right) \quad T_r > 1 \qquad \alpha = \alpha_0 + \omega\left(\alpha_1 - \alpha_0\right) \quad T_r \le 1$ $\alpha_k = T_r^{N_k\left(M_k - 1\right)} e^{L_k\left(1 - T_r^{N_k M_k}\right)} \quad k = 0,1,2,3$ $L_k, M_k,$ and N_k are universal constants
Boston-Mathias (Aspen Technology, 1994)	$\alpha = \left(\exp\left(\left\{\dfrac{\kappa}{2+\kappa}\right\}\left\{1 - T_r^{\left(1 + \frac{\kappa}{2}\right)}\right\}\right)\right)^2 \quad T_r > 1$ $\alpha = \left(1 + \kappa\left(1 - \sqrt{T_r}\right)\right)^2 \quad T_r \le 1$

Table 17. Volume-translated EOSs examined

Name	VT EOSs
VTPR EOS (Mathias *et al.*, 1989)	$$P = \frac{RT}{V^{UT} - b} - \frac{a_c \alpha}{V^{UT}(V^{UT} + b) + b(V^{UT} - b)}$$ $$V = V^{UT} + t + (V_c - V_c^{UT} - t)\left(\frac{\eta}{\eta + \delta}\right)$$ $$\delta = -\frac{\left(V^{UT}\right)^2}{RT}\left(\frac{\partial P}{\partial V^{UT}}\right)_T \qquad \eta = 0.41$$
HSVTvdW EOS (Kutney *et al.*, 1997)	$$P = \frac{RT}{V^{UT}}\left(\frac{\left(V^{UT}\right)^3 + b\left(V^{UT}\right)^2 + b^2 V^{UT} - b^3}{(V^{UT} - b)^3}\right) - \frac{a_c \alpha}{(V^{UT} + 2b)^2}$$ $$\alpha = \exp\left(\{1 - T_r\}\left\{\frac{\alpha_A}{T_r^{0.93}} + \alpha_B T_r^{0.75}\right\}\right)$$ $$V = V^{UT} + t + (V_c - V_c^{UT} - t)\left(\frac{8 V_r^{UT} T_r^{-9/2}}{\left(V_r^{UT}\right)^3 + \frac{13}{2}T_r^{-13/2} + \frac{1}{2}}\right)$$

I.3.2 Empirical Zeno Behavior

Contours for several values of Z are plotted for pure water for the vdW, RKS, and PR EOSs in Figure 37 through Figure 39 using parameters given in Table 18. For Z greater than 1.0, none of the models match the T_r–ρ_r values or curvature of the experimentally-correlated pure water data. This discrepancy might be expected as none of these EOSs had parameters fit in this region. However, in the lower density region, e.g. for $Z = 0.75$ in Figure 37, closer agreement between experimental data and the RKS and PR EOS predictions is observed, because the EOSs have approached the region of PVT space where the EOS parameters were fit. The differences between the plotted EOSs indicate that both the algebraic form and parameter values of the EOS influence the slope and curvature of the calculated Zeno lines.

I.3.2.1 Peng-Robinson (PR) EOS

The α model used in the EOS is considered and examined next. The PR EOS was chosen because of its wide acceptance and the existence of numerous α model treatments. Thus, one can examine the effect of α since it alters the attractive term of the EOS which, along the Zeno contour, should be balanced by the repulsive term. Models typically used for α show larger deviations from experimental behavior at higher temperatures.

Figure 40 compares several α models and clearly shows that the Twu *et al.* (1995) model is superior. Though not shown here, similar improvements were seen with the Twu *et al.* (1995) model over the original PR EOS for other Z-contours. It is well established that the original PR EOS α model form is inadequate for very high temperatures since α becomes negative. However, Figure 40 clearly shows that a well-formulated α model performs better, even if the model has not been regressed explicitly to the Zeno region of PVT space.

I.3.2.2 Redlich-Kwong-Soave (RKS) EOS

As shown in Figure 37 through Figure 39, the RKS EOS performed comparably to the PR EOS along the $Z = 0.75$, 1.00, and 1.25 isocompressibility contours. The effects of an α–model variation or volume translation for the RKS EOS model were not explored.

I.3.2.3 Hard-Sphere, Volume-Translated van der Waals (HSVTvdW) EOS

The final EOS feature examined was volume-translation. An example is shown for pure H_2O in Figure 41 using the VTPR EOS and the HSVTvdW EOS (see Table 17). In earlier work

(Kutney *et al.*, 1997), volumetric accuracy was improved substantially by volume translation. Thus, one might expect a close match between the HSVTvdW EOS Zeno line and the experimental Zeno line. However, this was not the case. By comparing the untranslated (HSUTvdW) and translated (HSVTvdW) forms of the EOS in Figure 41 with the same α model, one observes both a translation of the Zeno line and a significant change in curvature. The untranslated HSUTvdW EOS is also shown in Figure 41 with α fixed at 1.0 to demonstrate the substantial effect that the α model has on the Zeno line. In general, volume translation in the HSvdW model clearly affects the slope and curvature of the Zeno line, but the translation is far from uniform over the range of densities examined. As expected, there is substantial translation at high densities ($\rho_r > 1.0$), but the curvature in the Zeno line at lower densities was unexpected since the volume translation is reduced in that region. As shown in Figure 41, volume translation was also performed on the PR EOS using the method suggested by Mathias *et al.* (1989) resulting in comparable improvements to that of the Twu *et al.* (1995) α model.
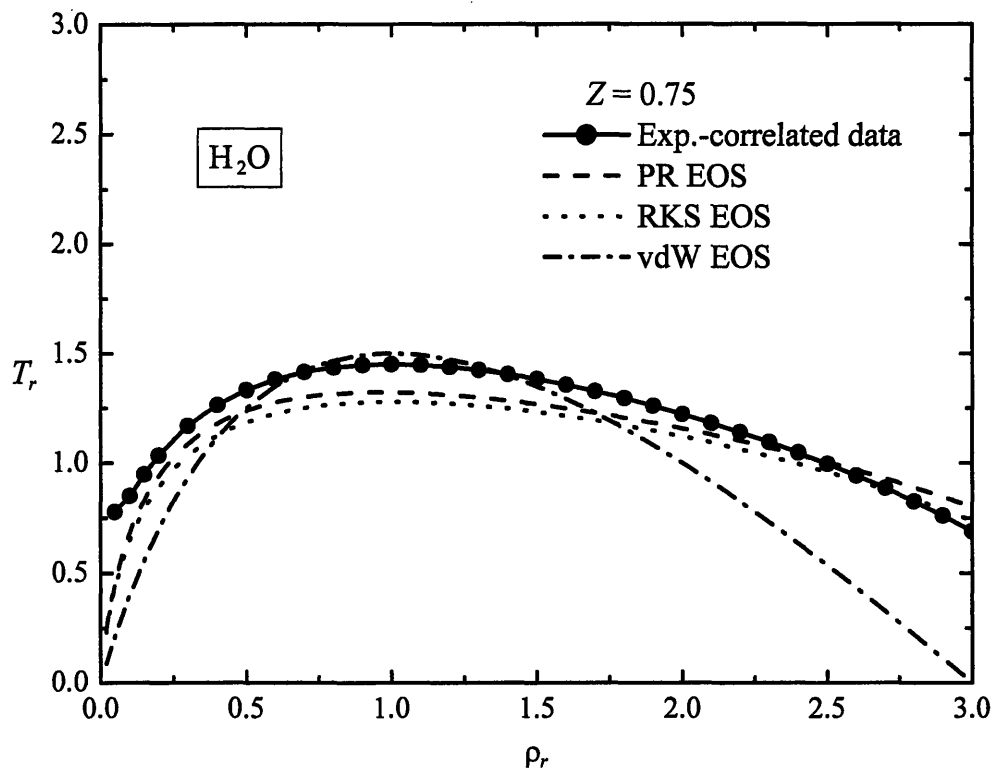
Figure 37. Predicted versus experimental $Z = 0.75$ contours for water as a function of T_r and ρ_r.
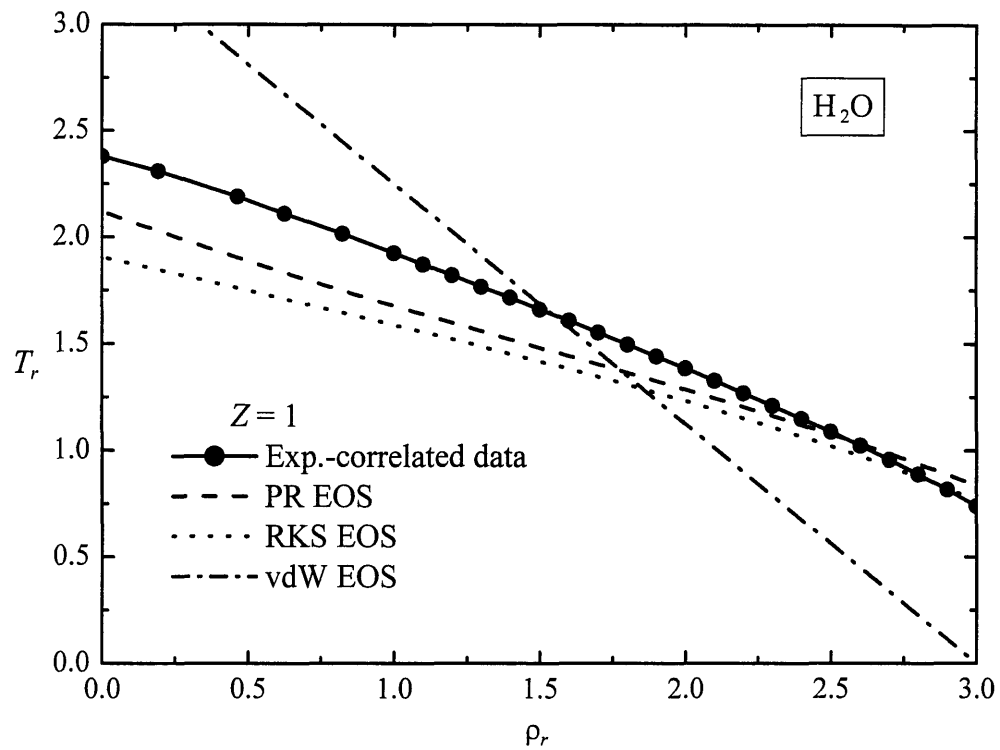
Figure 38. Predicted versus experimental $Z = 1$ Zeno line for water as a function of T_r and ρ_r.
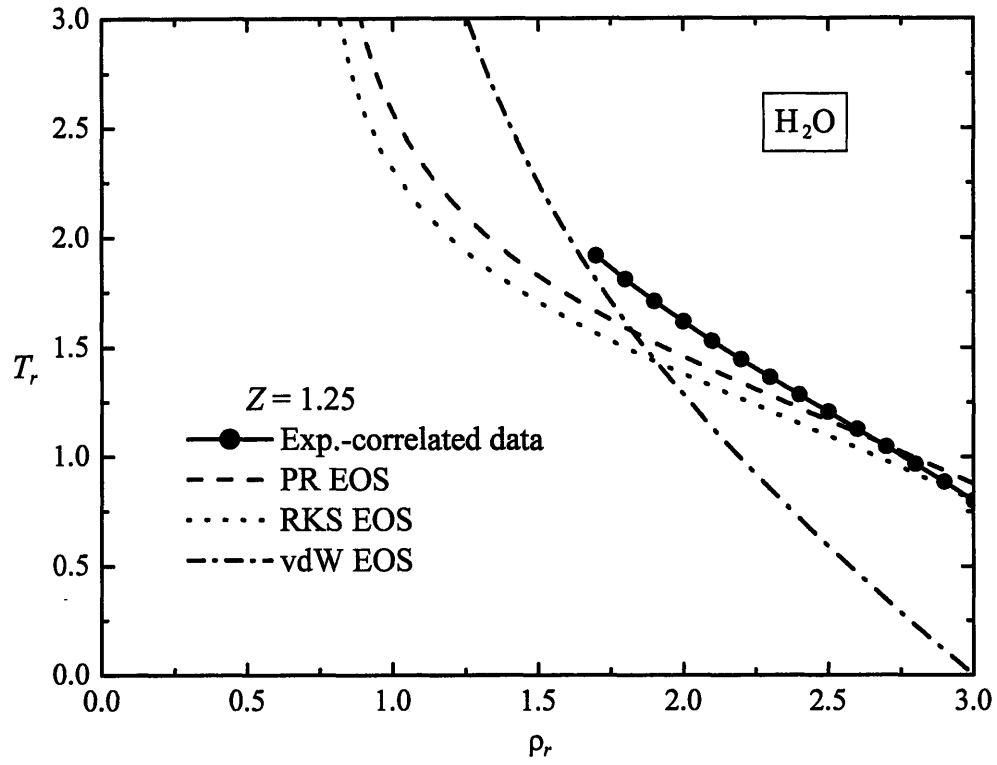
Figure 39. Predicted versus experimental $Z = 1.25$ contours for water as a function of T_r and ρ_r.

Table 18. Equation of state critical properties and parameters used for pure H_2O, CH_4, and CO_2 (T_c, P_c, and V_c values are based on available experimental data from several sources (Reid *et al.*, 1987; DIPPR, 1995))

EOS	T_c (°C)	P_c (bar)	a_c (m^{6}MPa/kgmol^2)	b (m^3/kgmol)	V_c (m^3/kgmol)	t (m^3/kgmol)	ω	α_A	α_B
H_2O									
vdW	374.1	220.9	0.553	0.0305	–	–	–	–	–
PR	374.1	220.9	0.599	0.0190	–	–	0.344	–	–
RKS	374.1	220.9	0.560	0.0211	–	–	0.344	–	–
VTPR	374.1	220.9	0.599	0.0190	0.0559	–0.0034	0.344	–	–
HSVTvdW	374.1	220.9	0.589	0.0060	0.0559	0.0048	–	0.105	1.038
CH_4									
PR	–82.62	45.95	0.250	0.0268	–	–	0.0105	–	–
HSVTvdW	–82.62	45.95	0.245	0.0085	0.0990	0.0140	–	0.037	0.501
CO_2									
PR	31.06	73.82	0.396	0.0267	–	–	0.225	–	–
HSVTvdW	31.06	73.82	0.390	0.0084	0.0939	0.0129	–	0.000	0.913
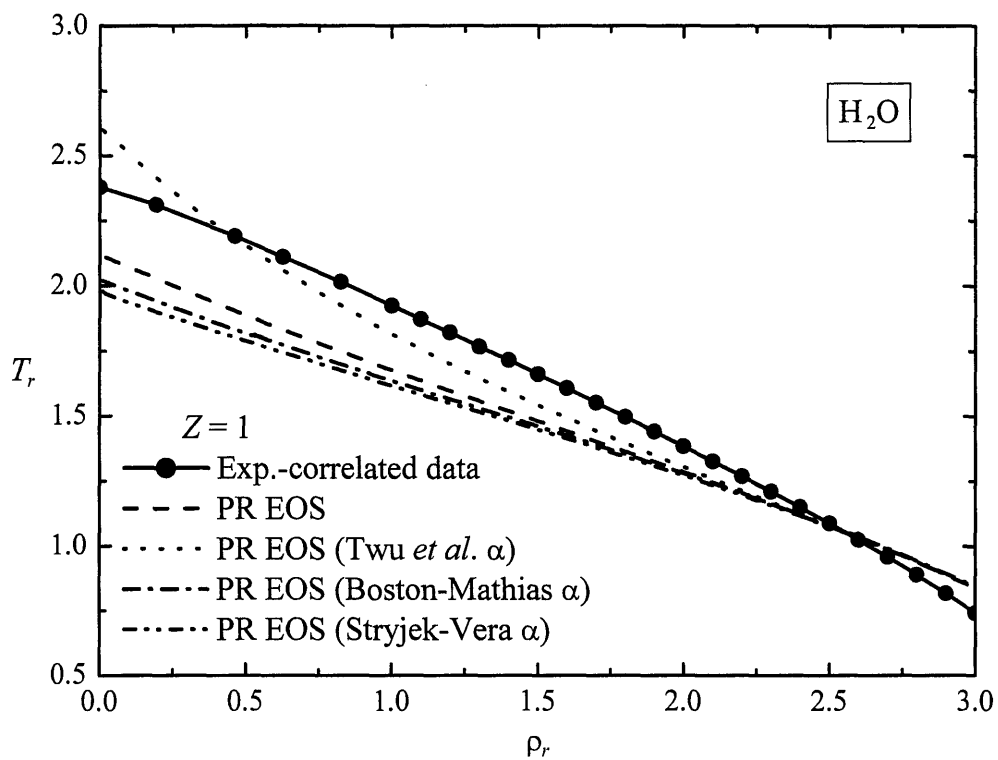
Figure 40. $Z = 1$ Zeno line for water for the PR EOS with several α parameter models. See Table 16 for the α parameter models.
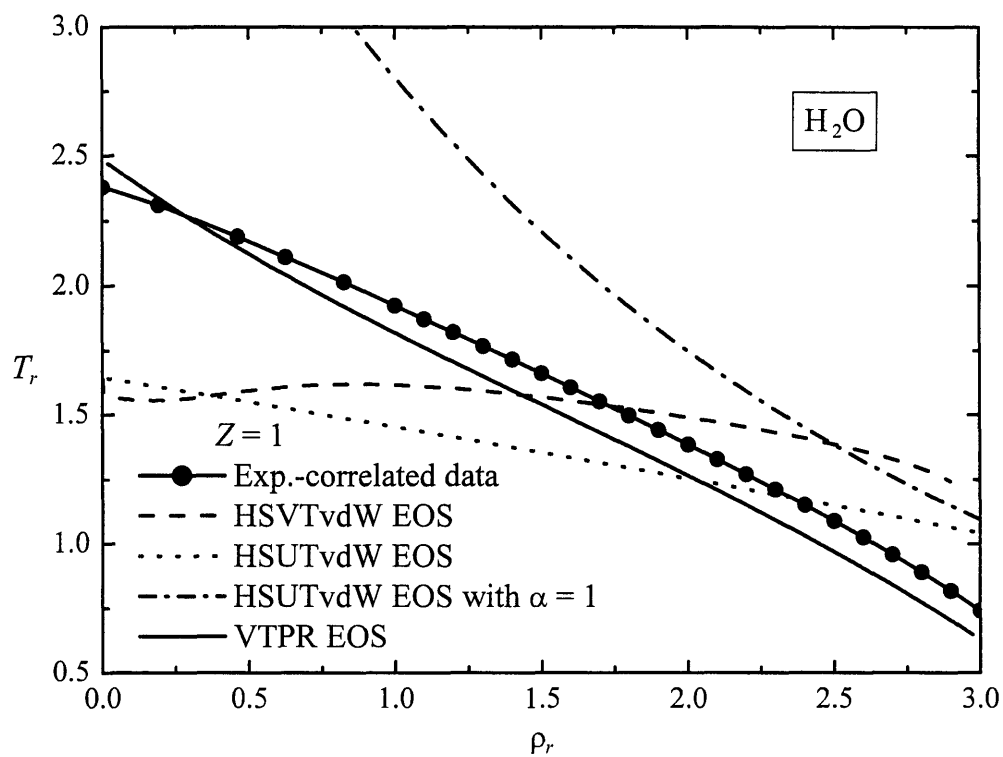
Figure 41. $Z = 1$ Zeno line for water for the volume translated VTPR EOS (Mathias *et al.*, 1989) and HSVTvdW EOS (Kutney *et al.*, 1997) including contours for the HSUTvdW EOS (without volume translation) and HSUTvdW EOS with $\alpha = 1$ (without volume translation).

I.3.2.4 Zeno-Line Fitting of the α Parameter

The results of these comparisons indicate that the forms of the α and volume-translation models have a significant effect on Zeno-line predictions. Given the general complexity of the EOS and the large number of α parameter treatments available, a new approach was formulated in order to determine how the α model itself affects the Zeno performance of an EOS. With the general form of an untranslated cubic EOS and the required water parameters a_c and b for the EOS (calculated from stability criteria), one can determine the values of α required to match the experimentally correlated Zeno data at various temperatures. These fit α values can then be compared to the values from a representative set of published α models. Figure 42 provides such a comparison for the PR EOS for several isocompressibility-factor contours, where it is noted that a common point at $\alpha(T_r = 1.0) = 1.0$ exists regardless of the magnitude of Z. The Twu *et al.* (1995) model appears to come closest to the fit α's.

Figure 43 shows results for similar calculations for the HSVTvdW EOS. Here one sees a larger separation between each fit α curve and some double-valued behavior. These curves imply that the α parameter will require a complex dependence on density as well as temperature. The simpler PR EOS formulation, however, does not show this large disparity, indicating that the mathematical form of the PR EOS is superior for matching isocompressibility-factor behavior. In fact, one could extrapolate this improvement further by hypothesizing that the "perfect EOS" might have a form such that the fit α values closely match experimental data and are expressible as a simple function of reduced temperature. The PR EOS with the Twu *et al.* (1995) α model comes reasonably close to meeting this criterion for pure H_2O.
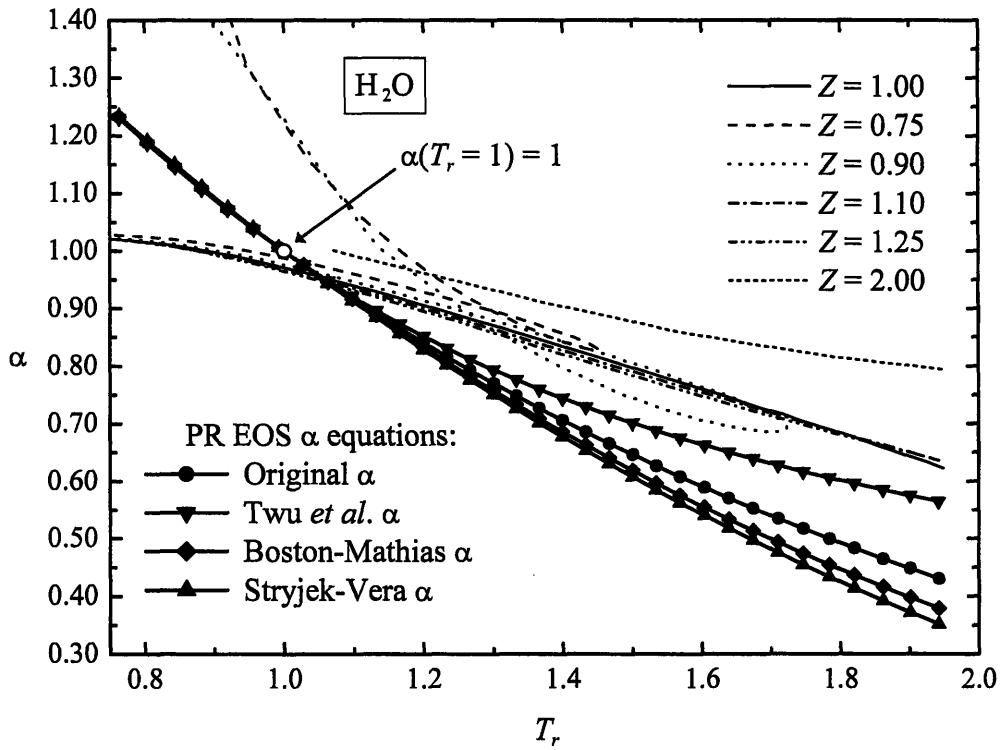
Figure 42. For the PR EOS, α values are fit to match experimentally-correlated water property data for several isocompressibility-factor conditions (thinner lines) and compared to published α equations which are independent of Z (thicker lines).

139
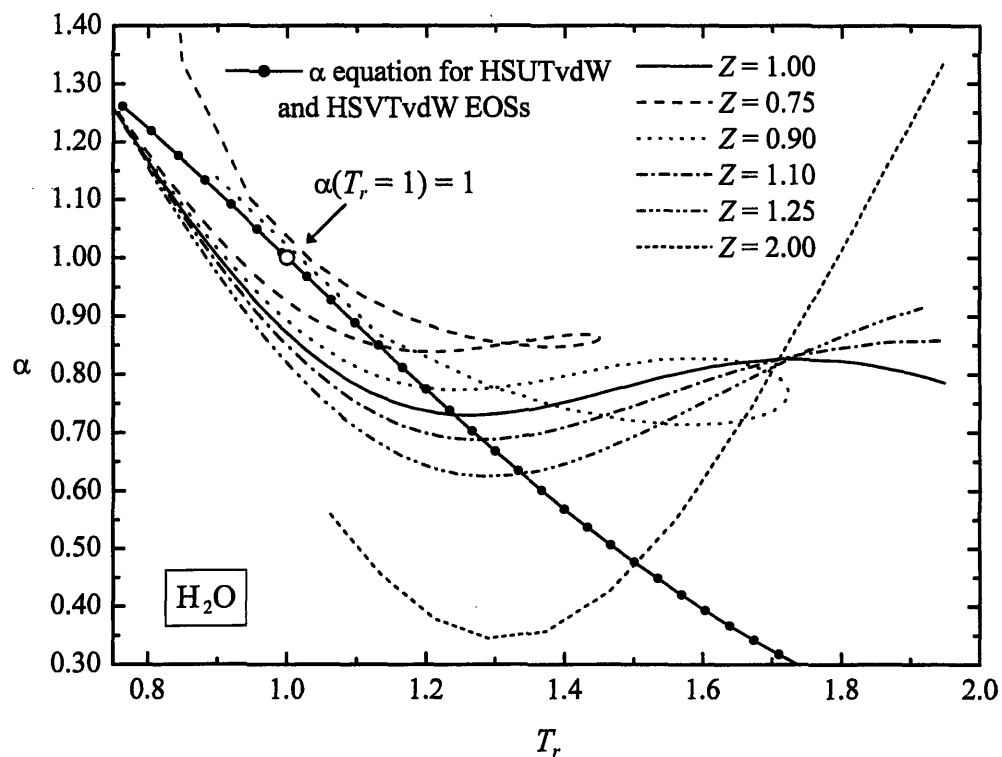
Figure 43. For the HSVTvdW EOS, α values are fit to match experimentally-correlated water property data for several isocompressibility-factor conditions and compared to the α equation actually used for the HSVTvdW and HSUTvdW EOSs.

I.3.3 Empirical EOS Zeno Lines for Pure Methane and Pure Carbon Dioxide

I.3.3.1 Methane

Zeno calculations were performed for pure CH_4 using the PR and HSVTvdW EOS models. Figure 44 compares the experimental Zeno line to predictions for several EOSs. The volume-translated HSVTvdW EOS shows dramatic curvature while the PR EOS with the Boston-Mathias α model shows an improvement over the original α and Twu *et al.* (1995) α models. The Zeno-line prediction using the Boston-Mathias α model approaches the experimental reduced Boyle temperature of methane ($T_{B,r} = 2.67$) at low density, confirming its usefulness for representing hydrocarbon properties. At a reduced density (ρ_r) of 0.2, the Twu *et al.* (1995) α is 0.56, but by reducing α to the Boston-Mathias α value of 0.50 and leaving the EOS repulsive contribution unchanged, then the correct $Z = 1$ temperature is predicted. The standard PR EOS Zeno line deviates more from the NIST data at low density, presumably because the PR EOS attractive term which contains α does not accurately represent the attractive effects and its compensation for repulsive effects is not complete.

I.3.3.2 Carbon Dioxide

Zeno calculations were also performed for pure CO_2 ($T_{B,r} = 2.35$) again using the PR and HSVTvdW EOS models. Figure 45 shows trends similar to those for pure methane given in Figure 44. However, in this case, the original PR EOS model matches the experimental data best.

Clearly, for these three representative fluids, species-dependent effects are not captured by customary critical point scaling. Using available cubic-type EOS models with reformulated α parameters and volume translations fitted to the Zeno condition was not sufficient to fully generalize the results. In addition, in Figure 45, results are plotted for the Song-Mason EOS which is based on a statistical mechanical perturbation model with an empirically-fitted constant ($\gamma = 1.303$) used to account for the temperature dependence of the second virial coefficient (Xu and Herschbach, 1992). It too falls short of providing an exact fit. Further research is required to find an EOS which can accurately model the Zeno line over the entire density and temperature regime. With an accurate model, one will not need density-dependent α models or variable
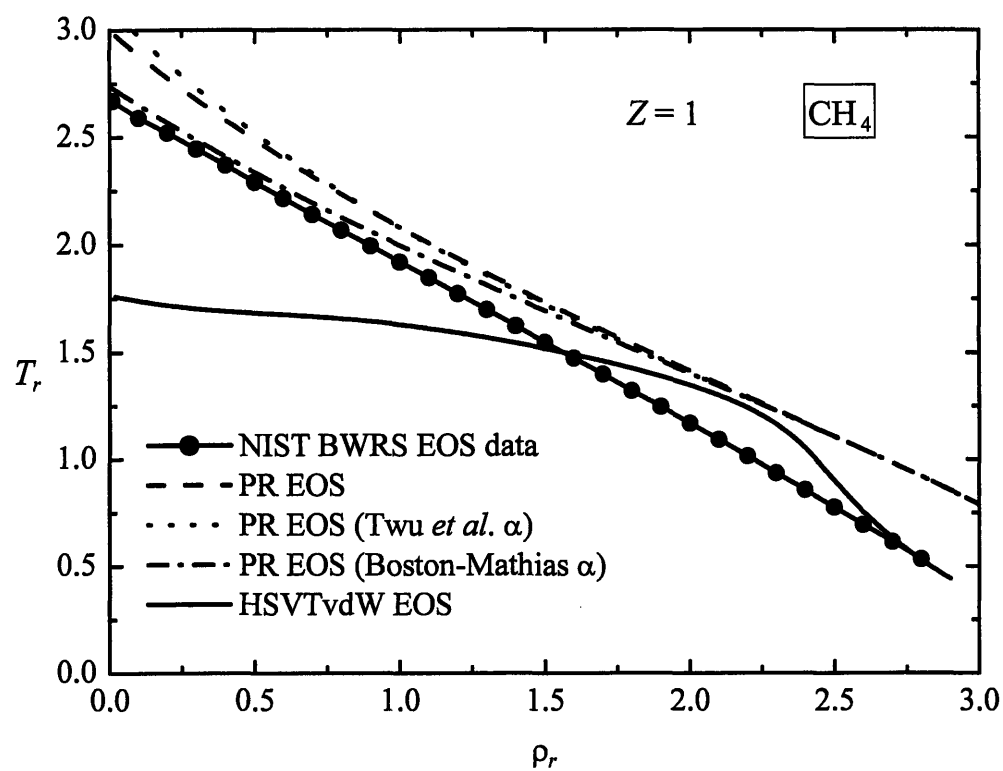
Figure 44. Experimental and predicted EOS $Z = 1$ Zeno lines for pure methane (Data source: McCarty and Arp (1992). See Table 15.).
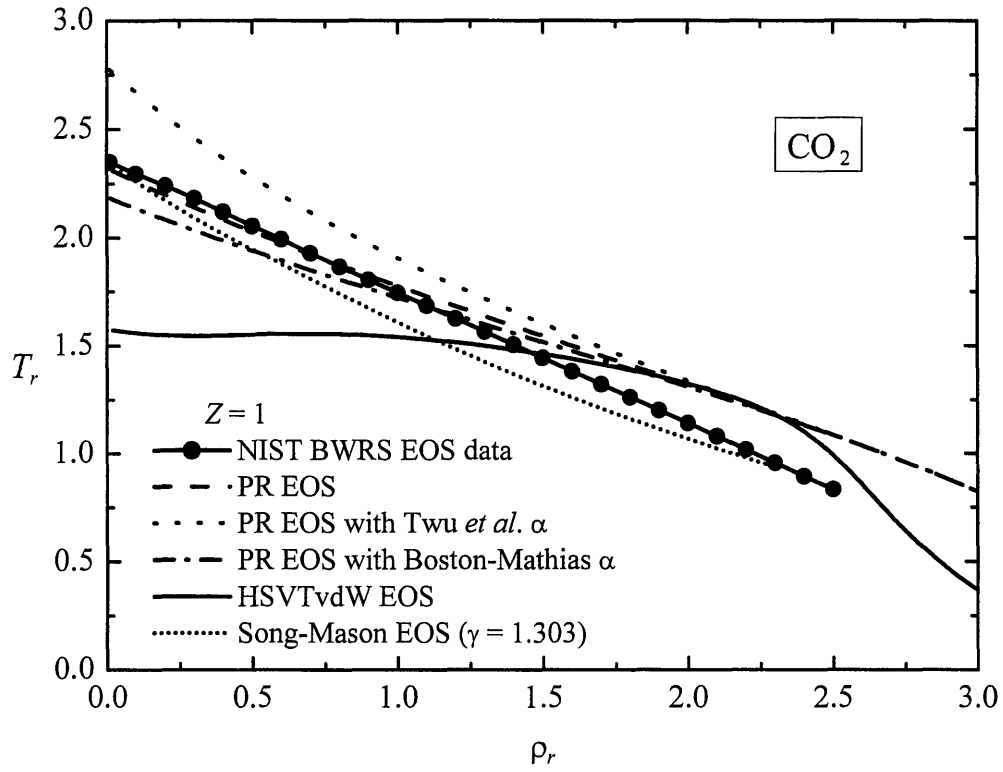
Figure 45. Experimental and predicted EOS $Z = 1$ Zeno line for pure carbon dioxide (Data source: McCarty and Arp (1992). See Table 15.).

volume translation to match Zeno behavior. Given these limitations of macroscopic EOS models, molecular simulation was used to probe molecular-level effects along the Zeno contour.

I.3.4 Molecular Simulation of Zeno Behavior

I.3.4.1 Potential Models and Computational Methods

A thorough molecular-simulation analysis has been conducted by M. Reagan and is explained in detail in Reagan (2000) and presented in a subsequent journal publication by Kutney *et al.* (2000). Only a brief review and select results are provided here.

The rigid Simple-Point-Charge (SPC) model for water is used for most of the molecular-simulation work and has previously been shown to provide accurate predictions of several water properties including the dielectric constant at ambient conditions (Berendsen *et al.*, 1981). The SPC model captures both short-range van der Waals interactions and long-range Coulombic interactions and as a result, predicts many important structural and electrostatic features of water (Berendsen *et al.*, 1981). Overall, the total intermolecular potential between two water molecules is given as a sum of Lennard-Jones and Coulombic interactions:

$$\Phi(r)_{water-water} = \Phi(r)_{Lennard-Jones}^{O-O} + \sum_{site-site} \Phi(r)_{Coulombic} \tag{84}$$

where

$$\Phi(r)_{Lennard-Jones} = 4\varepsilon_{ij}\left[\left(\frac{\sigma_{ij}}{r}\right)^{12} - \left(\frac{\sigma_{ij}}{r}\right)^{6}\right] \tag{85}$$

$$\Phi(r)_{Coulombic} = \frac{1}{4\pi\varepsilon_0}\frac{q_i q_j}{r}, \tag{86}$$

ε_0 is the vacuum permittivity $((Coulombs)^2\ kJ^{-1}\ mol\ nm^{-1})$, σ_{ij} is the diameter (nm), ε_{ij} is the potential well depth (kJ/mol), q_i is the point charge (Coulombs), and r is the site-site interatomic separation distance (nm). Additional assumptions and equations are also used in the SPC model and are described in Kutney *et al.* (2000) and Reagan (2000).

The SPC/E (Extended Simple Point Charge) model is also used for some simulations since it generates more accurate self-diffusivity predictions and a realistic critical point calculation. For example, Guissani and Guillot (1993) report a SPC/E critical temperature of

378.6°C and SPC/E critical density of 0.326 g/cm^3 which are close to the experimental values 374.1°C and 0.322 g/cm^3 (For comparison, $T_{c,SPC} = 313.9$°C and $\rho_{c,SPC} = 0.27$ g/cm^3).

To provide a basis of comparison for the SPC and SPC/E water results, M. Reagan also performed Molecular-Dynamics simulations using simple Lennard-Jones (LJ) soft spheres with a 6-12 potential (Kutney *et al.*, 2000; Reagan, 2000).

I.3.4.2 LJ, SPC, and SPC/E Simulation Results

Lennard-Jones $Z = 1$ simulation results are shown in Table 19 while SPC and SPC/E results are contained in Table 20 (Kutney *et al.*, 2000; Reagan, 2000). In addition, a range of compressibilities were computed at 367°C ($T_{r,SPC} = 1.0903$) at densities from 0.0059 to 0.881 g/cm^3 and are available in Table 21. Figure 46 is an isothermal plot of Z versus ρ_r at $T_r = 1.0903$ that compares the molecular simulation results given in Table 21 with experimentally correlated data for pure H_2O. The Zeno lines for SPC and SPC/E water are compared with experimental data in Figure 47.

The Zeno lines generated by Molecular-Dynamics simulations for both SPC and SPC/E water are similar and fall just above (for SPC) and below (for SPC/E) the experimentally-correlated $Z = 1$ line as shown in Figure 47. When properly scaled, the LJ model provides a linear fit as well, although it does not match experimental behavior on the Zeno contour as well as the SPC and SPC/E models. In earlier work, Ben-Amotz and Herschbach (1990a) showed similar results for Lennard-Jones fluids based on EOS and integral equation calculations (Nicolas *et al.*, 1979). For completeness, their results are also plotted on Figure 47. These comparisons indicate that all of these molecular simulation models capture the dynamic balance that exists between repulsive and attractive forces along the Zeno contour.

A SPC hydrogen-bonding analysis was also performed in order to examine the structure of water clusters and because there is widespread interest in water hydrogen bonding, especially at elevated temperatures and pressures. The combined distance-energy criteria of Kalinichev and Bass (1994) is often used to estimate the extent and the geometry of the hydrogen-bond network. The technique defines two water molecules to be hydrogen bonded if the O–H distance is less than 0.24 nm and the total water-water interaction energy is more negative than −10 kJ/mol. By sampling selected configurations from each simulation run that satisfy the Kalinichev and Bass

145

criteria, the average number of hydrogen bonds per molecule, $<n_{HB}>$, can be estimated and a matrix of connectivity for each simulated configuration can be generated.

Several $<n_{HB}>$'s for points on the Zeno line, as well as for ambient conditions and supercritical water at 450°C and 250 bar, are given in Table 22. Ambient water is known to have $<n_{HB}> = 3.2$, versus the SPC $<n_{HB}>$ value is 3.04. Knowing the complete matrix of connectivity for each independent configuration generated in the Molecular-Dynamics simulations, it is possible to determine the size and extent of hydrogen-bonded molecular clusters (Kalinichev and Churakov, 1999).

Cluster distributions are shown in Figure 48. As expected, the highest density system at 77°C shows a single large cluster containing 254 of the 256 molecules in the system. At 208°C, one still sees a predominance of large, percolating clusters that change size over time. By 367°C, despite only small changes in system density, a dramatically different liquid structure appears, with a large number of individual water molecules and groupings with less than 10 molecules as well as a wide distribution of clusters with sizes ranging from 10 to 200 molecules. Above 367°C, small groups of trimers, dimers, and single molecules begin to dominate as density decreases. Three-dimensional molecular visualizations of each SPC-calculated state point are shown in Figure 49 corresponding to the clustering depicted in two-dimensional projections shown in Figure 48.

Table 19. Lennard-Jones simulation results for $Z = 1$, the Zeno line

T (°C)	T_r	P (bar)	Z	ρ (g/cm^3)	ρ_r
49	0.549	748 ± 25	1.01 ± 0.03	0.504	1.87
208	0.819	681 ± 18	1.00 ± 0.02	0.308	1.14
367	1.090	349 ± 10	1.01 ± 0.03	0.118	0.44
508	1.331	150 ± 3	1.01 ± 0.04	0.042	0.15

Table 20. SPC and SPC/E model water simulation results for $Z = 1$, the Zeno line (95%-confidence-intervals uncertainties given for Z and P)

SPC Model

T (°C)	T_r	P (bar)	Z	ρ (g/cm^3)	ρ_r
77	0.6	1644 ± 52	1.01 ± 0.03	1.011	3.74
208	0.82	2044 ± 55	1.01 ± 0.02	0.914	3.39
367	1.09	2290 ± 49	1.01 ± 0.02	0.776	2.87
508	1.33	2296 ± 45	1.00 ± 0.02	0.643	2.38
637	1.55	2145 ± 39	1.00 ± 0.03	0.513	1.90
766	1.77	1858 ± 32	0.99 ± 0.03	0.393	1.45
1097	2.33	181 ± 17	1.00 ± 0.02	0.029	1.06

SPC/E Model

T (°C)	T_r	P (bar)	Z	ρ (g/cm^3)	ρ_r
77	0.54	1677 ± 54	1.01 ± 0.03	1.034	3.17
208	0.74	2095 ± 58	1.00 ± 0.03	0.949	2.91
367	0.98	2421 ± 52	1.00 ± 0.02	0.825	2.53
508	1.20	2490 ± 48	1.00 ± 0.02	0.698	2.14
637	1.40	2410 ± 42	1.00 ± 0.03	0.580	1.78
766	1.59	2316 ± 40	1.01 ± 0.03	0.483	1.48
1097	2.10	647 ± 21	1.00 ± 0.04	0.103	0.32

Table 21. SPC and SPC/E model water simulation results at $T_r = 1.0903$ data

SPC Model

P (bar)	Z	ρ (g/cm^3)	ρ_r
16.6	0.954	0.006	0.02
171	0.571	0.102	0.38
409	0.351	0.397	1.47
828	0.479	0.589	2.18
1624	0.770	0.718	2.66
1995	0.901	0.754	2.79
4157	1.61	0.881	3.26

SPC/E Model

P (bar)	Z	ρ (g/cm^3)	ρ_r
202	0.610	0.102	0.31
493	0.381	0.397	1.22
994	0.517	0.589	1.81
1921	0.820	0.718	2.20
2346	0.954	0.754	2.31
4617	1.61	0.881	2.70

Table 22. SPC hydrogen-bond simulation results

T (°C)	P (bar)	ρ (g/cm^3)	$<n_{HB}>$
77	1595	1.010	2.85
208	2043	0.914	2.31
367	2290	0.776	1.73
508	2296	0.643	1.28
637	2145	0.513	0.93
766	1858	0.393	0.66
1097	181	0.029	0.04
25	1	0.980	3.05
450	250	0.080	0.34
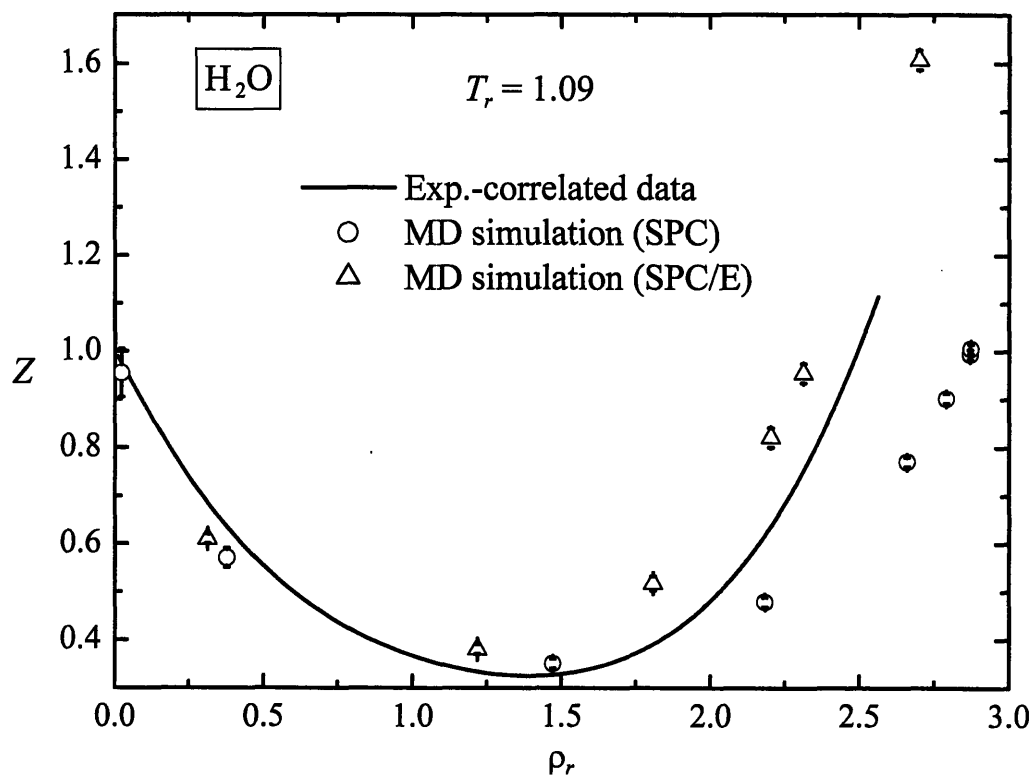
Figure 46. Molecular-Dynamics simulation of the $T_r = 1.09$ isotherm for water using the SPC and SPC/E models. A comparison with experimentally-correlated data given in Table 15 is shown.
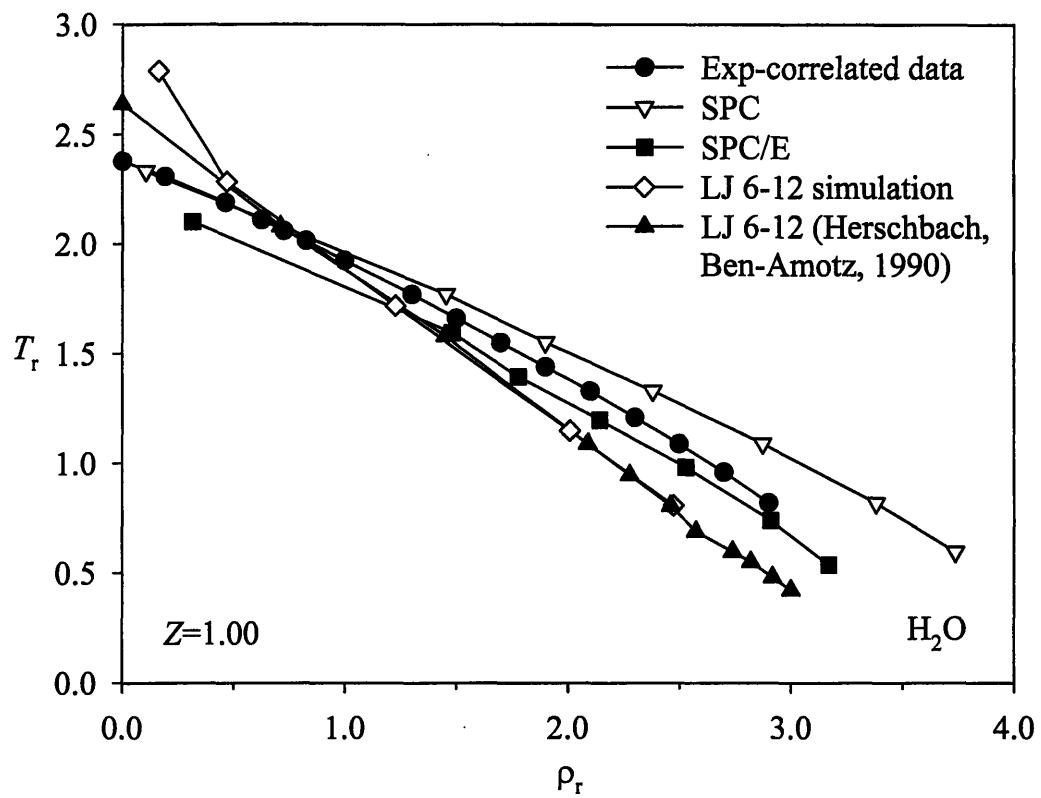
Figure 47. Molecular-Dynamics simulation of the Zeno line for water using the SPC, SPC/E, and LJ models. A comparison with experimentally-correlated data given in Table 15 is shown.
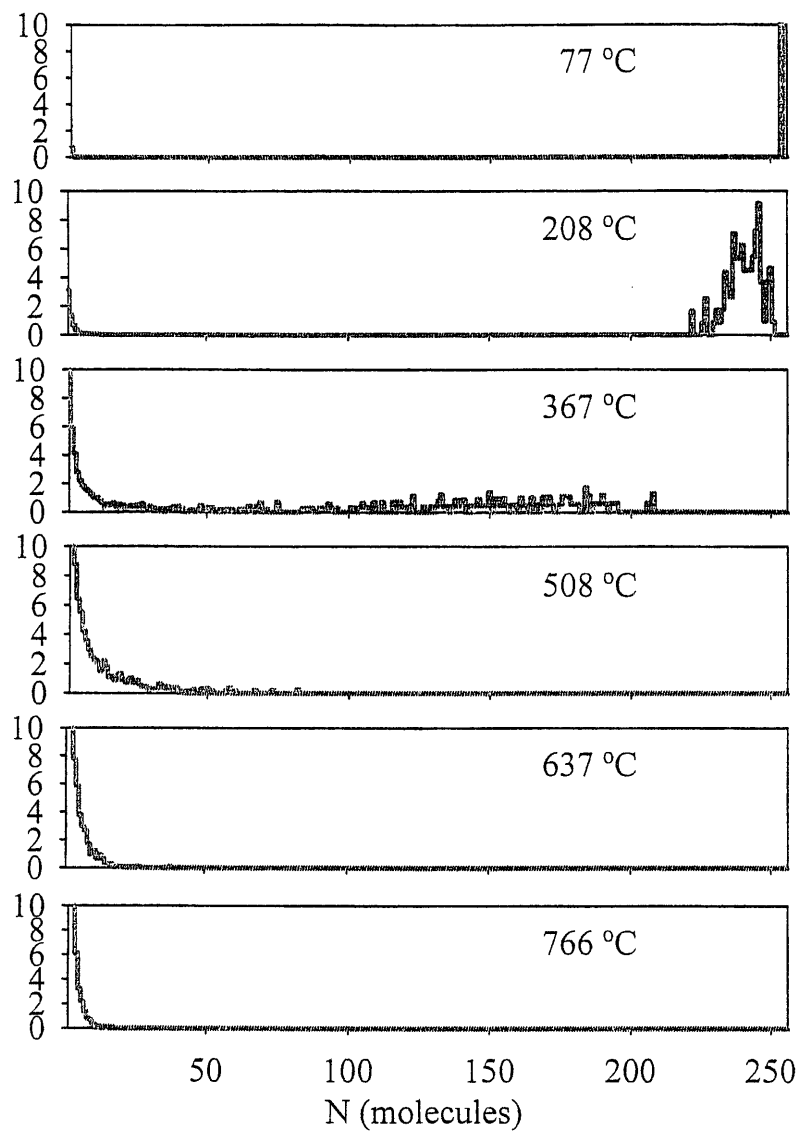
Figure 48. Cluster size distributions at points on the Zeno contour (see Table 20).

77 °C, 1595 bar, 1.01 g/cm

208 °C, 2043 bar, 0.914 g/cm

367 °C, 2290 bar, 0.776 g/cm

508 °C, 2296 bar, 0.643 g/cm

637 °C, 2145 bar, 0.513 g/cm

766 °C, 1858 bar, 0.393 g/cm

1097 °C, 181 bar, 0.029 g/cm
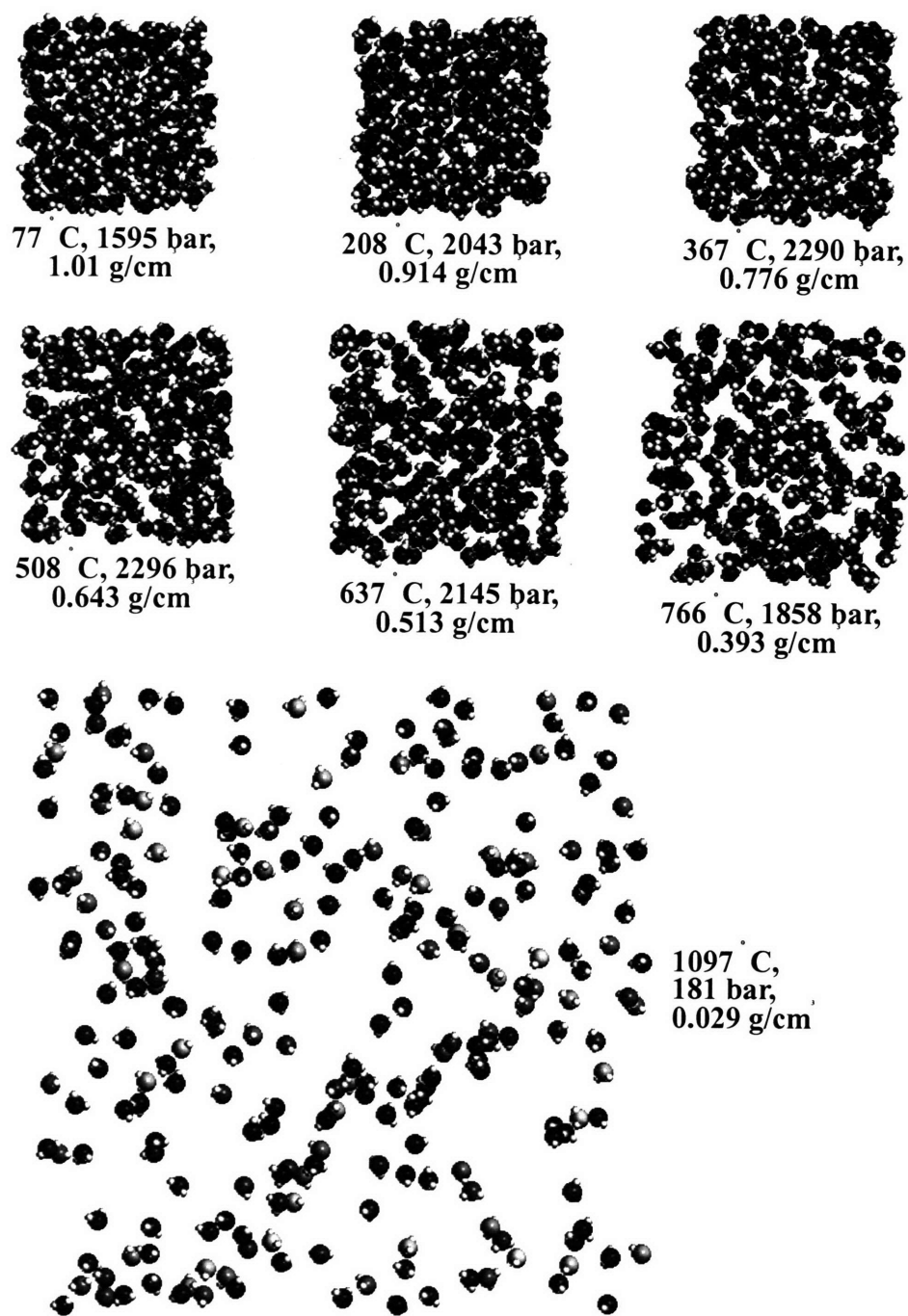
Figure 49. Two-dimensional projections of three-dimensional simulations of SPC water at points on the Zeno contour for seven different conditions of T and ρ (see Table 22).

I.3.5 Conclusions

The generic linearity of the $Z = 1$ contour in the T-ρ plane provides a quantitative criterion to evaluate and refine both macroscopic and molecular equations of state. By using critical-point scaling, species-dependent $Z = 1$ data can be partially generalized in a Corresponding-States framework. This observation has been used to examine if and how cubic equations of state could be fundamentally improved for three specific pure component cases (H_2O, CH_4, and CO_2). EOSs typically use parameters that are regressed from experimental *PVT* data which are far removed from the Zeno condition at high pressure and density. Thus, accurate Zeno line predictions indicate EOS robustness over a larger domain of *PVT* space.

Although the two-parameter van der Waals EOS yields a straight Zeno line (Batschinski, 1906; Ben-Amotz and Herschbach, 1990a), it does not match experimental observations even for simple fluids such as methane or argon. The Peng-Robinson EOS and other cubic EOSs show substantial improvement with reasonably close matches to empirical Zeno behavior with only one additional regressed parameter, α, which captures attractive interactions and is fit to vapor-liquid equilibrium data well outside the Zeno region. Modified PR EOSs with alternative α parameters can show improvements over the original PR EOS. In particular, the PR EOS with the Twu *et al.* (1995) α model shows excellent agreement with the Zeno conditions for water, implying that sensitivity to the magnitude and functional form of α may have a more fundamental connection to density-dependent interactions. A volume-translated PR EOS (VTPR EOS), which adds an adjustable parameter to provide improved estimates of high density *PVT* properties, provides substantially improved estimates of Zeno behavior. However, a hard-sphere volume-translated van der Waals EOS formulation (Kutney *et al.*, 1997) does not result in superior Zeno performance.

These comparisons indicate that, one should consider examining the $Z = 1$ contour to test for the observed universal linearity when developing an EOS. This Zeno criterion provides a species-independent check of the EOS robustness. When used effectively, new EOSs can be quickly compared to these observations and modified to increase accuracy.

Molecular simulations of Zeno behavior using SPC, SPC/E, and Lennard-Jones models for pure water match experimental behavior over a wide range of density, thereby confirming that these models can make water property predictions as accurate as pure component EOS predictions.

I.3.6 References

Aspen Technology (1994) Physical Properties Methods and Models – Reference Manual, Volume 2, Cambridge, MA.

Batschinski, A. (1906) "Abhandlungen über zustandsgleichung; abh. I: der orthometrische zustand." *Ann. Phys.*, **19**, 307–309.

Ben-Amotz, D. and Herschbach, D.R. (1990a) "Estimation of effective diameters for molecular fluids." *J. Phys. Chem.*, **94 (3)**, 1038–1047.

Ben-Amotz, D. and Herschbach, D.R. (1990b) "Correlation of Zeno ($Z = 1$) line for supercritical fluids with vapor liquid rectilinear diameters." *Israel J. Chem.*, **30**, 59–68.

Berendsen, H.J.C., Postma, J.P.M., van Gunsteren, W.F. and Hermans, J. (1981) "Interaction models for water in relation to protein hydration." *Intermolecular Forces*, Ed. by B. Pullman, Reidel and Dordrecht, 331–342.

Boushehri, A., Tao, F.M. and Mason, E.A. (1993) *J. Phys. Chem.*, **97 (11)**, 2711–2714.

Burshtein, A.I. (1974) "The origin of the "ideal gas curve"." *Russ. J. Phys. Chem.*, **8**, 1562–1566.

ChemicaLogic Corporation (1999) "SteamTab Companion V1.0." Based on the 1995 International Association for the Properties of Water and Steam (IAPWS) Formulation for the Thermodynamic Properties of Ordinary Water Substance for General and Scientific Use (IAPWS-95), Woburn, MA, .

DIPPR (1995) "Data compilation of pure compound properties." ASCII Files, NIST Standard Reference Data, Gaithersburg, MD.

Guissani, Y. and Guillot, B. (1993) *J. Phys. Chem.*, **98 (10)**, 8221–8235.

Haar, L., Gallagher, J.S. and Kell, G.S. (1984) *NIST standard reference database 10–steam tables*, Hemisphere Pub. Corp., New York, NY.

Holleran, E.M. (1967) "Linear relation of temperature and density at unit compressibility factor." *J. Chem. Phys.*, **47**, 5318–5324.

Holleran, E.M. (1968) "Interrelation of the virial coefficients." *J. Chem. Phys.*, **49**, 39–43.

Holleran, E.M. (1968) *J. Phys. Chem.*, **72**, 1230.

Holleran, E.M. (1969) *J. Phys. Chem.*, **73 (167)**, 3700.

Holleran, E.M. (1970) *Cryogenics*, **10**, 423.

Holleran, E.M. (1990) *Ind. Eng. Chem. Res.*, **29**, 632.

Holleran, E.M. and Hammes, J.P. (1975) *Cryogenics*, **15**, 95.

Holleran, E.M. and Jacobs, R.S. (1972) *Ind. Eng. Chem. Fundam.*, **11**, 272.

Holleran, E.M. and Sinka, J.V. (1971) *J. Phys. Chem.*, **55**, 4260.

Kalinichev, A.G. and Bass, J.D. (1994) *Chem. Phys. Lett.*, **231**, 301–307.

Kalinichev, A.G. and Churakov, S.V. (1999) *Chem. Phys. Lett.*, **302**, 411–417.

Kutney, M.C., Dodd, V.S., Smith, K.A., Herzog, H.J. and Tester, J.W. (1996) "Equations of state for supercritical process modeling." MIT Energy Laboratory, Cambridge, MA, MIT EL 94–003 (revised).

Kutney, M.C., Dodd, V.S., Smith, K.A., Herzog, H.J. and Tester, J.W. (1997) "A hard-sphere volume-translated van der Waals equation of state for supercritical process modeling. part 1. pure components." *Fluid Phase Equilibria*, **128**, 149–171.

Kutney, M.C., Reagan, M., Smith, K.A., Tester, J.W., and Herschbach, D.R. (2000) "The Zeno (Z = 1) behavior of equations of state: an interpretation across scales from macroscopic to molecular." *J. Phys. Chem. B*, **104 (40)**, 9513–9525.

Marrucho, I.M. and Ely, J.F. (1998) *Fluid Phase Equilibria*, **150–151**, 215–223.

Martin, J.J. (1967) *Ind. Eng. Chem.*, **59**, 34–56.

Mathias, P.M., Naheiri, T. and Oh, E.M. (1989) *Fluid Phase Equilibria*, **47**, 77–87.

McCarty, R.D. and Arp, V. (1992) NIST Standard Reference Database 12, NIST Thermophysical Properties of Pure Fluids Database, Version 3.1, NIST Standard Reference Data Program, Gaithersburg, MD.

Morsy, T.E. (1963) "Zum thermischen und kalorischen verhalten realer fluider stoffe." Doctoral dissertation, Karlsruhe, Germany.

Nedostup, V.I. (1970) "The use of the ideal gas curve in thermodynamic studies." *Russ. J. Phys. Chem.*, **44**, 1249–1250.

Nedostup, V.I. and Bekker, M.B. (1980) "Calculation of thermodynamic properties of mixtures of compressed gases." *High Temp.*, **18**, 869–871.

Nedostup, V.I. and Gal'kevich, E.P. (1976) "Behavioral features of the "ideal curves" of real gases." *High Temp.*, **14**, 972–975.

Nedostup, V.I. and Gal'kevich, E.P. (1980) "The "ideal curve" method in the thermodynamics of real gases and gas mixtures." *J. Eng. Phys.*, **38**, 424–429.

Nedostup, V.I., Gal'kevich, E.P., Kaminskii, E.S. and Bekker, M.B. (1988) "Canonic equation of state for imperfect gases in the high temperature and pressure ranges." *High Temp.*, **26**, 674–677.

Nicolas, J.J., Gubbins, K.E., Street, W.B. and Tildesley, D.J. (1979) *Molecular Physics*, **37 (5)**, 1429–1454.

Parsafar, G. and Mason, E.A. (1993) *J. Phys. Chem.*, **97 (35)**, 9048–9053.

Parsafar, G. and Mason, E.A. (1994) *J. Phys. Chem.*, **98 (7)**, 1962–1967.

Peng, D.-Y. and Robinson, D.B. (1976) *Ind. Eng. Chem., Fundam.*, **15**, 59–64.

Reagan, M.T. (2000) "Multiscale molecular modeling of aqueous systems from ambient to supercritical conditions." MIT Dept. of Chem. Eng., Doctoral dissertation, Cambridge, MA.

Reid, R.C., Prausnitz, J.M. and Poling, B.E. (1987) *The Properties of Gases and Liquids*, McGraw-Hill, 4th ed., New York, NY, .

Schaber, A. (1965) "Zum thermischen verhalten fluider stoffe." Doctoral dissertation, Karlsruhe, Germany, .

Serovskii, L.A. (1990) "Three-parameter modification of the van der Waals equation." *Russ. J. Phys. Chem.*, **64**, 334–336.

Soave, G.S. (1972) *Chem. Eng. Sci.*, **27**, 1197–1203.

Stryjek R. and Vera J.H. (1986) *Can J. Chem. Eng.*, **64**, 820–825.

Twu, C.H., Coon, J.E. and Cunningham, J.R. (1995) *Fluid Phase Equilibria*, **105**, 49–59.

van der Waals, J.D. (1873) "Over de continuiteit van den gas-en vloeistoftoestand." Doctoral dissertation, Leiden, Holland.

Vasserman, A.A. (1964) "Equation of state for nitrogen." *Russ. J. Phys. Chem.*, **38**, 1289–1291.

Xu, J. and Herschbach, D.R. (1992) *J. Phys. Chem.*, **96**, 2307–2312.

PART II – TRANSPORT-PROPERTY RESEARCH

II.1. Introduction and Background

In addition to a need for accurate thermodynamic properties for pure supercritical water and supercritical-water mixtures, there is also a need for accurate transport properties of these species. Transport properties are usually predicted using empirical or semi-empirical models and typically employ parameters that are regressed directly to experimental data. Transport properties govern heat and mass transfer and can potentially affect important phenomena in supercritical water including corrosion, reaction kinetics, salt nucleation, and salt precipitation. Transport modeling typically covers a wide range of applications including heat and mass transfer, fluid-mixing profiles, salt deposition, corrosion, species diffusion, and overall SCWO process and equipment simulations.

The transport property addressed in this dissertation section is molecular diffusivity. Pure water diffusivity data are available at typical SCWO conditions, but binary molecular-diffusivity data for aqueous mixtures are scarce. Compounding this scarcity is the concern that SCWO reactors intended to operate with maximum destruction efficiencies could possibly operate in a mass-transfer-limited mode due to limited availability of aqueous-mixture diffusivity data. For these reasons, this thesis section presents aqueous-mixture diffusivity data preceded by a discussion of

- molecular diffusivity,
- critical phenomena of transport properties,
- supercritical diffusivity publications,
- the nuclear magnetic resonance diffusivity-measurement approach, and
- the measurement apparatus.

Following the introduction of this dissertation's diffusivity data, an analysis of models with previously published data is presented.

159

II.1.1 Molecular Diffusivity

II.1.1.1 Diffusivity

Diffusion can be defined as the spontaneous permeation of "particles" through a collection of "particles." For a system in which the particles are molecules, molecular diffusion represents the permeation of molecules through a collection of molecules in contact with them and was first defined in a scientific manner by Berthollet in 1803 when he used the term "diffusion" to describe the movement of a dissolved salt particle away from salt crystals and into the bulk water solution (Tyrell and Harris, 1984). Later in 1808, Dalton stated that "the diffusion of gases through each other is effected by means of the repulsion belonging to the homogeneous particles (Simpson and Weiner, 1989)." The motion that is described by molecular diffusion develops due to a concentration gradient, although as will be discussed, the driving force is actually the chemical potential or free energy gradient. Molecular diffusion strives to minimize the gradient by equalizing the free energy throughout the system while increasing entropy and is dependent on the temperature, density, pressure, and concentration along with the molecule's shape, charge, size, and intramolecular interactions.

Close to an equilibrium condition in a simple system, the transfer rate of molecules (or mass) is proportional to the concentration gradient. The constant of proportionality is the diffusivity or the diffusion coefficient. Typical molecular diffusivities are presented in Table 23 which also demonstrates sensitivity to solute and temperature. Depending on the system in which molecular diffusion is occurring, distinct diffusion coefficients have also been defined in the context of Fick's First Law discussed below. Interdiffusion or mutual diffusion occurs when a single species i with a mutual diffusivity D_{ij} ($i \neq j$) diffuses through a multi-component system. Intradiffusion or tracer diffusion occurs when a portion of a single species i with a tracer diffusivity D_i is labeled and diffuses through a homogeneous system in which a concentration gradient exists for the labeled species i. Isotopic radioactive labeling was often used in the past, but other labeling techniques are also now available including nuclear-magnetic-resonance. Self-diffusion is a unique intradiffusion case, which occurs when the system has one only species, namely i, and has self-diffusivity defined as D_{ii}.

Table 23. Diffusivity examples (Atkins, 1990; Holz *et al.*, 2000)

Species	Temperature, T (°C)	Pressure, P (bar)	Diffusivity, $D_{12} \times 10^5$ (cm^2/s)
Solute effect			
H_2 in liquid CCl_4	25	1	9.75
O_2 in liquid CCl_4	25	1	3.82
CH_4 in liquid CCl_4	25	1	2.89
Sucrose in liquid H_2O	25	1	52.2
H_2O in liquid H_2O	25	1	2.30
CH_3OH in liquid H_2O	25	1	1.58
Temperature effect			
H_2O in liquid H_2O	25	1	2.30
H_2O in liquid H_2O	35	1	2.91
H_2O in liquid H_2O	45	1	3.59
H_2O in liquid H_2O	55	1	4.34
Ion effect			
H^+ in liquid H_2O	25	1	9.31
Na^+ in liquid H_2O	25	1	1.33

Examples of mutual, tracer, and self-molecular diffusivities are shown in Figure 50 for a n-dodecane (1) and n-octane (2) system. As the n-dodecane concentration increases, the mutual diffusivity (D_{12}) and the tracer diffusivities (D_1 and D_2) decrease. At the pure n-dodecane limit, the mutual diffusivity equals the n-octane tracer diffusivity (D_2). Correctly written as $\lim(D_{12}) \to D_2$ as $x_1 \to 1$, this observation has been verified theoretically (Tyrell and Harris, 1984). Conversely, $\lim(D_{12}) \to D_1$ as $x_1 \to 0$. It has also been shown that $D_{12} = D_{21}$ for binary systems (Kestin and Wakeham, 1988). Figure 50 also illustrates that there is not a simple relationship between either self-diffusivities (D_{11} and D_{22}) and mutual diffusivity (D_{12}). Although significant research effort has been invested, there are not any universal theories or formulas that correctly model diffusivities or hold for all binary systems (Cussler, 1997).

Fick was the first to develop an expression relating the mass-transfer-rate flux to the concentration gradient, and he based his theory on parallel research performed by Fourier for heat conduction and Ohm for current flow (Tyrell and Harris, 1984). Fick showed that the molar flux $\mathbf{J}_i$ is proportional to the driving force defined by the molar concentration gradient, which is often referred to as Fick's First Law of Diffusion:
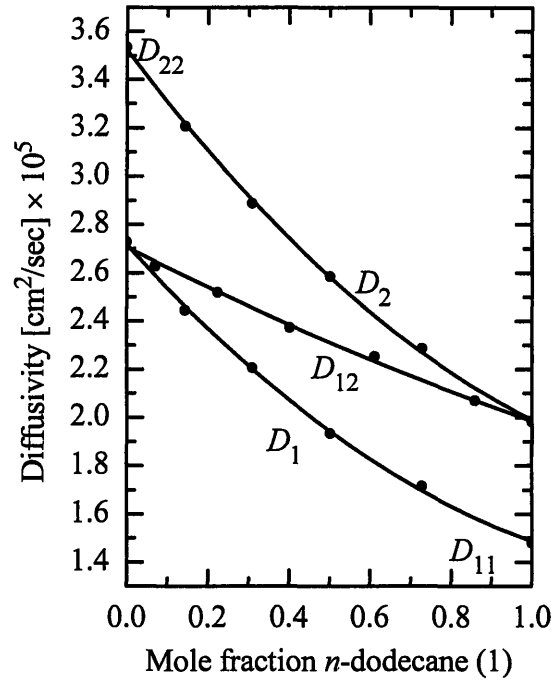
Figure 50. Diffusivities of n-dodecane (1) and n-octane (2) at 1 bar and 60°C (Van Geet and Adamson, 1964).

$$\mathbf{J}_i = -D_{ij}\nabla C_i \qquad (87)$$

where D_{ij} has dimensions length^2/time while for the Cartesian coordinate system

$$\nabla C_i = \left(\frac{\partial C_i}{\partial x}\right)_{y,z}\mathbf{i} + \left(\frac{\partial C_i}{\partial y}\right)_{x,z}\mathbf{j} + \left(\frac{\partial C_i}{\partial z}\right)_{x,y}\mathbf{k} \qquad (88)$$

The negative sign in Eq. (87) ensures that molecules are, on the average, transferred from higher to lower concentrations.

Fick was not entirely correct when he related the flux to the concentration gradient and called the proportionality constant diffusivity. To be theoretically correct, flux is proportional to the chemical potential gradient ($\nabla\mu_i$ or $d\mu_i/dz$ for one dimension). Correction terms involving activities, infinitely dilute diffusivities, and concentrations have been employed with some success (Poling et al., 2001).

Molecular diffusivity can be modeled using activation, free volume, hydrodynamic, and kinetic models (Tyrell and Harris, 1984). Hydrodynamic models are typically used for predicting properties of liquid-like fluids, while kinetic models are typically for gaseous predictions. Activation models are based on the Arrhenius concept where transition states must

162

be reached before diffusion may proceed and have resulted in semi-empirical diffusivity models of the following form

$$D = Ae^{\left(\frac{-E_a}{RT}\right)}$$

(89)

Once a molecule reaches an activated or energetic state, a diffusion "jump" may occur, but only a fraction of molecules should be activated. Unfortunately, compared to chemical-reaction kinetic values, activation energies are quite small for liquid-phase diffusivities and result in a significant proportion of activated molecules (Tyrell and Harris, 1984). Due to this substantial inconsistency, activation models should not be used for supercritical water diffusivity modeling, even though activation theories have had some success for other systems.

Based on the concept that vacant cages can form and then become occupied by random molecular movements, free volume models have also been used to model diffusivities but with limited success. For example, they have been used to accurately predict benzene self-diffusion coefficients and iodine-tetrachloromethane mutual diffusivities (Hildebrand, 1977). For benzene, n-heptane, n-decane, and some halogenated benzenes, Ertl and Dullien (1973) used

$$D_i = B'\left(\frac{\rho}{\rho_g} - 1\right)^m$$

(90)

in order to successfully predict tracer diffusivities. The terms B' and m are species-dependent fitted variables, and ρ_g is the limiting density at infinite viscosity (infinite viscosity typically corresponds to a liquid at its glass-transition point). Due to their limited modeling success, free volume models in their original forms were not considered for supercritical-water diffusivity modeling. Recently, however, hard sphere modeling researchers have incorporated free-volume concepts into their formulations and have had some success. This approach will be addressed shortly.

II.1.1.2 Hydrodynamic Theory of Diffusion

Since the level of understanding of liquid structure and interactions is far from complete, it should be no surprise that accurate theoretical liquid diffusivity models are not available. Nevertheless, semi-theoretical and idealized models are available, provide valuable insight into the diffusion mechanism in liquids, and allow diffusivity correlations to be developed.

Consider the case of a single rigid solute particle moving through a solvent continuum (at infinite dilution) where molecular motions are uncorrelated. The Nernst-Einstein equation relates the diffusion coefficient to temperature and the friction factor f, which represents the force necessary to make the particle move with unit velocity (or the inverse of the mobility, the steady-state particle velocity when under a unit force) (Bird *et al.*, 1960)

$$D_{12} = \frac{kT}{f} \tag{91}$$

Friction factor models continue to be difficult to develop and use due to the inadequate level of understanding of liquid structure, model assumptions, and model limitations.

Based on Stoke's 1903 analysis of a spherical particle with radius r_1 in creeping flow, classical hydrodynamic theory can relate the friction factor to the solvent viscosity

$$f = 6\pi\eta_2 r_1 \left(\frac{1 + \dfrac{2\eta_2}{\beta r_1}}{1 + \dfrac{3\eta_2}{\beta r_1}} \right) \tag{92}$$

where β is the sliding frictional coefficient between the diffusing sphere and the solvent liquid. Sliding friction varies between two limiting cases.

1. $\beta \to \infty$ where liquid solvent molecules completely wet the diffusing sphere, and there is "no slip" between them. For example, consider a large particle in a bath of low molecular weight solvent or where the solvent is a continuum (Tyrell and Harris, 1984). The friction factor reduces to

$$f = 6\pi\eta_2 r_1 \tag{93}$$

By substituting Eq. (93) into Eq. (91), the Stokes-Einstein equation results:

$$D_{12}^{SEns} = \frac{kT}{6\pi\eta_2 r_1} \tag{94}$$

2. $\beta \to 0$ where the liquid molecules do not wet and do not stick to the sphere, and there is slippage between them. The friction factor and reduced Nernst-Einstein equations are then

$$f = 4\pi\eta_2 r_1 \tag{95}$$

$$D_{12}^{SEs} = \frac{kT}{4\pi\eta_2 r_1} \tag{96}$$

The "slip" limit typically occurs when the solute and solvent molecules are approximately the same size or are alike as in the case for self-diffusivities. Given this observation, self-diffusivities of polar and non-polar liquids have been predicted using Eq. (96) with errors of ±12%.

For non-spherical particles, $e.g.$, macromolecules, the friction factor must be modified to account for the friction factor difference along each of the three dimensions (Kiado, 1974), but for this dissertation, it is beyond the scope of what is needed. Although these diffusivity models are derived for specialized cases, $i.e.$, the solute molecules should be much larger than the solvent molecules and the solution should be dilute, they nonetheless provide a basis for comparisons. They also provide a starting point for the development of more complex and accurate correlations.

The infinitely dilute assumption is often invalid for mixtures of interest and several investigators have attempted to account for solute concentrations. Batchelor introduced a simple first-order correction term using the solute volume fraction for a mixture of non-attracted hard spheres (Tyrell and Harris, 1984)

$$D_{12} = \frac{kT}{6\pi\eta_2 r_1}\left(1 + 1.45\phi_V\right) \tag{97}$$

This linear dependence on volume would always scale the diffusivity between 1.0 and 2.45, which is not always the case. Corrections based on activity coefficients have also been proposed. One of the simpler correlations is summarized by Kiado (1974), which starts with the solute chemical-potential gradient as developed by Hartley, Onsager, and Fuoss

$$\nabla\mu_1\big|_{T,P} = \frac{RT}{c_1}\left\{1 + \left(\frac{\partial\ln\gamma_1}{\partial\ln c_1}\right)_{T,P}\right\}\nabla c_1 \tag{98}$$

where γ_1 is the solute activity coefficient. For concentrated solutions, Hartley and Crank (1949) found that

$$D_{12} = \frac{kT}{\eta}\left(\frac{\partial\ln\gamma_1 x_1}{\partial\ln x_1}\right)_{T,P}\left(\frac{x_2}{\lambda_1} + \frac{x_1}{\lambda_2}\right) \tag{99}$$

165

where λ is the proportionality constant between the friction factor and species viscosity. If the λ's are assumed to be independent of concentration, then the model reduces to the form that was independently developed by Carman and Stein (1956) when they examined mixtures of ethyl iodide and n-butyl iodide

$$
\begin{aligned}
D_{12}^{CS} &= \frac{1}{\eta_{12}}\left(\frac{\partial \ln \gamma_1 x_1}{\partial \ln x_1}\right)_{T,P}\left(x_2\eta_2 D_1^{x_2 \to 0} + x_1\eta_1 D_2^{x_1 \to 0}\right) \\
&= \frac{1}{\eta_{12}}\left(\frac{\partial \ln \gamma_1 x_1}{\partial \ln x_1}\right)_{T,P}\left(x_2\eta_2 D_{12}^{\infty} + x_1\eta_1 D_{21}^{\infty}\right)
\end{aligned}
\tag{100}
$$

where η_{12} is the solution viscosity and D_{12}^{∞} is the mutual diffusivity of an infinitely dilute solution of i in species j (solvent). For each of these approaches, there are binary systems that are accurately modeled (less than 10% error). However, for complex systems such as associated solutions, these models often provide poor fits.

To provide practical predictive capabilities of hydrodynamic-based theories, numerous researchers have used experimental data in order to develop semi-empirical and empirical correlations for liquid-like diffusivities. One of the most widely used for infinitely dilute spherical mixtures is based on the work of Wilke and Chang (1955). They examined 285 points among 251 binary systems and achieved approximately 10% average error when they used

$$
D_{12}^{WC}[\text{cm}^2/\text{s}] = 7.4 \times 10^{-8}\frac{T[\text{K}]\sqrt{\phi_2 M_2[\text{g/mole}]}}{\eta_{12}[\text{cP}]V_{b1}^{0.6}[\text{cm}^3/\text{mole}]}
\tag{101}
$$

where ϕ_2 is a fitted dimensionless solvent association factor for "associated liquids such as water and other hydrogen-bonding solvents ... introduced to define the effective molecular weight of the solvent with respect to the diffusion process" (Wilke and Chang, 1955), V_{b1} is the solute liquid molar volume at the normal boiling point (NBP), and η_{12} is the solution viscosity but the solvent viscosity, η_2, is often used instead. Original association-factor values are reported in Table 24 along with values updated by more recent research (e.g., Hayduk and Laudie (1974) report $\phi_2 = 2.26$ for water at ambient conditions). Note that there is a strong correlation between the association factor and number of hydrogen bonds, as shown in Table 24, so caution must be exercised when using the Wilke-Chang correlation for hydrogen-bonded liquids that may experience changes in the number of hydrogen bonds, e.g., when they are heated. To this day,

this simple-to-use correlation is still regarded as one of the best available for liquid-like diffusivity predictions, although some replace the NBP molar volume with other expressions (*e.g.*, estimated molar volumes based on hydrated contact ion pair structures for supercritical aqueous salt mixtures (Butenhoff *et al.*, 1996)) and is often used as a precursor to more complicated expressions.

One such correlation was developed by Reddy and Doraiswamy (1967) where they eliminated the need for an association factor by using a ratio of solvent and solute molecular volume

$$D_{12}^{RD}[cm^2/s] = \Pi \frac{T[K]\sqrt{M_2[g/mole]}}{\eta_2[cP]V_1^{1/3}[cm^3/mole]V_2^{1/3}[cm^3/mole]} \quad \begin{array}{ll} V_2/V_1 \leq 1.5 & \Pi = 10^{-7} \\ V_2/V_1 > 1.5 & \Pi = 8.5 \times 10^{-8} \end{array} \quad (102)$$

Since volumes may not be available at some process conditions, NBP volumes are used instead. Using Eq. (102), they report a 13.5% deviation for 76 systems with $V_2/V_1 \leq 1.5$ and 18% deviation for 20 systems with $V_2/V_1 > 1.5$. Such a correlation further simplifies the need for data. However, by using NBP volumes, the accuracy of the Reddy-Doraiswamy prediction is at risk.

Table 24. Association factors for the Wilke-Chang correlation and ambient average number of hydrogen bonds (Wilke and Chang, 1955; Hayduk and Laudie, 1974; Kalinichev and Bass, 1997; Hoffmann and Conradi, 1998)

Species	ϕ_2	$<n_{HB}>$
Heptane	1.0	0.0
Ether	1.0	0.0
Benzene	1.0	0.0
Ethyl alcohol	1.5	0.8
Methyl alcohol	1.9	1.9
Water	2.6	
Updated water	2.26	3.2
Assuming linearity, $\phi_2 = 0.424<n_{HB}> + 1$ ($R^2 = 0.95$)		

Tyn and Calus proposed a correlation for infinitely dilute systems with equal-sized solute and solvent molecules since they correctly argue that the Stokes-Einstein equation assumes that "large, rigid spheres diffuse through a medium of small particles (Tyn and Calus, 1975a)." Their approach is different from the previously mentioned correlations because they focus on using parachors which are "secondary derived function(s) dependent of the primary properties of surface tension, density, and molecular weight." A parachor can be described then as "a measure of the effect of the forces due to molecular attraction on the molecular volumes." They point out several system limitations and write that their model has an overall absolute average error of 12.0% versus 16.5% for the Wilke-Chang correlation for the 113 self-diffusivities, 996 total data points, and 535 systems used. Poling *et al.* (2001) describe the limitations and give several examples of the Tyn-Calus correlation, which requires the surface tension of the system components at the conditions of interest since the parachors are slightly temperature dependent. Since system surface tensions are challenging to obtain at supercritical-water process conditions, the Tyn-Calus correlation is difficult to implement.

Other correlations based on other material properties such as heat of vaporization have been developed, but as is commonly the case, nearly all are regressed to numerous organic-solvent-based systems and to only a limited number of water-solvent-based systems. Of notable interest is the Lusis and Ratcliff (1968) correlation that specifically states in the article that water-solvent-based systems should not be used with their expression, although some researchers have used it for water systems despite this disclaimer (*e.g.*, Butenhoff *et al.*, 1996).

Hydrodynamic theories and the subsequent correlations are often extended for use at lower densities, higher temperatures, and for concentrated systems. At these conditions, many of these expressions are inaccurate, but are often refined in an attempt to improve their accuracy. For this dissertation and for comparison reasons only, these hydrodynamic-based expressions will be evaluated under SCWO-processing test conditions using many of the same refinements that have been previously proposed. They include the infinitely dilute mutual-diffusivity Stokes-Einstein, Wilke-Chang, and Reddy-Doraiswamy correlations.

II.1.1.3 Kinetic Theory of Diffusion

For the analysis of gas diffusivities, a fundamentally different approach based on the kinetic theory of gases is often used. From this simple theory of matter, equations of state and other physical property models can be developed. In its simplest (hard sphere) version, the kinetic theory of gases is based on four assumptions:

1. Gases are molecules that are in constant chaotic and random motion.

2. All molecules have an average kinetic energy proportional to kT, a mass m, and a diameter σ.

3. All molecules are negligible in size compared to the mean free path.

4. Perfectly elastic collisions are the only allowed interactions between molecules (Hirschfelder *et al.*, 1966).

With these assumptions, the root-mean-square speed of the molecules can be derived

$$c = \sqrt{\frac{3RT}{M}} \tag{103}$$

along with the Maxwell-Boltzmann distribution of velocities

$$f(v) = 4\pi v^2 \left(\frac{M}{2\pi RT}\right)^{3/2} \exp\left(-\frac{Mv^2}{2RT}\right) \tag{104}$$

The mean speed of the Maxwell-Boltzmann distribution can then be calculated along with the mean free path of a perfect gas, which is the product of the mean speed and the mean time between each collision (Atkins, 1990)

$$\bar{c} = \int v f(v) = \sqrt{\frac{8RT}{\pi M}} \tag{105}$$

$$\Lambda = \bar{c}\frac{V}{\sqrt{2}\sigma\bar{c}N_A} = \frac{RT}{\sqrt{2}\sigma N_A P} \tag{106}$$

Finally, it can be shown that the diffusivity of a pure perfect gas can be written as

$$D_{ii} = \frac{\bar{c}\Lambda}{3} = \frac{2(RT)^{3/2}}{3\pi^{1/2}\sigma N_A M^{1/2}P} \tag{107}$$

In real gases, molecules are not hard spheres and mixtures do not have the same size species. Thus, it is logical to expect refinements to the kinetic-gas-theory approach. For example, Chapman and Enskog, working independently, solved the Maxwell-Boltzmann

equation for a dilute, non-polar, monatomic, spherical binary gas mixture that has attractive and repulsive interactions (Hirschfelder et al., 1966; Chapman and Cowling, 1970; Tham and Gubbins, 1971; McLennan, 1989). Their result is what is commonly referred to as the Chapman-Enskog equation

$$D_{12}^E = \frac{3}{8}\sqrt{\frac{kT}{\pi M_{12}}}\frac{f_D}{n\sigma_{12}^2 \Omega_D}$$ (108)

where $M_{12} = 2/\{(1/M_1) + (1/M_2)\}$ [g/mol], n is molecular number density in the mixture, σ_{12} [Å] is the collision diameter, Ω_D is the collision integral for diffusion calculated from a intermolecular-potential function, and f_D is a correction term that is often unity unless there are unequal molecular masses and the light species is in trace amounts (Poling et al., 2001). To reiterate, interactions need to be elastic and instantaneous in order to ensure that only binary interactions occur and molecular velocities are not correlated, thereby assuring low densities and uncorrelated motion.

Using the ideal-gas law to express the number density, $n = P/kT$, and setting f_D to unity for molecular weights of the same order of magnitude, Eq. (108) reduces to (Poling et al., 2001)

$$D_{12}^E [\text{cm}^2/\text{s}] = 0.002663 \frac{T^{3/2}}{P[\text{bar}]\sigma_{12}^2[\text{Å}]\Omega_D \sqrt{M_{12}}}$$ (109)

where the superscript E stands for Chapman-Enskog. For non-polar gases, the Lennard-Jones (LJ) 12-6 potential function is often chosen to determine the collision integral and relates the intermolecular energy to the separation distance (r_i), potential-well depth (ε_i), and diameter (σ_i)

$$\psi_i = 4\varepsilon_i\left[\left(\frac{\sigma_i}{r_i}\right)^{12} - \left(\frac{\sigma_i}{r_i}\right)^6\right]$$ (110)

Using traditional mixing rules, the effective collision diameter and effective potential-well depth of a binary (12) mixture can be determined (Hirschfelder et al., 1966).

$$\sigma_{12} = \frac{\sigma_1 + \sigma_2}{2}$$ (111)

$$\varepsilon_{12} = \sqrt{\varepsilon_1\varepsilon_2} \quad \text{or} \quad \varepsilon_{12}/k = \sqrt{\frac{\varepsilon_1}{k}\frac{\varepsilon_2}{k}}$$ (112)

The effective-diameter combining rule (Eq. (111)) is theoretically correct for hard-sphere molecules while the effective well-depth rule (Eq. (112)) is semi-empirical and is based on successful property modeling. The theoretical underpinning for Eq. (112) comes from a simple interpretation of dispersion forces in a mixture (Hirschfelder *et al.*, 1966). With the effective collision diameter, effective well depth, and the temperature, the collision integral for diffusion (also written as $\Omega^{(1,1)*}$ in Hirschfelder *et al.* (1966) and $\Omega^{(1)}(1)$ in Chapman and Cowling (1970)) can be determined. Neufield *et al.* (1972) fit an expression to accurately determine and allow fast calculation of the collision integral for the LJ 6-12 potential

$$\Omega_D = \frac{1.06036}{(kT/\varepsilon_{12})^{0.15610}} + \frac{0.19300}{\exp(0.47635(kT/\varepsilon_{12}))} + \frac{1.03587}{\exp(1.52996(kT/\varepsilon_{12}))} + \frac{1.76474}{\exp(3.89411(kT/\varepsilon_{12}))}$$ (113)

Given that mixtures of interest may not be at low density, corrections have been developed to extend the kinetic-theory models to situations in which the mean free path is not large compared with the molecular diameters. Due to the smaller mean free path, dense-gas models can also account for a reduction of the collision frequency and can accommodate complex synchronized collisions rather than being limited to kinetic-gas-theory instantaneous binary collisions. Furthermore, there may now be molecular velocity correlation, all of which strain fundamental kinetic-gas-theory assumptions. One of the first attempts to account for dense gas effects was made by Enskog who used a collision-probability correction based on the belief that, for a hard sphere, there is a volume that the center of the sphere can no longer occupy when that sphere is in its collision state (Chapman and Cowling, 1970). The total restricted volume for the two spheres is the combination of the non-impacted sphere portion and the other colliding sphere. So as a result, the probability of molecular collisions is increased by $1/(1 - V_{sphere})$ per unit molecular volume. However, there is a competing factor that reduces the collision probability due to the shielding of one molecule by another and has been determined to be $(1 - 11/16\ V_{sphere})$ (Chapman and Cowling, 1970). The overall enhancement factor is the product of the two expressions. For hard spheres, the theoretical correction factor is

$$\chi = \frac{\left(1 - \dfrac{11\pi n\sigma^3}{96}\right)}{\left(1 - \dfrac{\pi n\sigma^3}{6}\right)} \quad \text{or} \quad \chi = \left(1 + \frac{5\pi N_A \rho \sigma^3}{96M}\right) \quad \text{for the first-order correction} \tag{114}$$

Refinements to Eq. (114) have been generated by Clausius (1879) and Boltzmann (1899), namely

$$\chi = 1 + \frac{5}{8}\left(\frac{\pi N_A \rho \sigma^3}{12M}\right) + 0.2869\left(\frac{\pi N_A \rho \sigma^3}{12M}\right)^2 + 0.1103\left(\frac{\pi N_A \rho \sigma^3}{12M}\right)^3 + \ldots \tag{115}$$

Thorne extended Enskog's methods to binary mixtures that resulted in an enhancement factor for dissimilar molecules (Chapman and Cowling, 1970)

$$\chi^{Thorne} = 1 + \frac{\pi N_A}{48}\left\{\frac{x_1 \rho_1 \sigma_1^3}{M_1}\left(4 - \frac{3\sigma_1}{\sigma_1 + \sigma_2}\right) + \frac{x_2 \rho_2 \sigma_2^3}{M_2}\left(4 - \frac{3\sigma_2}{\sigma_1 + \sigma_2}\right)\right\} + \ldots \tag{116}$$

However, this correction is not expected to significantly improve the accuracy of the kinetic-theory models since other phenomena are also affecting the dense-gas molecules. Nonetheless, the correction factor scales the low-density diffusivity prediction to the diffusivity at the density of interest using a low-density value such as the ideal-gas density (ρ^{ID}) at the same system pressure and temperature

$$D_{12}^{ET} = \frac{\rho^{ID}}{\rho \chi^{Thorne}} D_{12}^{E} \tag{117}$$

where the superscript ^{ET} signifies Enskog-Thorne. Other corrections have also been published in order to adjust for high pressure and dense systems. Takahashi (1974) developed a generalized chart based on self- and mutual-diffusivity values for gases at high pressures with an average deviation of 4.1% for the 27 systems investigated

$$D_{12}^{T} = \frac{P^{ID}}{P\chi^{Takahashi}} D_{12}^{E}\left(P = P^{ID}\right) = D_{12}^{E}\varsigma\left(1 - A^T/T_r^{B^T}\right)\left(1 - C^T/T_r^{E^T}\right) \tag{118}$$

where ς, A^T, B^T, C^T, and E^T are regressed values that are all a function of reduced pressure as shown in Table 25. For mixtures, linear combining rules (e.g., $T_r = T/T_c = T/\Sigma x_i T_{ci}$) are used to determine the critical mixture temperature and pressure to complete the list of formulas needed to use Takahashi's corresponding-states approach to correct for high pressure and dense systems.

Table 25. Table of coefficients for the Takahashi diffusivity correction (1974)

P_r	ς	A^T	B^T	C^T	E^T
≤ 0.1	1.01	0.038042	1.52267	0	0
≤ 0.2	1.01	0.067433	2.16794	0	0
≤ 0.3	1.01	0.098317	2.4291	0	0
≤ 0.4	1.01	0.13761	2.77605	0	0
≤ 0.5	1.01	0.175081	2.98256	0	0
≤ 0.6	1.01	0.216376	3.11384	0	0
≤ 0.8	1.01	0.314051	3.50264	0	0
≤ 1.0	1.02	0.385736	3.07773	0.141211	13.45454
≤ 1.2	1.02	0.514553	3.54744	0.278407	14
≤ 1.4	1.02	0.599184	3.61216	0.372683	10.009
≤ 1.6	1.02	0.557725	3.41882	0.504894	8.57519
≤ 1.8	1.03	0.593007	3.18415	0.678469	10.37483
≤ 2.0	1.03	0.696001	3.3766	0.665702	11.21674
≤ 2.5	1.04	0.79077	3.27984	0	0
≤ 3.0	1.05	0.5021	2.39031	0.602907	6.19043
≤ 4.0	1.06	0.837452	3.23513	0	0
≤ 5.0	1.07	0.89039	3.13001	0	0

Another approach correlated self-diffusivity for spherical non-polar gases using a virial expansion with universal parameters regressed from sub- and supercritical methane NMR self-diffusivity data (Dawson et al., 1970)

$$D_{11}^{D-HS} = \frac{\rho^{ID} D_{11}^{E}}{\rho \chi^{Dawson}} = \frac{\rho^{ID}}{\rho} D_{11}^{E} \bigg/ \left(1 + 0.053432\rho_r - 0.030182\rho_r^2 - 0.029725\rho_r^3\right) \qquad (119)$$

Although developed for a pure species, Eq. (119) could be adapted in order to predict mixture mutual diffusivities, but is limited to reduced densities of less than 2.5.

Returning to low density modeling, the Chapman-Enskog formulation was originally derived for non-polar molecules. Modifications have been introduced for polar molecules, and two will be summarized below that modify the intermolecular-potential function. Brokaw (1969) introduced a modification of the collision integral in order to account for the polarity of the mixture molecules, and it relied solely on the dipole moments for polar dependency (Poling et al., 2001). Eq. (109) is still used, but the following formulae are used to determine the collision integral Ω_D:

$$\Omega_D = \frac{1.06036}{(kT/\varepsilon_{12})^{0.15610}} + \frac{0.19300}{\exp(0.47635(kT/\varepsilon_{12}))} +$$
$$\frac{1.03587}{\exp(1.52996(kT/\varepsilon_{12}))} + \frac{1.76474}{\exp(3.89411(kT/\varepsilon_{12}))} + \frac{0.19\delta_{12}^2}{(kT/\varepsilon_{12})} \tag{120}$$

where

$$\delta_i = \frac{1}{2}\frac{\mu_{pi}^2}{\varepsilon\sigma_i^3} \sim \frac{1.94\times10^3\,\mu_{pi}^2}{V_{bi}T_{bi}} \tag{121}$$

μ_{pi} [Debyes] is the dipole moment for pure component i, T_{bi} is the normal-boiling-point temperature for pure component i, V_{bi} is the NBP molar volume,

$$\frac{\varepsilon_i}{k} = 1.18\big(1 + 1.3\delta_i^2\big)T_{bi} \tag{122}$$

$$\sigma_i = \left(\frac{1.585V_{bi}}{1+1.3\delta_i^2}\right)^{1/3} \tag{123}$$

$$\delta_{12} = \sqrt{\delta_1\delta_2} \tag{124}$$

$$\frac{\varepsilon_{12}}{k} = \sqrt{\frac{\varepsilon_1}{k}\frac{\varepsilon_2}{k}} \tag{125}$$

$$\sigma_{12} = \sqrt{\sigma_1\sigma_2} \tag{126}$$

The well depths and/or diameters can be calculated or be based on published or experimentally determined values.

The second approach starts by defining a modified LJ potential called the Stockmayer potential

$$\psi_i = 4\varepsilon_i\left[\left(\frac{\sigma_i}{r_i}\right)^{12} - \left(\frac{\sigma_i}{r_i}\right)^6\right] - \left(\frac{\mu_i\mu_j}{r_i^3}\right)(2\cos\theta_1\cos\theta_2 - \sin\theta_1\sin\theta_2\cos\varphi) \tag{127}$$

where θ_1 and θ_2 are the inclination angles of the axes of the two dipoles to the line joining the molecule centers and φ is the azimuthal angle between them (Monchick and Mason, 1961). Note that if one component is non-polar, Eq. (127) reduces to the LJ 6-12 potential. Unfortunately, unrealistic parameters were obtained when experimental data were used to determine the

parameters. For this reason, other approaches have been used including using a central field instead of dipole fields (Monchick and Mason, 1961)

$$\psi_i = 4\varepsilon_i \left[\left(\frac{\sigma_i}{r_i} \right)^{12} - \left(\frac{\sigma_i}{r_i} \right)^6 \right] - \left(\frac{\sigma_i}{r_i^3} \right) \delta_S \tag{128}$$

where δ_S is optimized according to pure parameter data such as viscosity or self-diffusivity. Monchick and Mason (1961) document the estimation procedure and provide values for the Stockmayer-potential parameters along with a table of diffusion collision-integral values as a function of kT/ε and δ_S. Numerical expressions to replace these tables have not been developed, but given the powerful computer capabilities available today, it would not be difficult to generate such expressions.

In addition to the kinetic-theory diffusivity models developed with strong theoretical underpinnings, many researchers have developed semi-empirical and empirical expressions for low-to-high densities relying on kinetic gas theory fundamentals. For example, Wilke and Lee (1955) developed an infinitely dilute mutual-diffusivity expression based on Eq. (108) where LJ 6-12 ε and σ parameters were estimated from pure component liquid NBP properties

$$D_{12}^{WL}[\text{cm}^2/\text{s}] = \frac{10^{-3} \left(3.03 - \frac{0.98}{\sqrt{M_{12}}} \right) T^{3/2}}{P\sigma_{12}^2 \Omega_D \sqrt{M_{12}}} \tag{129}$$

where

$$\frac{\varepsilon_i}{k} = 1.15 T_{bi} \tag{130}$$

$$\sigma_i = 1.18 V_{bi}^{1/3} \tag{131}$$

The collision integral was evaluated for particular values of ε_i and σ_i using the Eq. (111) and (112) combining formulae.

Mathur and Thodos (1965) used a novel approach to develop their relation for self-diffusivity. They started with the kinetic theory for diffusivity and the assumption that self-diffusivity is a function of critical constants, molecular weight along with the fact that diffusivity is a function of temperature and density or pressure. They found that for pressures close to one

175

atmosphere, self-diffusivity is most sensitive to temperature (Eq. (132)); for denser gases, temperature and density are the most appropriate parameters (Eq. (133)); and for liquids, temperature and pressure are the best to employ (Eq. (134)). By using dimensional analysis and experimental-data regression, Mathur and Thodos developed expressions for the following three cases

Normal pressures: $\quad D_{11}^{MT} [\text{cm}^2/\text{s}] = \dfrac{44 \times 10^{-5} P_{c1}^{2/3} [\text{atm}] T_{c1}^{5/6} T_{r1}^{1.716}}{\pi \sqrt{M_1}}$ for $T_{r1} \geq 1.5$

$$D_{11}^{MT} [\text{cm}^2/\text{s}] = \frac{2.427 \times 10^{-5} P_{c1}^{2/3} [\text{atm}] T_{c1}^{5/6} \left(7.907 T_{r1} - 1.66\right)^{1.338}}{\pi \sqrt{M_1}} \text{ for } T_{r1} < 1.5 \tag{132}$$

Elevated pressures: $\quad D_{11}^{MT} [\text{cm}^2/\text{s}] = \dfrac{10.7 \times 10^{-5} T_{c1}^{5/6} T_{r1}}{P_{c1}^{1/3} [\text{atm}] \rho_{r1} \sqrt{M_1}}$ for $0.15 \leq \rho_{r1} \leq 1.5$ $\tag{133}$

Liquid state: $\quad D_{11}^{MT} [\text{cm}^2/\text{s}] = \dfrac{3.67 \times 10^{-5} T_{c1}^{5/6} T_{r1}^{3.5}}{P_{c1}^{1/3} [\text{atm}] P_{r1}^{0.1} \sqrt{M_1}}$ for $\rho_{r1} > 2$ $\tag{134}$

The species used for the regressions include argon, krypton, xenon, nitrogen, and carbon dioxide. Although developed for pure species, by using combining and mixing rules, these correlations can be extended to predict mixture mutual diffusivities.

The kinetic theory of gases and its modifications introduced by multiple researchers offers several approaches to modeling supercritical mixture diffusivities. The non-polar and polar Chapman-Enskog equations, the Enskog-Thorne correction, the Takahashi correction, the Dawson correction, Wilke-Lee expression, and Mathur-Thodos expressions will be evaluated and compared with the data of this dissertation and with previously published measurements.

II.1.1.4 Hard-Sphere Theory of Diffusion

Another approach to predicting diffusivities is based on hard-sphere theory, which has its foundations in the kinetic theory of gases and usually begins with the Enskog-Thorne diffusivity equation for dense gases (Shenai et al., 1993). The basis of hard-sphere theory is that motion is correlated rather than uncorrelated for kinetic-gas theory due to the fact that molecular diameters are no longer negligible when compared to the mean free path. Furthermore, exchanges of energy are probable since molecules are no longer assumed to have kinetic-gas-theory length scales significantly smaller than the mean free path and to have infrequent binary collisions. A simple representation of the overall hard-sphere diffusivity can be written as

$$D_{12} = D_{12}^{HS} = A\zeta D_{12}^{ET}$$ (135)

where superscript ^{HS} stands for rough hard sphere. A is called the "roughness factor," and it attempts to correct for the angular-momentum exchange when molecules collide. Typically, the roughness factor is an adjustable parameter used to makeup any difference between theory and experiment, and it usually varies between 0.5 and 1.0.

The term ζ accounts for backscattering and hydrodynamic vortex formation in dense systems and is available only from molecular-dynamics simulation. Backscattering refers to the situation in which a collision between a light solute molecule and a heavy solvent molecule can reverse the direction of the solute molecule (Alder et al., 1970; Alder et al., 1974). Without a backscattering correction, the hard-sphere theory typically overestimates the diffusivity. Vortex formation around a moving heavier solute molecule can alter the velocities of neighboring molecules and is dependent on the momentum and, hence, the molecule mass (Alder et al., 1974; Tyrell and Harris, 1984). Without vortex formation taken into account, the hard-sphere theory typically underestimates the diffusivity.

At present, the molecular simulation required to represent all of the regimes of interest is incomplete thereby making calculation of the rough-hard-sphere (HS) diffusivity difficult. Furthermore, models resulting from the simulations are limited in number. A critique of several of these models is provided in Liu et al. (1998) and is summarized here. Several researchers start with the original Chapman-Enskog equation for a binary hard-sphere mixture so that they can use a radial distribution function that was provided by Alder et al. (1974)

$$D_{12}^E = \frac{3}{8}\sqrt{\frac{kT}{\pi M_{12}}} \frac{1}{n\sigma_{12}^2 g_{12}}$$ (136)

$$g_{12} = \frac{\sigma_1 g_{11} + \sigma_2 g_{22}}{2\sigma_{12}}$$ (137)

$$g_{ii} = \frac{1}{1-x} + \frac{3y_i}{2(1-x)^2} + \frac{y_i^2}{2(1-x)^3}$$ (138)

$$y_i = \frac{\pi}{6}\left(\frac{\sigma_j n_i \sigma_i^3 + \sigma_i n_j \sigma_j^3}{\sigma_j}\right)$$ (139)

$$x = \frac{\pi}{6}\left(n_i \sigma_i^3 + n_j \sigma_j^3\right)$$ (140)

177

or for self-diffusion (Liu *et al.*, 1998), the Carnahan-Starling (1969) expression

$$g = \frac{1 - \pi\sigma^3 n/12}{\left(1 - \pi\sigma^3 n/6\right)^3} \tag{141}$$

where n [molecules/length^3] is the number density. The backscattering and vortex-formation correction term, ζ, scales the smooth-hard-sphere (SHS) diffusivity (before roughness corrections are factored in) with the low density Chapman-Enskog diffusivity and is often written as D^{SHS}/D^E. There are several ways to determine this correction term including using the limited tables and figures provided by Alder *et al.* (1974) or Easteal and Woolf (1990), using the Erpenbeck and Wood (1991) $D^{EW\text{-}HS}/D^E$ expression, using the Sun and Chen (1985a) $D_1^{SC\text{-}HS}$ tracer expression which already incorporates D^E and a 0.7 roughness factor, or using the free-volume-based molecular-volume concept used by Liu *et al.* (1998). A fifth method proposed by Speedy (1987), which does not use long-time contributions (t $\to \infty$) in the diffusivity calculation, has been subject to noteworthy criticism by Erpenbeck and Wood (1991) due to this exclusion and, thus, will not be considered.

Erpenbeck and Wood (1991) (Valid for $1.6 < M/\rho V_0 < 25$)

$$\frac{D_{11}^{EW-HS}}{D_{11}^E} = 1 + 0.054034 \rho V_0/M + 6.3656\left(\rho V_0/M\right)^2 - 10.9425\left(\rho V_0/M\right)^3 \tag{142}$$

Sun and Chen (1985a)

$$D_1^{SC-HS}[\text{cm}^2/\text{s}] =$$

$$3.482 \times 10^{-6} \sigma_2[\text{Å}] \sqrt{\frac{RT}{M_2}} \left(\frac{M_2}{M_1}\right)^{0.167} \left(\frac{\sigma_2}{\sigma_1}\right) \left(\frac{M_2}{x_2\rho_2 V_0} - 1.383 \left(\frac{M_2}{M_1}\right)^{0.0165} \left(\frac{\sigma_1}{\sigma_2}\right)^{0.129}\right) \tag{143}$$

(Valid for $0.5 \le M_1/M_2 \le 4.0$, $0.5 \le \sigma_1/\sigma_2 \le 1.5$, and $1.5 \le M_2/x_2\rho_2 V_0 \le 3.0$.)

Liu *et al.* (1998)

$$\frac{D_{11}^{LSM-HS}}{D_{11}^E} = \exp\left(-\frac{0.75 n\sigma^3}{1.2588 - n\sigma^3}\right) \tag{144}$$

where V_0 [cm^3/molecule] is the solvent close-packed hard-sphere volume ($N_A\sigma_2^3/2^{1/2}$). Note that the LSM constants are actually fit to the Erpenbeck-Wood expression so this expression will behave in a similar fashion, but that the LSM expression later becomes part of the complete LSM diffusivity expression introduced next.

Using Eq. (144), Liu and coworkers had previously extended their self-diffusivity modeling efforts with good success to include mutual diffusivities for infinitely dilute solutes. However, they make it clear that their predictive tracer (TLSM) model is not successful for hydrogen-bonded molecules (Liu *et al.*, 1997 and 1998).

$$D_{12}^{TLSM-HS} = \frac{669.1 V_2}{N_A \sigma_{TLSM}^2} \sqrt{\frac{RT}{M_{12}}} \exp\left(-\frac{0.75 N_A \sigma_2^3 / V_2}{1.2588 - N_A \sigma_2^3 / V_2} - 0.27862 \frac{\varepsilon_{12}^{TLSM}}{kT}\right) \quad (145)$$

$$\sigma_{TLSM}^2 = \frac{2^{1/3} \sigma_{12}^2}{\left(1 + 1.2 \sqrt{\frac{kT}{\varepsilon_{12}^{TLSM}}}\right)^{1/3}} \quad (146)$$

$$\frac{\varepsilon_{12}^{TLSM}}{k} = \frac{\sqrt{\sigma_1^3 \sigma_2^3 \varepsilon_1 \varepsilon_2}}{k \sigma_{12}^3} \quad (147)$$

When the pure component Lennard-Jones values are adjusted in the TLSM model instead of using established values or values estimated from established correlations, the TLSM performance is significantly improved and was found to give acceptable predictions for hydrogen-bonded species. However, the model is no longer predictive using this regressed approach. Including sub- and supercritical water in their regressed analysis, they report an average deviation of 5.45% for their self-diffusivity predictions (Liu *et al.*, 1998). TLSM self-diffusivity predictions were further improved after their TLSM model was altered to include two additional adjustable parameters that are also regressed to available experimental data. The third parameter is an empirical temperature-dependent regressed parameter for the effective diameter while the fourth is the roughness factor that is used to take into account the coupling between translational and rotational momentum exchange during collisions (Liu and Macedo, 1995; Silva *et al.*, 1998). These tailored models limit their widespread use since they are no longer predictive models that do not require additional regressed terms or parameters. The TLSM-HS will be examined using available Lennard-Jones values and also with those values provided by the Liu, Silva, and Macedo research group.

Another approach to determining diffusivity was proposed by Eaton and Akgerman (1997) for their infinitely dilute mutual diffusivity model for supercritical fluids in many solvents, excluding water. They start with a MD-simulation-based correlation originally developed by Dymond (1974) and refined by Easteal and Woolf (1990). Dymond originally

showed that MD simulations of D^{SHS}/D^E could be consolidated into a series of straight lines with the following linear function

$$\frac{D_{12}^{SHS}}{D_{12}^E}\frac{1}{g_{12}}\frac{V}{V_0} = a\left(\left(\frac{V_2}{V_0}\right)^{\kappa} - \frac{b}{a}\right) \tag{148}$$

Eaton and Akgerman were able to derive relations for κ, a, and b, in part by developing functions for a and b which consolidate Dymond's straight lines into one single curve. As a result, κ was found to be $\sigma_1/\sigma_2 - 1/3$ for the systems studied by Eaton and Akgerman, and a & b were fit to the slope & intercept of the single curve. Their fit had an average absolute deviation of less than $\pm 1.5\%$ (Eaton and Akgerman, 1997). Next they added a roughness term, used the observation of Erkey and Akgerman (1989) that it is dependent on the ratio σ_1/σ_2, and fit it with experimental data. Infinitely dilute diffusivity measurements were obtained for 1-octene in supercritical ethane, hexane, and propane over a 41–290°C, 0.07–0.5 g/cm^3, and 44–124 bar range in their Taylor dispersion apparatus. These were then used to obtain two regression parameters. The final result is

$$D_{12}^{EA-HS}[cm^2/s] = 0.4924\sqrt{\frac{T}{M_{12}}}\left(\frac{\sigma_1}{\sigma_2}\right)^{1.7538}\frac{V_0[cm^3/mole]}{\sigma_{12}^2[\text{Å}]}\left(\left(\frac{V_2}{V_0}\right)^{\left(\frac{\sigma_2}{\sigma_1}-\frac{1}{3}\right)} - b_2\right) \tag{149}$$

$$b_2 = \frac{b}{a} = \left[-0.2440\left(\frac{\sigma_2}{\sigma_1}\right)^2 + 0.8491\left(\frac{\sigma_2}{\sigma_1}\right) + 0.6001\right]\left(\frac{M_1}{M_2}\right)^{-0.03587} \tag{150}$$

(Valid for $0.1 \le M_1/M_2 \le 1.67$, $0.5 \le \sigma_1/\sigma_2 \le 1.0$, and $1.5 \le V_2/V_0 \le 2.0$)

According to Eaton and Akgerman, Eqs. (149) and (150) estimate their measured diffusivities with an average absolute error of 4.01%. When compared to self-diffusivities of carbon dioxide, ethylene, toluene, and fluoromethane, Eqs. (149) and (150) predictions have an average absolute error of 3.64%. When their expressions were tested on 101 systems and over 1,500 data points, they report an error of 15.08%.

He (1997) used the general form of the Eaton-Akgerman equations and regressed two parameters to a complete set of data that spanned 107 binary systems with 10 solvents (water

was not considered) and 1,167 supercritical infinitely dilute data points. The resulting equation had an average absolute deviation of 7.5% for all of the data that were regressed

$$D_{12}^{H-HS} = \left[0.61614 + 3.0902 \exp\left(-0.87756 \frac{\sqrt{M_2 V_{c2}[\text{cm}^3/\text{mol}]}}{P_{c2}[\text{bar}]} \right) \right] 10^{-6} \left(V_2^k - 23 \right) \sqrt{\frac{T}{M_1}} \quad (151)$$

$$k = 1 \qquad \rho_{r2} \geq 1.2$$

$$(152)$$

$$k = 1 + \frac{\left(\rho_{r2} - 1.2 \right)}{\sqrt{M_2}} \qquad \rho_{r2} < 1.2$$

He and Yu (1998) attempted to improve high temperature diffusivity predictions by incorporating solvent density in a new correlation. The correlation they chose is based on Cohen and Turnbull's (1959) notion that molecular transport occurs by the movement of solute molecules into voids opened by solvent molecules in a grid, which is consistently changing and evolving

$$D_{12}^{HY-HS} = \begin{array}{l} \left[14.882 + 5.9081 \left(\frac{T_{c2} V_{c2}}{1000 M_2} \right) + 2.0821 \left(\frac{T_{c2} V_{c2}}{1000 M_2} \right)^2 \right] \times 10^{-5} \times \\ \exp\left(\frac{0.3887 V_{c2}}{0.23 V_{c2} - V_2} \right) \sqrt{\frac{T}{M_1}} \end{array} \quad (153)$$

As a result, the solute-molecule diffusivity is dependent on the movement of the solute, namely its velocity, and the probability of finding an empty void in the grid. For the 1,303 data points in 113 binary systems (again, water was not considered), Eq. (153) resulted in an 8.2% average absolute deviation. Predictions with this correlation will be performed in the analysis section.

When Fu et al. (2000) attempted to model solute contaminants in dense carbon dioxide, he recommended using the Enskog equation for predicting mutual diffusivities in liquid carbon dioxide, but not in supercritical carbon dioxide. They found that the Eaton-Akgerman model gives reasonably accurate predictions in liquid and supercritical carbon dioxide (1.1%–6.5% average absolute error). They also found that the TLSM model does not give satisfactory predictions (7.7%–27% and 6.8%–12% error for liquid and supercritical systems) (Fu et al., 2000).

Overall, the hard-sphere theory of diffusion is an area of active research, and refinements and new approaches appear when new experimental data become available. However since

1998, there have been essentially zero publications. Even with this publication stoppage, the previously published expressions provide another approach to model diffusivity, along with the kinetic- and hydrodynamic-theory diffusivity models. From this section, the Erpenbeck-Wood correction, Sun-Chen equation, TLSM equation, Eaton-Akgerman equation, He expression, and He-Yu expression will be evaluated for their performance in estimating supercritical mixture diffusivities. For the most part, these models are used for self-diffusivity or infinitely dilute mutual diffusivity predictions, but are not necessarily used to predict tracer and mutual diffusivities when there are concentrated species present. The next section explores theories and expressions developed for the real world possibility of mixtures that are not infinitely dilute.

II.1.1.5 Diffusivity Concentration Dependence

The concentration dependence of mutual and tracer diffusivities is a research area with very limited progress. Partly due to the lack of well-established and accurate predictive models for self- and binary diffusivity that can then used in concentration-weighted models and partly due to the lack of experimental data, there are only a few published correlations. For liquid systems, expressions have been developed to relate mutual diffusivity as a function of composition, but only a few are worth describing because of their generality and lack of accuracy (Poling *et al.*, 2001). One of the first to publish is Darken (1948) who related the mutual diffusivity to tracer diffusivity and mole fraction

$$D_{12}^D = \left(D_1 \big|_{x_1} x_1 + D_2 \big|_{x_2} x_2 \right) \alpha \tag{154}$$

where α is the thermodynamic correction factor

$$\alpha = \left(\frac{\partial \ln \gamma_1 x_1}{\partial \ln x_1} \right)_{T,P} = \left(\frac{\partial \ln \gamma_2 x_2}{\partial \ln x_2} \right)_{T,P} \tag{155}$$

The thermodynamic correction factor corrects for the fact that, for a binary system that is suddenly in a non-equilibrium state, the system can return to equilibrium with a diffusive flow that is related to the chemical-potential gradient, and not just a concentration gradient as is originally defined in Eq. (87). However, for low pressure gases, the thermodynamic correction factor is close to unity and is assumed to be one for most other applications (Poling *et al.*, 2001). However, according to Hardt *et al.* (1959), the Darken expression is not successful for modeling associated mixtures such as acetone and water.

Since tracer diffusivities are often unavailable, several researchers have focused on using infinitely dilute mutual diffusivities with limited success (Poling *et al.*, 2001). Vignes (1966) developed an expression for accurate fits of non-associated ideal or near-ideal systems

$$D_{12}^V = \left(\left(D_{21}^\infty \right)^{x_1} \left(D_{12}^\infty \right)^{x_2} \right) \alpha \qquad (156)$$

but is only partially successful for associated systems such as ethanol-water, acetone-water, and acetone-chloroform where the mean deviation is approximately 14% (Tyn and Calus, 1975b).

Leffler and Cullinan (1970) also had success when they scaled the Vignes relation with viscosities

$$D_{12}^{LC} = \left(\left(D_{21}^\infty \eta_1 \right)^{x_1} \left(D_{12}^\infty \eta_2 \right)^{x_2} \right) \alpha / \eta_{12} \qquad (157)$$

However, three different viscosities are required for their expression, and viscosity data of this nature are often unavailable. When compared with the Vignes relation, Tyn and Calus (1975b) did not find an advantage to using the Leffler-Cullinan relation for the associated systems, so it appears that this relation does not offer any advantage over the Vignes expression. A variation of the Vignes approach that was previously introduced and that is accurate for some associated and non-associated systems is the Carman and Stein relation (1956)

$$D_{12}^{CS} = \left(x_2 \eta_2 D_{12}^\infty + x_1 \eta_1 D_{21}^\infty \right) \alpha / \eta_{12} \qquad (100)$$

As before, limiting tracer diffusivities could be employed, however solution viscosities would also be needed.

Another approach is to use the inherent concentration dependence that several kinetic-theory-of-gas expressions have. The Eaton-Akgerman (1997), Erpenbeck-Wood (1991), and Liu *et al.* (1998) expressions have a density correction that could be exploited in order to weight diffusivity with respect to concentration. Furthermore, by using combining and mixing rules, the Mathur-Thodos and Wilke-Lee expressions and all of the intermolecular potential functions could be modified in order to have a concentration dependence. As a result, concentration expressions for diffusivity can be made, and they will be explored in Section II.5 of this dissertation.

In summary, many diffusivity models have been developed, each with benefits, yet also with shortcomings. Hydrodynamic-theory and kinetic-gas-theory based approaches have

become the standard when predicting diffusivities. Semi-empirical correlations are the mainstay, but there is still a low level of understanding regarding diffusivities and their dependence on concentration. Fundamental to all of these issues is the scarcity of diffusivity measurements, especially supercritical mixture diffusivities. Following a discussion about currently available supercritical data, this dissertation will then focus on NMR diffusivity measurements obtained during this dissertation and then examine many of the diffusivity models introduced in this section.

II.1.2 Critical Phenomena

II.1.2.1 Observations & Theories

Near the critical point, many thermodynamic and transport properties deviate substantially from their bulk mean value at any instance of time. Since supercritical-fluid processing can occur near the critical point, a discussion regarding these critical-phenomena deviations is, therefore, warranted. Observations of large deviations date to 1869 when Thomas Andrews (1869) reported a critical opalescence, *e.g.*, normally transparent fluids turning "milky" or opaque near or at the critical point.

The correlation length, ξ, is a measure over which these density deviations in one region are influenced by and can be correlated with density deviations in another region, and it has been shown to correlate with dimensionless temperature near the critical point (Bejan, 1997). When the critical temperature and critical density are closely approached, the correlation length diverges. Near the critical point, properties such as the correlation length are generally simulated with critical-scaling laws that are represented by truncated series

$$\xi \propto \lim_{|\Delta T_r| \to 0} \left(|\Delta T_r|^{-\nu} \left(1 + c_2 |\Delta T_r|^{-\nu'} + ... \right) \right) = |\Delta T_r|^{-\nu} = \left| \frac{T - T_c}{T_c} \right|^{-\nu} \tag{158}$$

For the correlation length, ν is a positive universal critical-exponent symbol. Regardless of the substance, with $T - T_c = 0.01$ K at the critical isochore, the correlation length of molecular interaction is approximately 100 nm, which is much larger than the typical 0.3 nm intermolecular distance of simple molecules far away from the critical point (Bejan, 1997). These large correlation lengths imply long-range density deviations which also vary slowly in time and result in increasing difficulty in achieving thermal equilibrium (Sengers, 1994).

It has also been well established that in the critical-point limit, phase transitions of different substances and systems behave similarly, *e.g.*, some thermodynamic properties diverge, thereby allowing the use of universal values for these property predictions. For properties that vanish at the critical point, a power series like Eq. (158) can be used with a positive exponent.

The critical-scaling law defined in Eq. (158) for the correlation length is regarded as the most accurate model for predicting properties of pure fluids and mixtures near the critical point. The scaling law is fashioned after the Ising-lattice model which is based on interactions between

185

cell elements in a d-dimensional lattice (Bejan, 1997). When the degrees of freedom or the order-parameter dimensionality is set to one ($n = 1$), each Ising-lattice cell has two possible discrete options, e.g., occupied or empty in the case of a unimolecular system or for a binary system without an empty cell, species one or two of the mixture. Critical-scaling laws are frequently based on the $d = 3$, $n = 1$ Ising case, but since there are slight variations between the original Ising exponents and theoretically and experimentally refined critical exponents, the critical-scaling laws are often described as Ising-like.

Further away from the critical point, properties are weaker functions of density and temperature and can be classically represented by mean-field values without having any deviations. Mean-field theory starts with the classical belief that a molecule interacts with all neighboring molecules in a similar fashion and that deviations from the mean value can be neglected (Bejan, 1997). When these deviations are neglected close to the critical point, the Helmholtz free-energy distribution of the system can be written in terms of a Taylor's series or, in this case, a Landau expansion. At the critical point, the Helmholtz free-energy representation remains finite and analytical and allows direct determination of mean-field critical exponents (Bejan, 1997; Sengers, 1994). These exponents match critical exponents that are derived from the van der Waal's equation of state (Bejan, 1997).

Universal exponents can be derived for the thermodynamic and transport properties of interest and have been confirmed experimentally for a large number of systems (Sengers, 1985; Bejan, 1997; Sakonidou et al., 1998; Sengers, 1994; Abdulkadirova et al., 2002; Anisimov et al., 2004). Thermodynamic properties are summarized in Table 26, while universal exponents for the Ising, Ising-like, and mean-field universality classes are listed in Table 27. Negative critical exponents will result in parameters diverging near the critical point, while parameters with positive critical-exponents will vanish. For the most part, mixtures exhibit similar trends, but as stated by Abdulkadirova and coworkers (2002), some pseudo-single-component properties exhibit weaker singularities including the isothermal compressibility and isobaric heat capacity for $|\Delta T_r| < 10^{-4}$, while the isochoric heat capacity continues to weakly diverge.

Table 26. Critical-phenomena power laws (Levelt-Sengers and Givens, 1993)

Property	System	Dependent variable	Independent variable	Power law
Coexistence curve (ρ)	One component	$\Delta\rho_r = (\rho_L - \rho_V)/\rho_c$	ΔT_r	$B|\Delta T_r|^\beta$
Coexistence curve	Two component	$|\Delta x|$	ΔT_r	$B|\Delta T_r|^\beta$
Coexistence curve (P)	One component	$P - P_c$	$\Delta\rho_r$	$D|\Delta\rho_r|^\delta$
Isothermal compressibility	One component	$\kappa_T = -(\partial V/\partial P)_T/V$	ΔT_r	$\Gamma|\Delta T_r|^{-\gamma}$
	Two component	$\kappa_T = -(\partial V/\partial P)_T/V$	$|\Delta T_r| <10^{-2}$ $|\Delta T_r| >10^{-2}$	$\Gamma'|\Delta T_r|^{-\alpha}$ $\Gamma|\Delta T_r|^{-\gamma}$
Isochoric heat capacity	One and two component	C_V	ΔT_r	$A|\Delta T_r|^{-\alpha}$
Isobaric heat capacity	One component	C_P	ΔT_r	$\propto \kappa_T$
	Two component	C_{Px}	$|\Delta T_r| <10^{-4}$ $|\Delta T_r| >10^{-4}$	$A'|\Delta T_r|^{-\alpha}$ $\propto \kappa_T$
Correlation length	One and two components	ξ	ΔT_r	$\xi_0|\Delta T_r|^{-\nu}$

Table 27. Critical-phenomena exponents for the Ising, Ising-like, and mean-field universality classes (Bejan, 1997; Anisimov *et al.*, 2004)

Universality class	α	β	δ	γ	ν
Ising ($d = 3$)	0.125	0.312	5.0	1.250	0.625
Ising-like & Wilson	0.110	0.325	4.8	1.241	0.630
Mean-field & van der Waals	0	0.5	3	1	0.5

Because the Ising, Ising-like, and mean-field universality classes have limited operating regimes, another universality class is often used when operating between two classes in order to improve property predictions. Aptly called "crossover theory", it usually has its own critical-exponent set, and experimental results indicate that crossover theories are sensitive to the type of species being modeled, e.g., polymers, ionic fluids, or simple fluids with short-range forces such as carbon dioxide and methane. The crossover to Landau's classical or mean-field class is also property dependent, but nonetheless occurs further away from the critical point when the Ising model begins to fail to capture classical behavior (Landau, 1966).

Sengers has estimated where the Ising model fails and where traditional methods cannot match observed critical phenomena (Sengers, 1994). Using renormalization-group theory, the secondary isothermal-compressibility critical exponent defined generically in Eq. (158) is 0.51 (Sengers, 1994), i.e.,

$$\kappa_T = c_1 |\Delta T_r|^{-\gamma} \left(1 + c_2 |\Delta T_r|^{0.51} + ...\right) \tag{159}$$

With this theory, long-range interactions not considered by the Ising model can now be included and properties can be repeatedly rescaled within a transformed correlation-length constraint. With this correction term and with c_2 of order one, $|\Delta T_r|$ must be less than 10^{-4} in order to keep the secondary correction shift under 1%. From this result, most asymptotic scaling laws are valid for only a very small reduced temperature range near the critical point ($|\Delta T_r| < 10^{-4}$) before secondary and mean-field terms can no longer be ignored.

There is still debate about when and if crossovers exist for ionic fluids since experimental evidence for systems with varying levels of ionic character do not always crossover back to the Ising regime (Levelt-Sengers and Givens, 1993; Pitzer, 1995). However, most researchers agree that for those particular systems, the crossover region may not have been entered due to the limitations of the experimental data and apparatus as the critical point is approached.

II.1.2.2 Transport Properties

In the classical approach, transport properties are not supposed to be affected near the critical point because properties such as thermal conductivity, λ; viscosity, η; and diffusivity, D, are dependent on short range molecular-level interactions and should not be affected by large

correlation lengths (Sengers, 1994). However as the critical region is approached, some properties are observed to show evidence of anomalous behavior due to a greater sensitivity to the dynamic behavior of critical deviations. Experimental evidence has shown that for mixtures, all three properties exhibit asymptotic qualities close to the liquid-liquid consolute critical point and even closer to the liquid-vapor plait critical point. Thermal conductivities and viscosities diverge weakly as temperature is reduced to the critical temperature, while mutual diffusivities vanish (Sakonidou *et al.*, 1998). For mixtures above $|\Delta T_r| > 10^{-2}$ and for pure components, thermal conductivities are strongly enhanced near the critical point while careful self-diffusivity measurements do not show any deviations at the critical point (Sakonidou *et al.*, 1998; Harris, 2002).

Dynamic renormalization-group theory and mode-coupling theory of critical dynamics are two theoretical approaches that have been developed to address critical effects of transport properties since critical effects cannot be adequately addressed by static models. These approaches shift from examining correlation lengths to the corresponding correlation times associated with critical-point deviations at the critical point. In addition, both approaches can account for large deviations that extend past intermolecular lengths and for nonequilibrium dynamics that affect transport properties and that are best described with hydrodynamic models (Sengers, 1994). Mode-coupled solutions to the Boltzmann-like kinetic equations that describe slowed-down motions near the critical point yield time-correlation functions of the critical deviations (Kawasaki, 1970). These frequency-based solutions are then used to obtain decay rates of concentration deviations and in the low frequency and large deviation limits near the critical point, obtain diffusivities (Senger, 1994). A fundamental review of dynamic and static approaches has been organized by Hohenberg and Halperin (1977).

II.1.2.2.1 Viscosity

Viscosity can be divided into a baseline η_b contribution and a critical-enhancement η_c contribution that can be represented by scaling laws (Sengers and Keyes, 1971)

$$\eta(\rho, T) = \eta_c(\rho, T) + \eta_b(\rho, T) \tag{160}$$

The background viscosity, η_b, is independent of the critical-point effects and is often further decomposed into an ideal-gas/low-density limit of viscosity and an excess viscosity

189

$$\eta_b(\rho,T) = \eta_{IG}(\rho \to 0,T) + \Delta\eta_{excess}(\rho,T) \tag{161}$$

For viscosity, renormalization-group theory and mode-coupling theory have both shown that the critical enhancement for viscosity is inversely proportional to the correlation length

$$\eta_c(T) \propto \xi^{-z} \propto |\Delta T_r|^{-\upsilon z} \propto |\Delta T_r|^{-\varphi} \tag{162}$$

where from a first order estimate, $z = 8/15\pi^2 = 0.054$ (Sengers, 1985). The exponent, z, has since been theoretically estimated to be 0.063 when higher order effects are included, thereby making the viscosity critical exponent, φ, equal to about 0.040 (Sengers, 1994). This small critical-point divergence is valid for pure fluids and binary mixtures and has been experimentally validated (Sengers, 1994; Luettmer-Strathman, 2002).

II.1.2.2.2 Diffusivity

The enhancements for mass-mutual diffusivity and thermal diffusivity can be derived with mode-coupling theory by starting with Onsager kinetic coefficients (Sengers, 1985; Anisimov et al., 1998). Using the Onsager expressions for thermal current and mass-diffusion current for a binary mixture

$$\mathbf{J}_q = -\delta'\nabla\mu - \gamma'\nabla T + \mu\mathbf{J}_d \tag{163}$$

$$\mathbf{J}_d = -\alpha'\nabla\mu - \beta'\nabla T \tag{164}$$

where α', β', γ', and $\delta' = \beta'T$ are the Onsager kinetic coefficients and $\mu = \mu_2 - \mu_1$, the mutual-mass diffusivity is

$$D_{\alpha'} = \frac{\alpha'}{\rho}\left(\frac{\partial\mu}{\partial x_2}\right)_{T,P} \tag{165}$$

where α' is equivalent to mass conductivity.

Isolating background and enhancement effects is the next key step during the analysis of critical-point diffusivity behavior. Using the decomposition approach previously used, the Onsager kinetic coefficient, α', can be written in terms of background, α'_b, and critical-enhancement, α'_c, contributions. Using mode-coupling theory, the enhancement solution takes

the form of the Stokes-Einstein equation in the hydrodynamic zero-frequency limit and diverges at the critical point according to

$$\alpha'_c = R_D \frac{k_B T \rho}{6\pi\eta_c\xi} \frac{M_1^2 M_2^2}{M_{12}^2} \left(\frac{\partial x_2}{\partial\mu}\right)_{T,P}$$ (166)

where M_{12} is the mole-fraction-weighted molecular mass (Kawasaki, 1970; Sengers, 1985). Solutions of the mode-coupling zero-frequency boundary conditions result in a first-order estimate of the universal dynamic-amplitude ratio, R_D, of one (Luettmer-Strathmann, 2002). Since diffusivity is proportional to the Onsager kinetic coefficient, the diffusivity critical-enhancement factor, D_{12c}, near a mixture consolute point can be extracted (Burstyn et al., 1980; Landau and Lifshitz, 1987)

$$D_{12c} = \frac{M_{12}^2 \rho \alpha'_c}{M_1^2 M_2^2} \left(\frac{\partial\mu}{\partial x_2}\right)_{T,P} = \frac{R_D k_B T}{6\pi\eta_c\xi}$$ (167)

Given that the critical exponents for viscosity and correlation length are $-\varphi = -0.040$ and $-\nu = -0.63$, respectively, the critical-phenomena power law and exponent take the following form

$$D_c \propto \left|\Delta T_r\right|^{(\nu+\varphi)} \propto \left|\Delta T_r\right|^{+0.67}$$ (168)

while the background term takes the form $\alpha'_b(\partial\mu/\partial x_2)_{T,P}/\rho$. The exponent +0.67 is reasonably close to the experimental critical-exponent value of +0.63 calculated from systems including phenol-water and aniline-cyclohexane, and its sign dictates that mass-mutual diffusivity vanishes at the critical point (Bak and Goldburg, 1969; Swinney and Henry, 1973). Diffusivities for an equimolar 3-methylpentane and nitroethane mixture are shown in Figure 51 and clearly show a decrease before experimental scattering affects alter the reported values for $T - T_c < 10^{-2}$ K (Burstyn et al., 1983). Once scattering effects are removed, mutual-diffusivity critical contributions have been shown to vanish.

Unlike mutual diffusivities, self-diffusivities do not vanish at the critical point, although their slopes may show some anomalous behavior usually due to impurities. Mutual diffusivities vanish because the large, dynamically slow critical-point deviations and their associated chemical-potential gradients give rise to only small driving forces. On the other hand, the self-

191
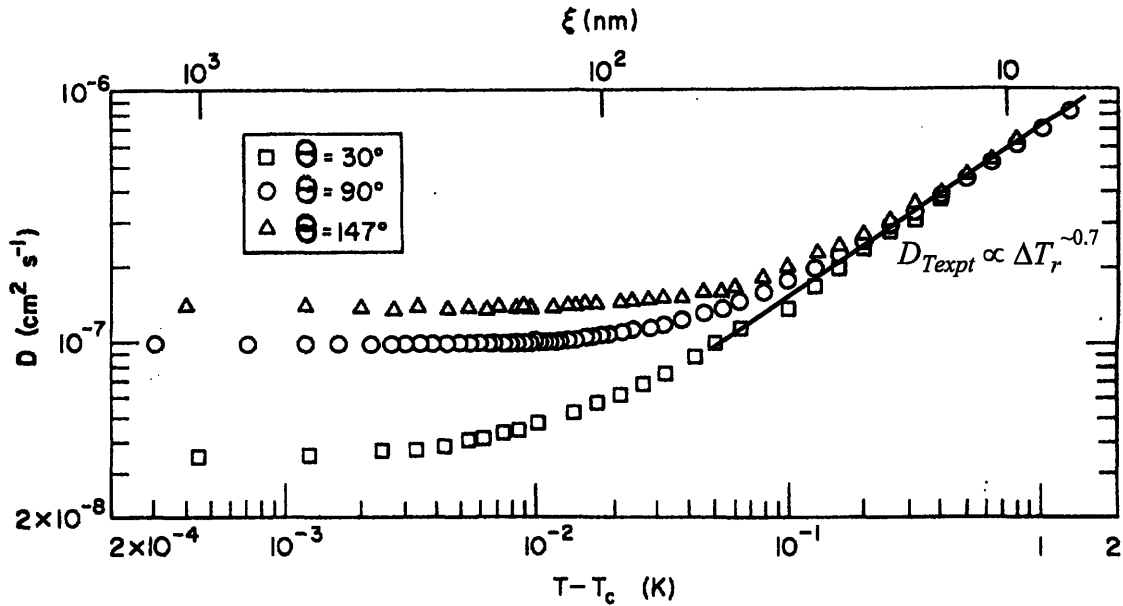
Figure 51. Mutual diffusivities of an equimolar 3-methylpentane and nitroethane mixture for three light-scattering angles, θ, where for $T - T_c > {\sim}0.05$ K, a diffusivity decrease of $v + \varphi \sim 0.7$ is observed (Source: Burstyn *et al.*, 1983). For $T - T_c < {\sim}0.05$ K, the measured diffusivity is dependent on the scattering angle due to experimental scattering effects which are later resolved.

diffusion driving force is associated with concentrations of labeled (*e.g.*, isotope-tagged A*) and unlabeled (A) species which are not directly affected by large critical-point deviations due to the chemical-exchange indifference and the lack of a chemical-potential gradient

$([\partial(\mu_A - \mu_B)/\partial x_B]_{T,P} = 0)$ in the dynamic analysis (Kawasaki, 1966). Multiple experimental studies corroborate this analysis. Harris reviewed chlorotrifluoromethane and carbon-dioxide self-diffusivity measurements made near the critical point with the NMR spin-echo technique and concluded that critical-point anomalies are not seen while Oosting and Trappeniers reported self-diffusivities for methane near the critical point without any irregularities (Oosting and Trappeniers, 1971; Harris, 2002). As shown in Figure 52, deviations or a divergence at the critical density ($\rho_r = \rho/\rho_c = 1$) do not appear to exist for the Oosting and Trappeniers data.

Xenon self-diffusivities for $|\Delta T_r| > 3 \times 10^{-4}$ were also measured with NMR and did not reveal any anomalies (Ehrlich and Carr, 1970). Sengers reports that self-diffusivity peculiarities near the critical point have not been reported in peer-reviewed literature, but that more sensitive experiments should be performed in order to explore this issue with greater detail (Sengers, 2003).
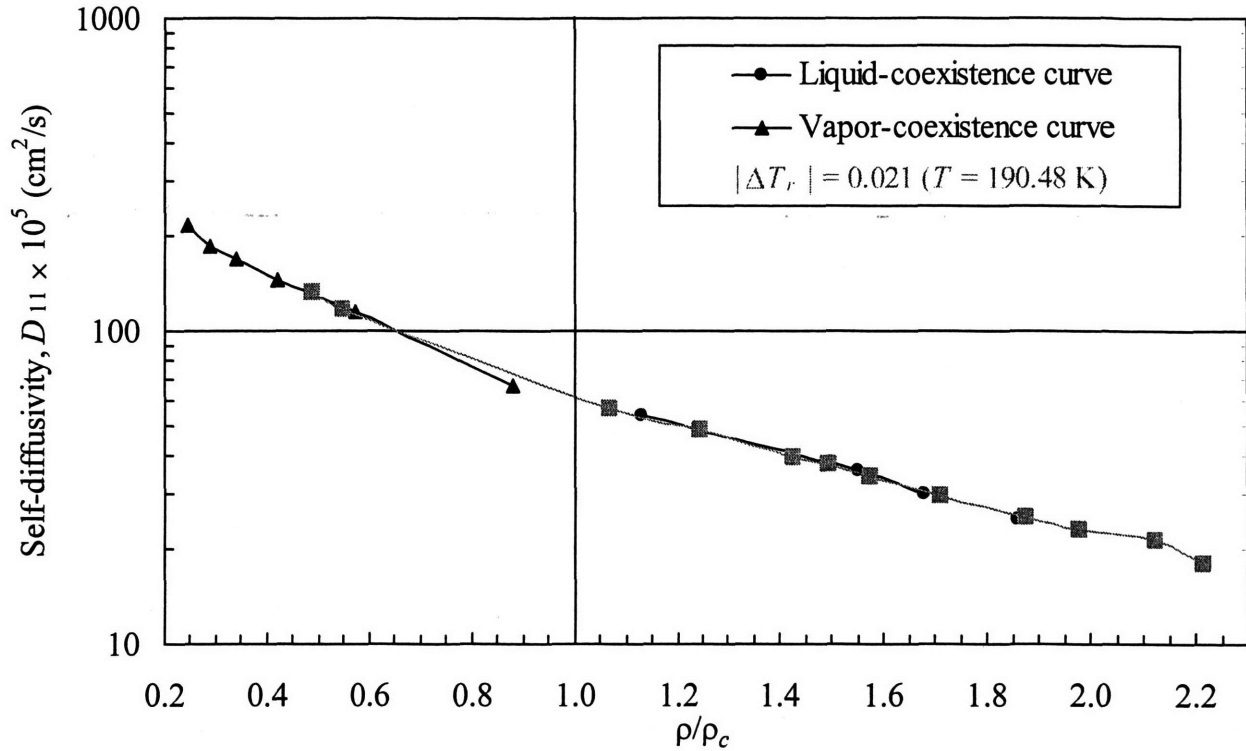
Figure 52. Methane self-diffusivity near and around the critical point for the liquid- and vapor-coexistence curves and the 190.48 K isotherm as reported by Oosting and Trappeniers (1971). Deviations and divergence are not evident (T_c = 190.6 K according to the authors).

Since pure fluid thermal diffusivities and binary-mutual diffusivities are related by their Onsager coefficients, their critical contributions are identical, and the thermal-diffusivity critical contribution is

$$D_{Tc} = \frac{R_D k_B T}{6\pi\eta_c\xi} \propto |\Delta T_r|^{(\nu+\varphi)} \propto |\Delta T_r|^{+0.67} \tag{169}$$

where the first-order estimate of the universal amplitude, R_D, is again one (Sengers, 1994). Pure species thermal diffusivities shrink at the critical point as shown in Figure 53 for carbon dioxide. Based on $\Delta T_r > 1 \times 10^{-4}$ thermal conductivity, heat capacity, and density data, the estimated critical exponent for carbon-dioxide is +0.79 which is close to the sulfur-hexafluoride critical-exponents of +0.83 and +0.89 calculated from experimental $|\Delta T_r| > 6 \times 10^{-4}$ saturated coexistence and critical isochore data, respectively (Sengers, 1994; Bejan, 1997). However, when sulfur-hexafluoride diffusivities were measured on Space-Shuttle Flight STS-65 in a low-gravity environment at temperatures closer to the critical point ($\Delta T_r > 4 \times 10^{-6}$) and when background contributions were assumed nonexistent, the critical exponent was estimated to be

+0.73 which is nearer to the theoretical $v + \varphi = +0.67$ value given by Eq. (169) (Wilkinson *et al.*, 1998). For comparison and as shown in Figure 54, the STS-65 exponent for $\Delta T_r > 10^{-4}$ is +0.88, which validates the previously reported exponent in this temperature range. Exponent differences of this magnitude between adjacent temperature ranges and different species are not unusual since transport properties with large exponents (*e.g.*, thermal and mass diffusivity) are sensitive to background contributions which are dependent on large species-dependent density deviations as the critical point is approached. Background contributions become significant further away from the critical point, and when they are neglected during critical-contribution analysis, the calculated critical-contribution exponent is erroneously large. On the other hand, background contributions become negligible closer to the critical point as seen in Figure 54 when the critical contribution with exponent +0.67 is the sole-contributing term in the model.

Unlike pure fluid thermal diffusivities which vanish near the critical point, thermal diffusivities for mixtures remain finite at the plait point primarily due to the mixture thermal conductivity remaining finite. Thermal-diffusivity calculations based on experimental thermal conductivities of equimolar methane-ethane mixtures substantiate these plait-point predictions (Sakonidou *et al.*, 1998).
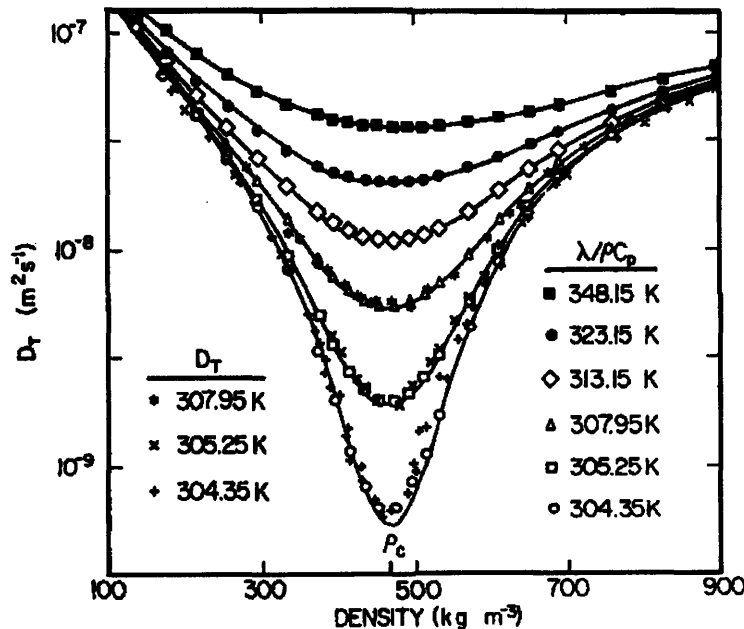
Figure 53. Experimental (D_T) and calculated ($\lambda/\rho C_P$) carbon-dioxide thermal diffusivities (symbols) clearly show a critical depression around the critical point ($T_c \sim 304.31$ K) and are similar to the theoretical solid lines calculated with Eq. (169) (Source: Sengers, 1994).

194
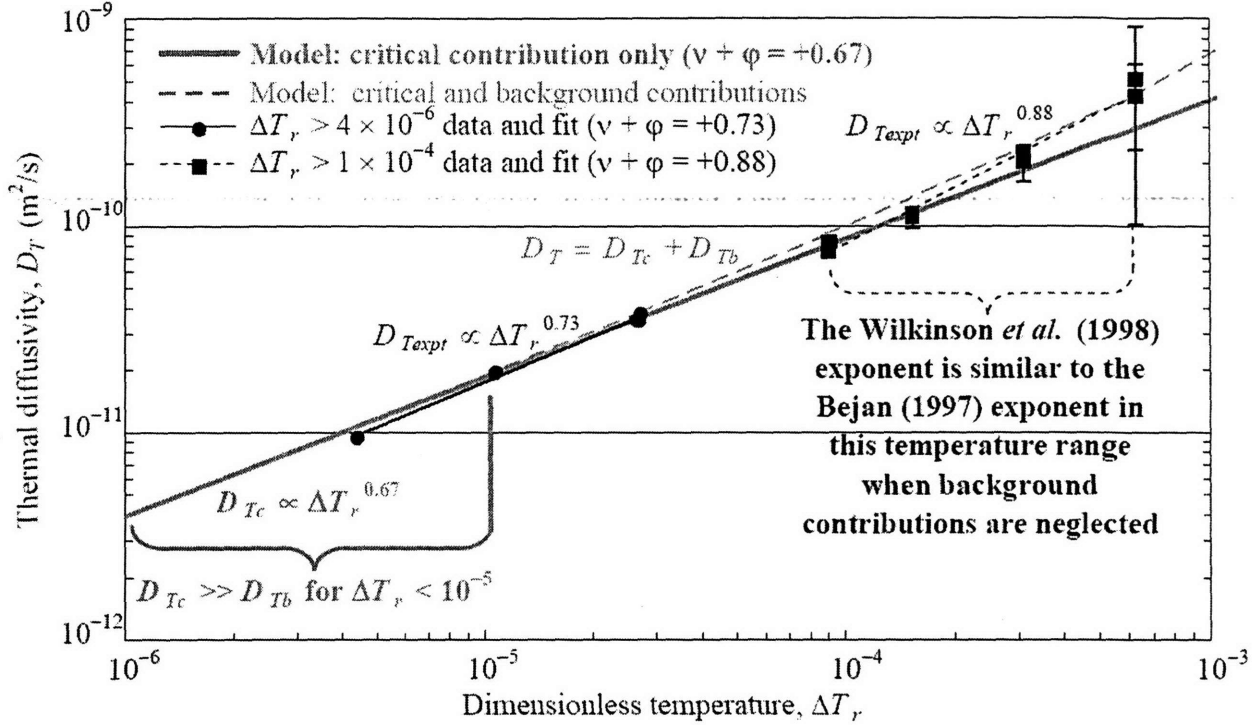
Figure 54. Critical exponents for the experimental (D_{Texpt}) sulfur-hexafluoride thermal diffusivities (symbols) differ depending on their proximity to the critical point, but clearly approach the theoretical exponent $\nu + \varphi = +0.67$ given by Eq. (169) (Wilkinson *et al.*, 1988). Background contributions become significant further away from the critical point, and when they are neglected during critical-contribution analysis, the calculated critical-contribution exponent is erroneously large. Experimental data are shown with the reported 95%-confidence-interval uncertainties.

II.1.2.2.3 Thermal Conductivity

Unlike viscosity and diffusivity at critical point, pure fluid thermal conductivity shows a significant enhancement (Sakonidou *et al.*, 1998). Thermal conductivity can also be decomposed into two additive terms which independently describe the critical-point enhancement and the background contribution. By rearranging the thermal-diffusivity definition

$$\lambda_c = D_{Tc}\rho C_{Pc} \tag{170}$$

and by using thermal-diffusivity enhancement defined in Eq. (169), the critical-enhancement term for thermal conductivity can be written

$$\lambda_c \propto \frac{C_{Pc}}{\eta_c \cdot \xi} \propto \frac{|\Delta T_r|^{-\gamma}}{|\Delta T_r|^{-\varphi} \cdot |\Delta T_r|^{-\upsilon}} \propto |\Delta T_r|^{\varphi+\upsilon-\gamma} \propto |\Delta T_r|^{\upsilon(1+z)-\gamma} \propto |\Delta T_r|^{-\psi} \tag{171}$$

The critical exponent, ψ, is calculated to be 0.57 and has been experimentally validated (Sengers, 1994).

For mixtures, the situation is quite different. Consensus has been recently achieved between theoretical and experimental results indicating that the enhancement is small, but finite for mixtures below $|\Delta T_r| < 10^{-2}$, scaling directly with the smaller enhancement to the isobaric heat-capacity (see Table 26). Also for mixtures, chemical-potential gradients are no longer zero and can no longer be neglected (Sakonidou et al., 1998).

Based on the experimental evidence and theoretical decomposition approach, accurate background models are required for correctly predicting transport-property critical effects. Traditional EOSs and their thermodynamic predictions are typically valid for $|\Delta T_r| > 10^{-2}$, however, for transport properties, the reduced temperature range is much larger. For example, thermal-conductivity enhancements for carbon dioxide are seen over a wide operating range covering $0.05 < \rho_r < 2$ and $0.8 < T_r < 1.4$ as shown in Figure 55 and clearly demonstrate that transport-property enhancements occur over a wide range and that accurate background terms are needed (Sengers, 1994).

Now that the discussion of thermodynamic and transport properties is complete, the focus can now shift to the limitations of critical-phenomena experiments performed in a normal terrestrial gravitational field. Although, temperature and density are the preferred control variables as the critical point is approached in order to minimize system perturbations, temperature and pressure are routinely controlled. Even so, density is difficult to control in a gravity-based environment. Near the critical point, gravitational forces induce large macroscopic density deviations due to the fluid weight and unavoidable fluid temperature variations, and therefore distort any light-scattering decay-rate measurements of the microscopic deviations (Sengers, 2003). Without gravity, macroscopic deviations will be reduced, and as a result, remaining density deviations will control the system and enable more accurate scattering experiments. Experiments of this nature could then confirm many of the critical exponents discussed in this section and resolve any lingering discrepancies. An example of this includes the thermal-diffusivity measurements made on Space Shuttle Flight STS-65 (Wilkinson et al., 1998).
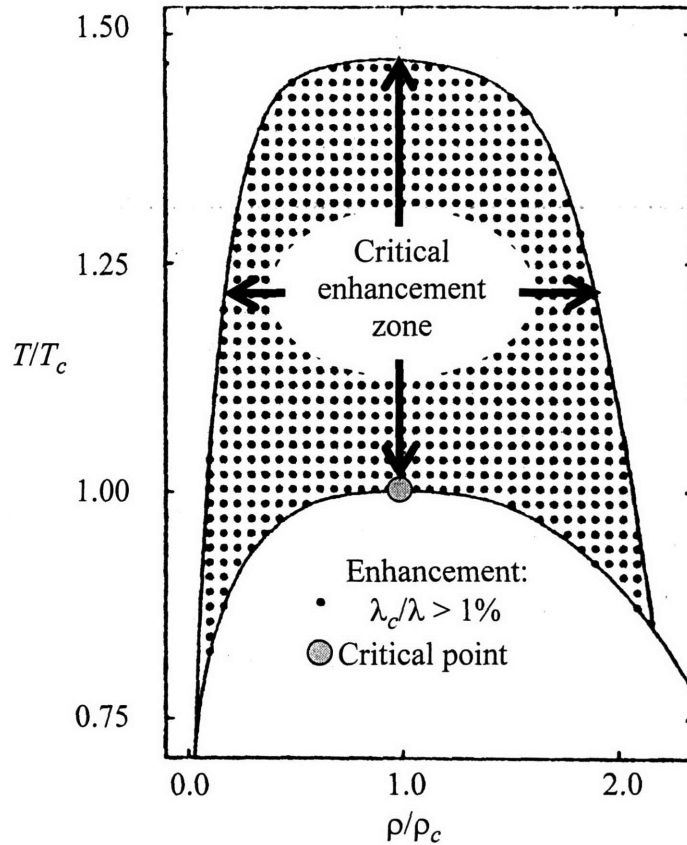
Figure 55. Stippled region and its borders show the thermal-conductivity enhancement for carbon dioxide where one percent or more of the total thermal conductivity is contributed by critical enhancements (Source: Sengers, 1994).

Clearly, critical phenomena influence thermodynamic and transport properties at and close to plait and consolute points for mixtures and critical points for pure species. In this dissertation, the diffusivity-model analysis will be improved when data influenced by critical phenomena are excluded from this analysis.

II.1.3 Supercritical Diffusivity Publications

The availability of supercritical diffusivity data is proportional to the ability to make measurements at these conditions and general interest in a particular component. Factors influencing the interest include whether specific diffusivity data are required or whether a particular species may be representative of a class such as electrolytes. The ability to measure the diffusivity is influenced by the operating conditions, which could be severe, and the measurement technique, which could be limited by the operating conditions or other technical limitations. For non-aqueous solutions near the critical point and for supercritical fluids, extensive lists have been developed and are summarized by He and Yu (1998) and Catchpole and King (1994). These lists primarily contain data for the solvent carbon dioxide, but contain data for other solvents such as ethylene, propane, methanol, ethanol, and sulfur hexafluoride. Supercritical self-diffusivities have also been measured for benzene (Asahi and Nakamura, 1997), toluene-d_8 (Baker et al., 1985), and methane (Dawson et al., 1970) while it should be noted that Balenovic et al. (1970) report subcritical mutual diffusivities for 11 binary dense-gas systems (combinations of helium, nitrogen, argon, hydrogen, and other simple organics up to 1360 atm), Sun and Chen (1985a and 1985b) report sub- and near-critical mutual diffusivities of several organics in n-hexane and cyclohexane, and later they report subcritical tracer diffusivities in dense ethanol, methanol, and 2-propanol (Sun and Chen, 1986 and 1987).

For aqueous systems, diffusivity data near the critical point are much more limited. Self-diffusivities for pure water have been reported by Lamb et al. (1981) for reduced temperatures $1.04 \leq T_r \leq 1.50$, by Krynicki et al. (1978) for $0.43 \leq T_r \leq 0.77$, and by Wilbur et al. (1976) for heavy water (D_2O) for $0.44 \leq T_r \leq 0.73$. Molecular simulations of supercritical water diffusivity have also been performed and match the experimental results within the uncertainty range (Kalinichev, 1993). Protonated diffusivity measurements and molecular-dynamic simulations are listed in Table 28 and Table 29, respectively, and are summarized in Figure 56 through Figure 58. In 1982, Weingärtner provided a reassessment for the self-diffusivity of liquid water in order to judge the results of a variety of work reporting widely varying diffusivities and reports the self-diffusivity of normal (protonated) water to be 2.30×10^{-5} cm^2/s at 25°C and 1 bar.

198

Table 28. Published pure (protonated) water diffusivity data near the critical point with calculated densities (with 95%-confidence-interval uncertainties) (Krynicki et al., 1978; Lamb et al., 1981; NIST, 1996)

Temperature, T (°C)	Calculated density (NIST, 1996), ρ_2 (g/cm^3)	Pressure, P (bar)	Reduced temperature, T_r	Reduced calculated density, ρ_{r2}	Reduced pressure, P_r	Self-diffusivity, $D_{22} \times 10^5$ (cm^2/s)
Lamb et al. (1981) data					
400	0.100	199	1.04	0.31	0.90	286 ± 57
400	0.122	221	1.04	0.38	1.00	243 ± 49
400	0.150	241	1.04	0.47	1.09	203 ± 41
400	0.203	265	1.04	0.63	1.20	161 ± 32
400	0.259	280	1.04	0.80	1.27	120 ± 24
400	0.298	291	1.04	0.93	1.32	112 ± 22
400	0.407	314	1.04	1.26	1.42	89.7 ± 18
400	0.505	378	1.04	1.57	1.71	70.0 ± 14
400	0.602	565	1.04	1.87	2.56	57.1 ± 11
400	0.701	1056	1.04	2.18	4.79	47.4 ± 9
500	0.093	256	1.19	0.29	1.16	326 ± 65
500	0.123	314	1.19	0.38	1.42	251 ± 50
500	0.150	359	1.19	0.47	1.63	213 ± 43
500	0.180	403	1.19	0.56	1.83	189 ± 38
500	0.250	491	1.19	0.78	2.23	141 ± 28
500	0.300	551	1.19	0.93	2.50	125 ± 25
500	0.401	691	1.19	1.25	3.13	95.6 ± 19
500	0.500	910	1.19	1.55	4.13	74.5 ± 15
500	0.599	1313	1.19	1.86	5.95	61.7 ± 12
600	0.100	336	1.35	0.31	1.52	361 ± 72
600	0.125	403	1.35	0.39	1.83	282 ± 56
600	0.150	467	1.35	0.47	2.12	242 ± 48
600	0.180	584	1.35	0.56	2.65	194 ± 39
600	0.250	696	1.35	0.78	3.16	156 ± 31
600	0.299	809	1.35	0.93	3.67	125 ± 25
600	0.399	1074	1.35	1.24	4.87	97.0 ± 19
600	0.499	1459	1.35	1.55	6.61	76.4 ± 15
700	0.100	397	1.50	0.31	1.80	471 ± 94
700	0.124	480	1.50	0.39	2.18	346 ± 69
700	0.150	568	1.50	0.47	2.57	285 ± 57
700	0.200	731	1.50	0.62	3.31	226 ± 45
700	0.250	893	1.50	0.78	4.05	172 ± 34
700	0.299	1060	1.50	0.93	4.81	155 ± 31
700	0.399	1455	1.50	1.24	6.60	108 ± 22
Krynicki et al. (1978) data					
2	1.000	0.007	0.43	3.11	0.00003	1.17 ± 0.1
10	1.000	0.012	0.44	3.11	0.0001	1.43 ± 0.1
25	0.997	0.032	0.46	3.10	0.0001	2.30 ± 0.2
50	0.988	0.124	0.50	3.07	0.001	3.89 ± 0.4
70	0.978	0.312	0.53	3.04	0.001	5.61 ± 1
90	0.965	0.701	0.56	3.00	0.003	7.42 ± 1
110	0.951	1.43	0.59	2.95	0.01	9.81 ± 1
130	0.935	2.70	0.62	2.90	0.01	12.8 ± 1

Table 28. Continued published pure (protonated) water diffusivity data

150	0.917	4.76	0.65	2.85	0.02	15.7 ± 2
175	0.893	8.93	0.69	2.77	0.04	19.6 ± 2
200	0.865	15.5	0.73	2.69	0.07	23.8 ± 2
225	0.834	25.5	0.77	2.59	0.12	280 ± 3
2	1.005	10	0.43	3.12	0.05	1.18 ± 0.1
2	1.014	30	0.43	3.15	0.14	1.20 ± 0.1
2	1.024	50	0.43	3.18	0.23	1.20 ± 0.1
2	1.032	70	0.43	3.21	0.32	1.18 ± 0.1
2	1.041	90	0.43	3.23	0.41	1.17 ± 0.1
2	1.049	110	0.43	3.26	0.50	1.16 ± 0.1
2	1.057	130	0.43	3.28	0.59	1.15 ± 0.1
2	1.064	150	0.43	3.30	0.68	1.14 ± 0.1
2	1.071	170	0.43	3.33	0.77	1.13 ± 0.1
10	1.004	10	0.44	3.12	0.05	1.45 ± 0.1
10	1.014	30	0.44	3.15	0.14	1.49 ± 0.1
10	1.022	50	0.44	3.17	0.23	1.50 ± 0.2
10	1.031	70	0.44	3.20	0.32	1.48 ± 0.1
10	1.039	90	0.44	3.23	0.41	1.46 ± 0.1
10	1.047	110	0.44	3.25	0.50	1.43 ± 0.1
10	1.054	130	0.44	3.27	0.59	1.41 ± 0.1
10	1.061	150	0.44	3.30	0.68	1.40 ± 0.1
10	1.068	170	0.44	3.32	0.77	1.39 ± 0.1
25	1.001	10	0.46	3.11	0.05	2.31 ± 0.2
25	1.010	30	0.46	3.14	0.14	2.34 ± 0.2
25	1.018	50	0.46	3.16	0.23	2.37 ± 0.2
25	1.026	70	0.46	3.19	0.32	2.39 ± 0.2
25	1.034	90	0.46	3.21	0.41	2.39 ± 0.2
25	1.042	110	0.46	3.23	0.50	2.38 ± 0.2
25	1.049	130	0.46	3.26	0.59	2.36 ± 0.2
25	1.056	150	0.46	3.28	0.68	2.33 ± 0.2
25	1.062	170	0.46	3.30	0.77	2.30 ± 0.2
50	0.992	10	0.50	3.08	0.05	3.90 ± 0.4
50	1.001	30	0.50	3.11	0.14	3.92 ± 0.4
50	1.009	50	0.50	3.13	0.23	3.95 ± 0.4
50	1.016	70	0.50	3.16	0.32	3.95 ± 0.4
50	1.024	90	0.50	3.18	0.41	3.94 ± 0.4
50	1.031	110	0.50	3.20	0.50	3.93 ± 0.4
50	1.038	130	0.50	3.22	0.59	3.89 ± 0.4
50	1.045	150	0.50	3.24	0.68	3.80 ± 0.4
50	1.051	170	0.50	3.26	0.77	3.74 ± 0.4
70	0.982	10	0.53	3.05	0.05	5.60 ± 0.6
70	0.991	30	0.53	3.08	0.14	5.55 ± 0.6
70	0.999	50	0.53	3.10	0.23	5.50 ± 0.6
70	1.006	70	0.53	3.13	0.32	5.44 ± 0.5
70	1.014	90	0.53	3.15	0.41	5.40 ± 0.5
70	1.021	110	0.53	3.17	0.50	5.31 ± 0.5
70	1.028	130	0.53	3.19	0.59	5.28 ± 0.5
70	1.034	150	0.53	3.21	0.68	5.21 ± 0.5
70	1.041	170	0.53	3.23	0.77	5.15 ± 0.5
90	0.970	10	0.56	3.01	0.05	7.40 ± 0.7
90	0.978	30	0.56	3.04	0.14	7.28 ± 0.7
90	0.987	50	0.56	3.06	0.23	7.20 ± 0.7

200

Table 28. Continued published pure (protonated) water diffusivity data

90	0.995	70	0.56	3.09	0.32	7.09 ± 0.7
90	1.002	90	0.56	3.11	0.41	6.97 ± 0.7
90	1.010	110	0.56	3.14	0.50	6.89 ± 0.7
90	1.017	130	0.56	3.16	0.59	6.79 ± 0.7
90	1.023	150	0.56	3.18	0.68	6.67 ± 0.7
90	1.030	170	0.56	3.20	0.77	6.59 ± 0.7
110	0.956	10	0.59	2.97	0.05	9.78 ± 1.0
110	0.965	30	0.59	3.00	0.14	9.66 ± 1.0
110	0.973	50	0.59	3.02	0.23	9.57 ± 1.0
110	0.982	70	0.59	3.05	0.32	9.44 ± 0.9
110	0.990	90	0.59	3.07	0.41	9.38 ± 0.9
110	0.997	110	0.59	3.10	0.50	9.21 ± 0.9
110	1.004	130	0.59	3.12	0.59	9.13 ± 0.9
110	1.011	150	0.59	3.14	0.68	9.01 ± 0.9
110	1.018	170	0.59	3.16	0.77	8.92 ± 0.9
130	0.940	10	0.62	2.92	0.05	12.7 ± 1
130	0.950	30	0.62	2.95	0.14	12.5 ± 1
130	0.959	50	0.62	2.98	0.23	12.3 ± 1
130	0.967	70	0.62	3.00	0.32	12.2 ± 1
130	0.976	90	0.62	3.03	0.41	12.0 ± 1
130	0.983	110	0.62	3.05	0.50	11.9 ± 1
130	0.991	130	0.62	3.08	0.59	11.8 ± 1
130	0.998	150	0.62	3.10	0.68	11.7 ± 1
130	1.005	170	0.62	3.12	0.77	11.6 ± 1
150	0.922	10	0.65	2.86	0.05	15.6 ± 2
150	0.933	30	0.65	2.90	0.14	15.3 ± 2
150	0.943	50	0.65	2.93	0.23	15.1 ± 2
150	0.952	70	0.65	2.96	0.32	14.9 ± 1
150	0.961	90	0.65	2.98	0.41	14.7 ± 1
150	0.969	110	0.65	3.01	0.50	14.4 ± 1
150	0.977	130	0.65	3.03	0.59	14.2 ± 1
150	0.984	150	0.65	3.06	0.68	14.0 ± 1
150	0.992	170	0.65	3.08	0.77	13.8 ± 1
175	0.898	10	0.69	2.79	0.05	19.4 ± 2
175	0.910	30	0.69	2.83	0.14	19.0 ± 2
175	0.921	50	0.69	2.86	0.23	18.7 ± 2
175	0.931	70	0.69	2.89	0.32	18.3 ± 2
175	0.940	90	0.69	2.92	0.41	18.0 ± 2
175	0.949	110	0.69	2.95	0.50	17.7 ± 2
175	0.958	130	0.69	2.97	0.59	17.4 ± 2
175	0.966	150	0.69	3.00	0.68	17.0 ± 2
175	0.974	170	0.69	3.02	0.77	16.7 ± 2
200	0.871	10	0.73	2.70	0.05	23.5 ± 2
200	0.885	30	0.73	2.75	0.14	22.8 ± 2
200	0.897	50	0.73	2.79	0.23	22.2 ± 2
200	0.908	70	0.73	2.82	0.32	21.6 ± 2
200	0.919	90	0.73	2.85	0.41	21.0 ± 2
200	0.929	110	0.73	2.88	0.50	20.4 ± 2
200	0.938	130	0.73	2.91	0.59	19.8 ± 2
200	0.946	150	0.73	2.94	0.68	19.2 ± 2
200	0.955	170	0.73	2.96	0.77	18.6 ± 2
225	0.840	10	0.77	2.61	0.05	27.8 ± 3

Table 28. Continued published pure (protonated) water diffusivity data

225	0.857	30	0.77	2.66	0.14	27.1 ± 3
225	0.871	50	0.77	2.70	0.23	26.5 ± 3
225	0.884	70	0.77	2.74	0.32	25.9 ± 3
225	0.895	90	0.77	2.78	0.41	25.3 ± 3
225	0.906	110	0.77	2.81	0.50	24.8 ± 2
225	0.916	130	0.77	2.85	0.59	24.1 ± 2
225	0.926	150	0.77	2.88	0.68	23.6 ± 2
225	0.935	170	0.77	2.90	0.77	22.9 ± 2

Table 29. Molecular-dynamic diffusivity simulations of pure water (Kalinichev, 1993 and NIST, 1996)

Temperature, T (°C)	Calculated density (NIST, 1996), ρ_2 (g/cm^3)	Pressure, P (bar)	Reduced temperature, T_r	Reduced calculated density, ρ_{r2}	Reduced pressure, P_r	Self-diffusivity, $D_{22} \times 10^5$ (cm^2/s)
400	0.167	250	1.04	0.52	1.13	196
499	0.528	994	1.19	1.64	4.51	76
357	0.693	570	0.97	2.15	2.58	37
407	0.972	6435	1.05	3.02	29.2	23
498	1.286	32000	1.19	3.99	145	11
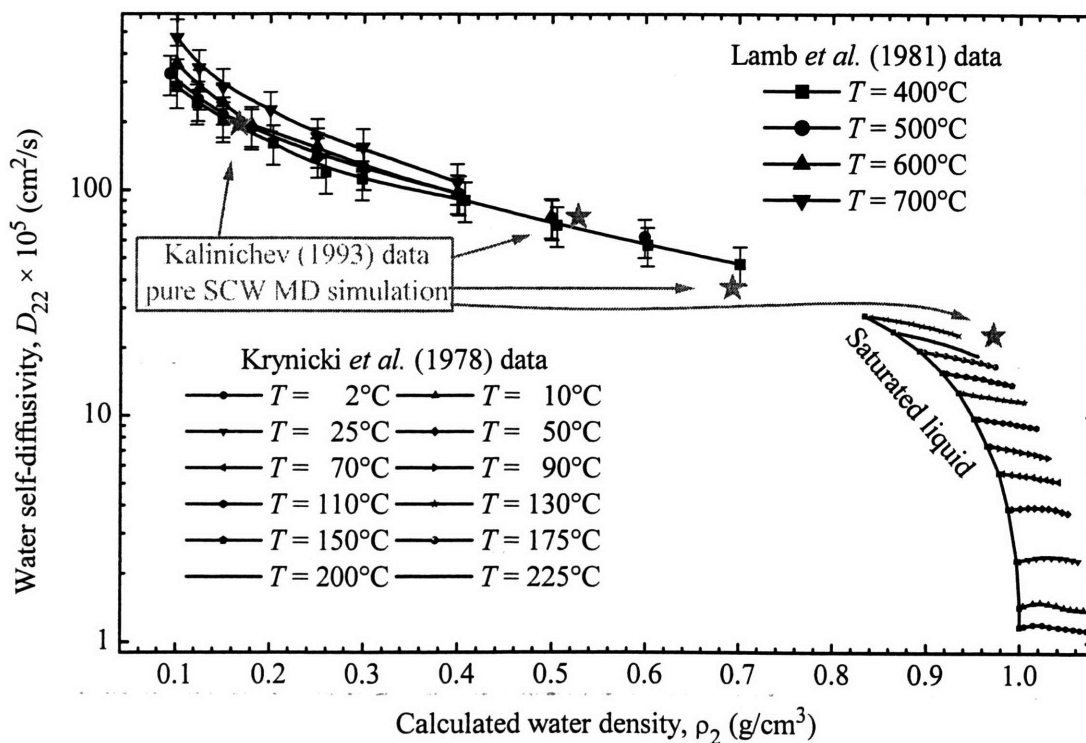
Figure 56. Water self-diffusivity measurements and simulations from NMR measurements and MD simulations, respectively, versus the calculated water density (Krynicki *et al.*, 1978; Lamb *et al.*, 1981; Kalinichev, 1993; NIST, 1996). Lamb *et al.* 95%-confidence-interval uncertainties are also shown.
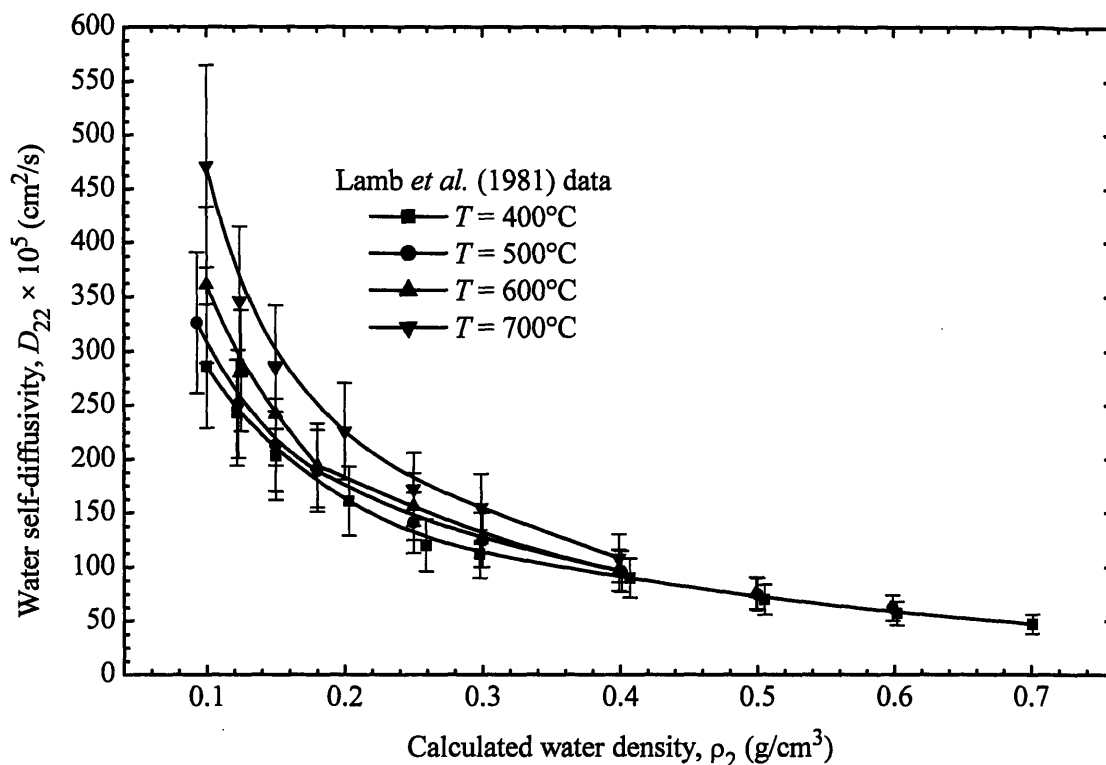
Figure 57. Water self-diffusivity measurements acquired using NMR and their 95%-confidence-interval uncertainties versus the calculated water density (Lamb *et al.*, 1981; NIST, 1996). Curves are intended to show general trends.
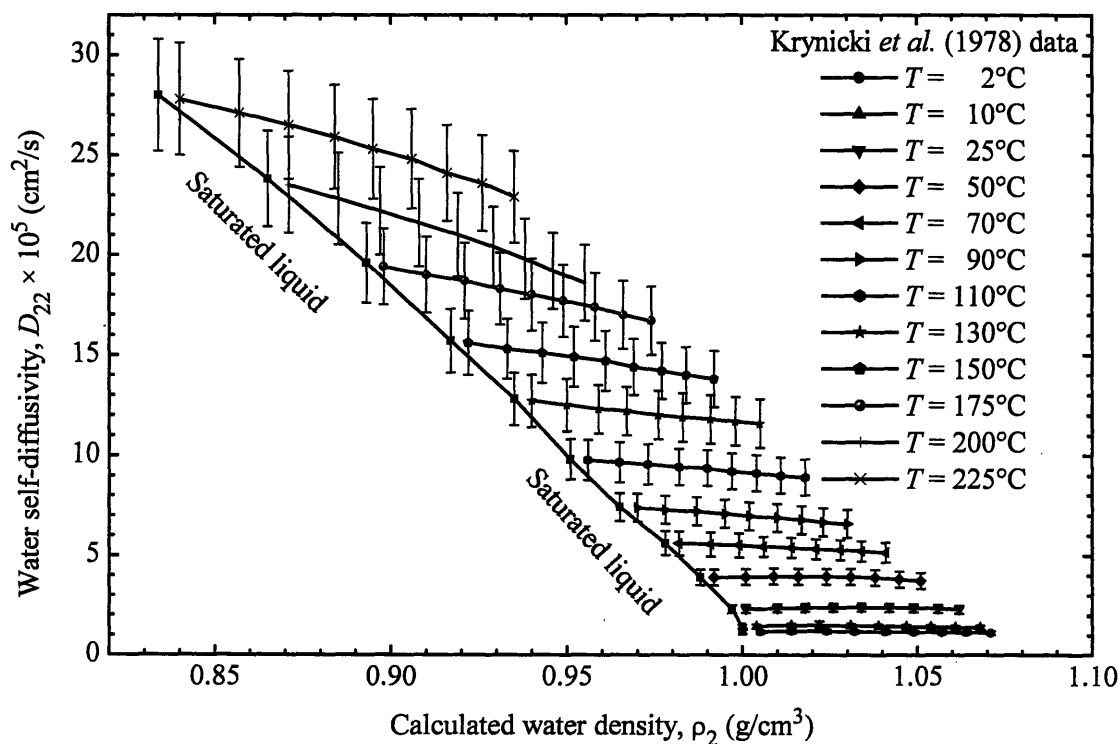
Figure 58. Water self-diffusivity measurements acquired using NMR and their 95%-confidence-interval uncertainties versus the calculated water density (Krynicki *et al.*, 1978; NIST, 1996).

For mixtures, data are also scant and are limited to

1. supercritical aqueous sodium-nitrate ($NaNO_3$) electrolyte-salt mixtures measured with the laser-induced grating method (Butenhoff *et al.*, 1996),

2. near-critical aqueous mixtures of hydroquinone and (potassium-) iodide ions at 240 bar measured with an electrical test cell (Flarsheim *et al.*, 1986),

3. sub- and near-critical aqueous binary mixtures of infinitely dilute inorganics (electrolytes) and organics (acetone and benzophenone) at 300 bar measured with the Taylor-Aris dispersion technique (Goemans, 1996), and

4. supercritical aqueous mixtures of infinitely dilute benzene at 250 bar measured with the Taylor-Aris dispersion technique (Bartle *et al.*, 1994).

These data are summarized in Table 30 and Table 31 and are shown in Figure 59 through Figure 61 as a function of pure water density. From Figure 60 and Figure 61, the iodide-ion data exhibit smoothness irregularities even with the 95%-confidence intervals shown, although the overall diffusivity trends are consistent with the other mixtures. For benzene, the data are also irregular, but are consistently isolated from the other datasets, thus raising suspicion about their accuracy. When plotted as a function of solution density in Figure 62, the benzene data are also outliers and thus, will not be used in the modeling analysis section. From further examination of Figure 62, the concentrated sodium-nitrate diffusivities no longer overlap and represent the only dataset that needs to be represented by mixture densities (Goemans, 1996).

In order to provide an overall picture of the available sub-, near, and supercritical diffusivity data, all of the data are plotted in Figure 63 where several trends can be seen. First, subcritical liquid diffusivities have higher densities and typically have lower diffusivities. Less dense and infinitely dilute supercritical-water mixtures have higher diffusivities, while concentrated aqueous mixtures have lower diffusivities. The dramatic diffusivity drops of the sodium-nitrate solutions are consistent with critical-point phenomena, but it should not be assumed that mixture diffusivities will always decrease at low densities. One region of Figure 63 that would benefit from additional data free of critical-phenomena effects is the low density supercritical region (0.1–0.4 g/cm^3, *i.e.*, the left side of Figure 63). Furthermore, understanding the concentration effect would be beneficial since SCWO processing conditions are not usually infinitely dilute.

Table 30. Aqueous sodium-nitrate(1) mutual diffusivity data along with calculated-pure-water densities (with 95%-confidence-interval uncertainties) (Butenhoff *et al.*, 1996; NIST, 1996)

Solute concentration (wt.%$_1$)	Solute mole fraction, x_1	Temperature, T (°C)	Calculated-pure-water density, ρ_2 (g/cm^3)	Pressure, P (bar)	Mutual diffusivity, $D_{12} \times 10^5$ (cm^2/s)
2.08%	0.004	450	0.285	409.5	13.0 ± 2
2.08%	0.004	450	0.308	425.1	14.7 ± 1
2.08%	0.004	450	0.343	450.1	17.0 ± 1
2.08%	0.004	450	0.402	500.0	19.8 ± 3
2.08%	0.004	450	0.446	550.3	18.3 ± 3
2.08%	0.004	450	0.480	600.1	20.2 ± 4
7.83%	0.018	400	0.225	271.6	10.6 ± 1
7.83%	0.018	400	0.246	276.9	12.1 ± 1
7.83%	0.018	400	0.357	300.0	15.8 ± 1
7.83%	0.018	400	0.475	350.0	20.1 ± 2
7.83%	0.018	400	0.523	399.9	21.2 ± 3
7.83%	0.018	400	0.578	500.0	23.2 ± 4
7.83%	0.018	400	0.612	600.0	21.7 ± 3
7.83%	0.018	450	0.282	407.3	1.42 ± 0.2
7.83%	0.018	450	0.286	410.3	2.72 ± 0.2
7.83%	0.018	450	0.305	422.8	6.35 ± 1
7.83%	0.018	450	0.322	435.0	9.04 ± 1
7.83%	0.018	450	0.343	450.1	11.4 ± 1
7.83%	0.018	450	0.375	475.0	14.6 ± 1
7.83%	0.018	450	0.402	500.0	17.1 ± 2
7.83%	0.018	450	0.446	550.1	20.3 ± 2
7.83%	0.018	450	0.480	600.0	21.7 ± 2
7.83%	0.018	450	0.506	650.0	23.1 ± 2
7.83%	0.018	450	0.528	700.0	23.1 ± 4
7.83%	0.018	450	0.547	750.0	24.8 ± 3
7.83%	0.018	450	0.564	800.0	24.7 ± 3
7.83%	0.018	450	0.591	900.0	24.0 ± 4
7.83%	0.018	500	0.294	544.0	4.0 ± 1
7.83%	0.018	500	0.299	550.2	5.4 ± 1
7.83%	0.018	500	0.339	600.1	12.2 ± 1
7.83%	0.018	500	0.406	700.0	19.6 ± 1
7.83%	0.018	500	0.457	800.1	22.7 ± 2
7.83%	0.018	500	0.497	900.0	25.0 ± 3
7.83%	0.018	500	0.529	1001.0	27.1 ± 4
20.3%	0.051	450	0.272	401.0	8.9 ± 0.4
20.3%	0.051	450	0.289	412.1	11.0 ± 1
20.3%	0.051	450	0.308	425.2	12.8 ± 2
20.3%	0.051	450	0.343	450.0	14.7 ± 2
20.3%	0.051	450	0.375	475.1	16.3 ± 1
20.3%	0.051	450	0.402	500.0	17.5 ± 2
20.3%	0.051	450	0.446	550.1	19.0 ± 2
20.3%	0.051	450	0.480	601.2	19.6 ± 3
20.3%	0.051	450	0.506	650.4	20.5 ± 2
20.3%	0.051	450	0.528	699.2	19.6 ± 2
20.3%	0.051	450	0.548	751.5	20.5 ± 3

Table 31. Published aqueous-mixture diffusivity data that are near or supercritical along with calculated-pure-water densities (with 95%-confidence-interval uncertainties) (NIST, 1996)

Solute concentration (wt.%$_1$)	Solute mole fraction, x_1	Temperature, T (°C)	Calculated-pure-water density, ρ_2 (g/cm^3)	Pressure, P (bar)	Mutual diffusivity, $D_{12} \times 10^5$ (cm^2/s)
Acetone(1)-water(2) ($2\sigma_T \sim 2$°C & $2\sigma_P \sim 2$ bar) (Goemans, 1996)
0.58%	0.002	25.1	1.010	300.7	0.958 ± 0.1
0.58%	0.002	100.0	0.972	299.7	3.59 ± 0.2
0.29%	0.001	200.2	0.884	300.2	10.6 ± 0.1
0.06%	0.000	299.8	0.751	299.7	25.9 ± 1
0.29%	0.001	300.3	0.750	300.1	24.5 ± 5
0.29%	0.001	300.0	0.751	300.0	25.2 ± 3
0.29%	0.001	350.1	0.644	301.6	43.6 ± 5
Benzophenone(1)-water(2) ($2\sigma_T \sim 2$°C & $2\sigma_P \sim 2$ bar) (Goemans, 1996)
0.01%	0.00001	100.0	0.972	300.4	2.28 ± 0.1
0.01%	0.00001	200.0	0.885	300.3	7.57 ± 1
0.001%	0.000001	300.0	0.751	299.6	19.1 ± 4
0.001%	0.000001	349.9	0.644	300.1	31.7 ± 10
Sodium nitrate(1)-water(2) ($2\sigma_T \sim 2$°C & $2\sigma_P \sim 2$ bar) (Goemans, 1996)
2.081%	0.004	24.4	1.010	300.0	1.78 ± 0.4
0.843%	0.002	50.6	1.000	299.5	2.62 ± 0.4
0.843%	0.002	100.2	0.972	300.6	4.49 ± 0.5
0.507%	0.001	149.8	0.933	299.6	7.32 ± 1
0.339%	0.001	200.0	0.885	300.0	10.5 ± 2
0.170%	0.0004	249.5	0.826	300.2	17.0 ± 1
0.170%	0.0004	299.9	0.751	299.8	19.2 ± 5
0.085%	0.0002	349.9	0.644	300.0	40.7 ± 13
Hydroquinone(1)-water(2) (Flarsheim et al., 1986)
~0.27%		25	1.008	240	0.74 ± 0.1
~0.28%		70	0.988	240	1.8 ± 1
~0.28%		100	0.969	240	2.7 ± 0.2
~0.30%		150	0.930	240	3.8 ± 0.6
~0.31%		200	0.881	240	7.9 ± 1
~0.33%		250	0.820	240	12 ± 2
~0.37%		300	0.741	240	19 ± 6
Iodide ions(1)-water(2) (Flarsheim et al., 1986)
~0.31%		25	1.008	240	1.4 ± 0.2
~0.32%		70	0.988	240	3.2 ± 0.2
~0.33%		100	0.969	240	4.6 ± 0.4
~0.34%		150	0.930	240	9.1 ± 1
~0.36%		200	0.881	240	16 ± 2
~0.39%		250	0.820	240	16 ± 2
~0.43%		300	0.741	240	22 ± 2
~0.51%		350	0.621	240	37 ± 8
~0.65%		375	0.486	240	49 ± 18
Benzene(1)-water(2) ($2\sigma_P \sim 4$ bar) (Bartle et al., 1994)
~0.1%	~0.0002	100	0.970	250	1.3 ± 0.3
~0.1%	~0.0002	150	0.930	250	1.7 ± 0.3
~0.1%	~0.0002	200	0.881	250	5.1 ± 1
~0.1%	~0.0002	250	0.821	250	5.4 ± 1
~0.1%	~0.0002	300	0.743	250	7.4 ± 1
~0.1%	~0.0002	350	0.625	250	25 ± 5
~0.1%	~0.0002	380	0.451	250	66 ± 13
~0.1%	~0.0002	400	0.167	250	160 ± 32
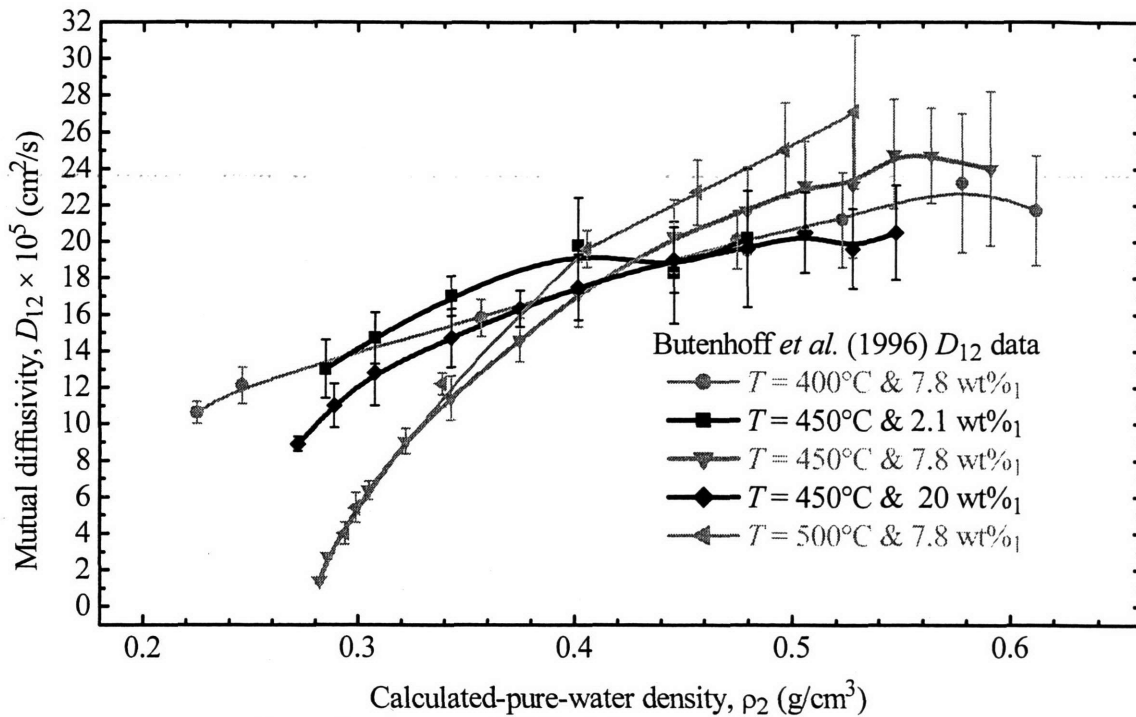
Figure 59. Aqueous sodium-nitrate mutual-diffusivity measurements reported as a function of calculated-pure-water density (Butenhoff *et al.*, 1996; NIST, 1996). Curves are intended to show general trends.
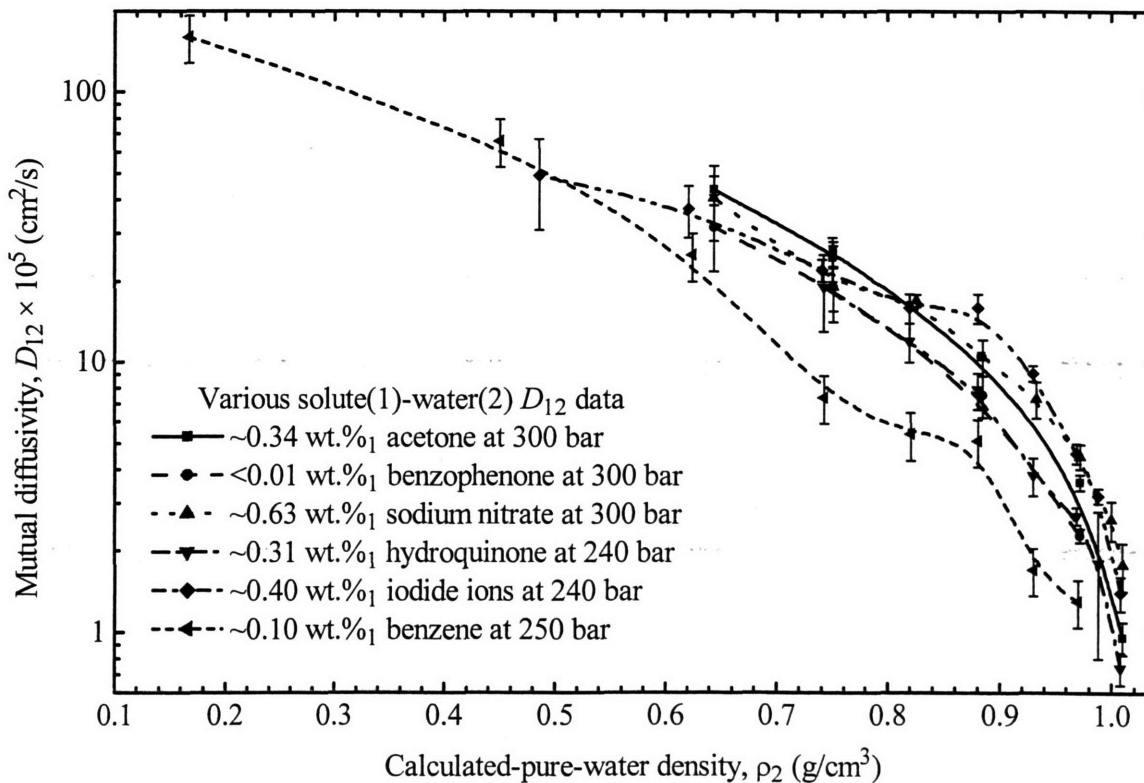
Figure 60. Aqueous-mutual-diffusivity measurements reported as a function of calculated-pure-water density (Flarsheim *et al.*, 1986; Bartle *et al.*, 1994; Goemans, 1996; NIST, 1996). Curves are intended to show general trends.

207
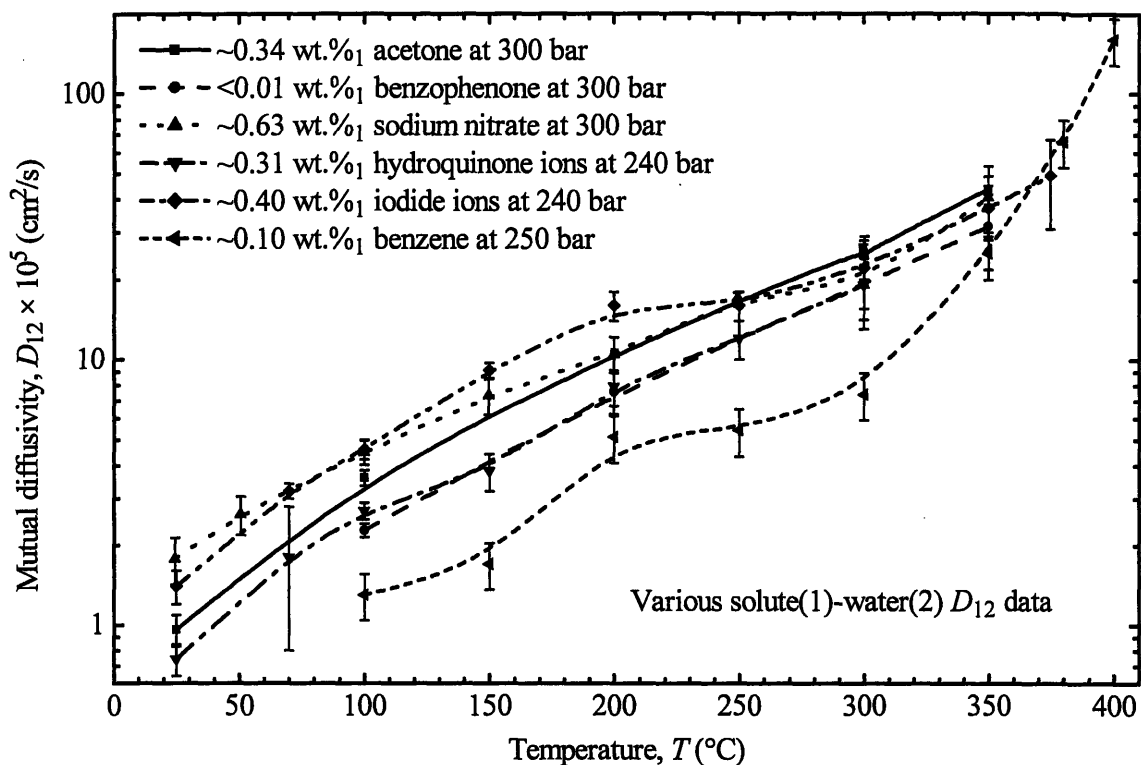
Figure 61. Aqueous-mutual-diffusivity measurements reported as a function of temperature (Flarsheim *et al.*, 1986; Bartle *et al.*, 1994; Goemans, 1996). Curves are intended to show general trends.
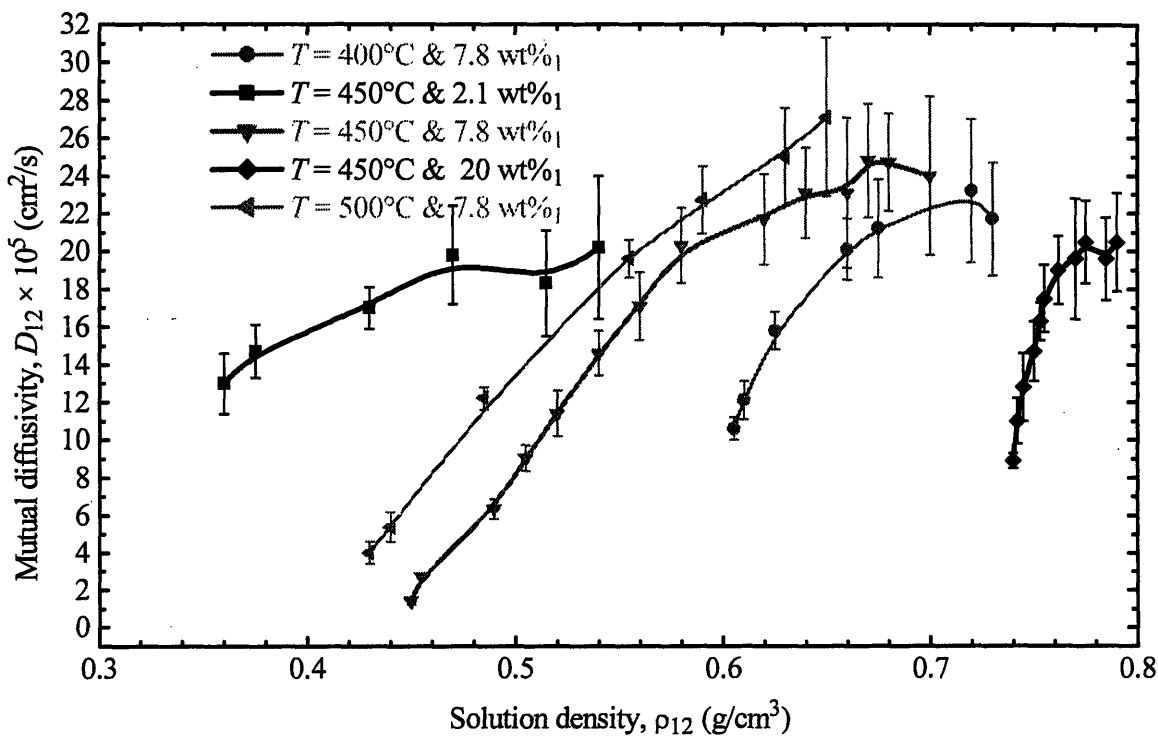
Figure 62. Aqueous sodium-nitrate mutual-diffusivity measurements plotted as a function of mixture solution density (Butenhoff *et al.*, 1996; Goemans, 1996). Curves are intended to show general trends.
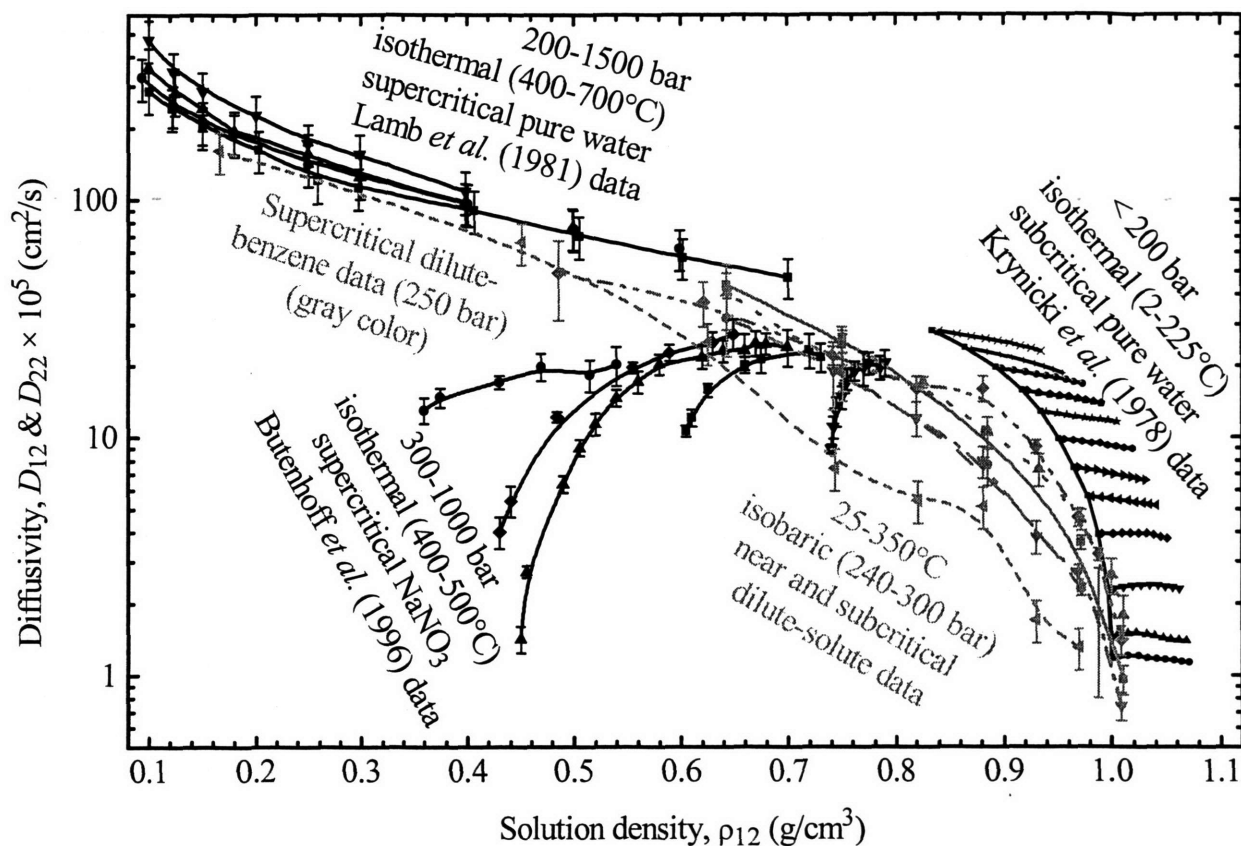
Figure 63. Global view of aqueous mutual and self-diffusivity measurements reported as a function of solution density (Krynicki *et al.*, 1978; Lamb *et al.*, 1981; Flarsheim *et al.*, 1986; Bartle *et al.*, 1994; Butenhoff *et al.*, 1996; Goemans, 1996; NIST, 1996). Curves are intended to show general trends.

Another anomaly to discuss involves the curvature of the 7.8 wt.%$_1$ sodium-nitrate curves in Figure 62. The authors speculate that dramatic diffusivity drops at lower density are due to critical-phenomena slowing near the critical-solution points (see Section II.1.2 for a critical-phenomena introduction). When 7.8 wt.%$_1$ diffusivity data are plotted as a function of pressure, slowing trends are seen for each of the 7.8 wt.%$_1$ diffusivity isotherms (Butenhoff *et al.*, 1996). They conclude that while the 450°C isotherm is close to the critical point, the 400°C and 500°C isotherms are further away from the plait point since they do not exhibit a drop comparable to 450°C data and that is characteristic of fluids near the critical point. Without accurate plait-point information, validating their conclusions is difficult.

However, if their assumption that the 500°C data are further away from the plait point is correct, then the 500°C diffusivities should not have a steep slope like that of the 450°C data. The 500°C data that they report have the same slope, implying that the 500°C data are closer to

the critical plait point. Due to this critical-point diffusivity decrease for each of their isotherms and the fact that much of the data is close to the critical-solution point, the data collected with the laser-induced-grating technique should not be used in the diffusivity-analysis section. In fact, for the diffusivity analysis performed by Butenhoff and coworkers, they tested correlations with the three densest data points which are least affected by critical effects for each concentration and temperature dataset so that their analysis was free of critical effects (Butenhoff *et al.*, 1996; Goemans, 1996). In order to avoid introducing diffusivity data possibly contaminated with critical effects, these data, along with the benzene data previously discussed, will not be used in the analysis section of this dissertation.

Ohmori and Kimura have recently performed molecular-dynamic simulations for sub- and supercritical water mixtures with oxygen and methane (2003), and these tracer diffusivities are contained in T and presented in Figure 64 and Figure 65 for oxygen and Figure 66 and Figure 67 for methane. When combined with all of the data used in the upcoming analysis section in Figure 68, the Ohmori and Kimura data are similar to and extend past the Lamb *et al.* (1981) data located in the low density supercritical regime.

Given the limited number of available diffusivities for supercritical aqueous solutions, especially with organic solutes, additional data would be useful in developing new and validating existing diffusivity models for supercritical water systems. Diffusivity measurements that address these issues are the focus of this dissertation, and this matter will be discussed further in Sections II.2 through II.4. The diffusivity models screened by the authors of the previously published supercritical diffusivity data will also be introduced in the diffusivity-analysis section.

Table 32. Published aqueous-mixture diffusivity simulation data along with calculated-pure-water densities (with 95%-confidence-interval uncertainties) (NIST, 1996; Ohmori and Kimura, 2003)

Solute concentration (wt.%$_1$)	Solute mole fraction, x_1	Temperature, T (°C)	Reported solution density, ρ_{12} (g/cm^3)	Calculated-pure-water density, ρ_2 (g/cm^3)	Pressure, P (bar)	Solute tracer diffusivity, $D_1 \times 10^5$ (cm^2/s)	Solvent tracer diffusivity, $D_2 \times 10^5$ (cm^2/s)
			Oxygen(1)-water(2)				
1.38%	0.0078	374	0.115	0.075	153	397 ± 18	228 ± 8
1.38%	0.0078	374	0.217	0.109	186	197 ± 6	114 ± 6
1.38%	0.0078	374	0.426	0.484	235	83 ± 6	72 ± 6
1.38%	0.0078	374	0.663	0.699	778	40 ± 4	44.6 ± 1.2
1.38%	0.0078	374	0.994	0.993	6550	16.5 ± 1	21.7 ± 0.6
1.38%	0.0078	400	0.217	0.135	231	182 ± 16	148 ± 6
1.38%	0.0078	500	0.115	0.097	266	391 ± 24	291 ± 20
1.38%	0.0078	500	0.217	0.182	406	183 ± 14	178 ± 14
1.38%	0.0078	500	0.426	0.431	745	89 ± 4	95 ± 6
1.38%	0.0078	500	0.663	0.682	1910	41 ± 6	55 ± 1.6
1.38%	0.0078	500	0.994	0.994	9270	20.4 ± 1	25.7 ± 1.4
1.38%	0.0078	600	0.115	0.105	349	388 ± 24	320 ± 16
1.38%	0.0078	600	0.217	0.199	581	189 ± 24	193 ± 10
1.38%	0.0078	600	0.426	0.429	1170	87 ± 6	104 ± 6
1.38%	0.0078	600	0.663	0.677	2820	47 ± 4	64 ± 4
1.38%	0.0078	700	0.115	0.108	427	401 ± 14	387 ± 18
1.38%	0.0078	700	0.217	0.206	750	218 ± 16	220 ± 12
1.38%	0.0078	700	0.426	0.430	1600	93 ± 4	110 ± 8
1.38%	0.0078	700	0.663	0.675	3730	57 ± 6	64 ± 4
			Methane(1)-water(2)				
0.70%	0.0078	374	0.115	0.076	155	355 ± 20	235 ± 8
0.70%	0.0078	374	0.217	0.112	188	187 ± 20	128 ± 6
0.70%	0.0078	374	0.426	0.500	242	78 ± 4	70.9 ± 2.8
0.70%	0.0078	500	0.115	0.099	269	384 ± 14	305 ± 20
0.70%	0.0078	500	0.217	0.187	413	203 ± 12	166 ± 6
0.70%	0.0078	500	0.426	0.441	766	81.5 ± 2	85 ± 4
0.70%	0.0078	600	0.115	0.106	352	405 ± 16	348 ± 6
0.70%	0.0078	600	0.217	0.201	587	210 ± 14	208 ± 16
0.70%	0.0078	600	0.426	0.437	1200	92 ± 6	103 ± 8
0.70%	0.0078	700	0.217	0.208	758	225 ± 16	223 ± 12
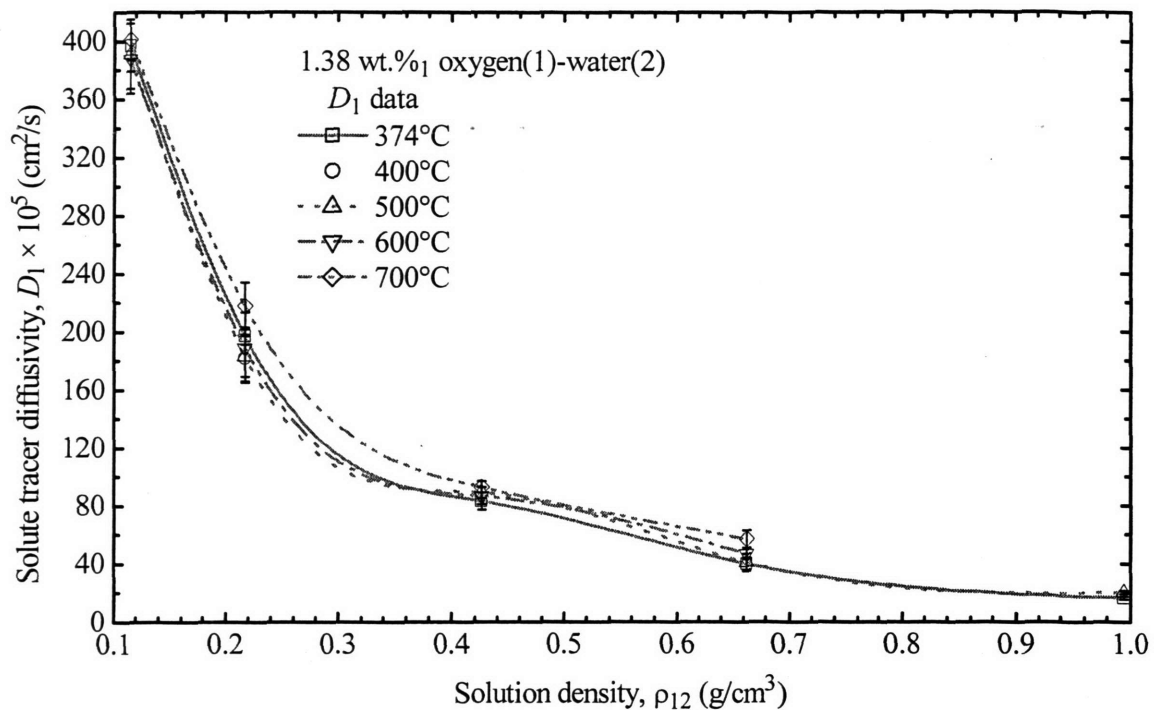
Figure 64. Simulated aqueous oxygen tracer diffusivities plotted as a function of mixture solution density for a 1.38 wt.%$_1$ oxygen-water mixture (Ohmori and Kimura, 2003). Curves are intended to show general trends.
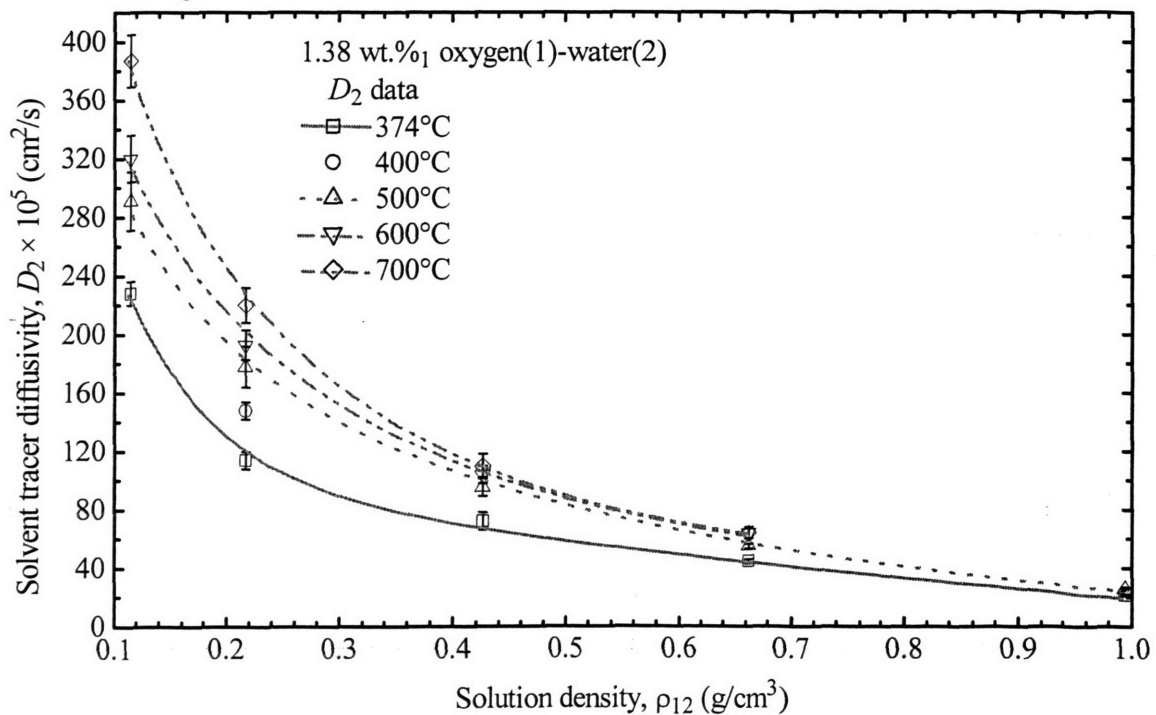
Figure 65. Simulated aqueous tracer diffusivities plotted as a function of mixture solution density for a 1.38 wt.%$_1$ oxygen-water mixture (Ohmori and Kimura, 2003). Curves are intended to show general trends.
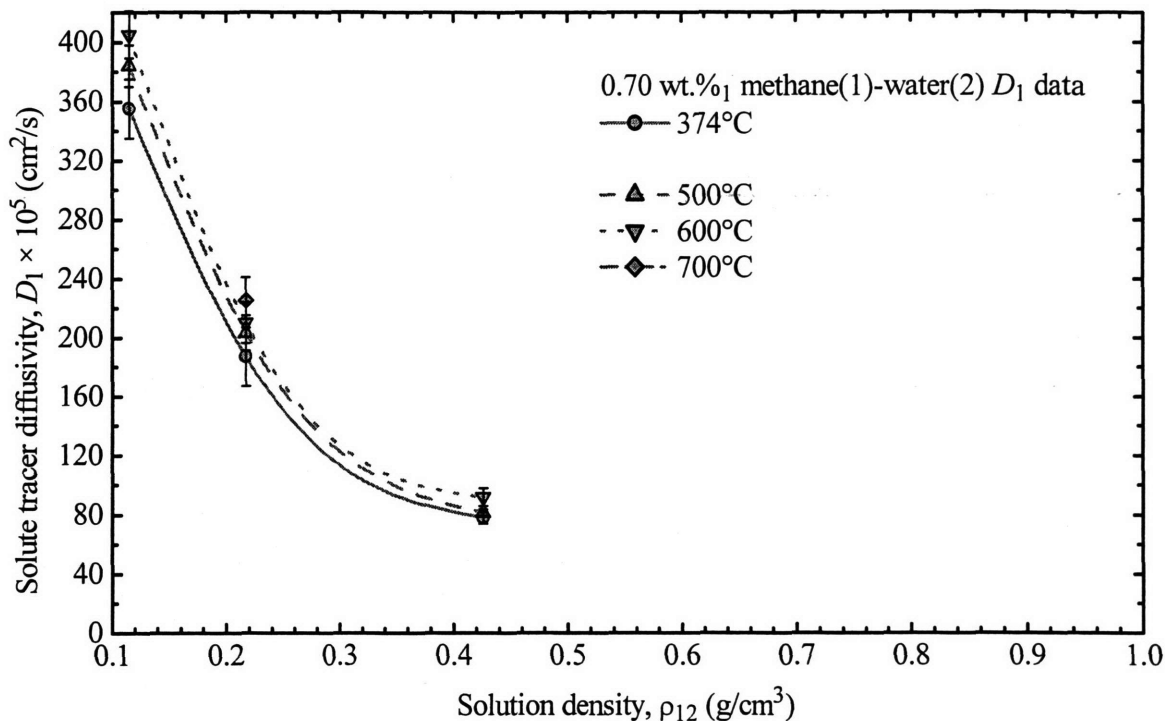
Figure 66. Simulated aqueous methane tracer diffusivities plotted as a function of mixture solution density for a 0.70 wt.%$_1$ methane-water mixture (Ohmori and Kimura, 2003). Curves are intended to show general trends.
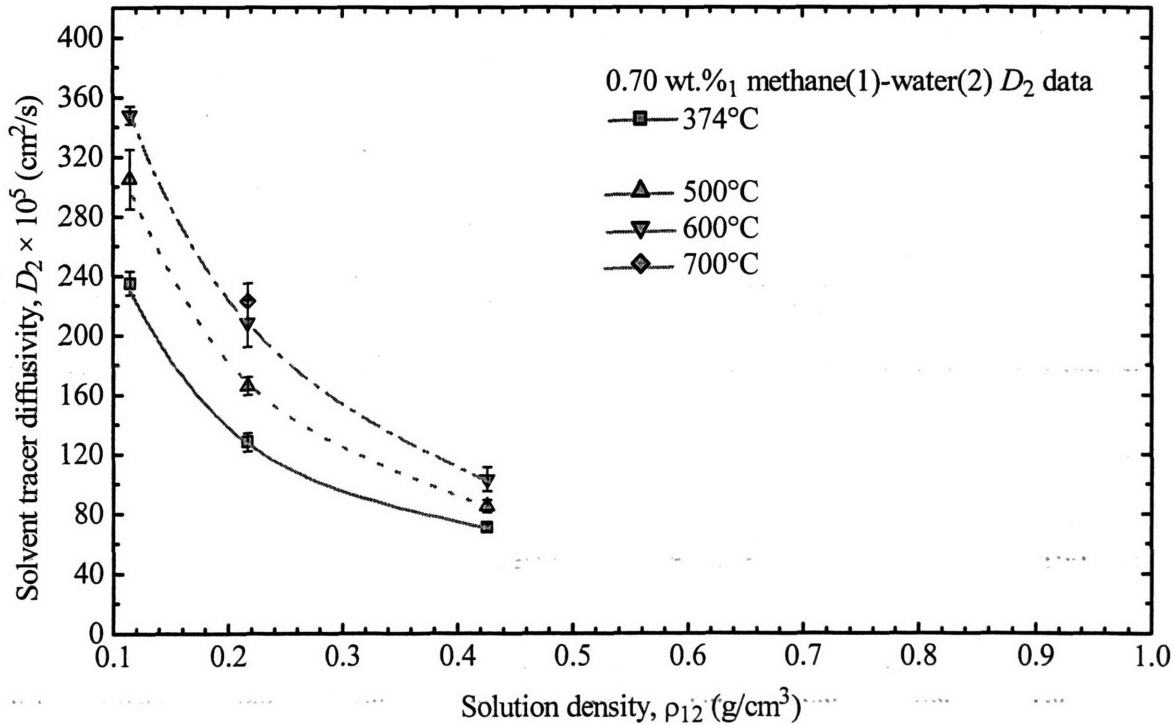
Figure 67. Simulated aqueous tracer diffusivities plotted as a function of mixture solution density for a 0.70 wt.%$_1$ methane-water mixture (Ohmori and Kimura, 2003). Curves are intended to show general trends.
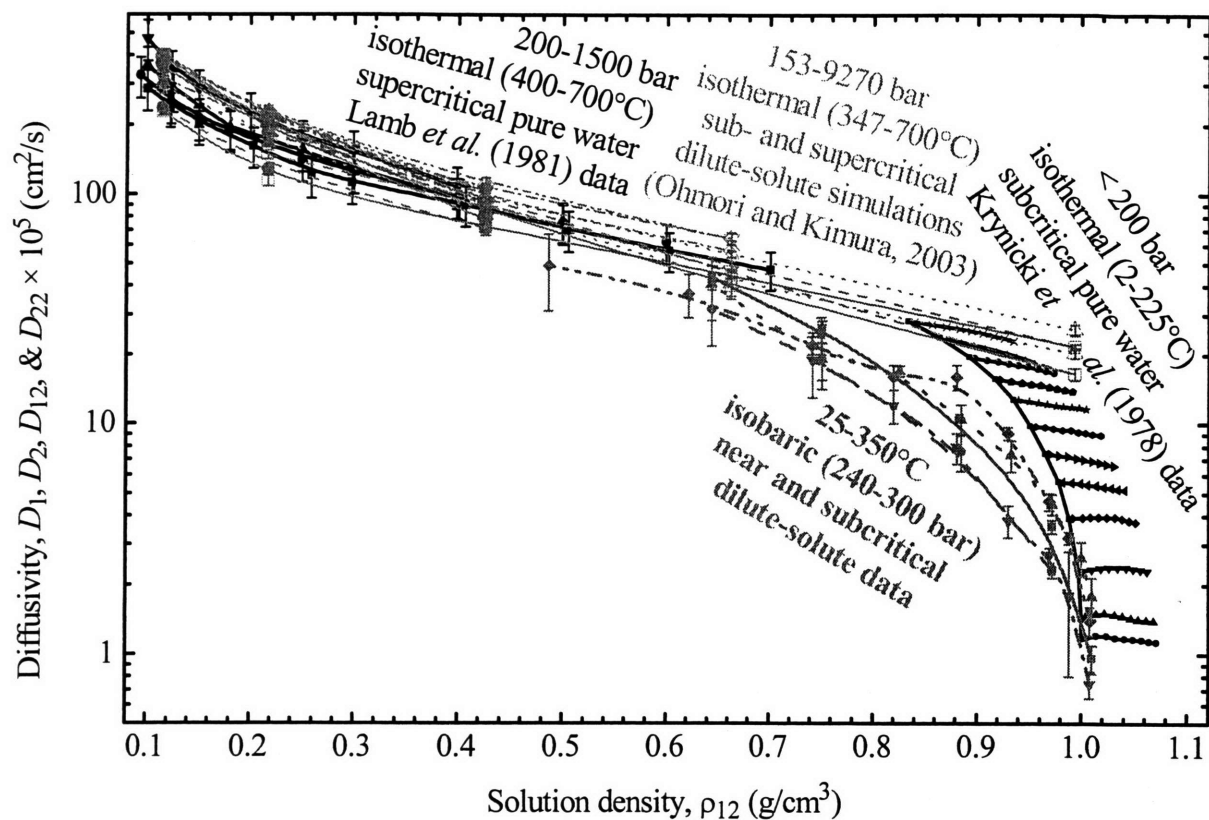
Figure 68. Global view of aqueous mutual and self-diffusivity measurements reported as a function of solution density (Krynicki *et al.*, 1978; Lamb *et al.*, 1981; Flarsheim *et al.*, 1986; Goemans, 1996; NIST, 1996; Ohmori and Kimura, 2003). Curves are intended to show general trends.

II.1.4 Nuclear Magnetic Resonance

Nuclear magnetic resonance (NMR) has been widely applied in many scientific fields including biology, chemistry, physics, and medicine, along with numerous engineering disciplines including nuclear, chemical, mechanical, and civil engineering. Since its first use in 1946 (Bloch *et al.*, 1946; Purcell *et al.*, 1946), NMR has evolved into a diagnostic tool capable of performing diffusivity, imaging, material characterization & differentiation, velocity, and acceleration experiments and has numerous chemistry and biology applications. Several of the key features of NMR are the non-invasive nature of sample and flow measurements; that NMR signals can be made sensitive to a variety of parameters including density, chemical shift, molecular motion, and NMR relaxation times; and that NMR is capable of measuring and resolving fast dynamic processes of order milliseconds.

II.1.4.1 NMR Diffusivity Measurement

The NMR diffusivity measurement is analogous to forced Rayleigh scattering. A spatial grating of the spin magnetization is created, and the attenuation induced by molecular diffusion is measured. One of most straightforward methods to explain NMR diffusivity measurements is to consider the magnetization grating across the sample. The wave vector $\mathbf{k}$ of the spin magnetization was introduced by Mansfield (1988) as

$$\Delta\mathbf{k}(\mathbf{G},t) = \frac{1}{2\pi}\int\gamma\mathbf{G}(t)dt \tag{172}$$

where $\mathbf{G}(t)$ is the time-dependent magnetic-field gradient. The detected NMR signal is the spatially invariant part of the spin magnetization modulated by the spin precession due to the gradient

$$S(\mathbf{k},t) \propto \exp(i\Delta\omega t)\exp(-t/T_2)\int\rho(\mathbf{r})\exp(2\pi i\Delta\mathbf{k}\cdot\mathbf{r})d\mathbf{r} \tag{173}$$

In the pulsed-gradient spin-echo (PGSE) measurements employed here, the spatial modulation of the spin magnetization is described by a single wave number whose amplitude attenuates as $\exp(-Dk^2 t)$. For those portions of the measurement when k is time dependent, the attenuation is $\exp(-\int Dk^2(t)dt)$. Since $k(t)$ is under experimental control, the diffusivity analysis from a series of measurements is straightforward. Finally, there are a variety of considerations associated with background gradients and hardware limitations that are well reviewed in the

literature (and Stejskal and Tanner, 1965; Hoult and Richards, 1975; Hoult and Richards, 1976; Callaghan and Xia, 1991; Price and Kuchel, 1991; Price et al., 1999).

II.1.4.2 NMR Probes for High Temperature and High Pressure Applications without Magnetic-Field Gradients

In addition to serving as a link between the spectrometer and sample, the NMR probe is assembled so that it can be placed easily in the magnet and can be able to reliably hold the sample vessel. When making measurements of samples held at elevated pressures and elevated temperatures, there is greater risk of harm for the operator, magnet, and the probe, so great care must be used. Numerous probe designs have been developed for a variety of high temperature or high pressures applications, and several will now be presented in chronological order.

In 1972 Jonas published the design of his probe that could achieve temperatures of 350°C and pressures of 5,000 bar with a Pyrex sample vessel and the RF coil placed inside a heavy walled, externally heated titanium cylinder (the probe is shown in Figure 69). High pressure seals were maintained at lower temperatures further away from the titanium heating zone. In 1979, DeFries and Jonas reported an improved design for their relaxation experiments with water (Lamb and Jonas, 1981) which could operate up to 700°C and 2,000 bar. As shown in Figure 70, the pressure-balanced sample cell (letter K) was made of alumina for corrosion resistance, and the design had the heater furnace (letter H) and RF coil (letter L) inside the argon-pressurized titanium cylinder (letter A).

In 1983, Shimokawa and Yamada made a probe for ^{13}C NMR experiments up to 550°C and 1,000 bar so that residues of thermal degradation of polyvinyl chloride could be monitored. The sample vessel material was not documented, but as shown in Figure 71, it was pressure balanced and placed inside a compact titanium alloy cylinder (2 cm ID, letter B) along with the heater (letter E) and RF coil (letter F). In 1990, Adler and coworkers reported ^{17}O spectra and relaxation for multiple ceramic samples using a water-cooled copper tube shaped to become the RF coil, which is then wrapped around the furnace containing the solid sample. The probe was reported to operate up to 1050°C as it sat in a cooling air stream at atmospheric pressure (the probe is shown in Figure 72). In 1992, Jonas and coworkers reported their work on a 6,000 bar probe along with other probes developed and previously discussed for use in their biological

studies. All of their results were below 100°C, had high resolution (0.003 ppm), and had high SNR (50), while the sample volumes (2 cm^3) were large.

In 1995, de Langen and Prins developed a heated titanium-alloy pressure vessel with the RF coil and pressure-balanced sample tube inside that could operate up to 10,000 bar and 337°C (the probe is shown in Figure 73). They report 5,500 bar proton relaxation data for polyethylene from 340 K through its melting line at 540 K.
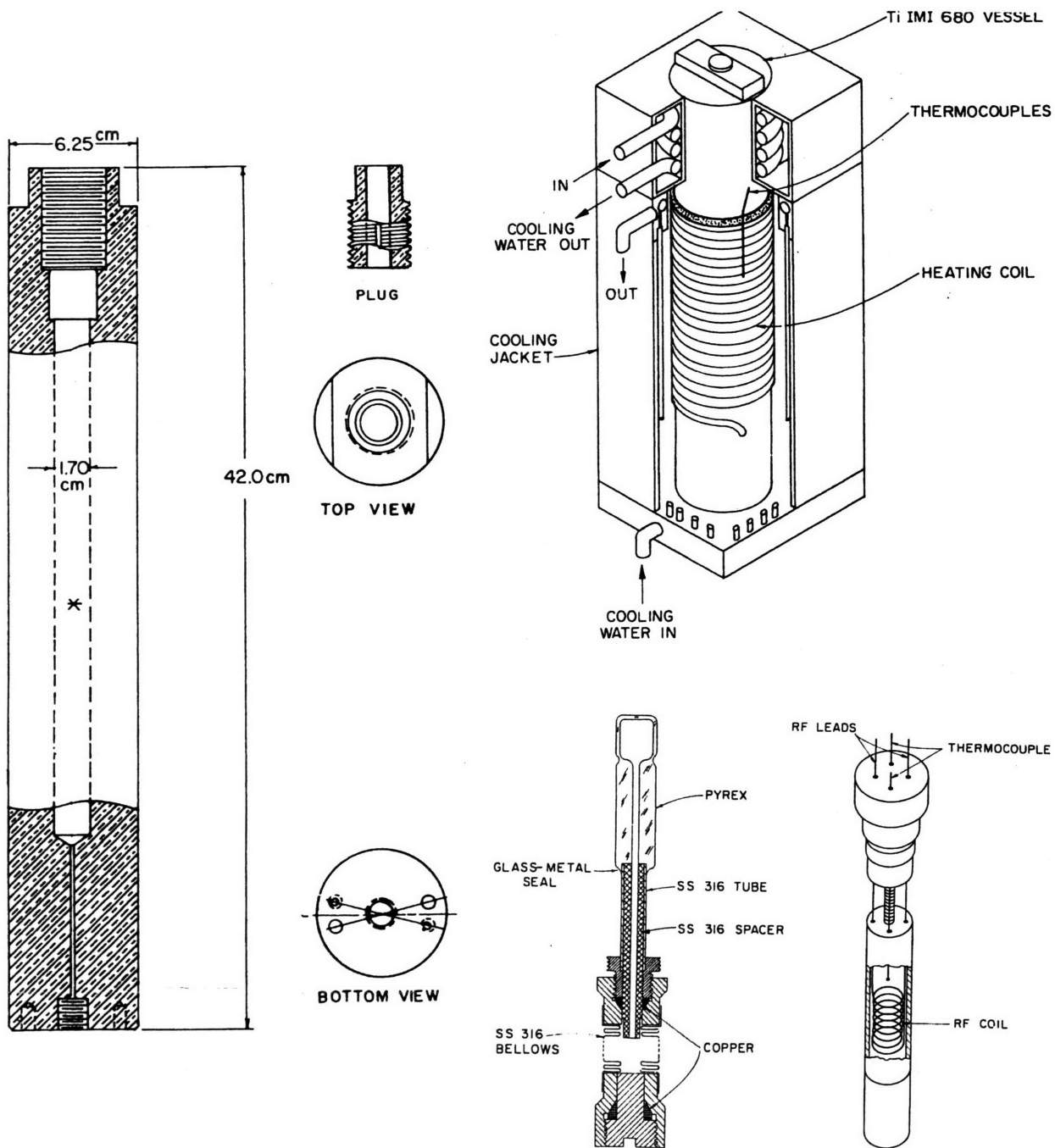
Figure 69. Illustrations of the high pressure NMR probe (Source: Jonas, 1972).
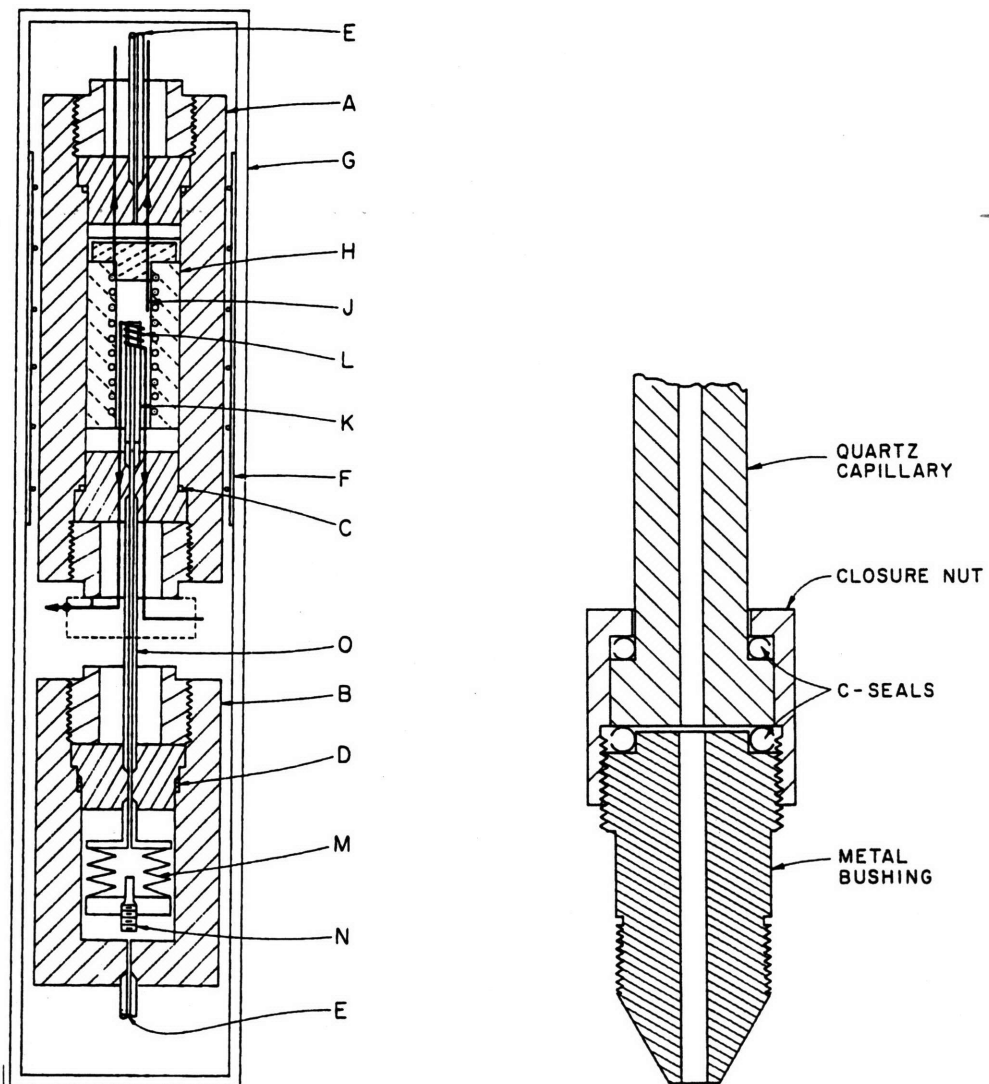
Figure 70. Illustrations of the high pressure NMR probe (Source: DeFries and Jonas, 1979).
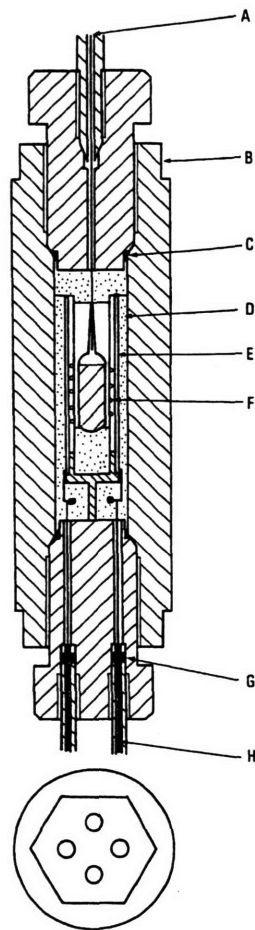
Figure 71. Illustrations of the high pressure NMR probe (Source: Shimokawa and Yamada, 1983).
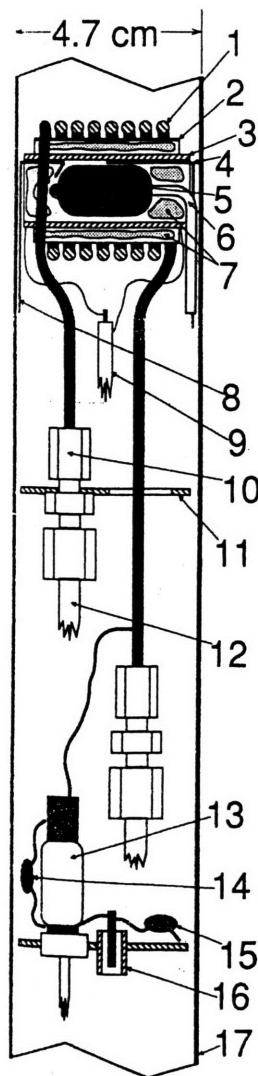
FIG. 2. Probe cross-section. (1) Copper NMR coil, 1/8-in. copper tubing. (2) Outer quartz furnace shell. (3) Annular furnace element. (4) Monitor thermocouple. (5) Sample. (6) Quartz sample tube containing $^{17}O_2$ gas. (7) Alumina fiber insulation. (8) Control thermocouple. (9) Coaxial furnace power lead. (10) Brass fitting. (11) Support plate. (12) Teflon water line. (13) Variable capacitor, 2 to 9 pf. (14) Fixed capacitor, 5 pf. (15) Fixed matching capacitor, $\cong 1300$ pf. (16) BNC radio frequency input/output. (17) Cylindrical brass probe body.
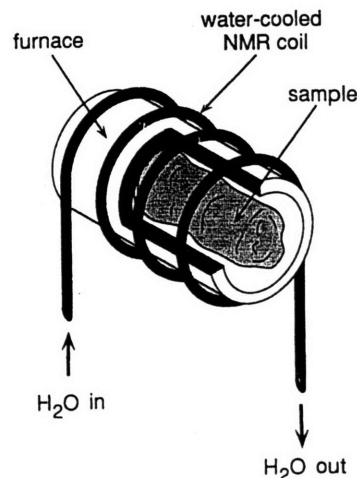
Figure 72. Illustrations of the high pressure NMR probe (Source: Adler *et al.*, 1990).
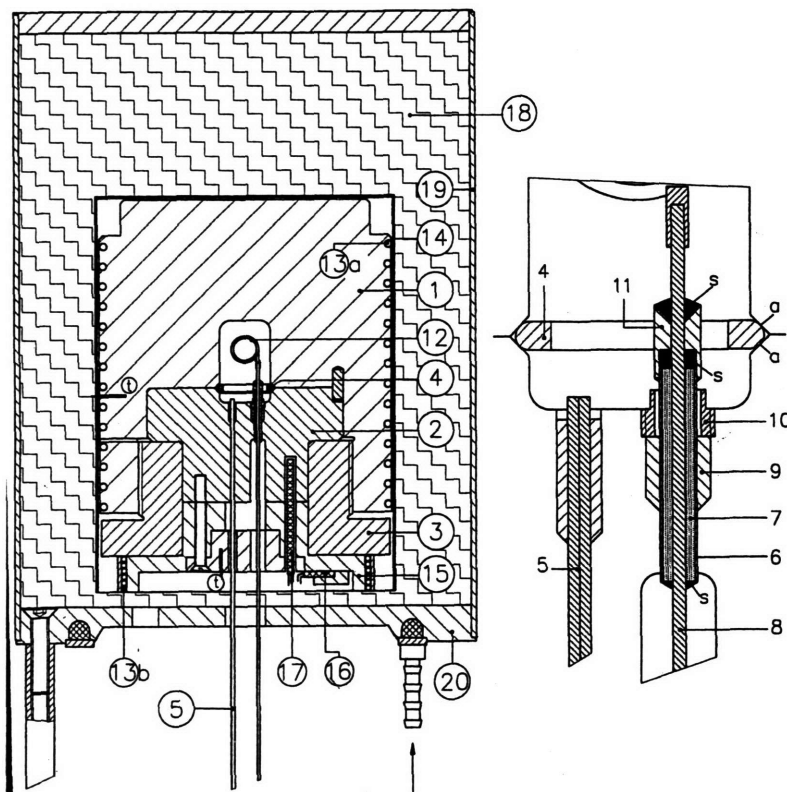
Figure 73. Illustrations of the high pressure NMR probe (Source: de Langen and Prins, 1995).

II.1.4.3 NMR Probes for High Temperature and High Pressure Applications with Magnetic-Field Gradients

All of the probes described in Section II.1.4.2 were used for relaxation measurements that did not require magnetic-field gradients. Unfortunately, only a limited number of NMR measurements are possible without gradients. If magnetic-field gradients are used, diffusivity experiments can be performed.

In 1985, Roe developed a high pressure sample tube (0.5 cm OD, 0.34 cm ID) made from sapphire that was mounted to a titanium valve assembly in order to perform high pressure experiments (the sample tube is shown in Figure 74). The closed-ended tube was glued and sealed to the metal with an epoxy adhesive and was quoted as operating safely at 140 bar, although the hydrostatic burst point of the tube was 1,000 bar (the seal was still intact during an actual pressure test). Experiments with different nuclei were performed and had 0.0014 ppm resolutions. In 1991, Horvath and Ponce redesigned Roe's sample tube by simplifying the titanium valve connected to the sapphire tube. The novel features of the Roe (1985) and Horvath

and Ponce (1991) sample tubes include that the 0.5 cm OD tube could be swapped with the standard 0.5 cm OD NMR sample tube. In addition, the sample tube could be precharged and pressurized away from the magnet before being placed in the magnet and probe. Their tube, which is manufactured by Saphikon, Inc. (Milford, NH), is glued in place with an aluminum-based polyamide adhesive in order to generate the high pressure seal (the sample tube is shown in Figure 75). In 1995, Yonker and coworker's novel design used fused-silica capillary tubing that was looped multiple times in a 0.5 cm NMR tube in order to study protonated organometallic reactions at ambient temperatures up to 1,000 bar (the sample tube is shown in Figure 76). They also report proton chemical shifts of subcritical propane and supercritical ethylene, supercritical-xenon chemical shifts (^{129}Xe), and local shielding of near-critical sulphur hexafluoride (^{19}F). Unfortunately, their apparatus is limited to low temperatures due to tensile-strength reduction at higher temperatures, and they only report less than 68°C data.
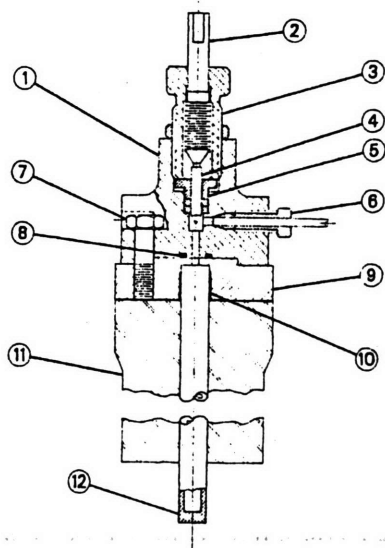
Figure 74. Illustrations of the high pressure NMR probe (Source: Roe, 1985).
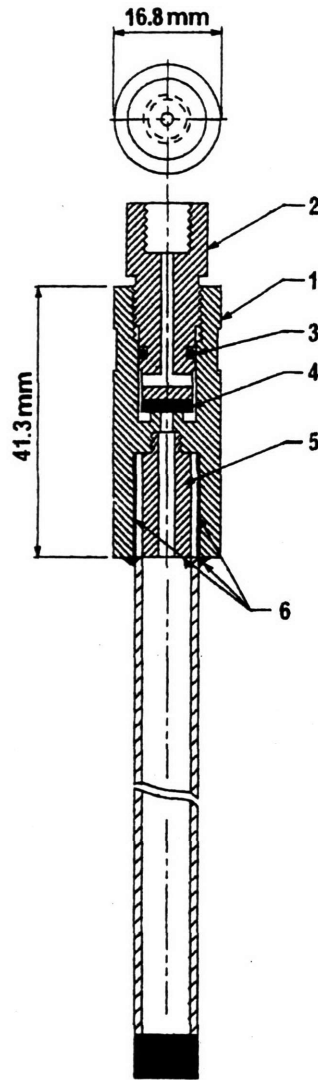
Figure 75. Illustrations of the high pressure NMR probe (Source: Horvath and Ponce, 1991).
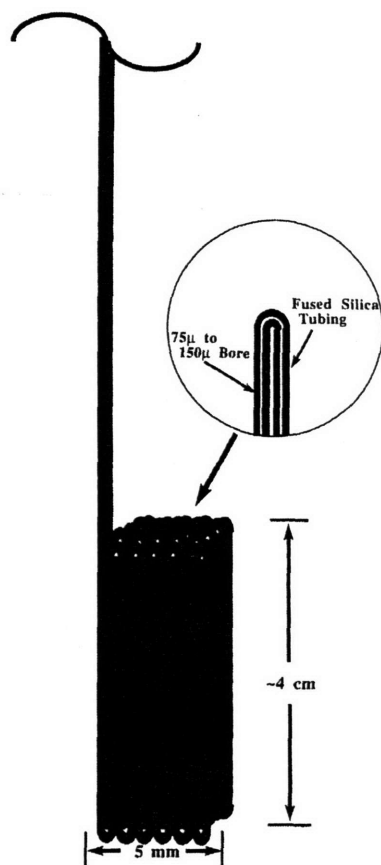
Figure 76. Illustrations of the high pressure NMR sample tube (Source: Yonker *et al.*, 1995).

In 1996, Bai and coworkers modified the designs of Roe, Horvath, and Ponce by decoupling pressure and temperature. Since the previous sample tubes were sealed with a constant volume, an increase in temperature would increase the vapor pressure. Bai removed the valve door assembly, placed a pressure-balanced movable piston inside the sample tube that connects the sample tube to capillary tubing, and pressurized the back of the piston and the volume of the valve assembly (the sample tube is shown in Figure 77). They were now able to control the pressure by regulating the backside pressure of the piston, and add samples through the access port and capillary tubing of the back face of the piston. They reported ^{13}C spin-lattice relaxation times for carbon dioxide from 30 to 300 bar and 15 to 70°C.
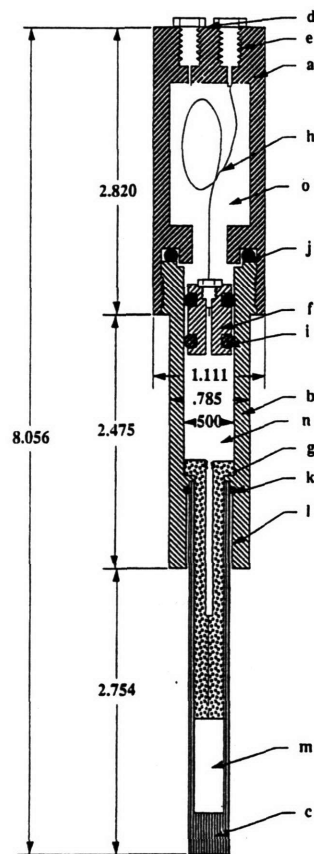
Figure 77. Illustrations of the high pressure NMR probe (Source: Bai *et al.*, 1996). Note the sample-tube restriction used to isolate the sample from the piston and capillary feed tubing in order to minimize natural convection.

In 1999, Gaemers and coworkers built a sapphire tube assembly similar to Bai's but without the piston and used one access port in the metal body to pressurize (up to ~100 bar) and the second to monitor the pressure with a transducer (the sample tube is shown in Figure 78). The last example of a closed-ended tube is that from Haake and coworkers (1998) who used a Pyrex tube with a pressurized port in order to perform sub- and supercritical xenon experiments up to 80 bar and 70°C. In all of these designs, the sample is measured at one end of the sample tube and the sample inside this end would be difficult to change since the access ports for new samples are all located at the other end of the tube.
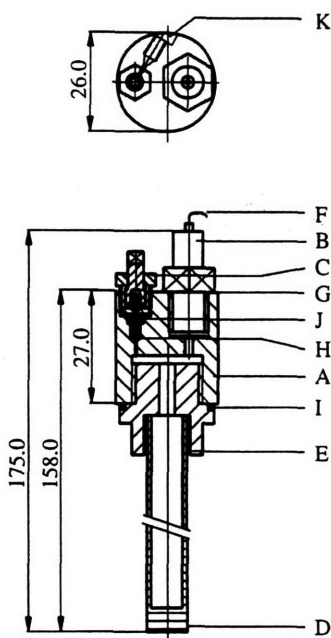
Figure 78. Illustrations of the high pressure NMR probe (Source: Gaemers *et al.*, 1999).

One of the most important features about these last approaches is that standard NMR probes can be used, including probes which have gradient sets that are built into the probe or gradient sets that permanently line the superconducting magnet which the probes sit in. As a result, more interesting NMR experiments can be performed including imaging experiments. However, the tube-to-metal interface does not allow the use of high temperatures that are needed for SCW studies.

In 1996, Matenaar and coworkers designed and built a pressure vessel similar to those of Jonas, but were able to include a gradient set (#11) between the pressure vessel and the RF coil (#10) and sample (the probe is shown in Figure 79). The gradient set was formed on a MACOR® (a Corning machinable ceramic) base, and the probe was able to operate up to 2,000 bar and 400°C for their molten-salt ([23]Na) diffusion studies.
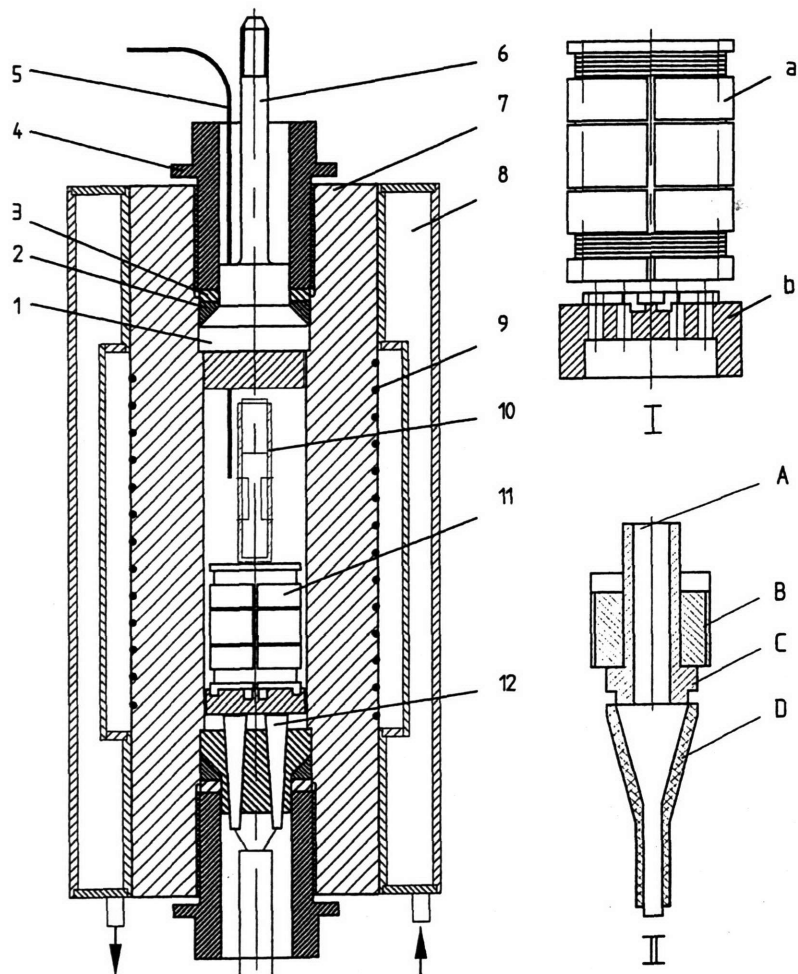
Figure 79. Illustrations of the high pressure NMR probe (Source: Matenaar *et al.*, 1996).

In 1997, Hoffmann and Conradi simplified Jonas's design in order to make chemical shift measurements for pure water, pure ethanol, and pure methanol (Hoffman and Conradi, 1997a; Hoffman and Conradi, 1997b; Hoffman and Conradi, 1998). Nonetheless, they report shifts up to 400 bar and 600°C with 0.1 ppm FWHM water peaks. Their probe also contains a one-axis gradient coil located on top of the cooling coils covering their titanium-alloy pressurize vessel (the probe and its argon-pressure-balanced sample cell is shown in Figure 80).
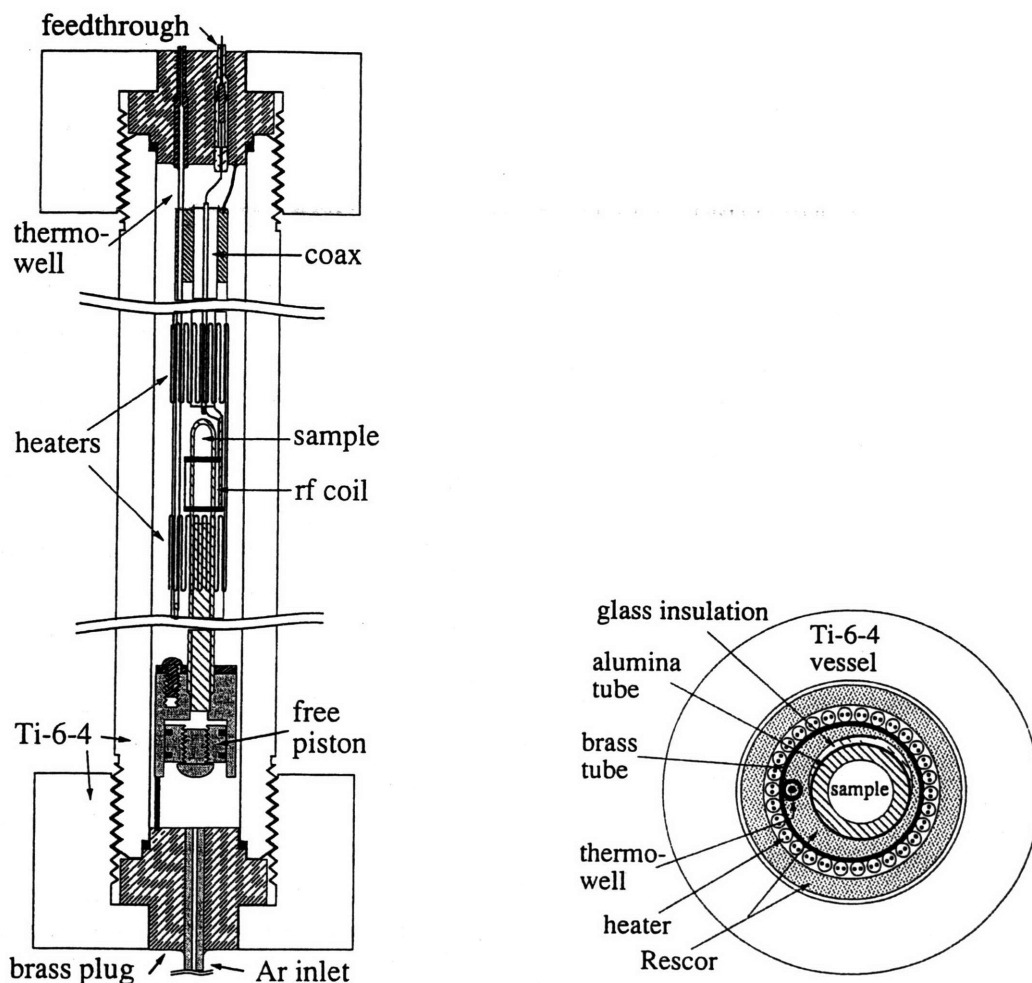
Figure 80. Illustrations of the high pressure NMR probe (Source: Hoffmann and Conradi, 1997a).

Also in 1997, Matubayasi and coworkers report their probe design for their studies (1997a and 1997b) of hydrogen bonding in sub- and supercritical water. Their water sample is sealed in a small quartz capillary, which is then placed in a standard 0.5 cm NMR tube filled with the heat transfer fluid DEMNUM S-200 (Daikin Co.). This tube is then placed in a vertical bore magnet and is placed inside the RF coil. A double-walled cylindrical Dewar is located between the sample tube and the RF coil and is used as an insulator to keep the RF coil cool while hot nitrogen gas flows past the sample tube (the probe is shown in Figure 81). The Dewar tube functions as a thermal insulator since the gap between the double set of walls is sealed and placed under vacuum, thereby reducing the thermal conductivity and heat-transfer coefficient across the Dewar wall. The nitrogen that is flowing past the sample tube is heated upstream with an electrical heater located inside the Dewar. Temperatures up 400°C are reported, and since the

sample capillary is sealed, the maximum pressure is estimated to be 260 bar based on their reported density of 0.19 g/cm^3. A noteworthy feature is the use of a cool RF coil since the SNR is inversely dependent on the temperature (Hoult and Richards, 1976). Only Matubayasi *et al.* (1997b) and Adler *et al.* (1990) use a low temperature coil with a high temperature sample. However, Matubayasi's coil has a much larger diameter which reduces the RF-coil filling factor, and consequently, the SNR.
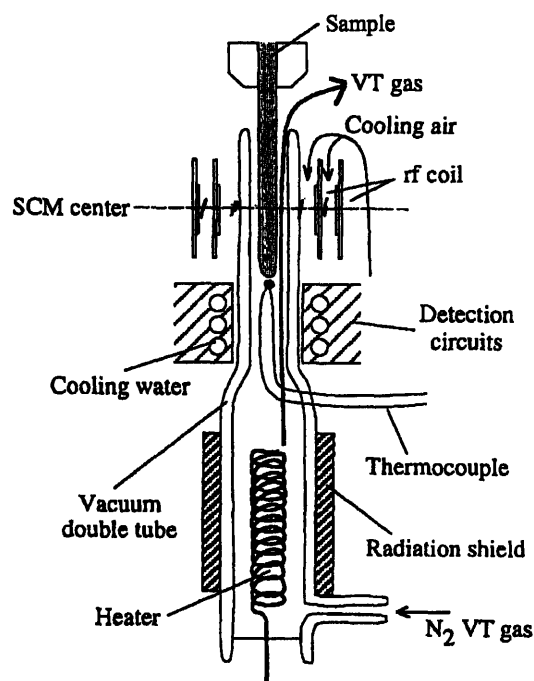
Figure 81. Illustrations of the high pressure NMR probe (Source: Matubayasi *et al.*, 1997b).

All of these probes have their various advantages and limitations, but one aspect never addressed is using the probe for monitoring molecular motion besides mentioning that measurements can be made. Furthermore, these probes offer little in terms of fast, convenient replacement of sample within the same sample vessel and within the actual location surrounded by the RF coil.

II.1.5 References

Abdulkadirova, Kh. S. , Kostrowicka, A., Wyczalkowska, Anisimov, M.A., and Sengers, J.V. (2002) "Thermodynamic properties of mixtures of H_2O and D_2O in the critical region." *J. Chem. Phys.*, **116 (11)**, 4597–4610.

Adler, S.B., Michaels, J.N. and Reimer, J.A. (1990) "A compact, high temperature nuclear magnetic resonance probe for use in a narrow-bore superconducting magnet." *Rev. Sci. Instrum.*, **61 (11)**, 3368–3371.

Alder, B.J., Alley, W.E., and Dymond, J.H. (1974) "Studies in molecular dynamics.XIV. mass and size dependence of the binary diffusion coefficient." *J. Chem. Phys.*, **61 (4)**, 1415–1420.

Alder, B.J., Gass, D.M., and Wainwright, T.E. (1970) "Studies in molecular dynamics.VIII. the transport coefficients for a hard-sphere fluid." *J. Chem. Phys.*, **53 (10)**, 3813–3826.

Andrews, T. (1869) "On the continuity of the gaseous and liquid states of matter." *Phil. Trans. Royal Soc.*, **159**, 575–590.

Anisimov, M.A., Agayan, V.A., Povodyrev, A.A., Sengers, J.V., and Gorodetskii, E.E. (1998) "Two-exponential decay of dynamic light scattering in near-critical fluid mixtures." *Phys. Rev. E*, **57**, 1946–1961.

Asahi, N. and Nakamura, Y. (1997) "NMR study of liquid and supercritical benzene." *Ber. Bunsenges. Phys. Chem.*, **101 (5)**, 831–836.

Atkins, P.W. (1990) *Physical Chemistry*, W.H. Freeman and Co., 4th ed., New York, NY.

Bai, S., Taylor, C.M., Mayne, C.L., Pugmire, R.J., and Grant, D.M. (1996) "A new high pressure sapphire nuclear magnetic resonance cell." *Rev. Sci. Instrum.*, **67 (1)**, 240–243.

Bak, C.S. and Goldburg, W.I. (1969) "Light scattering in an impure binary liquid mixture near the critical point." *Phys. Rev. Lett.*, **23 (21)**, 1218–1220.

Baker, E.S., Brown, D.R., Lamb, D.M., and Jonas, J. (1985) "Self-diffusion in compressed supercritical toluene-d_8." *J. Chem. Eng. Data*, **30**, 141–143.

Balenovic, Z., Myers, M.N., and Giddings, J.C. (1970) "Binary diffusion in dense gases to 1360 atm by the chromatographic peak-broadening method." *J. Chem. Phys.*, **52 (2)**, 915–922.

Bartle, K.D., Carroll, J.L., Clifford, A.A., and Smith, L. (1994) "Measurement of the diffusion coefficient of benzene in liquid and supercritical water." Internal correspondence.

Bejan, A. (1997) *Advanced Engineering Thermodynamics*, John Wiley & Sons, Inc., New York, NY.

Bird, R.B., Stewart, W.E., and Lightfoot, E.N. (1960) *Transport Phenomena*, John Wiley & Sons, Inc., New York, NY.

Bloch, F., Hansen, W.W., and Packard, M. (1946) "Nuclear induction." *Phys. Rev.*, **70**, 474.

Boltzmann, L. (1899) *Proc. Amsterdam*, 403.

Brokaw, R.S. (1969) "Predicting transport properties of dilute gases." *Ind. Eng. Chem. Proc. Des. Dev.*, **8 (2)**, 240–253.

Burstyn, H.C., Sengers, J.V., Bhattacharjee, J.K., and Ferrell, R.A. (1983) "Dynamic scaling function for critical fluctuations in classical fluids." *Phys. Rev. A*, **28 (3)**, 1567–1578.

Burstyn, H.C., Sengers, J.V., and Esfandiari, P. (1980) "Stokes-Einstein diffusion of critical fluctuations in a fluid." *Phys. Rev. A*, **22 (1)**, 282–284.

Butenhoff, T.J., Goemans, M.G.E. and Buelow, S.J. (1996) "Mass diffusion coefficients and thermal diffusivity in concentrated hydrothermal $NaNO_3$." *J. Phys. Chem.*, **100**, 5982–5992.

Callaghan, P.T. and Xia, Y. (1991) "Velocity and diffusion imaging in dynamic NMR microscopy." *J. Mag. Res.*, **91**, 326–352.

Carman, P.C. and Stein, L.H. (1956) *Trans. Faraday Soc.*, **52**, 619.

Carnahan, N.F. and Starling, K.E. (1969) "Intermolecular repulsions and the equation of state for fluids/equation of state for nonattractive rigid spheres." *J. Chem. Phys.*, **51**, 635–636.

231

Catchpole, O.J. and King, M.B. (1994) "Measurement and correlation of binary diffusion coefficients in near critical fluids." *Ind. Eng. Chem. Res.*, **33**, 1828–1837.

Chapman, S. and Cowling T.G. (1970) *The Mathematical Theory of Non-uniform Gases*, Cambridge University Press, Cambridge, UK.

Clausius, R. (1879) *Mech. Warmetheorie*, **3**, 57, 2nd ed..

Cohen, M.H. and Turnbull, D. (1959) "Molecular transport in liquids and glasses." *J. Chem. Phys.*, **31**, 1164.

Cussler, E.L. (1997) *Diffusion: Mass Transfer in Fluid Systems*, Cambridge University Press, 2nd ed., Cambridge, UK.

Darken, L.S. (1948) Trans. Am. Inst. Mining Metall. Engrs., **175**, 184.

Dawson, R., Khoury, F., and Kobayashi, R. (1970) "Self-diffusion measurements in methane by pulsed nuclear magnetic resonance." *AIChE J.*, **16 (5)**, 725–729.

de Langen, M. and Prins, K.O. (1995) "NMR probe for high pressure and high temperature." *Rev. Sci. Instrum.*, **66 (11)**, 5218–5221.

Defries, T.H. and Jonas, J. (1979) "NMR probe for high-pressure and high-temperature experiments." *J. Mag. Reson.*, **35**, 111–119.

Dymond, J.H. (1974) "Corrected Enskog theory and the transport coefficients of liquids." *J. Chem. Phys.*, **60 (3)**, 969–973.

Easteal, A.J. and Woolf, L.A. (1990) "Tracer diffusion in hard-sphere liquids from molecular dynamics simulations." *Chem. Phys. Lett.*, **167 (4)**, 329–333.

Eaton, A.P. and Akgerman, A. (1997) "Infinite-dilution diffusion coefficients in supercritical fluids." *AIChE J.*, **36**, 923–931.

Ehrlich, R.S. and Carr, H.Y. (1970) "Xenon self-diffusion near the critical point and on the liquid branch of the coexistence curve." *Phy. Rev. Let.*, **25 (6)**, 341–344.

Erkey, C. and Akgerman, A. (1989) "Translational rotational coupling parameters for mutual diffusion in normal alkanes." *AIChE J.*, **35 (11)**, 1907–1911.

Erpenbeck, J.J. and Wood, W.W. (1991) "Self-diffusion coefficient for the hard-sphere fluid." *Phys. Rev. A*, **43 (8)**, 4254–4261.

Ertl, H. and Dullien, F.A.L. (1973) "Self-diffusion and viscosity of some liquids as a function of temperature [NMR measurements]." *AIChE J.*, **19 (6)**, 1215–1223.

Flarsheim, W.M., Tsou, Y.M., Trachtenberg, I., Johnston, K.P., and Bard, A.J. (1986) "Electrochemistry in near-critical and supercritical fluids. 3. Studies of Br⁻, I⁻, and hydroquinone in aqueous solutions." *J. Phys. Chem.*, **90**, 3857–3862.

Fu, H.F., Coelho, L.A.F., and Matthews, M.A. (2000) "Diffusion coefficients of model contaminants in dense CO_2." *J. Supercritical Fluids*, **18**, 141–155.

Gaemers, S., Luyten, H., Ernsting, J.M., and Elsevier, C.J. (1999) "Multinuclear magnetic resonance studies under pressure of gases and in supercritical media employing a novel titanium-sapphire high-pressure cell with pressure sensor." *Mag. Res. Chem.*, **37**, 25–30.

Goemans, M.G.E. (1996) "Molecular diffusion and mass transfer in subcritical and supercritical water." *University of Texas at Austin*, Doctoral dissertation, Austin, TX.

Haake, M., Goodson, B.M., Laws, D.D., Brunner, E., Cyrier, M.C., Havlin, R.H., and Pines, A. (1998) "NMR of supercritical laser-polarized xenon." *Chem. Phys. Lett.*, **292 (4-6)**, 686–690.

Hardt, A.P., Anderson, D.K., Rathbun, R., Mar, B.W., and Babb, A.L. (1959) "Self-diffusion in liquids. II. comparison between mutual and self-diffusion coefficients." *J. Phys. Chem.*, **63 (12)**, 2059–2061.

Harris, K.R. (2002) "Comment on 'Self-diffusion near the liquid-vapor critical point.'" *J.Chem. Phys.*, **116 (14)**, 6379–6380.

Hartley, G.S. and Crank, J. (1949) *Trans. Faraday Soc.*, **45**, 801.

Hayduk, W. and Laudie, H. (1974) "Prediction of diffusion coefficients for nonelectrolytes in dilute aqueous solutions." *AIChE J.*, **20 (3)**, 611–615.

He, C.H. (1997) "Prediction of binary diffusion coefficient of solutes in supercritical solvents." *AIChE J.*, **43 (11)**, 2944–2947.

He, C.H. and Yu, Y.S. (1998) "New equation for infinite-dilution diffusion coefficients in supercritical and high-temperature liquid solvents." *Ind. Eng. Chem. Res.*, **37**, 3793–3798.

Hildebrand, J.H. (1977) *Viscosity and Diffusivity: A Predictive Treatment*, John Wiley & Sons, Inc., New York, NY.

Hirschfelder, J.O., Curtiss, C.F. and Bird, R.B. (1966) *Molecular Theory of Gases and Liquids*, Wiley, 2nd ed., New York, NY.

Hoffmann, M.M. and Conradi, M.S. (1997a) "Nuclear magnetic resonance probe for supercritical water and aqueous solutions." *Rev. Sci. Instrum.*, **68 (1)**, 159–164.

Hoffmann, M.M. and Conradi, M.S. (1997b) "Are there hydrogen bonds in supercritical water?." *J. Am. Chem. Soc.*, **119**, 3811–3817.

Hoffmann, M.M. and Conradi, M.S. (1998) "Are there hydrogen bonds in supercritical methanol and ethanol?." *J. Phys. Chem. B*, **102 (1)**, 263–271.

Hohenberg, P.C. and Halperin, B.I. (1977) "Theory of dynamic critical phenomena." *Rev. Mod. Phys.*, **49 (3)**, 435–479.

Holz, M., Heil, S.R., and Sacco, A. (2000) "Temperature-dependent self-diffusion coefficients of water and six selected molecular liquids for calibration in accurate ^{1}H NMR PFG measurements." *Phys. Chem. Chem. Phys.*, **2**, 4740–4742.

Horváth, I.T. and Ponce, E.C. (1991) "New valve design for high-pressure sapphire tubes for NMR measurements." *Rev. Sci. Instrum.*, **62 (4)**, 1104–1105.

Hoult, D.I. and Richards, R.E. (1975) "Critical factors in the design of sensitive high resolution nuclear magnetic resonance spectrometers." *Proc. Roy. Soc. London A*, **A344 (1638)**, 311–340.

Hoult, D.I. and Richards, R.E. (1976) "The signal-to-noise ratio of the nuclear magnetic resonance experiment." *NMR in Biomedicine: The Physical Basis*, 102–116.

Jonas, J. (1972) "Nuclear magnetic resonance measurements at high pressure." *Rev. Sci. Instrum.*, **43 (4)**, 643–649.

Jonas, J., Koziol, P., Peng, X., Reiner, C., and Campbell, D.M. (1992) "High-resolution NMR spectroscopy at high pressures." *J. Mag. Res. B*, **102**, 299-309.

Kalinichev, A.G. (1993) "Molecular dynamics and self-diffusion in supercritical water." *Ber. Bunsenges. Phys. Chem.*, **97 (7)**, 872–876.

Kalinichev, A.G. and Bass, J.D. (1997) "Hydrogen bonding in supercritical water. 2. computer simulations." *J. Phys. Chem. A*, **101**, 9720–9727.

Kawasaki, K. (1966) "Diffusion constants near the critical point for time-dependent Ising models. iii. Self-diffusion constant*." *Phy. Rev.*, **150 (1)**, 285–290.

Kawasaki, K. (1970) "Kinetic equations and time correlation functions of critical fluctuations." *Ann. Phys.*, **61**, 1–56.

Kestin, J. and Wakeham, W.A. (1988) Transport Properties of Fluids: Thermal Conductivity, Viscosity, and Diffusion Coefficient, Hemisphere Publishing Co., New York, NY.

Kiado, A. (1974) Transport Phenomena in Aqueous Solutions.

Krynicki, K., Green, C.D., and Sawyer, D.W. (1978) "Pressure and temperature dependence of self-diffusion in water." *Discuss. Far. Soc.*, **66**, 199–208.

Lamb, W.J., Hoffman, G.A., and Jonas, J. (1981) "Self-diffusion in compressed supercritical water." *J. Chem. Phys.*, **74 (12)**, 6875–6880.

Lamb, W.J. and Jonas, J. (1981) "NMR study of compressed supercritical water." *J. Chem. Phys.*, **74 (2)**, 913–921.

Landau, L.D. (1966) *Electrodynamics of continuous media*, Pergamon, New York, NY.

Landau, L.D. and Lifshitz, E.M. (1987) *Fluid Mechanics*, Pergamon, 2nd ed., New York, NY.

Leffler, J. and Cullinan, H.T. (1970) "Variation of liquid diffusion coefficients with composition. binary systems." *Ind. Eng. Chem. Fundam.*, **9 (1)**, 84–87.

Levelt-Sengers, J.M.H. and Givens, J.A. (1993) "Critical-behavior of ionic fluids." *Mol. Phys.*, **80 (4)**, 899–913.

Liu, H. and Macedo, E.A. (1995) "Accurate correlations for the self-diffusion coefficients of CO_2, CH_4, C_2H_4, H_2O, and D_2O over wide ranges of temperature and pressure." *J. Supercritical Fluids*, **8**, 310–317.

Liu, H., Silva, C.M., and Macedo, E.A. (1997) "New equations for tracer diffusion coefficients of solutes in supercriticial and liquid solvents based on the Lennard-Jones fluid model." *Ind. Eng. Chem. Res.*, **36**, 246–252.

Liu, H., Silva, C.M., and Macedo, E.A. (1998) "Unified approach to the self-diffusion coefficients of dense fluids over wide ranges of temperature and pressure-hard-sphere, square-well, Lennard-Jones and real substances." *Chem. Eng. Sci.*, **53 (13)**, 2403–2422.

Lusis, M.A. and Ratcliff, G.A. (1968) "Diffusion in binary liquid mixtures at infinite dilution." *Can. J. Chem. Eng.*, **46**, 385–387.

Luettmer-Strathmann, J. (2002) "Thermodiffusion in the critical region." *Thermal Nonequilibrium Phenomena in Fluid Mixtures*, W. Koehler and S. Wiegand editors, Springer-Verlag, Heidelberg.

Mansfield, P. (1988) "Imaging by nuclear magnetic resonance." *J. Phys. E*, **21**, 18–30.

Matenaar, U., Richter, J. and Zeidler, M.D. (1996) "High-temperature—high-pressure NMR probe for self-diffusion measurements in molten salts." *J. Mag. Res. A*, **122**, 72–75.

Mathur, G.P. and Thodos, G. (1965) "The self-diffusivity of substances in the gaseous and liquid state." *AIChE J.*, **11 (4)**, 613–616.

Matubayasi, N., Wakai, C. and Nakahara, M. (1997a) "NMR study of water structure in super- and subcritical conditions." *Phys. Rev. Lett.*, **78 (13)**, 2573–2576.

Matubayasi, N., Wakai, C. and Nakahara, M. (1997b) "Structural study of supercritical water." I. nuclear magnetic resonance spectroscopy." *J. Chem. Phys.*, **107 (21)**, 9133–9140.

McLennan, J.A. (1989) "Boltzmann-equation for a dissociating gas." *J. Stat. Phys.*, **57 (3-4)**, 887–905.

Monchick, L. and Mason, E.A. (1961) "Transport properties of polar gases." *J. Chem. Phys.*, **35 (3)**, 1676–1697.

Neufield, P.D., Janzen, A.R., and Aziz, R.A. (1972) "Empirical equations to calculate 16 of the transport collision integrals $\Omega l,s*$ for the Lennard-Jones (12-6) potential." *J. Chem. Phys.*, **57 (3)**, 1100–1102.

NIST (1996) NIST standard reference database 10–steam tables, Boulder, CO.

Ohmori, T. and Kimura, Y. (2003) "Translational diffusion of hydrophobic solutes in supercritical water studied by molecular dynamics simulations." *J. Chem. Phys.*, **119 (14)**, 7328–7334.

Oosting, P.H. and Trappenjers, N.J. (1971) "Proton-spin-lattice relaxations and self-diffusion in methanes III. interpretation of proton-spin-lattice relaxation experiments." *Physica*, **51**, 395–417.

Pitzer, K.S. (1995) "Ionic fluids: near-critical and related properties." *J. Phys. Chem.*, **99**, 13070–13077.

Poling, B.E., Prausnitz, J.M., and O'Connell, J.P. (2001) " *The Properties of Gases and Liquids*,McGraw-Hill, 5th ed., New York, NY.

Price, W.S. and Kuchel, P.W. (1991) "Effect of nonrectangular field gradient pulses in the Stejskal and Tanner (diffusion) "pulse sequence." *J. Mag. Reson.*, **94**, 133–139.

Price, W.S., Hayamizu, K., Ide, H., and Arata, Y. (1999) "Strategies for diagnosing and alleviating artifactual attenuation associated with large gradient pulses in PGSE NMR diffusion measurements." *J. Mag. Reson.*, **139**, 205–212.

Purcell, E.M., Torrey, H.C., and Pound, R.V. (1946) "Resonance absorption by nuclear magnetic moments in a solid." *Phys. Rev.*, **69**, 37–38.

Reddy, K.A. and Doraiswamy, L.K. (1967) "Estimating liquid diffusivity." *Ind. Eng. Chem. Fundam.*, **6 (1)**, 77–79.

Roe, D.C. (1985) "Sapphire NMR tube for high-resolution studies at elevated pressure." *J. Mag. Res.*, **63**, 388–391.

Sakonidou, E.P., van den Berg, H.R., ten Seldam, C.A., and Sengers, J.V. (1998) "The thermal conductivity of an equimolar methane-ethane mixture in the critical region." *J. Chem. Phys.*, **109 (2)**, 717–736.

Sengers, J.V. (1985) "Transport properties of fluids near critical points." *Int. J. Thermophys.*, **6 (3)**, 203–232.

Sengers, J.V. (1994) "Effects of critical fluctuations on the thermodynamic and transport properties of supercritical fluids." *Supercrit. Fluids*, 231–271.

Sengers, J.V. (2003) Private communication.

Sengers, J.V. and Keyes, P.H. (1971) "Scaling of the thermal conductivity near the gas-liquid critical point." *Phys. Rev. Lett.*, **26 (2)**, 70–73.

Shenai, V.M., Hamilton, B.L., and Matthews, M.A. (1993) "Diffusion in liquid and supercritical fluid mixtures." *ACS Symp. Ser., No. 514*, 92–103.

Shimokawa, S. and Yamada, E. (1983) "A ^{13}C NMR probe for high-temperature and high-pressure experiments." *J. Mag. Res.*, **51**, 103–109.

Silva, C.M., Liu, H., and Macedo, E.A. (1998) "Models for self-diffusion coefficients of dense fluids, including hydrogen-bonding substances." *Chem. Eng. Sci.*, **53 (13)**, 2423–2429.

Simpson, J. and Weiner, E. (1989) *Oxford English Dictionary*, Clarendon Press, 2nd ed., New York, NY.

Speedy, R.J. (1987) "Diffusion in the hard sphere fluid." *Mol. Phys.*, **62**, 509.

Stejskal, E.O. and Tanner, J.E. (1965) "Spin diffusion measurements: spin echoes in the presence of a time-dependent field gradient." *J. Chem. Phys.*, **42 (1)**, 288–292.

Stokes, G.G. (1903) *Mathematical and Physical Papers*, 3, Cambridge University Press.

Sun, C.K.J. and Chen, S.H. (1985a) "Tracer diffusion of aromatic hydrocarbons in *n*-hexane up to the supercritical region." *Chem. Eng. Sci.*, **40 (12)**, 2217–2224.

Sun, C.K.J. and Chen, S.H. (1985b) "Tracer diffusion of aromatic hydrocarbons in liquid cyclohexane up to its critical temperature." *AIChE J.*, **31 (9)**, 1510–1515.

Sun, C.K.J. and Chen, S.H. (1986) "Tracer diffusion in dense ethanol: a generalized correlation for nonpolar and hydrogen-bonded solvents." *AIChE J.*, **32**, 1367.

Sun, C.K.J. and Chen, S.H. (1987) "Tracer diffusion in dense methanol and 2-propanol up to supercritical region: understanding of solvent molecular association and development of an empirical correlation." *Ind. Eng. Chem. Res.*, **26**, 815.

Swinney, H.L. and Henry, D.L. (1973) "Dynamics of fluids near the critical point: decay rate of order-parameter fluctuations." *Phys. Rev. A*, **8 (5)**, 2586–2617.

Takahashi, S. (1974) "Preparation of a generalized chart for the diffusion coefficients of gases at high pressures." *J. Chem. Eng. Jpn.*, **7 (6)**, 417–420.

Tham, M.K. and Gubbins, K.E. (1971) "Kinetic theory of multicomponent dense fluid mixtures of rigid spheres." *J. Chem. Phys.*, **55 (1)**, 268–279.

Tyn, M.T. and Calus, W.F. (1975a) "Diffusion coefficients in dilute binary liquid mixtures." *J. Chem. Eng. Data*, **20 (1)**, 106–109.

Tyn, M.T. and Calus, W.F. (1975b) "Temperature and concentration dependence of mutual diffusion coefficients of some binary liquid systems." *J. Chem. Eng. Data*, **20 (3)**, 310–316.

Tyrell, H.J.V. and Harris, K.R. (1984) *Diffusion in Liquids-A Theoretical and Experimental Study*, Butterworth, London.

Van Geet, A.L. and Adamson, A.W. (1964) "Diffusion in liquid hydrocarbon mixtures." *J. Phys. Chem.*, **64 (2)**, 238–246.

Vignes, A. (1966) "Diffusion in binary solutions. variation of diffusion coefficient with composition." *Ind. Eng. Chem. Fundam.*, **5 (2)**, 189–199.

Wilbur, D.J., DeFreis, T., and Jonas, J. (1976) "Self-diffusion in compressed liquid heavy water." *J. Chem. Phys.*, **65 (5)**, 1783–1786.

Wilkinson, R.A., Zimmerli, G.A., Hao, H., Moldover, M.R., Berg, R.F., Johnson, W.L., Ferrell, R.A., and Gammon, R.W. (1998) "Equilibration near the liquid-vapor critical point in microgravity." *Phys. Rev. E*, **57 (1)**, 436–448.

Weingärtner, H. (1982) "Self diffusion in liquid water. a reassessment." *Zeitschrift für Physikalische Chemie Neue Folge*, **132**, 129–149.

Wilke, C.R. and Chang, P. (1955) "Correlations of diffusion coefficients in dilute solutions." *AIChE J.*, **1**, 264–270.

Wilke, C.R. and Lee, C.Y. (1955) "Estimation of diffusion coefficients for gases and vapors." *Ind. Eng. Chem.*, **47 (6)**, 1253–1257.

Yonker, C.R., Zemanian, T.S., Wallen, S.L., Linehan, J.C. and Franz, J.A. (1995) "A new apparatus for the convenient measurement of NMR spectra in high-pressure liquids." *J. Mag. Res. A*, **113**, 102–107.

II.2. Objectives and Approach

SCW binary diffusivity data are scarce and difficult to obtain due to the limited ability to make diffusivity measurements at harsh SCWO process conditions. NMR is a technique that has been successfully used to accurately measure diffusivities and has been used at SCWO conditions to measure pure supercritical water properties such as chemical shift, self-diffusivity, and relaxation effects (Lamb *et al.*, 1981; Lamb and Jonas, 1981; Hoffmann and Conradi, 1997). Furthermore, up to now, SCW NMR measurement samples are contained in closed vessels so changing sample composition is rather difficult and time consuming. Some designs have incorporated a piston so that pressure, and hence, density could be altered while temperature could be easily adjusted, but none have been capable of flowing new sample into the sample region in order to deliver new sample or, possibly, examine molecular motion such as molecular velocity.

The first objective for this part of the dissertation is to design and construct a SCW NMR apparatus capable of making SCW measurements under flowing conditions for the reasons described above. Validating apparatus performance and measurement capacity will be achieved by confirming SCW self-diffusivity data of Lamb *et al.* (1981). A second objective is to use this system to measure diffusivities of a binary system in order to generate additional binary diffusivity data and consists of tracer diffusivity experiments for three different concentrations of a model aqueous mixture, namely acetone(1)-water(2). The third objective is to use the collected data for the development and validation of diffusivity models. Kinetic-gas and hydrodynamic theories will be tested in order to determine their accuracy with the collected and previously published data. The following three sections address each of these objectives.

II.2.1 References

Hoffmann, M.M. and Conradi, M.S. (1997) "Nuclear magnetic resonance probe for supercritical water and aqueous solutions." *Rev. Sci. Instrum.*, **68 (1)**, 159–164.

Lamb, W.J., Hoffman, G.A., and Jonas, J. (1981) "Self-diffusion in compressed supercritical water." *J. Chem. Phys.*, **74 (12)**, 6875–6880.

Lamb, W.J. and Jonas, J. (1981) "NMR study of compressed supercritical water." *J. Chem. Phys.*, **74 (2)**, 913–921.

II.3. SCW NMR Apparatus Design and Fabrication

The SCW NMR apparatus is composed of several major components which will be described in this section. The NMR experimental details will be discussed prior to the introduction of the NMR probe assembly. The probe assembly discussion will follow. The focus of this section then shifts to its subsystems such as thermal and high temperature features, pressure and flow capabilities, measurements, controls, NMR circuitry, and safety features.

II.3.1 Pulsed Gradient Spin Echo Technique

The PGSE experiment employed here used eight dummy scans, CYCLOPS phase cycling, and signal averaging (depending on the signal strength and by repeating the phase cycling four to six times for a total of sixteen to twenty-four scans) (Hoult and Richards, 1975). Maximum gradient strengths, G_{max}, were determined at each experimental condition in order to achieve sufficient attenuation of the multi-peak spectra, while the gradient strength was varied from near zero, G_{min}, (smallest signal attenuation) to the maximum value, G_{max} (greatest signal attenuation) in approximately twelve steps. The sequence used is illustrated in Figure 82. The gradient was calibrated using water at atmospheric conditions (25°C and 1 atmosphere) where the water self-diffusivity is $(2.299 \pm 0.005) \times 10^{-5}$ cm^2/s (Weingärtner, 1982; Holz et al., 2000). An example of the data processing is shown in Figure 83 where the stacked plot clearly shows increasing attenuation from each of the scans, while Figure 84 and Figure 85 show the diffusivity-calculation results of for acetone and water, respectively.
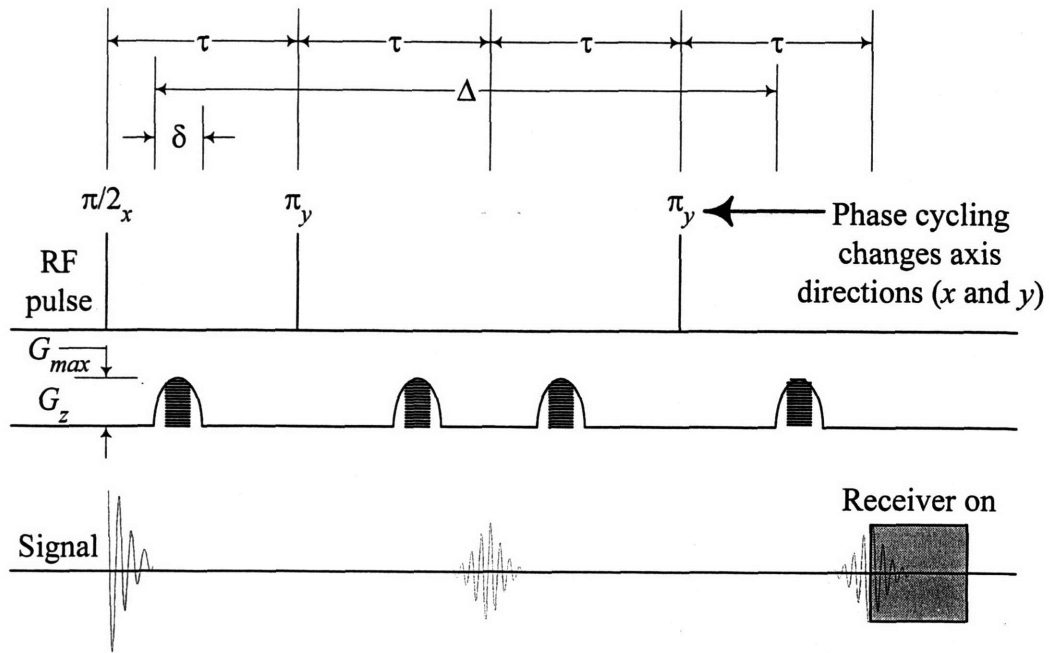
Figure 82. PGSE sequence used for the SCW NMR diffusivity experiments.
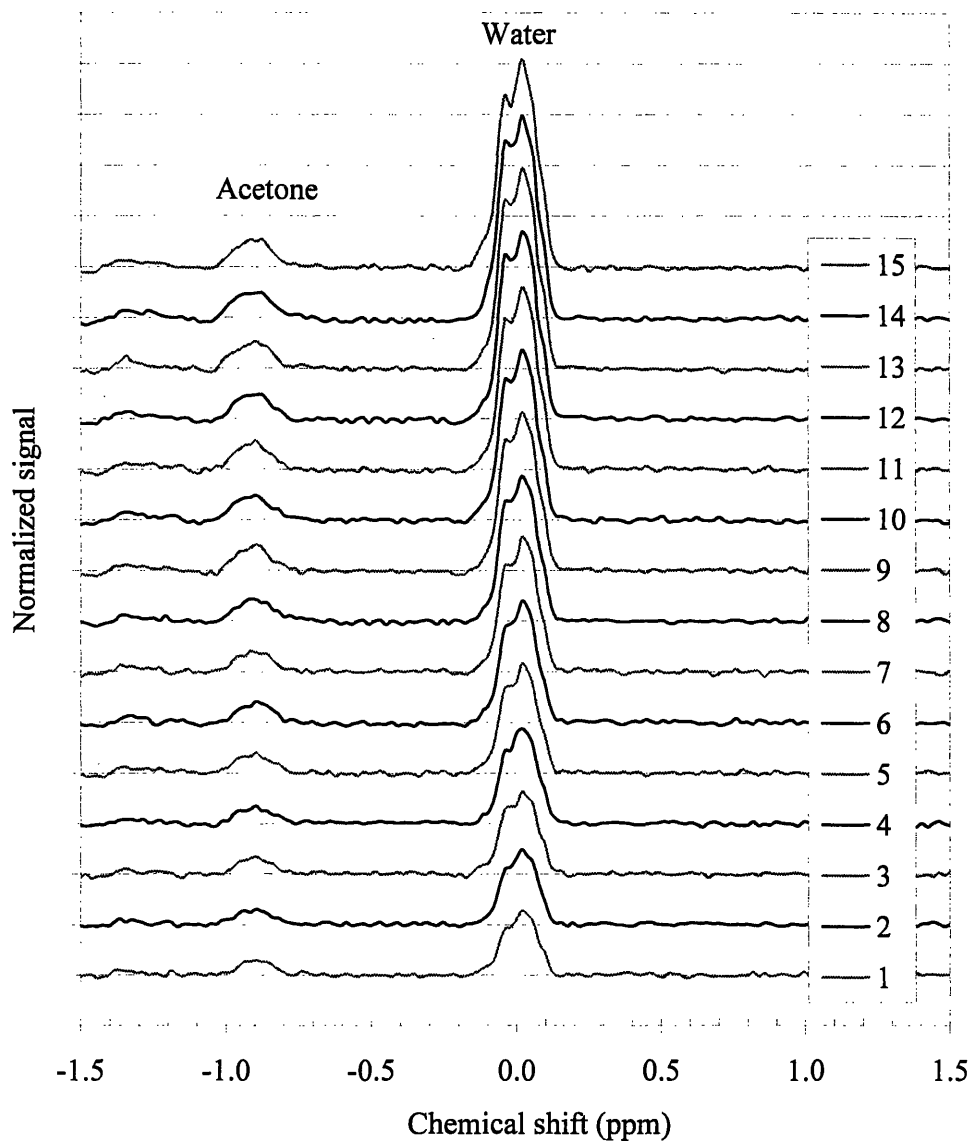
Figure 83. Stacked plot example of a binary mixture showing two separate chemically shifted peaks (left peak is acetone while water is on the right). The area of each peak for each of the varying-gradient-strength scans is determined and is then used to calculate the tracer diffusivity for acetone and for water. The conditions for this experiment are 400°C, 0.10 g/cm^3, and 40 wt.%$_1$ acetone(1)-water(2).

```
f:/nmr/2001_nmr/pgsevg2/12/ser117        Δ = 16025. μs
{10, 13, 2002}    D = 0.001537856 ± 0.00009878 cm²/sec
Peak: Ace   PHO = 243      G = 1.57 G/cm
```

$$2/\pi(g\delta\gamma)^2(4\Delta-\delta)$$
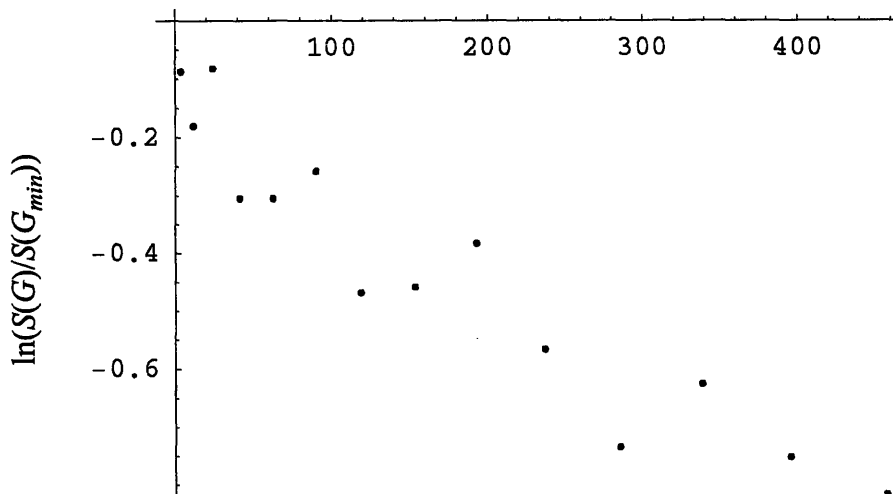
Figure 84. Acetone(1) tracer-diffusivity plot for the data shown in Figure 83 $(-m = D_1 = (154 \pm 10) \times 10^{-5} \text{ cm}^2/\text{s}$ where 10 is the estimated standard deviation). The conditions for this experiment are 400°C, 0.10 g/cm^3, and 40 wt.%$_1$ acetone(1)-water(2).


```
f:/nmr/2001_nmr/pgsevg2/12/ser117        Δ = 16025. μs
{5, 26, 2002}    D = 0.002490219 ± 0.0000367 cm²/sec
Peak: H2O   PHO = 243      G = 1.57 G/cm
```

$$2/\pi(g\delta\gamma)^2(4\Delta-\delta)$$
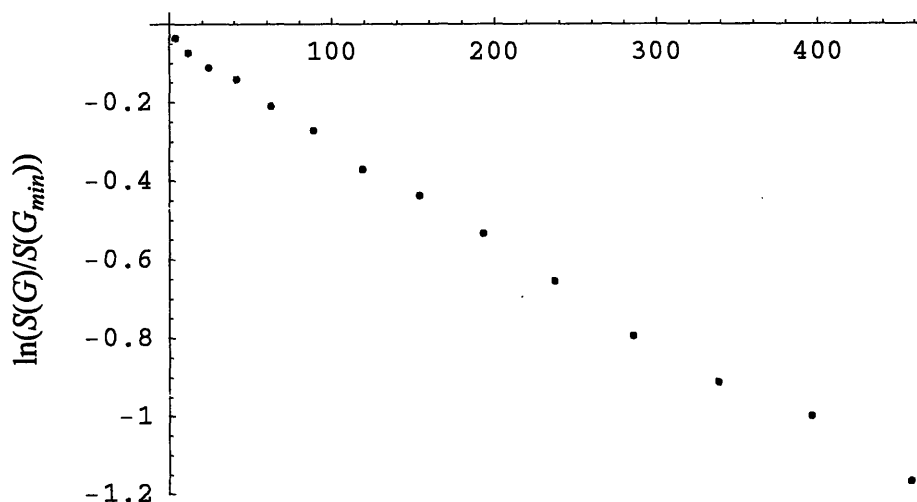
Figure 85. Water(2) tracer-diffusivity plot for the data shown in Figure 83 $(-m = D_2 = (249 \pm 4) \times 10^{-5} \text{ cm}^2/\text{s}$ where 4 is the estimated standard deviation). The conditions for this experiment are 400°C, 0.10 g/cm^3, and 40 wt.%$_1$ acetone(1)-water(2).

II.3.2 NMR Probe Assembly

II.3.2.1 High Temperature Features

The approaches used by other researchers have resulted in either sample tubes that are used in standard commercial NMR probes or thick-walled metallic pressure vessels that can be pressure balanced with thin-walled sample tubes (Hoffmann and Conradi, 1997; Matubayasi *et al.*, 1997). Both cases could be adapted for flow at high temperatures, but none have published such data. The design by Matubayasi and coworkers (1997) offers several features that were transferred to this researcher's SCW NMR probe including the use of a vacuum Dewar and hot gas to maintain a high temperature. The hot gas is a safety concern since this gas has to be cooled. The hot gas was designed to mix downstream with cooling gas, which is used to keep the magnet bore and other temperature-sensitive components cool. Early tests with Dewars showed that a significant radial temperature ($\Delta T = 10°C$ at 350°C) could exist inside the Dewar if the outside temperature were ambient when the Dewar vacuum was not actively pumped. From these tests, the Dewar was modified to be actively pumped during high temperature exposure in order to minimize heat loss. In order to minimize radiation heat losses, the surface emissivity was lowered by silver coating the internal Dewar surfaces. The final design of the Dewar that was prepared by H.S. Martin, Inc. (NJ) and used in this research is shown in Figure 86.

To further reduce temperature variation near the sample tube, the hot gas flowing in the Dewar was forced to turn around in an annular section in order to behave like a counter-current heat exchanger. As a result, the Dewar inner wall was heated with recycled hot gas flowing away from the sample, and temperature gradients were minimized near the sample region (See Figure 87). Typical air-flow rates were 150 SCFH (limited by the building compressor) and typical annular exhaust temperatures were 400°C. The Dewar outer wall registered 35°C for a 520°C inlet-hot-air temperature and a 500°C sweet-spot temperature. Over approximately 40 cm of the Dewar, this 20°C difference yields an approximate axial temperature gradient of $-2°C/cm$ which is close to the $-3 \pm 3°C/cm$ that was estimated from temperature readings of thermocouples mounted in known axial positions on the NMR sample vessel.

A vacuum turbo-pump was used to evacuate the Dewar before and during all experiments. Temperature monitoring confirmed that the Dewar functioned as an insulator since

500°C/cm radial-temperature gradients were often seen across the Dewar double wall. Since the vacuum equipment had to be placed outside the shielded magnet room, ¼" ID copper tubing joined the vacuum pump to the valve mounted on the NMR probe assembly, which was connected to a flexible 321 stainless-steel vacuum tube (Swagelok 321-4-x-24-b2). The flexible tubing was connected directly to the Dewar pump port. Isofrax™ 1260C (Unifrax) thermal insulation was used to provide additional thermal resistance in areas where airflow was not needed and in any gaps. Pieces of one-inch thick blankets were cut and molded where necessary. 40 CFM of 20°C cooling air was provided by a R4110-2 regenerative blower (Gast Manufacturing Inc., MI) and a counter-current air-water heat exchanger (HF-202-HY-1P, Young Radiator Co., OH). Additional cooling-flow details will be provided when the NMR electrical circuit is discussed (see Section II.3.2.5).

Pump port   7.4 cm OD & 7.0 cm ID

5.7 cm OD & 5.4 cm ID

Length = 44.5 cm
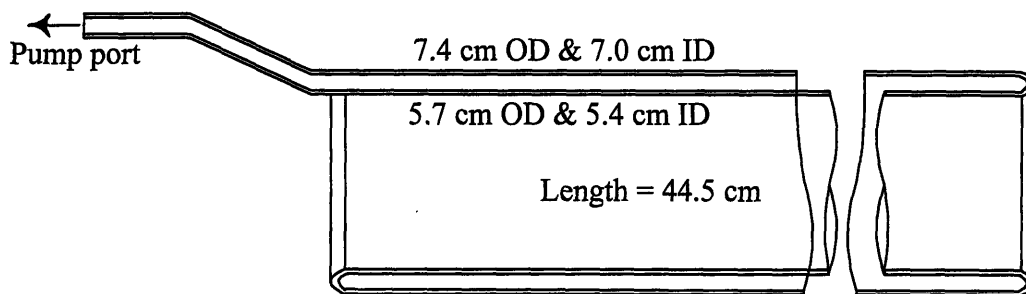
Figure 86. Rendering of the silver-coated quartz dual-walled Dewar with a 3/8" pumping port in order to actively pump and improve thermal-insulation properties.

Top cross-section of the 152 cm long magnet and shim-set bore

20 cm

cool air

vacuum
hot air
hot air
Dewar
cool air
cool air

a)

Bottom cross-section of the 152 cm long magnet and shim-set bore

cool air

10 cm

vacuum
hot air
hot air
Dewar
cool air
cool air
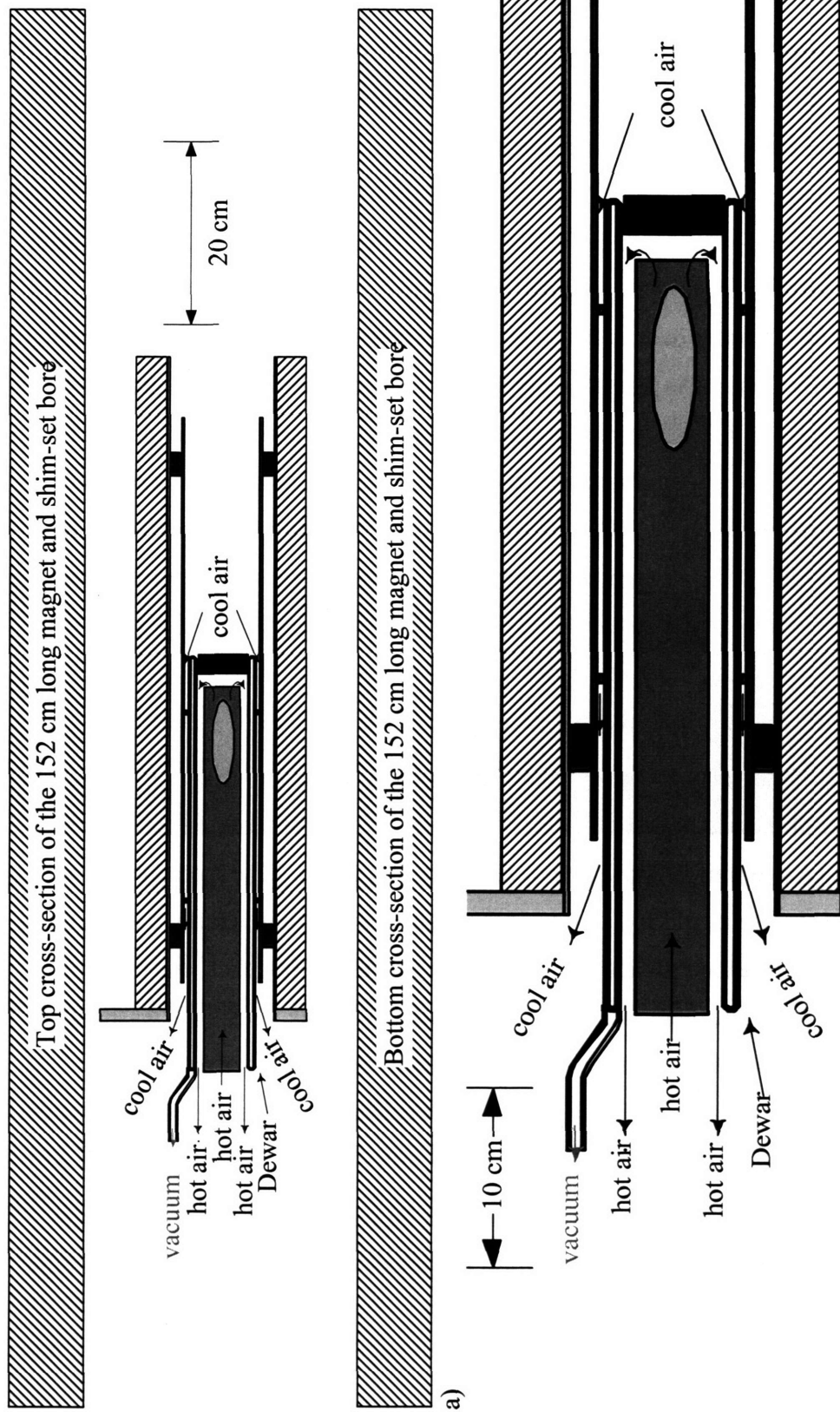
b)

Figure 87. Top picture (a) shows the Dewar placed within the gradient set lined with a fiber-reinforced polymer (FRP) cylinder that house and supports all SCW NMR components and shields the gradient set. Bottom close-up (b) shows the flow path for the hot air in the insulated (not shown) copper-foil cylinder (0.020" thick, 4 cm OD), for the counter-current hot air between the copper and Dewar, and for the cooling air between the Dewar and a second FRP tube shown with dark-grey support feet. The light-grey oval represents the magnet sweet spot and the sample vessel location.

245

II.3.2.2 SCW Pressure and Flow Features

II.3.2.2.1 High temperature and high pressure sample vessel

With the sample vessel heated, attention can now turn to pressurizing and flowing the sample. Because SCW mixtures are well known to be chemically and mechanically corrosive (*e.g.*, chemical attack and pitting), the choice of materials to house SCW is limited, but well documented (Downey *et al.*, 1995; Cline, 2000). Inconel alloy 625 and Hastelloy alloy C276 are the materials of choice for non-chlorinated SCWO systems. However, metal will interfere with RF energy so it cannot be used to store the sample fluid in the vicinity of the RF coil. Furthermore, magnetic metals must be avoided in order to prevent these materials from being accelerated and potentially flying. As a result, only high nickel and stainless-steel alloys are considered. For high temperature, high pressure applications, the best non-metallic option is sapphire, which is single crystal aluminum oxide. Saphikon, Inc. (Milford, NH) is a reputable supplier of custom-made sapphire tubes (Horvath and Ponce, 1991). However, their tubes have been used in the past for high pressure studies, but not for high pressure and high temperature studies. The temperature must remain low because epoxy adhesives are often used to join the sapphire tube to any other surface, and epoxies have a temperature limit of approximately 00°C. A new approach is needed to seal sapphire with metal at high temperatures and pressures.

High pressure and high temperature sapphire sealing is rather difficult, but not impossible, and in the MIT supercritical fluids research group, it is quite common to use sapphire-to-metal seals (Armellini, 1993; Dipippo, 1998; Hodes, 1998). One method used to seal sapphire windows is to use a gold foil O-ring at the high pressure fluid interface when these windows are tightened in a threaded socket-gland (nut) arrangement. However, due to thermal expansion coefficient differences, there is a tendency for the seal to leak. Bellevue washers placed between the gland and window are now used since their angled surface provides additional compression force and compensates for thermal expansion effects that may lessen the force holding the seal.

Using this type of sealing technique would not work on typical closed-ended sapphire tubes since there is not a sealing surface. The solution is the world's first flanged sapphire tube
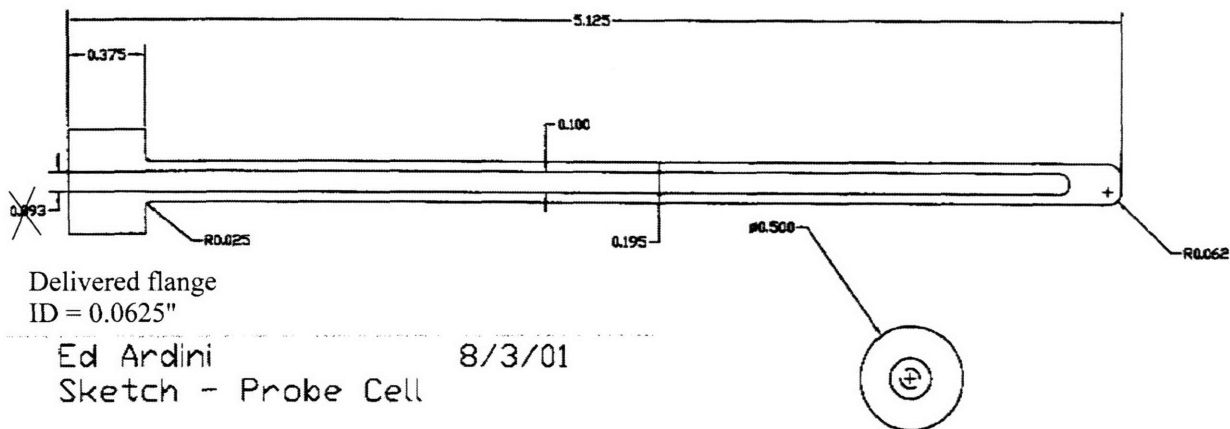
Figure 88. Saphikon print (in inches) for the flanged, closed-ended SCW NMR sample tube.
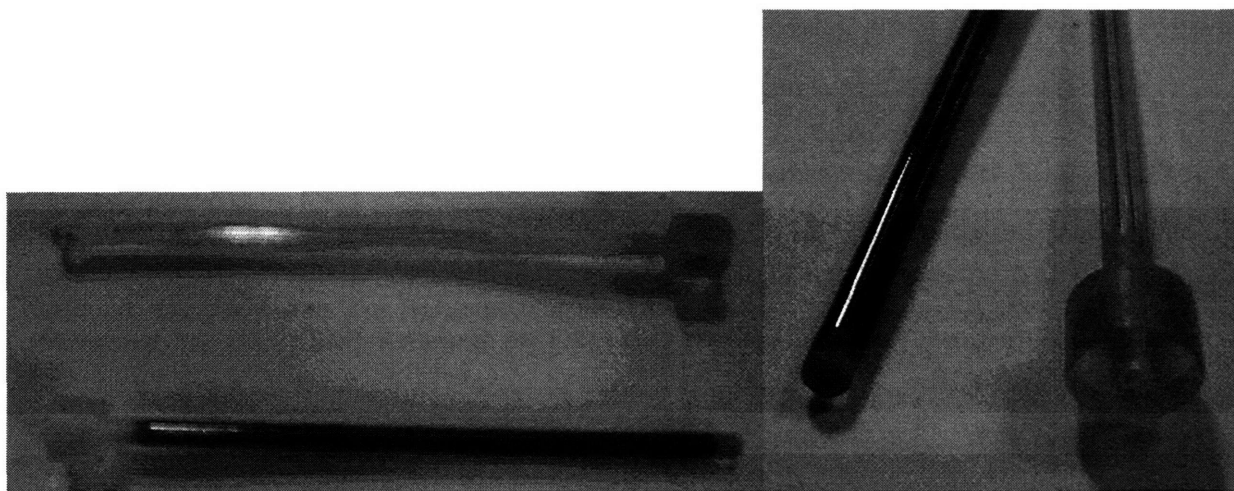
Figure 89. Pictures of the Saphikon flanged, closed-ended SCW NMR sample tubes.

for use in high pressure, high temperature SCW NMR studies. Saphikon Inc. was able to provide flanged sapphire tubes as drawn in Figure 88 and shown in Figure 89.

The tube was designed to avoid metal and RF interaction and to avoid bounded diffusion. Using a 5" (12.7 cm) length would ensure that large metal fittings would not interfere with the NMR RF energy. Bounded diffusion is a concern for large diffusivities and occurs when a diffusing molecule impacts a surface instead of another molecule or when the spin magnetization is weakened by excessive spin dephasing. The resulting diffusivity is artificially skewed, unless further experiments are performed to compensate for bounded diffusion. Typically, in a bounded-diffusion environment, the measured diffusivity often reaches a limit, *e.g.*, due to

repeated impacts with vessel walls. Bounded diffusion requires knowledge of the distance that a molecular could randomly travel during the NMR experiment along with the intrinsic length scale that a spin may travel during one revolution (2π radians) of precession. Assuming a diffusivity of 0.02 cm^2/s, an experimental scan time of 100 ms, the average RMS distance can be estimated

$$x_{RMS} = \sqrt{2Dt} = 0.063\,\text{cm} = 0.025"$$ (174)

Wayne and Cotts (1966) derived a dephasing bounded-diffusion relationship in terms of the gradient strength and the length scale so that precession-related bounded diffusion which artificially increases the spin-magnetization attenuation and inflates the calculated diffusivity can be avoided

$$\frac{\gamma Gl^3}{D} \leq 1 \text{ for bounded diffusion}$$ (175)

Using a 0.5 G/cm gradient strength, the critical length for bounded diffusion is 0.021 cm = 0.008". Using the inner diameter of the sapphire tube (0.1" (0.254 cm)), $\gamma Gl^3/D = 1700$, which is three orders of magnitude larger than the bounded-diffusion criterion. For this reason and due to the fact that diffusion is monitored axially (not radially), bounded diffusion is not expected to occur for the SCW NMR experiments.

For the probe used in this study, the sample tube is required to interface with a standard High Pressure Equipment Co. (HiP, Erie, PA) Hastelloy C276 fitting. Purchased fittings and hardware were altered and machined in order to mate with the sapphire sample tube. One end of a Hastelloy C276 60-21HF6 connector was machined and polished in order to have a scratch-free surface that could maintain a high pressure, high temperature seal. The other end was left intact so that a standard HiP connection could be made. A drawing of the socket and a picture of the modified parts, along with a Bellevue washer used to produce the high temperature, high pressure seal, are shown in Figure 90. When a gold foil washer is used to cushion the large area between the sapphire and fitting sealing surfaces, microscopic crevices or holes that could form a leak path are filled, and 300 bar pressures can be reached. Four stacked Inconel Bellevue washers (Key Bellevilles Inc.) are also used in order to provide sufficient sealing force at elevated temperatures. Without completely compressing the washers, a room temperature torque

of 120 inch-lbs (13.6 N-m) was sufficient to maintain 300 bar seals at 400°C. If the washers are ever fully compressed, then they become permanently deformed and cannot be used again.
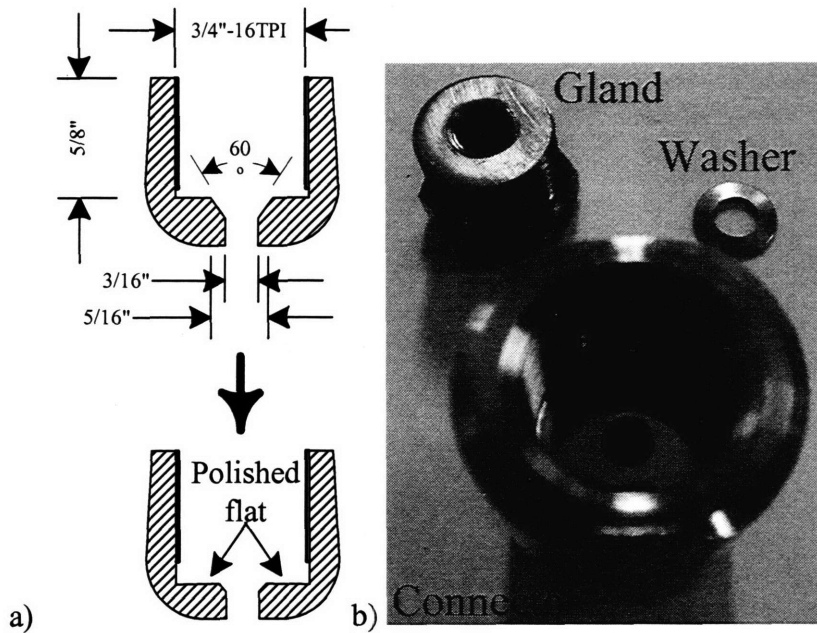
Figure 90. (a) Drawing of HiP socket before and after machining and (b) Pictures of the modified connector with the polished sealing surface (mirror-like), the gland with its face flattened, and one of the four Bellevue washers used together to maintain the seal.

Given the success reported in the literature, C-seals were considered as a sealing method since an increased pressure-differential increases the force between the seal and the other sealing faces (Jonas, 1972; DeFries and Jonas, 1979). Silver-plated Inconel 600 C-seals from Garlock Helicoflex (U5214-00500 SEB) were used to seal the flanged sample tube and a modified HiP connector, but had difficulty maintaining pressure at high temperatures. The failure is based on the creation of a second seal between the flange and connector surfaces. As a result, the C-seal pressure-differential lessened as pressure increased between the C-seal and the second seal. Eventually, the second seal would leak to the atmosphere and the primary C-seal pressure differential would momentarily increase and reseal the C-seal preventing any system pressure drop. Unfortunately, this leak cycle would repeat so this method was shelved in favor of the previously discussed gold-film method. It should be noted that at ambient temperature, C-seals leaks were not observed up to the tested pressure of 400 bar, indicating that the C-seals were under greater stress at higher temperatures.

II.3.2.2.2 Flow and pressurization system

To be able to place fluid into the sample tube, a delivery system had to be developed. The best approach is to use a small nozzle or inner feed tube to deliver new fluid in a co-annular configuration. Not only does a tube placed near the end of the sample tube ensure that new sample is delivered, it provides a means to have macroscopic motion, *i.e.*, convection. Furthermore, the additional volume restriction from the inner tube in the non-sampled part of the sapphire tube reduces the flow induced by thermal gradients and thereby makes the end of the tube appear to be a sample bulb. A nozzle made out of 0.032" (0.8 mm) OD stainless-steel tubing was used to deliver fluid inside the sample vessel (MicroGroup, Inc., Medway, MA). Since small amounts of metal can be located near the RF coil and since metal thermocouples were already offset 1.9 cm from the coil, using a metal nozzle with a similar offset did not affect the NMR signal. In order to avoid interfering with the internal thermocouple, the nozzle had a larger offset of 2.3 cm and will be described in more detail shortly.

The delivery and return flow path must start and end on the same side of the magnet due to the annular flow design and the layout of other probe components including the RF electrical circuit. Using standard flow fittings, the inner flow can be delivered so that new sample fluid can reach the tip of the sapphire sample vessel. These fittings are kept cool, used to hold and support the sample holder in a cantilevered position, and are located in the air-mixing zone on the left side of the magnet drawing shown in Figure 91. Pictures of the NMR probe are shown in Figure 92. The 13/64" ID, 3/8" OD stainless-steel 316 tubing (HiP) that was used for fluid containment and as an arm to hold the sample tube served its purpose well by not bowing, leaking (failing), or becoming magnetic due to thermal cycling.
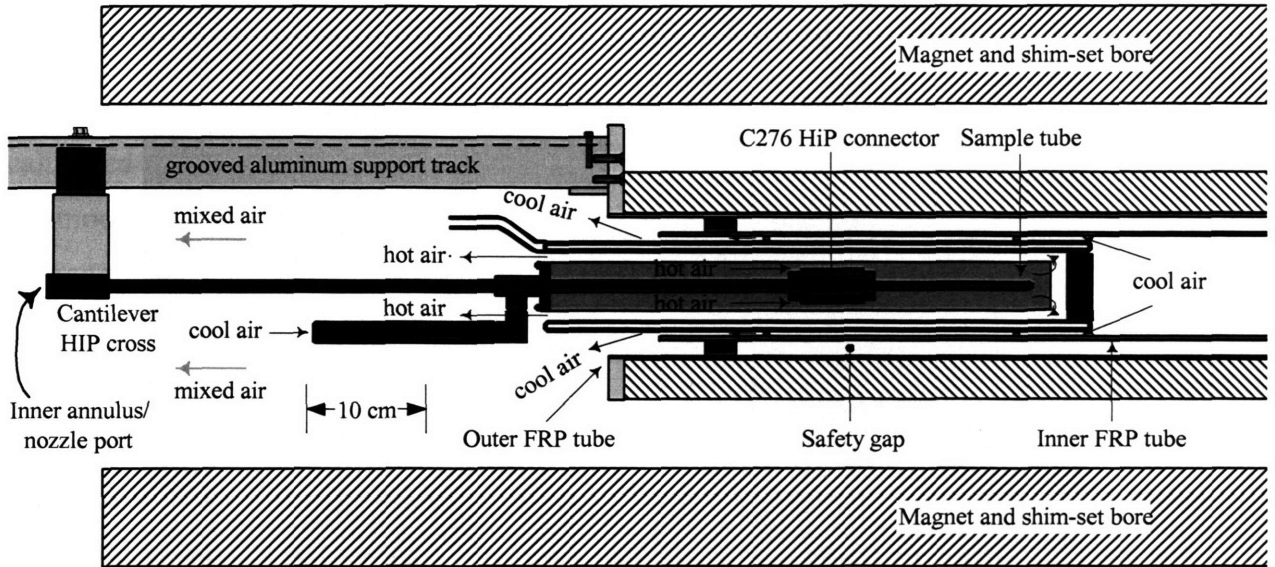
Figure 91. NMR probe visualization showing the sample tube, connector, and cantilevered feed tubing that is anchored in the exhaust region on the left. Also shown is the Ohmic heater that heats air which heats the inner annular core. This hot air is eventually mixed with ample cooling air under the aluminum support track prior to exiting the magnet bore.

251
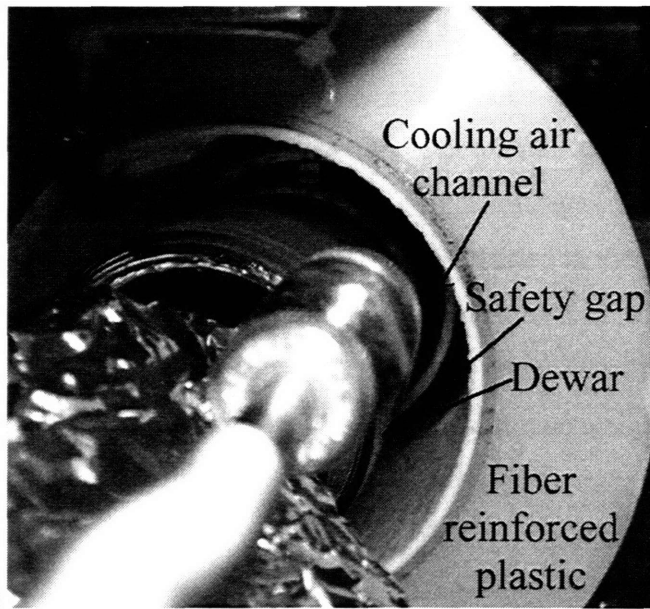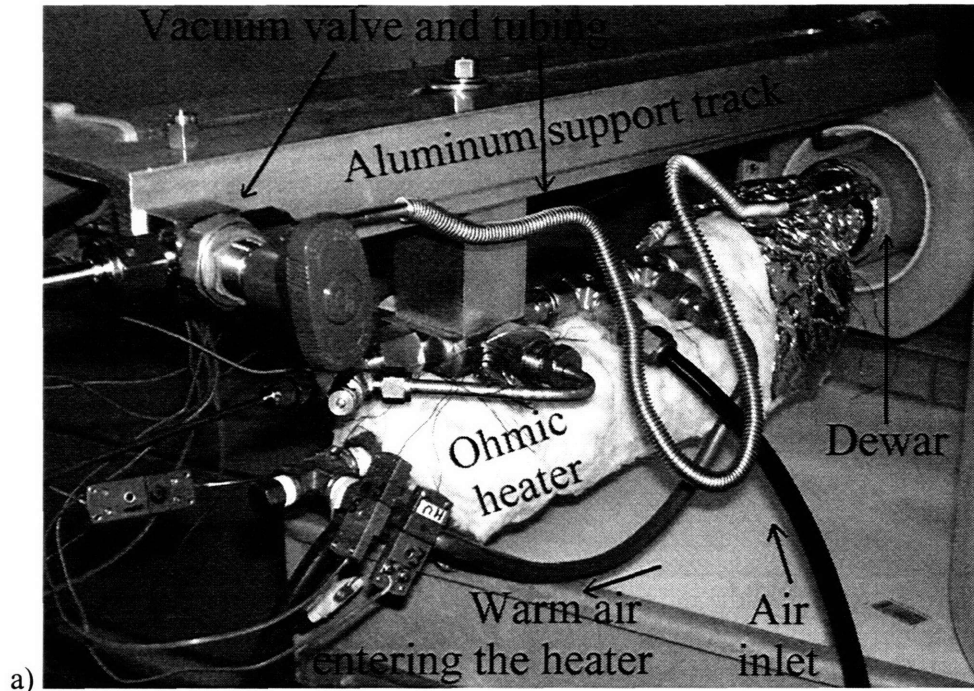
Figure 92. Pictures of the NMR probe assembly. (a) Mixing zone region which shows the Inconel 625 inner annular feed tube (0.125" (3.2 mm) OD) entering the cantilevered HiP cross fitting mounted to the aluminum support track, the insulated Ohmic heater, and the Dewar that is located in the fiber-reinforced plastic (FRP) probe body. (b) Close-up view of the outer FRP support tube, which shows a second FRP tube supporting the Dewar and forms the cooling air channel. Hot air leaves the Dewar and immediately mixes with the much larger flow of cooling air.

II.3.2.3 Process-Condition Measurement and Control Features

Temperature and pressure within the NMR probe are independently controlled using calibrated thermocouples and a pressure transducer. Ungrounded Nicrosil/Nisil Type N thermocouples (Omega Technologies Co., CT) were used to control the sample temperature and to monitor multiple locations so that axial and radial temperature gradients could be determined. They were NIST-traceable calibrated at 400°C, 450°C, 500°C, 550°C, and 600°C, and the 0.020" OD thermocouples were within 0.4°C of the actual temperatures (Refer to Omega Technologies Co. catalog for NIST calibration information). Type N thermocouples were chosen because of their low level of magnetic-field interaction since the two conductors are non-magnetic nickel-chromium alloys. The Inconel 600 sheath was left isolated from the thermocouple wires and junction (ungrounded) in order to reduce electrical noise and grounding loops. One 0.0625" (1.6 mm) OD thermocouple with an exposed junction (no sheath coverage) was permanently positioned ~4 cm past the Ohmic heater (001-10009 Convectronics), but before the air flow was diverted to the main axial section. The exposed junction was partially covered in order to minimize radiation effects from the glowing-red heater elements. The heater was powered with a Variac transformer that was manually adjusted until a temperature of interest was reached. Four-foot-long, 0.020" (0.5 mm) OD ungrounded thermocouples were strung along the inside of the flow system to near the end of the sample tube and secured to the sample-tube surface.

Early tests had two thermocouples located inside the sample tube and two located externally separated axially in order to determine the internal and external temperature gradients. When calculated at 400°C and 450°C, the −0.3°C/cm and −0.4°C/cm (± 0.3°C/cm (95% confidence interval)) temperature gradients are nearly the same since they fall within the range of the temperature measurements. Due to space limitations within the sample tube, only one thermocouple could be installed internally during the actual SCW NMR experiments. The external ones were arranged to measure radial temperature gradients since it was observed that these gradients were larger than the axial gradients. For the SCW NMR experiments, the thermocouple configuration is shown in Figure 93. By having knowledge of thermocouple locations, thermal gradients, and temperatures, the average sample volume temperature can be estimated along its variation during the NMR data collection. Temperatures were scanned and stored every two seconds (0.5 Hz) using a personal computer running Omega data acquisition
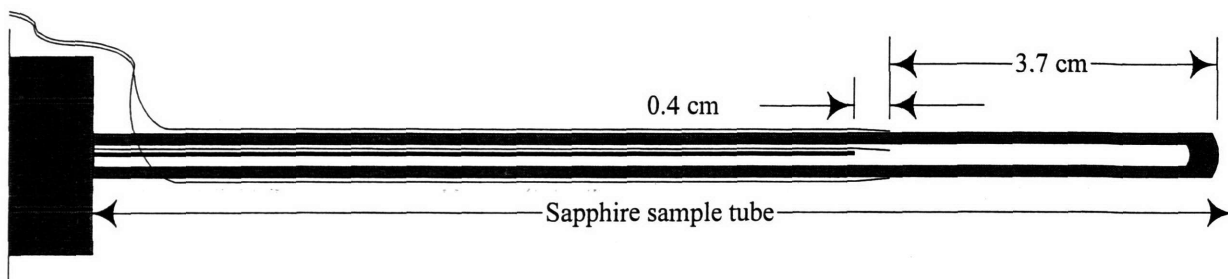
Figure 93. 0.02" OD thermocouple placement in and around the sapphire sample tube (note that the RF coil is not displayed). Two thermocouples are secured above and below the tube, while one is internal with its vertical location unknown. The inner nozzle is shown and appears as a thick solid line in the sample tube.

hardware (WB-ASC 12-bit DAQ card) and software with 60 Hz filtering enabled in order to remove house voltage signal interference. Other thermocouples were placed in the annular regions where hot and cold air were flowing, along with one in the mixed air region of Figure 92a and one mounted to the bottom outer diameter of the main FRP tube.

Pressure is monitored with a 5,000 psig (340 bar) PX945 pressure transducer (Omega Technologies Co.). Since the transducer has magnetic components, it was located near the base of the magnet where the high pressure sample feed and return lines are located. It was mounted to a wood panel that was secured to the floor and that also housed a pneumatic four-way control valve. The control valve allows automatic isolation of the NMR probe and the pumping station (Bertram Controls Corp., CT). In order to verify the pressure accuracy, the pressure was verified with transducers used by the MIT Supercritical Fluids Group. The flow diagram and layout is shown conceptually in Figure 94. A chromatography pump was used to pump and pressurize the sample. Pure water is stored in a 10 gallon (37.9 L) polypropylene tank where it is continuously deaerated with helium gas. This deaeration technique has been shown to remove oxygen from water solutions (DiNaro, 1999). A Millipore filtering unit equipped with reverse-osmosis, carbon filtering, and ultraviolet filtering provided the deionized, filtered water. A switching valve allowed the pump to siphon from a second reservoir containing the experimental aqueous organic mixture.

Following the pumping, the aqueous mixture is brought to the base of the magnet where it can be diverted back to the pumping station or flowed through the NMR probe depending on the position of the four-way control valve as shown in Figure 94. Flow enters the NMR probe
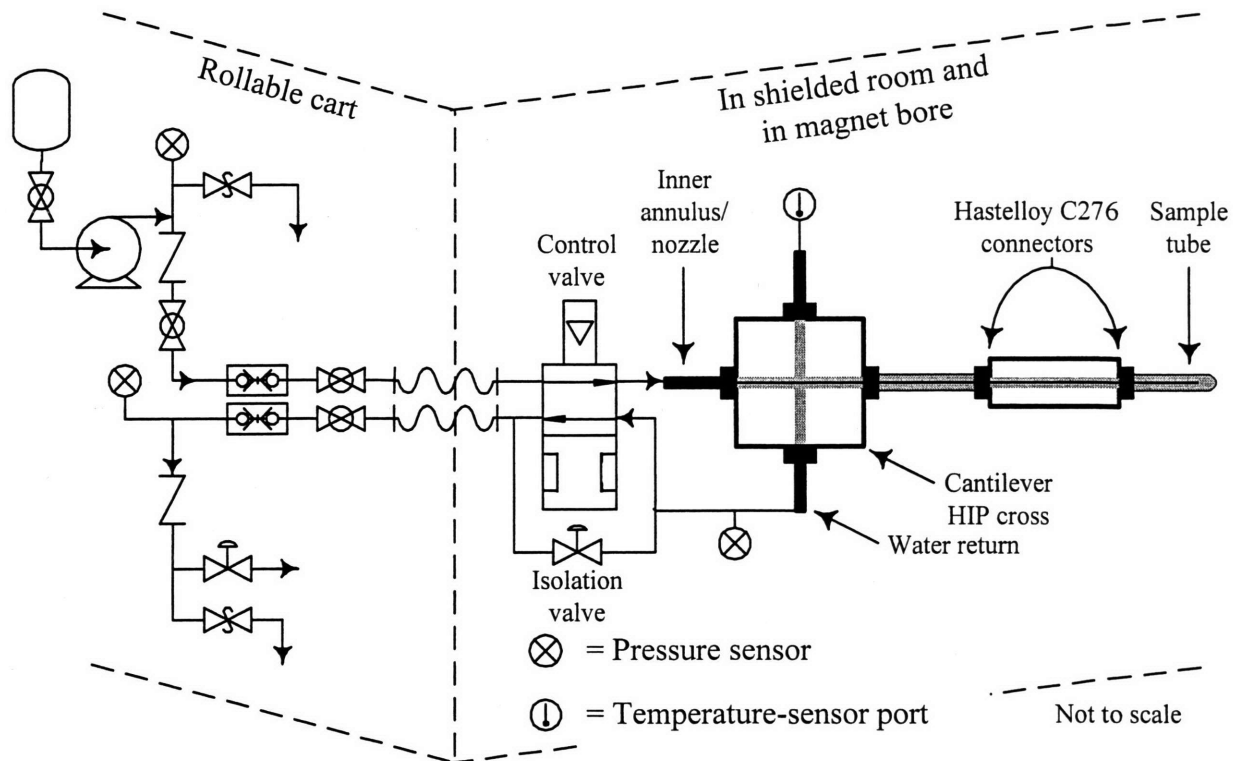
Figure 94. Flow diagram and layout of the flow system including the pumping station and hardware near and in the magnet.

system through the inner annular tube (0.0625" (1.6 mm) ID, 0.125" (3.2 mm) OD, Inconel 625). This tube is then stepped down twice to smaller diameter tubing (0.020" (0.5 mm) ID, 0.032" (0.8 mm) OD, SS316) with 0.042" (1.1 mm) ID, 0.0625" (1.6 mm) OD SS321 tubing in order for the inner-tube outer diameter to clear the sapphire-tube inner diameter. The seals between the larger and smaller tubes are achieved by crimping the tubes together. Since the seal is pressure balanced, there is essentially zero driving force for the seal to leak. After passing through the sample tube, the return flow passes counter-currently through the 3/8" (9.5 mm) OD stainless-steel 316 tubing before it is diverted back to the magnet base through the HiP cross fitting that serves as the support for the cantilever tubing. At the magnet base, the pressure is measured. When there is little or no flow, the pressure does not fluctuate. At higher flow rates when the pump strokes are more frequent and a pressure drop develops from the flow restrictions between the sample tube and pressure transducer, fluctuations can be as high as 5 bar. The flow passes through the control valve once more before it is depressurized through a manually adjusted back-pressure regulator (BP-66, Go).

Flow through the NMR probe   Flow diverted around the NMR probe
(open isolation valve keeps NMR probe pressurized)
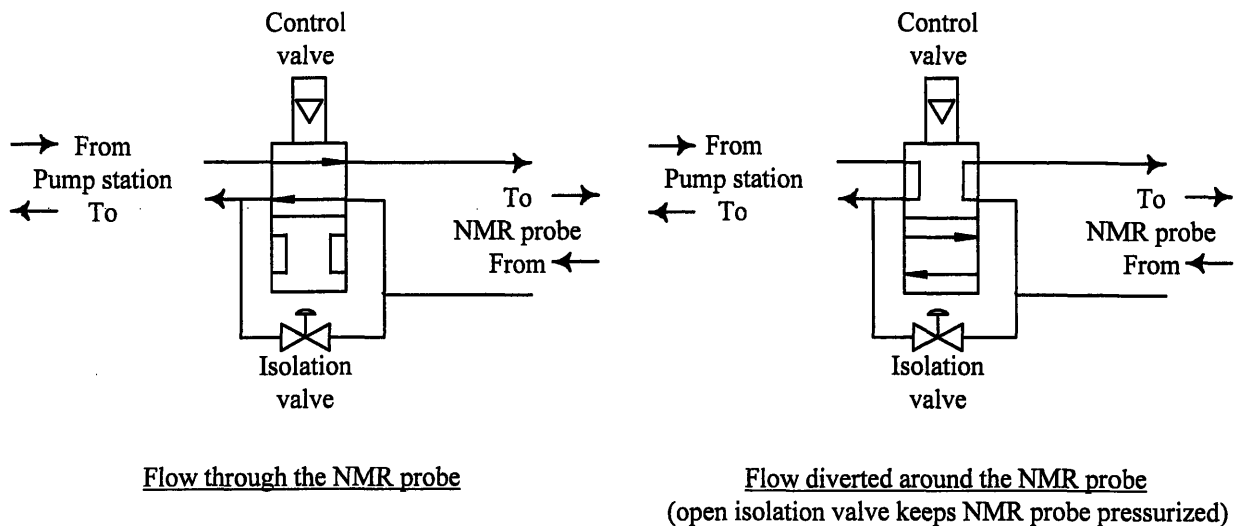
Figure 95. Flow pathways for the four-way control valve. With the isolation valve closed, configuration a) allows flow through the NMR probe, while configuration b) isolates the NMR probe while flow continues from and to the pumping station.

II.3.2.4 Nuclear-Magnetic-Resonance Electrical-Circuit Features

An RF coil must surround the sample of interest and is designed to be slightly larger than the sample tube. Given the location, the coil temperature is approximately that of the sample. A 1 cm long, saddle-shape RF coil was constructed with one piece of 0.2 cm diameter copper wire (Callaghan, 1993). The coil is connected to the NMR probe circuit that must be operating at a near ambient temperature since the variable capacitors and solder junctions will fail at temperatures above 100°C. To ensure that the electrical circuit operates at an acceptably low temperature, cooling air is used.

The RF circuit used for proton NMR requires that it be tuned to 200.14 MHz and have the load impedance matched to 50 Ω. In order for the variable capacitors to have sensitivity around 200.14 MHz, they must have a small capacitance range (1–10 pf). The circuit used appears in Figure 96. Electrical arcing occurred during the use of high power pulses, so the power was lowered to 75 W by using two 3dB attenuators for a total of 6dB attenuation. Although the $\pi/2$ pulse time increased slightly to 10 μs, the arcing was eliminated, and the NMR experiment produced repeatable results.

A close up view of the electrical circuit and support is shown in Figure 97, while the overall NMR probe assembly is shown in Figure 98. A picture of the completed NMR probe is shown in Figure 99.

256
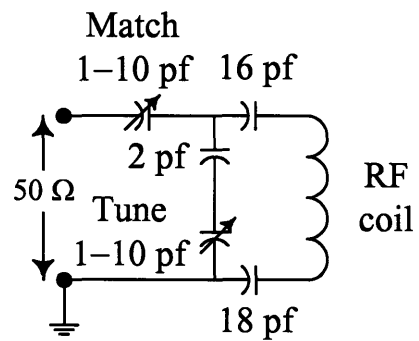
Figure 96. RF electrical circuit used for 200.14 MHz ^{1}H measurements.
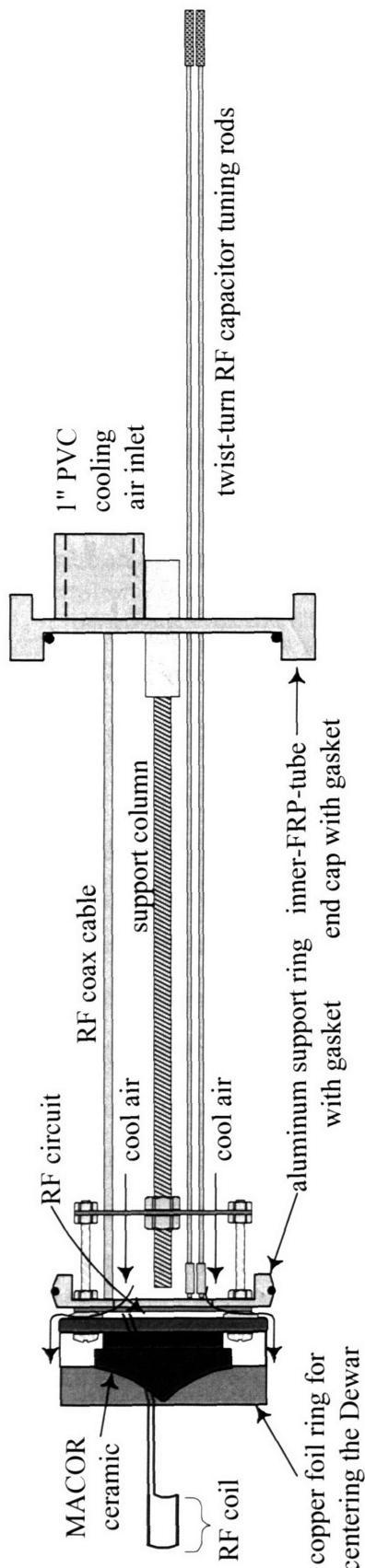
Figure 97. Drawing of the RF electrical circuit and support. Cooling air enters through the PVC port before passing the inner opening of the support ring and moving past the Dewar outer diameter (not shown). The RF circuit is fastened to the left of the support ring. The coax cable leads to a BNC jack mounted on the FRP end cap.
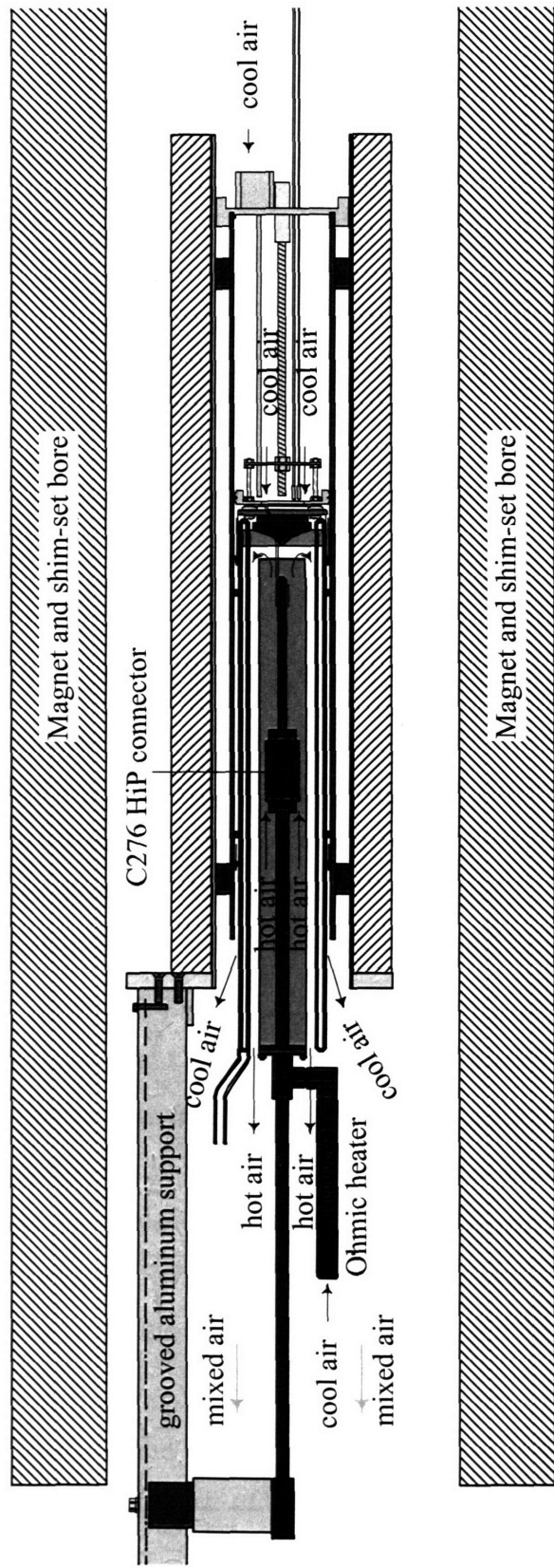
Figure 98. NMR probe assembly drawing with the RF electrical circuit and support in place. The entire SCW NMR probe is shown.

258
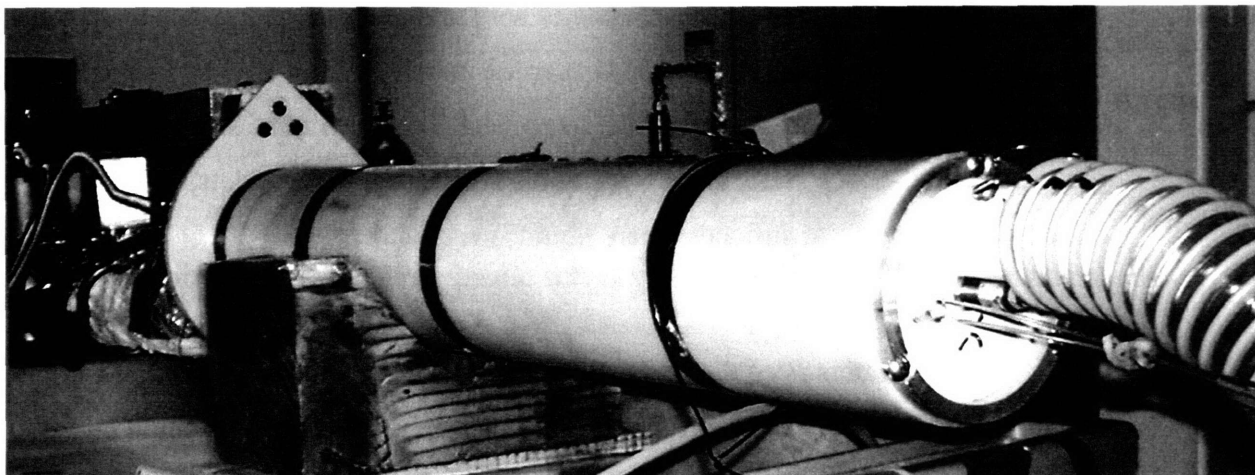
Figure 99. Picture of NMR probe assembly showing on the right side: the outer FRP support tube, the electrical probe end cap with connected cooling airline (and tethered screw to lock the cooling airline in place), and RF tuning rods under the airline. On the left side, the aluminum support track is connected to the outer FRP support tube. Black tape on the FRP provides extra thickness and cushioning for the probe when it is inserted in the magnet gradient set.

II.3.2.5 Safety

Safety to both the operator and magnet was of utmost concern requiring strategies and techniques for several parts of the experimental system. For the pumping station, high pressure tubing was isolated behind polycarbonate windows (1/2" (1.3 cm) thick GE Lexan). Pressure relief valves were used to prevent unsafe pressure surges. Due to the high magnetic field strength generated by the magnet, several rules are required to protect operators and the magnet. First, magnetic materials must be isolated or kept a sufficient distance from the magnet in order to minimize attractive forces. Thus, the pumping station, the vacuum pump, and the blower/heat exchanger were located outside of the shielded room. Furthermore, magnetic or slightly magnetic objects that had to be located in the shielded room were secured so that they could not be pulled towards the magnet. For operators, the common safety rules were in place including no pacemakers, magnetic-encoded cards, or analog watches.

In terms of the NMR probe assembly, since there are numerous hazards, it is appropriate to discuss them in terms of their energy hazard category.

II.3.2.5.1 Electrical energy

Since the heater consumes up to 15 amps of current, it is considered hazardous. All wires were electrically insulated and secured to minimize wear and

259

tear on wire feedthroughs. Nichrome heater wire is slightly magnetic, and there is a chance for wire movement when placed near the magnet. These heating elements were contained in a quartz tube in order to prevent contact with the surrounding metal grounding tube. Since water and other liquids are nearby, wire, outlets, and junction boxes were kept off flat surfaces where liquids may collect.

II.3.2.5.2 Thermal energy

Since heaters raise the temperature of the fluid and of neighboring materials, burns are a possibility. The NMR probe was designed so that surfaces could be held and operators would not be harmed. Hot surfaces were insulated as best as possible in order for protection and to minimize heat loss. Multiple barrier layers were in place in order to prevent hot objects from touching any magnet component including the gradient set. The magnet bore was lined on both ends with 1/8" (3.2 mm) thick high temperature insulation and 1/8" (3.2 mm) thick acrylic tubing that extended past the magnet and into the shielded room. This tube would act as a barrier for any hot materials or projectiles that may come in contact with the magnet bore.

FRP tubes and plates were used to line and protect the gradient set. They served a dual role since they were also used to support and contain the entire NMR probe. A continuously monitored thermocouple was attached to the outer surface of the FRP tube where a hot projectile may land if the sample tube failed. The inner FRP tube placed in the outer FRP tube was held in place with feet, located at 12, 4, and 8 o'clock and in two axial locations. The resulting ½" (1.3 cm) gap between the tubes was used as a safety gap in case of a sample tube and inner FRP tube failure. In such a catastrophic event, the ¼" (6.4 mm) OD plastic tubing winded inside the gap would have cold nitrogen gas (from a liquid nitrogen tank) flowing rapidly in order to cool the gap. Further, it was reasoned that if a hot object did touch the tubing, the tubing would melt and gas would immediately start to flow out of that opening and start cooling that hot object. Fortunately, the inner FRP was never damaged, and the gas tubing system was never used.

Inside the inner FRP, approximately 40 CFM of 20°C cooling air was flowing in order to keep the Dewar outer diameter cool. This air stream is the first

line of defense for thermal deviations when the Dewar fails (it occurred once when the sample tube failed). This air also protected the mixed region inside the magnet bore (see Figure 87) from excessive temperatures as was described in the text.

In the case of a power failure, the control computer, blower, heater, pump, vacuum pump, and pneumatic valves would shutdown and the following sequence of events would take place

- Dewar vacuum valve would be closed to maintain a vacuum in the Dewar and its insulation;

- Control valve would isolate the probe from flow and maintain pressure;

- House compressed air would flow through the non-powered heater and follow the normal route;

- Cold nitrogen gas would immediately flow between the inner and outer FRP gap in order to keep the FRP tubes and gradient set cool along with flow near the aluminum support track;

- If the house compressed air failed, then a separate cylinder of nitrogen gas is ready to be used to replace the lost compressed air; and

- These steps would to be followed until the power is restored and the entire SCW NMR system is inspected.

If a high pressure, high temperature fluid line failed, then depending on it location the steps above would be followed to ensure that thermal energy is safely dissipated. The heater would be shut off while the blower would still be used to generate cooling air in order to dissipate the heat. Any generated hazardous waste is properly contained, and all contaminated areas are decontaminated.

II.3.2.5.3 Mechanical energy associated with compressive energy

The control valve is pneumatically controlled and has moving parts that are pinching hazards. The metal support housing of the valve adequately cover the moving parts, but nonetheless, a small hazard exists. High pressure lines are a mechanical hazard due to the stored energy in the compressed fluid. The steps listed above for a high pressure, high temperature failure would be followed. Any

generated hazardous waste is properly contained, and all contaminated areas are decontaminated.

II.3.2.5.4 Hazardous materials

Personal protective equipment is used to handle chemicals and other hazardous materials. Protective gloves are used when chemicals are handled. Waste chemicals were handled according to MIT Safety Office guidelines and properly stored and tagged prior to removal by staff. For spills, the generated hazardous waste is properly contained, and all contaminated areas are decontaminated.

II.3.2.6 System Startup and Shutdown

II.3.2.6.1 Startup

The best-known method to reach supercritical conditions is to heat slowly ($< 10°C/min$ above 200°C) at a pressure below 100 bar in order to reduce the tensile and thermal stresses on the system, sample tube, and sample-tube seal. During this time, water can slowly be pumped through the system, but pumping will delay reaching thermal equilibrium. Instead, the control valve can be switched to recirculate mode and the exposure valve opened in order for the NMR probe to equilibrate its pressure with the pumping station and quickly achieve thermal equilibrium. The following list summarizes the key steps in preparing the NMR system for SCW NMR measurements and important rates to lower the likelihood of system damage.

1. Prior to pumping, purge water supply with helium in order to remove dissolved oxygen.

2. Pump down on Dewar with turbo pump in order to reach the lowest possible pressure and have the greatest insulation character.

3. Temporarily turn on the liquid pump and flush the entire system at high flow (~10 cm^3/min) at ambient pressure.

4. Turn on cooling-air blower and heat exchanger water flow (> 6 L/min).

5. Setup emergency cooling systems.

6. Verify data acquisition system functionality and perform any ambient NMR experiments.

262

7. Recirculate the water flow, but open the exposure valve and begin any under 100 bar operations.

8. Turn on the heater compressed air and the heater in order to slowly start heating the system with ~50°C increments in order to maintain a less than 10°C/min sample-tube temperature rise.

9. The 10°C/min temperature rate increase should not be exceeded at temperatures above 200°C or the thermal stress may damage the sample tube.

10. At steady-state, perform necessary experiments with low or no flow.

II.3.2.6.2 Shutdown

Shutdown follows the startup procedure in reverse order and with opposite commands. Thermal stress dictates a slow cool-down rate with a low flow rate and pressure. The heater should not be turned off, and the compressed air flow should not be increased. Slowly ramp the heater down to achieve a less than 20°C/min ramp-down rate. By following these procedures, the sample tube should not be damaged.

II.3.3 References

Armellini, F.J. (1993) "Phase equilibria and precipitation phenomena of sodium chloride and sodium sulfate in sub- and supercritical water." *MIT Dept. of Chem. Eng.*, Doctoral dissertation, Cambridge, MA.

Callaghan, P.T. (1993) *Principles of Nuclear Magnetic Resonance Microscopy*, Oxford University Press, New York, NY.

Cline, J.A. (2000) "Experimental and ab initio investigations into the fundamentals of corrosion, in the context of supercritical water oxidation systems." *MIT Dept. of Chem. Eng.*, Doctoral dissertation, Cambridge, MA.

Defries, T.H. and Jonas, J. (1979) "NMR probe for high-pressure and high-temperature experiments." *J. Mag. Reson.*, 35, 111–119.

DiNaro, J.L. (1999) "Oxidation of benzene in supercritical water: experimental measurements and development of an elementary reaction mechanism." *MIT Dept. of Chem. Eng.*, Doctoral dissertation, Cambridge, MA.

Dipippo, M.M. (1998) "Phase behavior of inorganic salts in sub- and supercritical water." *MIT Dept. of Chem. Eng.*, Doctoral dissertation, Cambridge, MA.

Downey, K.W., Snow, R.H., Hazlebeck, D.A., and Roberts, A.J. (1995) "Corrosion and chemical agent destruction." Research on supercritical water oxidation of hazardous military wastes." *ACS Symp. Ser., No. 608*, 30 (5), 313.

Jonas, J. (1972) "Nuclear magnetic resonance measurements at high pressure." *Rev. Sci. Instrum.*, 43 (4), 643–649.

Hodes, M.S. (1998) "Measurement and modeling of deposition rates from near-supercritical, aqueous, sodium sulfate and potassium sulfate solutions to a heated cylinder." *MIT Dept. of Mech. Eng.*, Doctoral dissertation, Cambridge, MA.

Hoffmann, M.M. and Conradi, M.S. (1997) "Nuclear magnetic resonance probe for supercritical water and aqueous solutions." *Rev. Sci. Instrum.*, 68 (1), 159–164.

Holz, M., Heil, S.R., and Sacco, A. (2000) "Temperature-dependent self-diffusion coefficients of water and six selected molecular liquids for calibration in accurate 1H NMR PFG measurements." *Phys. Chem. Chem. Phys.*, 2, 4740–4742.

Horváth, I.T. and Ponce, E.C. (1991) "New valve design for high-pressure sapphire tubes for NMR measurements." *Rev. Sci. Instrum.*, 62 (4), 1104–1105.

Hoult, D.I. and Richards, R.E. (1975) "Critical factors in the design of sensitive high resolution nuclear magnetic resonance spectrometers." *Proc. Roy. Soc. London A*, A344 (1638), 311–340.

Matubayasi, N., Wakai, C. and Nakahara, M. (1997) "Structural study of supercritical water." I. nuclear magnetic resonance spectroscopy." *J. Chem. Phys.*, 107 (21), 9133–9140.

Wayne and Cotts (1966) "Nuclear-magnetic-resonance study of self-diffusion in a bounded medium." *Phys. Rev.*, 151 (1), 264–272.

Weingärtner, H. (1982) "Self diffusion in liquid water. a reassessment." *Zeitschrift für Physikalische Chemie Neue Folge*, 132, 129–149.

II.4. Diffusivity Measurements

Using the NMR probe, diffusivity experiments can be performed at SCW conditions for both pure water and selected model aqueous mixtures at several temperatures, densities, and for the mixtures, at several concentrations. Acetone was chosen as the model solute for the mixture experiments for the following reasons:

1. It has sufficient proton (^{1}H) density and NMR signal;

2. It has low hydrolysis rates in SCW so that the mixture composition is constant during an NMR experiment;

3. For the investigated concentrations, it is miscible with water at ambient conditions where it is stored and pumped; and

4. Its critical temperature, pressure, and density (235.05°C, 47.01 bar, 0.278 g/cm^3) are lower than those for pure water, resulting in lower mixture critical properties, thus ensuring a supercritical mixture when the acetone concentration is increased (See Table 33 for critical values for several materials).

Low SCW hydrolysis rates were confirmed with twenty-minute-long NMR spectroscopy experiments. During these experiments, spectra were collected every few minutes and acetone signal intensities did not decrease or shift. The process conditions were chosen to address the following:

1. Pure supercritical water results could be compared with the results of Lamb *et al.* (1981) in order to validate the NMR probe;

2. First-of-its-kind measurements of pure water in the subcritical, low pressure, high temperature range in order to identify low density diffusivity trends;

3. First-of-its-kind measurements of aqueous organic mixtures at sub- and supercritical conditions at several concentrations.

In order to separate density from temperatures effects on diffusivity, a series of experiments were conducted at constant pure water density for several temperatures. Since temperature and pressure are the process-control variables, densities were calculated using the

265

Table 33. Critical parameters for several materials

Material	$T_c{}^a$ (°C)	$P_c{}^a$ (bar)	$V_c{}^a$ (m^3/kmol)	Z_c = $P_c V_c / R T_c$
Acetone	235.05	47.01	0.2090	0.2326
Ammonia	132.40	112.775	0.0724	0.2422
Benzene	288.95	48.940	0.2590	0.2710
Carbon dioxide	31.06	73.821	0.0939	0.2741
Ethanol	239.35	61.37	0.1670	0.2406
Ethylene	9.19	50.404	0.1290	0.2770
Methane	−82.62	45.979	0.0990	0.2874
Nitrogen	−146.89	33.980	0.0896	0.2900
Oxygen	−118.57	50.430	0.0734	0.2886
Water	374.14	220.899	0.0559	0.2295

^{a} Obtained from Braker and Mossman, 1980; Walas, 1985; Sato $et\ al.$, 1991; Poling $et\ al.$, 2001.

NIST steam-table EOS for pure water in order to identify the pressures that would be required to generate isochoric (constant density) data at a specified temperature (NIST, 1996). For mixtures, the pure water EOS was also used since mixture densities have not been measured for the acetone-water mixture at sub- and supercritical conditions, and experimental solution densities are, therefore, not available. Other EOSs could have been used, but for consistency (especially at low concentrations), the pure water density formulation was used.

Preliminary experiments indicated that concentrated acetone(1)-water(2) solutions were required in order to have sufficient acetone NMR signal-to-noise ratios (SNRs). Infinitely dilute solutions would have been ideal to measure acetone tracer diffusivities, since the tracer diffusivity would then equal the infinitely dilute mutual diffusivity (Tyrell and Harris, 1984). At concentrations other than infinitely dilute, the mutual diffusivity and solute tracer diffusivity are not equal as is shown in Section II.1.1.1. The acetone(1) concentrations used are 20 wt.%$_1$, 40 wt.%$_1$, and 60 wt.%$_1$ (± 0.3 wt.%$_1$ (95%-confidence-interval uncertainties)), which correspond to acetone mole fractions, x_1, of 0.0724, 0.171, and 0.319 (± 0.6%) and the following approximated pseudo-single-component critical-mixture properties (T_c, P_c, & ρ_c):

- 20 wt.%$_1$: 363.9°C, 208.0 bar, & 0.319 g/cm^3,
- 40 wt.%$_1$: 350.1°C, 190.8 bar, & 0.315 g/cm^3, and
- 60 wt.%$_1$: 329.6°C, 165.2 bar, & 0.308 g/cm^3.

The chosen temperatures and densities are matched to the previously published near and supercritical self-diffusivities, while the process-condition set is expanded to include lower densities and an intermediate temperature (450°C). NMR-probe-safety issues prevent higher temperatures and densities from being investigated. The test matrix is shown in Table 34.

The PGSE NMR diffusivity sequence was used, but because of the order of magnitude difference in diffusivities over these process conditions, the gradient strength and pulse times were adjusted in order to obtain sufficient attenuation of the NMR signal. If one or more td1 scans had intensities near the background noise level due to significant attenuation, then the gradient strength was reduced to lower the extent of attenuation. Typically, the PGSE gradients varied between 0.5 and 2.1 G/cm with $\delta = 5$ ms and $\Delta = 10$ ms. At each process condition shown in Table 34, at least three experiments are performed, and the calculated diffusivities are averaged. Since there is a small sample size (small number of degrees of freedom), Student's t-distribution is used to estimate the standard deviation at the 95% confidence interval (Devore, 1990). During the approximately five-minute-long experiment, temperature and pressure drifts will occur. The experiment will be considered an outlier, and datum will not be used if the temperature and pressure variations exceed thresholds determined by the following conditions:

- For each set of isothermal (400°C, 450°C, or 500°C) experiments, an overall average temperature is calculated using each individual experiment average temperature. If the overall average temperature is outside of the 95% confidence interval for an individual experiment, then this individual experiment is considered an outlier and its datum is not used in the future analysis.

- A similar approach is used to filter pressure outliers. Individual experiments are considered outliers if their 95% confidence intervals do not include the average pressure calculated to match the desired density. With the outliers removed, overall temperature, pressure, and density averages are then recalculated.

Table 34. Temperature, pure water density, concentration, and (calculated) pressure experimental matrix

Calculated pressure (bar) - experimental 60 $wt.\%_0$, 40 $wt.\%_1$, 20 $wt.\%_1$, and 0 $wt.\%_1$ aqueous organic solution data

T (°C)	p(pure H_2O)=0.025 g/cm³				0.05 g/cm³				0.10 g/cm³				0.15 g/cm³				0.20 g/cm³				0.225 g/cm³				0.250 g/cm³			
Acetone $wt.\%_1$ →	60%	40%	20%	0%	60%	40%	20%	0%	60%	40%	20%	0%	60%	40%	20%	0%	60%	40%	20%	0%	60%	40%	20%	0%	60%	40%	20%	0%
400		69.0				125.1				199.5				240.9				264.0				271.7				277.9		
450		76.7				140.6				236.4																		
500		83.3				155.3				271.1																		

= Data not collected

Table 35. Range of temperatures, pure water densities, concentrations, and pressures studied following temperature and pressure outlier filtering (95% confidence intervals are used to represent the reported standard deviations)

Experimental pressure (bar) - experimental 60 $wt.\%_0$, 40 $wt.\%_1$, 20 $wt.\%_1$, and 0 $wt.\%_1$ aqueous organic solution data

T (°C)	p(pure H_2O)=0.0253±0.0001 g/cm³				0.0494 ± 0.0001 g/cm³				0.0977 ± 0.0001 g/cm3				0.1423 ± 0.0003 g/cm³				0.1838 ± 0.0004 g/cm³				0.2206 ± 0.0007 g/cm³				0.257 ± 0.002 g/cm³			
Acetone $wt.\%_1$ →	60%	40%	20%	0%	60%	40%	20%	0%	60%	40%	20%	0%	60%	40%	20%	0%	60%	40%	20%	0%	60%	40%	20%	0%	60%	40%	20%	0%
404.3 ± 0.3	70.5	70.2	70.2	69.7	125.6	125.3	125.2	125.5	200.0	199.9	199.8	199.5	241.1	240.7	240.7	241.2	264.4	264.2	263.9	264.4	279.1	278.2	278.5		289.0	288.9	289.6	
455 ± 2	76.4	79.8			140.4	140.3	140.8		236.7	237.2	236.6																	
506 ± 4	84.4	81.7			155.6	155.0	154.6		271.3	271.1	271.3																	

= Data not collected

The resulting process conditions are shown in Table 35. Note that the temperature averages for the three temperature datasets are 404°C, 455°C, and 506°C. With the process conditions well defined, the diffusivity measurement results are now presented.

II.4.1 Pure Water Results and Analysis

Pure water (0 wt.%$_1$) self-diffusivities were measured first in order to validate the SCW NMR probe and the self-diffusivities reported by Lamb *et al.* (1981). Table 36 presents the data collected and the previously published results. The data are also compared in Figure 100. The density is determined with the NIST Steam-Table EOS while the uncertainty in density is calculated by using the worst case of experimental temperature and pressure deviation (maximum of $\left|\rho\left(\overline{T}+\Delta T, \overline{P}-\Delta P\right)-\rho\left(\overline{T}, \overline{P}\right)\right|$ and $\left|\rho\left(\overline{T}-\Delta T, \overline{P}+\Delta P\right)-\rho\left(\overline{T}, \overline{P}\right)\right|$) (NIST, 1996).

From a review of the data and Figure 100, it appears that there is an excellent agreement between Lamb *et al.* (1981) data and the data collected in the SCW NMR probe, given the uncertainty in the measurements.

II.4.2 Binary Organic Aqueous Mixture Results

The tracer diffusivities of acetone(1) and water(2) are shown next in Table 37 as a function of acetone concentration, experimental temperature, calculated-pure-water density, and the experimental pressure. The density is calculated in a similar fashion as described earlier, even though the mixture density is altered by the addition of acetone solute. The discussion with mixture densities follows shortly.

The diffusivity data are plotted as a function of the calculated-pure-water density in a series of figures:

- Figure 101 contains acetone tracer-diffusivity data at 404.3°C for several concentrations as a function of density.

- Figure 102 contains water tracer and self-diffusivity data at 404.3°C for several concentrations as a function of density.

- Figure 103 contains tracer and self-diffusivity data at 404.3°C for several concentrations as a function of calculated-pure-water density. Acetone and pure

269

Table 36. Pure water self-diffusivities at sub- and supercritical water conditions, including Lamb *et al.* (1981) data (with 95%-confidence-interval uncertainties)

Experimental temperature, T (°C)	Calculated-pure-water density, ρ_2 (g/cm^3)	Experimental pressure, P (bar)	Measured self-diffusivity, $D_{22} \times 10^5$ (cm^2/s)	Lamb *et al.*, $D_{22} \times 10^5$ (cm^2/s)
402.7 ± 0.2	0.0247 ± 0.0003	69.7 ± 0.8	1291 ± 21	
403 ± 2	0.0498 ± 0.0005	125.5 ± 0.5	628 ± 5	
404 ± 1	0.0976 ± 0.0009	199.5 ± 0.5	298 ± 22	
400	0.100	199		286 ± 57
400	0.122	221		243 ± 49
403.2 ± 0.6	0.144 ± 0.001	241.2 ± 0.7	201 ± 15	
400	0.150	241		203 ± 41
403 ± 1	0.188 ± 0.004	264.4 ± 0.8	166 ± 15	
400	0.203	265		161 ± 32
400	0.259	280		120 ± 24
400	0.298	291		112 ± 22
400	0.407	314		90 ± 18
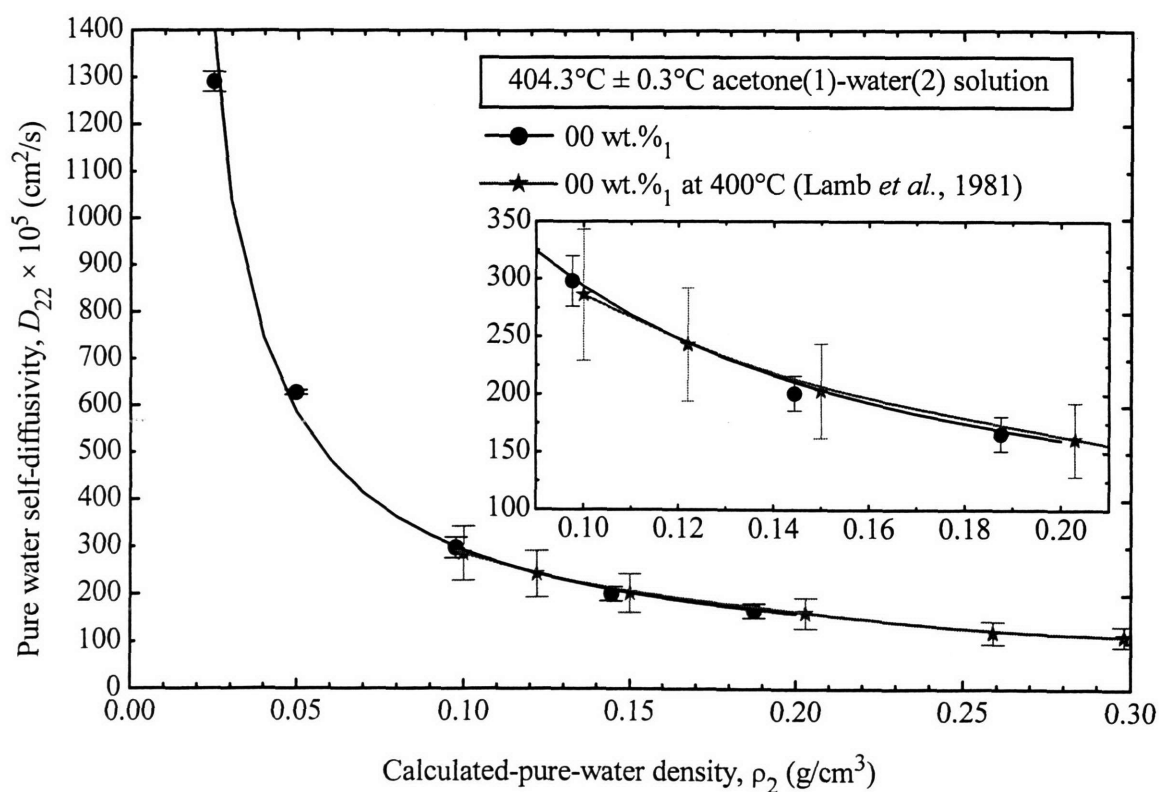
Figure 100. Pure water self-diffusivities at 404.3°C (with 95%-confidence-interval uncertainties) including a close-up view of the overlapping data. Curves are intended to show general trends.

Table 37. Acetone(1)-water(2) tracer diffusivities at sub- and supercritical water conditions (with 95%-confidence-interval uncertainties)

Acetone concentration (wt.%$_1$) = x_1	Experimental temperature, T (°C)	Calculated-pure-water density, ρ_2 (g/cm^3)	Experimental pressure, P (bar)	Acetone tracer diffusivity, $D_1 \times 10^5$ (cm^2/s)	Water tracer diffusivity, $D_2 \times 10^5$ (cm^2/s)
20 = 0.0724	409 ± 2	0.0246 ± 0.0005	70 ± 1	<<SNR	1282 ± 378
20 = 0.0724	404.4 ± 0.8	0.0494 ± 0.0002	125.2 ± 0.5	374 ± 98	588 ± 23
20 = 0.0724	404 ± 1	0.0977 ± 0.0008	200 ± 1	168 ± 12	282 ± 12
20 = 0.0724	403.2 ± 0.1	0.144 ± 0.001	240.7 ± 0.7	130 ± 10	239 ± 8
20 = 0.0724	404.1 ± 0.9	0.182 ± 0.005	264 ± 1	106 ± 18	189 ± 5
20 = 0.0724	402 ± 3	0.234 ± 0.003	278.5 ± 0.9	87 ± 32	177 ± 16
20 = 0.0724	404.4 ± 0.1	0.258 ± 0.001	289.6 ± 0.3	85 ± 22	168 ± 20
20 = 0.0724	455.3 ± 0.4	0.0494 ± 0.0003	140.8 ± 0.8	514 ± 26	828 ± 70
20 = 0.0724	456.5 ± 0.8	0.0973 ± 0.0008	236.6 ± 0.4	295 ± 31	351 ± 10
20 = 0.0724	506 ± 1	0.049 ± 0.001	155 ± 3	615 ± 56	938 ± 112
20 = 0.0724	504 ± 5	0.099 ± 0.002	271.3 ± 0.8	352 ± 36	383 ± 9
40 = 0.171	403 ± 1	0.025 ± 0.0004	70.2 ± 0.9	585 ± 45	943 ± 103
40 = 0.171	402.5 ± 0.3	0.0497 ± 0.0001	125.3 ± 0.3	300 ± 40	470 ± 37
40 = 0.171	403 ± 1	0.098 ± 0.001	199.9 ± 0.7	150 ± 36	253 ± 33
40 = 0.171	404.3 ± 0.4	0.1418 ± 0.0008	240.7 ± 0.3	143 ± 23	275 ± 35
40 = 0.171	404.1 ± 0.1	0.184 ± 0.001	264.2 ± 0.6	121 ± 15	221 ± 4
40 = 0.171	404 ± 1	0.217 ± 0.002	278.2 ± 0.8	98 ± 9	201 ± 76
40 = 0.171	404 ± 1	0.255 ± 0.003	288.9 ± 0.9	86 ± 31	190 ± 8
40 = 0.171	452.7 ± 0.7	0.0260 ± 0.0001	79.8 ± 0.1	766 ± 25	1202 ± 76
40 = 0.171	455.2 ± 0.9	0.0492 ± 0.0002	140.3 ± 0.5	460 ± 32	640 ± 10
40 = 0.171	454.7 ± 0.4	0.0984 ± 0.0004	237.2 ± 0.4	217 ± 71	310 ± 81
40 = 0.171	500.9 ± 0.7	0.0244 ± 0.0005	82 ± 2	958 ± 47	1475 ± 21
40 = 0.171	505 ± 1	0.0494 ± 0.0001	155 ± 0.4	580 ± 63	803 ± 2
40 = 0.171	504.8 ± 0.8	0.098 ± 0.001	271 ± 1	286 ± 107	369 ± 26
60 = 0.319	402.8 ± 0.2	0.0251 ± 0.0004	70.5 ± 0.9	656 ± 15	982 ± 7
60 = 0.319	403 ± 1	0.0497 ± 0.0002	125.6 ± 0.5	305 ± 17	480 ± 36
60 = 0.319	404 ± 1	0.097 ± 0.001	200.0 ± 0.6	174 ± 30	307 ± 10
60 = 0.319	404.2 ± 0.9	0.142 ± 0.001	241.1 ± 0.6	133 ± 7	218 ± 32
60 = 0.319	404 ± 1	0.184 ± 0.001	264.4 ± 0.6	117 ± 24	204 ± 28
60 = 0.319	404.3 ± 0.7	0.2202 ± 0.0008	279.1 ± 0.4	91 ± 9	184 ± 9
60 = 0.319	403.7 ± 0.4	0.262 ± 0.003	289.0 ± 0.1	80 ± 9	180 ± 7
60 = 0.319	456 ± 1	0.0246 ± 0.0001	76.4 ± 0.2	782 ± 34	1205 ± 74
60 = 0.319	455 ± 1	0.0492 ± 0.0002	140.4 ± 0.1	466 ± 85	632 ± 204
60 = 0.319	456.0 ± 0.5	0.0975 ± 0.0005	236.7 ± 0.6	252 ± 51	357 ± 30
60 = 0.319	504.8 ± 0.6	0.025 ± 0.001	84 ± 3	888 ± 98	1189 ± 101
60 = 0.319	506.5 ± 0.3	0.0494 ± 0.0005	156 ± 1	554 ± 138	785 ± 19
60 = 0.319	507 ± 2	0.0979 ± 0.0007	271 ± 1	349 ± 18	441 ± 180

water data from this study are shown side by side in order to compare their calculated-pure-water-density trends. Also included are the pure water self-diffusivity data from Lamb *et al.* (1981).

- Figure 104 contains tracer and self-diffusivity data at 455°C for several concentrations as a function of calculated-pure-water density.

- Figure 105 contains tracer and self-diffusivity data at 506°C for several concentrations as a function of calculated-pure-water density.

The following figures contain pure-calculated-water isochors as a function of temperature or concentration.

- Figure 106 contains acetone tracer-diffusivity data for several isochors as a function of temperature.

- Figure 107 contains water tracer and self-diffusivity data for several isochors as a function of temperature.

- Figure 108 contains acetone tracer-diffusivity data for several 404.3°C isochors as a function of concentration.

- Figure 109 contains water tracer-diffusivity data for several 404.3°C isochors as a function of concentration.

- Figure 110 contains acetone and water tracer-diffusivity data for several 455°C isochors as a function of concentration.

- Figure 111 contains acetone and water tracer-diffusivity data for several 506°C isochors as a function of concentration.

- Figure 112 contains acetone and water tracer-diffusivity data for several 0.025 g/cm^3 isotherms as a function of concentration.

- Figure 113 contains acetone and water tracer-diffusivity data for several 0.049 g/cm^3 isotherms as a function of concentration.

- Figure 114 contains acetone and water tracer-diffusivity data for several 0.098 g/cm^3 isotherms as a function of concentration.
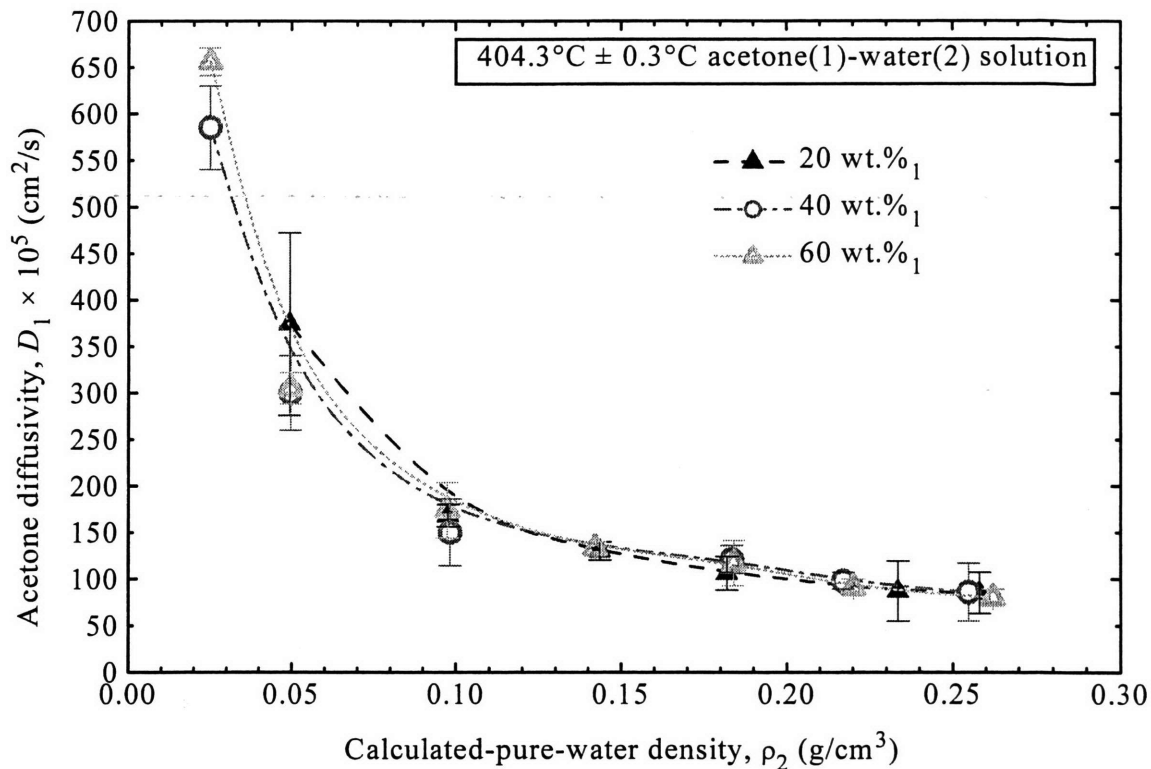
Figure 101. Acetone tracer diffusivities at 404.3°C (with 95%-confidence-interval uncertainties). Curves are intended to show general trends.
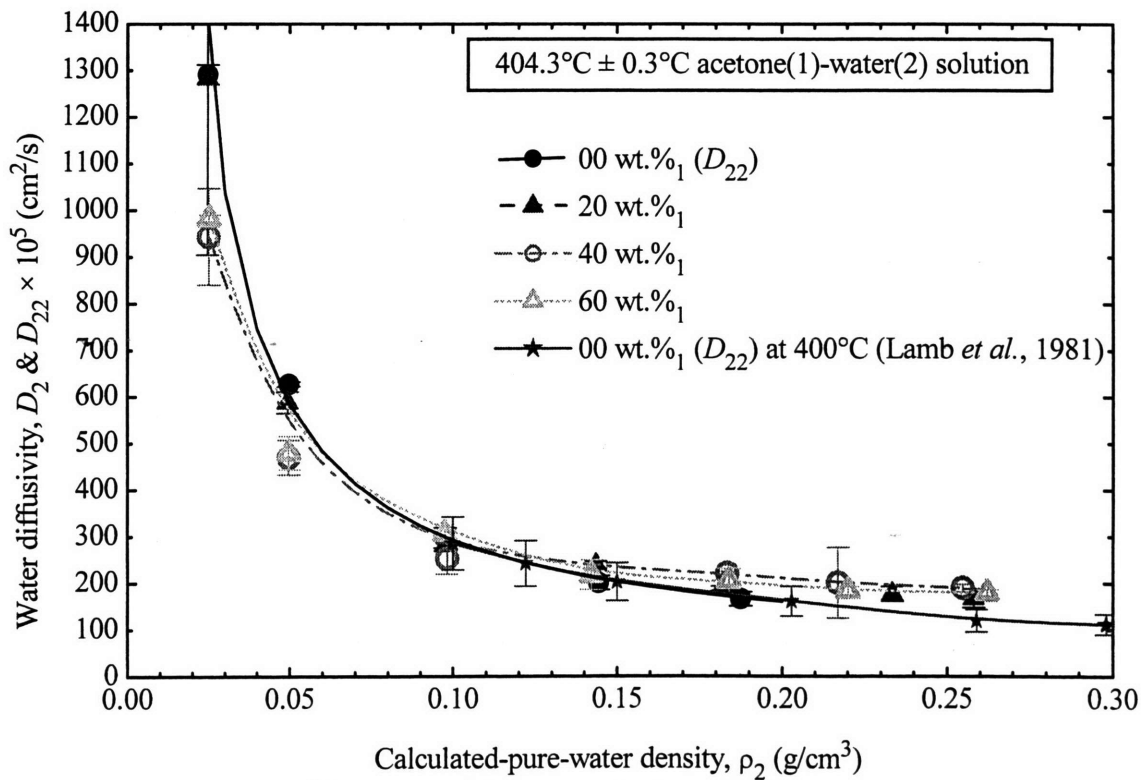
Figure 102. Water diffusivities at 404.3°C (with 95%-confidence-interval uncertainties). Curves are intended to show general trends.
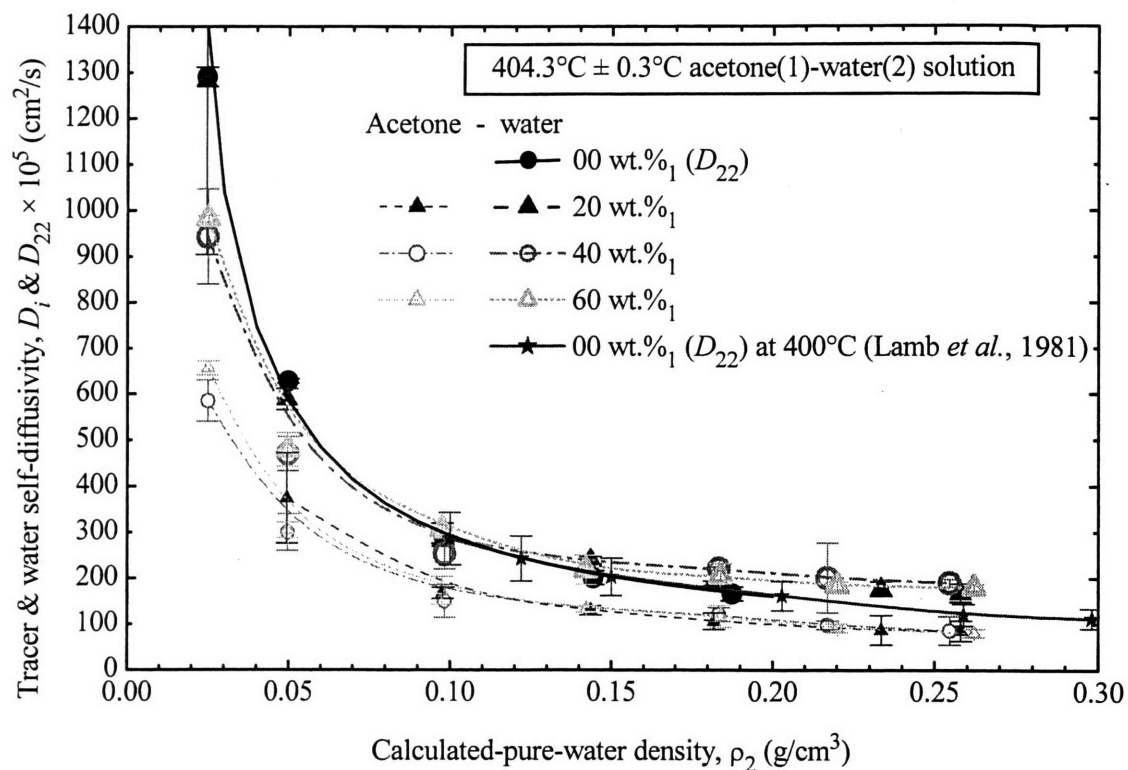
Figure 103. Acetone and water diffusivities at 404.3°C (with 95%-confidence-interval uncertainties). Curves are intended to show general trends.
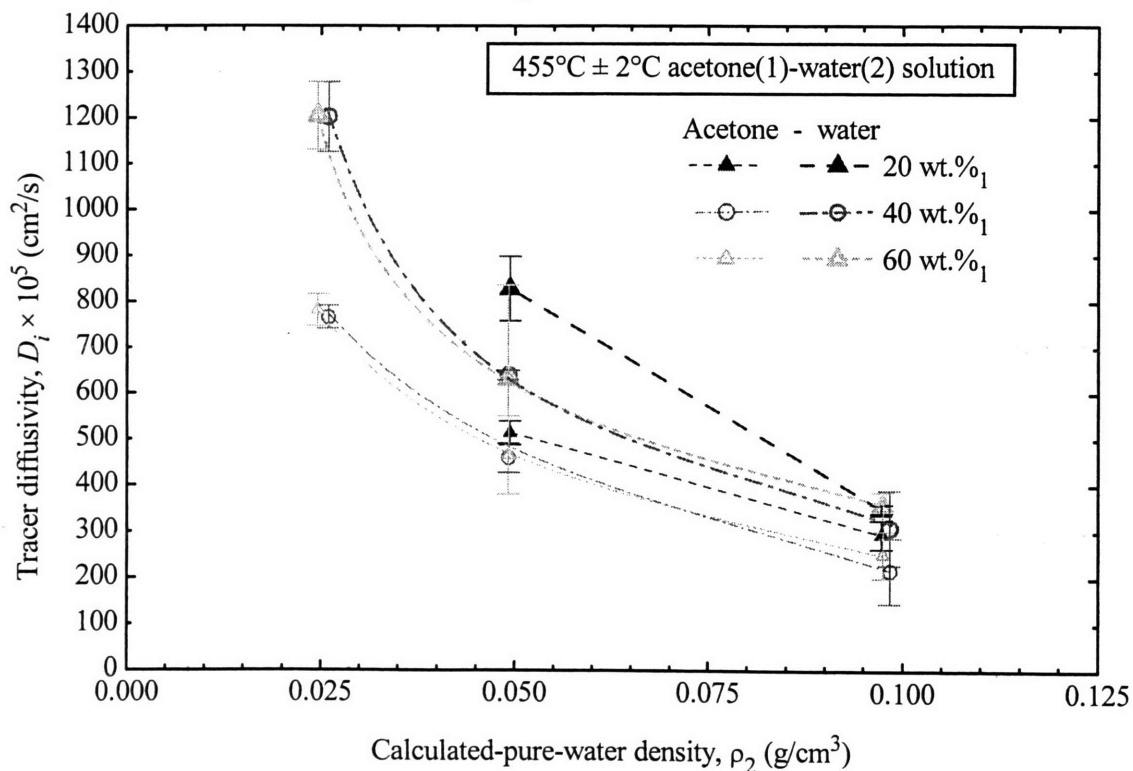
Figure 104. Tracer diffusivities at 455°C (with 95%-confidence-interval uncertainties). Curves are intended to show general trends.
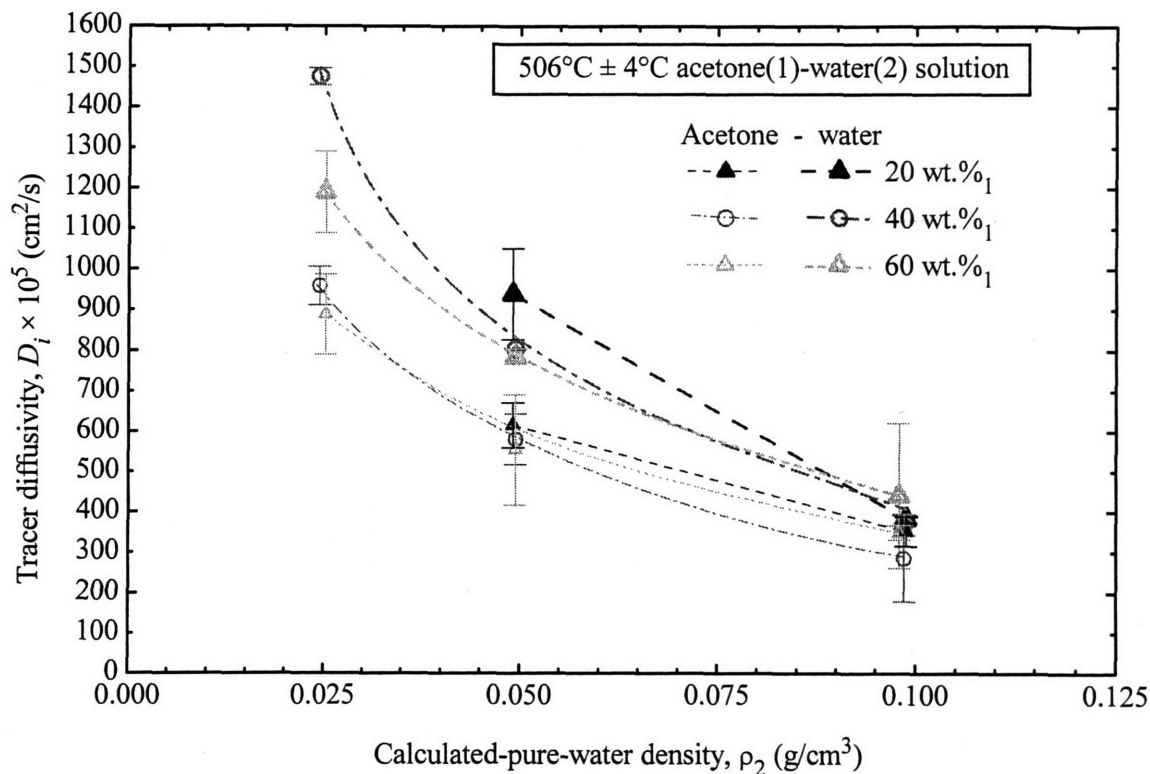
Figure 105. Tracer diffusivities at 506°C (with 95%-confidence-interval uncertainties). Curves are intended to show general trends.
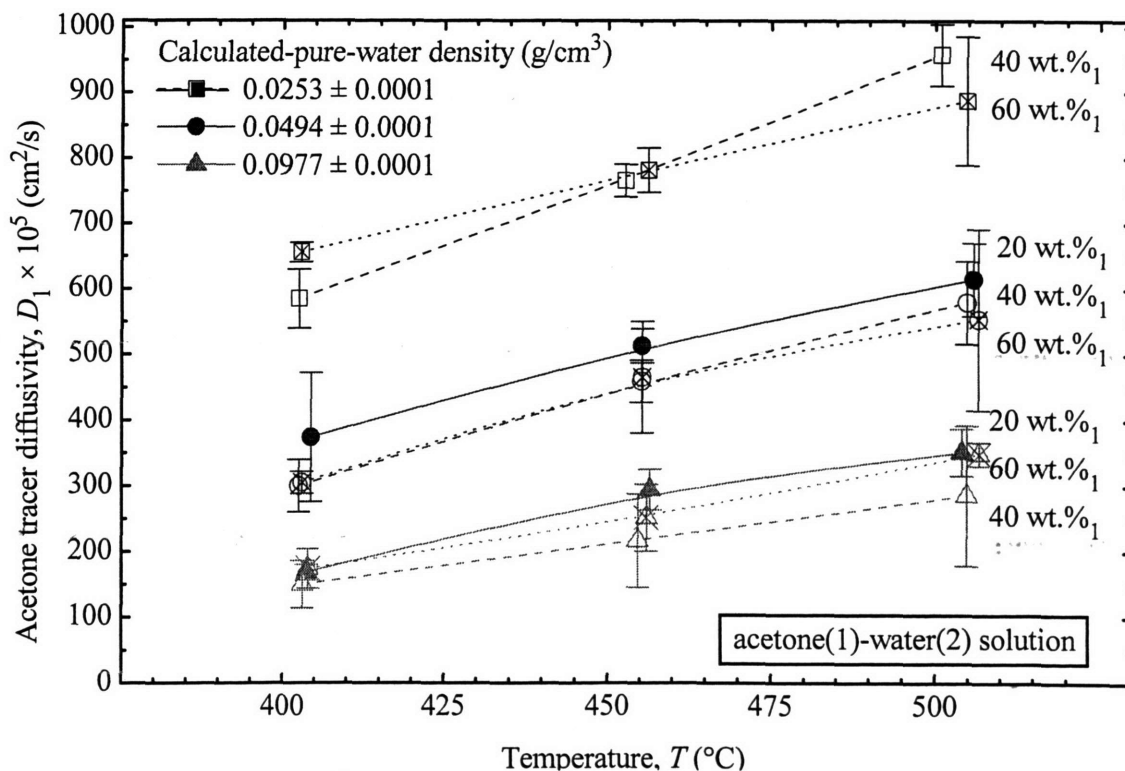
Figure 106. Acetone tracer diffusivities for several isochors as a function of temperature (with 95%-confidence-interval uncertainties). Curves are intended to show general trends.
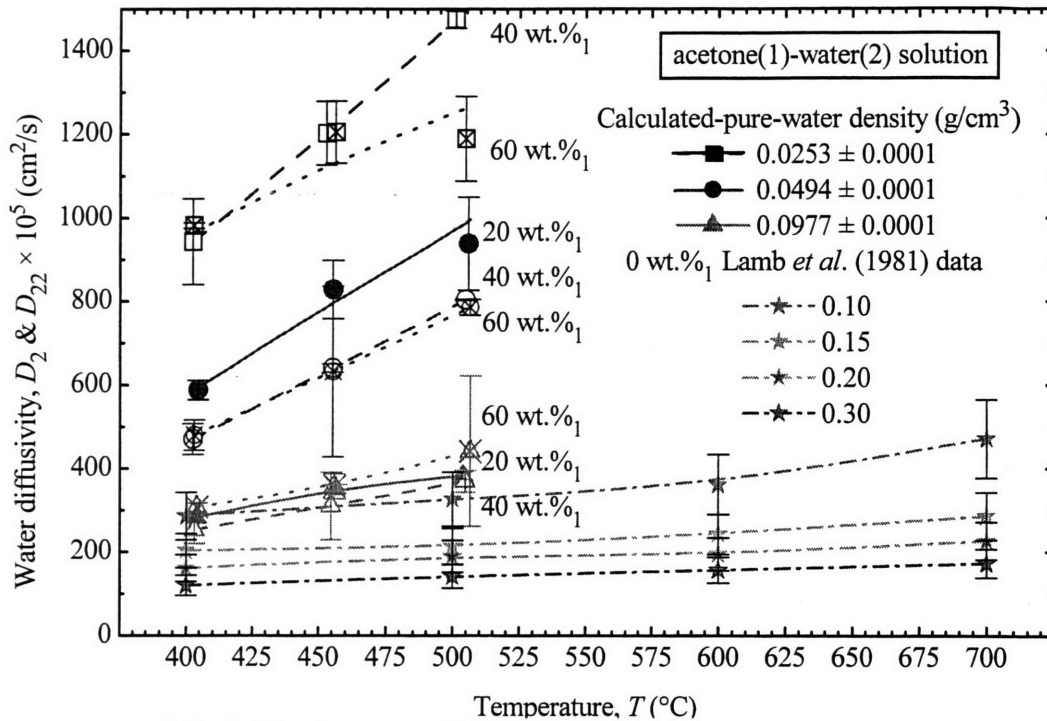
Figure 107. Water diffusivities for several isochors as a function of temperature (with 95%-confidence-interval uncertainties). Curves are intended to show general trends.
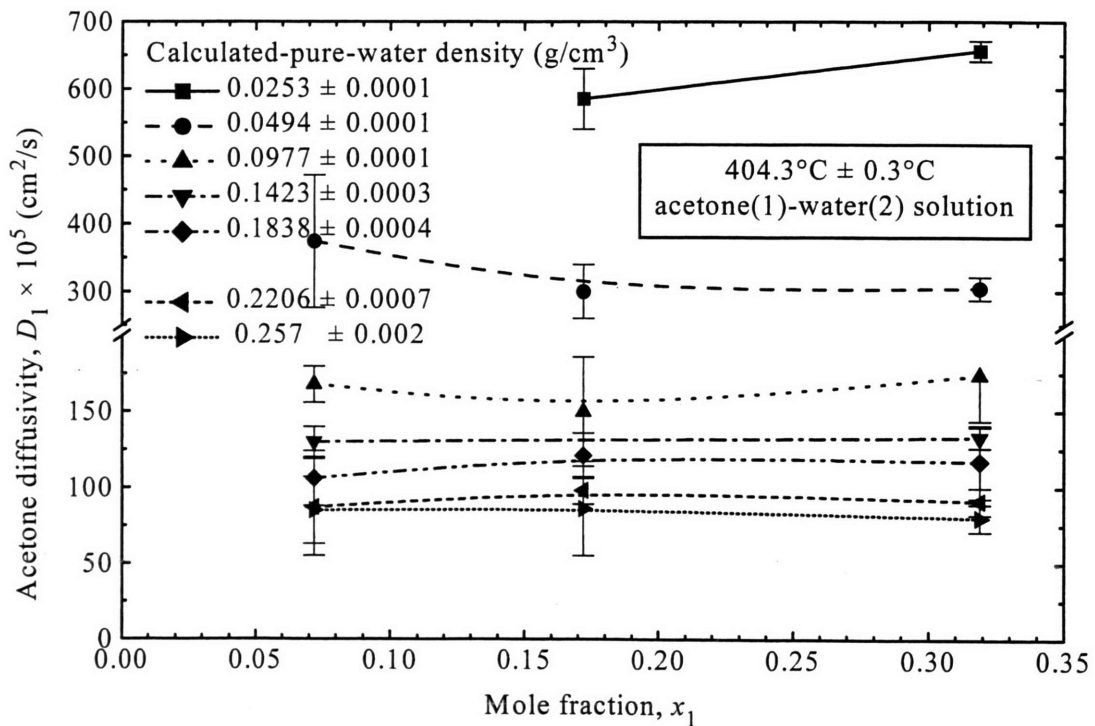
Figure 108. Acetone tracer diffusivities for several isochors as a function of concentration at 404.3°C (with 95%-confidence-interval uncertainties). Curves are intended to show general trends.
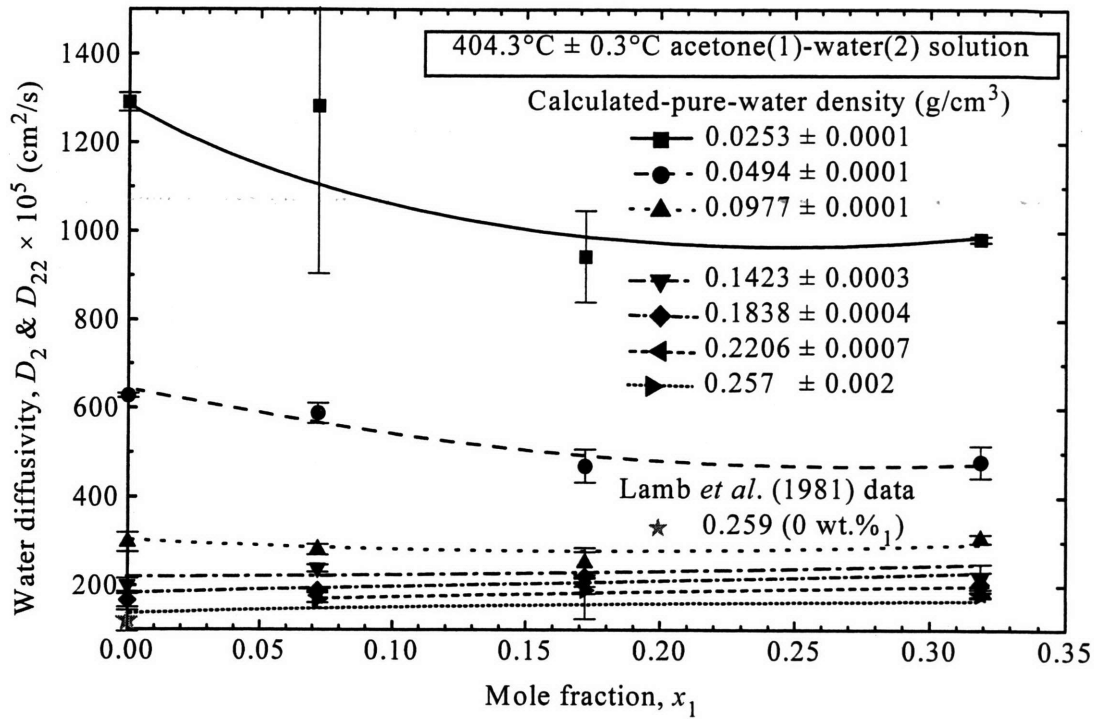
Figure 109. Water diffusivities for several isochors as a function of concentration at 404.3°C (with 95%-confidence-interval uncertainties). Curves are intended to show general trends.
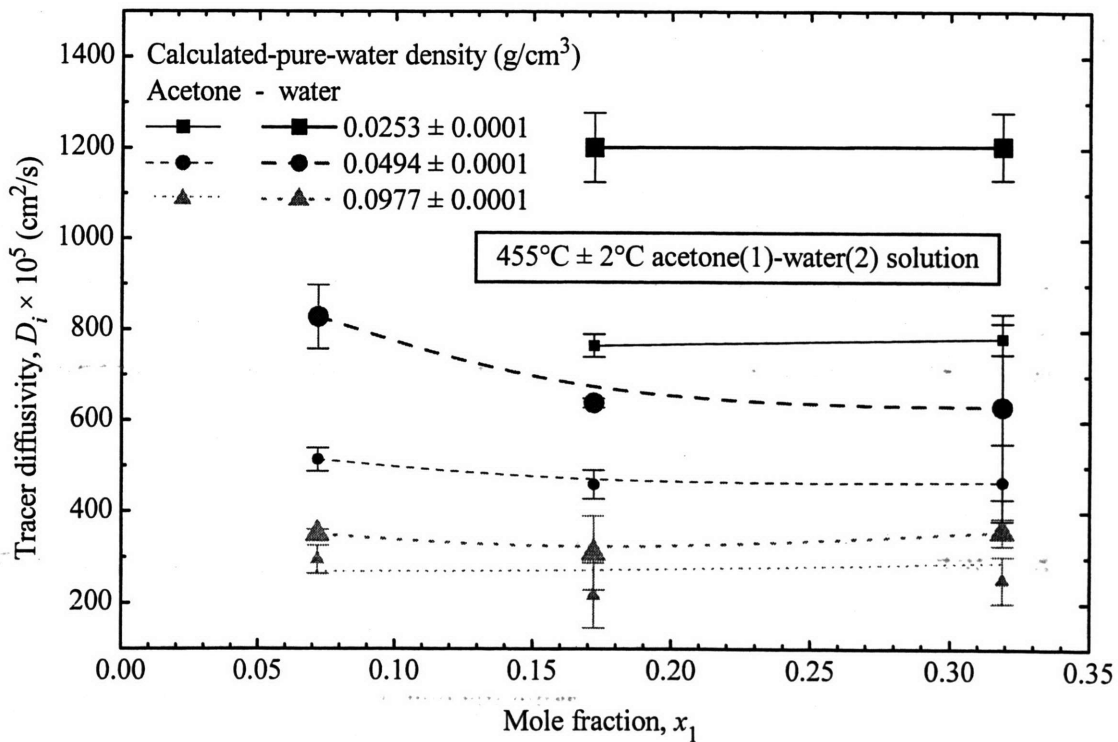
Figure 110. Acetone and water diffusivities for several isochors as a function of concentration at 455°C (with 95%-confidence-interval uncertainties). Curves are intended to show general trends.
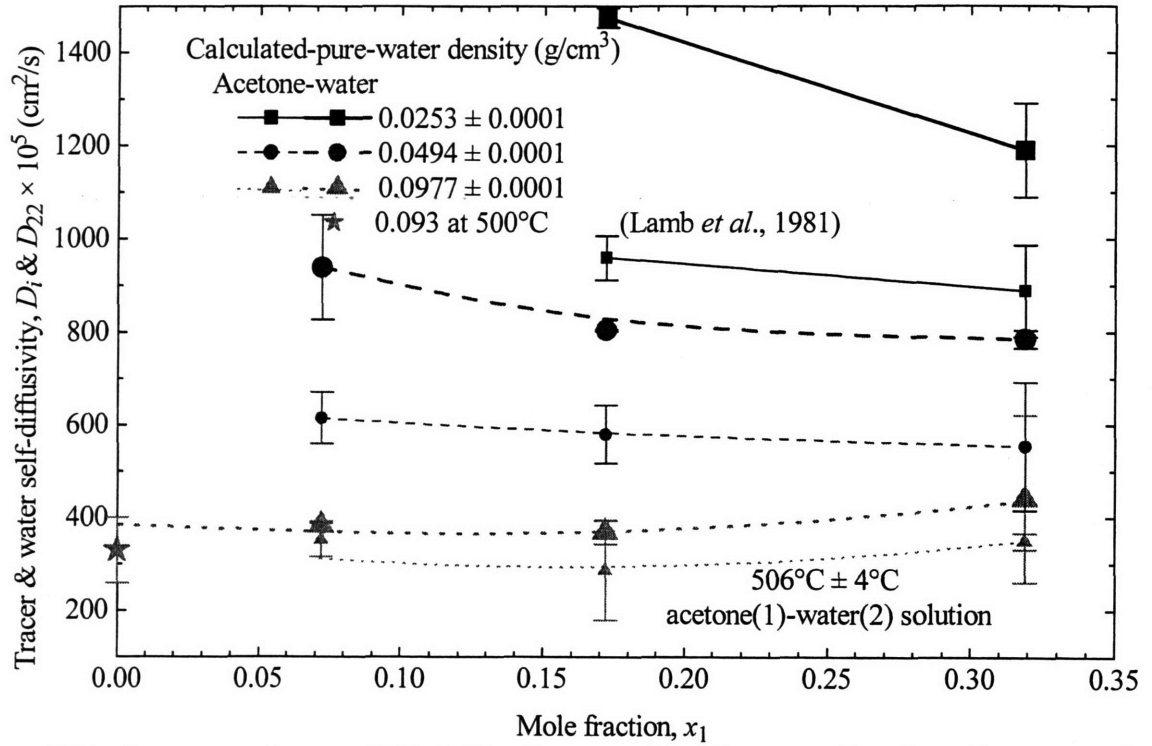
Figure 111. Acetone and water diffusivities for several isochors as a function of concentration at 506°C (with 95%-confidence-interval uncertainties). Curves are intended to show general trends.
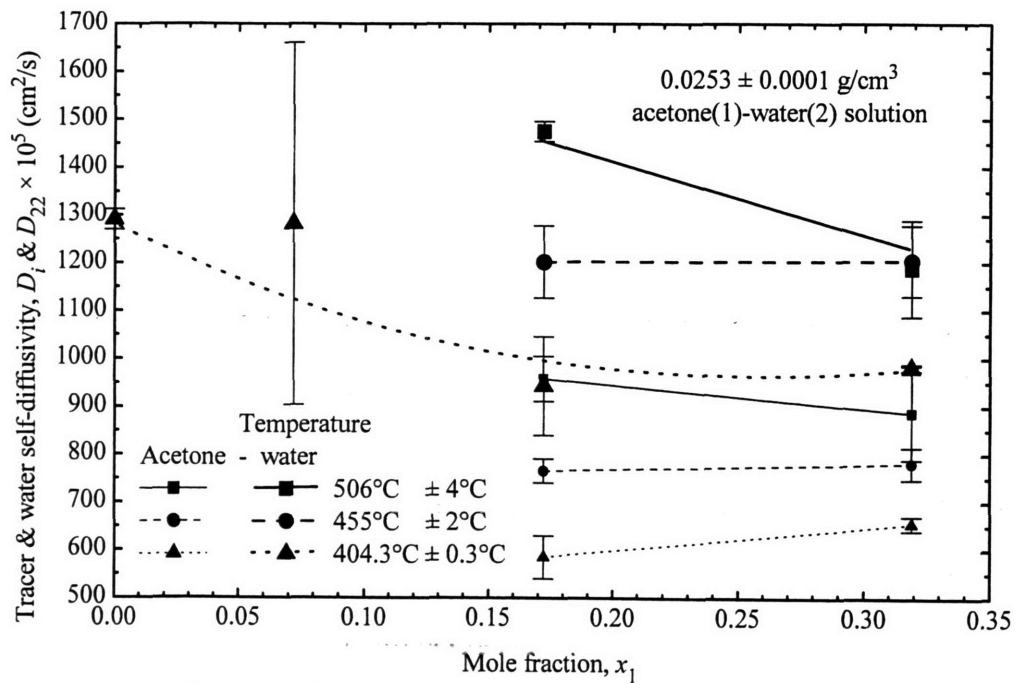
Figure 112. Acetone and water diffusivities for several isotherms as a function of concentration for 0.025 g/cm^3 (with 95%-confidence-interval uncertainties). Curves are intended to show general trends.
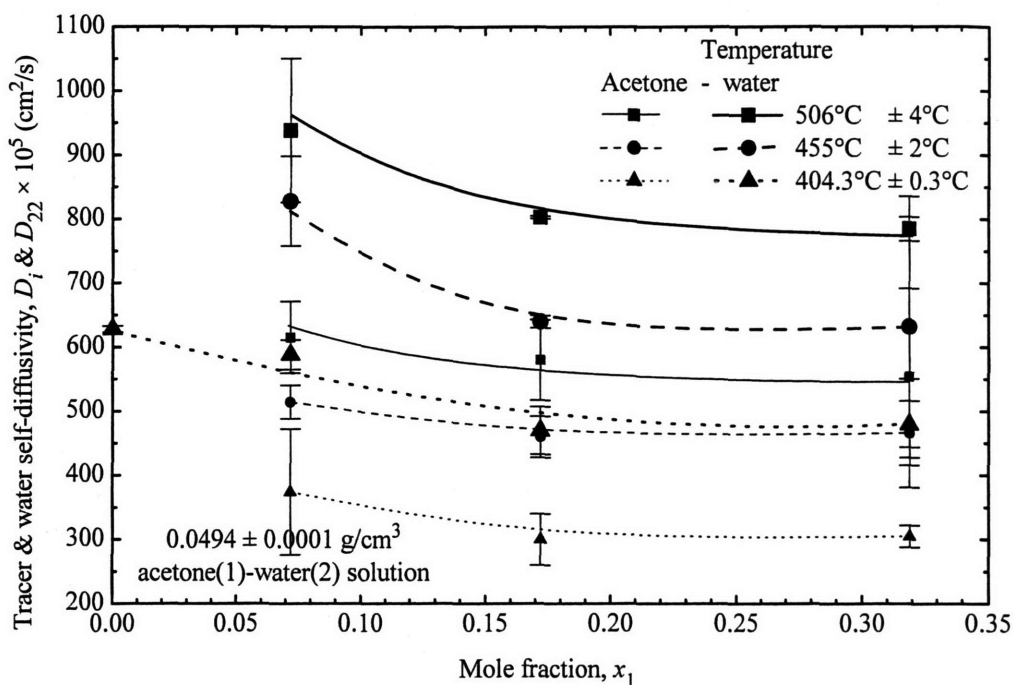
Figure 113. Acetone and water diffusivities for several isotherms as a function of concentration for 0.049 g/cm^3 (with 95%-confidence-interval uncertainties). Curves are intended to show general trends.
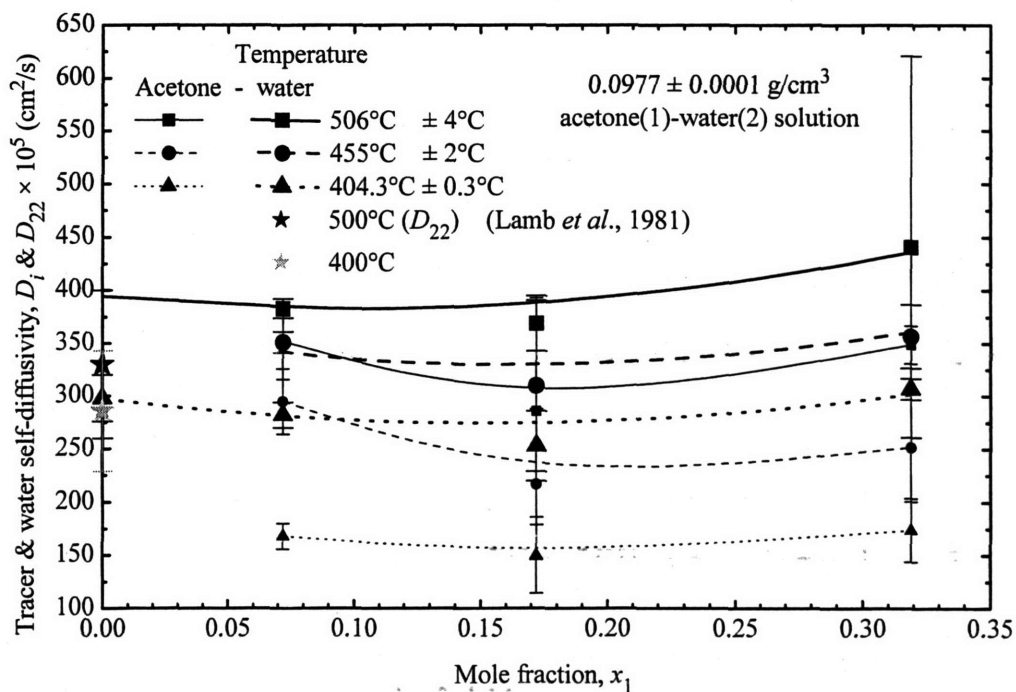
Figure 114. Acetone and water diffusivities for several isotherms as a function of concentration for 0.098 g/cm^3 (with 95%-confidence-interval uncertainties). Curves are intended to show general trends.

II.4.3 Binary Organic Aqueous Mixture Results with Mixture Densities

In order to correct the density representation for mixture diffusivities when acetone is present and to avoid the use of calculated-pure-water densities, the mixture densities can either be measured or estimated for all of the experimental process conditions. Experimental density data are not available, so mixture densities will be estimated using an equation of state. As shown in the first part of this dissertation, EOS predictions can be inaccurate, so caution must be employed when relying on EOS results, even when an EOS has been validated with experimental data.

In an attempt to identify a suitable EOS that could predict mixture densities for the acetone-water diffusivity experiments, several EOSs were examined. The first tests were performed on pure water since water is the major component in the experiments performed. Furthermore, since acetone and water have similar properties (*e.g.*, polar, hydrogen bonded, reasonably close critical temperatures, and completely miscible) and since acetone *PVT* data is scarce, identifying an EOS with accurate water predictions is an appropriate first step in identifying an EOS for mixture-density predictions. Water predictions were compared to reference values calculated with the NIST Steam-Table EOS at the experimental process conditions (NIST, 1996). Starting with the Ideal-Gas Law and comparing its density ratio with the Steam-Table EOS, the extent of ideality was found to be low in the supercritical region (density ratio = $0.70 \pm 0.40_{95\%}$), as is evident in Table 38. The Ideal-Gas Law is a poor choice for modeling dense fluids.

An EOS that has more accurate dense-fluid property predictions and that is recommended for SCWO applications is the Schwartzentruber-Renon EOS (Peneloux *et al.*, 1982; Modell *et al.*, 2000). Often referred to as the SR-POLAR EOS, this EOS has six-regressed-parameters (c_0, c_1, c_2, q_0, q_1, q_2) and reduces to the RKS EOS when five parameters are set to zero (denominator parameter c_2 should not be set to zero) (Aspen Technology, 1994).

$$P = \frac{RT}{V + c - b} - \frac{a}{(V + c)(V + c + b)} \tag{176}$$

Table 38. Pure water density predictions for the SCW/NMR mixture process conditions for several EOSs including subcritical-water, **supercritical-water**, and *overall* statistics

Temperature, T (°C)	Pressure, P (bar)	Calculated-pure-water density, ρ_2 (g/cm³) (NIST, 1996)	Ideal-gas-law water density ratio, ρ_2^{ID}/ρ_2	Untranslated SR-POLAR water density ratio, ρ_2^{SRUT}/ρ_2	Translated SR-POLAR^M water density ratio, ρ_2^{SRM}/ρ_2	Translated two-point-fit SR-POLAR water density ratio, ρ_2^{SR}/ρ_2
408.7	70.2	0.0246	0.905	1.009	1.033	1.033
404.4	125.2	0.0494	0.811	0.992	1.042	1.042
403.8	199.8	0.0977	0.654	0.962	1.067	1.066
403.2	**240.7**	**0.1436**	**0.537**	**0.918**	**1.080**	**1.079**
404.1	**263.9**	**0.1820**	**0.464**	**0.892**	**1.116**	**1.116**
402.2	**278.5**	**0.2336**	**0.382**	**0.799**	**1.054**	**1.054**
404.4	**289.6**	**0.2581**	**0.359**	**0.804**	**1.099**	**1.099**
455.3	140.8	0.0494	0.848	1.151	1.055	1.055
456.5	236.6	0.0973	0.722	1.307	1.103	1.103
505.8	154.6	0.0491	0.877	1.313	1.057	1.057
504.0	**271.3**	**0.0988**	**0.765**	**1.761**	**1.094**	**1.094**
402.5	70.2	0.0250	0.902	0.994	1.019	1.019
402.5	125.3	0.0497	0.809	0.986	1.036	1.036
403.1	199.9	0.0983	0.651	0.956	1.061	1.060
404.3	**240.7**	**0.1418**	**0.543**	**0.929**	**1.093**	**1.092**
404.1	**264.2**	**0.1835**	**0.461**	**0.888**	**1.112**	**1.111**
404.4	278.2	0.2171	0.410	0.858	1.131	1.131
404.3	288.9	0.2547	0.363	0.809	1.104	1.104
452.7	79.8	0.0260	0.917	1.105	1.025	1.025
455.2	140.3	0.0492	0.848	1.150	1.054	1.054
454.7	237.2	0.0984	0.718	1.300	1.096	1.095
500.9	81.7	0.0244	0.935	1.206	1.021	1.021
504.8	155.0	0.0494	0.874	1.309	1.054	1.054
504.8	**271.1**	**0.0985**	**0.767**	**1.765**	**1.097**	**1.097**
402.8	70.5	0.0251	0.902	0.996	1.020	1.020
403.0	125.6	0.0497	0.809	0.987	1.037	1.037
404.0	200.0	0.0975	0.657	0.965	1.071	1.070
404.2	**241.1**	**0.1421**	**0.543**	**0.931**	**1.095**	**1.095**
404.1	**264.4**	**0.1840**	**0.460**	**0.886**	**1.110**	**1.110**
404.3	**279.1**	**0.2202**	**0.405**	**0.853**	**1.127**	**1.127**
403.7	**289.0**	**0.2622**	**0.353**	**0.787**	**1.074**	**1.074**
456.2	76.4	0.0246	0.923	1.110	1.030	1.030
455.3	140.4	0.0492	0.848	1.150	1.054	1.054
456.0	236.7	0.0975	0.721	1.305	1.101	1.101
504.8	84.4	0.0252	0.934	1.215	1.027	1.027
506.5	155.6	0.0494	0.875	1.315	1.057	1.057
506.6	**271.3**	**0.0979**	**0.770**	**1.780**	**1.105**	**1.104**
Subcritical water		mean:	0.83	1.12	1.05	1.05
Subcritical water		$\sigma_{95\%}$:	0.19	0.27	0.05	0.05
Supercritical water		**mean:**	**0.52**	**1.08**	**1.10**	**1.10**
Supercritical water		$\sigma_{95\%}$:	**0.31**	**0.80**	**0.04**	**0.04**
Overall		*mean:*	*0.70*	*1.09*	*1.07*	*1.07*
Overall		$\sigma_{95\%}$:	*0.40*	*0.52*	*0.07*	*0.07*

$$c = c_0 + \frac{c_1}{1 + c_2 - T_r} \qquad \text{for } T_r \leq 1$$

$$c = b + \frac{c_1 \left(\dfrac{c_2\{c_0 - b\}}{c_1} + 1 \right)^2}{1 + c_2 \left(\dfrac{c_2\{c_0 - b\}}{c_1} + 1 \right) - T_r} \qquad \text{for } T_r > 1 \tag{177}$$

$$a = 0.45724 \alpha R^2 T_c^2 / P_c \tag{178}$$

$$b = 0.08664 R T_c / P_c \tag{179}$$

$$\sqrt{\alpha} = 1 + \left(0.48508 + 1.55171\omega - 0.15613\omega^2\right)\left(1 - \sqrt{T_r}\right) - q_0\left(1 - \sqrt{T_r}\right)\left(1 + q_1 T_r + q_2 T_r^2\right)$$

$$\sqrt{\alpha} = \exp\left(\left(1 - T_r^d\right)\left(1 - \frac{1}{d}\right)\right) \quad \text{for } T_r > 1 \qquad \uparrow \text{ for } T_r \leq 1 \uparrow \tag{180}$$

$$d = 1 + \frac{\left(0.48508 + 1.55171\omega - 0.15613\omega^2\right)}{2} - q_0\left(1 + q_1 + q_2\right)$$

For mixtures, Lorentz-Berthelot combining rules are used to develop mixture relations

$$a = \sum_i \sum_j x_i x_j \sqrt{a_i a_j}\left(1 - k_{a,ij} - l_{ij}\left(x_i - x_j\right)\right) \tag{181}$$

$$b = \sum_i \sum_j x_i x_j \left(\frac{b_i + b_j}{2}\right)\left(1 - k_{b,ij}\right) \tag{182}$$

$$c = \sum_i x_i c_i \tag{183}$$

where the following binary-interaction parameters can be regressed, *e.g.*, to phase-equilibria data

$$k_{a,ij} = k_{a0,ij} + k_{a1,ij}T + k_{a2,ij}/T \tag{184}$$

$$l_{ij} = l_{0,ij} + l_{1,ij}T + l_{2,ij}/T \tag{185}$$

$$k_{b,ij} = k_{b0,ij} + k_{b1,ij}T + k_{b2,ij}/T \tag{186}$$

$$k_{a,ij} = k_{a,ji} \tag{187}$$

$$l_{ij} = -l_{ji} \tag{188}$$

$$k_{b,ij} = k_{b,ji} \tag{189}$$

Density improvements are possible with the use of three regressed volume-translation parameters (c_0, c_1, c_2). In Aspen Plus^{TM}, these parameters can be simultaneously regressed with the three other parameters (q_0, q_1, q_2,), which are automatically regressed to vapor pressures generated from the extended Antoine formulation. With the untranslated SR-POLAR EOS, the Table 38 water-density ratio is closer to unity, but has a large range (ratio = $1.09 \pm 0.52_{95\%}$) and significant deviations (ratios ≤ 1.8), implying that this EOS does not significantly improve upon the Ideal-Gas Law. The untranslated SR-POLAR parameters are listed in Table 39.

Using the SR-POLAR parameters optimized by Modell *et al.* (2000) with several hundred density and enthalpy data points, the water-density ratio for the SR-POLAR^M is $1.07 \pm 0.07_{95\%}$ which is a significant improvement over the previously discussed EOSs. The SR-POLAR^M parameters are also shown in Table 39, but its optimization approach is not suitable for acetone since hundreds of acetone data points are not available.

Since acetone data points are available at ambient conditions, the SR-POLAR EOS for water was re-regressed using several ambient water data points in order to check the two-point-fit SR-POLAR EOS for water. Specifically, the six SR-POLAR water parameters were re-regressed using only two ambient liquid density points ($P = 1$ bar, $T = 25°C$ & $90°C$, $\rho = 0.997$ g/cm^3 & 0.965 g/cm^3) and Antoine vapor pressures. The resulting translated-water SR-POLAR

Table 39. SR-POLAR parameters regressed for the EOS mixture-density analysis*

Parameter	Untranslated-water SR-POLAR	Translated-water SR-POLAR^M (^{M} = Modell *et al.*, 2000)	Translated-water SR-POLAR (two point fit)	Translated-acetone SR-POLAR (two point fit)	Translated-ethanol SR-POLAR (two point fit)
c_0	-	−0.00149	−0.00114	0.0118	0.00704
c_1	-	0.00702	0.00711	0.00320	0.00155
c_2	-	0.446	0.466	0.0509	0.0117
q_0	0.0670	0.0671	0.0412	−0.332	−0.393
q_1	−0.630	−0.630	0.236	0.0609	−0.0447
q_2	−1.15	−1.15	1.60	−1.89	−1.85

*Pure component parameters used for the simulations, $\omega_{acetone} = 0.306$ and $\omega_{water} = 0.345$. Critical constants are listed in Table 33.

parameters are similar to the SR-POLAR^M volume-translated parameters and are listed in Table 39. The overall water-density ratios for the process conditions are the same as shown in Table 38 (ratio = $1.07 \pm 0.07_{95\%}$), implying that when the SR-POLAR EOS is regressed with two ambient densities and vapor pressures, the translated SR-POLAR EOS can be extrapolated to supercritical conditions with acceptable density errors (<10%) for fluids behaving like water. Using the same approach, two ambient densities for acetone (P = 1 bar, T = 25°C & 50°C, ρ = 0.785 g/cm^3 & 0.756 g/cm^3), along with ASPEN PLUS™ vapor pressures, were used to regress the six SR-POLAR parameters for pure acetone. The parameters for acetone are presented in Table 39. Unfortunately, the acetone SR-POLAR predictions at the experimental process conditions cannot be verified since experimental PVT data are not available at these PT conditions.

Since densities of pure water (Steam-Table, SR-POLAR^M, and SR-POLAR) and pure acetone are now made, the next activity is to determine the mixture density. For non-ideal solutions, volumetric changes due to mixing exist, thereby requiring that partial volumetric properties be used to determine the mixture volume

$$V = \sum_i x_i \hat{V}_i \ \ e.g., \text{for a binary mixture}, V_{12} = x_1 \hat{V}_1 + x_2 \hat{V}_2 = x_1 \left(\frac{\partial N V}{\partial N_1} \right)_{P,T} + x_2 \left(\frac{\partial N V}{\partial N_2} \right)_{P,T} \quad (190)$$

Another approach to determine the mixture volume is to use the volume change attributed to mixing which is often referred to as the excess volume

$$V = V_{12} = x_1 V_1 + x_2 V_2 + V^E \quad (191)$$

One advantage to this approach is that pure species volumes are used instead of partial molar volumes, however excess properties are also scarce. Without these non-ideality corrections, these mixture formulae reduce to formulae reserved for ideal solutions.

Another approach is to use combining rules. Some combining rules have a rational basis, while others are completely empirical. Options include weighting volume, mass, or density (inverted volume) while the scaling could be by mass, mole, or volume fractions. The Lorentz-Berthelot combining rule is often used and treats the mixture as an ideal solution of pure species weighted by their respective mole fractions

$$V = \sum_i x_i V_i, \text{ e.g., for a binary mixture, } V = V_{12} = x_1 V_1 + x_2 V_2 \qquad (192)$$

For a binary system, the mixture-density would be

$$\rho = \rho_{12} = \frac{x_1 MW_1 + x_2 MW_2}{x_1 \dfrac{MW_1}{\rho_1} + x_2 \dfrac{MW_2}{\rho_2}} \qquad (193)$$

In order to identify an appropriate mixture method for determining mixture densities of the acetone-water system, methods were compared using experimental PVT data. Since experimental data are not available for the acetone-water system, high pressure and high temperature data for another aqueous hydrogen-bonded-organic system were used. Safarov and Shakhverdiev (2001) report mixture densities for several concentrated (25, 50, and 75 wt.%$_1$) ethanol(1)-water(2) solutions from 1–600 bar and 25–250°C. Their data are presented in Table 40 and are estimated to have a 0.05–0.10% error. Using these densities, the mixture-density approaches can be evaluated. Since pure ethanol parameters are needed for the SR-POLAR EOS, two ambient densities ($P = 1$ bar, $T = 25$°C & 70°C, $\rho = 0.787$ g/cm^3 & 0.740 g/cm^3) are used to determine these parameters, which are summarized in Table 39.

Before testing the mixture-density approaches, pure water density ratios were calculated using the SR-POLAR and Steam-Table EOSs in order to check the robustness of the SR-POLAR EOS. The average density ratios of the untranslated and volume-translated SR-POLAR EOSs are $0.73 \pm 0.02_{95\%}$ and $1.00 \pm 0.02_{95\%}$, respectively, indicating that the two-point volume-translated SR-POLAR EOS is accurate for dense fluids (see Table 41 for the pure water volume-translated density ratios). Next, the Lorentz-Berthelot combining rule was evaluated with the ethanol-water PVT data:

- SR-POLAR ethanol(1) and Steam-Table water(2) volumes weighted by mole fractions and

- SR-POLAR ethanol(1) and SR-POLAR water(2) volumes weighted by mole fractions

Table 40. Experimental ethanol(1)-water(2) solution mixture densities at several concentrations, temperatures, and pressures (Safarov and Shakhverdiev, 2001)

Acetone concentration (wt.%$_1$) = x_1	Temperature, T (°C)	Pressure, P (bar)							
		1	50	100	200	300	400	500	600
		Mixture density, ρ_{12} (g/cm^3)							
25 = 0.115	25	0.958	0.960	0.962	0.965	0.969	0.972	0.976	0.980
25 = 0.115	50	0.939	0.942	0.945	0.950	0.953	0.957	0.961	0.966
25 = 0.115	75	0.919	0.922	0.925	0.930	0.935	0.939	0.943	0.948
25 = 0.115	100		0.902	0.905	0.911	0.916	0.921	0.925	0.930
25 = 0.115	125		0.879	0.883	0.891	0.897	0.903	0.909	0.915
25 = 0.115	150		0.850	0.855	0.864	0.873	0.880	0.886	0.893
25 = 0.115	175		0.812	0.820	0.833	0.845	0.855	0.863	0.872
25 = 0.115	200		0.771	0.781	0.799	0.814	0.826	0.838	0.848
25 = 0.115	250		0.642	0.659	0.704	0.735	0.759	0.777	0.793
50 = 0.281	25	0.909	0.911	0.914	0.918	0.923	0.926	0.932	0.935
50 = 0.281	50	0.888	0.890	0.893	0.898	0.902	0.908	0.913	0.917
50 = 0.281	75	0.864	0.868	0.871	0.878	0.884	0.889	0.895	0.900
50 = 0.281	100		0.845	0.849	0.856	0.862	0.868	0.875	0.881
50 = 0.281	125		0.819	0.823	0.831	0.838	0.845	0.851	0.858
50 = 0.281	150		0.789	0.795	0.805	0.813	0.821	0.827	0.835
50 = 0.281	175		0.748	0.761	0.778	0.790	0.799	0.806	0.812
50 = 0.281	200		0.699	0.712	0.734	0.755	0.767	0.778	0.787
50 = 0.281	250			0.555	0.625	0.663	0.690	0.711	0.724
75 = 0.540	25	0.854	0.857	0.860	0.866	0.871	0.876	0.880	0.885
75 = 0.540	50	0.831	0.835	0.838	0.844	0.850	0.856	0.861	0.867
75 = 0.540	75	0.809	0.813	0.817	0.824	0.830	0.837	0.843	0.850
75 = 0.540	100		0.789	0.793	0.801	0.809	0.816	0.823	0.830
75 = 0.540	125		0.760	0.766	0.777	0.787	0.796	0.805	0.812
75 = 0.540	150		0.725	0.734	0.749	0.763	0.774	0.785	0.794
75 = 0.540	175		0.680	0.693	0.715	0.732	0.747	0.759	0.771
75 = 0.540	200		0.627	0.646	0.676	0.698	0.716	0.732	0.745
75 = 0.540	250			0.506	0.575	0.619	0.649	0.673	0.693

Table 41. Pure water density ratio of the volume-translated SR-POLAR and Steam-Table EOSs at the experimental Safarov and Shakhverdiev (2001) process conditions (NIST, 1996)

Temperature, T (°C)	Pressure, P (bar)							
	1	50	100	200	300	400	500	600
	Pure water density ratio, ρ_2^{SR} / ρ_2							
25	1.000	0.999	0.998	0.996	0.993	0.991	0.989	0.987
50	0.998	0.998	0.997	0.995	0.994	0.993	0.991	0.990
75	0.999	0.999	0.998	0.997	0.997	0.996	0.995	0.994
100		1.001	1.001	1.000	1.000	1.000	1.000	0.999
125		1.003	1.003	1.004	1.004	1.005	1.005	1.006
150		1.005	1.006	1.007	1.009	1.010	1.011	1.013
175		1.005	1.007	1.010	1.013	1.015	1.018	1.020
200		1.004	1.006	1.011	1.016	1.020	1.024	1.027
250		0.987	0.994	1.006	1.017	1.026	1.034	1.041
Mean:	0.9991	1.000	1.001	1.003	1.005	1.01	1.01	1.02
$\sigma_{95\%}$:	0.0004	0.006	0.005	0.005	0.008	0.01	0.01	0.02
Overall:	$1.00 \pm 0.02_{95\%}$							

which resulted in mixture density ratios of $1.11 \pm 0.28_{95\%}$ and $1.11 \pm 0.29_{95\%}$, respectively, for the 196 mixture-density points compared. Ratios for these two cases are summarized in Table 42 and Table 43. Given the large density-ratio variations observed with the mole-fraction weighted volumes especially between 50 and 300 bar, which is the process pressure range used for the NMR diffusivity experiments, other density-weighting approaches were investigated.

When the pure component densities are weighted by their respective mole fractions,

$$\rho = \sum_i x_i \rho_i \ \ e.g., \text{for a binary mixture}, \rho = \rho_{12} = x_1 \rho_1 + x_2 \rho_2 \tag{194}$$

the average SR-POLAR(1)-Steam-Table(2) density ratio is $1.05 \pm 0.06_{95\%}$ while the average SR-POLAR(1)-SR-POLAR(2) density ratio is $1.06 \pm 0.07_{95\%}$. The individual density ratios are presented in Table 44 and Table 45 and do not exhibit the large variations that were evident with weighted-volume approaches. The density-weighted mixture method is superior to the volume-weighted approach for the ethanol-water system evaluated and has acceptable error for dense fluids, which are usually difficult to predict.

By employing mixing and combining rules, EOSs can also calculate mixture properties by treating a mixture as a pseudo-single component. As shown in Eq. (184) through Eq. (189), the SR-POLAR model uses combining rules for evaluating its a, b, and c terms, and was tested for its ethanol-water density predictions. With all of the binary-interaction parameters set to zero

287

(by default), the average density ratio of the SR-POLAR(12) EOS is $0.96 \pm 0.06_{95\%}$ for the ratios shown Table 46. Without binary parameters, the SR-POLAR(12) EOS is slightly more accurate than the previously discussed EOSs for the dense ethanol-water system investigated.

Another option is to regress the binary-interaction parameters, but as previously discussed, binary data at the conditions of interest are not available. As reported by Modell *et al.* (2000), another approach that is included in ASPEN PLUS™ is to fit these parameters to activity coefficients generated from internal UNIFAQ correlations. Since these activity coefficients are based on ambient temperature data with low, vapor-like and high, liquid-like densities, the resulting SR-POLAR EOS densities at intermediate supercritical densities are interpolated densities, not extrapolated. Using this approach, the ethanol-water binary parameters were estimated to be $k_{0,ij} = -0.0656$, $k_{2,ij} = -1.46$, $l_{0,ij} = 0.0754$, and $l_{2,ij} = -19.0$. As shown in Table 47, the average density ratio of the SR-POLAR(12) EOS with binary parameters is $0.98 \pm 0.06_{95\%}$, a slight improvement over the zeroed binary-parameter predictions. Note that the binary parameters appear to only offset the density as indicated by the same uncertainty. So, for the dense ethanol-water system investigated, the SR-POLAR(12) EOSs with or without binary parameters are slightly better than the SR-POLAR(1)-Steam-Table(2) EOS and SR-POLAR(1)-SR-POLAR(2) EOS mixture approaches previously discussed.

Table 42. SR-POLAR(1)-Steam-Table(2) volume-weighted mixture-density ratios at several concentrations, temperatures, and pressures (NIST, 1996; Safarov and Shakhverdiev, 2001)

Ethanol concentration (wt.%$_1$) = x_1	Temperature, T (°C)	Pressure, P (bar)							
		1	50	100	200	300	400	500	600
		Mixture-density ratio, $\rho_1^{SR\ STM}/\rho_{12}$							
25 = 0.115	25	0.975	1.041	0.920	0.871	1.043	1.043	1.043	1.043
25 = 0.115	50	0.980	0.917	1.050	0.866	1.050	1.050	1.050	1.049
25 = 0.115	75	0.981	0.913	0.856	1.058	1.056	1.056	1.056	1.055
25 = 0.115	100		0.904	0.844	1.062	1.061	1.060	1.059	1.059
25 = 0.115	125		0.891	0.830	1.065	1.063	1.061	1.059	1.057
25 = 0.115	150		0.878	0.816	1.074	1.069	1.066	1.064	1.061
25 = 0.115	175		0.866	0.808	1.085	1.077	1.071	1.067	1.062
25 = 0.115	200		0.848	0.809	1.099	1.087	1.078	1.071	1.065
25 = 0.115	250		0.415	0.629	1.159	1.123	1.100	1.084	1.072
	Mean:	0.979	0.9	0.8	1.0	1.07	1.07	1.06	1.058
	$\sigma_{95\%}$:	0.003	0.2	0.1	0.1	0.02	0.02	0.01	0.009
50 = 0.281	25	0.968	1.097	0.915	1.095	1.094	1.095	1.093	1.093
50 = 0.281	50	0.969	0.912	1.111	1.109	1.109	1.107	1.105	1.104
50 = 0.281	75	0.969	0.907	1.124	1.120	1.118	1.115	1.112	1.110
50 = 0.281	100		0.896	1.134	1.130	1.127	1.124	1.120	1.117
50 = 0.281	125		0.882	1.147	1.142	1.138	1.134	1.131	1.127
50 = 0.281	150		0.864	1.160	1.152	1.147	1.142	1.139	1.134
50 = 0.281	175		0.849	1.181	1.162	1.152	1.147	1.142	1.141
50 = 0.281	200		0.832	1.224	1.196	1.172	1.162	1.153	1.148
50 = 0.281	250			1.451	1.306	1.246	1.209	1.185	1.174
	Mean:	0.969	0.91	1.2	1.16	1.15	1.14	1.13	1.13
	$\sigma_{95\%}$:	0.001	0.08	0.1	0.06	0.05	0.03	0.03	0.03
75 = 0.540	25	0.972	1.166	1.164	1.162	1.160	1.158	1.158	1.155
75 = 0.540	50	0.973	1.186	1.184	1.181	1.177	1.173	1.171	1.168
75 = 0.540	75	0.966	1.202	1.199	1.194	1.190	1.185	1.181	1.176
75 = 0.540	100		1.218	1.214	1.207	1.201	1.196	1.191	1.186
75 = 0.540	125		1.239	1.232	1.221	1.211	1.204	1.196	1.190
75 = 0.540	150		1.268	1.256	1.238	1.223	1.212	1.201	1.193
75 = 0.540	175		1.316	1.295	1.266	1.243	1.226	1.213	1.201
75 = 0.540	200		1.383	1.349	1.299	1.267	1.244	1.225	1.212
75 = 0.540	250			1.593	1.419	1.334	1.285	1.252	1.227
	Mean:	0.971	1.25	1.3	1.24	1.22	1.21	1.20	1.19
	$\sigma_{95\%}$:	0.004	0.07	0.1	0.08	0.05	0.04	0.03	0.02

Overall: $1.11 \pm 0.28_{95\%}$

289

Table 43. SR-POLAR(1)-SR-POLAR(2) volume-weighted mixture-density ratios at several concentrations, temperatures, and pressures (Safarov and Shakhverdiev, 2001)

Ethanol concentration (wt.%$_1$) = x_1	Temperature, T (°C)	Pressure, P (bar)							
		1	50	100	200	300	400	500	600
		Mixture-density ratio, $\rho_1^{SR} \rho_2^{SR} / \rho_{12}$							
25 = 0.115	25	0.975	1.040	0.919	0.870	1.036	1.034	1.032	1.030
25 = 0.115	50	0.979	0.916	1.047	0.865	1.043	1.042	1.041	1.038
25 = 0.115	75	0.980	0.912	0.856	1.055	1.053	1.052	1.050	1.048
25 = 0.115	100		0.904	0.844	1.063	1.061	1.060	1.059	1.058
25 = 0.115	125		0.892	0.830	1.070	1.068	1.066	1.064	1.063
25 = 0.115	150		0.879	0.817	1.082	1.079	1.076	1.076	1.074
25 = 0.115	175		0.868	0.809	1.096	1.091	1.087	1.086	1.083
25 = 0.115	200		0.849	0.810	1.111	1.104	1.100	1.096	1.093
25 = 0.115	250		0.414	0.629	1.166	1.142	1.128	1.121	1.116
	Mean:	0.978	0.9	0.8	1.0	1.08	1.07	1.07	1.07
	$\sigma_{95\%}$:	0.002	0.2	0.1	0.1	0.03	0.03	0.03	0.03
50 = 0.281	25	0.968	1.095	0.914	1.091	1.087	1.086	1.081	1.080
50 = 0.281	50	0.969	0.912	1.108	1.104	1.102	1.098	1.095	1.093
50 = 0.281	75	0.969	0.907	1.122	1.117	1.114	1.111	1.107	1.104
50 = 0.281	100		0.896	1.135	1.130	1.127	1.124	1.120	1.116
50 = 0.281	125		0.883	1.150	1.146	1.143	1.140	1.137	1.133
50 = 0.281	150		0.865	1.167	1.161	1.157	1.153	1.153	1.149
50 = 0.281	175		0.850	1.189	1.173	1.167	1.164	1.163	1.163
50 = 0.281	200		0.833	1.232	1.210	1.190	1.185	1.180	1.179
50 = 0.281	250			1.443	1.314	1.266	1.240	1.225	1.222
	Mean:	0.968	0.91	1.2	1.16	1.15	1.15	1.14	1.14
	$\sigma_{95\%}$:	0.001	0.08	0.2	0.07	0.05	0.05	0.05	0.05
75 = 0.540	25	0.972	1.165	1.161	1.156	1.153	1.148	1.145	1.140
75 = 0.540	50	0.973	1.184	1.181	1.175	1.170	1.164	1.161	1.156
75 = 0.540	75	0.966	1.200	1.197	1.191	1.186	1.179	1.175	1.169
75 = 0.540	100		1.219	1.215	1.208	1.201	1.196	1.191	1.186
75 = 0.540	125		1.242	1.236	1.226	1.217	1.210	1.202	1.197
75 = 0.540	150		1.274	1.264	1.248	1.233	1.224	1.215	1.208
75 = 0.540	175		1.323	1.304	1.278	1.259	1.245	1.234	1.225
75 = 0.540	200		1.388	1.357	1.313	1.287	1.269	1.254	1.245
75 = 0.540	250			1.584	1.428	1.357	1.319	1.294	1.277
	Mean:	0.971	1.25	1.3	1.25	1.23	1.22	1.21	1.20
	$\sigma_{95\%}$:	0.004	0.08	0.1	0.08	0.06	0.05	0.05	0.04

Overall: $1.11 \pm 0.29_{95\%}$

Table 44. SR-POLAR(1)-Steam-Table(2) <u>density-weighted</u> mixture-density ratios at several concentrations, temperatures, and pressures (NIST, 1996; Safarov and Shakhverdiev, 2001)

Ethanol concentration (wt.%$_1$) = x_1	Temperature, T (°C)	Pressure, P (bar)							
		1	50	100	200	300	400	500	600
		Mixture-density ratio, $\rho_1^{SR\ STM}{}_2 / \rho_{12}$							
25 = 0.115	25	1.015	1.016	1.016	1.017	1.018	1.018	1.019	1.019
25 = 0.115	50	1.024	1.024	1.023	1.023	1.024	1.024	1.024	1.023
25 = 0.115	75	1.031	1.030	1.029	1.029	1.029	1.029	1.029	1.028
25 = 0.115	100		1.033	1.032	1.032	1.032	1.032	1.032	1.032
25 = 0.115	125		1.036	1.035	1.033	1.033	1.032	1.031	1.030
25 = 0.115	150		1.042	1.041	1.040	1.038	1.036	1.036	1.035
25 = 0.115	175		1.057	1.055	1.050	1.046	1.043	1.041	1.038
25 = 0.115	200		1.074	1.072	1.065	1.060	1.056	1.052	1.049
25 = 0.115	250		1.131	1.145	1.100	1.073	1.055	1.043	1.034
	Mean:	1.02	1.05	1.05	1.04	1.04	1.04	1.03	1.03
	$\sigma_{95\%}$:	0.02	0.07	0.08	0.05	0.04	0.03	0.02	0.02
50 = 0.281	25	1.032	1.032	1.031	1.031	1.031	1.032	1.029	1.030
50 = 0.281	50	1.041	1.041	1.041	1.041	1.041	1.040	1.038	1.038
50 = 0.281	75	1.050	1.049	1.048	1.046	1.046	1.045	1.044	1.043
50 = 0.281	100		1.052	1.052	1.052	1.051	1.051	1.049	1.048
50 = 0.281	125		1.056	1.057	1.058	1.058	1.059	1.059	1.057
50 = 0.281	150		1.062	1.062	1.064	1.065	1.066	1.068	1.066
50 = 0.281	175		1.078	1.074	1.070	1.071	1.074	1.076	1.079
50 = 0.281	200		1.103	1.109	1.108	1.101	1.104	1.104	1.107
50 = 0.281	250		1.224	1.144	1.110	1.089	1.075	1.072	
	Mean:	1.04	1.06	1.08	1.07	1.06	1.06	1.06	1.06
	$\sigma_{95\%}$:	0.02	0.05	0.12	0.07	0.05	0.05	0.05	0.05
75 = 0.540	25	1.034	1.034	1.033	1.031	1.031	1.029	1.029	1.027
75 = 0.540	50	1.043	1.042	1.041	1.040	1.038	1.037	1.036	1.034
75 = 0.540	75	1.044	1.044	1.044	1.043	1.043	1.042	1.041	1.039
75 = 0.540	100		1.045	1.045	1.046	1.046	1.047	1.046	1.045
75 = 0.540	125		1.046	1.048	1.049	1.050	1.050	1.049	1.049
75 = 0.540	150		1.051	1.053	1.056	1.055	1.056	1.055	1.055
75 = 0.540	175		1.066	1.070	1.074	1.075	1.076	1.077	1.076
75 = 0.540	200		1.088	1.105	1.115	1.121	1.124	1.126	1.129
75 = 0.540	250		1.114	1.081	1.055	1.040	1.030	1.021	
	Mean:	1.04	1.05	1.06	1.06	1.06	1.06	1.05	1.05
	$\sigma_{95\%}$:	0.01	0.03	0.06	0.05	0.05	0.06	0.06	0.07

<u>Overall:</u> $1.05 \pm 0.06_{95\%}$

Table 45. SR-POLAR(1)-SR-POLAR(2) <u>density-weighted</u> mixture-density ratios at several concentrations, temperatures, and pressures (Safarov and Shakhverdiev, 2001)

Ethanol concentration (wt.%$_1$) = x_1	Temperature, T (°C)	Pressure, P (bar)							
		1	50	100	200	300	400	500	600
		Mixture-density ratio, $\rho_1^{SR}\rho_2^{SR}/\rho_{12}$							
25 = 0.115	25	1.015	1.015	1.014	1.013	1.012	1.010	1.009	1.007
25 = 0.115	50	1.023	1.022	1.020	1.018	1.018	1.017	1.016	1.014
25 = 0.115	75	1.030	1.028	1.028	1.027	1.025	1.025	1.024	1.023
25 = 0.115	100		1.034	1.033	1.032	1.032	1.032	1.032	1.031
25 = 0.115	125		1.038	1.038	1.037	1.037	1.037	1.036	1.035
25 = 0.115	150		1.047	1.047	1.047	1.046	1.046	1.047	1.047
25 = 0.115	175		1.063	1.062	1.060	1.058	1.057	1.058	1.057
25 = 0.115	200		1.078	1.079	1.077	1.075	1.075	1.075	1.074
25 = 0.115	250		1.117	1.138	1.107	1.090	1.080	1.075	1.073
	Mean:	1.02	1.05	1.05	1.05	1.04	1.04	1.04	1.04
	$\sigma_{95\%}$:	0.01	0.06	0.08	0.06	0.05	0.05	0.05	0.05
50 = 0.281	25	1.032	1.031	1.030	1.028	1.025	1.025	1.021	1.020
50 = 0.281	50	1.040	1.040	1.039	1.037	1.036	1.034	1.031	1.030
50 = 0.281	75	1.049	1.048	1.047	1.044	1.043	1.042	1.040	1.038
50 = 0.281	100		1.053	1.053	1.052	1.052	1.051	1.049	1.047
50 = 0.281	125		1.059	1.060	1.061	1.062	1.063	1.063	1.061
50 = 0.281	150		1.066	1.067	1.070	1.073	1.074	1.077	1.077
50 = 0.281	175		1.082	1.079	1.079	1.082	1.086	1.090	1.095
50 = 0.281	200		1.106	1.114	1.118	1.115	1.120	1.124	1.129
50 = 0.281	250		1.218	1.150	1.125	1.111	1.104	1.107
	Mean:	1.04	1.06	1.1	1.07	1.07	1.07	1.07	1.07
	$\sigma_{95\%}$:	0.02	0.05	0.1	0.08	0.07	0.07	0.07	0.07
75 = 0.540	25	1.034	1.033	1.031	1.029	1.027	1.024	1.023	1.020
75 = 0.540	50	1.042	1.040	1.039	1.038	1.035	1.033	1.032	1.029
75 = 0.540	75	1.043	1.043	1.043	1.042	1.041	1.039	1.038	1.035
75 = 0.540	100		1.045	1.046	1.047	1.046	1.047	1.046	1.045
75 = 0.540	125		1.048	1.049	1.051	1.052	1.053	1.051	1.052
75 = 0.540	150		1.054	1.056	1.060	1.060	1.062	1.062	1.062
75 = 0.540	175		1.069	1.074	1.080	1.083	1.085	1.086	1.087
75 = 0.540	200		1.090	1.109	1.122	1.130	1.136	1.139	1.144
75 = 0.540	250		1.110	1.085	1.065	1.055	1.049	1.045
	Mean:	1.04	1.05	1.06	1.06	1.06	1.06	1.06	1.06
	$\sigma_{95\%}$:	0.01	0.04	0.06	0.06	0.06	0.07	0.07	0.08

Overall: $1.06 \pm 0.07_{95\%}$

292

Table 46. SR-POLAR(12), <u>zero-binary-parameter</u> mixture-density ratios at several concentrations, temperatures, and pressures (Safarov and Shakhverdiev, 2001)

Ethanol concentration (wt.%$_1$) = x_1	Temperature, T (°C)	Pressure, P (bar)							
		1	50	100	200	300	400	500	600
		Mixture-density ratio, $\rho_{12}^{SR} / \rho_{12}$							
25 = 0.115	25	0.969	0.969	0.968	0.968	0.967	0.966	0.964	0.963
25 = 0.115	50	0.972	0.971	0.970	0.969	0.969	0.969	0.968	0.966
25 = 0.115	75	0.975	0.974	0.973	0.973	0.972	0.973	0.972	0.971
25 = 0.115	100		0.974	0.974	0.974	0.975	0.975	0.976	0.976
25 = 0.115	125		0.975	0.975	0.975	0.975	0.976	0.977	0.977
25 = 0.115	150		0.979	0.979	0.980	0.981	0.982	0.984	0.985
25 = 0.115	175		0.992	0.992	0.991	0.991	0.992	0.995	0.996
25 = 0.115	200		1.014	1.013	1.013	1.014	1.017	1.019	1.021
25 = 0.115	250		0.978	0.981	0.961	0.954	0.953	0.954	0.956
	Mean:	0.972	0.98	0.98	0.98	0.98	0.98	0.98	0.98
	$\sigma_{95\%}$:	0.006	0.03	0.03	0.03	0.03	0.04	0.04	0.04
50 = 0.281	25	0.957	0.957	0.956	0.955	0.953	0.953	0.950	0.950
50 = 0.281	50	0.958	0.958	0.958	0.957	0.957	0.956	0.955	0.954
50 = 0.281	75	0.959	0.958	0.958	0.957	0.957	0.957	0.956	0.956
50 = 0.281	100		0.955	0.956	0.957	0.958	0.960	0.959	0.959
50 = 0.281	125		0.952	0.954	0.958	0.961	0.964	0.966	0.967
50 = 0.281	150		0.950	0.953	0.958	0.964	0.969	0.974	0.977
50 = 0.281	175		0.959	0.958	0.961	0.969	0.978	0.986	0.994
50 = 0.281	200		0.985	0.992	1.002	1.006	1.018	1.028	1.038
50 = 0.281	250		0.926	0.903	0.904	0.908	0.912	0.923
	Mean:	0.958	0.96	0.96	0.96	0.96	0.96	0.97	0.97
	$\sigma_{95\%}$:	0.002	0.02	0.03	0.05	0.05	0.06	0.06	0.06
75 = 0.540	25	0.962	0.962	0.961	0.959	0.958	0.956	0.956	0.954
75 = 0.540	50	0.962	0.962	0.961	0.961	0.960	0.959	0.959	0.957
75 = 0.540	75	0.956	0.957	0.957	0.958	0.959	0.959	0.959	0.958
75 = 0.540	100		0.949	0.951	0.954	0.957	0.959	0.960	0.961
75 = 0.540	125		0.942	0.945	0.950	0.954	0.958	0.959	0.962
75 = 0.540	150		0.935	0.940	0.949	0.954	0.960	0.964	0.968
75 = 0.540	175		0.937	0.946	0.960	0.970	0.979	0.986	0.991
75 = 0.540	200		0.949	0.971	0.998	1.018	1.033	1.045	1.056
75 = 0.540	250		0.797	0.847	0.860	0.870	0.877	0.883
	Mean:	0.960	0.95	0.9	0.95	0.95	0.96	0.96	0.97
	$\sigma_{95\%}$:	0.008	0.02	0.1	0.08	0.08	0.08	0.09	0.09

<u>Overall:</u> 0.96 ± 0.06$_{95\%}$

Table 47. SR-POLAR(12), <u>binary-parameter</u> mixture-density ratios at several concentrations, temperatures, and pressures (Safarov and Shakhverdiev, 2001)

Ethanol concentration (wt.%$_1$) = x_1	Temperature, T (°C)	Pressure, P (bar)							
		1	50	100	200	300	400	500	600
		Mixture-density ratio, $\rho_{12}^{SR} / \rho_{12}$							
25 = 0.115	25	0.974	0.974	0.973	0.973	0.971	0.970	0.969	0.967
25 = 0.115	50	0.979	0.978	0.977	0.975	0.975	0.974	0.973	0.971
25 = 0.115	75	0.983	0.982	0.981	0.980	0.979	0.979	0.979	0.977
25 = 0.115	100		0.984	0.983	0.983	0.983	0.983	0.983	0.983
25 = 0.115	125		0.986	0.986	0.985	0.985	0.986	0.985	0.985
25 = 0.115	150		0.993	0.993	0.993	0.993	0.993	0.995	0.995
25 = 0.115	175		1.010	1.009	1.007	1.006	1.006	1.007	1.007
25 = 0.115	200		1.037	1.035	1.032	1.032	1.033	1.034	1.036
25 = 0.115	250		1.017	1.016	0.989	0.978	0.973	0.972	0.973
	Mean:	0.979	1.00	0.99	0.99	0.99	0.99	0.99	0.99
	σ95%:	0.009	0.04	0.04	0.04	0.04	0.04	0.04	0.04
50 = 0.281	25	0.965	0.964	0.963	0.962	0.960	0.960	0.957	0.956
50 = 0.281	50	0.968	0.968	0.967	0.966	0.966	0.964	0.962	0.961
50 = 0.281	75	0.971	0.970	0.969	0.968	0.967	0.967	0.965	0.964
50 = 0.281	100		0.970	0.970	0.970	0.970	0.971	0.970	0.969
50 = 0.281	125		0.970	0.971	0.973	0.975	0.977	0.979	0.978
50 = 0.281	150		0.973	0.974	0.978	0.982	0.985	0.989	0.990
50 = 0.281	175		0.989	0.985	0.986	0.991	0.997	1.003	1.011
50 = 0.281	200		1.028	1.030	1.034	1.034	1.044	1.050	1.059
50 = 0.281	250			0.990	0.945	0.937	0.935	0.936	0.944
	Mean:	0.968	0.98	0.98	0.98	0.98	0.98	0.98	0.98
	σ95%:	0.006	0.04	0.04	0.05	0.05	0.06	0.07	0.07
75 = 0.540	25	0.968	0.967	0.966	0.964	0.963	0.961	0.960	0.958
75 = 0.540	50	0.970	0.969	0.968	0.967	0.966	0.964	0.964	0.962
75 = 0.540	75	0.965	0.965	0.965	0.965	0.966	0.965	0.965	0.963
75 = 0.540	100		0.960	0.961	0.964	0.965	0.967	0.967	0.968
75 = 0.540	125		0.955	0.958	0.961	0.964	0.967	0.968	0.970
75 = 0.540	150		0.954	0.957	0.963	0.967	0.971	0.974	0.977
75 = 0.540	175		0.963	0.969	0.978	0.985	0.992	0.998	1.002
75 = 0.540	200		0.990	1.004	1.023	1.038	1.051	1.060	1.070
75 = 0.540	250			0.856	0.876	0.881	0.886	0.891	0.894
	Mean:	0.967	0.97	0.96	0.96	0.97	0.97	0.97	0.97
	σ95%:	0.005	0.02	0.08	0.08	0.08	0.08	0.09	0.09

<u>Overall:</u> 0.98 ± 0.06$_{95\%}$

294

Given the apparent success of validating the mixture-density approaches, the SR-POLAR(1)-Steam-Table(2) EOS with weighted densities is selected over the SR-POLAR(12) EOS in order to calculate mixture densities for the experiments performed. The reasons are six fold:

1. As shown in Table 48, the average mixture-density ratio calculated for the ethanol-water validation work is reasonable ($0.90 < \rho_{12}^{EOS}/\rho_{12} < 1.10$) and is nearly the best.

2. Overestimating mixture densities (ratio = 1.10 for the ethanol-water system) will allow density effects to be compared in the mutual-diffusivity analysis. Since diffusivities are density dependent and since pure-water-calculated densities underestimate the mixture density, diffusivities based on these density approaches should represent the lowest and highest possible values. Values that are similar imply that pure-water-calculated-based diffusivities are sufficient and mixture-based diffusivities can be represented by the pure-water-based counterparts.

3. By using the Steam-Table EOS for the water component, density inaccuracies will be reduced as the mixture becomes dilute (and eventually becomes pure water) since the Steam-Table EOS is more accurate than the SR-POLAR(12) EOS for pure water predictions. This approach also prevents density discontinuities since they would exist if mixture-density predictions were made using the SR-POLAR(12) EOS for dilute mixtures and then predictions were made using the NIST Steam-Table EOS for pure water.

4. Only two readily available liquid densities are needed (in addition to vapor pressures provided by ASPEN PLUS™ in order to regress the six SR-POLAR pure component parameters.

5. Furthermore, binary parameters would not be needed.

6. The difference in acetone-water mixture-density predictions between the SR-POLAR(12) EOS with and without binary parameters is only -0.2% ± 0.8%$_{95\%}$ for the set of experimental process conditions, indicating that binary parameters do not significantly affect acetone-water mixture densities.

295

With the EOS and mixture-density choices selected, the mixture densities can be calculated for the experimental process conditions, and they are shown in Table 49.

In the worst-case scenario, the SR-POLAR acetone density may have up to 10% error (especially for supercritical densities which show a larger deviation). Since the acetone density does not contribute more than a third ($x_1 = 0.32$) to the mixture density, then the mixture-density error can be estimated to be less than 4%, but in order to be cautious, the mixture error should be doubled to 8%. Although 8% may seem rather large, it is comparable to several of the diffusivity 95%-confidence-interval uncertainties. With the mixture densities approximated, plots of diffusivity as a function of the mixture density can be shown. Tracer-diffusivity data are again tabulated in Table 50 with the calculated mixture density, while Figure 101 through Figure 105 are re-plotted in Figure 115 through Figure 119.

Table 48. Average mixture-density ratios for several mixture-density approaches when compared to experimental ethanol(1)-water(2) mixture-density data, ρ_{12} (Safarov and Shakhverdiev, 2001)

Approach for the 196 data points examined	Mixture-density ratio	Mean $\pm \sigma_{95\%}$
Volume & mole-fraction weighted SR-POLAR(1)-SR-POLAR(2)	$\rho_1^{SR} \rho_2^{SR} / \rho_{12}$	1.11 ± 0.29
Volume & mole-fraction weighted SR-POLAR(1)-Steam-Table(2)	$\rho_1^{SR} \rho_2^{STM} / \rho_{12}$	1.11 ± 0.28
Density & mole-fraction weighted SR-POLAR(1)-SR-POLAR(2)	$\rho_1^{SR} \rho_2^{SR} / \rho_{12}$	1.06 ± 0.07
Density & mole-fraction weighted SR-POLAR(1)-Steam-Table(2)	$\rho_1^{SR} \rho_2^{STM} / \rho_{12}$	1.05 ± 0.06
Internally (a, b, & c) weighted, zeroed-binary-parameters SR-POLAR(12)	$\rho_{12}^{SR} / \rho_{12}$	0.96 ± 0.06
Internally (a, b, & c) weighted, regressed-binary-parameters SR-POLAR(12)	$\rho_{12}^{SR} / \rho_{12}$	0.98 ± 0.06

Table 49. Mixture-density predictions using the SR-POLAR and Steam-Table EOSs for the subcritical and **supercritical** process conditions

Acetone concentration (wt.%$_1$) = x_1	Temperature, T (°C)	Pressure, P (bar)	Translated SR-POLAR acetone density, ρ_1^{SR} (g/cm^3)	Calculated-pure-water density, ρ_2 (g/cm^3) (NIST, 1996)	Calculated mixture density, $\rho = \rho_1^{SR} \, {}_2^{STM}$ (g/cm^3)
20 = 0.0724	408.7	70.2	0.1034	0.0247	0.030
20 = 0.0724	404.4	125.2	0.2510	0.0494	0.064
20 = 0.0724	403.8	199.8	0.4602	0.0978	0.124
20 = 0.0724	**403.2**	**240.7**	**0.5583**	**0.1435**	**0.174**
20 = 0.0724	**404.1**	**263.9**	**0.6068**	**0.1830**	**0.214**
20 = 0.0724	**402.2**	**278.5**	**0.6418**	**0.2347**	**0.264**
20 = 0.0724	**404.4**	**289.6**	**0.6591**	**0.2595**	**0.288**
20 = 0.0724	455.3	140.8	0.2335	0.0495	0.063
20 = 0.0724	**456.5**	**236.6**	**0.4429**	**0.0974**	**0.122**
20 = 0.0724	505.8	154.6	0.2198	0.0492	0.062
20 = 0.0724	**504.0**	**271.3**	**0.4354**	**0.0989**	**0.123**
40 = 0.171	402.5	70.2	0.1057	0.0250	0.039
40 = 0.171	402.5	125.3	0.2540	0.0498	0.085
40 = 0.171	403.1	199.9	0.4618	0.0983	0.161
40 = 0.171	**404.3**	**240.7**	**0.5558**	**0.1417**	**0.213**
40 = 0.171	**404.1**	**264.2**	**0.6074**	**0.1837**	**0.257**
40 = 0.171	**404.4**	**278.2**	**0.6359**	**0.2192**	**0.291**
40 = 0.171	**404.3**	**288.9**	**0.6577**	**0.2571**	**0.326**
40 = 0.171	452.7	79.8	0.1069	0.0260	0.040
40 = 0.171	455.2	140.3	0.2325	0.0493	0.081
40 = 0.171	**454.7**	**237.2**	**0.4473**	**0.0986**	**0.159**
40 = 0.171	500.9	81.7	0.0967	0.0245	0.037
40 = 0.171	504.8	155.0	0.2212	0.0494	0.079
40 = 0.171	**504.8**	**271.1**	**0.4340**	**0.0986**	**0.156**
60 = 0.319	402.8	70.5	0.1063	0.0251	0.051
60 = 0.319	403.0	125.6	0.2541	0.0498	0.115
60 = 0.319	404.0	200.0	0.4601	0.0978	0.214
60 = 0.319	**404.2**	**241.1**	**0.5569**	**0.1424**	**0.275**
60 = 0.319	**404.1**	**264.4**	**0.6078**	**0.1842**	**0.319**
60 = 0.319	**404.3**	**279.1**	**0.6380**	**0.2227**	**0.355**
60 = 0.319	**403.7**	**289.0**	**0.6596**	**0.2635**	**0.390**
60 = 0.319	456.2	76.4	0.0999	0.0246	0.049
60 = 0.319	455.3	140.4	0.2325	0.0493	0.108
60 = 0.319	**456.0**	**236.7**	**0.4440**	**0.0977**	**0.208**
60 = 0.319	504.8	84.4	0.0999	0.0252	0.049
60 = 0.319	506.5	155.6	0.2211	0.0495	0.104
60 = 0.319	**506.6**	**271.3**	**0.4319**	**0.0981**	**0.205**

Table 50. Acetone(1)-water(2) tracer diffusivities at sub- and **supercritical** water conditions (with 95%-confidence-interval uncertainties)

Acetone concentration (wt.%$_1$) = x_1	Experiment temperature, T (°C)	Calculated mixture density, ρ (g/cm^3)	Experimental pressure, P (bar)	Acetone(1) tracer diffusivity, $D_1 \times 10^5$ (cm^2/s)	Water(2) tracer diffusivity, $D_2 \times 10^5$ (cm^2/s)
20 = 0.0724	409 ± 2	0.030	70 ± 1	<<SNR	1282 ± 378
20 = 0.0724	404.4 ± 0.8	0.064	125.2 ± 0.5	374 ± 98	588 ± 23
20 = 0.0724	404 ± 1	0.124	200 ± 1	168 ± 12	282 ± 12
20 = 0.0724	**403.2 ± 0.1**	**0.174**	**240.7 ± 0.7**	**130 ± 10**	**239 ± 8**
20 = 0.0724	**404.1 ± 0.9**	**0.214**	**264 ± 1**	**106 ± 18**	**189 ± 5**
20 = 0.0724	**402 ± 3**	**0.264**	**278.5 ± 0.9**	**87 ± 32**	**177 ± 16**
20 = 0.0724	**404.4 ± 0.1**	**0.288**	**289.6 ± 0.3**	**85 ± 22**	**168 ± 20**
20 = 0.0724	455.3 ± 0.4	0.063	140.8 ± 0.8	514 ± 26	828 ± 70
20 = 0.0724	**456.5 ± 0.8**	**0.122**	**236.6 ± 0.4**	**295 ± 31**	**351 ± 10**
20 = 0.0724	506 ± 1	0.062	155 ± 3	615 ± 56	938 ± 112
20 = 0.0724	**504 ± 5**	**0.123**	**271.3 ± 0.8**	**352 ± 36**	**383 ± 9**
40 = 0.171	403 ± 1	0.039	70.2 ± 0.9	585 ± 45	943 ± 103
40 = 0.171	402.5 ± 0.3	0.085	125.3 ± 0.3	300 ± 40	470 ± 37
40 = 0.171	403 ± 1	0.161	199.9 ± 0.7	150 ± 36	253 ± 33
40 = 0.171	**404.3 ± 0.4**	**0.213**	**240.7 ± 0.3**	**143 ± 23**	**275 ± 35**
40 = 0.171	**404.1 ± 0.1**	**0.257**	**264.2 ± 0.6**	**121 ± 15**	**221 ± 4**
40 = 0.171	**404 ± 1**	**0.291**	**278.2 ± 0.8**	**98 ± 9**	**201 ± 76**
40 = 0.171	**404 ± 1**	**0.326**	**288.9 ± 0.9**	**86 ± 31**	**190 ± 8**
40 = 0.171	452.7 ± 0.7	0.040	79.8 ± 0.1	766 ± 25	1202 ± 76
40 = 0.171	455.2 ± 0.9	0.081	140.3 ± 0.5	460 ± 32	640 ± 10
40 = 0.171	**454.7 ± 0.4**	**0.159**	**237.2 ± 0.4**	**217 ± 71**	**310 ± 81**
40 = 0.171	500.9 ± 0.7	0.037	82 ± 2	958 ± 47	1475 ± 21
40 = 0.171	505 ± 1	0.079	155 ± 0.4	580 ± 63	803 ± 2
40 = 0.171	**504.8 ± 0.8**	**0.156**	**271 ± 1**	**286 ± 107**	**369 ± 26**
60 = 0.319	402.8 ± 0.2	0.051	70.5 ± 0.9	656 ± 15	982 ± 7
60 = 0.319	403 ± 1	0.115	125.6 ± 0.5	305 ± 17	480 ± 36
60 = 0.319	404 ± 1	0.214	200 ± 0.6	174 ± 30	307 ± 10
60 = 0.319	**404.2 ± 0.9**	**0.275**	**241.1 ± 0.6**	**133 ± 7**	**218 ± 32**
60 = 0.319	**404 ± 1**	**0.319**	**264.4 ± 0.6**	**117 ± 24**	**204 ± 28**
60 = 0.319	**404.3 ± 0.7**	**0.355**	**279.1 ± 0.4**	**91 ± 9**	**184 ± 9**
60 = 0.319	**403.7 ± 0.4**	**0.390**	**289 ± 0.1**	**80 ± 9**	**180 ± 7**
60 = 0.319	456 ± 1	0.049	76.4 ± 0.2	782 ± 34	1205 ± 74
60 = 0.319	455 ± 1	0.108	140.4 ± 0.1	466 ± 85	632 ± 204
60 = 0.319	**456 ± 0.5**	**0.208**	**236.7 ± 0.6**	**252 ± 51**	**357 ± 30**
60 = 0.319	504.8 ± 0.6	0.049	84 ± 3	888 ± 98	1189 ± 101
60 = 0.319	506.5 ± 0.3	0.104	156 ± 1	554 ± 138	785 ± 19
60 = 0.319	**507 ± 2**	**0.205**	**271 ± 1**	**349 ± 18**	**441 ± 180**
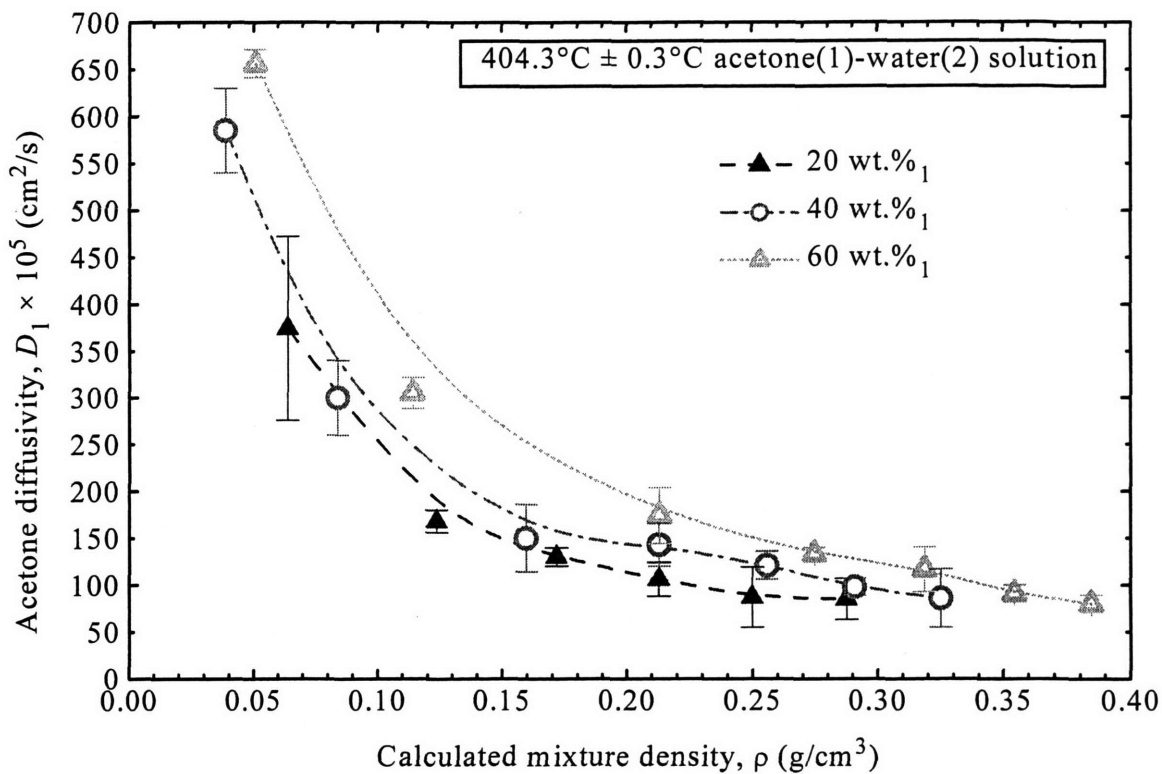
Figure 115. Acetone tracer diffusivities at 404.3°C (with 95%-confidence-interval uncertainties). Curves are intended to show general trends.
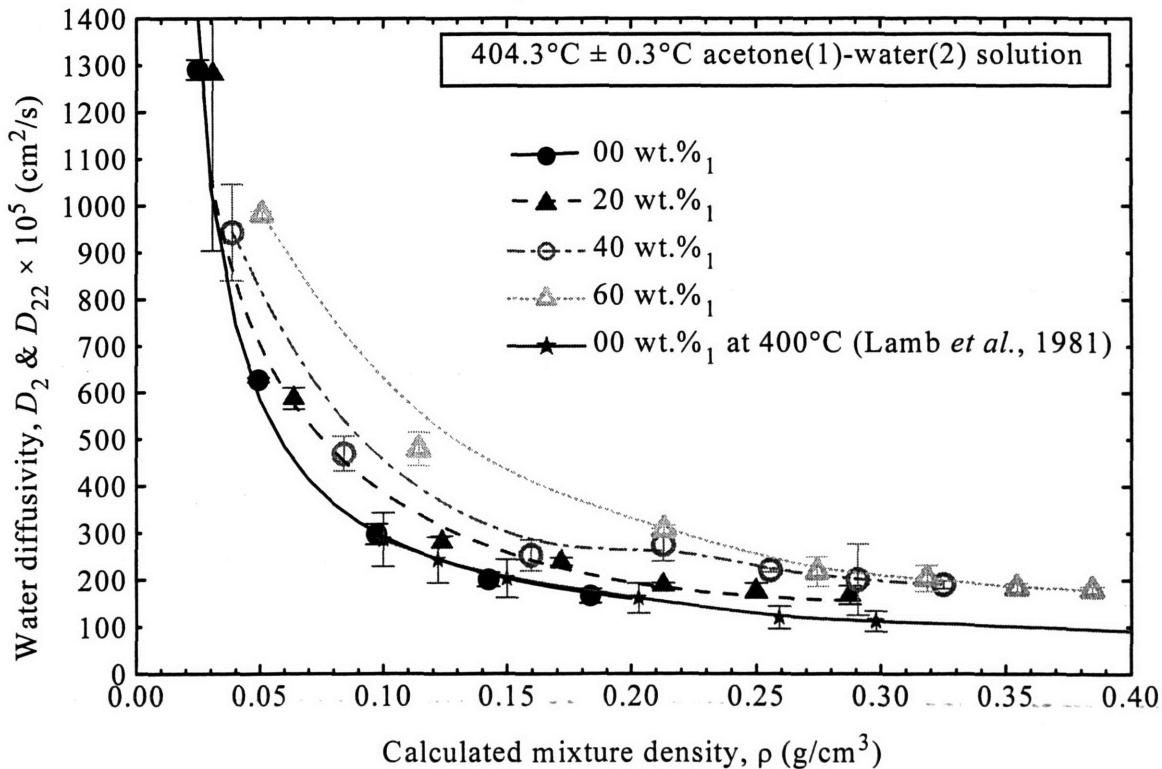
Figure 116. Water diffusivities at 404.3°C (with 95%-confidence-interval uncertainties). Curves are intended to show general trends.
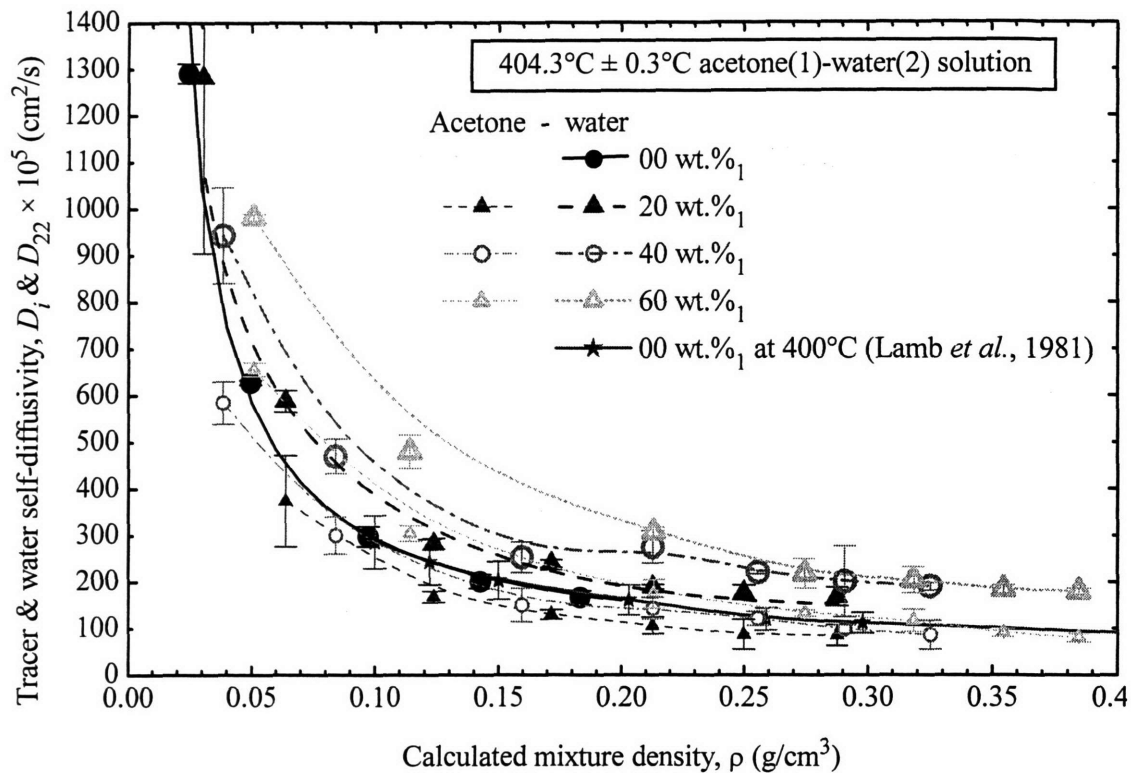
Figure 117. Acetone and water diffusivities at 404.3°C (with 95%-confidence-interval uncertainties). Curves are intended to show general trends.
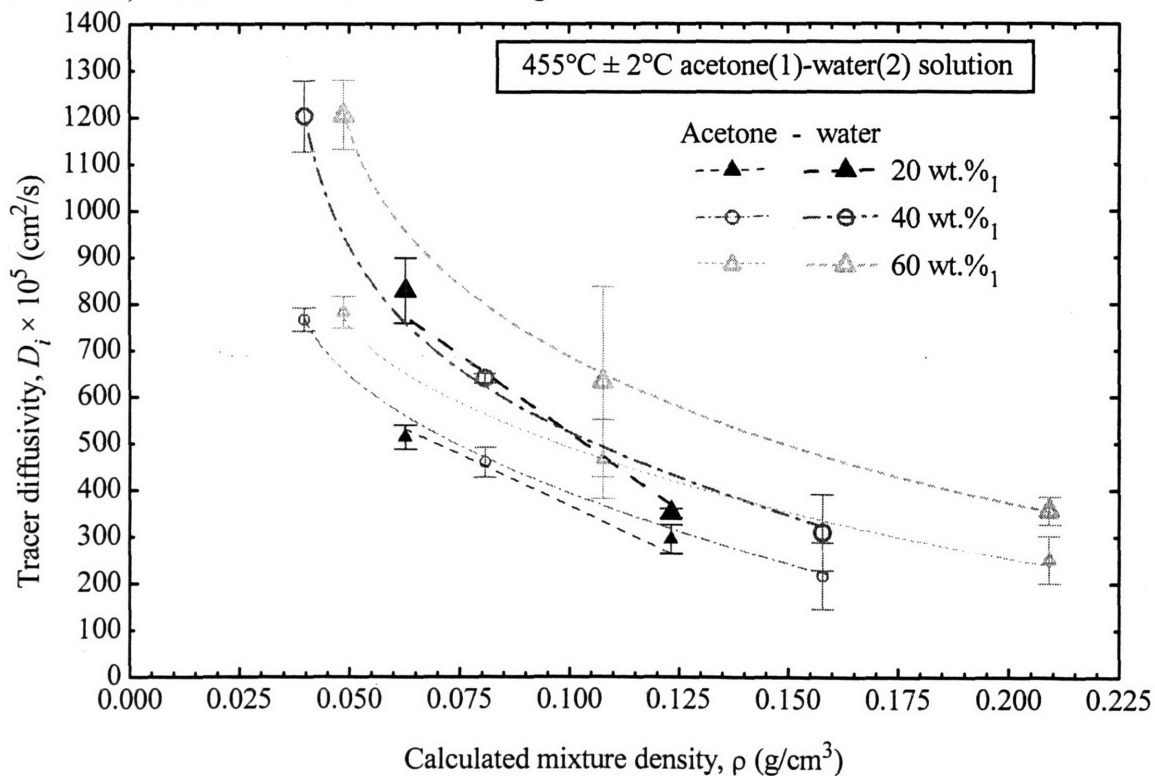
Figure 118. Tracer diffusivities at 455°C (with 95%-confidence-interval uncertainties). Curves are intended to show general trends.
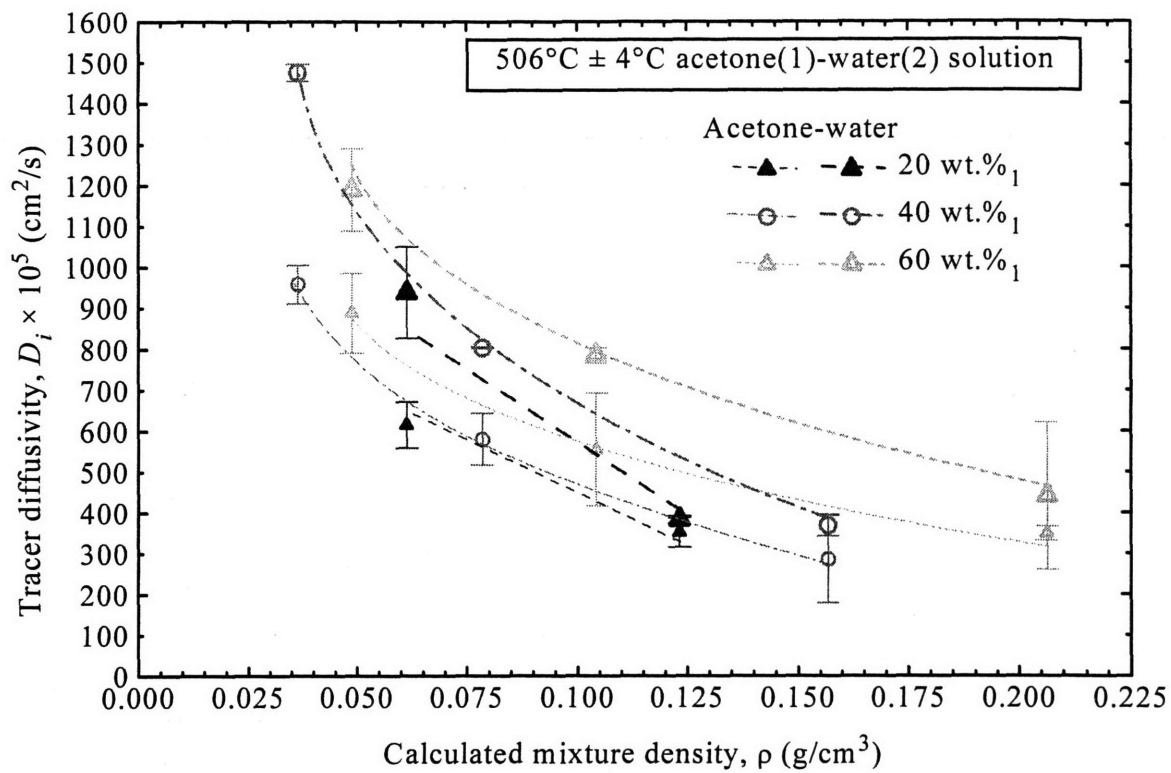
Figure 119. Tracer diffusivities at 506°C (with 95%-confidence-interval uncertainties). Curves are intended to show general trends.

II.4.4 Analysis and Discussion

This section will focus on observed diffusivity trends and on the estimation of infinitely dilute mutual diffusivities, D_{12}^{∞}, from acetone tracer diffusivities.

II.4.4.1 Diffusivity Trends

The diffusivity dependence on concentration shows trends similar to those seen in the literature. For example, tracer and mutual diffusivities often reach a minimum at low solute concentrations as is shown in Figure 120 for an acetone-water mixture at several temperatures, in Figure 121 for an acetone-n-butylacetate mixture at several temperatures, and in Figure 122 for an acetone-water mixture at 25°C. Note that the Figure 122 acetone-water tracer-diffusivity data do not agree at concentrated solutions, but show similar minima near mole fractions of 0.2. The published data show temperature trends and slope changes near the diffusivity minima that are also visible in the data of this dissertation (see Figure 112 through Figure 114). For example, at lower densities and higher temperatures, there appears to be an increase in diffusivity as infinite dilution is approached.

Ferrario *et al.* (1990) report hydrogen-bonding simulation results for several systems including ambient acetone-water. They report that the jump in diffusivity at higher acetone concentrations correlates to the significant disruption of the water-water hydrogen-bonding network and the formation of coordinated solute-water species. These species are linked less than the original water-water network and support greater molecular movement. They also find that, at low solute concentrations, the solute has enhanced-receptor qualities that further stabilize the hydrogen-bonding network and lead to diffusivity minima near ~0.3 mole fractions. The minima can be seen in ambient data (see Figure 122) and in the high temperature, high pressure data (see Figure 112 through Figure 114). Hydrogen bonding is known to exist in high temperature and high pressure SCWO (Hoffmann and Conradi, 1997), and acetone appears to behave in a similar fashion as it does at ambient conditions.

For the 40 wt.%1 data, an anomaly exists that is associated with day-to-day repeatability since measurements around 0.20 g/cm3 were taken on different days with different solutions. In order to demonstrate that other data are not affected, Figure 123 and Figure 124 show the day of
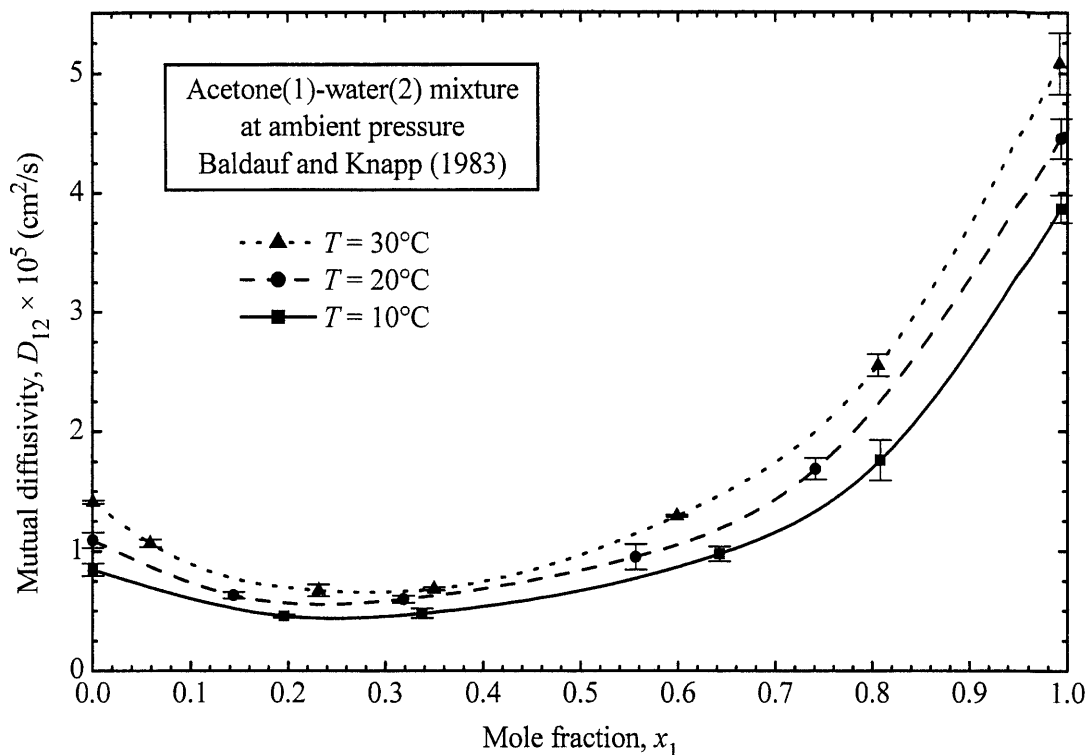
Figure 120. Mutual diffusivity for an acetone(1)-water(2) mixture at ambient pressure with 95%-confidence-interval uncertainties (Baldauf and Knapp, 1983). The diffusivity minima appear to shifts from ~0.3 to ~0.2 as the temperature is lowered.
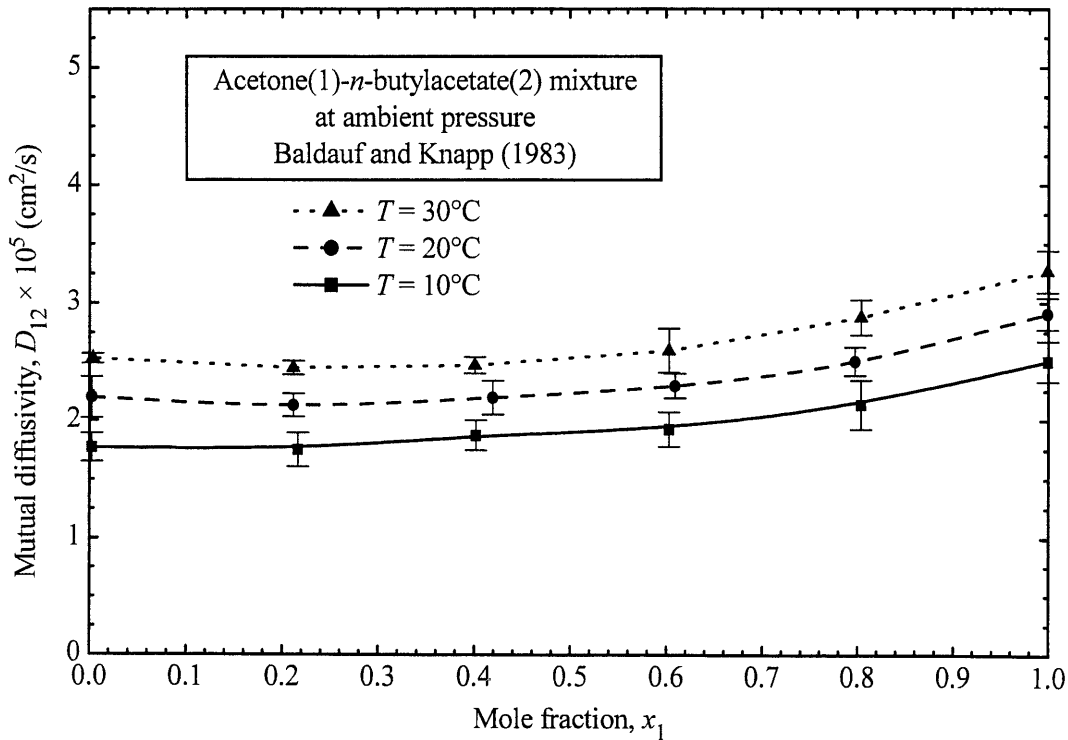
Figure 121. Mutual diffusivity for an acetone(1)-n-butylacetate(2) mixture at ambient pressure with 95%-confidence-interval uncertainties (Baldauf and Knapp, 1983). The diffusivity minima are sensitive to temperature, and for $T = 10°C$, the minimum is at $x_1 \sim 0$.
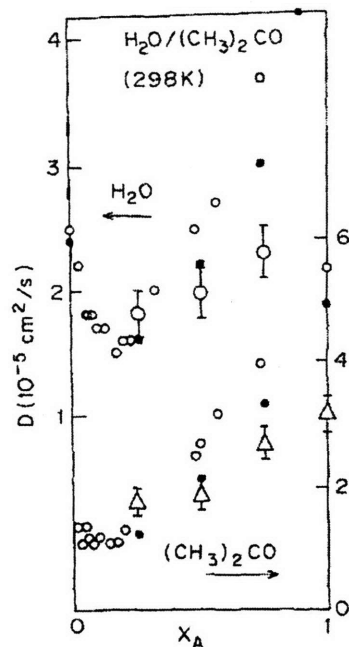
Figure 122. Tracer diffusivities for an acetone(A)-water mixture at 25°C. Small solid and open circles are experimental data from two sources, while the large open circles, triangles, and squares are MD-simulated data for water and acetone, respectively (Source: Ferrario *et al.*, 1990).

collection for all of the multi-day 404°C experimental data. The 60 wt.%$_1$ data are consistent during the two-day collection period. The only anomaly is for the 40 wt.%$_1$ solution which may have been more dilute for the low-density, day-two experiments and been more concentrated for the denser experiments on day four.

II.4.4.2 Infinitely Dilute Mutual Diffusivities

Infinitely dilute mutual diffusivities can now be estimated by extrapolating isochoric and isothermal acetone-tracer-diffusivity data to zero acetone concentration. This extrapolation will be performed using the calculated mixture-density diffusivity data (Table 50) and the calculated-pure-water-density diffusivity data (Table 37) although these pure-water-density results will be suspect due to the use of the pure water densities. Weighted second-order fits ($y = b + mx + nx^2$) were made for several isochoric data sets extracted from density-versus-diffusivity figures including Figure 115. These fits are summarized in Table 51, and note that other isochoric data sets could be extracted. Data from Table 50 cannot be used since mixture densities are not

304
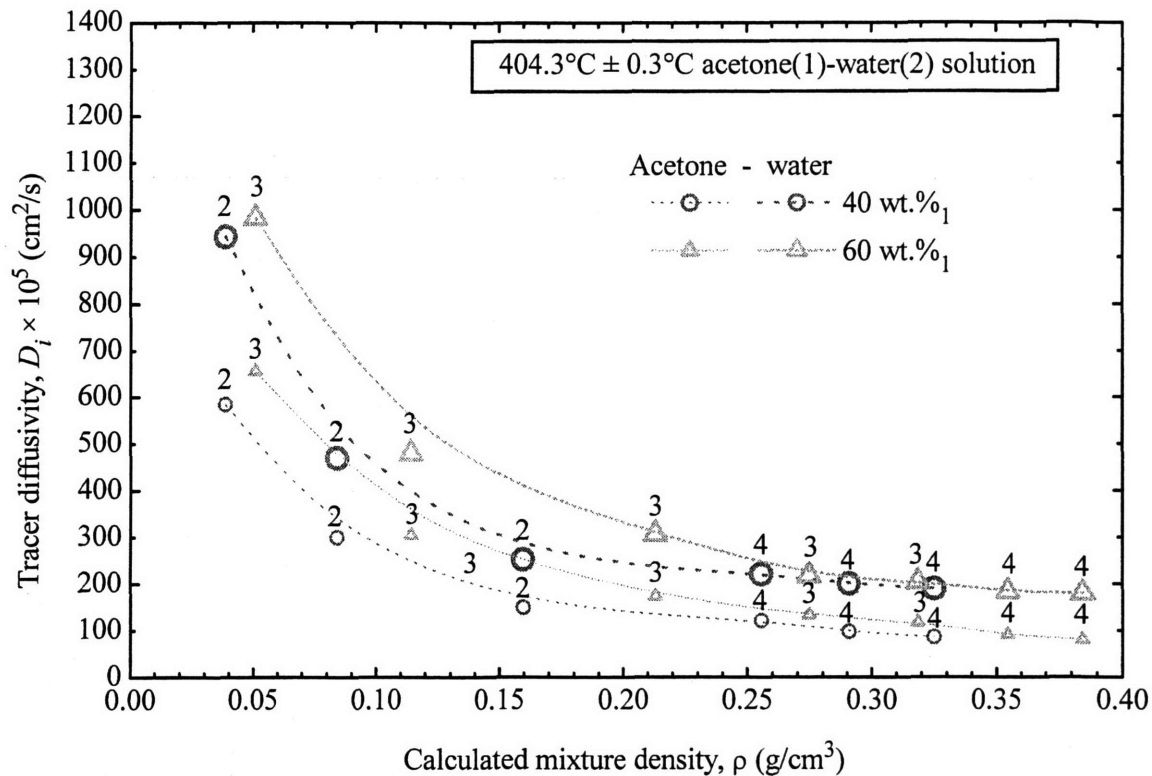
Figure 123. Tracer diffusivities at 404°C showing the day number of collection with curves. 40 wt.%$_1$ and 60 wt.%$_1$ had multiple collection days, and only 40 wt.%$_1$ exhibits an anomaly.
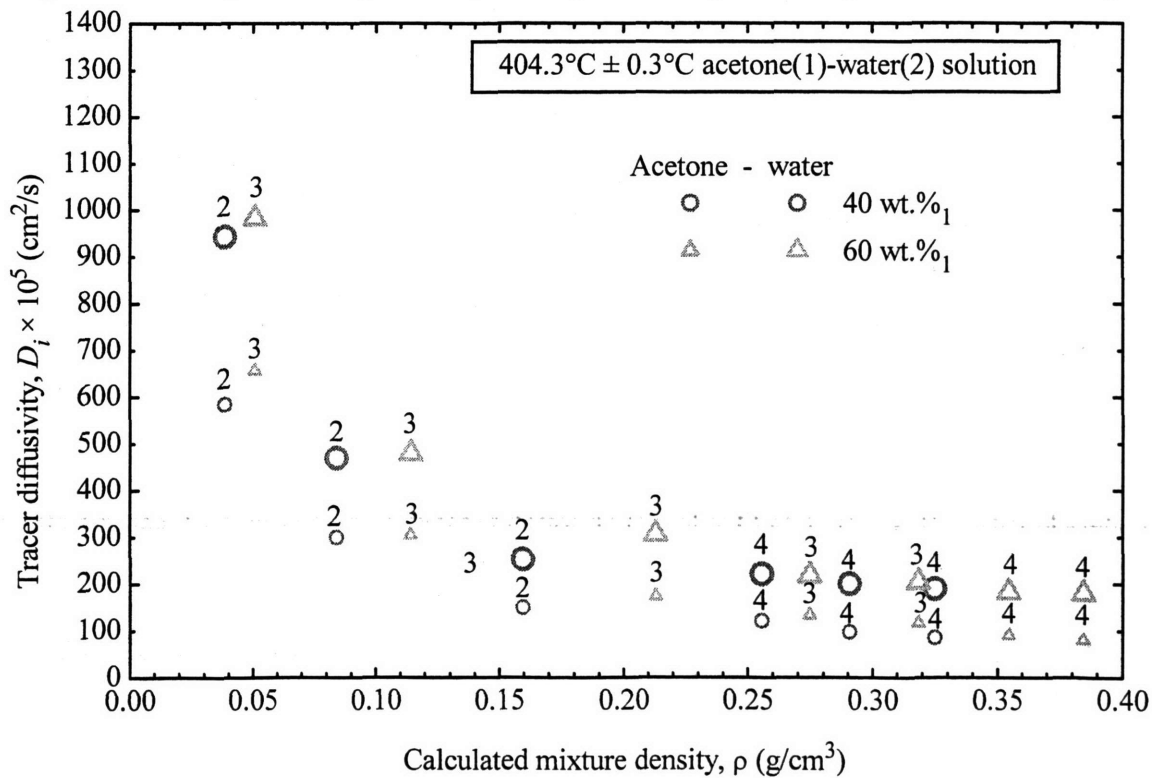
Figure 124. Tracer diffusivities at 404°C showing the day number of collection. Concentrations of 40 wt.%$_1$ and 60 wt.%$_1$ had multiple collection days, and only 40 wt.%$_1$ exhibits an anomaly.

identical and cannot be clustered together. Due to data scattering and uncertainty below 0.2 g/cm^3 mixture densities, 404°C isochore-data estimation is limited to the region above 0.2 g/cm^3.

Three isochore sets are estimated from Figure 115 and are plotted in Figure 125 in order to estimate the infinitely dilute mutual diffusivity. Similar tracer-diffusivity trends are seen since the mutual diffusivity exponentially decreases near the critical point and becomes relatively linear with density at higher densities. Diffusivity also increases with temperature, but further analysis will follow when diffusivity models and functional dependencies are validated.

Extrapolations are also performed on pure-water-density isochors that have at least three data points, and the extrapolated infinitely dilute mutual diffusivities are presented in Table 52 and are shown in Figure 126. These extrapolations allow a comparison of the mutual diffusivity using two distinct mixture density sets. The reported uncertainty is rather large, but this is due to the small number of data points, which also have large uncertainties. These results are consistent with the results obtained using mixture-water isochors, and all are shown in Figure 127. There appears to be acceptable agreement between the mutual diffusivities extrapolated from different isochoric dataset approaches (pure water versus mixture densities).

Table 51. Extrapolated infinitely dilute mutual diffusivities, $D_{12}{}^\infty$, and their corresponding process conditions (with 95%-confidence-interval uncertainties)

Temperature, T (°C)	Mixture density, ρ (g/cm^3)	Pressure, P (bar)	Infinitely dilute mutual diffusivity, $D_{12}{}^\infty \times 10^5$ (cm^2/s)
404	0.22	278	86 ± 20
404	0.26	289	70 ± 30
404	0.30	299	57 ± 20
455	0.05	142	520 ± 80
455	0.10	240	380 ± 100
506	0.05	157	680 ± 150
506	0.10	275	440 ± 180
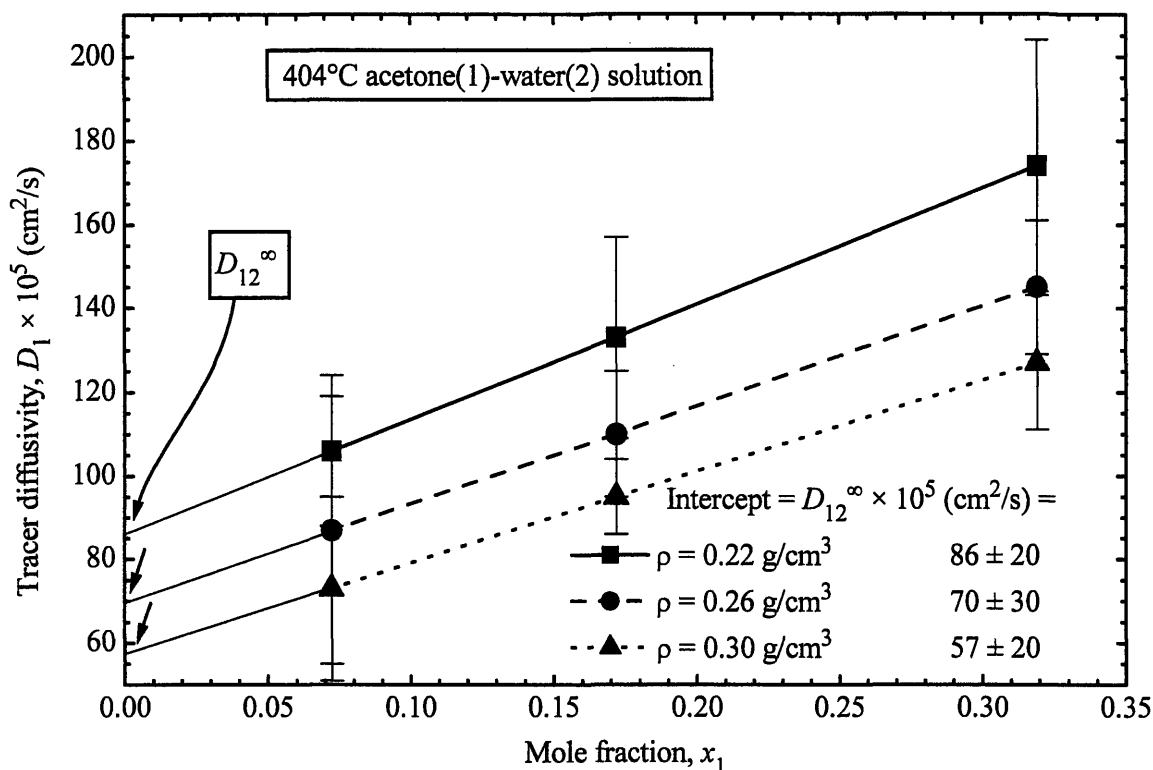
Figure 125. Tracer and extrapolated infinitely dilute mutual diffusivities at 404°C for several calculated mixture densities (with 95%-confidence-interval uncertainties).

Table 52. Extrapolated infinitely dilute mutual diffusivities, D_{12}^{∞}, for several temperatures and calculated-pure-water densities (with 95%-confidence-interval uncertainties)

Experimental temperature, T (°C)	Calculated-pure-water density, ρ_2 (g/cm^3)	Experimental pressure, P (bar)	Infinitely dilute mutual diffusivity, $D_{12}^{\infty} \times 10^5$ (cm^2/s)
404	0.0494	125	500 ± 200
404	0.0977	200	200 ± 60
404	0.1838	264	90 ± 50
404	0.2206	279	70 ± 70
404	0.257	289	80 ± 70
455	0.0494	141	580 ± 80
455	0.0977	237	300 ± 100
506	0.0494	155	700 ± 200
506	0.0977	271	400 ± 200

307
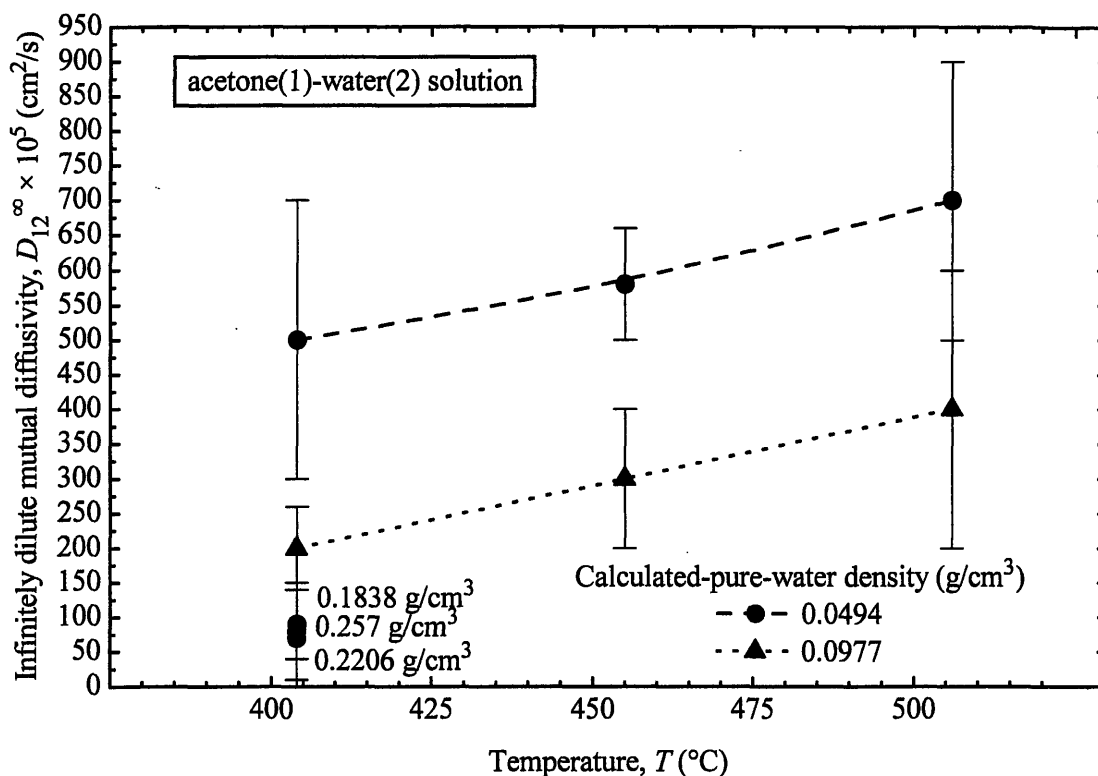
Figure 126. Infinitely dilute mutual diffusivities for acetone-water mixtures as a function of temperature (with 95%-confidence-interval uncertainties).
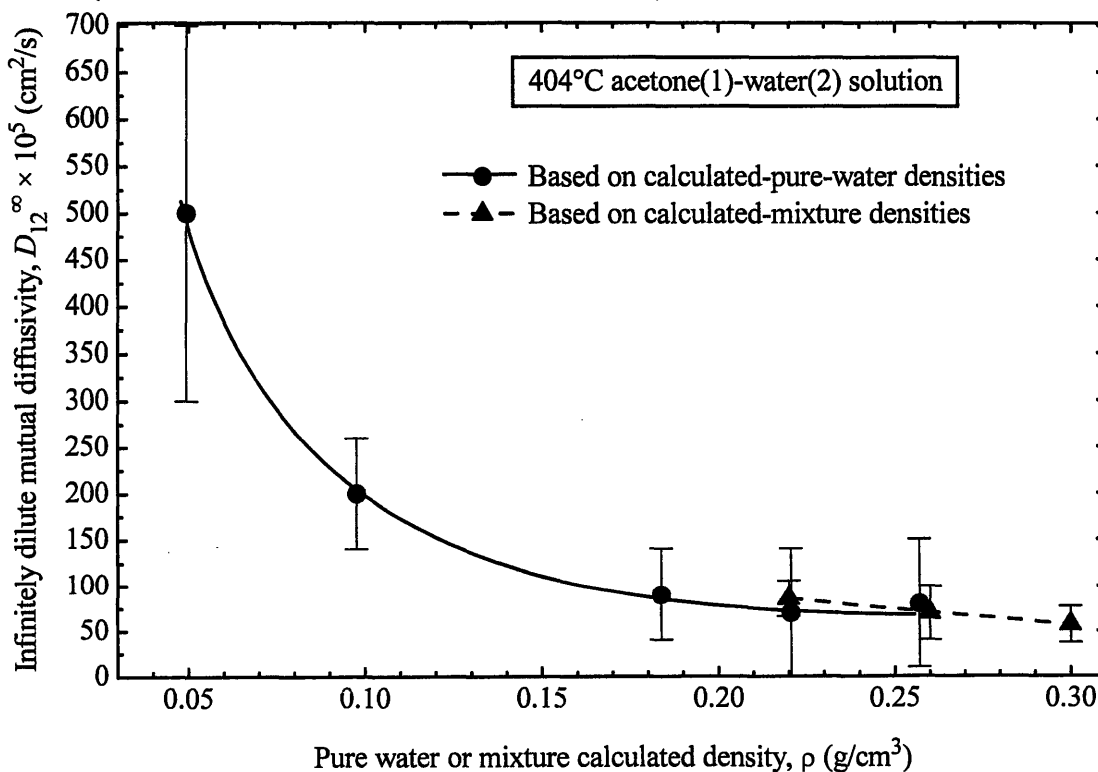
Figure 127. Infinitely dilute mutual diffusivities at 404°C based on extrapolation with calculated-pure-water densities and calculated-mixture densities (with 95%-confidence-interval uncertainties).

When Table 51 and Table 52 are compared, the analyses with two different isochoric data sets yield similar results, which should be expected given that less than 30 mole% of acetone is used. The pure-water-isochore diffusivities are within the uncertainty of the mixture-isochore diffusivities indicating that the pure-water-isochore tracer diffusivities could be used to determine the infinitely dilute mutual diffusivities, and surely be used to generate, *e.g.*, temperature trends. The agreement also holds at higher densities where one expects that the difference between density models is the largest and where the extrapolated infinitely dilute mutual diffusivities could deviate. That is not evident from the data presented in Figure 127. At low densities, ideal behavior ensures that density predictions would be similar and would yield comparable infinitely dilute mutual diffusivities. Additional infinitely dilute mutual diffusivities can be extrapolated since one is not limited to the density values used in Table 51 and Table 52. Further analysis of these mutual diffusivities will be performed in the next section when diffusivity models are investigated in order to validate the diffusivity models and their functional dependences.

II.4.5 References

Aspen Technology (1994) Physical Properties Methods and Models – Reference Manual, Volume 2, Cambridge, MA.

Baldauf, W. and Knapp, H. (1983) "Experimental adetermination of diffusion coefficients, viscosities, densities and refractive indexes of 11 binary liquid systems." *Ber. Bunsenges. Phys. Chem.*, **87**, 304–309.

Braker, W. and Mossman, A.L. (1980) *Matheson Gas Data Book*, 6th ed., Lyndurst, NJ.

Devore, J.L. (1990) *Probability and Statistics for Engineering and the Sciences*, Brooks/Cole Publishing Co., 3rd ed., Pacific Grove, CA.

Ferrario, M., Haughney, M., McDonald, I.R., and Klein, M.L. (1990) "Molecular-dynamics simulation of aqueous mixtures: methanol, acetone, and ammonia." *J. Chem. Phys.*, **93** (7), 5156–5166.

Hoffmann, M.M. and Conradi, M.S. (1997) "Nuclear magnetic resonance probe for supercritical water and aqueous solutions." *Rev. Sci. Instrum.*, **68** (1), 159–164.

Lamb, W.J., Hoffman, G.A., and Jonas, J. (1981) "Self-diffusion in compressed supercritical water." *J. Chem. Phys.*, **74** (12), 6875–6880.

Modell, M., Panagiotopoulos, A.Z. and Kutney, M.C. (2000) "Modeling and simulation of the thermodynamic properties of water and SCW mixtures." Joint ISHR & ICSTR Meeting, Kochi, Japan.

NIST (1996) NIST standard reference database 10–steam tables, Boulder, CO.

Peneloux, A., Rauzy, E. and Freze, R. (1982) "A consistent correction for Redlich-Kwong-Soave volumes." *Fluid Phase Equilibria*, **8**, 7–23.

Poling, B.E., Prausnitz, J.M., and O'Connell, J.P. (2001) *The Properties of Gases and Liquids*, McGraw-Hill, 5th ed., New York, NY.

Sato, H., Watanabe, K., Levelt-Sengers, J.M.H., Gallagher, J.S., Hill, P.G., Straub, J. and Wagner, W. (1991) "Sixteen thousand evaluated experimental thermodynamic property data for water and steam.'" *J. Phy. Chem. Ref. Data*, **20**, 1023–1044.

Safarov, D.T. and Shakhverdiev, A.N. (2001) "Investigation of the thermophysical properties of ethyl alcohol + water solutions." *High Temp.*, **39** (3), 395–400.

Tyrell, H.J.V. and Harris, K.R. (1984) *Diffusion in Liquids-A Theoretical and Experimental Study*, Butterworth, London.

Walas, S.M. (1985) *Phase Equilibria in Chemical Engineering*, Butterworth-Heinemann, Stoneham, MA.

II.5. Diffusivity Modeling

In this final section, diffusivity models will be evaluated against previously discussed data so that models with greater accuracy and versatility can be recommended for SCWO modeling applications. The compared models are based on hydrodynamic, kinetic, and hard-sphere theories of diffusion, while the referenced diffusivity data include:

- experimental pure water self-diffusivities,
- experimental aqueous dilute-solute mutual diffusivities,
- experimental aqueous concentrated-solute tracer diffusivities, and
- simulated aqueous dilute-solute tracer diffusivities.

The 303 sub- and supercritical-water data points span an order of magnitude of densities (0.1 to 1.1 g/cm^3) and temperatures from ambient to supercritical-water temperatures (25°C to 700°C) and ensure a wide supercritical-processing window for examining the selected diffusivity models. The previously published data are contained in Section II.1.3 and visually summarized in Figure 68, while the acetone tracer and mutual diffusivities collected in this thesis are listed in Section II.4's Table 36, Table 50, and Table 51.

The models evaluated in this analysis were previously introduced in Section II.1.1.2 through Section II.1.1.4 and are listed in Table 53. Prior to examining each diffusivity model and offering modeling recommendations, constants and properties that are employed in these models are introduced.

II.5.1 Species Constants and Properties

All of the diffusivity models examined employ species-dependent constants or parameters. These parameters include critical properties, phase-change temperatures and volumes, and 6-12 Lennard-Jones (LJ) constants since the Lennard-Jones intermolecular potential function is employed. The solutes compared are acetone, benzene, benzophenone, hydroquinone, iodide ions (potassium-iodide salt), methane, oxygen, and sodium-nitrate. Critical properties for water and the solutes investigated are listed in Table 54, while molecular weights, acentric factors, and phase-change properties are listed in Table 55.

Table 53. Diffusivity models evaluated in this analysis

Model		Section
Hydrodynamic theory of diffusion		II.5.2.1
Stokes-Einstein equation with the no-slip condition		II.5.2.1.1
Stokes-Einstein equation with the slip condition		II.5.2.1.1
Wilke-Chang equation		II.5.2.1.2
Reddy-Doraiswamy equation	(original form)	II.5.2.1.3
	(with NBP-volumes)	II.5.2.1.3
Kinetic theory of diffusion		II.5.2.2
Chapman-Enskog equation		II.5.2.2.1
CE equation with the Enskog-Thorne correction		II.5.2.2.1.1
Weighted CE equation with the ET correction		II.5.2.2.1.1
CE equation with the Takahashi correction		II.5.2.2.1.2
CE equation with the Dawson HS correction		II.5.2.2.1.3
CE equation with the Erpenbeck-Wood HS correction		II.5.2.2.1.4
Polar Chapman-Enskog equation		II.5.2.2.2
Polar CE equation with the Enskog-Thorne correction		II.5.2.2.2
Polar, weighted CE equation with the ET correction		II.5.2.2.2
Polar CE equation with the Takahashi correction		II.5.2.2.2
Polar CE equation with the Dawson HS correction		II.5.2.2.2
Wilke-Lee equation		II.5.2.2.3
WL equation with the Enskog-Thorne correction		II.5.2.2.3
WL equation with the Takahashi correction		II.5.2.2.3
WL equation with the Dawson HS correction		II.5.2.2.3
Mathur-Thodos equations		II.5.2.2.4
Hard-Sphere Theory of Diffusion		II.5.2.3
Sun-Chen equation		II.5.2.3.1
Eaton-Akgerman equation		II.5.2.3.2
He equation		II.5.2.3.3
He-Yu equation		II.5.2.3.4
Tracer Liu-Silva-Macedo equation		II.5.2.3.5

Table 54. Pure component critical properties used in this modeling analysis (Braker and Mossman, 1980; Walas, 1985; Sato *et al.*, 1991; Poling *et al.*, 2001; Knovel, 2004; NIST, 2004)

Species	Critical temperature, T_c (°C)	Critical pressure, P_c (bar)	Critical density, ρ_c (cm^3/mol)	Critical compressibility, Z_c
Water	373.9	220.6	0.322	0.229
Acetone	235	47.01	0.278	0.232
Benzophenone	543	30.0	0.308	0.262
Hydroquinone	549	74.5	0.367	0.327
Iodide ion (used KI values)	2601	214.5	0.549	0.207
Methane	-83	46.0	0.162	0.287
Oxygen	-119	50.4	0.435	0.289
Sodium nitrate	Constants were not found and not estimated			

Note that the iodide-ion properties are based on its salt, potassium iodide, except for its molecular weight. The normal-boiling-point (NBP) molar volume for acetone in Table 55 has several entries and includes the published 77.5 cm^3/mole value and a temperature-dependent list developed and used by Goemans (1996) during his modeling analysis. For consistency reasons, his list is not used during this analysis. The temperature-dependent volumes were computed after he used his experimental data and the Stokes-Einstein equation to calculate the effective Stokes-Einstein radii, thereby enabling his Stokes-Einstein predictions to be flawless! Goemans used this volume-estimation technique so that he could compensate for hydrogen-bonding effects since molecular volume scales according to the static dielectric constant (Goemans, 1996). As a result of using variable boiling volumes, hydrogen-bonding effects could be included in his evaluated models that normally do not have such corrections (the Wilke-Chang association factor was preset to one during the Goemans' analysis in order to not overcompensate). Since the current analysis attempts, as much as possible, to compare diffusivity models with traditional calculation approaches and with constant properties that do not vary, 77.5 cm^3/mole is used for the boiling molar volume of acetone. Similarly, fixed volumes and ratios are used for benzophenone, instead of Goemans' temperature-dependent lists.

Table 55. Additional pure component properties used in this modeling analysis
(Braker and Mossman, 1980; Walas, 1985; Sato et al., 1991; Poling et al., 2001; Knovel, 2004; NIST, 2004)

Species	Molecular weight, MW (g/mol)	Acentric factor, ω	Melting temperature (at $P = 1$ bar), T_m (°C)	Normal boiling temperature (at $P = 1$ bar), T_b (°C)	Normal boiling molar volume (at $P = 1$ bar), V_b (cm³/mol)
Water	18.015	0.344	0.0	100	18.8
Acetone	58.08	0.306	−94	55.9	77.5
Acetone (Goemans, 1996)		.	For consistency, these data are not used (77.5 is used):		$\left\{\begin{array}{l} 43.3 \text{ at } 25°C \\ \& 100°C \\ 28.5 \text{ at } 200°C \\ 29.5 \text{ at } 300°C \\ 13.1 \text{ at } 350°C \end{array}\right.$
Benzophenone	182.2	0.545	48	306	211
Benzophenone (Goemans, 1996)		For consistency, these data are not used (211 is used):			$\left\{\begin{array}{l} 233 \text{ at } 100°C \\ 99.1 \text{ at } 200°C \\ 53.4 \text{ at } 300°C \\ 53.4 \text{ at } 350°C \end{array}\right.$
Hydroquinone	110.1	0.686	170	285	134
Iodide ion	126.9	0.585 (KI value)	733 (KI value)	1324 (KI value)	78.3 (KI value)
Methane	16.04	0.011	−183	−162	37.8
Oxygen	32.00	0.022	−218	−183	28.1
Sodium nitrate	84.99		308		76.5 (Goemans, 1996)

The 6-12 Lennard-Jones constants are presented in Table 56 and include, for comparison, Goemans' estimates that are inappropriately back-calculated from the Stokes-Einstein equation. As noted earlier, these estimates will not be used in this analysis. Benzophenone and hydroquinone radii are estimated after scaling the van der Waals volumes for benzene, acetone, benzophenone, and hydroquinone and are not significantly different from the benzophenone values back-calculated by Goemans (Knovel, 2004). These similarities indicate that Goemans' experimental diffusivities are reasonable which are also evident in Figure 60 and Figure 68.

Since densities are also required during this analysis and experimental density data are not available, EOS predictions are used. Densities of experimental dilute aqueous solutions and pure water are predicted with the NIST Steam Table (NIST, 1996). Mixture densities for the experimental acetone diffusivities have been estimated using EOSs in Section II.4.3. Mixture densities of the MD-simulated aqueous-methane and aqueous-oxygen systems are provided by

Ohmori and Kimura (2003). When solvent close-packed hard-sphere molar volumes are needed, they are set equal to $V_0 = 2^{-1/2}N_A\sigma_2{}^3$ for all systems, including concentrated systems when the packed volumes will be partially influenced by the solute.

Solvent viscosities are also needed, and they are estimated with the NIST Steam Table since water is the solvent (NIST, 1996). For concentrated mixtures, solution viscosities may be noticeably different from the pure water viscosities, so solution viscosities have also been estimated. Concentrated-solution viscosities were approximated with the Rogers and Pitzer (1982) approach that was used for concentrated sodium-chloride solutions. In this concentration-dependent approach, the solution viscosity is set equal to the pure water viscosity evaluated at the solution density (instead of the pure water density). For example, solution viscosity is an estimated 34% larger for the most dense and concentrated acetone solution (0.39 g/cm^3 & 60 wt.%$_1$) used in this analysis.

Table 56. Pure component 6-12 Lennard-Jones properties used in this modeling analysis

Species	Well-depth potential, ε/k (K)	Radius, r (Å)
Water	363 (Lienhard and Lienhard, 2002)	$1.375 - 0.0011(T[°C] - 25)$ (Wilhelm, 1973)
Acetone	560 (Lienhard and Lienhard, 2002)	2.28 (Lienhard and Lienhard, 2002)
Acetone Goemans (1996)	Goemans (1996) back-calculated estimates are not used (2.28 is used):	2.41 at 25°C & 100°C 2.29 at 200°C 1.98 at 300°C 1.57 at 350°C
Benzophenone Goemans (1996)	Goemans (1996) back-calculated estimates are not used (3.7 is used):	3.98 at 100°C 3.56 at 200°C 1.95 at 300°C & 350°C
Benzophenone	640 (estimated from critical properties (Perry, 1984))	3.7 (estimate larger than benzene: 2.67 (Lienhard and Lienhard, 2002))
Hydroquinone	630 (estimated from critical properties (Perry, 1984))	3.0 (estimate larger than benzene: 2.67 (Lienhard and Lienhard, 2002))
Iodide ion	1900 (estimated from KI critical properties (Perry, 1984))	2.20 (iodine ionic radius (Atkins, 1990))
Methane	148.6 (Lienhard and Lienhard, 2002)	1.88 (Lienhard and Lienhard, 2002)
Oxygen	106.7 (Lienhard and Lienhard, 2002)	1.73 (Lienhard and Lienhard, 2002)
Sodium nitrate	1000 (estimated from melting volume (Perry, 1984))	3.12 ($NaNO_3$-$4H_2O$ (Goemans, 1996))

II.5.2 Diffusivity-Model Analysis

Due to the large number of diffusivity models and data points examined during this analysis, it is necessary to consolidate and simplify the reporting process. For this reason, x-y scatter plots with fixed ranges are used to display the results of each model. Mixture density is shown on the abscissa, while the ordinate displays the ratio of calculated and experimental diffusivities, D_{calc}/D_{expt} where D_{calc} is the model prediction and D_{expt} is the experimental diffusivity.

Ideally, the plotted ratios should all be unity, but finding such an accurate model is unlikely. Diffusivity ratios, for the most part, should remain inside the range $0.5 < D_{calc}/D_{expt} < 2.0$ in order for the model to be considered worthy for SCW diffusivity modeling. Models that fall within this range can replicate temperature, density, and species dependencies fairly well and should extend to other SCW systems in a straightforward manner. Multiple excursions beyond this range indicate that the diffusivity predictions are poor and that these models should be considered suspect. Multiple excursions may be caused by poor model form or inherent model limitations. For example, some models are limited to a specific density regime such as low ($\rho < \sim 0.5$ g/cm^3) or high ($\rho > \sim 0.5$ g/cm^3) density. Plotted ratios may also be skewed by experimental-data inaccuracies, although these effects are minimized by qualitatively examining the isothermal and isobaric trends and by using the same experimental diffusivities in every modeling-analysis plot. Later in this analysis, experimental uncertainties and their scatter-plot impact will be discussed.

To judge the performance of each model, three performance zones will be used in order to classify both low and high mixture-density prediction capabilities. These zones are summarized in Table 57. Two scatter plots are shown for each model since it is difficult to distinguish all of the plotted data. The first plot contains mutual diffusivities (D_{12}) and solute tracer diffusivities (D_1), while the second plot focuses on water and contains pure water self-diffusivities (D_{22}) and water tracer diffusivities (D_2) for models that can provide such data. Examples of the plots that are shown with fixed legend symbols are shown in Figure 128. Diffusivity ratios for models that have limited prediction capabilities are consolidated in a single plot instead of two. Average diffusivity ratios and their corresponding 95%-confidence-interval uncertainties are also reported for the low density range and high density range.

Top plot legend:

- ▣ <0.01 wt.%1-benzophenone D12 at 300 bar
- ◉ ~0.63 wt.%1-sodium-nitrate D12 at 300 bar
- △ ~0.31 wt.%1-hydroquinone D12 at 240 bar
- ◇ ~0.40 wt.%1-iodide-ions D12 at 240 bar
- − ~0.34 wt.%1-acetone D12 at 300 bar (Goemans)
- ✳ ~0.00 wt.%1-acetone D12 (Kutney)
- ■ 404°C 20 wt.%1-acetone D1
- ▢ 404°C 40 wt.%1-acetone D1
- ▢ 404°C 60 wt.%1-acetone D1
- + 455°C 20 wt.%1-acetone D1
- × 455°C 40 wt.%1-acetone D1
- ✕ 455°C 60 wt.%1-acetone D1
- ● 506°C 20 wt.%1-acetone D1
- ○ 506°C 40 wt.%1-acetone D1
- ○ 506°C 60 wt.%1-acetone D1
- × 374°C 1.38 wt.%1-oxygen D1
- ⌗ 400°C 1.38 wt.%1-oxygen D1
- ◈ 500°C 1.38 wt.%1-oxygen D1
- ▲ 600°C 1.38 wt.%1-oxygen D1
- ✦ 700°C 1.38 wt.%1-oxygen D1
- + 374°C 0.70 wt.%1-methane D1
- ◌ 500°C 0.70 wt.%1-methane D1
- △ 600°C 0.70 wt.%1-methane D1
- ▽ 700°C 0.70 wt.%1-methane D1

Bottom plot legend:

- ■ 400°C D22
- ● 500°C D22
- ▲ 600°C D22
- ◆ 700°C D22
- ◘ 404°C D22 (Kutney)
- ○ Saturated water D22
- ▫ 25°C D22
- · 50°C D22
- × 70°C D22
- − 90°C D22
- + 110°C D22
- ⁓ 130°C D22
- × 150°C D22
- ⁓ 175°C D22
- ▲ 200°C D22
- ◆ 225°C D22
- ■ 404°C 20 wt.%1-acetone D2
- ▢ 404°C 40 wt.%1-acetone D2
- ▢ 404°C 60 wt.%1-acetone D2
- + 455°C 20 wt.%1-acetone D2
- × 455°C 40 wt.%1-acetone D2
- ✕ 455°C 60 wt.%1-acetone D2
- ● 506°C 20 wt.%1-acetone D2
- ○ 506°C 40 wt.%1-acetone D2
- ○ 506°C 60 wt.%1-acetone D2
- · 374°C 1.38 wt.%1-oxygen D2
- ⌗ 400°C 1.38 wt.%1-oxygen D2
- ◈ 500°C 1.38 wt.%1-oxygen D2
- ▲ 600°C 1.38 wt.%1-oxygen D2
- ◆ 700°C 1.38 wt.%1-oxygen D2
- + 374°C 0.70 wt.%1-methane D2
- ◌ 500°C 0.70 wt.%1-methane D2
- △ 600°C 0.70 wt.%1-methane D2
- ▽ 700°C 0.70 wt.%1-methane D2

Figure 128. Scatter plot templates used to display diffusivity-model predictions. The top plot contains ratios of mutual diffusivities (D_{12}) and solute tracer diffusivities (D_1), while the bottom plot contains ratios of pure water self-diffusivities (D_{22}) and water tracer diffusivities (D_2).

Table 57. Modeling-analysis performance zones for SCW mixture densities

Zone color	Zone range	Model judgment & recommendation
Black [F]	$0.25 > D_{calc}/D_{expt} > 4.0$	Failed and not recommended for use
Grey	$0.25 < D_{calc}/D_{expt} < 0.5$ $2.0 < D_{calc}/D_{expt} < 4.0$	Use with Caution
White [A]	$0.5 < D_{calc}/D_{expt} < 2.0$	Gives Adequate predictions

Low density performance indicator ← ▯▯ → High density performance indicator
on the left   ($\rho < \sim 0.5$ g/cm^3)   on the right   ($\rho > \sim 0.5$ g/cm^3)

II.5.2.1 Hydrodynamic Theory of Diffusion

II.5.2.1.1 Stokes-Einstein Equation

The first hydrodynamic model evaluated is the Stokes-Einstein (SE) equation with slip variations first discussed in Section II.1.1.2. The no-slip (Eq. (94)) and slip (Eq. (96)) conditions were examined and are shown in Figure 129 through Figure 132 and Figure 133 through Figure 136, respectively. In both cases, the low density predictions are inaccurate since a key hydrodynamic-theory requirement is not met. Viscous forces no longer dominate at low densities, thereby limiting the range of the Stokes-Einstein equation. For dense predictions using pure water viscosities, the no-slip equation underestimates the mutual diffusivities shown in Figure 129 and the self-diffusivities shown in Figure 130. The effectiveness of using mixture viscosities, instead of pure solvent viscosities, is evaluated for concentrated-solute diffusivities and is visually shown in Figure 131 for solute and Figure 132 for solvent tracer diffusivities. As explained earlier, mixture viscosity is computed using the mixture density and is another approach that can introduce concentration dependence into the diffusivity calculation. Self-diffusivity and infinitely dilute diffusivity predictions will not change, so they are not plotted. In all cases, calculated diffusivities are smaller with the larger mixture viscosities, including in the low density region where hydrodynamic models are considered invalid.

The no-slip Stokes-Einstein equation evaluated in its original form is rated: [F][A]
(mean low & high density diffusivity ratios: $0.5 \pm 0.5_{95\%}$ & $0.9 \pm 0.3_{95\%}$)
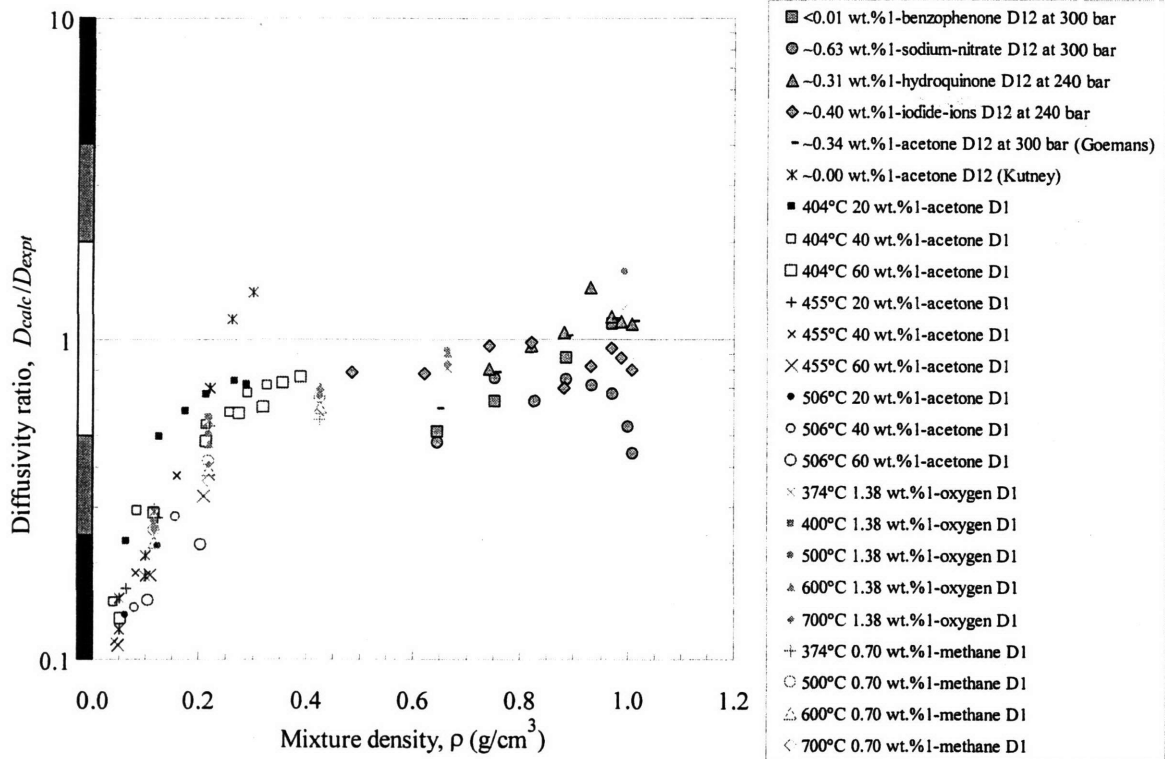
Figure 129. Stokes-Einstein D_{12} and D_1 predictions using the no-slip condition (6 in denominator), pure water viscosities, and solute radii ($r = r_1$).
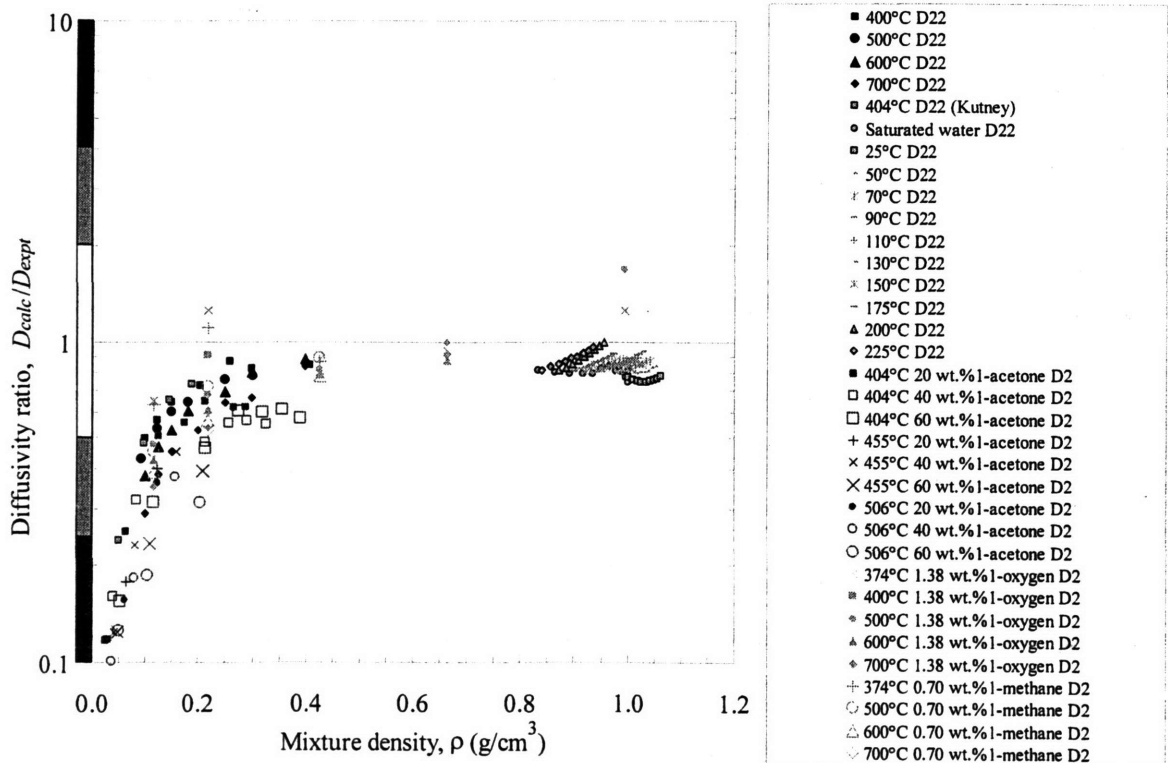
Figure 130. Stokes-Einstein D_{22} and D_2 predictions using the no-slip condition (6 in denominator), pure water viscosities, and solvent radii ($r = r_2$).
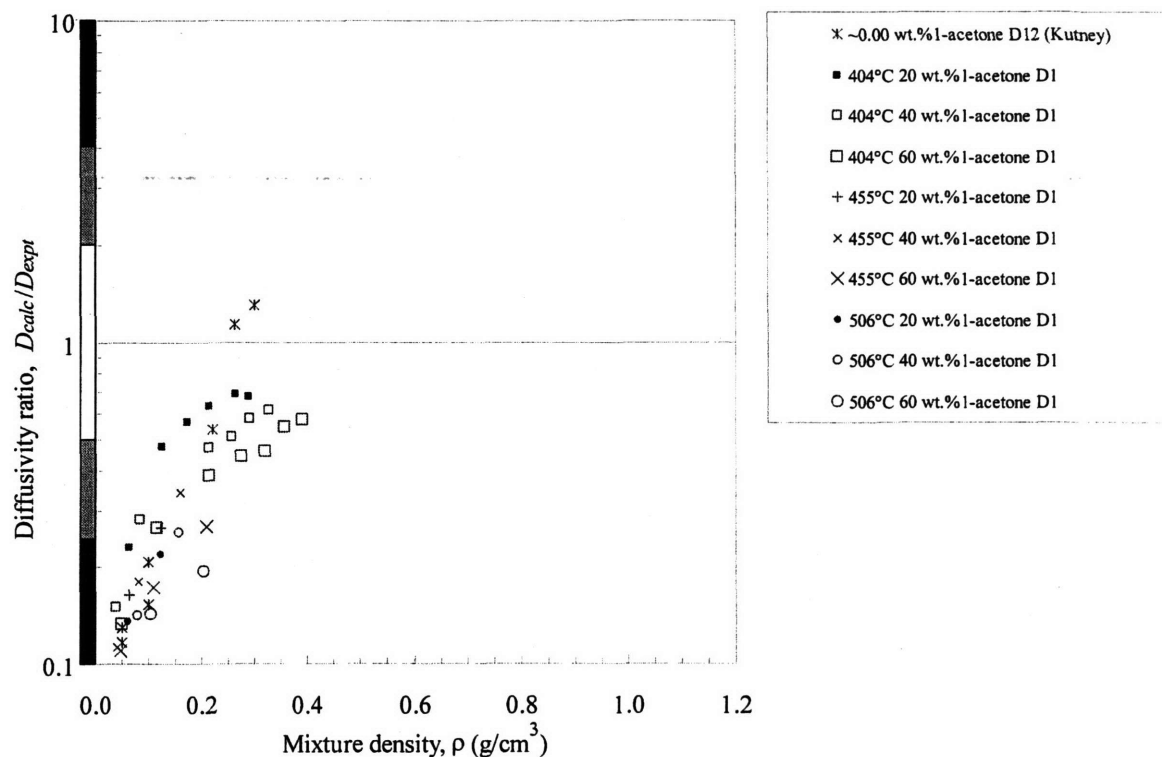
Figure 131. Stokes-Einstein D_{12} and D_1 predictions using the no-slip condition (6 in denominator), mixture viscosities, and solute radii ($r = r_1$).
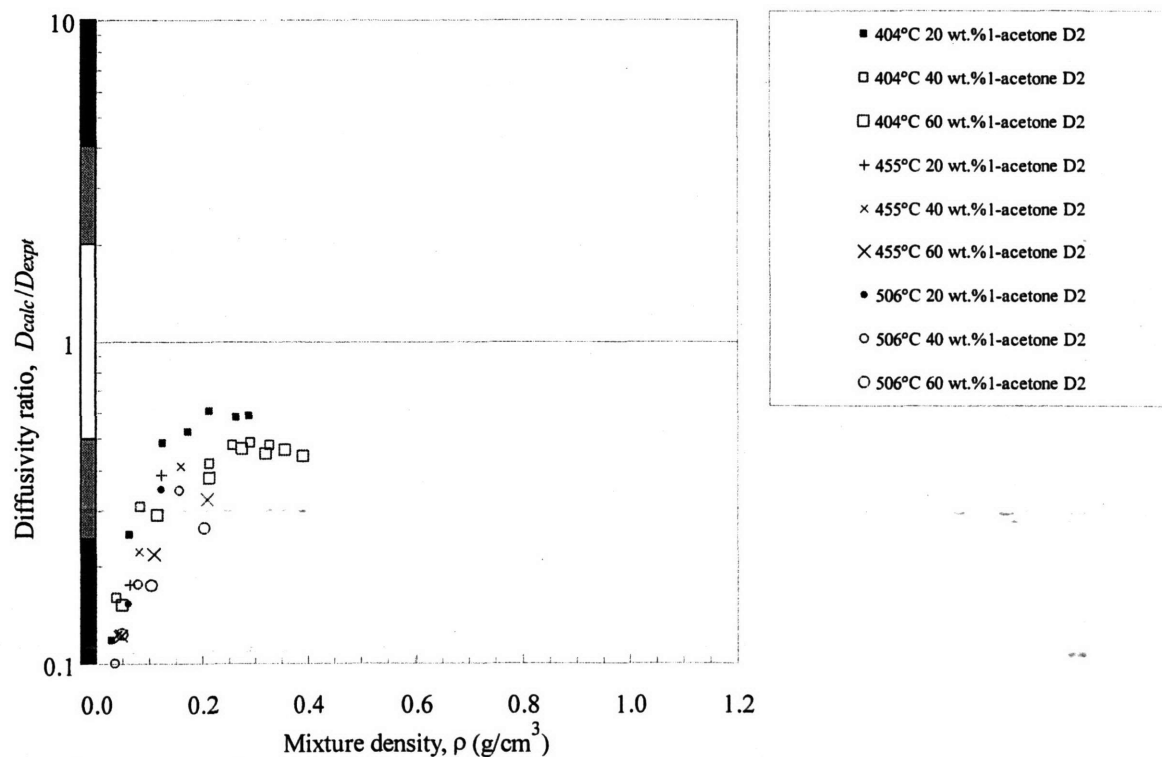
Figure 132. Stokes-Einstein D_{22} and D_2 predictions using the no-slip condition (6 in denominator), mixture viscosities, and solvent radii ($r = r_2$).

321

Predictions with the slip Stokes-Einstein equation are similar to the no-slip predictions and observed trends, except that the dense predictions are 6/4 = 50% larger as seen in Figure 133 and Figure 134. As predicted and as seen, the dense slip self-diffusivities are more accurate since the slip limit typically occurs when the solute and solvent molecules are approximately the same size. When calculated with mixture viscosities, concentrated slip diffusivities are reduced as shown in Figure 135 and Figure 136. For dense solutions, the equivalent reduction will improve the slip Stokes-Einstein model accuracy.

The slip Stokes-Einstein equation evaluated in its original form is rated: Γ A
(mean low & high density diffusivity ratios: $0.7 \pm 0.8_{95\%}$ & $1.3 \pm 0.4_{95\%}$)

The final approach used to examine the Stokes-Einstein model for supercritical water self-diffusivities was also used by Lamb *et al.* (1981). In their work, they used their experimental results in order to determine the ideal slip coefficients, C_{SE}, and showed the density range where the Stokes-Einstein model is reasonably accurate. Their coefficient plots are updated in this dissertation with additional data and results in the same conclusions previously stated. Mutual and solute tracer diffusivities are shown in Figure 137 while self- and solvent tracer diffusivities are shown in Figure 138. When mixture viscosities are used, the computed solute and solvent tracer coefficients are slightly reduced and are presented in Figure 139 and Figure 140, respectively. The ideal coefficients are mostly between the slip and no-slip limits and suggest that water systems are represented by a mixture of slip and no-slip states. Results outside this band indicate that the system is not well represented by hydrodynamic behavior and theory. This is clearly the case at low densities.
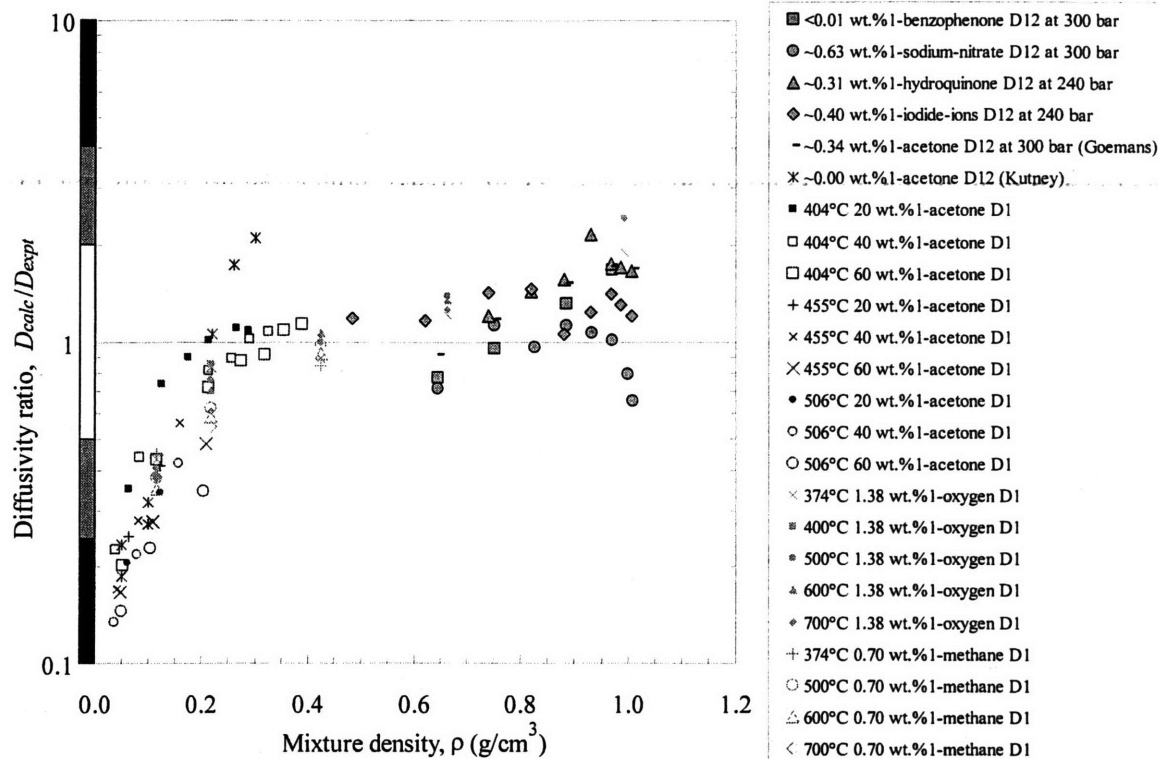
Figure 133. Stokes-Einstein D_{12} and D_1 predictions using the slip condition (4 in denominator), pure water viscosities, and solute radii ($r = r_1$).
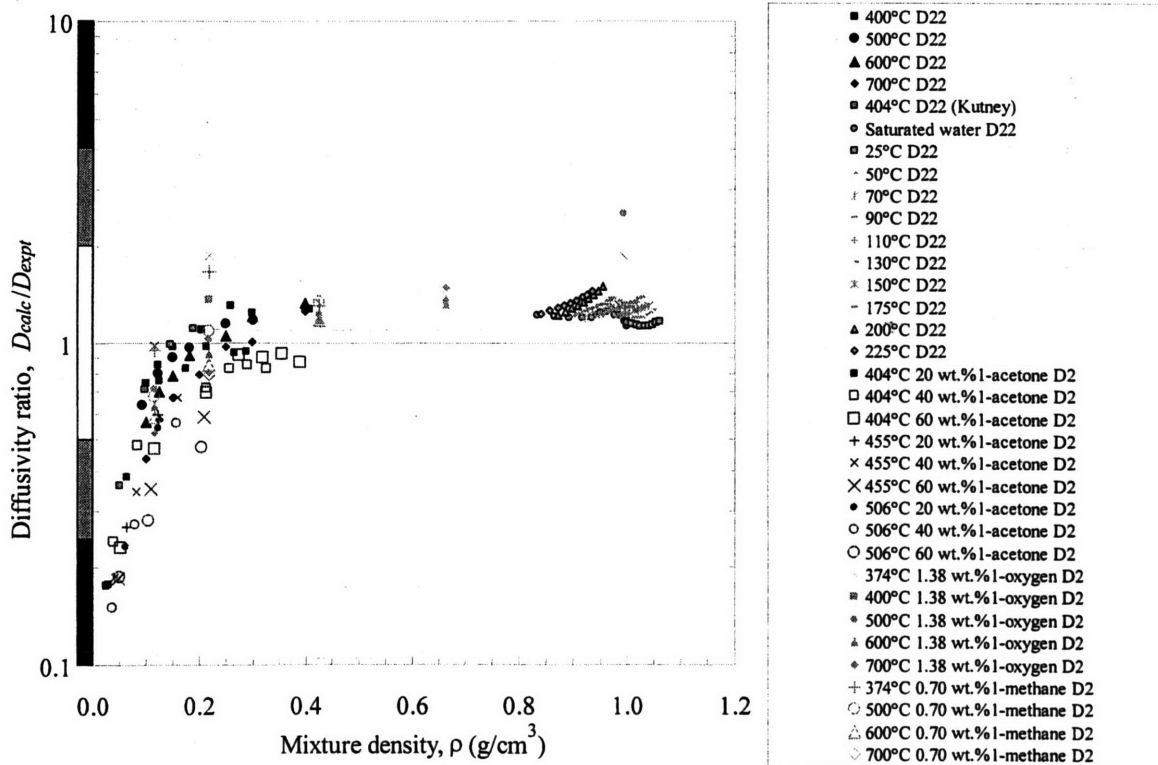
Figure 134. Stokes-Einstein D_{22} and D_2 predictions using the slip condition (4 in denominator), pure water viscosities, and solvent radii ($r = r_2$).
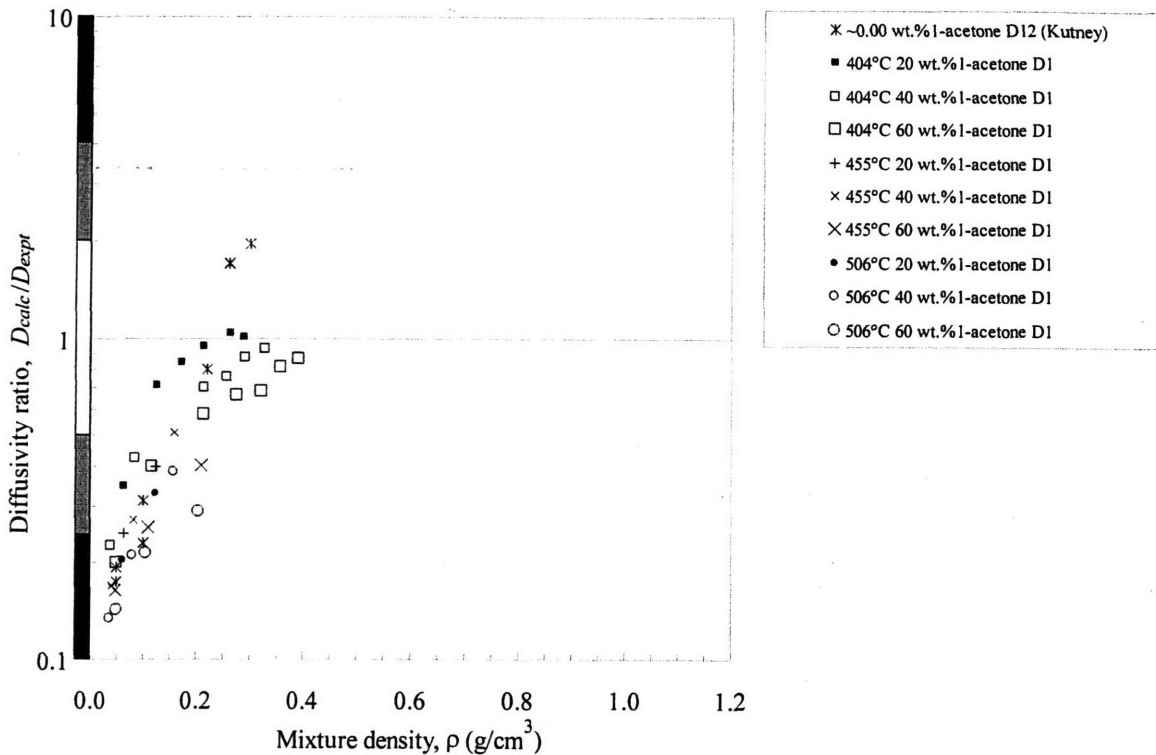
Figure 135. Stokes-Einstein D_{12} and D_1 predictions using the slip condition (4 in denominator), mixture viscosities, and solute radii ($r = r_1$).
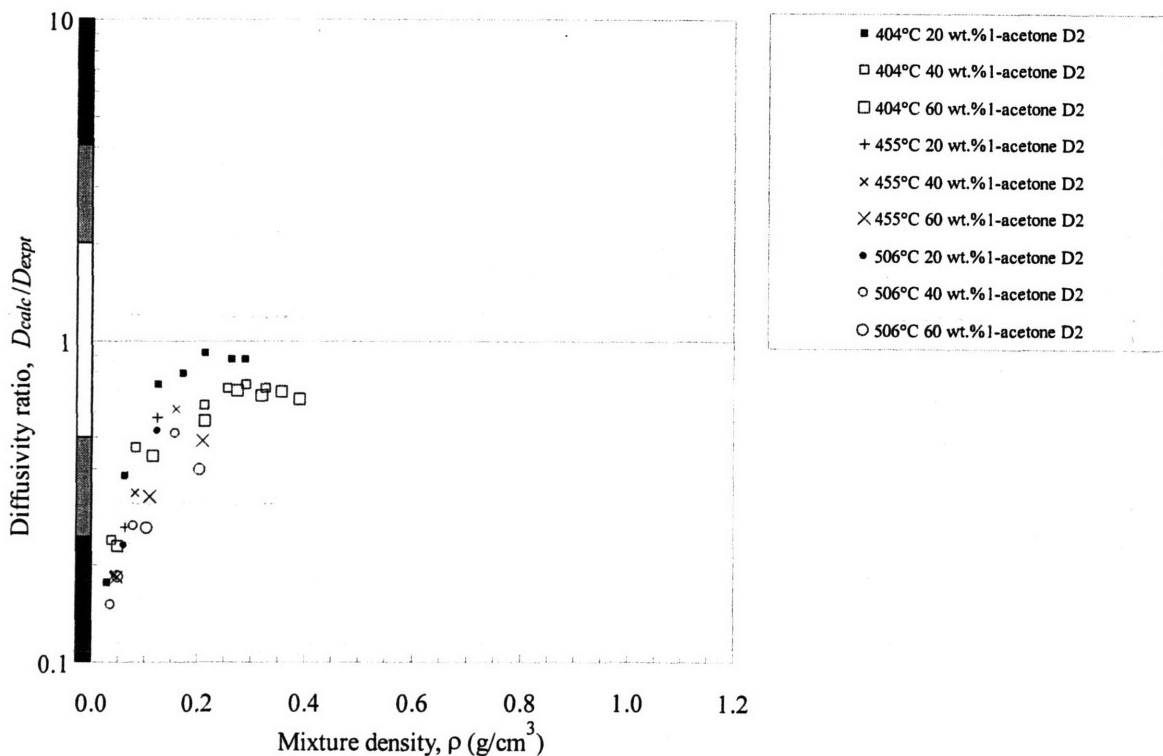
Figure 136. Stokes-Einstein D_{22} and D_2 predictions using the slip condition (4 in denominator), mixture viscosities, and solvent radii ($r = r_2$).

324
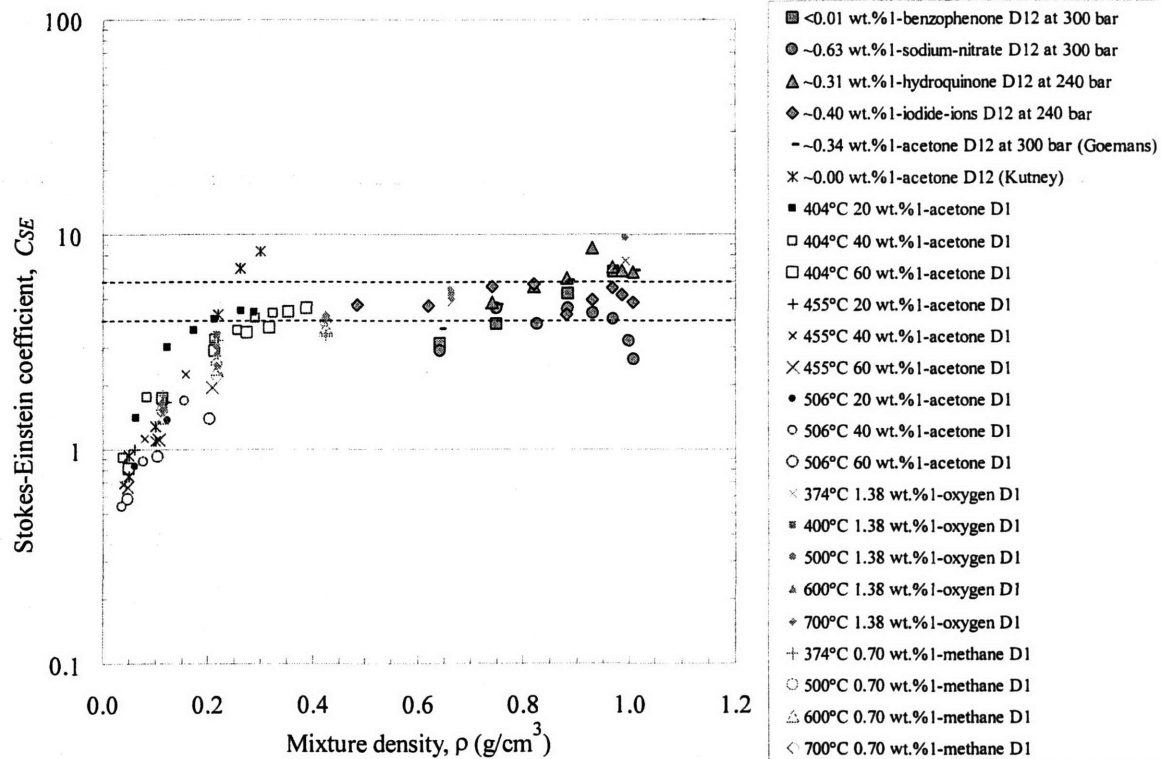
Figure 137. Stokes-Einstein C_{SE} predictions for D_{12} and D_1 using pure water viscosities and solute radii ($r = r_1$).
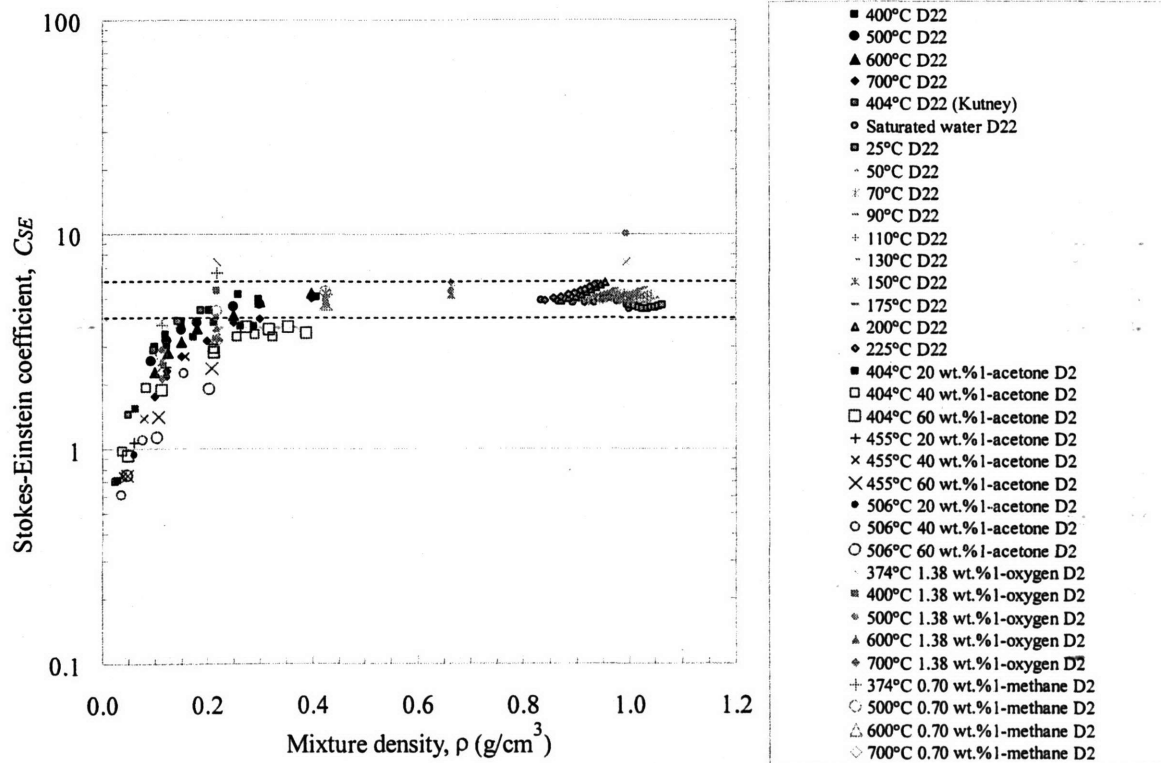
Figure 138. Stokes-Einstein C_{SE} predictions for D_{22} and D_2 using pure water viscosities and solvent radii ($r = r_2$).
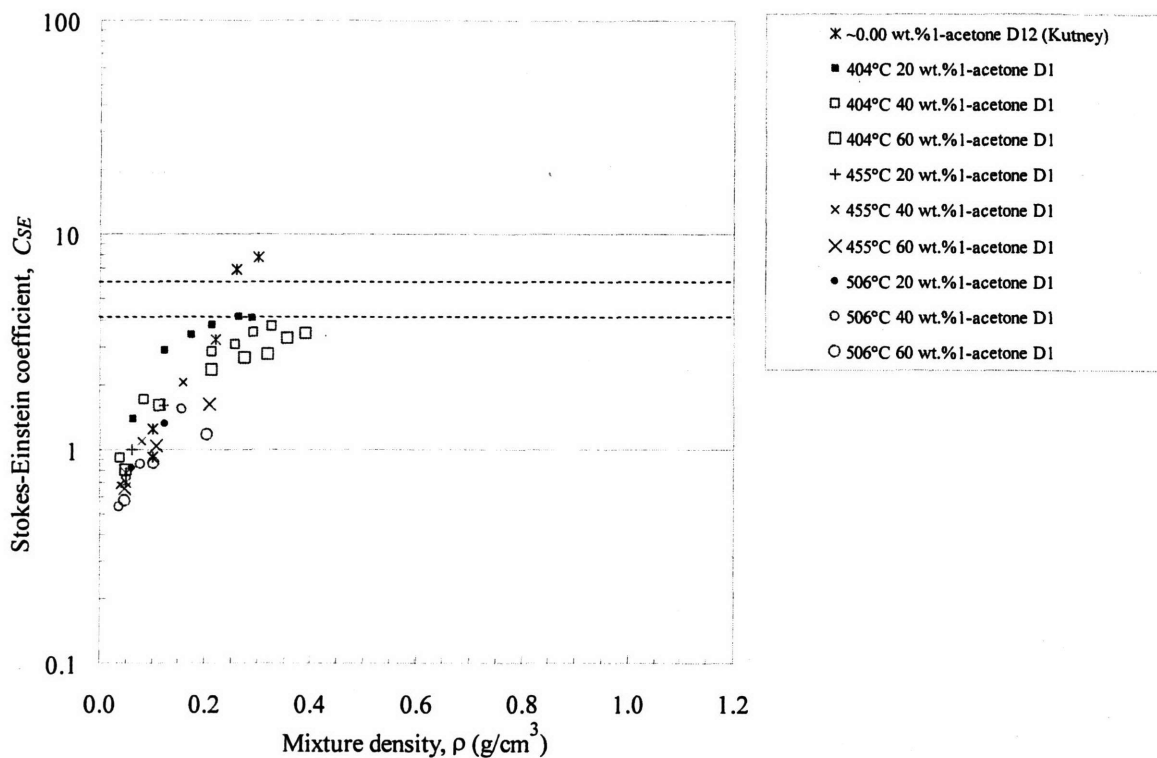
Figure 139. Stokes-Einstein C_{SE} predictions for D_{12} and D_1 using mixture viscosities and solute radii ($r = r_1$).
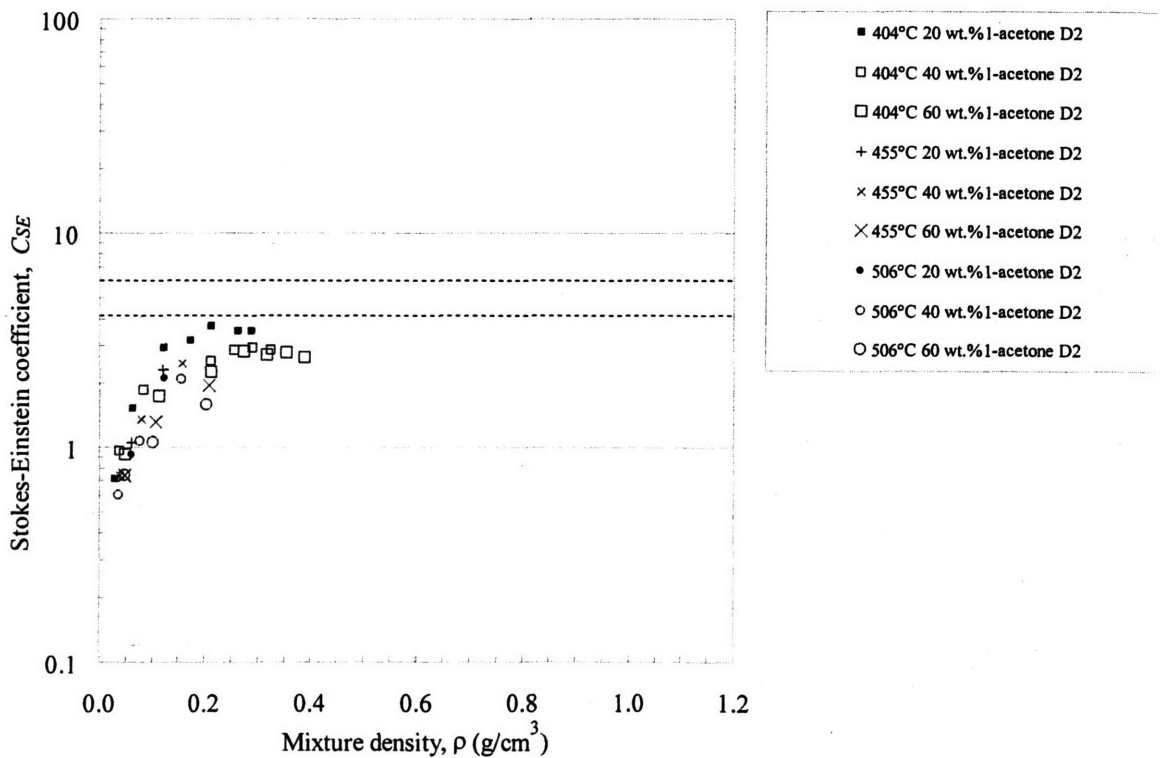
Figure 140. Stokes-Einstein C_{SE} predictions for D_{22} and D_2 using mixture viscosities and solvent radii ($r = r_2$).

326

II.5.2.1.2 Wilke-Chang Equation

Although the Wilke-Chang equation presented in Eq. (101) has a hydrodynamic-theory foundation, the final form was chosen following the fitting of several constants to several hundred high density binary systems over a tenfold solution-viscosity range. Given their approach and fitting region, the Wilke-Chang equation performs adequately for the dense systems evaluated in this analysis as shown in Figure 141 when pure water solvent viscosities over a hundredfold range are used. However, the predictions are inaccurate in the low density region since the Stokes-Einstein criteria are no longer met and since this region is outside the original range of this model. When larger mixture viscosities are employed for concentrated tracer diffusivities, predictions become slightly smaller and worse as seen in Figure 142. However, at higher densities, these reductions will likely improve the Wilke-Chang accuracy for concentrated systems since predictions are currently overestimated with the pure solvent viscosity.

The Wilke-Chang equation evaluated in its original form is rated: F A

(mean low & high density diffusivity ratios: $0.5 \pm 0.5_{95\%}$ & $1.2 \pm 0.4_{95\%}$)

In an attempt to expand the use of the Wilke-Chang correlation for systems with unknown normal-boiling-point volumes, solute volumes were replaced with the solute molar volumes at the condition of interest (i.e., the system temperature, density, and pressure). Diffusivities which have readily available solute densities are plotted in Figure 143. Liquid-like self-diffusivities are not altered since the molar volumes hardly differ. Underestimated dense acetone mutual diffusivities are now larger and similar to the self-diffusivity predictions, even though the Wilke-Chang equation is specifically developed with normal-boiling-point volumes. The convergence of self- and mutual predictions at high density may be a significant result and should be validated with other systems. Low density predictions became obviously smaller and worse since the molar volume significantly increases. As shown in earlier figures as well as in Figure 144, mixture viscosities reduce the predictions when solute molar volumes are used.
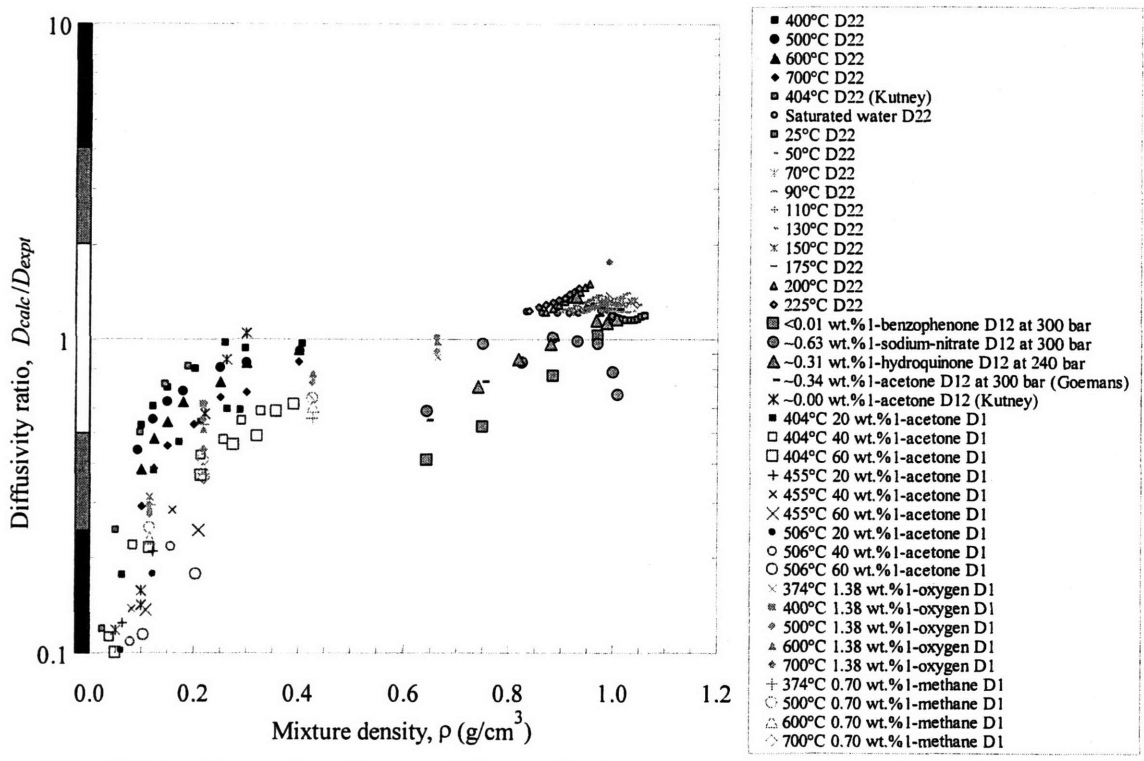
Figure 141. Wilke-Chang D_{22}, D_{12}, and D_1 predictions using pure water viscosities, constant solute normal-boiling-point volumes, and temperature- and density-dependent solvent association factors.

Legend (Figure 141):
- ■ 400°C D22
- ● 500°C D22
- ▲ 600°C D22
- ◆ 700°C D22
- ▫ 404°C D22 (Kutney)
- ○ Saturated water D22
- ▣ 25°C D22
- - 50°C D22
- * 70°C D22
- ~ 90°C D22
- + 110°C D22
- ~ 130°C D22
- × 150°C D22
- - 175°C D22
- ▲ 200°C D22
- ◆ 225°C D22
- ▨ <0.01 wt.%1-benzophenone D12 at 300 bar
- ◉ ~0.63 wt.%1-sodium-nitrate D12 at 300 bar
- ▲ ~0.31 wt.%1-hydroquinone D12 at 240 bar
- ~ ~0.34 wt.%1-acetone D12 at 300 bar (Goemans)
- ✻ ~0.00 wt.%1-acetone D12 (Kutney)
- ■ 404°C 20 wt.%1-acetone D1
- ▫ 404°C 40 wt.%1-acetone D1
- □ 404°C 60 wt.%1-acetone D1
- + 455°C 20 wt.%1-acetone D1
- × 455°C 40 wt.%1-acetone D1
- ✕ 455°C 60 wt.%1-acetone D1
- • 506°C 20 wt.%1-acetone D1
- ○ 506°C 40 wt.%1-acetone D1
- ○ 506°C 60 wt.%1-acetone D1
- × 374°C 1.38 wt.%1-oxygen D1
- ⁂ 400°C 1.38 wt.%1-oxygen D1
- ✿ 500°C 1.38 wt.%1-oxygen D1
- ▲ 600°C 1.38 wt.%1-oxygen D1
- ✦ 700°C 1.38 wt.%1-oxygen D1
- + 374°C 0.70 wt.%1-methane D1
- ◔ 500°C 0.70 wt.%1-methane D1
- △ 600°C 0.70 wt.%1-methane D1
- ◇ 700°C 0.70 wt.%1-methane D1

Figure 142. Wilke-Chang D_{12} and D_1 predictions using mixture viscosities, constant solute normal-boiling-point volumes, and temperature- and density-dependent solvent association factors (D_{22} predictions do not change).

Legend (Figure 142):
- ✻ ~0.00 wt.%1-acetone D12 (Kutney)
- ■ 404°C 20 wt.%1-acetone D1
- ▫ 404°C 40 wt.%1-acetone D1
- □ 404°C 60 wt.%1-acetone D1
- + 455°C 20 wt.%1-acetone D1
- × 455°C 40 wt.%1-acetone D1
- ✕ 455°C 60 wt.%1-acetone D1
- • 506°C 20 wt.%1-acetone D1
- ○ 506°C 40 wt.%1-acetone D1
- ○ 506°C 60 wt.%1-acetone D1

328
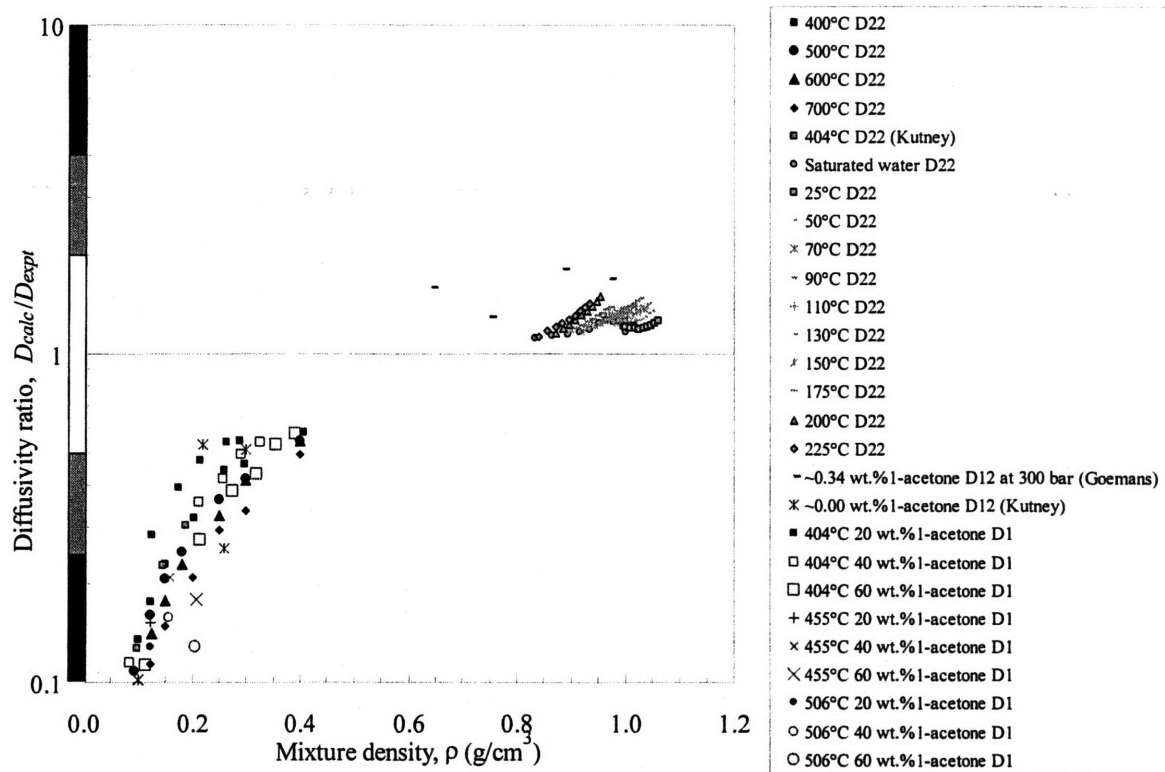
Figure 143. Wilke-Chang D_{22}, D_{12}, and D_1 predictions using pure water viscosities and temperature- and density-dependent solvent association factors and solute volumes.
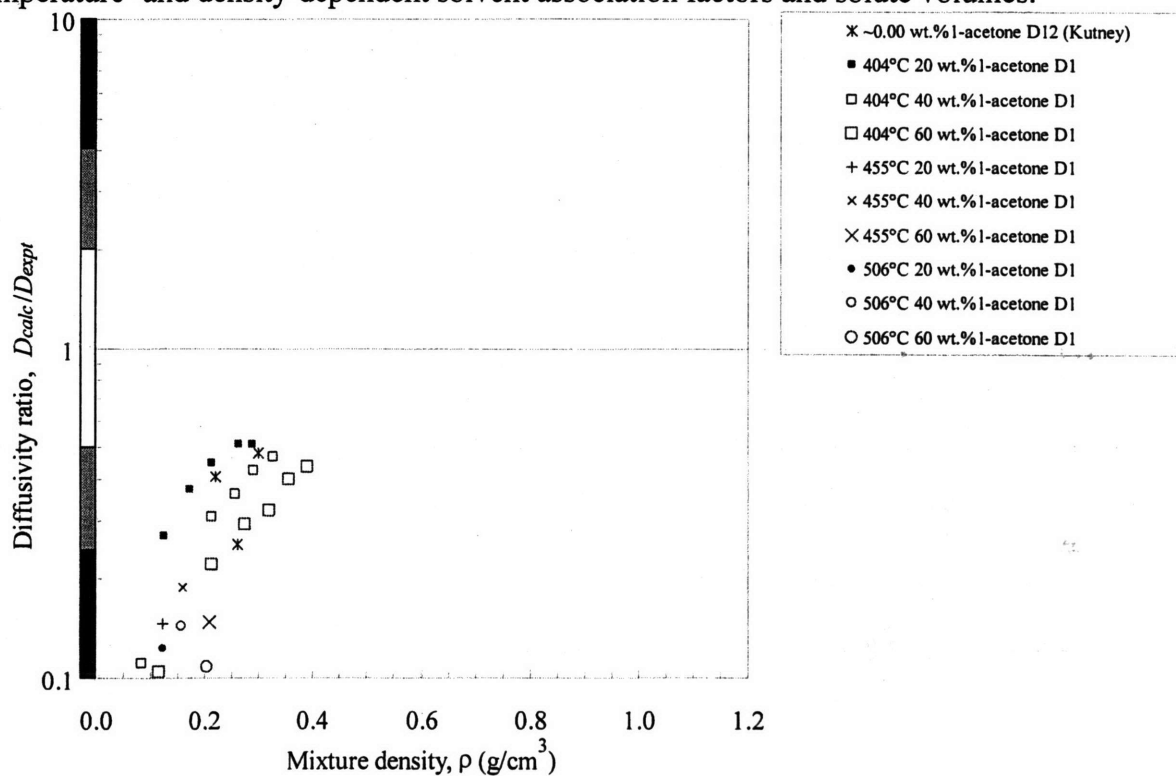
Figure 144. Wilke-Chang D_{12} and D_1 predictions using mixture viscosities and temperature- and density-dependent solvent association factors and solute volumes.

II.5.2.1.3 Reddy-Doraiswamy Equation

The Reddy-Doraiswamy equation defined in Eq. (102) eliminated the need for solute normal-boiling-point volumes and solvent association factors and, instead, requires solute and solvent molar volumes. Designed specifically for liquid diffusivities, the predictions were found to be significantly better than the Wilke-Chang predictions according to Reddy-Doraiswamy, especially for systems when water is the solute (25% error rather than 100%) (Reddy and Doraiswamy, 1967). Results with molar volumes for this analysis are contained in Figure 145 and are noticeably closer to one and more accurate for the liquid water self-diffusivities. Liquid-like acetone mutual diffusivities are overestimated and comparable to the Wilke-Chang predictions that are made with molar volumes. Low density predictions are inaccurate and not significantly different from the Wilke-Chang predictions that are made with molar volumes.

When normal-boiling-point properties are used instead of volumetric properties, the Reddy-Doraiswamy liquid self-diffusivities do not change substantially as seen in Figure 146. For species that are now included in Figure 146, their Reddy-Doraiswamy predictions are remarkably good indicating that the Reddy-Doraiswamy equation provides acceptable estimates of high density diffusivity. Low density predictions are also improved when normal-boiling-point volumes are used, but are still considered inaccurate. Predictions for densities between 0.3 and 0.5 g/cm^3 are fairly accurate and fall within a smaller band, indicating that this equation can predict diffusivities for a wider range than the Wilke-Chang and Stoke-Einstein equations.

Finally, when mixture viscosities are used instead of pure solvent viscosities, the predictions are slightly worse and are consistent with Wilke-Chang and Stokes-Einstein equations using mixture viscosities. These mixture results are shown in Figure 147.

The Reddy-Doraiswamy equation evaluated in its original form is rated: $\boxed{F}$ $\boxed{A}$ (mean low & high density diffusivity ratios: $0.6 \pm 0.6_{95\%}$ & $1.0 \pm 0.4_{95\%}$)

The Reddy-Doraiswamy equation evaluated with NBP volumes is rated for densities greater than 0.3 g/cm^3: (low & high mean ratios: $0.2 \pm 0.4_{95\%}$ & $1.0 \pm 0.2_{95\%}$) $\boxed{C}$ $\boxed{A}$
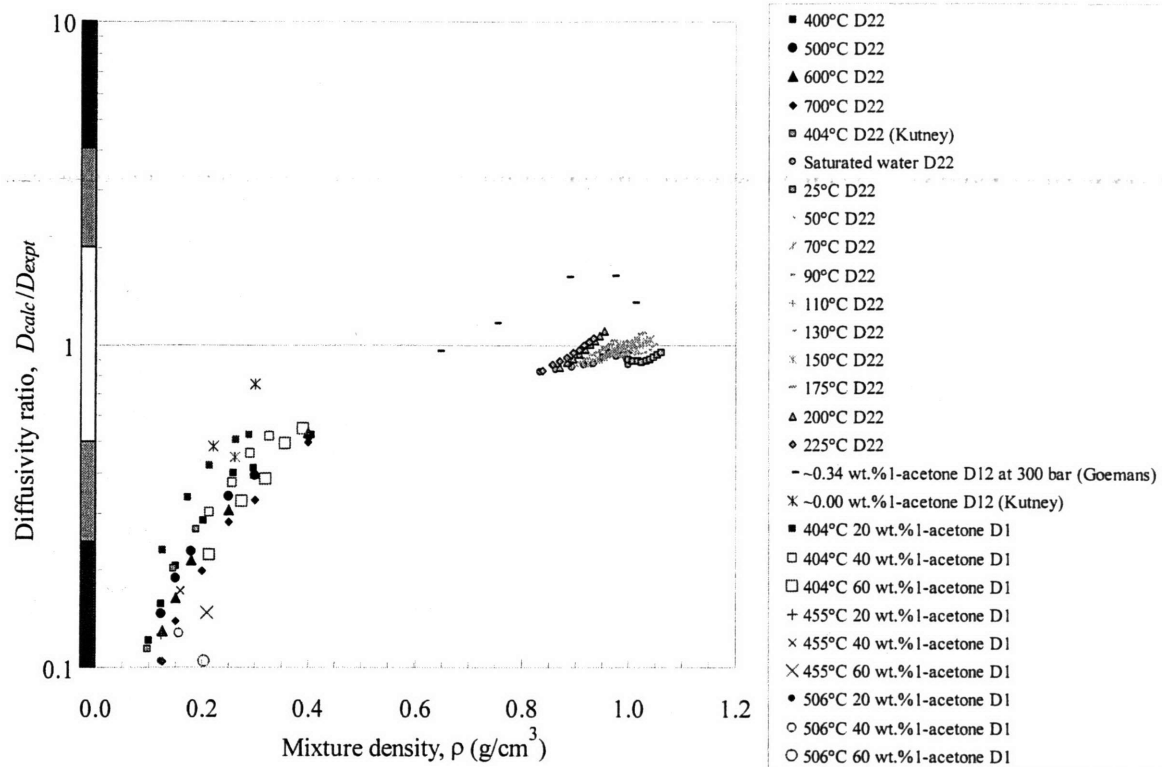
Figure 145. Reddy-Doraiswamy D_{22}, D_{12}, and D_1 predictions using pure water viscosities and temperature- and density-dependent solute volumes.
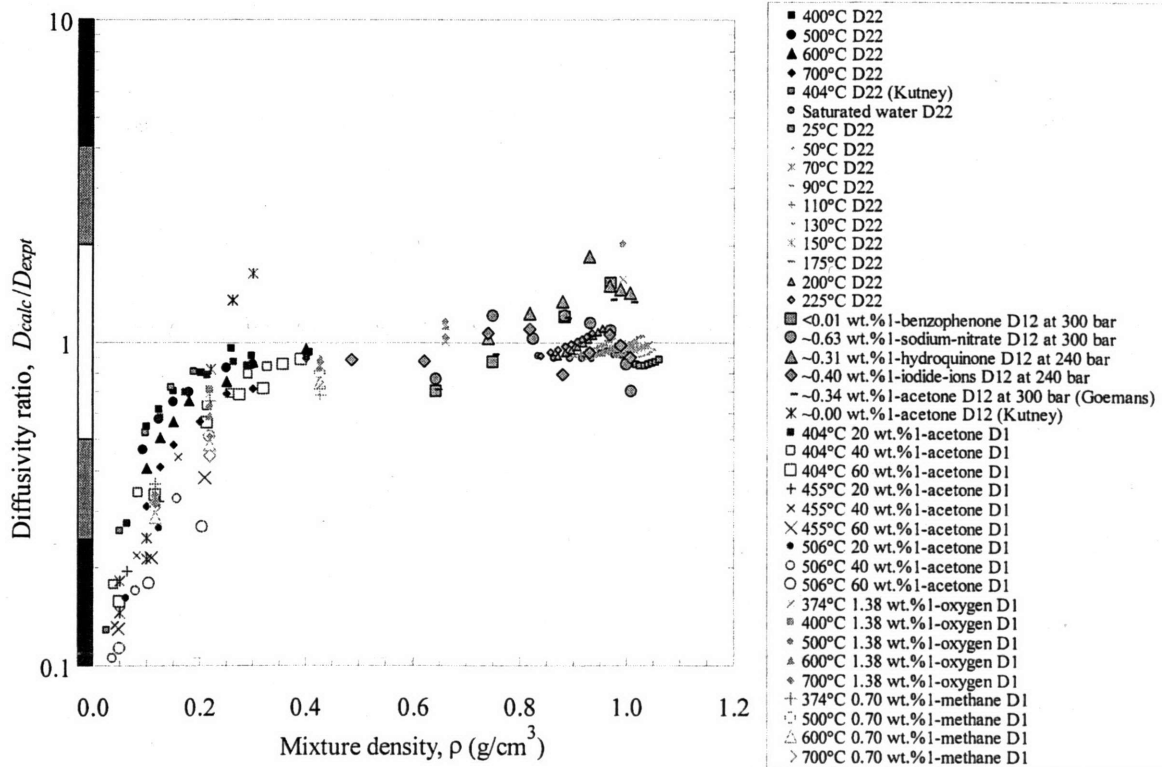
Figure 146. Reddy-Doraiswamy D_{22}, D_{12}, and D_1 predictions using pure water viscosities and constant solute and solvent normal-boiling-point volumes.
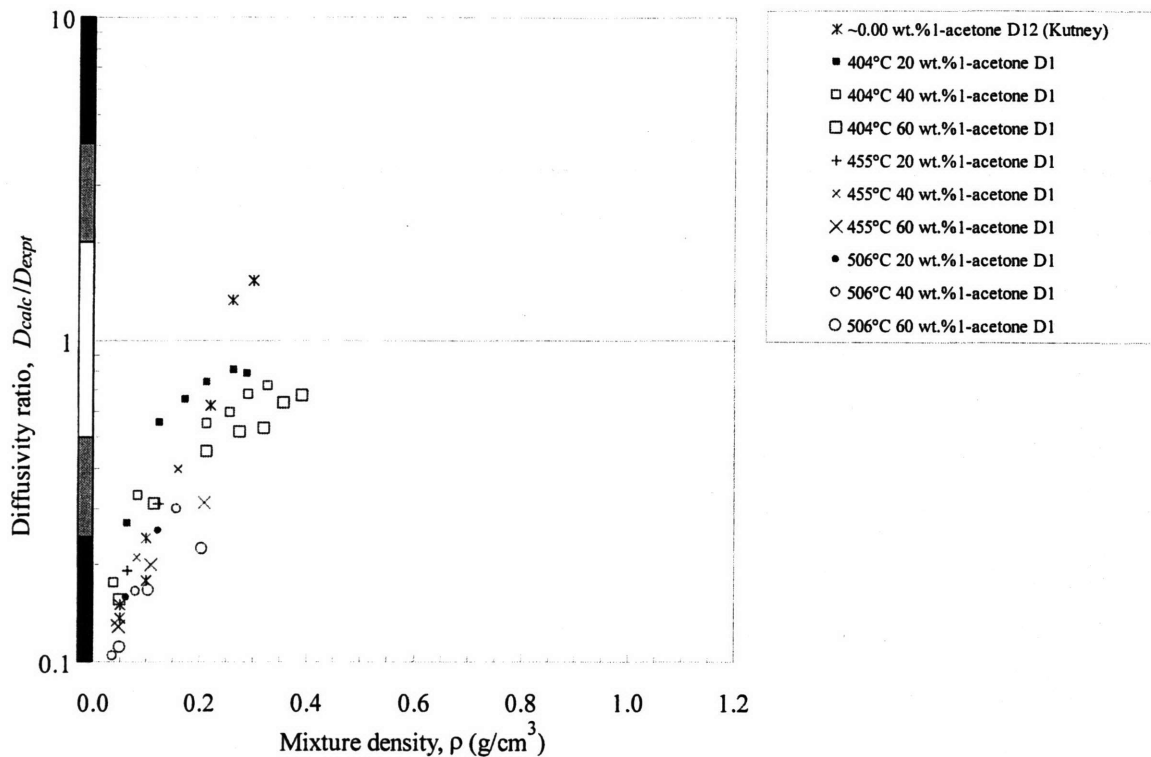
Figure 147. Reddy-Doraiswamy D_{12} and D_1 predictions using mixture viscosities and constant solute and solvent normal-boiling-point volumes (D_{22} predictions do not change).

The NBP-volume equation is not recommended for 0.3 g/cm^3 densities or less: **F** **A** (mean low & high density diffusivity ratios: $0.2 \pm 0.4_{95\%}$ & $1.0 \pm 0.2_{95\%}$)

All three examined hydrodynamic models perform well in the liquid density regime, but they cannot extend to the low density region. As reflected in Table 58, the Reddy-Doraiswamy correlation is the only hydrodynamic model that can be used with acceptable accuracy for mixture densities greater than 0.3 g/cm^3 when normal-boiling-point molar volumes are employed. Also, it is the only model which has subcritical self-diffusivity ratios centered on one as seen in Figure 146. Mean diffusivity ratios and their corresponding uncertainties are presented in Figure 148, and this figure visually demonstrates the success of all the hydrodynamic models at high densities, especially the Reddy-Doraiswamy correlation. From this analysis, solvent viscosities should be used in these models, since mixture viscosities always reduce the diffusivity ratios. With the hydrodynamic-theory analysis complete, the kinetic-theory analysis will be discussed next.

332

Table 58. Low and high density performance rankings for the
hydrodynamic diffusivity models evaluated in this analysis

Model	Section	Density Low | High	
Hydrodynamic theory of diffusion	II.5.2.1		
Stokes-Einstein equation with the no-slip condition	II.5.2.1.1	F	A
Stokes-Einstein equation with the slip condition	II.5.2.1.1	F	A
Wilke-Chang equation	II.5.2.1.2	F	A
Reddy-Doraiswamy equation (original form)	II.5.2.1.3	F	A
(>0.3 g/cm^3 with NBP-volumes)	II.5.2.1.3	C	A

Average diffusivity ratio with 95%-confidence-interval uncertainties

Figure 148. Low and high density mean diffusivity ratios with 95%-confidence-interval uncertainties for the hydrodynamic diffusivity models evaluated in this analysis.

333

II.5.2.2 Kinetic Theory of Diffusion

The kinetic-theory analysis first begins with the Chapman-Enskog equation in its original form before any corrections are employed. These corrections are needed to extend the kinetic-theory models from its low density origin to higher densities where the mean free path is not large compared to the molecular diameters. Following discussion of the Chapman-Enskog corrections, semi-empirical models will be discussed.

II.5.2.2.1 Chapman-Enskog Equation

Chapman-Enskog diffusivity is calculated with Eq. (109) and the Lennard-Jones 6-12 collision integral (Eq. (113)). Unweighted combining rules are used to calculate the effective collision diameter (Eq. (111)), the effective potential well depth (Eq. (112)), and the molecular weight ($M_{12} = 2/\{(1/M_1) + (1/M_2)\}$). Results using the original formulation of the Chapman-Enskog equation with unweighted combining rules are provided in Figure 149 for the systems with known Lennard-Jones constants. Although Figure 149 appears to be accurate at low density, it has high density shortcomings as seen when the ordinate is expanded in Figure 150. High density predictions are clearly poor and immediately lead to the need for higher density corrections.

Prior to correcting the Chapman-Enskog formulation, attempts were made to introduce concentration dependence into the model since tracer-diffusivity data are available at several concentrations. Diffusivities with mole-fraction-weighted molecular weights and Lennard-Jones parameters were evaluated first. Molecular weight and the collision diameter were linearly weighted, *i.e.*, $M_{12} = x_1 M_1 + x_2 M_2$ and $\sigma_{12} = x_1 \sigma_1 + x_2 \sigma_2$, while the potential well depth was arbitrarily weighted with $\varepsilon_{12} = \varepsilon_1^{x_1} \varepsilon_2^{x_2}$. Weighting infinitely dilute mutual diffusivities in this fashion essentially neglect the solute contributions since all mixtures wind up having solvent-like properties. Results with this combined weighting are contained in Figure 151 and Figure 152. Diffusivity ratios increase and are observably worse over the entire density range. Also note that infinitely dilute mutual diffusivities are now similar to self-diffusivities since solute effects are purged.
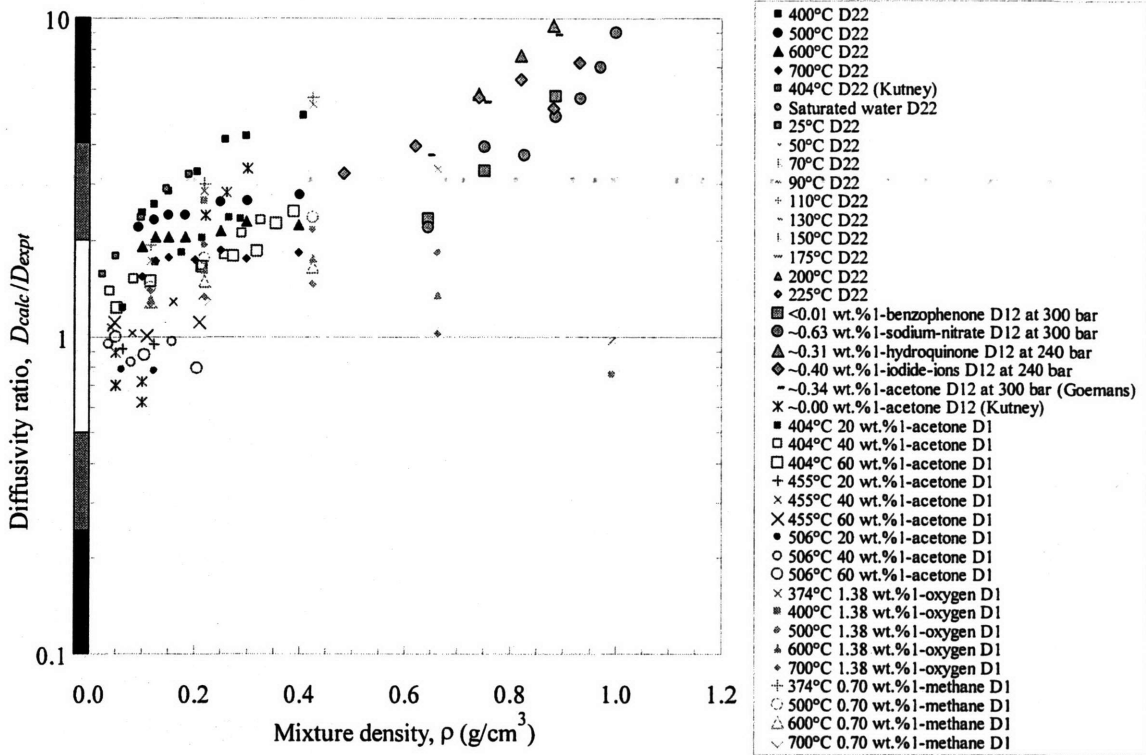
Figure 149. Chapman-Enskog D_{22}, D_{12}, and D_1 predictions using **unweighted** molecular weight and Lennard-Jones parameters.
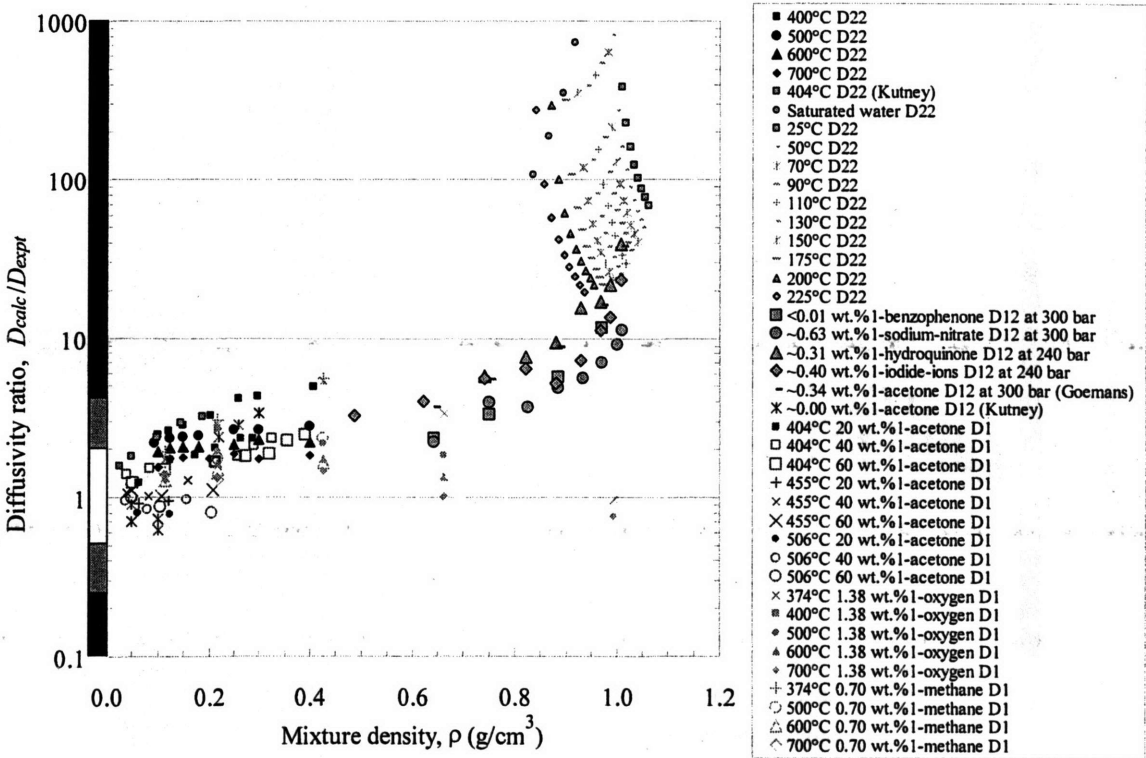
Figure 150. Chapman-Enskog D_{22}, D_{12}, and D_1 predictions using **unweighted** molecular weight and Lennard-Jones parameters and shown with a larger ordinate range.
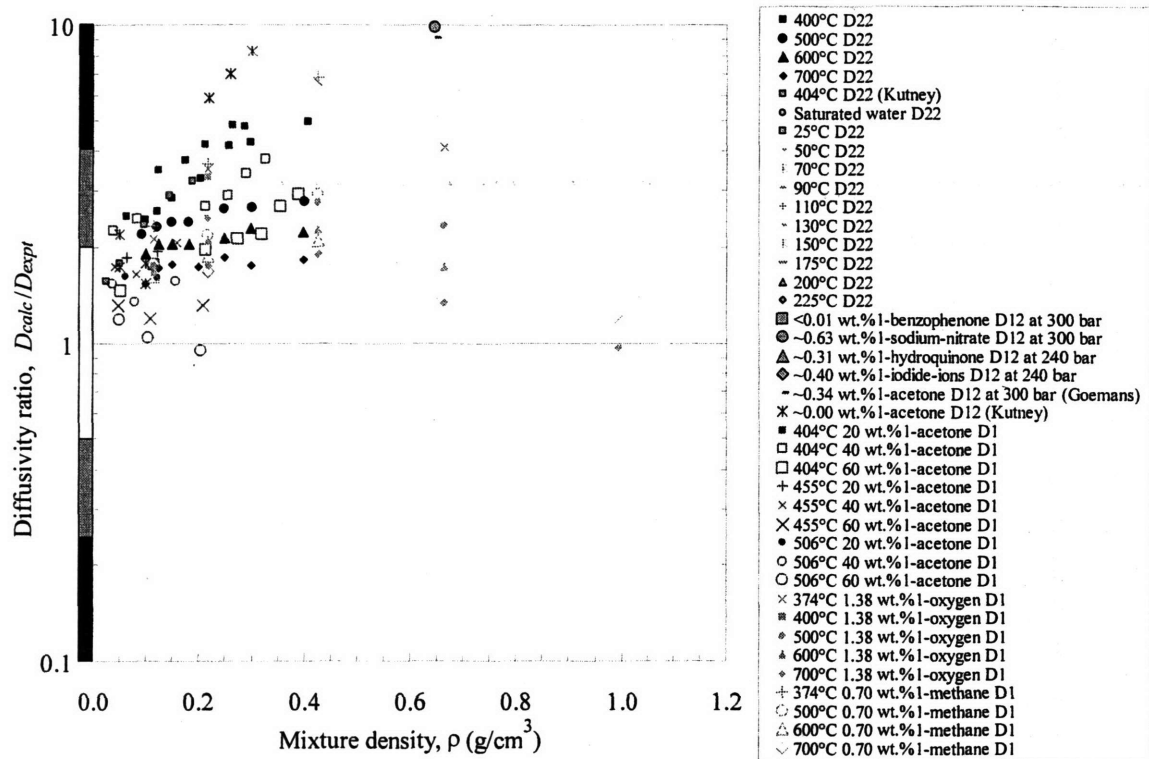
Figure 151. Chapman-Enskog D_{22}, D_{12}, and D_1 predictions using **weighted** molecular weight and Lennard-Jones parameters.
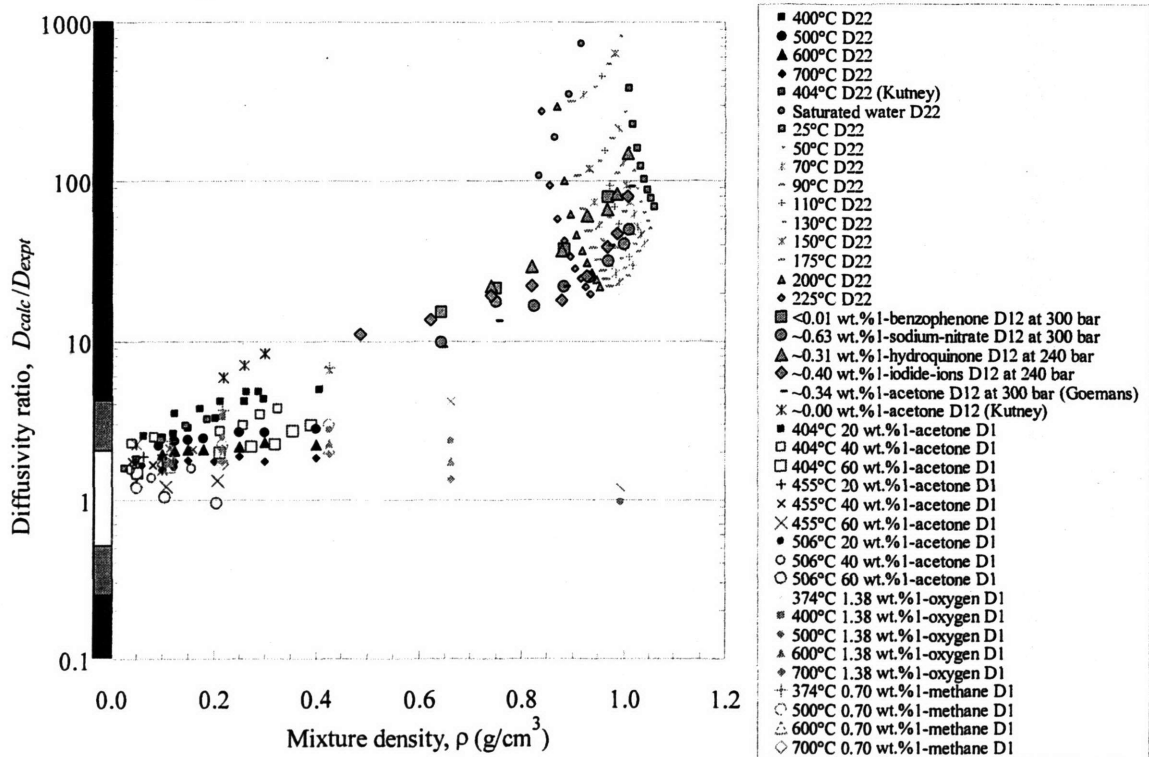
Figure 152. Chapman-Enskog D_{22}, D_{12}, and D_1 predictions using **weighted** molecular weight and Lennard-Jones parameters and shown with a larger ordinate range.

In order to understand which weighting term contributes to the deteriorating predictions, weighting is only performed for the molecular weight. The results, as seen in Figure 153 and Figure 154, are nearly equivalent with the original Chapman-Enskog predictions, thereby implying that the Lennard-Jones weighting is the source of the weighting-prediction deterioration. As a final check, when the Lennard-Jones terms are the only terms weighted, the predictions are significantly worse as verified in Figure 155 and Figure 156. In all cases the predictions are inadequate which indicate that the uncorrected Chapman-Enskog equation is not appropriate for use in supercritical-water diffusivity modeling.

The Chapman-Enskog equation in its original unweighted form is rated: C F
(mean low & high density diffusivity ratios: $2 \pm 2_{95\%}$ & $>10 \pm >10_{95\%}$)
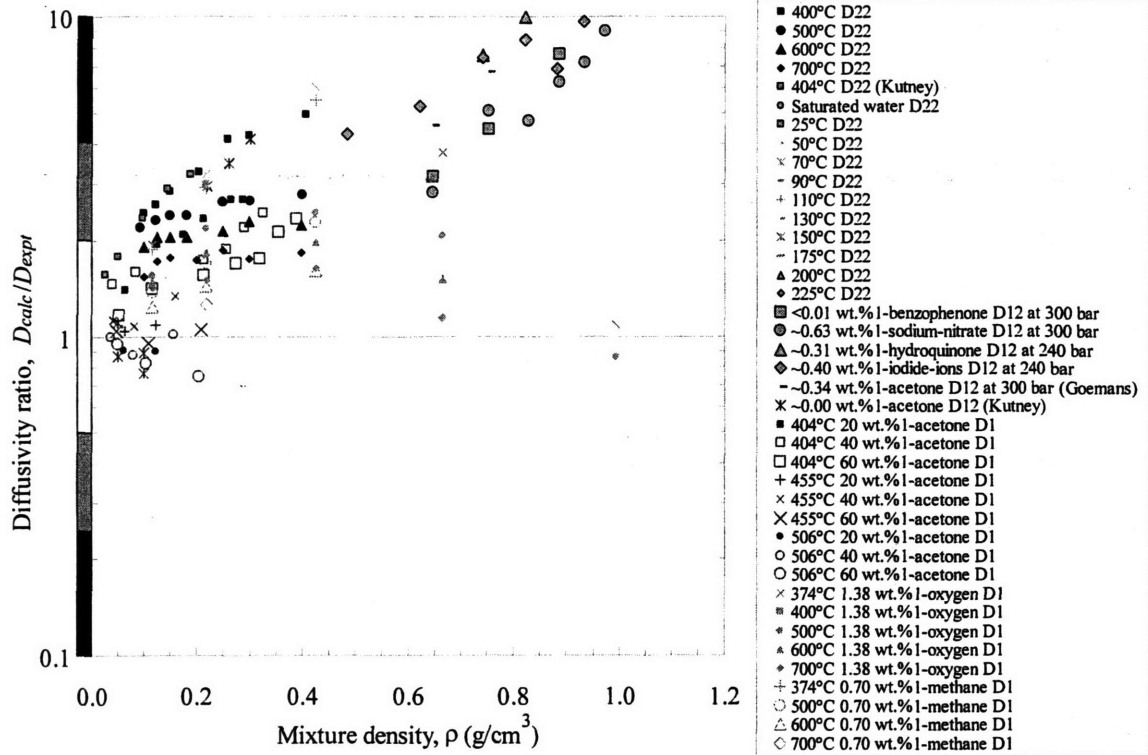
Figure 153. Chapman-Enskog D_{22}, D_{12}, and D_1 predictions using **weighted** molecular weight and **unweighted** Lennard-Jones parameters.
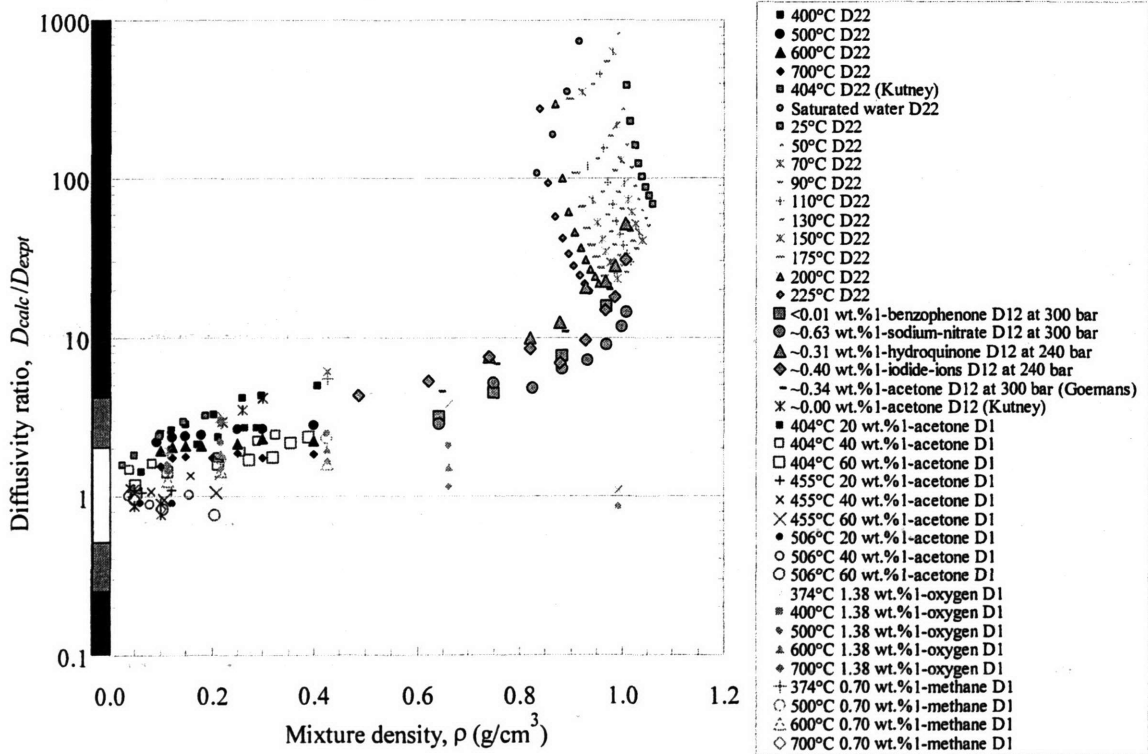
Figure 154. Chapman-Enskog D_{22}, D_{12}, and D_1 predictions using **weighted** molecular weight and **unweighted** Lennard-Jones parameters and shown with a larger ordinate range.

338
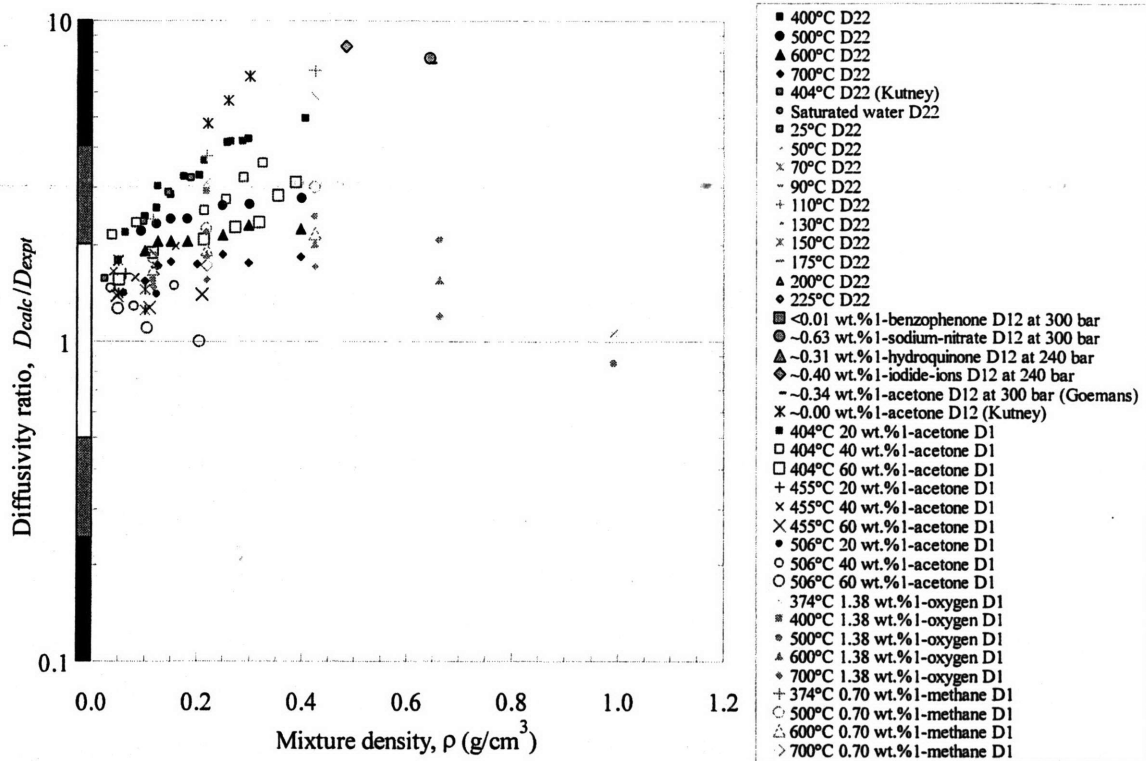
Figure 155. Chapman-Enskog D_{22}, D_{12}, and D_1 predictions using **unweighted** molecular weight and **weighted** Lennard-Jones parameters.
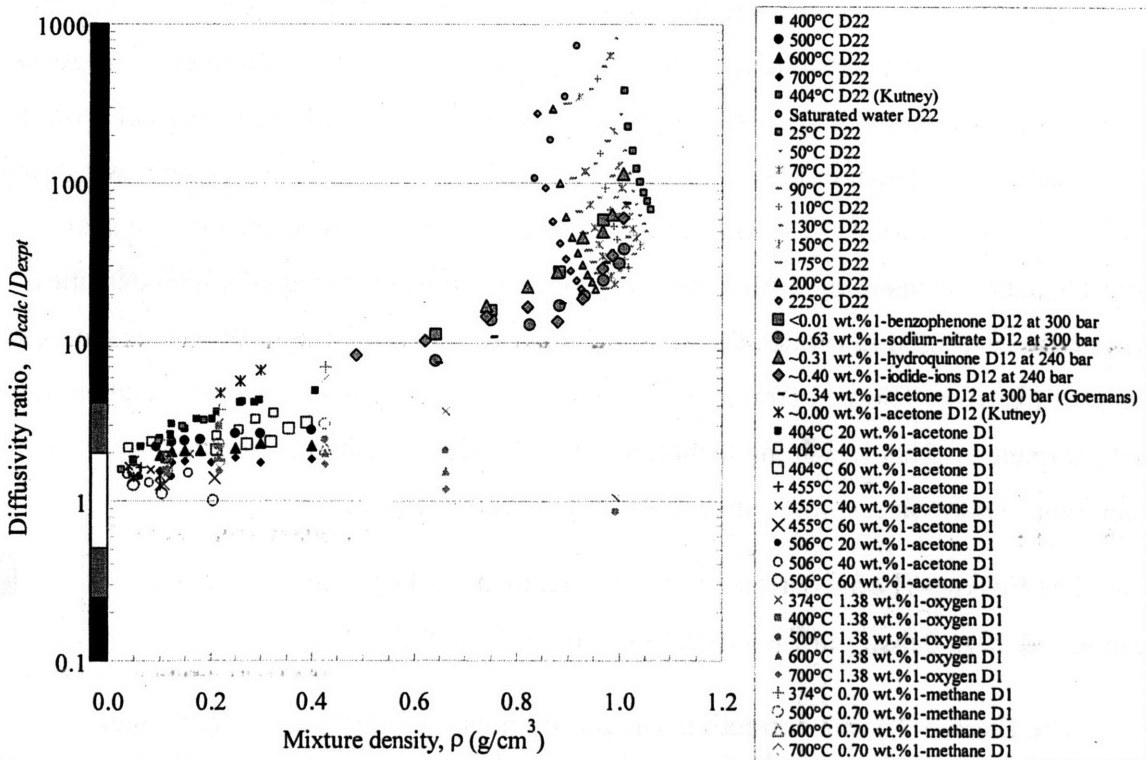
Figure 156. Chapman-Enskog D_{22}, D_{12}, and D_1 predictions using **unweighted** molecular weight and **weighted** Lennard-Jones parameters and shown with a larger ordinate range.

II.5.2.2.1.1 Chapman-Enskog Equation with the Enskog-Thorne Correction

Since the Chapman-Enskog model is not normally extended beyond the ideal-gas region, several approaches have been developed in order to compensate for this limitation. The first correction explored in this dissertation is developed by Enskog and Thorne and is introduced in Eq. (117). Their correction factor scales the low density diffusivity to the diffusivity at the density of interest using a density-dependent correction factor. As seen in Figure 157, the Enskog-Thorne correction reduces the higher density diffusivities an order of magnitude compared to the uncorrected Chapman-Enskog results in Figure 149 and Figure 150. For the most part, self-diffusivities are overestimated, while tracer and mutual diffusivities are underestimated. Since molecular weights, well-depths, and diameters are the only terms that induce this partition, weighting effects were also investigated.

When the Chapman-Enskog weighting approach previously tested is used and all three terms are weighted, the partition is greatly reduced as seen in Figure 158. For dilute solutes, this mole-fraction weighting approach reduced the partition since the solute contribution becomes effectively zero. For this reason, the diffusivities approach the self-diffusivity values which are, of course, unchanged using any weighting approach. In order to understand which term contributed to the partition reduction, molecular-weight weighting is performed first. As seen in Figure 159, the weighted-molecular-weight results are nearly similar to the original Enskog-Thorne predictions shown in Figure 157, thereby implying that the Lennard-Jones weighting is the origin for the partition reduction. The weighted-Lennard-Jones corrections are shown in Figure 160, and the resulting diffusivities are fairly accurate, except at very high densities. Based on these weighting results, the partition between self- and other diffusivities seen with the unweighted Enskog-Thorne correction can be reduced by using mole-fraction-weighted Lennard-Jones parameters. This weighting technique also provides a method to incorporate concentration dependence. Otherwise, solute concentration is unaccounted for.

The Enskog-Thorne correction of the Chapman-Enskog equation is rated: **C F**
(mean low & high density diffusivity ratios: $1.0 \pm 0.7_{95\%}$ & $2 \pm 3_{95\%}$)

The Enskog-Thorne correction using mole-fraction-weighted Lennard-Jones
terms is rated: (mean low & high density diffusivity ratios: $1.2 \pm 0.5_{95\%}$ & $2 \pm 3_{95\%}$) **A F**

Figure 157. Chapman-Enskog D_{22}, D_{12}, and D_1 predictions with the Enskog-Thorne correction using **unweighted** molecular weight and Lennard-Jones parameters.

Figure 158. Chapman-Enskog D_{22}, D_{12}, and D_1 predictions with the Enskog-Thorne correction using **weighted** molecular weight and Lennard-Jones parameters.

Figure 159. Chapman-Enskog D_{22}, D_{12}, and D_1 predictions with the Enskog-Thorne correction using **weighted** molecular weight and **unweighted** Lennard-Jones parameters.

Figure 160. Chapman-Enskog D_{22}, D_{12}, and D_1 predictions with the Enskog-Thorne correction using **unweighted** molecular weight and **weighted** Lennard-Jones parameters.

II.5.2.2.1.2 Chapman-Enskog Equation with the Takahashi Correction

The next correction evaluated is the Takahashi correction defined in Eq. (118) using experimentally regressed parameters contained in Table 25. These parameters were fit to a collection of organic and inert mutual diffusivities over a reduced temperature and pressure range of $0.88 \leq T_r \leq 6.41$ and $0.02 \leq P_r \leq 9.83$, respectively (Takahashi, 1974). When this correction is applied to the original Chapman-Enskog equation as shown in Figure 161, the low density predictions are significantly improved, but still overestimate the diffusivity. Also, these predictions do not resemble the bimodal Enskog-Thorne predictions which were minimized with weighted Lennard-Jones parameters. At high densities the Takahashi correction results in significant errors and is essentially unusable since the Takahashi correction becomes negative for the majority of low temperature ($T_r \leq 0.88$) and high pressure diffusivity data.

The Takahashi correction is inherently mole-fraction-weighted since mole-fraction-weighted reduced temperatures and pressures are used throughout the calculation. Weighting calculations were also performed using mole-fraction-weighted molecular weights and Lennard-Jones parameters. As seen in Figure 162, accuracy is not improved with the weighted Chapman-Enskog terms, and high density predictions are still not possible. As previously noted, the weighting minimizes the solute contribution, and the predicted diffusivities essentially mimic the water self-diffusivities. Duplicating the analysis approach used earlier, the weighting effect is examined first using unweighted Lennard-Jones parameters and mole-fractioned-weighted molecular weights (see Figure 163) followed by the unweighted molecular weights and weighted Lennard-Jones parameters (see Figure 164). As previously seen, the Lennard-Jones weighting has the strongest influence to force the diffusivity to match self-diffusivity values. Neither of these schemes are worthy of recommendation, but they clearly indicate that weighting can result in significant prediction modifications.

The Takahashi correction of the Chapman-Enskog equation is rated: C F

(mean low & high density diffusivity ratios: $1 \pm 1_{95\%}$ & $>10 \pm >10_{95\%}$)

Figure 161. Chapman-Enskog D_{22}, D_{12}, and D_1 predictions with the Takahashi correction using **unweighted** molecular weight and Lennard-Jones parameters.

Figure 162. Chapman-Enskog D_{22}, D_{12}, and D_1 predictions with the Takahashi correction using **weighted** molecular weight and Lennard-Jones parameters.

344

Figure 163. Chapman-Enskog D_{22}, D_{12}, and D_1 predictions with the Takahashi correction using **weighted** molecular weight and **unweighted** Lennard-Jones parameters.

Figure 164. Chapman-Enskog D_{22}, D_{12}, and D_1 predictions with the Takahashi correction using **unweighted** molecular weight and **weighted** Lennard-Jones parameters.

345

II.5.2.2.1.3 Chapman-Enskog Equation with the Dawson HS Correction

The next Chapman-Enskog modification discussed is the Dawson correction which attempts to correct for non-ideal densities of spherical non-polar gases (Dawson *et al.*, 1970). Introduced in Eq. (119), this volume virial expansion is based on the theoretical argument that the self-diffusivity of dense hard spheres can be written in terms of the compressibility (Douglass *et al.*, 1961). The fixed Dawson constants were fit from experimental methane sub- and supercritical self-diffusivities. Due to success of this correction for other gases such as hydrogen, krypton, and carbon dioxide, it is evaluated for sub- and supercritical water and its mixtures. For every mixture, reduced density is estimated using mixture density and the mole-fraction-weighted critical density given by Eq. (194). When combined with the original Chapman-Enskog equation, the Dawson correction is successful in reducing low density diffusivities to acceptable levels as shown in Figure 165. Dense predictions are poor and significantly drop off due to the mathematical form of the Dawson correction. As noted in earlier in this dissertation, this correction is limited to reduced densities of less than 2.5, otherwise, it becomes negative.

Figure 165. Chapman-Enskog D_{22}, D_{12}, and D_1 predictions with the Dawson hard-sphere correction using **unweighted** molecular weight and Lennard-Jones parameters.

To complete the analysis, the Dawson correction is separately tested with mole-fraction-weighted Chapman-Enskog terms including when molecular weight is weighted, Lennard-Jones parameters are weighted, and when all three are weighted. When all three are weighted (see Figure 166), tracer and mutual diffusivities increase while their diffusivity ratios become noticeably imprecise (self-diffusivities obviously remain the same). When molecular weight is weighted, the low density predictions become slightly less accurate as seen in Figure 167, while the denser mixture diffusivities become markedly more accurate. Finally, as revealed in Figure 168, the Lennard-Jones-weighted ratios are similar to the substandard case when all three parameters are weighted.

In principle, the Dawson correction is similar to the Takahashi correction because both are limited to low density predictions due to their choice of regressed datasets. Both significantly improve the Chapman-Enskog predictions in the low density regime, but are not recommended for higher densities.

As a result, the Dawson correction of the Chapman-Enskog equation is rated: [A] [F]
(mean low & high density diffusivity ratios: $1.2 \pm 0.6_{95\%}$ & $0.4 \pm 0.5_{95\%}$)

Figure 166. Chapman-Enskog D_{22}, D_{12}, and D_1 predictions with the Dawson hard-sphere correction using **weighted** molecular weight and Lennard-Jones parameters.
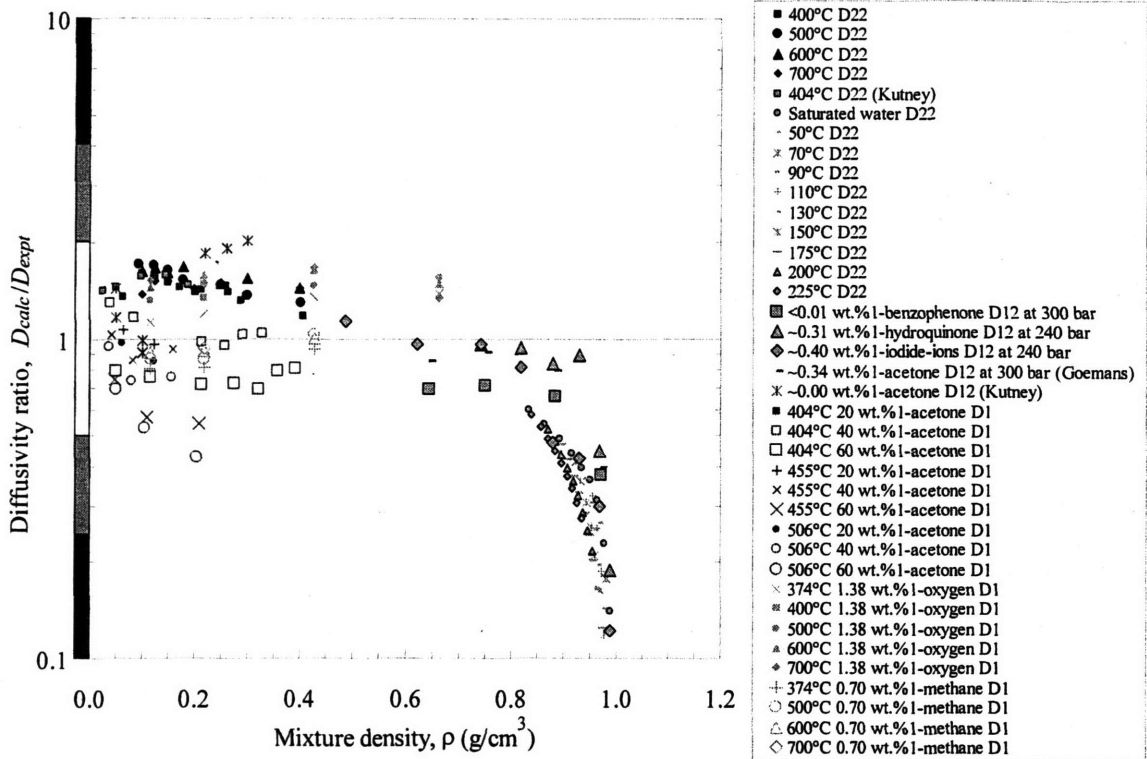
Figure 167. Chapman-Enskog D_{22}, D_{12}, and D_1 predictions with the Dawson hard-sphere correction using **weighted** molecular weight and **unweighted** Lennard-Jones parameters.
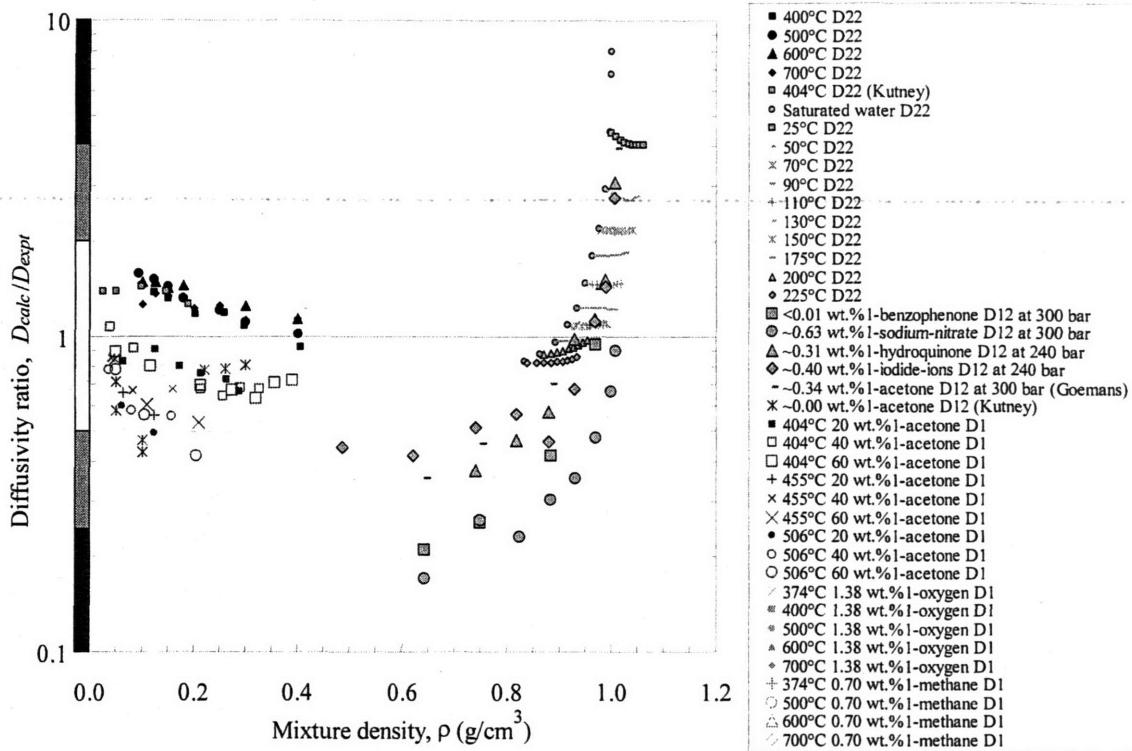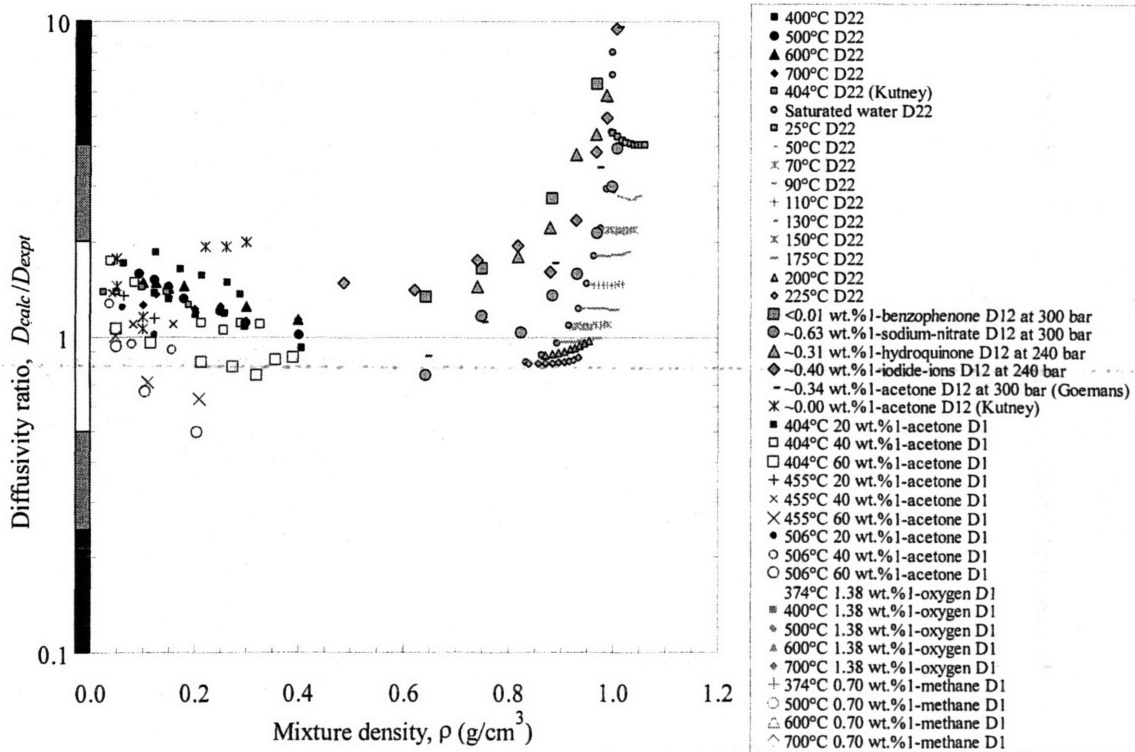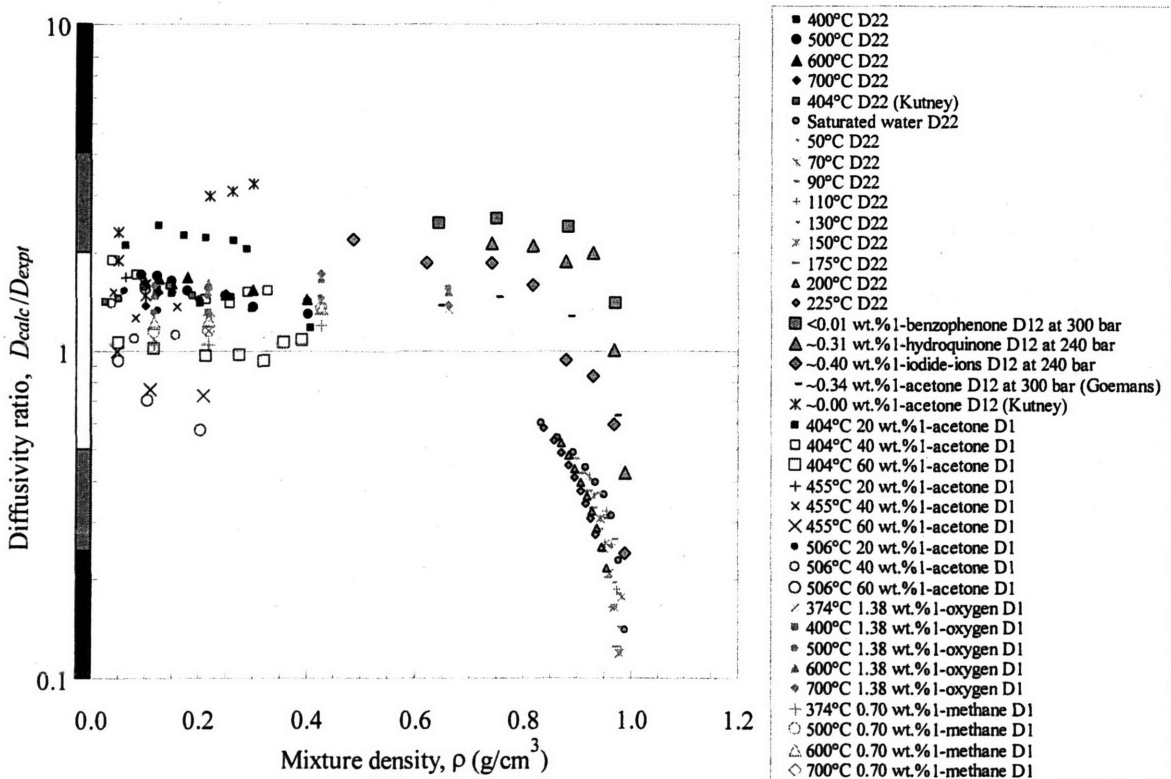

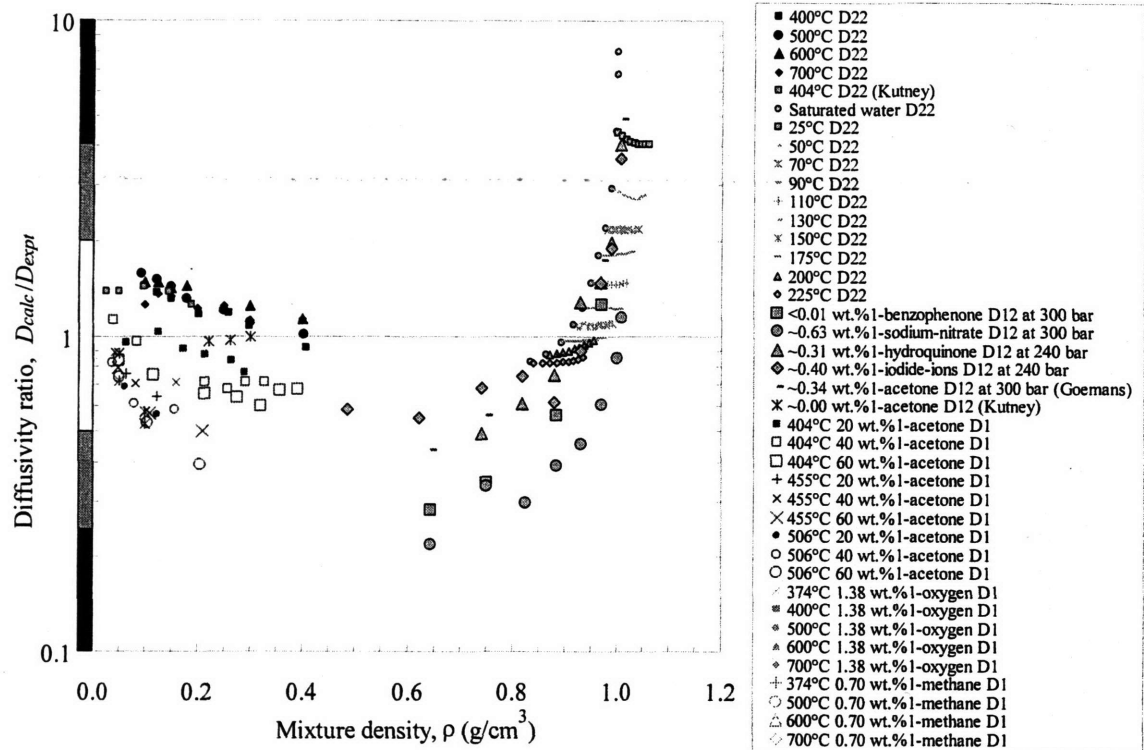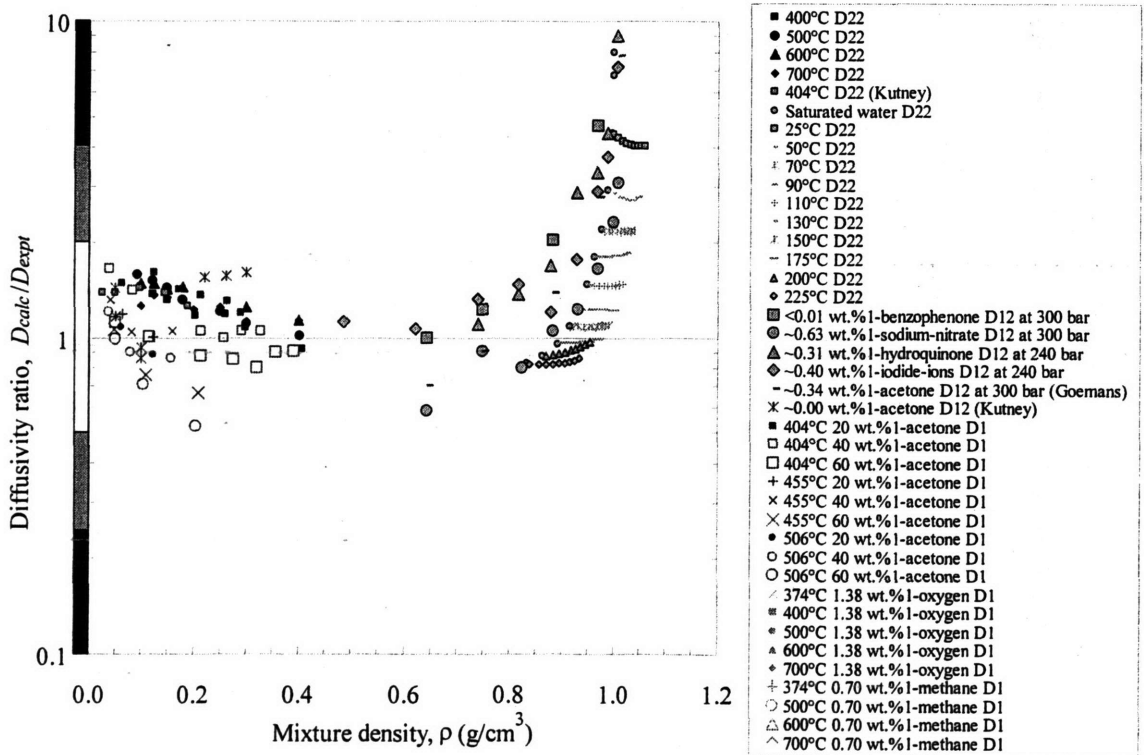Figure 168. Chapman-Enskog D_{22}, D_{12}, and D_1 predictions with the Dawson hard-sphere correction using **unweighted** molecular weight and **weighted** Lennard-Jones parameters.

II.5.2.2.1.4Chapman-Enskog Equation with the Erpenbeck-Wood HS Correction

The correction developed by Erpenbeck and Wood for self-diffusivities of hard-sphere fluids is based on Monte-Carlo simulations performed for $1.6 \leq V/V_0 \leq 25$ reduced-volume ratios. Presented in Eq. (142), the coefficients are based solely on their simulation work and are not regressed to experimental data. Their simulations include backscattering and vortex-formation effects that are included in hard-sphere theories and that are described in Section II.1.1.4. When applied to the original Chapman-Enskog equation, the Erpenbeck-Wood correction performed poorly over the entire density range as seen in Figure 169.

The form of their correction is mathematically similar to the Dawson correction previously discussed, but it is fundamentally superior since this correction varies between 0.84 and 1.34 and can never become negative. However, the failure of this correction is in part due to its lack of flexibility since all of the universal constants are regressed from theoretical, and not experimental, results. Due to its failure to improve low density predictions, the Erpenbeck-Wood analysis is stopped.

The Erpenbeck-Wood correction of the Chapman-Enskog equation is rated: ▮ ▮

(mean low & high density diffusivity ratios: $2 \pm 2_{95\%}$ & $>10 \pm >10_{95\%}$)
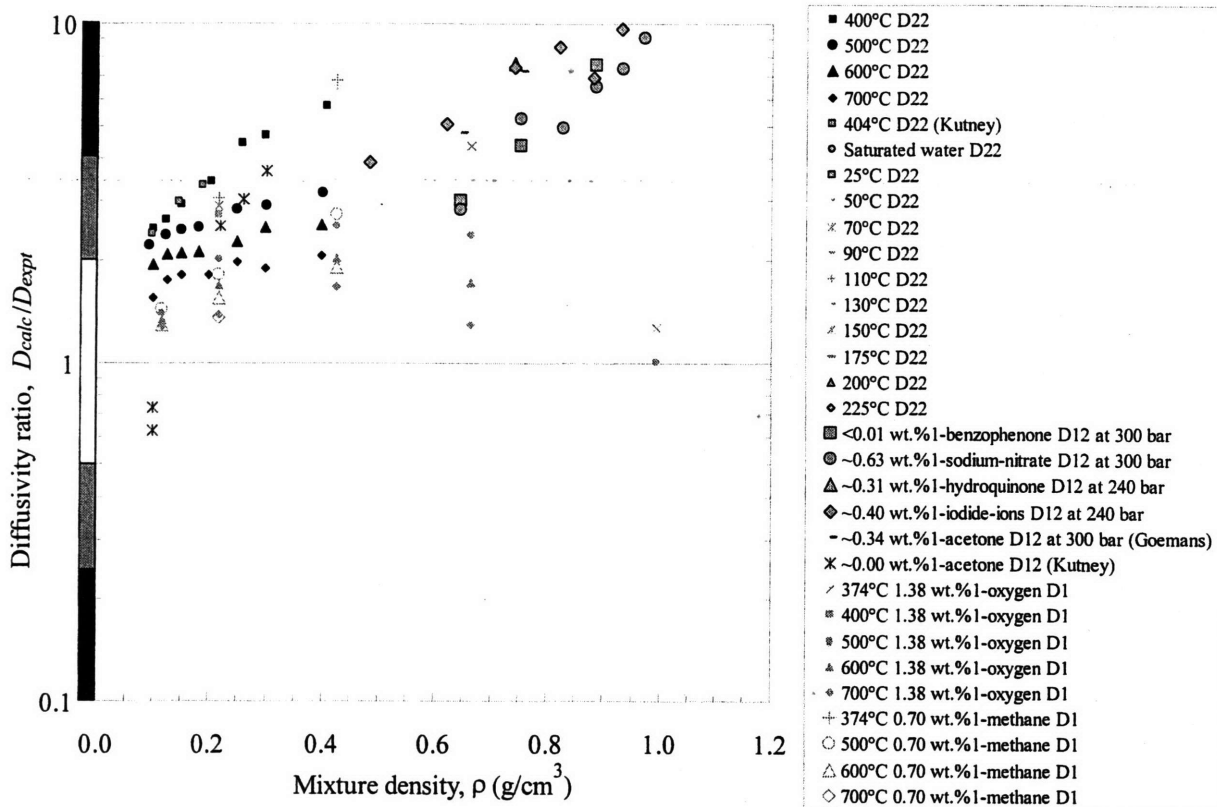
Figure 169. Chapman-Enskog D_{22}, D_{12}, and dilute D_1 predictions with the Erpenbeck-Wood hard-sphere correction using **unweighted** molecular weight and Lennard-Jones parameters.

II.5.2.2.2 Polar Chapman-Enskog Equation

Since water is polar even while it is supercritical, it is reasonable to consider polar modifications of the Chapman-Enskog equation. The Brokaw approach affixes a polar correction term onto the non-polar Lennard-Jones collision integral (Eq. (120)). This binary term is dependent on the dipole moment of both components and will be ineffective if either component is non-polar (*i.e.*, no correction if the solvent is polar and the solute is not). Reliance on the dipole moment exclusively is a potential drawback of the Brokaw method since dipole moments may not fully account for all polarity effects. Nonetheless, the Brokaw correction is tested for water self-diffusivities and acetone-water mutual and tracer diffusivities.

Using Brokaw's recommended values for water ($\delta_2 = 0.95$ for 0 to 1000°C) and acetone ($\delta_1 = 0.63$ for 0 to 300°C), the original Chapman-Enskog equation is reexamined (Brokaw, 1969). Compared to the non-polar results in Figure 149, the polar Chapman-Enskog approach shown in Figure 170 is not noticeably different at low densities, but the mean diffusivity is

350

reduced approximately 6% for low density predictions. At high densities, the reduction is 10% (but still greater than the current ordinate scale) since temperatures of these dense datasets are usually lower and collision integrals are usually larger at these higher densities. Due to the rather small improvement observed, the remaining analysis will be brief.

When the Enskog-Thorne, Takahashi, and Dawson corrections are applied to the unweighted polar Chapman-Enskog equation, the resulting downward shifts are the same since these corrections only scale the Chapman-Enskog predictions. Accordingly, the low and high density predictions are reduced by approximately 6% and 10%, respectively, for each approach. The Enskog-Thorne correction is updated in Figure 171, while the non-polar equation is in Figure 157. The Takahashi results are in Figure 172 and Figure 161, respectively, while the Dawson corrections are in Figure 173 and Figure 165. The polar offset does not change the diffusivity-ratio scatter, but since supercritical self-diffusivities are overestimated, the downward offset shifts diffusivity ratios closer to one, thus improving their accuracy in all cases. The Enskog-Thorne supercritical self-diffusivity predictions are the most accurate so far.

The polar correction does provide some benefit, especially self-diffusivity predictions as just noted. However, this benefit is outweighed by disadvantages including the lack of data for other solutes, the complete reliance on dipole moments, and the uncorrected case of a non-polar solute and polar water solvent mixture. In summary, the polar correction is straightforward and offers greater accuracy for low density predictions of water self-diffusivity. For water mixtures, the correction is not recommended.

The Chapman-Enskog equation with its polar correction is still rated:　　　　　C **F**
(mean low & high density diffusivity ratios: $2 \pm 2_{95\%}$ & $>10 \pm >10_{95\%}$)

The Enskog-Thorne correction of the polar Chapman-Enskog equation is rated:　　C **F**
(mean low & high density diffusivity ratios: $0.9 \pm 0.6_{95\%}$ & $2 \pm 2_{95\%}$)

The Enskog-Thorne correction using mole-fraction-weighted Lennard-Jones
terms is rated (note that it is not shown): $(1.1 \pm 0.5_{95\%}$ & $2 \pm 2_{95\%})$　　**A** C

The Takahashi correction of the polar Chapman-Enskog equation is rated:　　C **F**
(mean low & high density diffusivity ratios: $1.4 \pm 0.9_{95\%}$ & $>10 \pm >10_{95\%}$)

The Dawson correction of the polar Chapman-Enskog equation is rated:　　**A** **F**
(mean low & high density diffusivity ratios: $1.1 \pm 0.6_{95\%}$ & $0.3 \pm 0.6_{95\%}$)

351
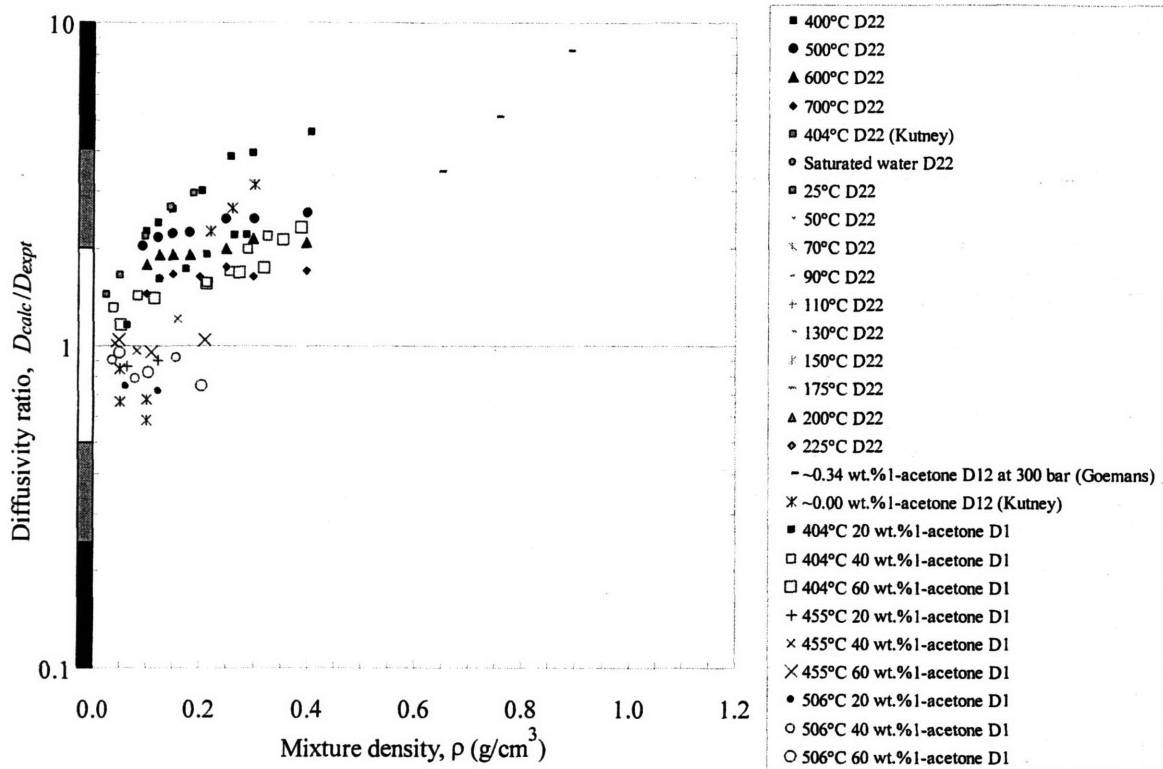
Figure 170. Polar Chapman-Enskog D_{22}, D_{12}, and D_1 predictions using **unweighted** molecular weight and Lennard-Jones parameters.
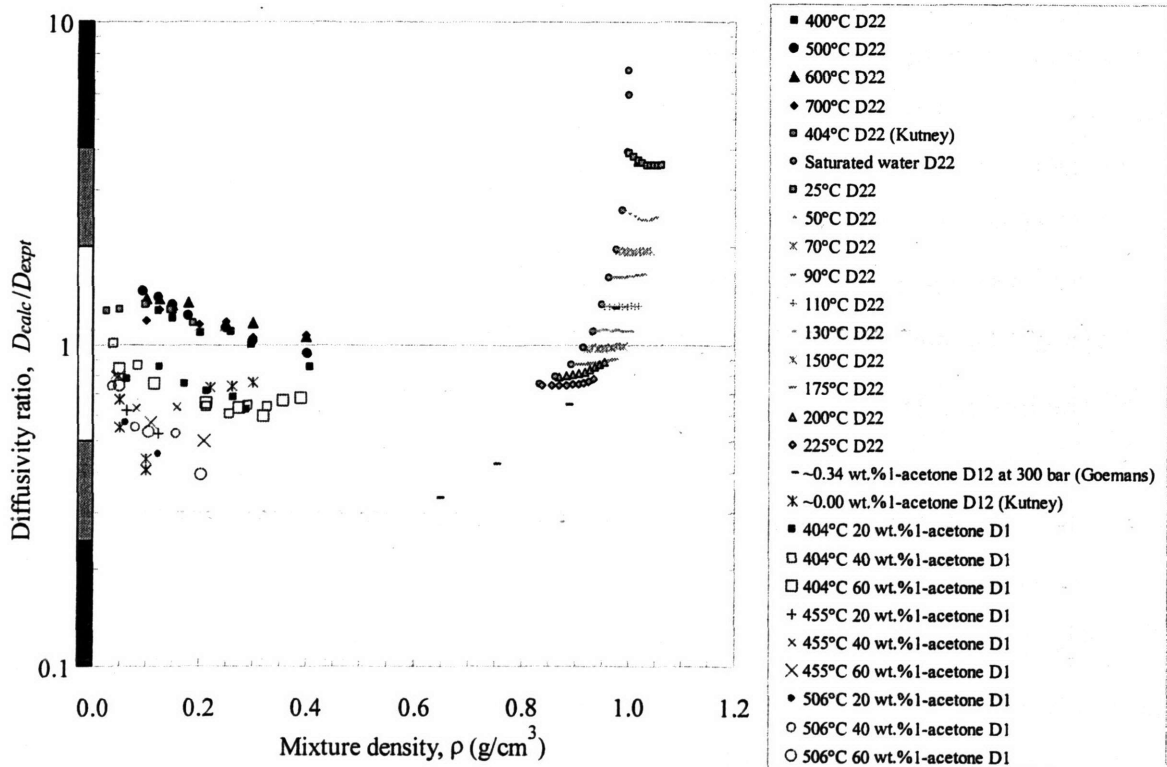
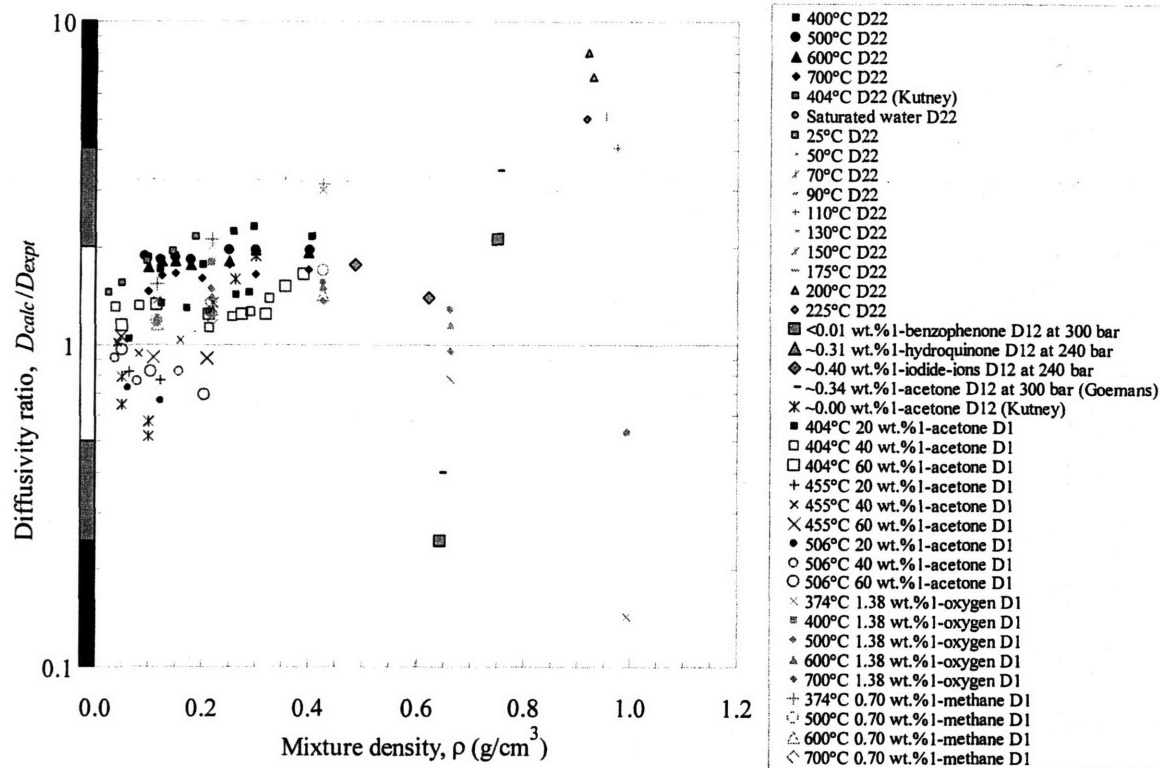Figure 171. Polar Chapman-Enskog D_{22}, D_{12}, and D_1 predictions with the Enskog-Thorne correction using **unweighted** molecular weight and Lennard-Jones parameters.
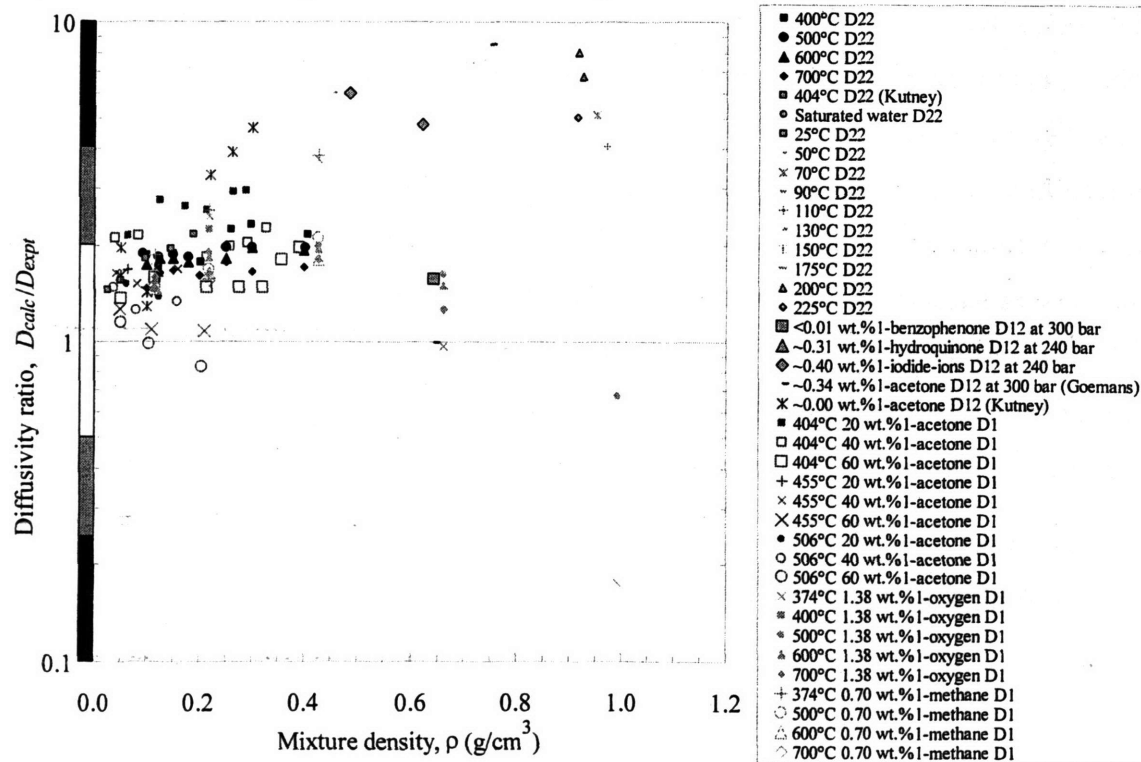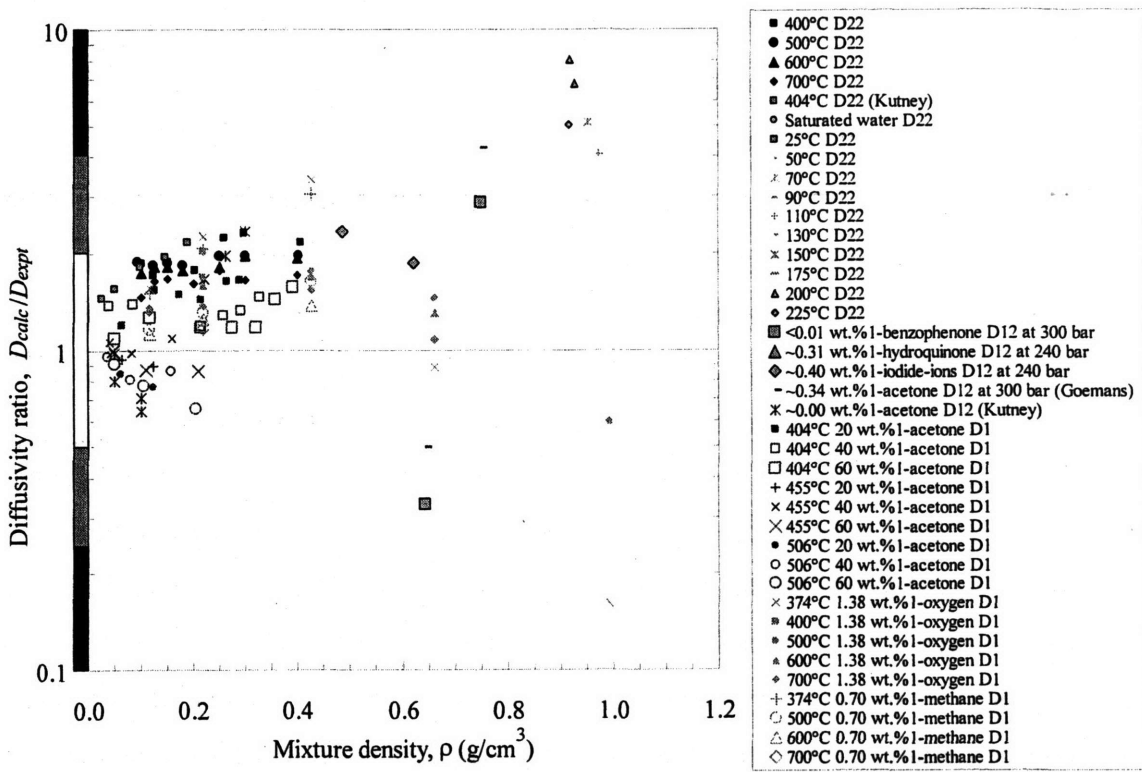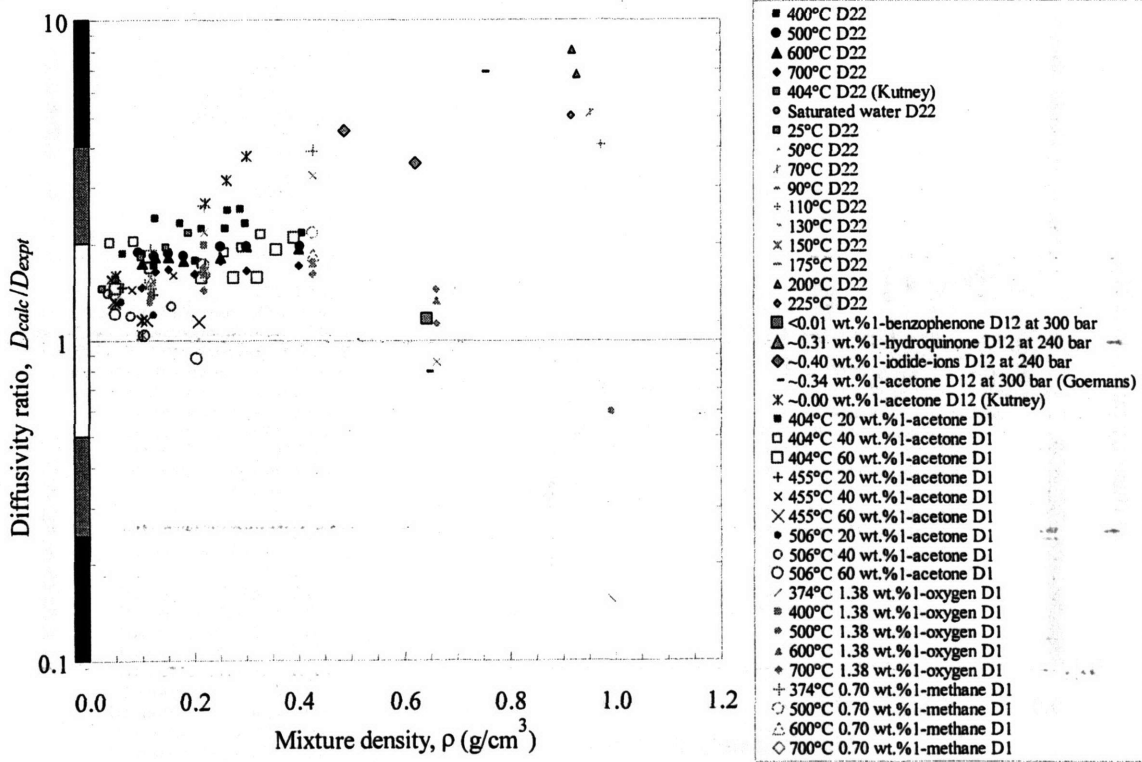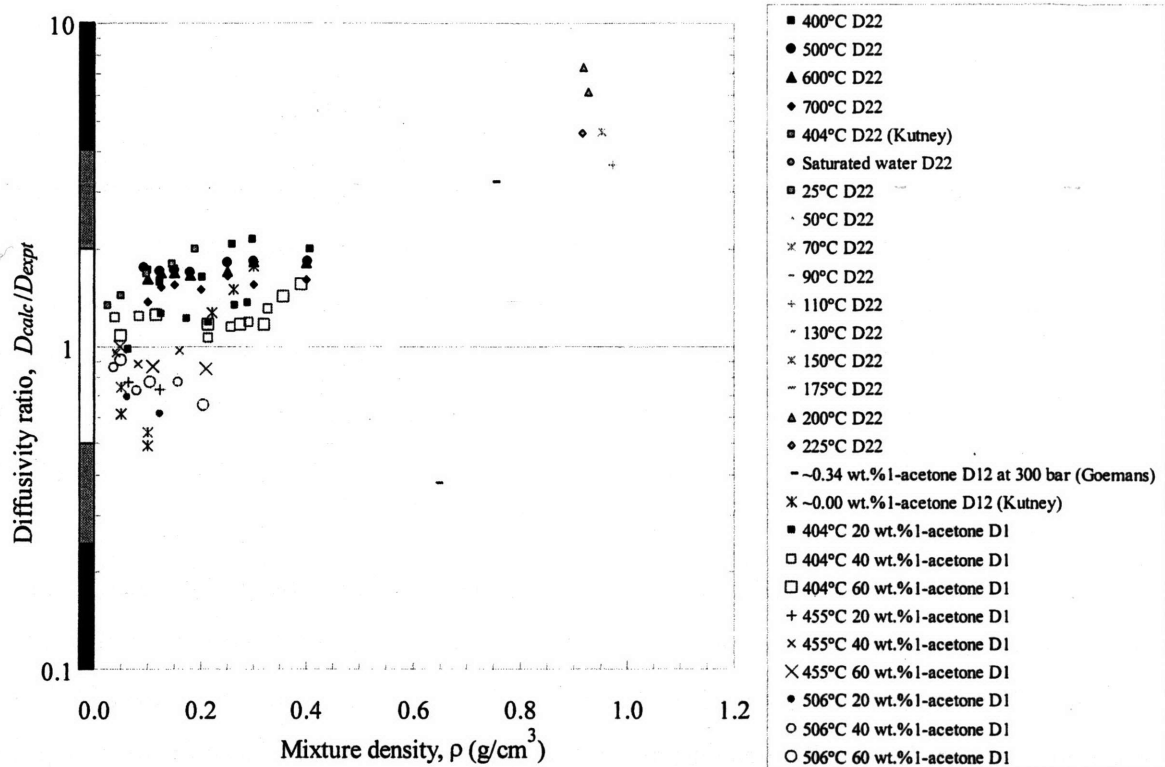
Figure 172. Polar Chapman-Enskog D_{22}, D_{12}, and D_1 predictions with the Takahashi correction using **unweighted** molecular weight and Lennard-Jones parameters.
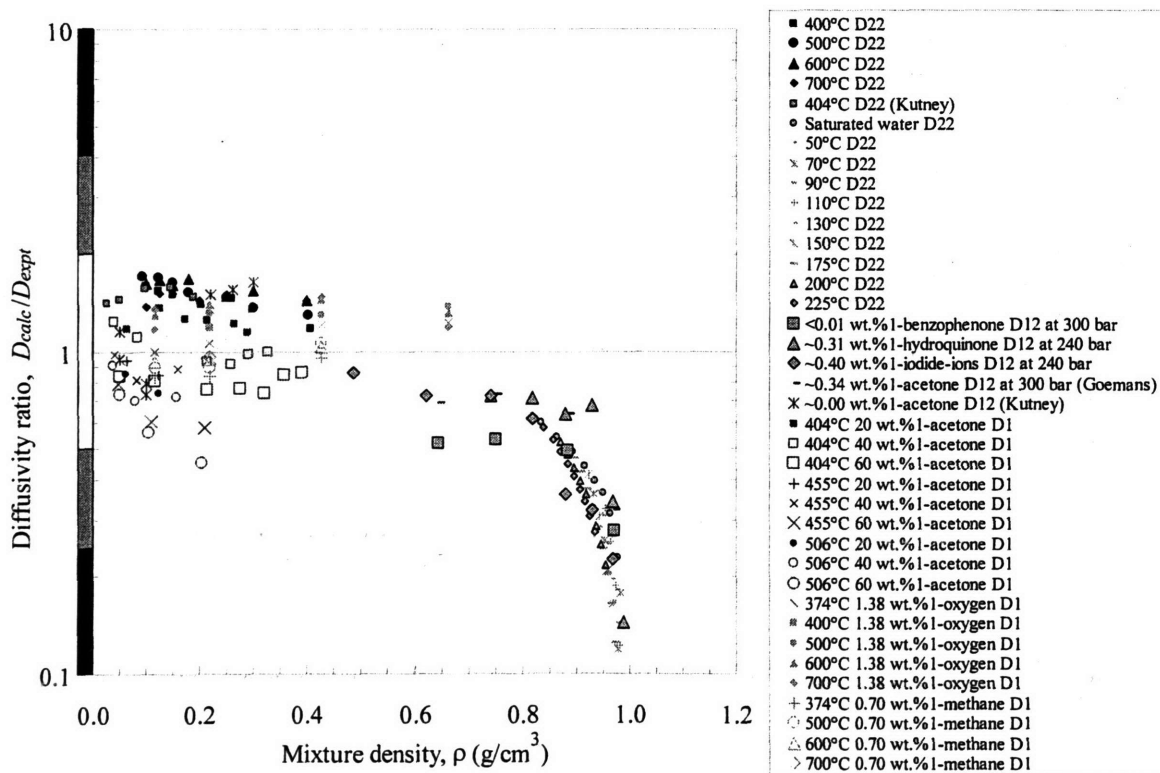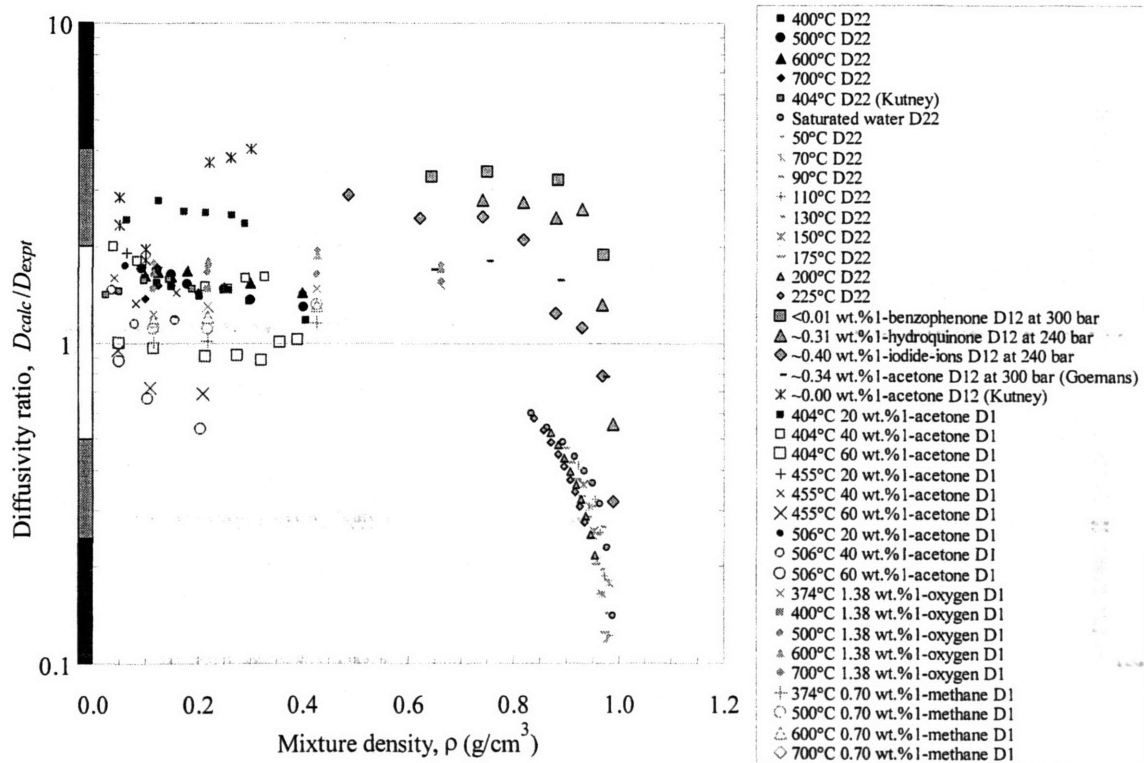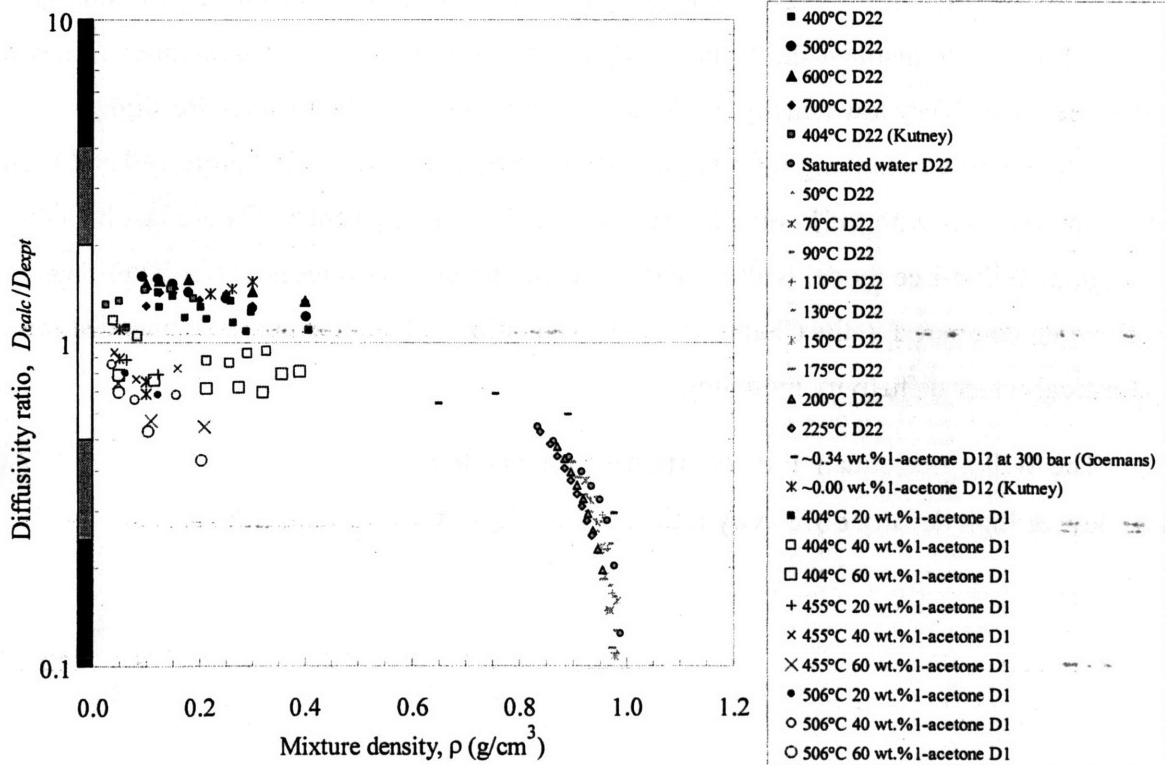

Figure 173. Polar Chapman-Enskog D_{22}, D_{12}, and D_1 predictions with the Dawson hard-sphere correction using **unweighted** molecular weight and Lennard-Jones parameters.

353

II.5.2.2.3 Wilke-Lee Equation

The Wilke-Lee equation is adapted from a model developed by Hirschfelder, Bird, and Spotz (Wilke-Lee, 1955). Hirschfelder *et al.* estimated the diffusivity for pairs of non-polar gases with the Lennard-Jones potential function, but Wilke and Lee utilized a larger database of gaseous diffusivities and identified several trends that simplified the model form and increased its robustness and accuracy. The resulting model is defined in Eq. (129) and by default, uses estimates of Lennard-Jones parameters calculated from normal-boiling-point temperatures and molar volumes. It is functionally similar to the Chapman-Enskog model, but since LJ terms have been estimated with experimental data, it is supposed to be more accurate than the uncorrected Chapman-Enskog equation.

Since Lennard-Jones values are also available (see Table 56), the Wilke-Lee equation will also be evaluated with these known values (compared to the default estimated values). Wilke-Lee diffusivity predictions are first made with the estimated values in Figure 174 followed by those with known Lennard-Jones parameters in Figure 175. As is the case for the Chapman Enskog and as expected, the high density self-diffusivity predictions are inaccurate and off the current ordinate since the Wilke-Lee model is a kinetic-gas theory model meant for ideal-gas systems. Figure 176 displays the Wilke-Lee predictions with known Lennard-Jones values with a larger ordinate. Very low density predictions with the estimated LJ values are slightly improved compared to the original Chapman-Enskog equation shown in Figure 149 and Figure 150, but predictions with the known LJ values do not reveal any benefit. These results indicate that original Wilke-Lee model with its additional empirical work does not offer additional benefit when compared to the Chapman-Enskog equation. Thus, it is not recommended for supercritical-water diffusivity modeling.

The Wilke-Lee equation in its original form is rated:

C F

(mean low & high density diffusivity ratios: $1.4 \pm 1.3_{95\%}$ & $>10 \pm >10_{95\%}$)

354
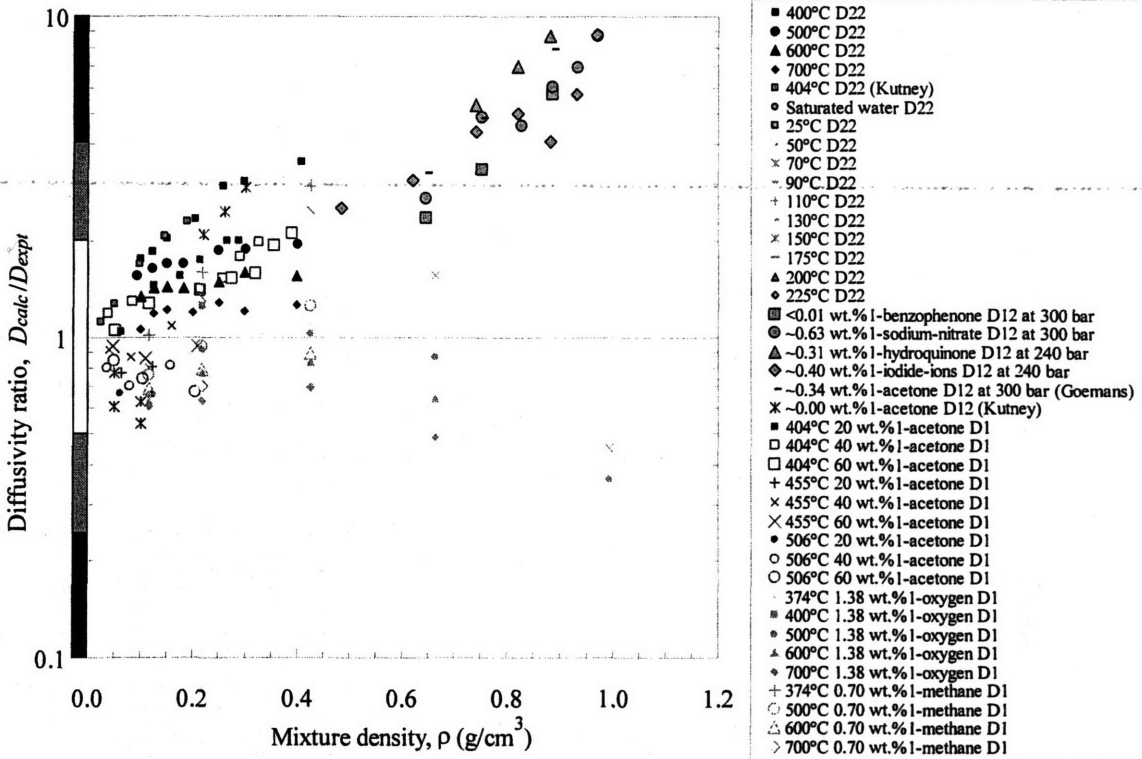
Figure 174. Wilke-Lee D_{22}, D_{12}, and D_1 predictions using Wilke-Lee-estimated Lennard-Jones parameters.
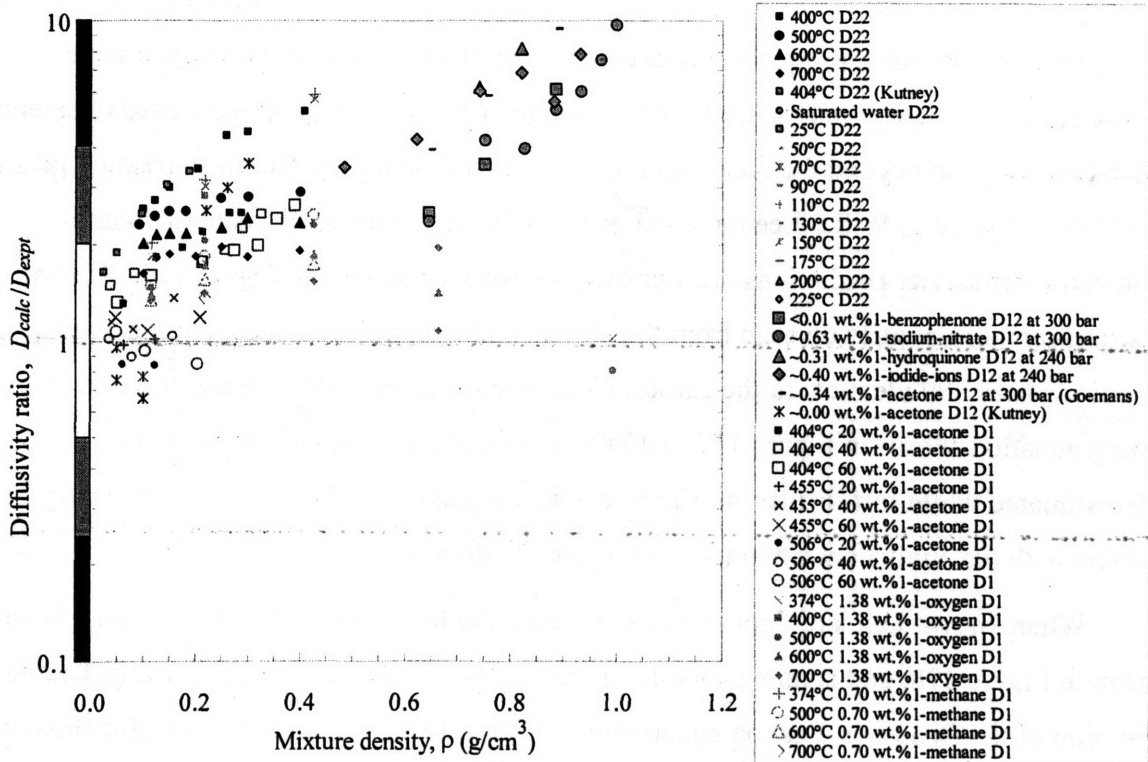
Figure 175. Wilke-Lee D_{22}, D_{12}, and D_1 predictions using known Lennard-Jones parameters.
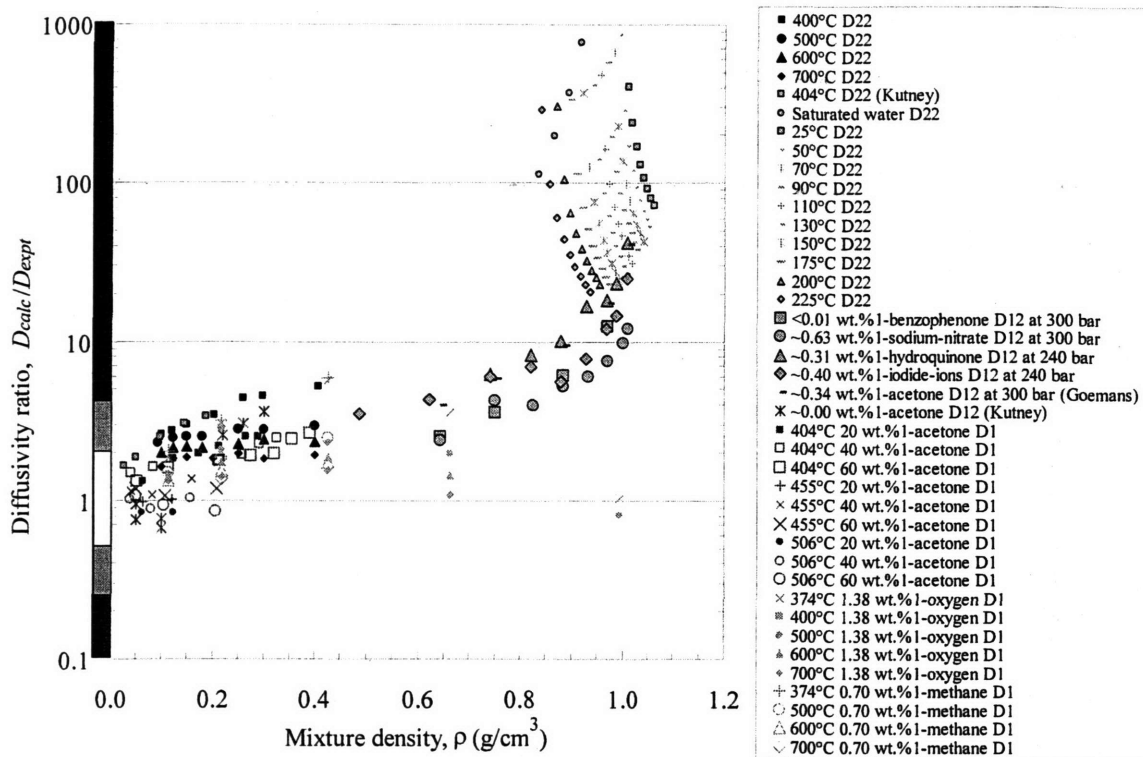
Figure 176. Wilke-Lee D_{22}, D_{12}, and D_1 predictions using known Lennard-Jones parameters and shown with a larger ordinate range.

Since the Wilke-Lee equation is developed for ideal-gas-like densities, the same approaches that were previously used for the Chapman-Enskog equation were used to extend the Wilke-Lee equation beyond the ideal-gas region. When the Enskog-Thorne correction given in Eq. (117) is applied to Wilke-Lee equation using Wilke-Lee-estimated Lennard-Jones parameters, diffusivity predictions are significantly reduced as seen in Figure 177. At low densities, self-diffusivities diverge from the mutual and tracer diffusivities, but the overall response is basically identical to the Enskog-Thorne correction of the unweighted Chapman-Enskog equation shown in Figure 157. At higher densities, mutual diffusivities are underestimated while self-diffusivities predictions are scattered above one, but are nearly identical with the equivalent Chapman-Enskog predictions.

When known Lennard-Jones values are used, the low density bimodal response is smaller as seen in Figure 178, and is now generally underestimated compared to the Enskog-Thorne correction of the Chapman-Enskog equation (see Figure 157). Higher density self-diffusivities are scattered about the ratio one which makes the Wilke-Lee equation a better choice for high densities when the Wilke-Lee equation is used with known Lennard-Jones parameters.

356
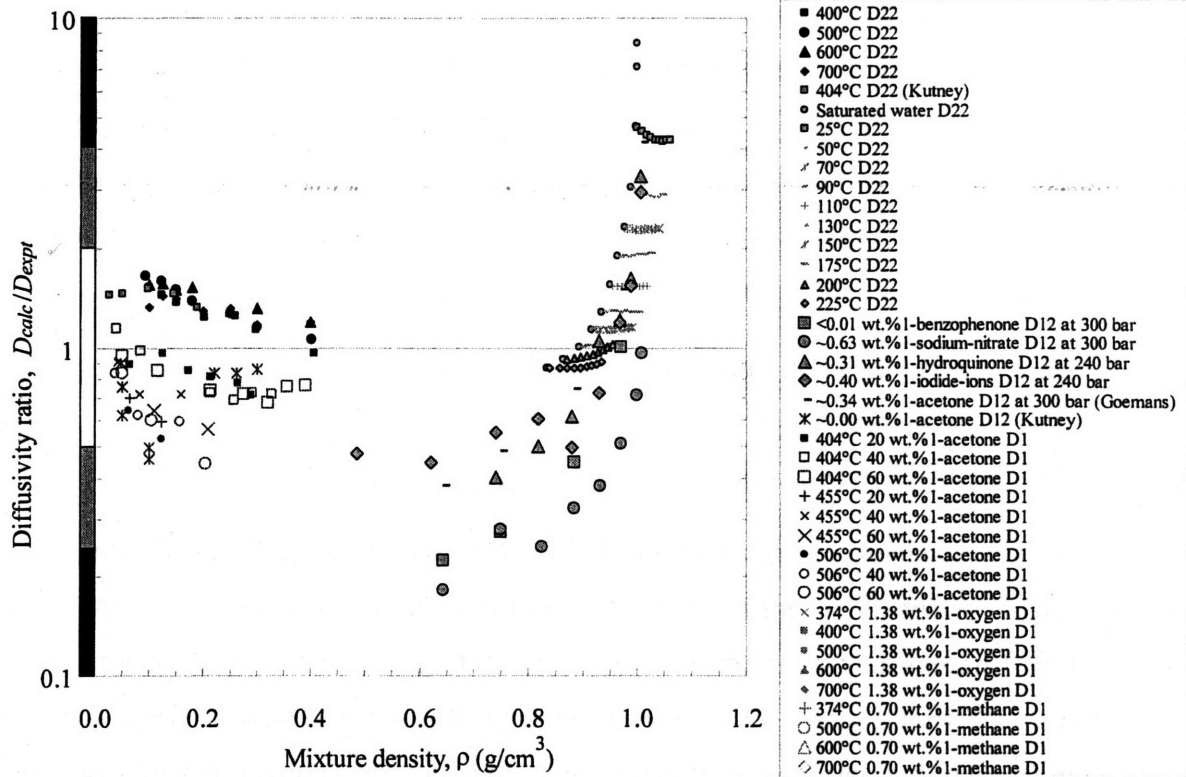
Figure 177. Wilke-Lee D_{22}, D_{12}, and D_1 predictions with the Enskog-Thorne correction using Wilke-Lee-estimated Lennard-Jones parameters.
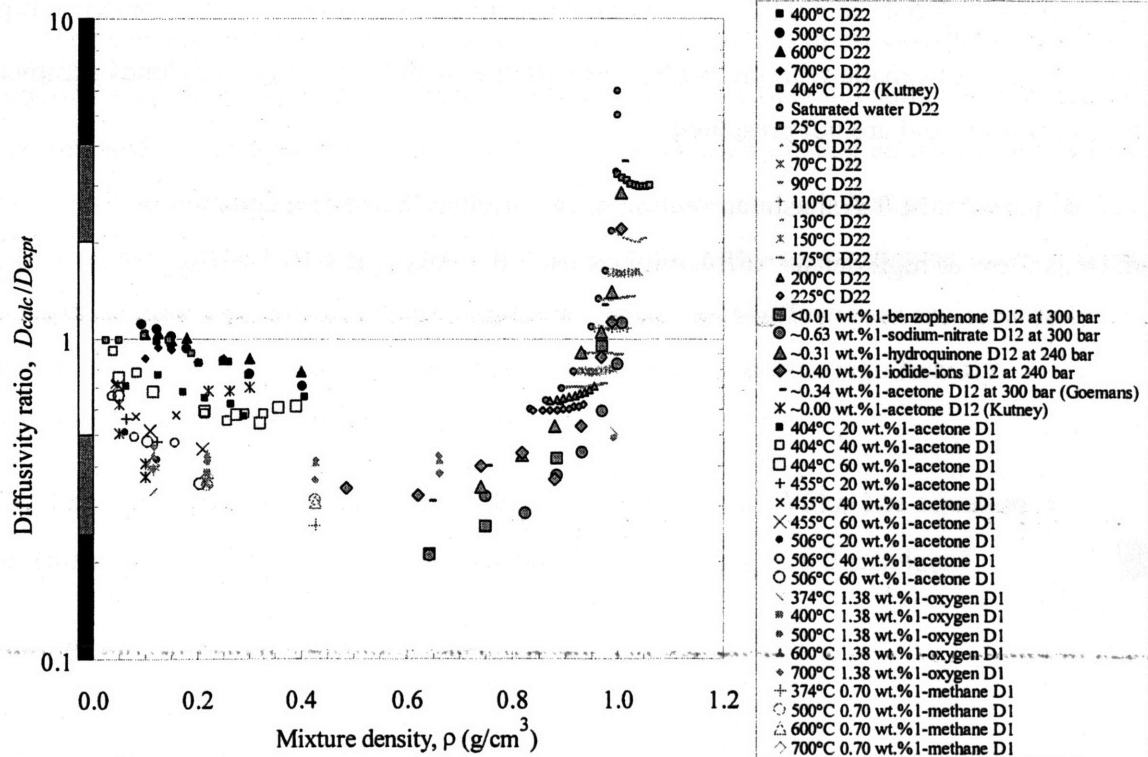
Figure 178. Wilke-Lee D_{22}, D_{12}, and D_1 predictions with the Enskog-Thorne correction using known Lennard-Jones parameters.

357

While the estimated-Lennard-Jones results at low densities are superior to the results calculated with known parameters, the high density predictions are worse. Since the Enskog-Thorne correction of the Wilke-Lee model with known parameters provides somewhat balanced results with high density predictions scattered around one and low density predictions equal to or under one, this model comes close to the results of the Enskog-Thorne correction using mole-fraction-weighted Lennard-Jones terms.

The Enskog-Thorne correction of the Wilke-Lee equation employing known Lennard-Jones parameters is rated:

C F

(mean low & high density diffusivity ratios: $1.0 \pm 0.7_{95\%}$ & $2 \pm 3_{95\%}$)

Using the Takahashi correction shown in Eq. (118) and the Wilke-Lee-estimated Lennard-Jones constants, low density predictions are predicted with sufficient accuracy as seen in Figure 179. These results are superior to the equivalent Takahashi-corrected Chapman-Enskog results shown in Figure 161. However, the high density predictions are large and are not shown on the current ordinate. As mentioned earlier, the Takahashi correction is fit to a collection of organic and inert mutual diffusivities over a reduced temperature and pressure range of $0.88 \leq T_r \leq 6.41$ and $0.02 \leq P_r \leq 9.83$, respectively, but is not intended for dense liquid systems. Predictions made with the Wilke-Lee equation with known Lennard-Jones parameters were less accurate and are not presented.

As a result, the Takahashi correction of the original Wilke-Lee equation is rated: (mean low & high density diffusivity ratios: $1.0 \pm 0.6_{95\%}$ & $>10 \pm >10_{95\%}$)

A F
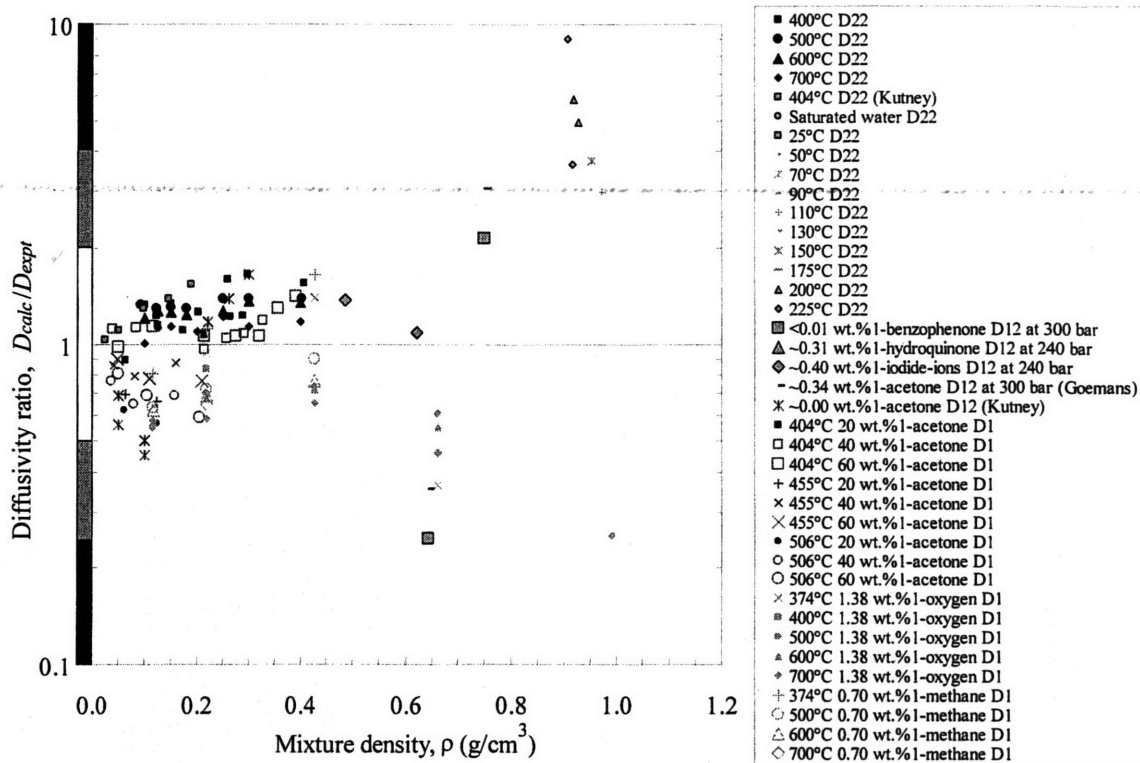
Figure 179. Wilke-Lee D_{22}, D_{12}, and D_1 predictions with the Takahashi correction using Wilke-Lee-estimated Lennard-Jones parameters.

The Dawson correction that is shown in Eq. (119) and that improves Chapman-Enskog predictions is also applied to the Wilke-Lee equation when the default estimated Lennard-Jones values are used. Compared to the Dawson-corrected Chapman-Enskog equation, Wilke-Lee diffusivity ratios are further reduced as shown in Figure 180, and as a result, improve low density supercritical self-diffusivity predictions. On the other hand, due to the shift downward, multiple tracer diffusivities are now significantly underestimated. Self-diffusivities are accurately modeled, but as the density is increased, the predictions will become significantly underestimated along with other diffusivities.

For these reasons, the Dawson correction of the original Wilke-Lee equation is rated: (mean low & high density diffusivity ratios: $0.8 \pm 0.5_{95\%}$ & $0.3 \pm 0.4_{95\%}$)

400°C D22
500°C D22
600°C D22
700°C D22
404°C D22 (Kutney)
Saturated water D22
50°C D22
70°C D22
90°C D22
110°C D22
130°C D22
150°C D22
175°C D22
200°C D22
225°C D22
<0.01 wt.%1-benzophenone D12 at 300 bar
~0.31 wt.%1-hydroquinone D12 at 240 bar
~0.40 wt.%1-iodide-ions D12 at 240 bar
~0.34 wt.%1-acetone D12 at 300 bar (Goemans)
~0.00 wt.%1-acetone D12 (Kutney)
404°C 20 wt.%1-acetone D1
404°C 40 wt.%1-acetone D1
404°C 60 wt.%1-acetone D1
455°C 20 wt.%1-acetone D1
455°C 40 wt.%1-acetone D1
455°C 60 wt.%1-acetone D1
506°C 20 wt.%1-acetone D1
506°C 40 wt.%1-acetone D1
506°C 60 wt.%1-acetone D1
374°C 1.38 wt.%1-oxygen D1
400°C 1.38 wt.%1-oxygen D1
500°C 1.38 wt.%1-oxygen D1
600°C 1.38 wt.%1-oxygen D1
700°C 1.38 wt.%1-oxygen D1
374°C 0.70 wt.%1-methane D1
500°C 0.70 wt.%1-methane D1
600°C 0.70 wt.%1-methane D1
700°C 0.70 wt.%1-methane D1

Diffusivity ratio, D_{calc}/D_{expt}

Mixture density, ρ (g/cm^3)

Figure 180. Wilke-Lee D_{22}, D_{12}, and D_1 predictions with the Dawson correction using Wilke-Lee-estimated Lennard-Jones parameters.

In summary, the Wilke-Lee predictions are similar to the Chapman-Enskog results, although a slight improvement is seen when the original formulation with estimated Lennard-Jones parameters is used. Of course, the use of estimated parameters in empirical models always raises suspicion, but if known values are used, then the Wilke-Lee equation is nearly identical to the Chapman-Enskog equation. Ideal-gas Corrections offer some benefit and their results are summarized below.

The Wilke-Lee equation in its original form is rated:
(mean low & high density diffusivity ratios: $1.4 \pm 1.3_{95\%}$ & $>10 \pm >10_{95\%}$)

The Enskog-Thorne correction of the Wilke-Lee equation employing known Lennard-Jones parameters is rated: (low & high mean ratios: $1.0 \pm 0.7_{95\%}$ & $2 \pm 3_{95\%}$)

The Takahashi correction of the original Wilke-Lee equation is rated:
(mean low & high density diffusivity ratios: $1.0 \pm 0.6_{95\%}$ & $>10 \pm >10_{95\%}$)

The Dawson correction of the original Wilke-Lee equation is rated:
(mean low & high density diffusivity ratios: $0.8 \pm 0.5_{95\%}$ & $0.3 \pm 0.4_{95\%}$)

Although there is not a clear advantage for low density predictions, low density self-diffusivity predictions using the Dawson-corrected Wilke-Lee equation have the least scatter and are the best yet observed during this analysis.

II.5.2.2.4 Mathur-Thodos Equations

The semi-empirical Mathur-Thodos diffusivity approach is based upon dimensional analysis and experimental-data regression and is considered unconventional compared to the other kinetic-gas theory approaches. As shown in Eqs. (132) through (134), three self-diffusivity equations are used to cover a wide range of temperatures and densities. Since gases at atmospheric pressures are not included in this analysis, Eq. (132) will not be evaluated. This multi-equation approach will have discontinuities near the equation crossover points which will introduce prediction discrepancies when switching between equations. Additional user scrutiny is required whenever such predictions are made. Since this analysis also includes mutual and tracer diffusivities, the Mathur-Thodos equations are modified so that these predictions can be made. Mixture densities are used along with mole-fraction-weighted properties including molecular weights and critical temperatures, densities, and pressures.

Water self-diffusivities predictions are shown in Figure 181. Most high density diffusivity ratios are less than one, but they have less scatter compared to models previously discussed. In particular, low temperature diffusivity ratios (less than 100°C) are nearly one, while high temperature diffusivity ratios are below one. The predictions are remarkable given that the model was originally developed with simple, non-hydrogen-bonded gases such as argon, carbon dioxide, krypton, nitrogen, and xenon. At low densities, the agreement is superior than others in this analysis so far and is likely due to the fact that hydrogen bonding is less prevalent at these conditions.

Mutual and solute-tracer diffusivities are shown next in Figure 182, and although diffusivity-ratio points are scattered at most densities, the predictions lie near a diffusivity ratio of one. Over 95% of the predictions lie in the acceptable region, and this indicates that the Mathur-Thodos model can simulate reasonable diffusivities for supercritical-water systems over a wide density range.
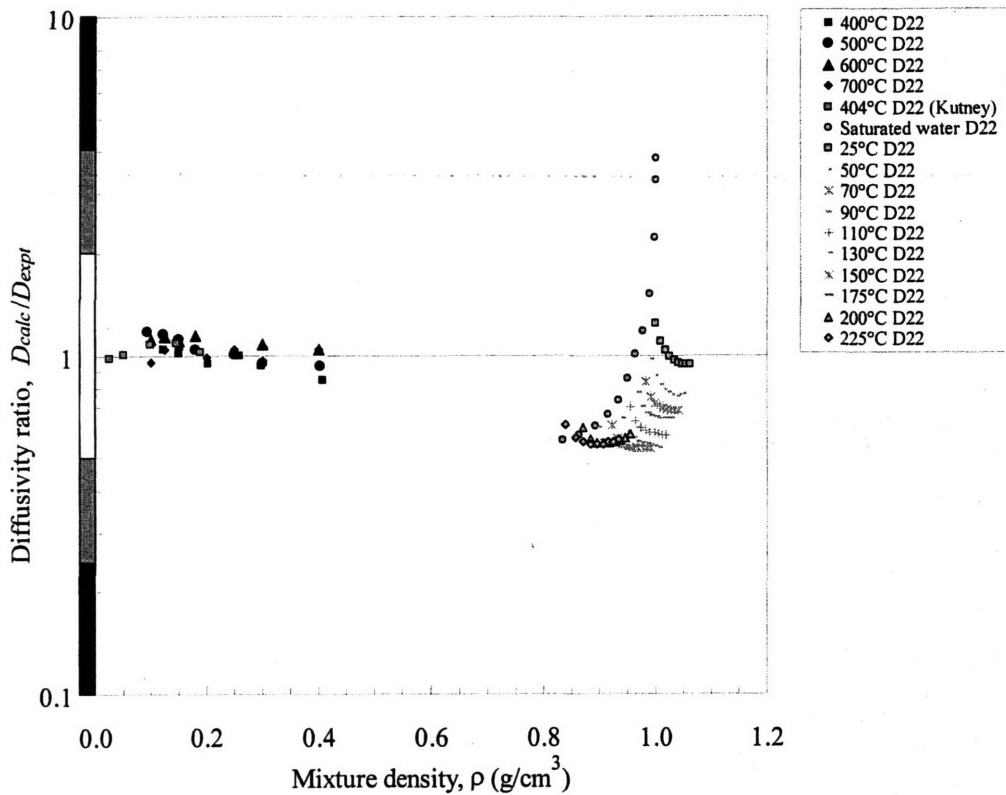
Figure 181. Mathur-Thodos D_{22} predictions using the low and high density formulae.
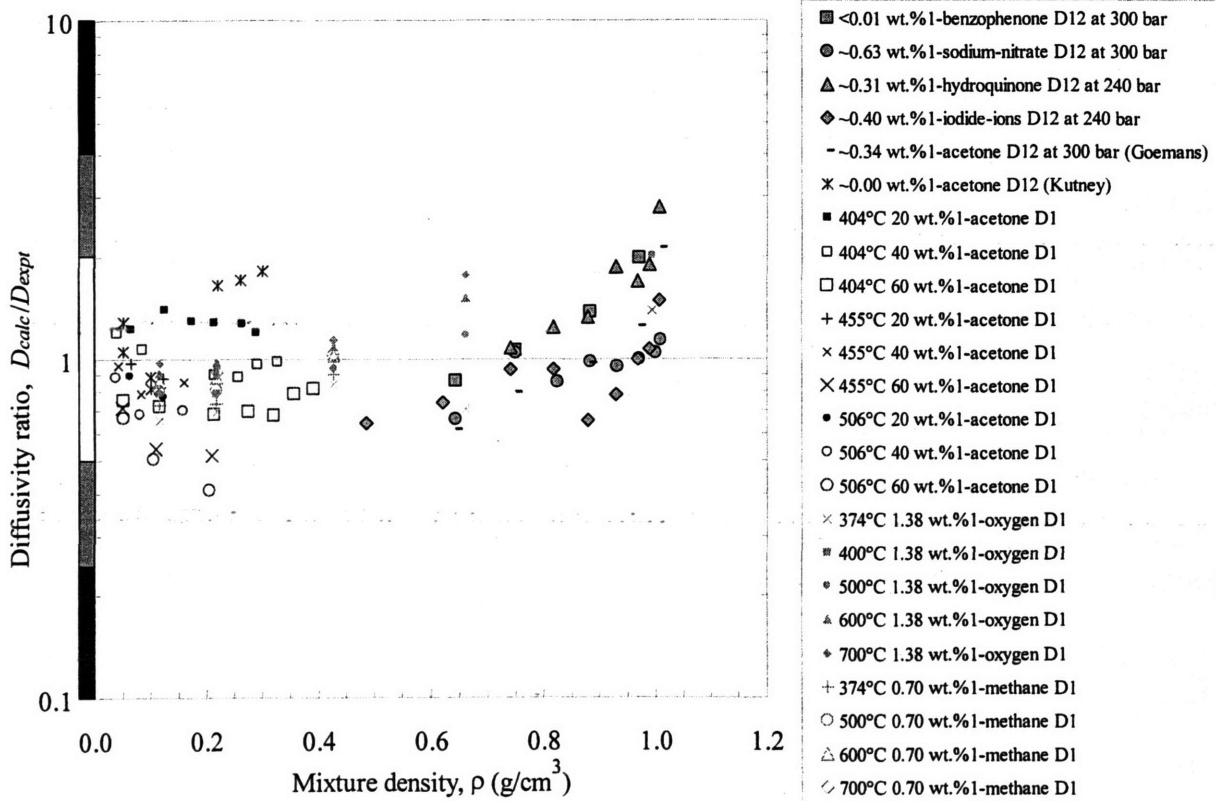
Figure 182. Mathur-Thodos D_{12} and D_1 predictions using the low and high density formulae.

Solvent tracer diffusivities were also computed and are plotted in Figure 183 along with the previously discussed self-diffusivities. The tracer predictions are clearly underestimated and clustered, yet they can be easily explained. Due to the simplistic binary-weighting approach, calculated Mathur-Thodos predictions cannot be differentiated (solute D_{1calc} = solvent D_{2calc}). As a result, the computed diffusivity ratios are calculated with identical Mathur-Thodos predictions. Since the experimental solvent diffusivities are always larger than the solute values, the resulting solvent diffusivity ratios (D_{2calc}/D_{2expt}) will always be smaller than the solute diffusivity ratios (D_{1calc}/D_{1expt}) and hence, underestimated.

The accuracy of the solute-diffusivity predictions clearly establish that the current weighting scheme used in the Mathur-Thodos model should be used for solute, and not solvent, tracer predictions. What is unclear is why the small contribution from solute critical properties results in accurate solute predictions, yet makes the solvent predictions worse. When using the current mixture-weighted mixture rules (*i.e.*, for mole-fraction weighted critical properties) for concentrated acetone tracer diffusivities, the Mathur-Thodos predictions are automatically reduced $27 \pm 3\%$, $40 \pm 9\%$, and $60 \pm 5\%$ for the 20 wt.$_1$%, 40 wt.$_1$%, and 60 wt.$_1$% solutions, respectively, from their equivalent pure water counterpart. Yet, the experimental water tracer diffusivities never decrease more than 30% from their equivalent self-diffusivities. As a result, the solvent tracer diffusivity ratios will become worse as the solution becomes concentrated when this simplistic weighting approach is used. Conversely, the benefits of this concentration-weighting method include smooth, continuous predictions as the system becomes more dilute and the lack of the usual discontinuity at infinite dilution when traditional LJ rules are employed (*e.g.*, Eq. (111) and Eq. (112)). Other weighting schemes can possibly avoid the solvent-tracer-accuracy issue, but are much more likely to be complicated.

Now that the significant drop in solvent-tracer accuracy can be explained in terms of the current concentration-weighting approach, solvent tracer diffusivities are no longer included in the Mathur-Thodos analysis. When the other predictions are combined in Figure 184, the plotted diffusivity ratios are scattered about one symmetrically along the entire abscissa with limited excursions into the caution zone. For these reasons, the Mathur-Thodos kinetic-gas-theory-based approach is superior at predicting self-, mutual, and solute-tracer diffusivities than the other examined models.
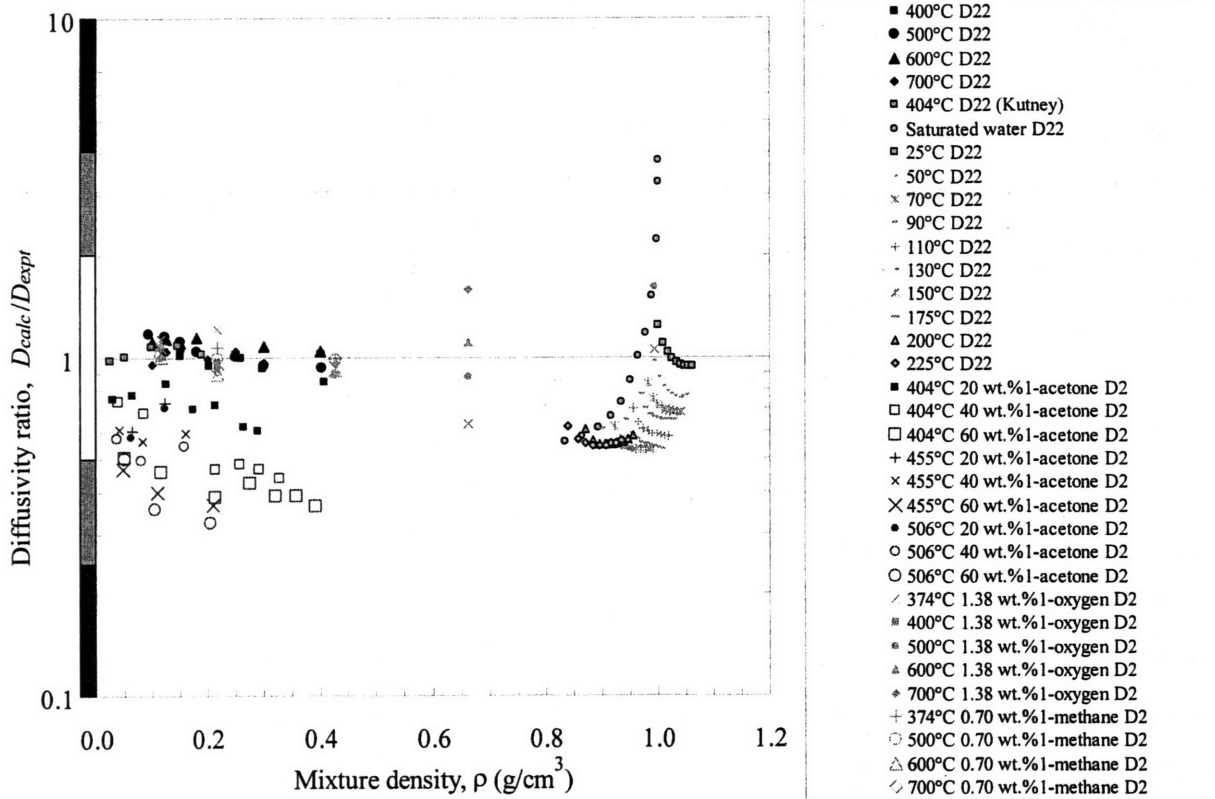
Figure 183. Mathur-Thodos D_{22} and D_2 predictions using the low and high density formulae.
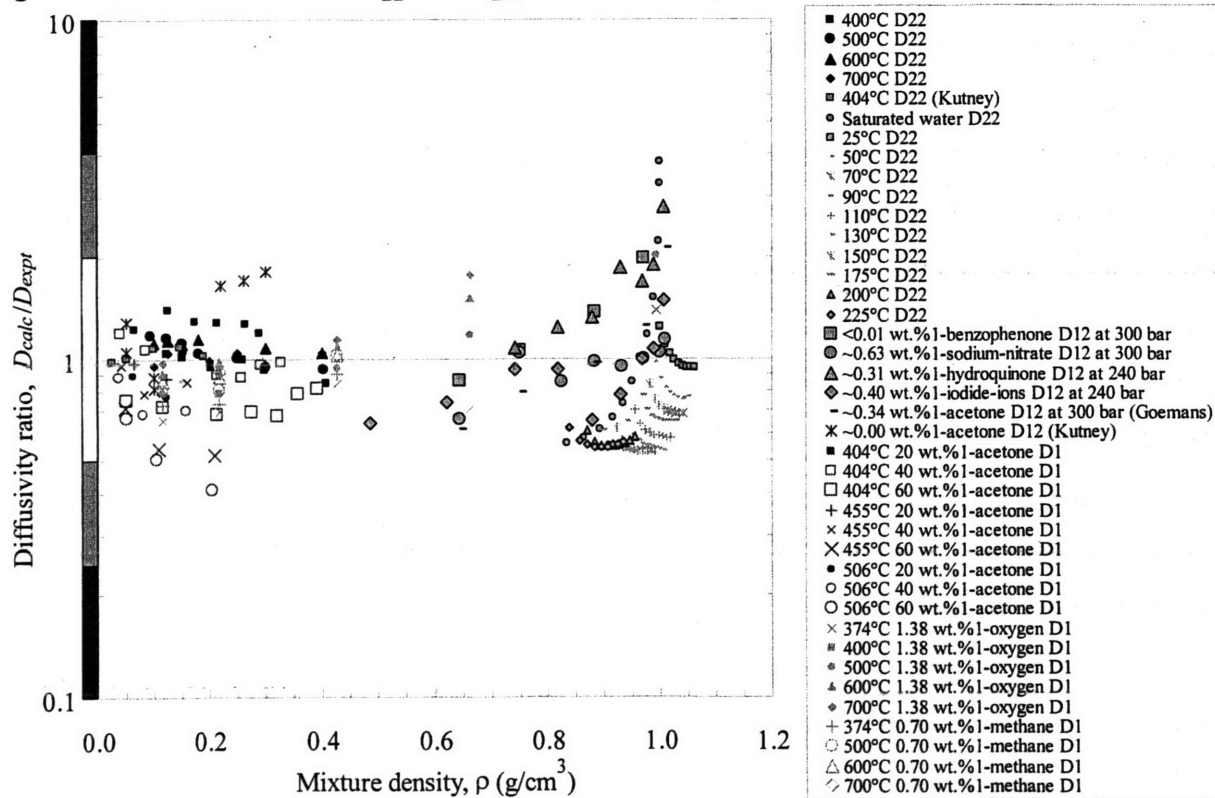
Figure 184. Mathur-Thodos D_{22}, D_{12}, and D_1 predictions using the low and high density formulae.

Based on the Mathur-Thodos performance in Figure 184, the Mathur-Thodos approach with mixture density and mole-fraction-weighted parameters is rated: $\boxed{A}\boxed{A}$ (mean low & high density diffusivity ratios: $1.0 \pm 0.5_{95\%}$ & $0.9 \pm 1.0_{95\%}$)

A summary of the performance for each of the investigated kinetic-theory models is given in Table 59 while mean diffusivity ratios with uncertainties are plotted in Figure 185. Nearly all kinetic-theory models have unacceptable accuracies at higher densities (>0.5 g/cm^3), except for the empirical Mathur-Thodos equations or for models adjusted with the Enskog-Thorne correction. The Mathur-Thodos approach is currently the only model that is considered reliable for low and high density predictions of sub- and supercritical water systems. It is also unique in that it can be computed with critical properties, molecular weight, and operating conditions (*i.e.*, temperature, density, and pressure) and is not dependent on potential functions. Reliable low density predictions can also be made with the original or polarity-adjusted Chapman-Enskog equations corrected with either the Enskog-Thorne or Dawson modifications. The Takahashi-corrected Wilke-Lee equation is successful for low density diffusivity predictions, but its Lennard-Jones parameters are estimated which casts doubt about extending it to untested water systems.

It is apparent from Figure 185 that low density kinetic-gas-theory predictions are more accurate than the hydrodynamic-theory predictions. In general, the low density kinetic mean diffusivity ratios have less variability, while the high density ones have more. The Mathur-Thodos diffusivity ratios are centered about one, but have larger high density uncertainties than the hydrodynamic models. Given its success in predicting low density diffusivities and its reliable high density predictions, the Mathur-Thodos model currently is the recommended model for supercritical-water diffusivity predictions.

Table 59. Low and high density performance rankings for the hydrodynamic- and kinetic-based diffusivity models evaluated in this analysis

Model	Section	Density Low	High
Hydrodynamic theory of diffusion	II.5.2.1		
Stokes-Einstein equation with the no-slip condition	II.5.2.1.1	F	A
Stokes-Einstein equation with the slip condition	II.5.2.1.1	F	A
Wilke-Chang equation	II.5.2.1.2	F	A
Reddy-Doraiswamy equation (original form)	II.5.2.1.3	F	A
(>0.3 g/cm^3 with NBP-volumes)	II.5.2.1.3	C	A
Kinetic theory of diffusion	II.5.2.2		
Chapman-Enskog equation	II.5.2.2.1	C	F
CE equation with the Enskog-Thorne correction	II.5.2.2.1.1	C	F
Weighted CE equation with the ET correction	II.5.2.2.1.1	A	F
CE equation with the Takahashi correction	II.5.2.2.1.2	C	F
CE equation with the Dawson HS correction	II.5.2.2.1.3	A	F
CE equation with the Erpenbeck-Wood HS correction	II.5.2.2.1.4	F	F
Polar Chapman-Enskog equation	II.5.2.2.2	C	F
Polar CE equation with the Enskog-Thorne correction	II.5.2.2.2	C	F
Polar, weighted CE equation with the ET correction	II.5.2.2.2	A	C
Polar CE equation with the Takahashi correction	II.5.2.2.2	C	F
Polar CE equation with the Dawson HS correction	II.5.2.2.2	A	F
Wilke-Lee equation	II.5.2.2.3	C	F
WL equation with the Enskog-Thorne correction	II.5.2.2.3	C	F
WL equation with the Takahashi correction	II.5.2.2.3	A	F
WL equation with the Dawson HS correction	II.5.2.2.3	C	F
Mathur-Thodos equations	II.5.2.2.4	A	A

Figure 185. Low and high density mean diffusivity ratios with 95%-confidence-interval uncertainties for the hydrodynamic- and kinetic-based diffusivity models evaluated in this analysis.

II.5.2.3 Hard-Sphere Theory of Diffusion

II.5.2.3.1 Sun-Chen Equation

The first approach discussed in this section is the tracer-diffusivity expression developed by Sun and Chen because it is based completely upon MD hard-sphere simulation results. It also includes a roughness correction that is used to adjust for angular-momentum exchanges when molecules collide. The Sun-Chen model is defined in Eq. (143) and is convenient to use because Chapman-Enskog variables, such as potential-function parameters and collision integrals, are not needed.

Their approach should be limited to systems where $0.5 \leq M_1/M_2 \leq 4.0$, $0.5 \leq \sigma_1/\sigma_2 \leq 1.5$, and $1.5 \leq M_2/x_2\rho_2V_0 \leq 3.0$ since their modification is based on MD data with these restrictions. Of the three-hundred data points in this analysis, only 120 meet these criteria. Those valid points are the high density self-diffusivities between 25°C and 225°C. The other 180 data points fail to satisfy one or more of the criteria, but nonetheless, are included in the analysis in order to test the extendibility of the Sun-Chen model.

Later on, Sun and Chen customized their model for n-hexane systems by performing a linear regression with their experimental n-hexane diffusivities and assumed $\sigma_i = V_{ci}^{1/3}$. However, the resulting semi-empirical model is intended for n-hexane systems and is not applicable to other fluid systems. For this reason, the generic form defined in Eq. (143) will be evaluated.

Mutual diffusivities along with solute tracer diffusivities determined with the generic form are shown in Figure 186. Low and high density results are clustered about one, even though these data do not meet the original model criteria. The only exceptions to this are the simulated oxygen and methane datasets which are consistently underestimated. Self-diffusivity predictions are also plotted in Figure 186. Low density self-diffusivities are reliably centered about one and come close to matching the Mathur-Thodos performance seen in Figure 181. However, the diffusivity ratios have a larger distribution since the diffusivity ratios are greater than one at very low densities and decrease as the density increases. The Mathur-Thodos ratios do not show this behavior and have near-zero slopes. The high density self-diffusivities are also centered about one, but their scatter is worse than the Mathur-Thodos results. The Sun-Chen

results are surprisingly accurate given that this model is fit to computer-simulated tracer diffusivities (experimental data are not regressed). In addition, the Sun-Chen model requires only a small list of parameters (*e.g.*, molecular diameters and weights), yet it can reliably simulate supercritical self-diffusivities over ranges that do not satisfy the original regression criteria.

Based on these results, the Sun-Chen model is rated:

(mean low & high density diffusivity ratios: $0.9 \pm 0.5_{95\%}$ & $1 \pm 2_{95\%}$)
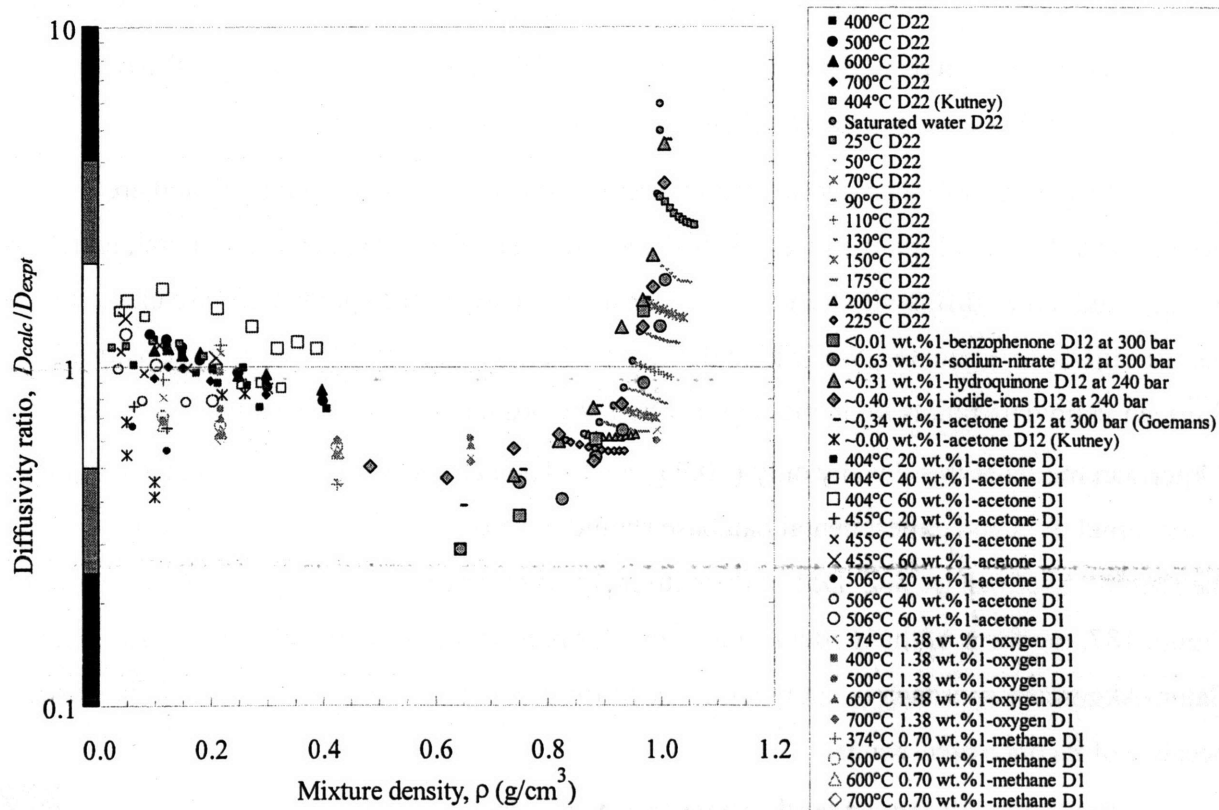
Figure 186. Sun-Chen D_{22}, D_{12}, and D_1 predictions using the default model.

II.5.2.3.2 Eaton-Akgerman Equation

In contrast to the Sun-Chen methodology, Eaton and Akgerman used a semi-empirical approach in order to develop an expression for infinitely dilute mutual diffusivities. Starting with Dymond's hard-sphere expression which was developed from MD data, Eaton and Akgerman used experimental supercritical carbon-dioxide diffusivities and additional MD data in order to identify model trends and eliminate the need for several arduous terms such as the collision integral (Eaton and Akgerman, 1997). With their model form simplified, two remaining constants are estimated from experimental 1-octene diffusivities in ethane, propane, and hexane and are permanently fixed. So while the Sun-Chen model is based entirely on MD simulations, the Eaton-Akgerman formulae shown in Eq. (149) and Eq. (150) are based on experimental data that they fit their model to and then conveniently evaluate their model with.

Due to their dependence on MD simulations, their model is limited to $0.1 \leq M_1/M_2 \leq 1.67$, $0.5 \leq \sigma_1/\sigma_2 \leq 1.0$, and $1.5 \leq V_2/V_0 \leq 2.0$. Only fourteen out of 303 data points in this analysis satisfy these constraints and are considered valid. Seven of the fourteen points are part of the 25°C self-diffusivity dataset, while the remaining five and two are part of the 50°C and 70°C datasets, respectively. Since the Sun-Chen model is successful modeling diffusivities outside of its MD range, the Eaton-Akgerman model is also examined.

Mutual and solute-tracer diffusivity predictions are shown in Figure 187 and are inaccurate at low and high densities. Self-diffusivities are also shown and, in general, match the mutual- and tracer-diffusivity trends. Low density diffusivity-ratio predictions are closer to one, but are still underestimated, while high density predictions steadily increase with density. The fourteen valid data points lie in the region where the ordinate is one, thus validating the Eaton-Akgerman model at this density only (~0.9 g/cm^3). The narrow width illustrates that a much wider simulation and experimental database should have been used during the development of the Eaton-Akgerman model. Due to the extremely wide range of diffusivity ratios observed in Figure 187, the form of the model is unsuitable for predicting supercritical diffusivities. The Eaton-Akgerman approach is not recommended for predicting supercritical-water diffusivities because of its poor predictions.

The Eaton-Akgerman hard-sphere-theory approach is rated:

(mean low & high density diffusivity ratios: $0.4 \pm 0.5_{95\%}$ & $2 \pm 3_{95\%}$)

II.5.2.3.3 He Equation

Whereas the Eaton-Akgerman model is developed using data from three solvents, He uses ten solvents and a much larger diffusivity database during the development of his model. The He model originates with the Eaton and Akgerman version of the Dymond model, but He regresses and develops new terms since He's database is much larger. The resulting model is presented in Eq. (151) and requires less inputs than the Eaton-Akgerman model. It is claimed to have better results due in part to the 1,167 point database that spans a solvent reduced-temperature range of $1.00 \leq T_{r2} \leq 1.78$ and a reduced-density range of $0.21 \leq \rho_{r2} \leq 2.29$. Despite the use of this larger database, He starts with the extended Dymond model that is based on MD simulations with $0.1 \leq M_1/M_2 \leq 1.67$, $0.5 \leq \sigma_1/\sigma_2 \leq 1.0$, and $1.5 \leq V_2/V_0 \leq 2.0$ limits (He, 1997). He never mentions that these constraints may hinder or restrict the extension of his model to the larger range of experimental data.
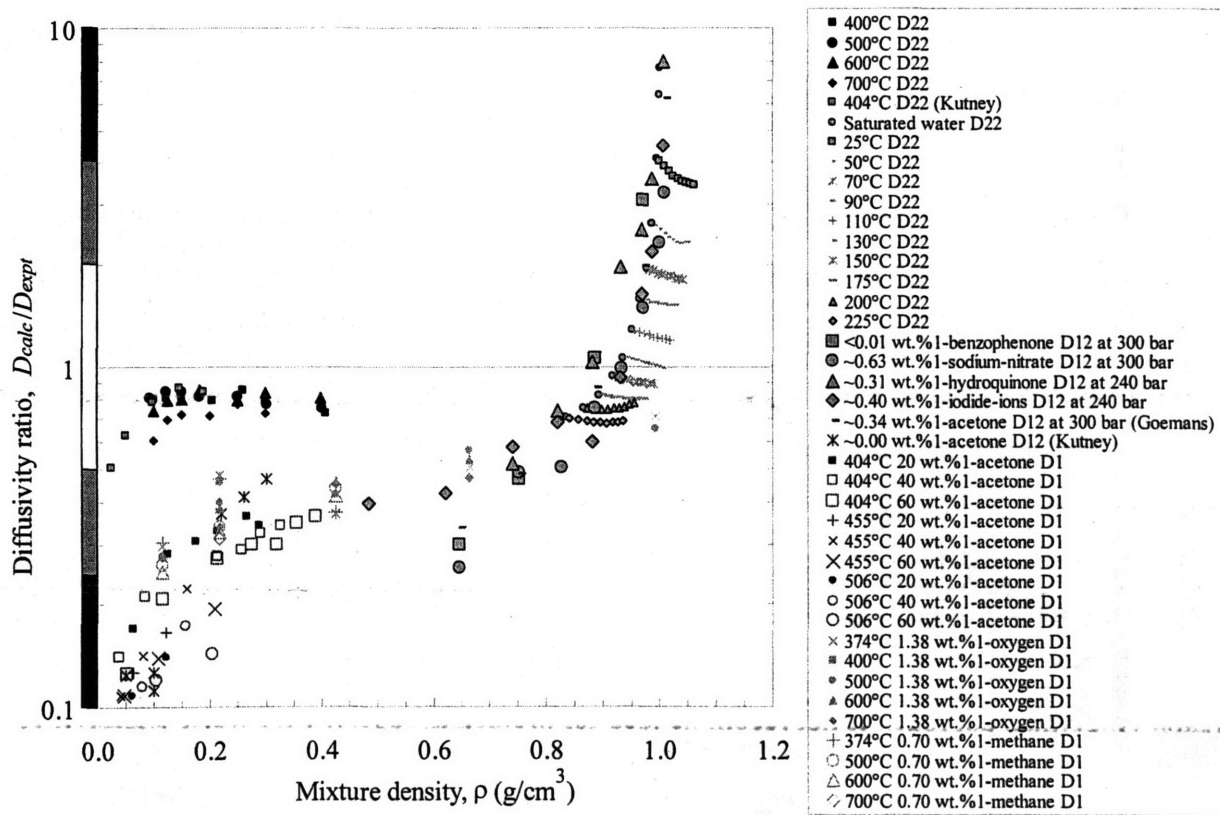
Figure 187. Eaton-Akgerman D_{22}, D_{12}, and D_1 predictions using the default model.

In fact, the Eaton-Akgerman and He models are regressed to data that extend past the MD boundaries used during the model development, and the Eaton-Akgerman results clearly illustrate how poor these extrapolations are. For the He model, the results are worse than the Eaton-Akgerman results (see Figure 188). For example, high density predictions are negative since the reduced density is greater than 2.29 and outside the regressed range of the He database. These results demonstrate that semi-empirical models need to be validated for the systems of interest before they are qualified for use. This is especially important when models are developed with experimental data which are beyond the fundamental limits of the model. The evaluation performed here indicates that the He correlation is not suitable for supercritical-water diffusivity modeling.

The He hard-sphere-theory approach is rated:

F   F

(mean low & high density diffusivity ratios: $0.3 \pm 0.2_{95\%}$ & $<0.1 \pm <0.1_{95\%}$)
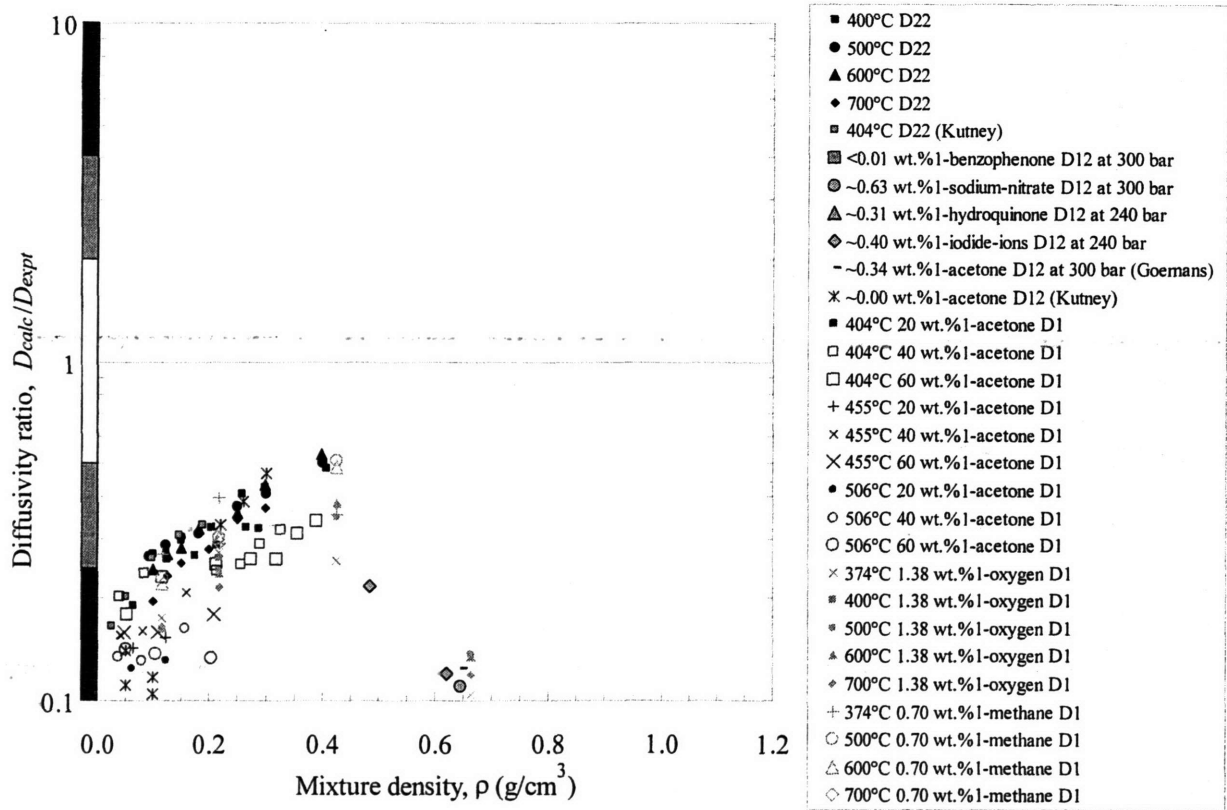
Figure 188. He D_{22}, D_{12}, and D_1 predictions using pure water solvent properties.

II.5.2.3.4 He-Yu Equation

Since He and Yu were not satisfied with the He model for high temperature liquids, they developed a new correlation to improve these and supercritical infinitely dilute diffusivity predictions. They used the Cohen and Turnbull notion that molecular transport occurs by the movement of solute molecules into voids opened by solvent molecules in a grid, which is constantly changing and evolving (He and Yu, 1998). With a larger 1,303-point database, the He-Yu correlation is formed from experimental data that span from $0.70 \leq T_{r2} \leq 1.78$, $0.22 \leq \rho_{r2}$ ≤ 2.62, and $58.1 \leq MW_1 \leq 885$. MD simulations are not used so the He-Yu expression is free of additional constraints that limit the Eaton-Akgerman and He expressions.

The He-Yu model, as shown in Eq. (153), does not explicitly depend on the solvent close-packed hard-sphere molar volume, V_0, because He and Yu use an estimate of $0.23V_{c2}$. Results from the default model with the He-Yu estimated volume are presented before the results with the real hard-sphere volume are presented. Diffusivity ratios are reported in Figure 189 using the default He-Yu V_0 expression. High density diffusivity predictions are underestimated, along with diffusivity ratios with densities smaller than 0.2 g/cm^3. Predictions for densities in between are reasonable.

The actual close-packed volume is roughly 40% smaller than the He-Yu estimated volume. When the real volume is used in the He-Yu model instead of $0.23V_{c2}$, high density predictions are significantly increased as seen in Figure 190. The diffusivity ratios are also scattered more and as a result, imply that the He-Yu model should not be used for dense-fluid predictions. The low density predictions are unchanged since the hard-sphere volumes are negligible compared to the actual volumes in the exponential term in Eq. (153). Volumes are large because molecules are no longer packed together. Due to the poor low density performance along with the difficulty of predicting liquid-like diffusivities, the He-Yu model is not recommended for supercritical-water diffusivity predictions.

Therefore, the He-Yu hard-sphere-theory approach is rated: ▮ ▮

(mean low & high density diffusivity ratios: $0.7 \pm 0.8_{95\%}$ & $2 \pm 3_{95\%}$)
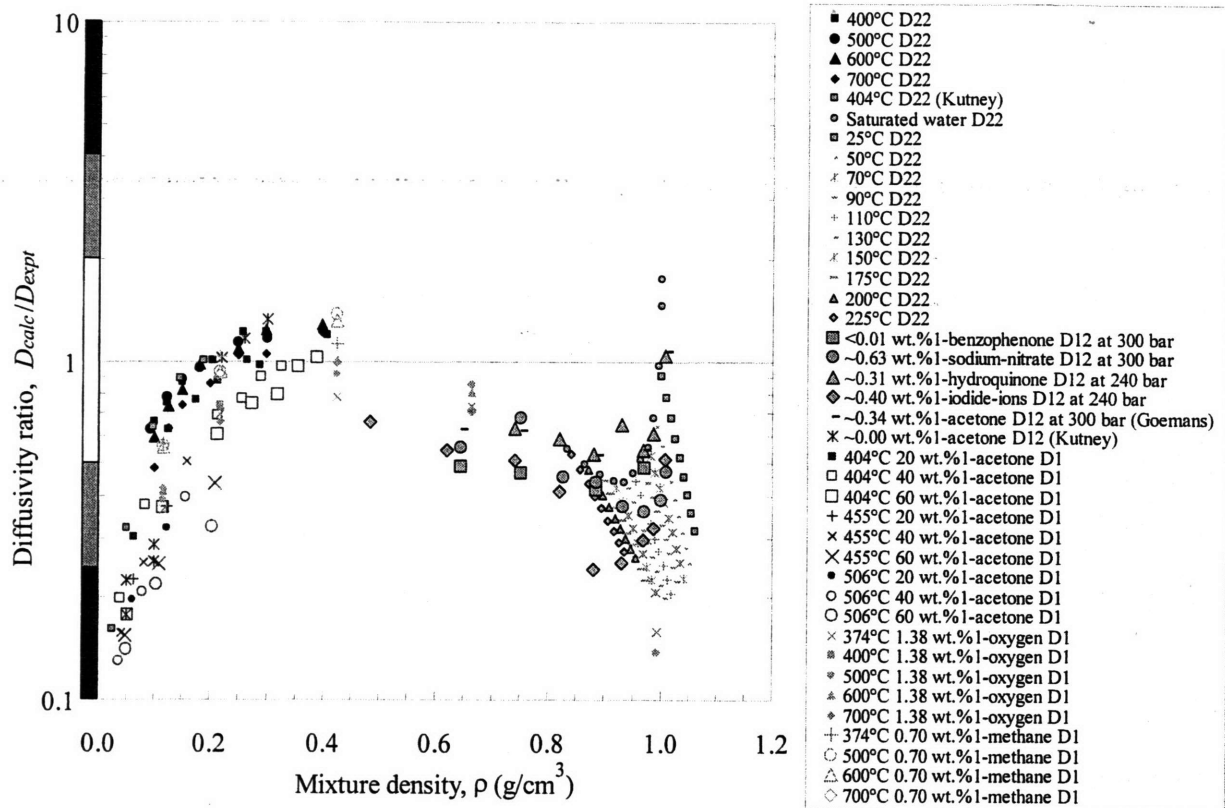
Figure 189. He-Yu D_{22}, D_{12}, and D_1 predictions using He-Yu's estimated V_0.
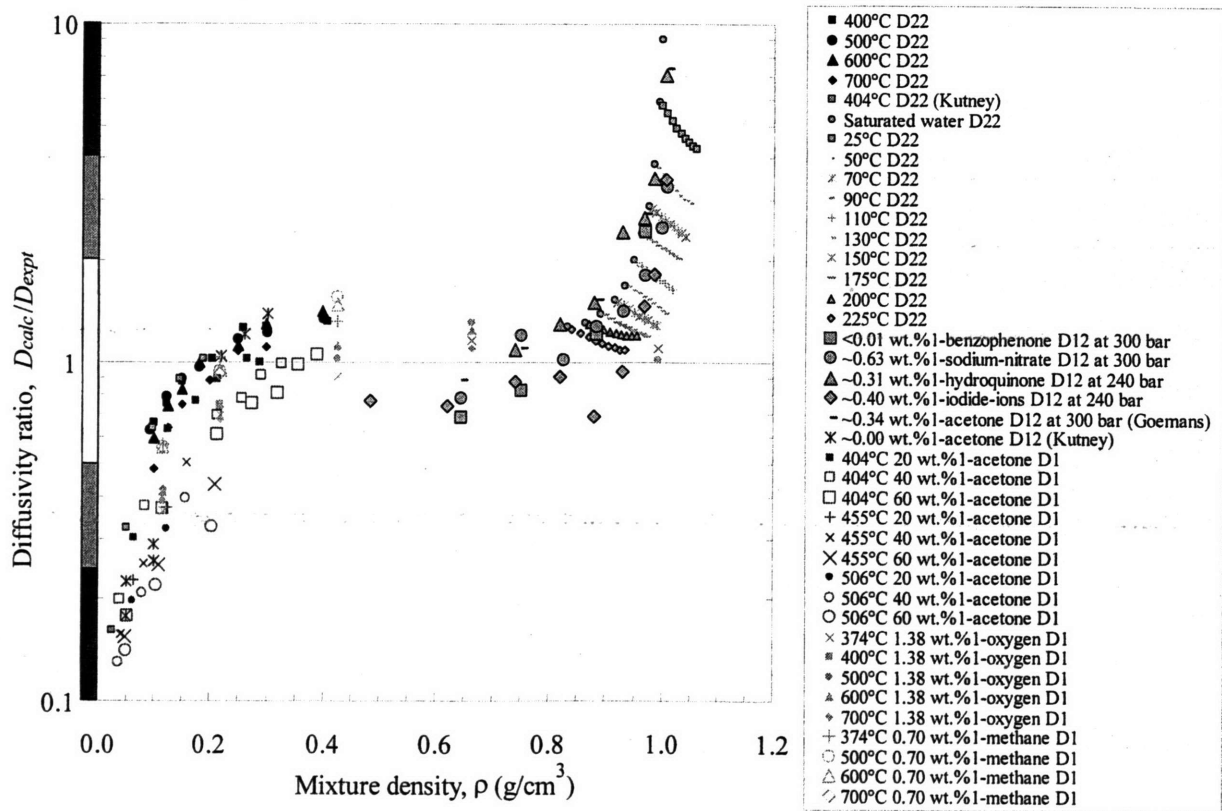
Figure 190. He-Yu D_{22}, D_{12}, and D_1 predictions using the real experimental V_0.

II.5.2.3.5 Tracer Liu-Silva-Macedo Equation

The final hard-sphere model evaluated is developed by Liu, Silva, and Macedo (LSM). They start with a free-volume-theory expression for hard spheres, and following development work with MD simulations, they generate a kinetic-theory correction. MD-related restrictions for their self-diffusivity correction are never discussed. The resulting expression is defined in Eq. (144) and is the foundation for their overall expression. Next, they insert a pseudo-activation-energy term into the exponential grouping in order to replicate statistical-mechanics results which suggest that a temperature-dependent attractive correction is needed for Lennard-Jones fluids (Chung, 1966; Liu and Macedo, 1995). Note that when densities and interaction energies are small (e.g., in the ideal-gas limit), the modified expression correctly reduces to unity.

With their database of over forty substances and 1,500 self-diffusivity data points, they developed the LSM self-diffusivity model that is the basis of their work. Recently, they extended the LSM model so that infinitely dilute mutual diffusivities can be predicted. Defined in Eq. (145), the Tracer LSM (TLSM) model reduces to the LSM form when predicting self-diffusivities. The TLSM model requires molecular weights, volume, temperature, the effective hard-sphere diameter, σ_{TLSM}, which is defined in Eq. (146), and the effective well-depth potential, ε^{TLSM}, which is defined in Eq. (147). Effective hard-sphere theory corrects for differences between perfect Lennard-Jones fluids and real fluids that sometimes have weaker attractive interactions. These differences are noticeable often at low temperatures and high densities. For the LSM and TLSM models, the effective diameter in Eq. (146) is based upon the effective hard-sphere correction developed by Ben-Amotz and Herschbach (1990).

In order to further improve the accuracy of their LSM and TLSM models, Liu and coworkers opted to regress the normally fixed Lennard-Jones values with the data in their database. They write that the Lennard-Jones well-depth potential and diameter can be made adjustable for species in their diffusivity database since these diffusivities are already known, and the additional regression often improves the model accuracy (Liu et al., 1998). In most cases, the regressed Lennard-Jones values are similar to the known values, indicating that the model form reasonably simulates the system.

Regressed Lennard-Jones parameters for hydrogen-bonded species are significantly different from the known values and imply that the LSM model is not well suited for hydrogen-bonded species. For example, water self-diffusivity predictions are improved when a well-depth of $\varepsilon_2/k = 3789$ K and diameter of $\sigma_2 = 1.53$ Å are used instead of the accepted values of 363 K and ~2.66 Å (see Table 60 for differences of other species). Using the regressed water constants, the average-absolute deviation is approximately 30% for all of the 118 water self-diffusivities in their database, yet only 12% for the 34 supercritical self-diffusivities. Since these percentages are higher than for other examined species, Liu et $al.$ (1998) do not recommend using the two-parameter TLSM model for water. Instead, they recommend their empirical model with four adjustable parameters for hydrogen-bonded species. This complicated model is not evaluated because this analysis avoids models that require regression of parameters for each species.

For species that are not part of the original regressed database, Liu and coworkers recommend using the following generalized equations provided by Silva et $al.$ (1998) for both Lennard-Jones parameters, even if values are available in the literature

$$\frac{\varepsilon_i}{k} = 0.774 T_{ci} \qquad (197)$$

$$\sigma_i = \sqrt[3]{0.17791 + 11.779\left(\frac{T_{ci}}{P_{ci}}\right) - 0.049029\left(\frac{T_{ci}}{P_{ci}}\right)^2} \qquad (198)$$

These relations will not be used because Lennard-Jones values are available in Table 56, and they have been used already throughout the analysis.

Table 60. Known and the TLSM-regressed pure component 6-12 Lennard-Jones properties

Species	Known well-depth potential, ε/k (K)	Known radius, r (Å)	TLSM well-depth potential, ε/k (K)	TLSM radius, r (Å)
Water	363	$1.375 - 0.0011(T[°C] - 25)$	3789	0.765
Acetone	560	2.28	333	2.34
Methane	149	1.88	167	1.79
Source	Lienhard and Lienhard, 2002	Wilhelm, 1973 (water); Lienhard and Lienhard, 2002	Liu et $al.$, 1998	

Since differences are expected between regressed and known Lennard-Jones based predictions, the TLSM model will be examined with both sets of values. With known Lennard-Jones values and the default TLSM equations (Eq. (145), Eq. (146), and Eq. (147)), low density mutual- and solute-tracer-diffusivity predictions are reasonably accurate as observed in Figure 191 while high density diffusivity ratios are scattered and underestimated. Simulated methane and oxygen diffusivity ratios straddle one along the entire abscissa. Using known Lennard-Jones values, self-diffusivities are overestimated in Figure 192 for both low and high densities. Since solvent and solute tracer diffusivities are identical when calculated with the TLSM model and since experimental solvent diffusivities are always larger than the equivalent solute diffusivities, the solvent diffusivity ratios in Figure 192 will be smaller than the solute diffusivity ratios in Figure 191. Due to this numerical limitation, water tracer diffusivities for the acetone-water systems will be underestimated. Likewise, water tracer diffusivities are overestimated at low densities and become underestimated at higher densities for the methane and oxygen datasets.
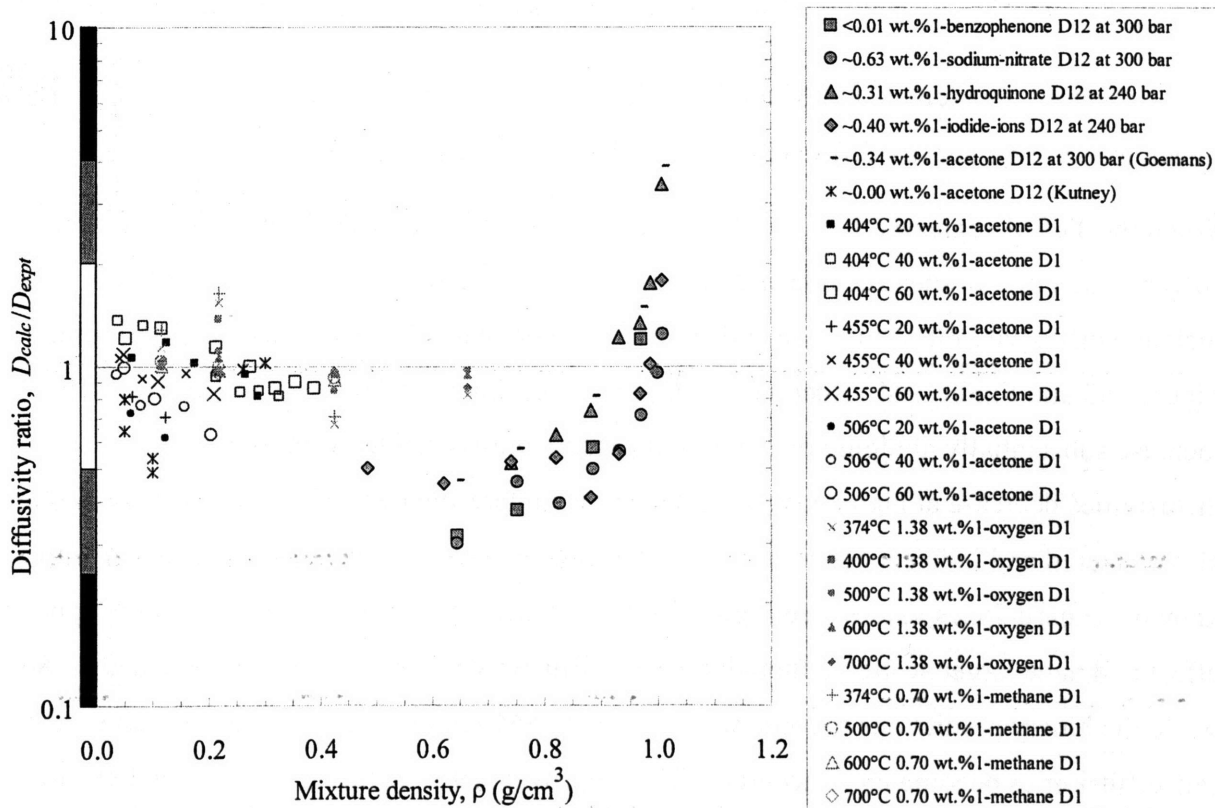
Figure 191. TLSM D_{12} and D_1 predictions using the original formulation and known LJ values.
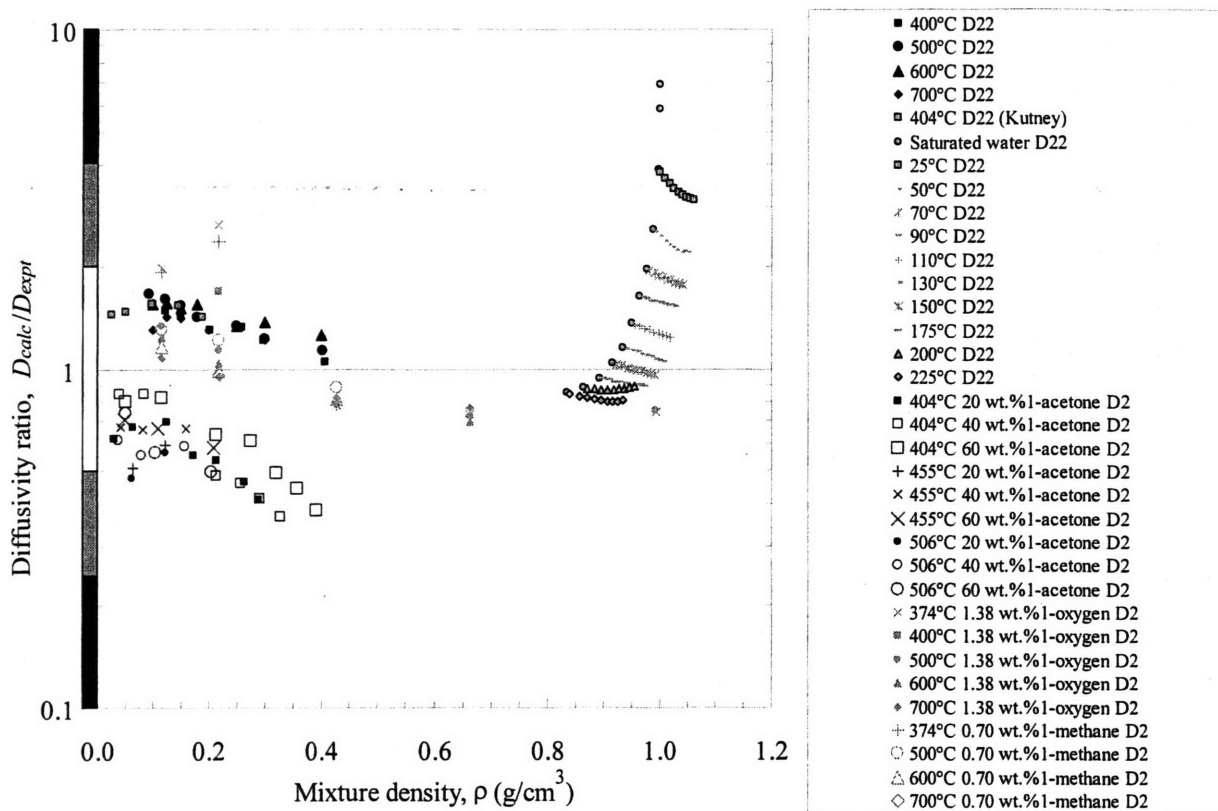
Figure 192. TLSM D_{22} and D_2 predictions using the original formulation and known LJ values.

Overall, the default TLSM model with known LJ values is rated:

(mean low & high density diffusivity ratios: $1.1 \pm 0.6_{95\%}$ & $1 \pm 2_{95\%}$)

When the TLSM-regressed Lennard-Jones values that are listed in Table 60 are used for the solvent water and solutes acetone and methane, several differences are observed. On the whole, methane diffusivity ratios increase and are now overestimated by approximately 30% as seen in Figure 193 and Figure 194. Acetone tracer predictions improve slightly at low densities, but increase substantially at higher densities and become unreasonable. Conversely, self-diffusivities decrease at high densities and are now underestimated. These self-diffusivities are also clustered and indicate better model performance compared to the model calculated with known Lennard-Jones values (see Figure 192). Low density self-diffusivities show the opposite effect and have larger scatter, although the self-diffusivity ratios are scattered around one. So while the binary predictions become worse using TLSM-regressed Lennard-Jones values, the self-diffusivities become more accurate. This improvement is expected because the Lennard-Jones values were optimized with the experimental data that this model is being tested with.
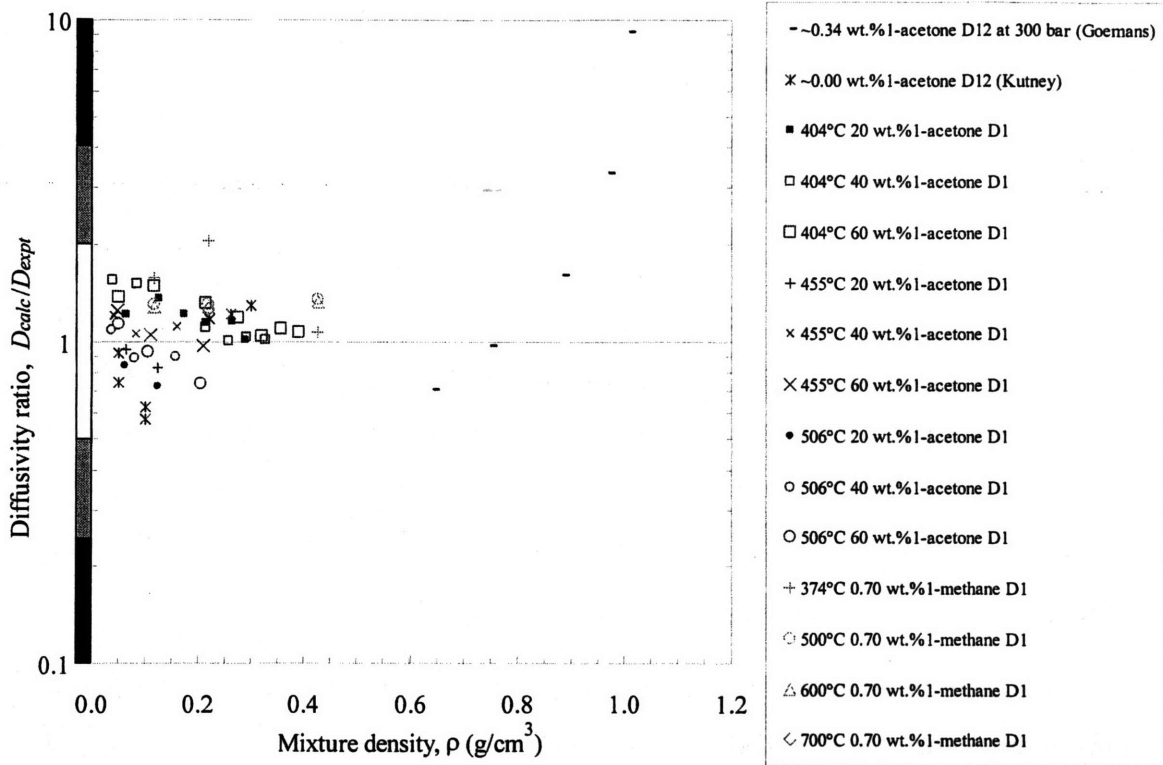
Figure 193. TLSM D_{12} and D_1 predictions using the original formulation and TLSM-regressed LJ values.

Figure 194. TLSM D_{22} and D_2 predictions using the original formulation and TLSM-regressed LJ values.

379
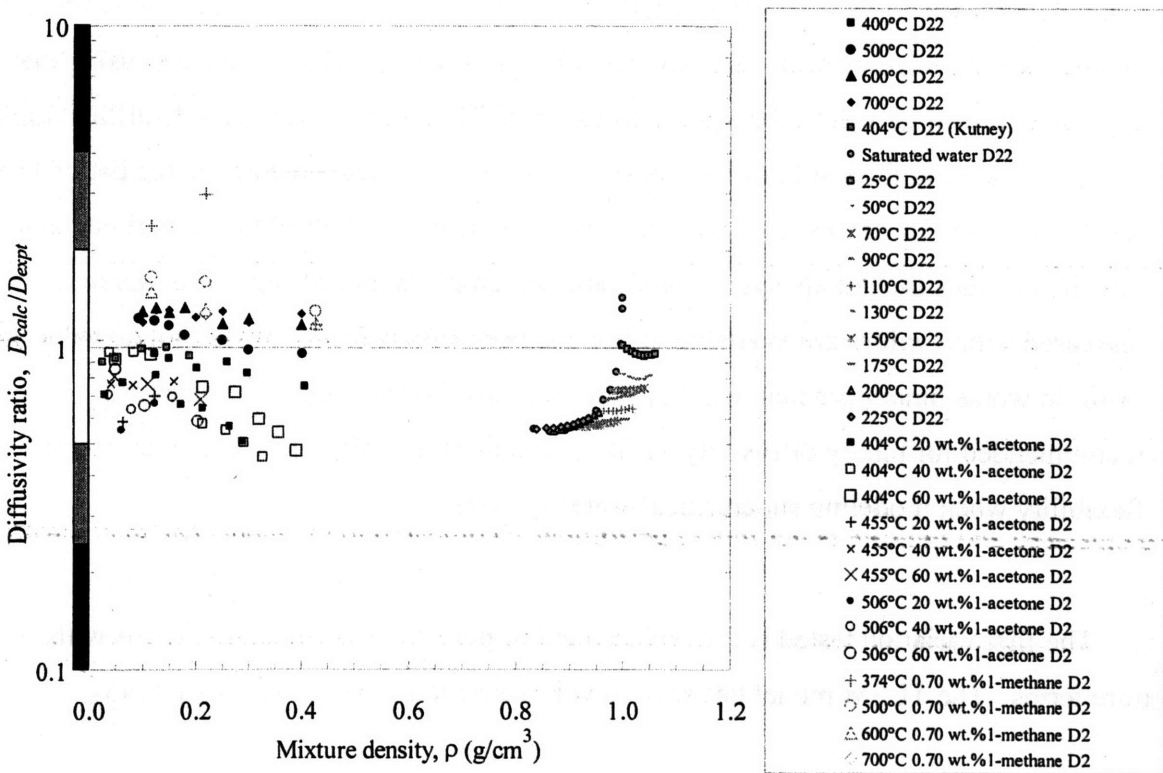
The default TLSM model with TLSM-regressed LJ values is rated:

(mean low & high density diffusivity ratios: $1.1 \pm 0.5_{95\%}$ & $1 \pm 2_{95\%}$)

Now that the original formulation of the TLSM model has been evaluated, variations will be explored in order to further increase the accuracy of the TLSM model. The following variations will be tested.

1. Use mixture volumetric properties instead of solvent properties since Liu *et al.* developed the TLSM model for infinitely dilute solutes which do not need mixture properties. For concentrated systems, the volumetric terms are not always adequately represented by pure solvent properties and therefore, it is appropriate to consider using mixture terms. For the first test, the solvent density (ρ_2) and the solvent diameter (σ_2) will be replaced with the mixture density (ρ) and the effective diameter (σ_{TLSM}), respectively.

2. Weigh the other unweighted terms since there have been past instances when weighing these terms improve the overall model accuracy. In particular, the unweighted σ_{12}, ε_{TLSM}, and M_{12} terms will be replaced with weighted versions. Finally, use TLSM-regressed LJ values for water and known LJ values for the solute. Since the ultimate goal is to accurately predict diffusivities for supercritical water and its systems, it is reasonable to consider using the TLSM-regressed LJ values for water because they will result in accurate self-diffusivities. Since only around forty solutes have been regressed by Liu and coworkers, the list of TLSM-regressed solute LJ values is small. This limitation is due to the fact that experimental solute self-diffusivities are not always available and therefore, cannot be regressed. Even if regressed solute values are available, it has just been shown that regressed solute values result in worse binary predictions. For these reasons, known solute LJ values are recommended for binary diffusivity TLSM predictions and offer the highest degree of flexibility when modeling supercritical-water systems.

The first variation tested is the replacement of pure solvent volumetric terms with mixture terms. The TLSM model has several volumetric terms as shown in Eq. (145)

$$D_{12}^{TLSM-HS} = \frac{669.1 M_2}{\rho_2 N_A \sigma_{TLSM}^2} \sqrt{\frac{RT}{M_{12}}} \cdot$$
$$\exp\left(-\frac{0.75\rho_2 N_A \sigma_2^3 / M_2}{1.2588 - \rho_2 N_A \sigma_2^3 / M_2} - 0.27862 \frac{\varepsilon_{12}^{TLSM}}{kT}\right)$$

(145)

$$\sigma_{TLSM}^2 = \frac{2^{1/3} \sigma_{12}^2}{\left(1 + 1.2\sqrt{\frac{kT}{\varepsilon_{12}^{TLSM}}}\right)^{1/3}}$$

(146)

$$\frac{\varepsilon_{12}^{TLSM}}{k} = \frac{\sqrt{\sigma_1^3 \sigma_2^3 \varepsilon_1 \varepsilon_2}}{k\sigma_{12}^3}$$

(147)

$$\sigma_{12} = \frac{\sigma_1 + \sigma_2}{2}$$

(111)

$$M_{12} = \frac{2}{1/M_1 + 1/M_2}$$

(199)

Since the pure solvent number density $(\rho_2 N_A \sigma_2{}^3)$ is influenced by the addition of solute, it is appropriate to convert this term into a mixture number density. Since the effective hard-sphere diameter is solute weighted and appears elsewhere in the TLSM model, all solvent diameters in Eq. (145) are replaced with the effective diameter. The solvent density is also replaced with the mixture density which results in the following TLSM model

$$D_{12}^{TLSM-HS} = \frac{669.1 M_{12}}{\rho N_A \sigma_{TLSM}^2} \sqrt{\frac{RT}{M_{12}}} \cdot$$
$$\exp\left(-\frac{0.75\rho N_A \sigma_{TLSM}^3 / M_{12}}{1.2588 - \rho N_A \sigma_{TLSM}^3 / M_{12}} - 0.27862 \frac{\varepsilon_{12}^{TLSM}}{kT}\right)$$

(200)

$$\sigma_{TLSM}^2 = \frac{2^{1/3} \sigma_{12}^2}{\left(1 + 1.2\sqrt{\frac{kT}{\varepsilon_{12}^{TLSM}}}\right)^{1/3}}$$

(146)

$$\frac{\varepsilon_{12}^{TLSM}}{k} = \frac{\sqrt{\sigma_1^3 \sigma_2^3 \varepsilon_1 \varepsilon_2}}{k\sigma_{12}^3}$$

(147)

$$\sigma_{12} = \frac{\sigma_1 + \sigma_2}{2}$$

(111)

$$M_{12} = \frac{2}{1/M_1 + 1/M_2}$$

(199)

It is crucial that any change that improves binary predictions and introduces concentration dependence does not negatively impact infinitely dilute or pure solvent predictions. When the mixture volume reduces to the solvent volume in the infinitely dilute and pure solvent limit, the original LSM model is intentionally reformed.

Mutual and tracer diffusivity ratios with known LJ values are shown in Figure 195. Compared to the original predictions shown in Figure 191, the low density diffusivity predictions are scattered more, but still lie about the diffusivity ratio of one. High density predictions are worse, and some results are off the ordinate scale. The extreme values are the result of using an unweighted combining rule (Eq. (111)) which is used in Eq. (147) and then cubed in the TLSM equation (Eq. (146)). On the other hand, the self-diffusivity predictions do not change as seen in Figure 196 since Eq. (200) reduces to the original LSM model when solutes are not present.

When the TLSM-regressed LJ values are used instead of known values for methane, acetone, and water systems, similar trends are seen. Mutual and tracer diffusivities are dispersed more as shown in Figure 197. However, high density mutual diffusivities in Figure 197 are overestimated compared to those in Figure 193 when solvent volumetric terms are used. Self-diffusivity ratios that are plotted in Figure 198 do not change at low densities, but decrease slightly at high densities because effective diameters are used in the hard-sphere exponential term (compared to when the solvent diameters are used in Figure 194).

The original TLSM model (Eq. (145)) cannot have concentration dependence since it is specifically designed for self- and infinitely dilute mutual diffusivities. By weighting volumetric parameters in Eq. (200), predictions are now dependent on the system concentration, but are scattered more. This increased scattering can be explained in terms of unweighted energy terms such as the hard-sphere diameter, and this issue will be addressed next. Both models still reduce to the original LSM form for self-diffusivity predictions.
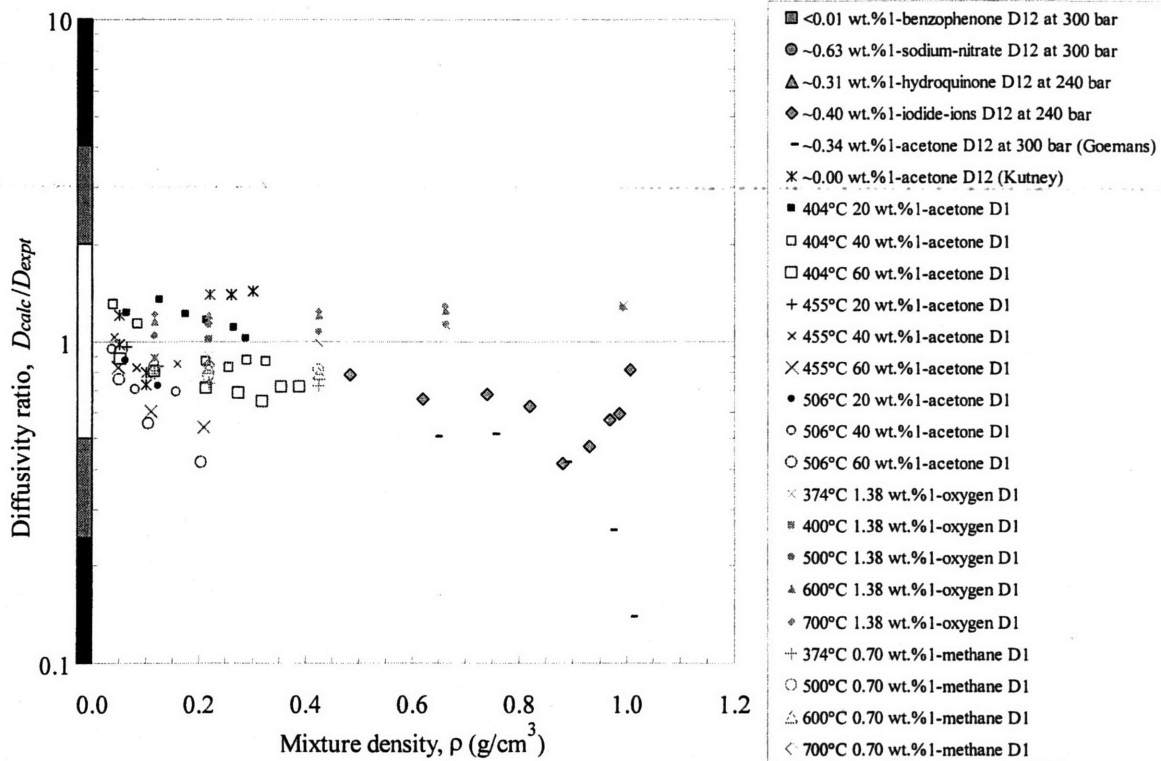
Figure 195. TLSM D_{12} and D_1 predictions using known LJ values, mole-fraction-weighted V_2, and all $\sigma_2 = \sigma_{TLSM}$.

Figure 196. TLSM D_{22} and D_2 predictions using known LJ values, mole-fraction-weighted V_2, and all $\sigma_2 = \sigma_{TLSM}$.

383
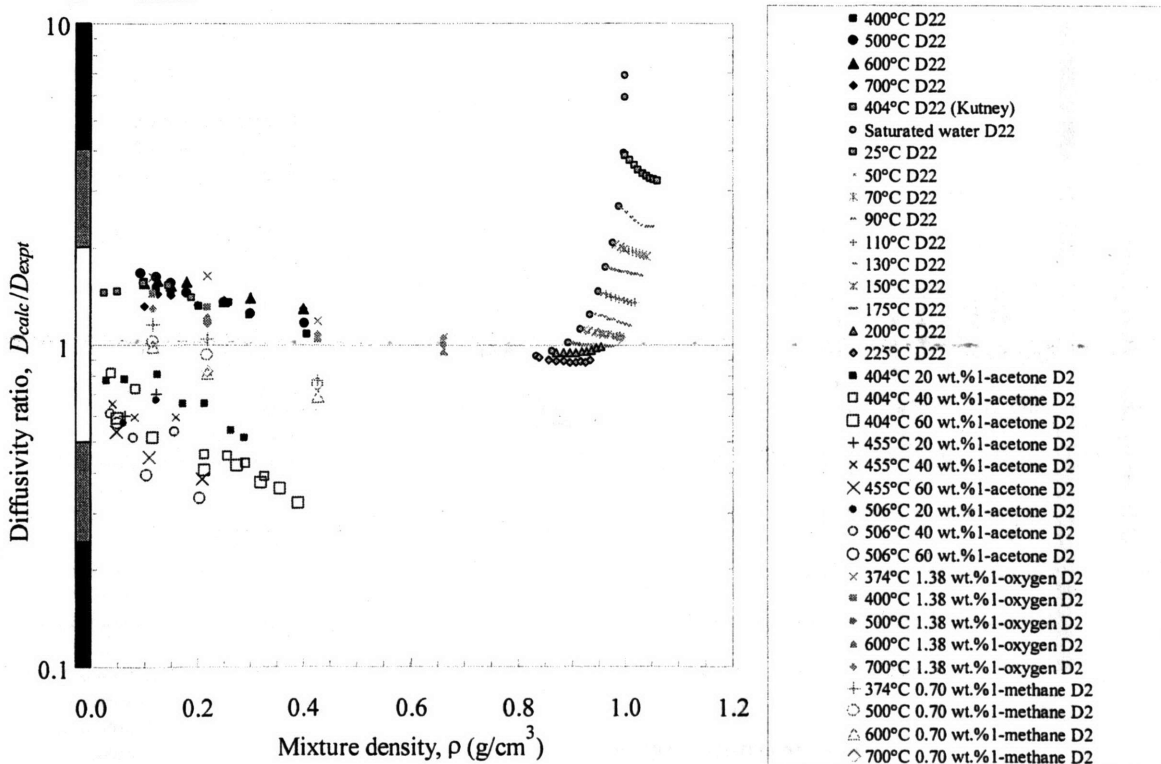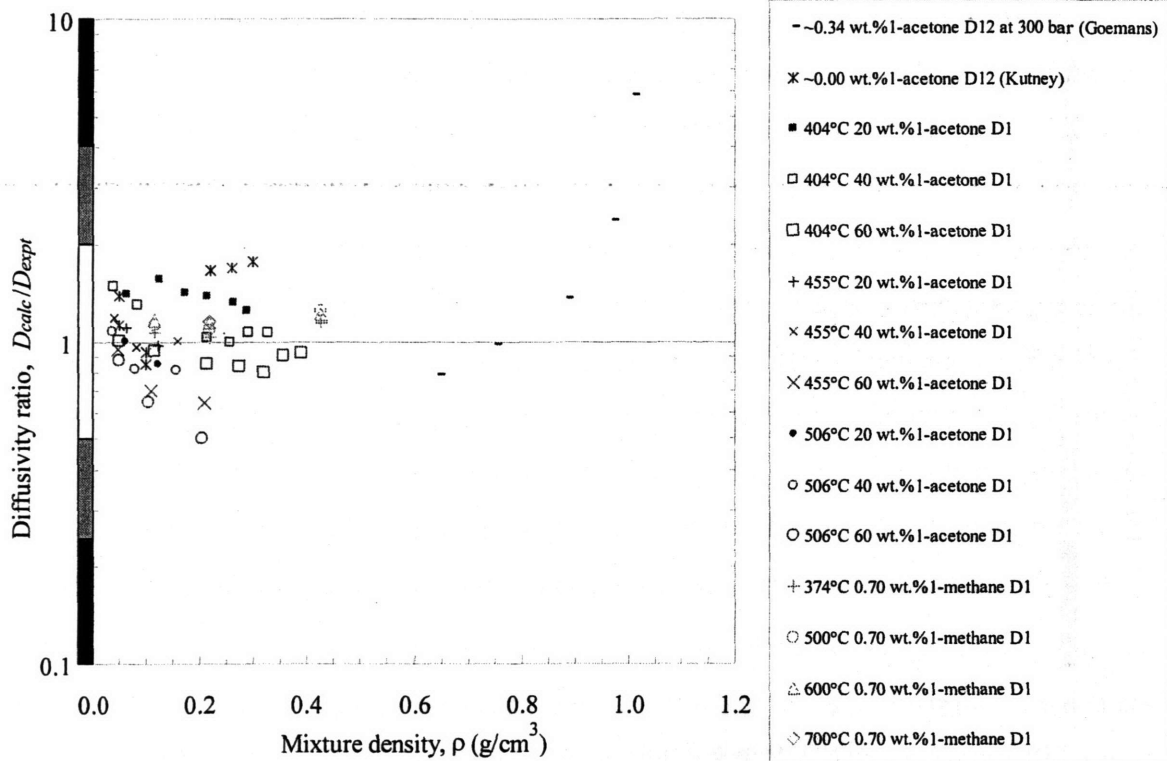
Figure 197. TLSM D_{12} and D_1 predictions using TLSM-regressed LJ values, mole-fraction-weighted V_2, and all $\sigma_2 = \sigma_{TLSM}$.
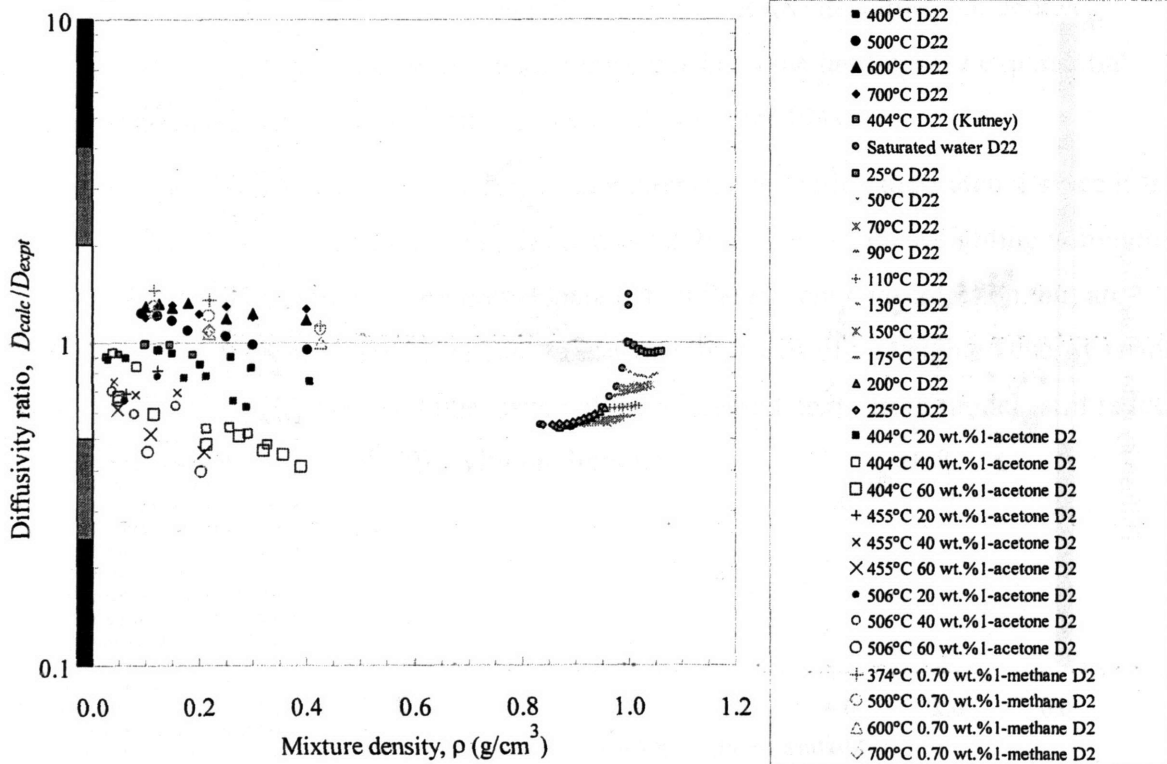
Figure 198. TLSM D_{22} and D_2 predictions using TLSM-regressed LJ values, mole-fraction-weighted V_2, and all $\sigma_2 = \sigma_{TLSM}$.

In order to avoid abnormally large mean molecular diameters and predictions for larger solute species, several terms are weighted. The well-depth potential will be weighted according to Eq. (202). The mean molecular diameter will be represented by a linear mole-fraction combination of diameters as defined in Eq. (203). These changes introduce concentration dependence in a simple fashion and avoid a significant change to the term when solute is added to the system. To be consistent with the other weighted terms, the mixture molecular weight is the last term scaled, and it is defined in Eq. (204).

$$D_{12}^{TLSM-HS} = \frac{669.1 M_{12}}{\rho N_A \sigma_{TLSM}^2} \sqrt{\frac{RT}{M_{12}}} \cdot$$
$$\exp\left(-\frac{0.75 \rho N_A \sigma_{TLSM}^3 / M_{12}}{1.2588 - \rho N_A \sigma_{TLSM}^3 / M_{12}} - 0.27862 \frac{\varepsilon_{12}^{TLSM}}{kT}\right) \tag{201}$$

$$\sigma_{TLSM}^2 = \frac{2^{1/3} \sigma_{12}^2}{\left(1 + 1.2 \sqrt{\frac{kT}{\varepsilon_{12}^{TLSM}}}\right)^{1/3}} \tag{146}$$

$$\frac{\varepsilon_{12}^{TLSM}}{k} = \frac{\varepsilon_1^{x_1} \varepsilon_2^{x_2}}{k} \tag{202}$$

$$\sigma_{12} = x_1 \sigma_1 + x_2 \sigma_2 \tag{203}$$

$$M_{12} = x_1 M_1 + x_2 M_2 \tag{204}$$

TLSM predictions can be made with known LJ values now that all mixture terms are weighted with respect to mole fraction. Mutual and solute-tracer diffusivities using Eqs. (201), (146), (202), (203), and (204) are plotted in Figure 199, while self-diffusivities are shown in Figure 200. High density mutual diffusivities are no longer larger than the ordinate scale, but are still overestimated and dispersed compared to the original predictions shown in Figure 191. Likewise, low density predictions are larger and scattered more compared to the original predictions in Figure 191, although there is less scatter for the oxygen and methane tracer results over its density range. Self-diffusivities are identical to those in Figure 196 because the combining rules are ineffective when modeling pure species.
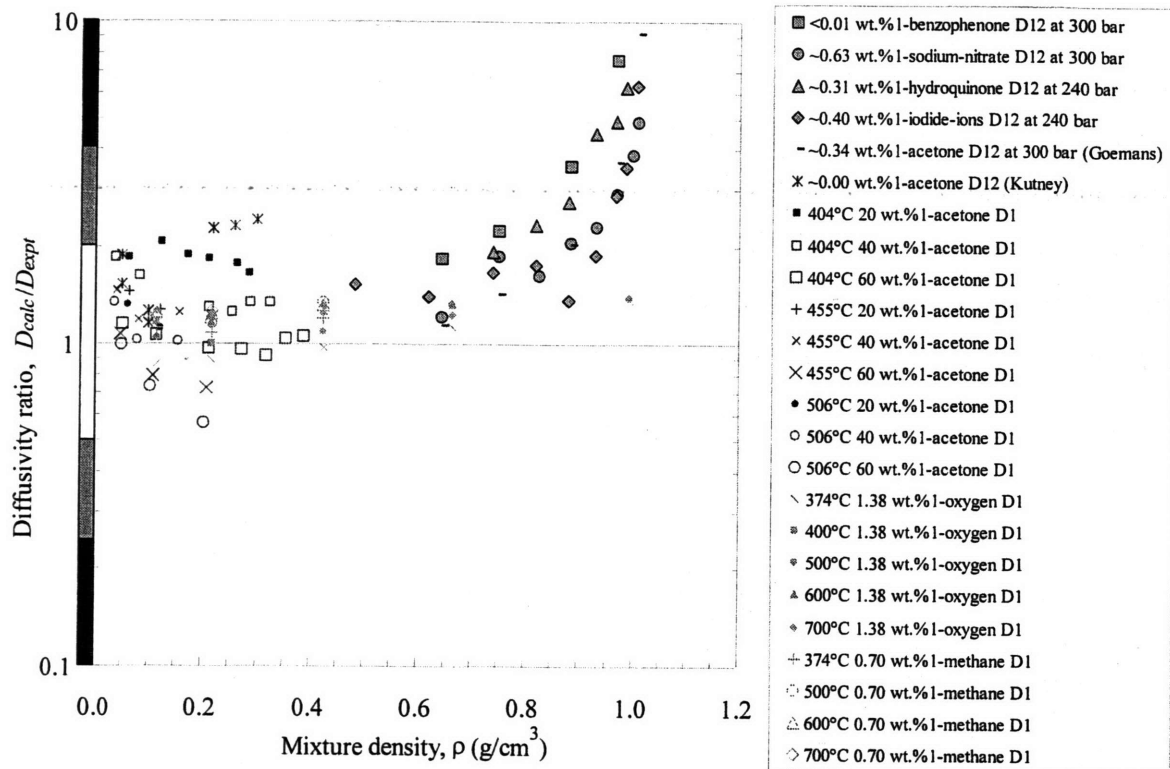
Figure 199. TLSM D_{12} and D_1 predictions using known LJ values, mole-fraction-weighted V_2, $\sigma_2 = \sigma_{TLSM}$, and mole-fraction-weighted σ_{12}, $\varepsilon_{12}^{TLSM} = \varepsilon_{12}$, & MW_{12}.

Legend for Figure 199:
- ▣ <0.01 wt.%1-benzophenone D12 at 300 bar
- ◉ ~0.63 wt.%1-sodium-nitrate D12 at 300 bar
- △ ~0.31 wt.%1-hydroquinone D12 at 240 bar
- ◇ ~0.40 wt.%1-iodide-ions D12 at 240 bar
- – ~0.34 wt.%1-acetone D12 at 300 bar (Goemans)
- ✳ ~0.00 wt.%1-acetone D12 (Kutney)
- ■ 404°C 20 wt.%1-acetone D1
- ◻ 404°C 40 wt.%1-acetone D1
- □ 404°C 60 wt.%1-acetone D1
- + 455°C 20 wt.%1-acetone D1
- × 455°C 40 wt.%1-acetone D1
- ✕ 455°C 60 wt.%1-acetone D1
- • 506°C 20 wt.%1-acetone D1
- ○ 506°C 40 wt.%1-acetone D1
- ○ 506°C 60 wt.%1-acetone D1
- ＼ 374°C 1.38 wt.%1-oxygen D1
- ▦ 400°C 1.38 wt.%1-oxygen D1
- ✿ 500°C 1.38 wt.%1-oxygen D1
- ▲ 600°C 1.38 wt.%1-oxygen D1
- ◆ 700°C 1.38 wt.%1-oxygen D1
- ＋ 374°C 0.70 wt.%1-methane D1
- ⬭ 500°C 0.70 wt.%1-methane D1
- △ 600°C 0.70 wt.%1-methane D1
- ◇ 700°C 0.70 wt.%1-methane D1

Figure 200. TLSM D_{22} and D_2 predictions using known LJ values, mole-fraction-weighted V_2, $\sigma_2 = \sigma_{TLSM}$, and mole-fraction-weighted σ_{12}, $\varepsilon_{12}^{TLSM} = \varepsilon_{12}$, & MW_{12}.

Legend for Figure 200:
- ■ 400°C D22
- ● 500°C D22
- ▲ 600°C D22
- ◆ 700°C D22
- ▣ 404°C D22 (Kutney)
- ○ Saturated water D22
- ▦ 25°C D22
- · 50°C D22
- ⅰ 70°C D22
- ˷ 90°C D22
- + 110°C D22
- · 130°C D22
- ⅹ 150°C D22
- ⁻ 175°C D22
- ▲ 200°C D22
- ◆ 225°C D22
- ▣ <0.01 wt.%1-benzophenone D12 at 300 bar
- △ ~0.06 wt.%1-hydroquinone D12 at 240 bar
- ◆ ~0.40 wt.%1-iodide-ions D12 at 240 bar
- ■ 404°C 20 wt.%1-acetone D2
- ◻ 404°C 40 wt.%1-acetone D2
- □ 404°C 60 wt.%1-acetone D2
- + 455°C 20 wt.%1-acetone D2
- × 455°C 40 wt.%1-acetone D2
- ✕ 455°C 60 wt.%1-acetone D2
- • 506°C 20 wt.%1-acetone D2
- ○ 506°C 40 wt.%1-acetone D2
- ○ 506°C 60 wt.%1-acetone D2
- ⁄ 374°C 1.38 wt.%1-oxygen D2
- ▦ 400°C 1.38 wt.%1-oxygen D2
- ✿ 500°C 1.38 wt.%1-oxygen D2
- ▲ 600°C 1.38 wt.%1-oxygen D2
- ◆ 700°C 1.38 wt.%1-oxygen D2
- ＋ 374°C 0.70 wt.%1-methane D2
- ⬭ 500°C 0.70 wt.%1-methane D2
- △ 600°C 0.70 wt.%1-methane D2
- ◇ 700°C 0.70 wt.%1-methane D2

Based on the previous TLSM results with different combinations of weighting and mixture properties, an optimum approach for modeling diffusivity of sub- and supercritical-water systems has been developed. This approach is dependent on the solute concentration, so the TLSM model is no longer limited to infinitely dilute predictions. In addition, experimental solute self-diffusivities are not needed in order to regress the solute Lennard-Jones parameters used in the TLSM model. Instead, solute Lennard-Jones parameters can be estimated using critical-constant correlations in case known parameters are unavailable. Solute molecular weight is the only other solute property that is required.

Given that the solvent in this analysis is always water and since the most accurate self-diffusivity results are obtained with the TLSM-regressed Lennard-Jones values (see Table 60), TLSM-regressed Lennard-Jones values are recommended for use when using the TLSM model to predict diffusivities of sub- and supercritical water systems. Solvent molecular weight and density at the process condition of interest are the only other solvent properties that are required.

Using the original TLSM model contained in Eqs. (145) and (146) along with the mole-fraction-weighted mixture well-depth, diameter, and molecular weight defined in Eqs. (202), (203), and (204), the recommended TLSM equation set is complete.

$$D_{12}^{TLSM-HS} = \frac{669.1 M_2}{\rho_2 N_A \sigma_{TLSM}^2} \sqrt{\frac{RT}{M_{12}}} \cdot$$

$$\exp\left(-\frac{0.75 \rho_2 N_A \sigma_2^3 / M_2}{1.2588 - \rho_2 N_A \sigma_2^3 / M_2} - 0.27862 \frac{\varepsilon_{12}^{TLSM}}{kT}\right) \tag{145}$$

$$\sigma_{TLSM}^2 = \frac{2^{1/3} \sigma_{12}^2}{\left(1 + 1.2 \sqrt{\frac{kT}{\varepsilon_{12}^{TLSM}}}\right)^{1/3}} \tag{146}$$

$$\frac{\varepsilon_{12}^{TLSM}}{k} = \frac{\varepsilon_1^{x_1} \varepsilon_2^{x_2}}{k} \tag{202}$$

$$\sigma_{12} = x_1 \sigma_1 + x_2 \sigma_2 \tag{203}$$

$$M_{12} = x_1 M_1 + x_2 M_2 \tag{204}$$

Using known solute Lennard-Jones values, the diffusivity can be simply computed since regression is no longer necessary. This equation set is nearly identical to the set published by

Liu and coworkers. In fact, the only differences are the use of mole-fraction-weighted well-depths, diameters, and molecular weights and that they recommend using regressed Lennard-Jones values for the solvent and the solute.

As stated earlier, it is recommended to use available solute Lennard-Jones values since experimental solute self-diffusivities are not consistently available. Using TLSM-regressed water values is recommended since these values provide the most accurate sub- and supercritical water self-diffusivity predictions.

Mutual and tracer diffusivities using the recommended TLSM model are shown in Figure 201. Low density tracer predictions are scattered about one and are all reasonable. Accuracy is fairly consistent for the oxygen and methane tracer predictions as density increases, although the diffusivity ratios are scattered at low densities. High density mutual diffusivities are slightly overestimated, but are reasonable. Above densities of 1 g/cm^3, the results become significantly overestimated and demonstrate the need for a high density limit for the TLSM model. At very low densities, the TLSM model approaches the diffusivity ratio of one which indicates that the model can accurately represent ideal-gas-like diffusivities in the region where kinetic-gas theories dominate.

Water self-diffusivities are shown in Figure 202 and are also reasonable over the entire abscissa. At the low density supercritical conditions, the predictions are slightly overestimated but are clustered together reasonably well. At high density, low temperature self-diffusivities are accurate due to the use of regressed-TLSM Lennard-Jones values. Higher temperature predictions are clustered below the unity diffusivity ratio and are also reasonable. When known values are used, the high density, high temperature predictions are similar to those in Figure 200 and are unreasonable. The solvent tracer diffusivity ratios for the simulated oxygen and methane systems are accurate and clustered together over its entire density range. Water tracer diffusivity ratios are also plotted in Figure 202 and are underestimated for two reasons. First, solvent and solute tracer diffusivities are identical in the TLSM calculation. Second, the experimental water data are always larger, thereby making the prediction ratios always smaller.
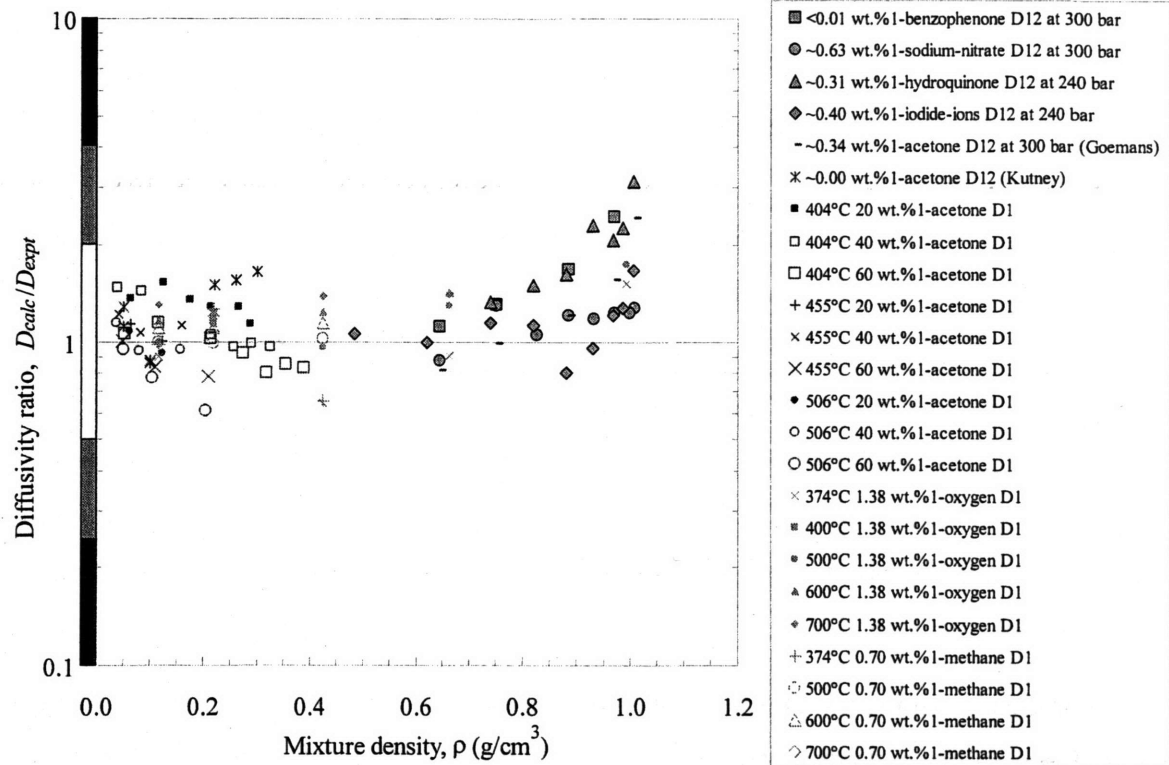
Figure 201. TLSM D_{12} and D_1 predictions using known-solute(1) & TLSM-regressed-water(2) Lennard-Jones values and mole-fraction-weighted σ_{12}, $\varepsilon_{12}^{TLSM} = \varepsilon_{12}$, & MW_{12}.
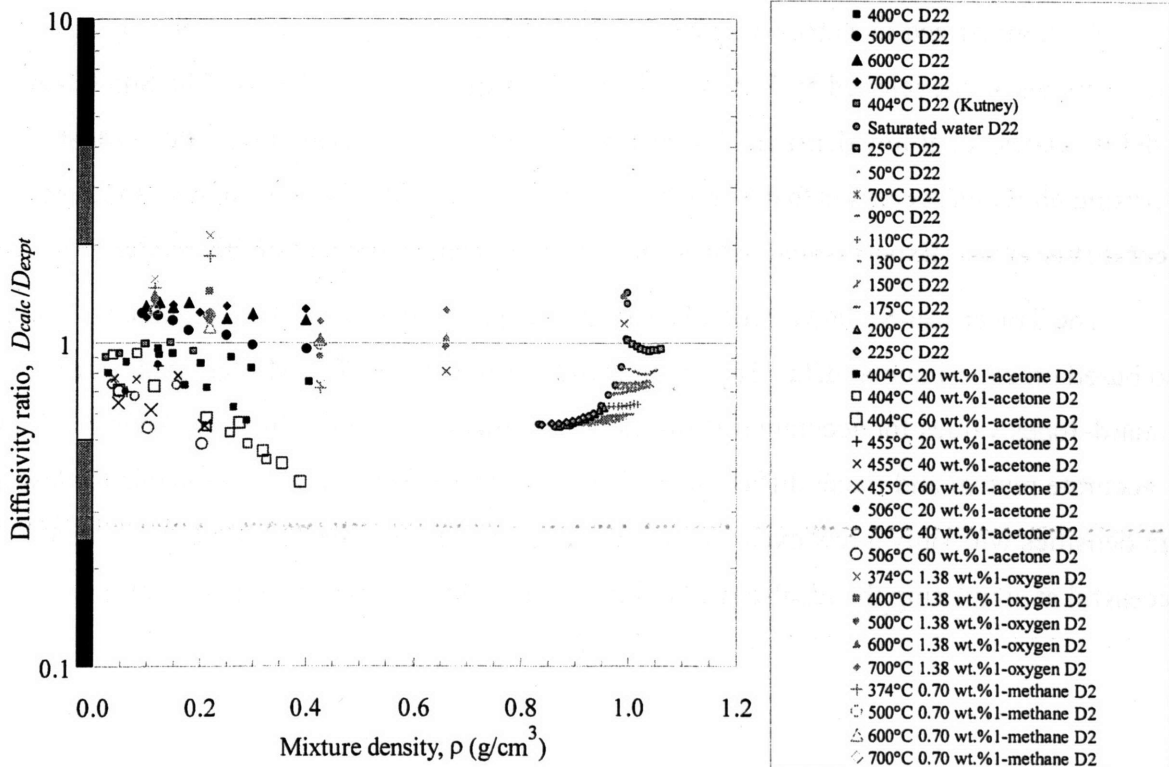
Figure 202. TLSM D_{22} and D_2 predictions using known-solute(1) & TLSM-regressed-water(2) LJ values and mole-fraction-weighted σ_{12}, $\varepsilon_{12}^{TLSM} = \varepsilon_{12}$, & MW_{12}.

All of these results indicate that the TLSM model using known-solute and TLSM-regressed-solvent Lennard-Jones values and Eqs. (145), (146), (202), (203), and (204) can reasonably predict self-, mutual, and tracer diffusivities over a large process regime. When these data are combined together (without the secondary solvent tracer diffusivities) in Figure 203, several conclusions can be drawn. First, low density predictions remain inside the acceptable zone with no excursions into the caution zone. They are scattered symmetrically about the diffusivity ratio of one, although low temperature (400°C) self-diffusivities are slightly underestimated, and the other self-diffusivities are overestimated. Second, high density predictions are scattered about the diffusivity ratio of one, but are bimodal. The underestimated predictions are primarily self-diffusivities, while the overestimated predictions are mainly mutual diffusivities. Nevertheless, the TLSM predictions are reasonable and are the best yet observed in this hard-sphere theory section.

For these reasons, the TLSM model with known-solute and TLSM-regressed-solvent Lennard-Jones values and calculated with Eqs. (145), (146), (202), (203), and (204) is rated: (mean low & high density diffusivity ratios: $1.0 \pm 0.4_{95\%}$ & $0.9 \pm 1.0_{95\%}$) $\boxed{A}\boxed{A}$

As summarized in Table 61 and Table 62 and Figure 204, the most promising hard-sphere models are developed by Sun and Chen (1985) and Liu *et al.* (1998). The Sun-Chen model is successful at low densities, but its high density predictions are inaccurate. Most surprising about its success is that Sun-Chen model is based entirely on computer-simulated tracer diffusivities. Experimental data are not used in the development of this model.

The Tracer Liu-Silva-Macedo (TLSM) model is also based on MD simulations, but it is also based on experimental data. The recommended version uses TLSM-regressed water Lennard-Jones values for accurate self-diffusivity predictions, while solutes use known values for accurate mutual and tracer diffusivities. The resulting predictions are reasonable for low and high densities with only a few excursions into the caution zone. The TLSM model is also successful at simulating the ideal-gas-like regime where kinetic-gas theories are valid.

Figure 203. TLSM D_{22}, D_{12}, and D_1 predictions using known-solute(1) & TLSM-regressed-water(2) LJ values and mole-fraction-weighted σ_{12}, $\varepsilon_{12}^{TLSM} = \varepsilon_{12}$, & MW_{12}.

The legend of the figure reads:

- 400°C D22
- 500°C D22
- 600°C D22
- 700°C D22
- 404°C D22 (Kutney)
- Saturated water D22
- 25°C D22
- 50°C D22
- 70°C D22
- 90°C D22
- 110°C D22
- 130°C D22
- 150°C D22
- 175°C D22
- 200°C D22
- 225°C D22
- <0.01 wt.%1-benzophenone D12 at 300 bar
- ~0.63 wt.%1-sodium-nitrate D12 at 300 bar
- ~0.31 wt.%1-hydroquinone D12 at 240 bar
- ~0.40 wt.%1-iodide-ions D12 at 240 bar
- ~0.34 wt.%1-acetone D12 at 300 bar (Goemans)
- ~0.00 wt.%1-acetone D12 (Kutney)
- 404°C 20 wt.%1-acetone D1
- 404°C 40 wt.%1-acetone D1
- 404°C 60 wt.%1-acetone D1
- 455°C 20 wt.%1-acetone D1
- 455°C 40 wt.%1-acetone D1
- 455°C 60 wt.%1-acetone D1
- 506°C 20 wt.%1-acetone D1
- 506°C 40 wt.%1-acetone D1
- 506°C 60 wt.%1-acetone D1
- 374°C 1.38 wt.%1-oxygen D1
- 400°C 1.38 wt.%1-oxygen D1
- 500°C 1.38 wt.%1-oxygen D1
- 600°C 1.38 wt.%1-oxygen D1
- 700°C 1.38 wt.%1-oxygen D1
- 374°C 0.70 wt.%1-methane D1
- 500°C 0.70 wt.%1-methane D1
- 600°C 0.70 wt.%1-methane D1
- 700°C 0.70 wt.%1-methane D1

Table 61. Low and high density performance rankings for the hydrodynamic-, kinetic-, and hard-sphere-based diffusivity models evaluated in this analysis

Model	Section	Density Low	High
Hydrodynamic theory of diffusion	II.5.2.1		
Stokes-Einstein equation with the no-slip condition	II.5.2.1.1	F	A
Stokes-Einstein equation with the slip condition	II.5.2.1.1	F	A
Wilke-Chang equation	II.5.2.1.2	F	A
Reddy-Doraiswamy equation (original form)	II.5.2.1.3	F	A
(>0.3 g/cm^3 with NBP-volumes)	II.5.2.1.3	C	A
Kinetic theory of diffusion	II.5.2.2		
Chapman-Enskog equation	II.5.2.2.1	C	F
CE equation with the Enskog-Thorne correction	II.5.2.2.1.1	C	F
Weighted CE equation with the ET correction	II.5.2.2.1.1	A	F
CE equation with the Takahashi correction	II.5.2.2.1.2	C	F
CE equation with the Dawson HS correction	II.5.2.2.1.3	A	F
CE equation with the Erpenbeck-Wood HS correction	II.5.2.2.1.4	F	F
Polar Chapman-Enskog equation	II.5.2.2.2	C	F
Polar CE equation with the Enskog-Thorne correction	II.5.2.2.2	C	F
Polar, weighted CE equation with the ET correction	II.5.2.2.2	A	C
Polar CE equation with the Takahashi correction	II.5.2.2.2	C	F
Polar CE equation with the Dawson HS correction	II.5.2.2.2	A	F
Wilke-Lee equation	II.5.2.2.3	C	F
WL equation with the Enskog-Thorne correction	II.5.2.2.3	C	F
WL equation with the Takahashi correction	II.5.2.2.3	A	F
WL equation with the Dawson HS correction	II.5.2.2.3	C	F
Mathur-Thodos equations	II.5.2.2.4	A	A
Hard-Sphere Theory of Diffusion	II.5.2.3		
Sun-Chen equation	II.5.2.3.1	A	C
Eaton-Akgerman equation	II.5.2.3.2	F	F
He equation	II.5.2.3.3	F	F
He-Yu equation	II.5.2.3.4	F	F
Tracer Liu-Silva-Macedo equation (known LJ values)	II.5.2.3.5	C	C
Tracer Liu-Silva-Macedo equation (regressed LJ values)	II.5.2.3.5	A	C
Tracer Liu-Silva-Macedo equation (known(1)-regressed(2))	II.5.2.3.5	A	A

Table 62. Low and high density mean diffusivity ratios and 95%-confidence-interval uncertainties for the hydrodynamic-, kinetic-, and hard-sphere-based diffusivity models evaluated in this analysis

Model	Low			High
		Density		
Hydrodynamic theory of diffusion				
Stokes-Einstein equation with the no-slip condition	0.5 ± 0.5	F	A	0.9 ± 0.3
Stokes-Einstein equation with the slip condition	0.7 ± 0.8	F	A	1.3 ± 0.4
Wilke-Chang equation	0.5 ± 0.5	F	A	1.2 ± 0.4
Reddy-Doraiswamy equation (original form)	0.6 ± 0.6	F	A	1.0 ± 0.4
(>0.3 g/cm^3 with NBP-volumes)	0.2 ± 0.4	C	A	1.0 ± 0.2
Kinetic theory of diffusion				
Chapman-Enskog equation	2 ± 2	C	F	$>10 \pm >10$
CE equation with the Enskog-Thorne correction	1.0 ± 0.7	C	F	2 ± 3
Weighted CE equation with the ET correction	1.2 ± 0.5	A	F	2 ± 3
CE equation with the Takahashi correction	1 ± 1	C	F	$>10 \pm >10$
CE equation with the Dawson HS correction	1.2 ± 0.6	A	F	0.4 ± 0.5
CE equation with the Erpenbeck-Wood HS correction	2 ± 2	F	F	$>10 \pm >10$
Polar Chapman-Enskog equation	2 ± 2	C	F	$>10 \pm >10$
Polar CE equation with the Enskog-Thorne correction	0.9 ± 0.6	C	F	2 ± 2
Polar, weighted CE equation with the ET correction	1.1 ± 0.5	A	C	2 ± 2
Polar CE equation with the Takahashi correction	1.4 ± 0.9	C	F	$>10 \pm >10$
Polar CE equation with the Dawson HS correction	1.1 ± 0.6	A	F	0.3 ± 0.6
Wilke-Lee equation	1 ± 1	C	F	$>10 \pm >10$
WL equation with the Enskog-Thorne correction	1.0 ± 0.7	C	F	2 ± 3
WL equation with the Takahashi correction	1.0 ± 0.6	A	F	$>10 \pm >10$
WL equation with the Dawson HS correction	0.8 ± 0.5	C	F	0.3 ± 0.4
Mathur-Thodos equations	1.0 ± 0.5	A	A	0.9 ± 1.0
Hard-Sphere Theory of Diffusion				
Sun-Chen equation	0.9 ± 0.5	A	C	1 ± 2
Eaton-Akgerman equation	0.4 ± 0.5	F	F	2 ± 3
He equation	0.3 ± 0.2	F	F	$<0.1 \pm <0.1$
He-Yu equation	0.7 ± 0.7	F	F	2 ± 3
Tracer Liu-Silva-Macedo equation (known LJ values)	1.1 ± 0.6	C	C	1.4 ± 2.0
Tracer Liu-Silva-Macedo equation (regressed LJ values)	1.1 ± 0.5	A	C	0.8 ± 2.0
Tracer Liu-Silva-Macedo equation (known(1)-regressed(2))	1.1 ± 0.4	A	A	0.9 ± 0.9
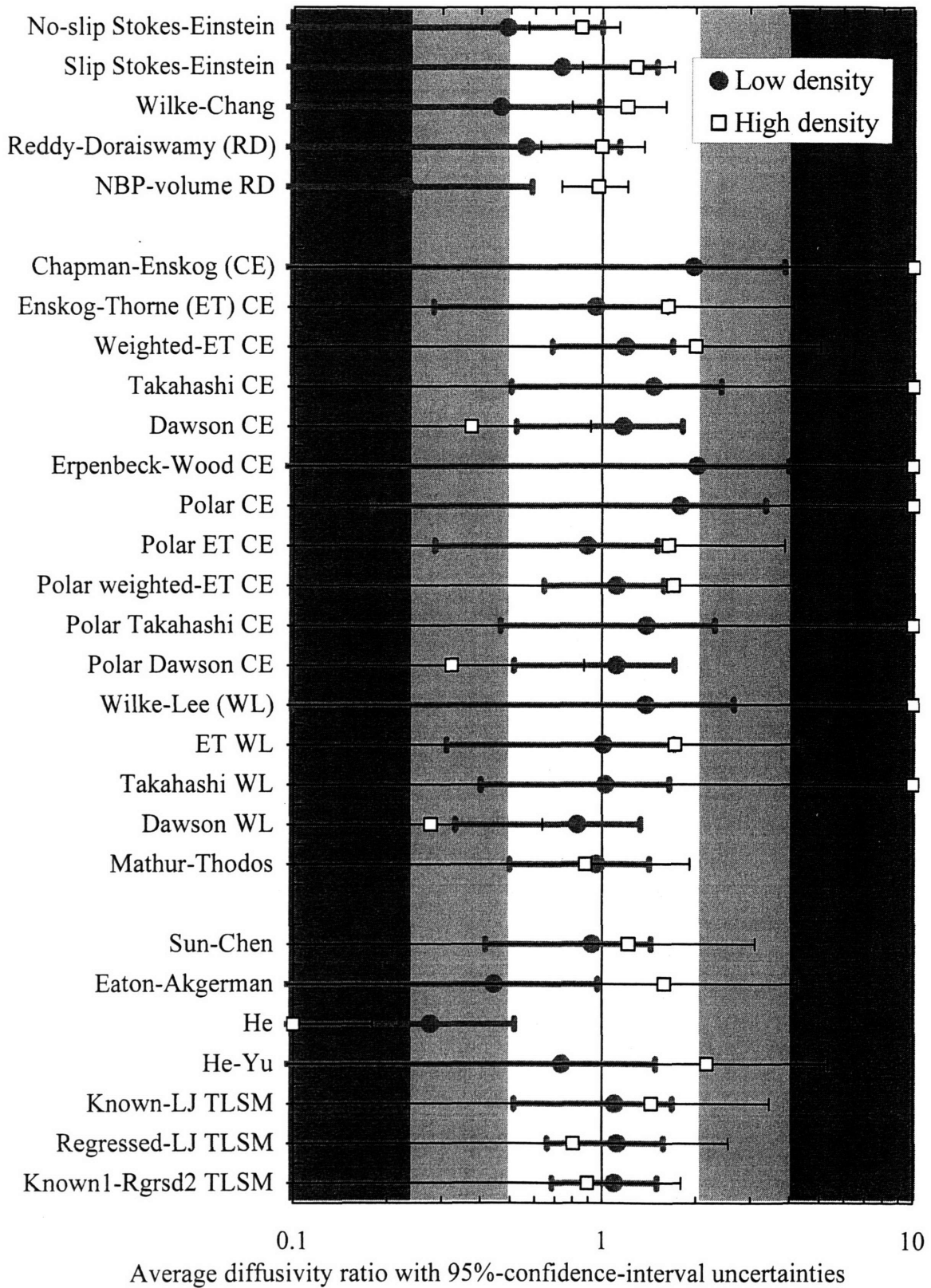
Figure 204. Low and high density mean diffusivity ratios and uncertainties for the hydrodynamic-, kinetic-, and hard-sphere-based diffusivity models evaluated in this analysis.

II.5.3 Discussion and Error Analysis

With the initial analysis of each model complete and the results summarized concisely in Table 61 and Table 62, the focus can now shift to summarizing the recommendations of the analysis before an error analysis is performed. The hydrodynamic-theory analysis reveals that low density (<0.5 g/cm^3) diffusivity predictions are inaccurate. Dense predictions are reasonable for all of the models evaluated. The most accurate results were obtained using the Reddy-Doraiswamy equation when normal-boiling-point volumes are used instead of the default approach (which uses volumes at the condition of interest).

$$D_{12}^{RD}[\text{cm}^2/\text{s}] = \Pi \frac{T[\text{K}]\sqrt{M_2[\text{g/mole}]}}{\eta_2[\text{cP}]V_1^{NBP1/3}[\text{cm}^3/\text{mole}]V_2^{NBP1/3}[\text{cm}^3/\text{mole}]}$$

(102)

$$V_2^{NBP}/V_1^{NBP} \leq 1.5 \quad \Pi = 10^{-7}$$
$$V_2^{NBP}/V_1^{NBP} > 1.5 \quad \Pi = 8.5 \times 10^{-8}$$

As seen is Table 61, this model is recommended for densities greater than 0.3 g/cm^3. Predictions at lower densities are inaccurate as seen in Figure 146. Another noteworthy feature is the lack of scattered data for high density predictions, especially for the water self-diffusivities. The recommended form of the Reddy-Doraiswamy equation is independent of concentration so predictions are insensitive to the solute concentration and cannot be distinguished (Reddy and Doraiswamy, 1967). Even though the Reddy-Doraiswamy results are accurate over a wide density range, only a few of these data points are at supercritical conditions. Since this analysis is focused on identifying models that can accurately predict diffusivities for sub- and supercritical water systems and this model has poor prediction capabilities for a majority of the supercritical data, the Reddy-Doraiswamy model cannot be recommended for subcritical-water diffusivity modeling.
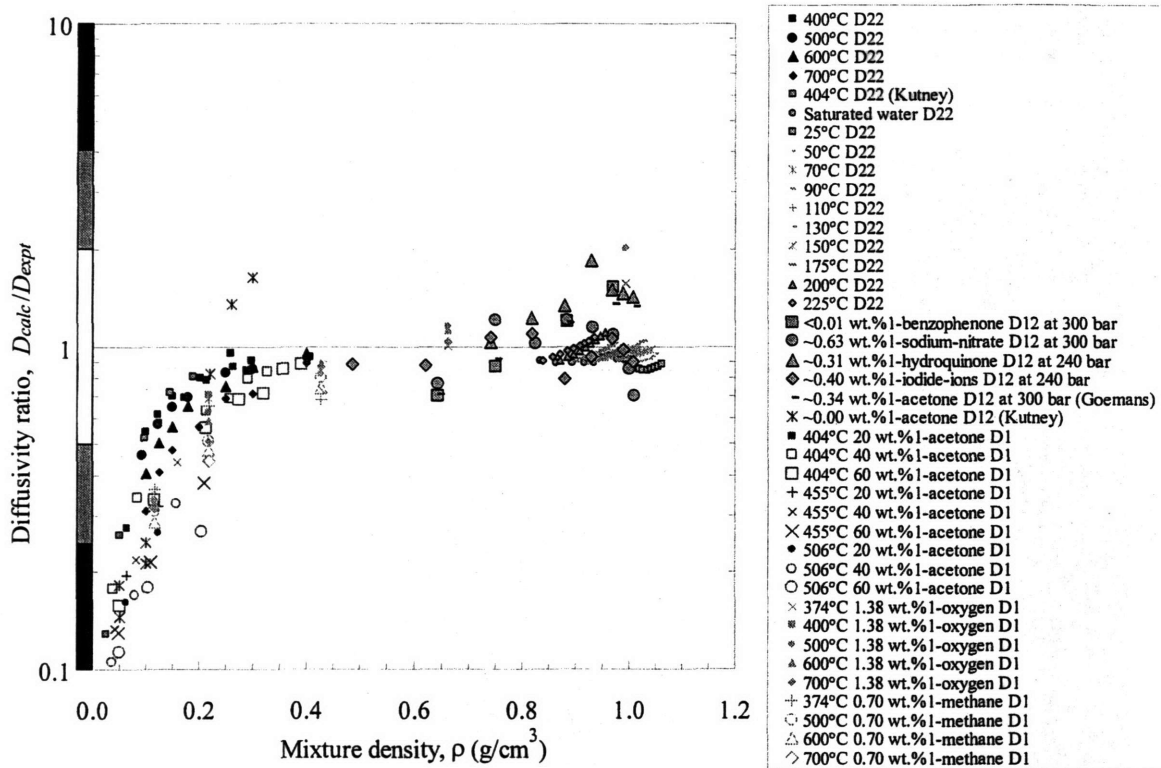
Figure 146. Reddy-Doraiswamy D_{22}, D_{12}, and D_1 predictions using pure water viscosities and constant solute and solvent normal-boiling-point volumes.

The Mathur-Thodos self-diffusivity model is rated the best overall kinetic-theory model due to its accuracy along the entire density range (Mathur and Thodos, 1965)

Normal pressures:
$$D_{11}^{MT}[cm^2/s] = \frac{44 \times 10^{-5} P_{c1}^{2/3}[atm]T_{c1}^{5/6}T_{r1}^{1.716}}{\pi\sqrt{M_1}} \text{ for } T_{r1} \geq 1.5$$

$$D_{11}^{MT}[cm^2/s] = \frac{2.427 \times 10^{-5} P_{c1}^{2/3}[atm]T_{c1}^{5/6}\left(7.907T_{r1} - 1.66\right)^{1.338}}{\pi\sqrt{M_1}} \text{ for } T_{r1} < 1.5$$

(132)

Elevated pressures:
$$D_{11}^{MT}[cm^2/s] = \frac{10.7 \times 10^{-5} T_{c1}^{5/6}T_{r1}}{P_{c1}^{1/3}[atm]\rho_{r1}\sqrt{M_1}} \text{ for } 0.15 \leq \rho_{r1} \leq 1.5$$

(133)

Liquid state:
$$D_{11}^{MT}[cm^2/s] = \frac{3.67 \times 10^{-5} T_{c1}^{5/6}T_{r1}^{3.5}}{P_{c1}^{1/3}[atm]P_{r1}^{0.1}\sqrt{M_1}} \text{ for } \rho_{r1} > 2$$

(134)

When extended to mixtures using mole-fraction-weighted terms instead of solute terms, the predictions fall into the acceptable zone as seen in Figure 184. The scatter is larger than the Reddy-Doraiswamy scatter, but low density predictions are reasonably accurate. Needing only

critical constants, molecular weights, and densities, the Mathur-Thodos approach is simple to use and is accurate for sub- and supercritical-water diffusivity predictions. On the other hand, this multi-equation approach will have discontinuities when switching between the different equations and will lead to prediction discrepancies.

The TLSM model is the other model that performed admirably. As indicated in Table 61, the best results were obtained when known Lennard-Jones well-depths and diameters were used for the solute and TLSM-regressed Lennard-Jones values were used for the solvent water. The model is extended to concentrated systems by employing simple mole-fraction-weighted terms that are written below

$$D_{12}^{TLSM-HS} = \frac{669.1 M_2}{\rho_2 N_A \sigma_{TLSM}^2} \sqrt{\frac{RT}{M_{12}}} \cdot$$
$$\exp\left(-\frac{0.75 \rho_2 N_A \sigma_2^3 / M_2}{1.2588 - \rho_2 N_A \sigma_2^3 / M_2} - 0.27862 \frac{\varepsilon_{12}^{TLSM}}{kT} \right)$$

(145)

$$\sigma_{TLSM}^2 = \frac{2^{1/3} \sigma_{12}^2}{\left(1 + 1.2 \sqrt{\frac{kT}{\varepsilon_{12}^{TLSM}}} \right)^{1/3}}$$

(146)

$$\frac{\varepsilon_{12}^{TLSM}}{k} = \frac{\varepsilon_1^{x_1} \varepsilon_2^{x_2}}{k}$$

(202)

$$\sigma_{12} = x_1 \sigma_1 + x_2 \sigma_2$$

(203)

$$M_{12} = x_1 M_1 + x_2 M_2$$

(204)

Results with these formulae are shown in Figure 203 and are nearly identical to the Mathur-Thodos results that are shown in Figure 184. The agreement is remarkable given that the Mathur-Thodos equation set is based upon dimensional analysis. Likewise, average absolute deviations (AAD) at any temperature show a similar trend for the Mathur-Thodos and TLSM models as seen in the second section of Table 63. The second section also shows that the modified TLSM expression has smaller uncertainties than the Mathur-Thodos equation set and the TLSM model when known Lennard-Jones values or regressed Lennard-Jones values are used for both species. The third section of Table 63 contains AAD statistics for predictions above 400°C, while the fourth section contains statistics for only supercritical predictions. Statistics

397
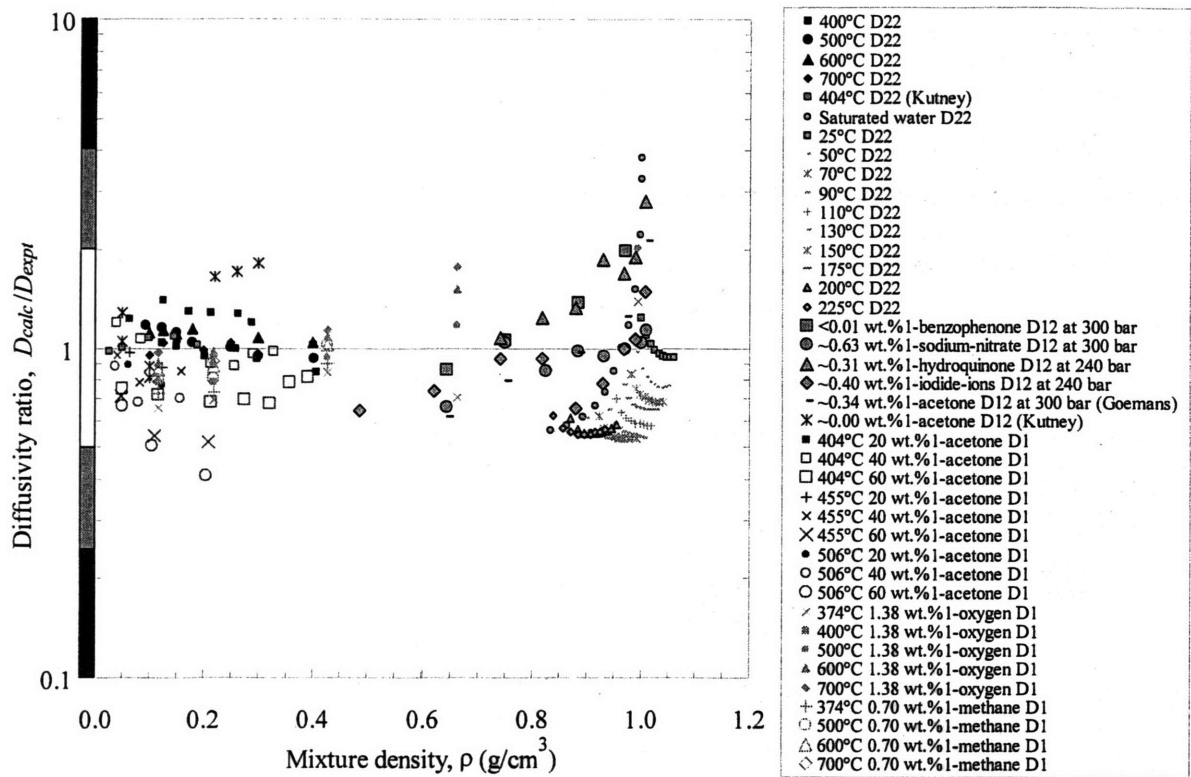
Figure 184. Mathur-Thodos D_{22}, D_{12}, and D_1 predictions using low and high density formulae.
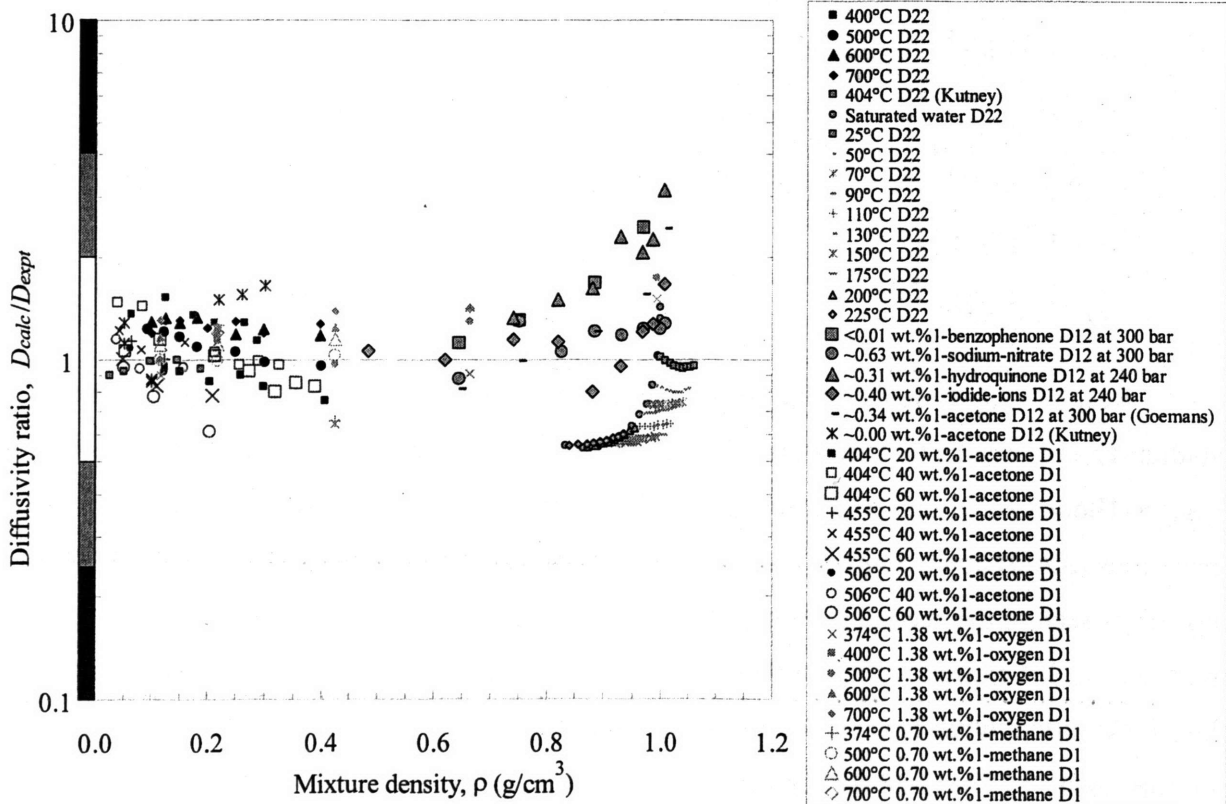
Figure 203. TLSM D_{22}, D_{12}, and D_1 predictions using known-solute(1) & TLSM-regressed-water(2) LJ values and mole-fraction-weighted σ_{12}, $\varepsilon_{12}^{TLSM} = \varepsilon_{12}$, & MW_{12}.

Table 63. Low and high density mean diffusivity ratios and corresponding average absolute deviations along with 95%-confidence-interval uncertainties for the Mathur-Thodos and Tracer Liu-Silva-Macedo diffusivity models evaluated in this analysis

Model	Overall density Low & High	Density Low			High

$$\text{Mean diffusivity ratios} = \frac{\sum_i^n \left(D_{calc}/D_{expt} \right)_i}{n}$$

Model	Low & High	Low			High
Mathur-Thodos equations	0.9 ± 0.8	1.0 ± 0.5	A	A	0.9 ± 1.0
TLSM equation (known LJ values)	1.3 ± 1.6	1.1 ± 0.6	C	C	1.4 ± 2.0
TLSM equation (regressed LJ values)	0.9 ± 1.4	1.1 ± 0.5	A	C	0.8 ± 2.0
TLSM equation (known(1)-regressed(2))	1.0 ± 0.8	1.1 ± 0.4	A	A	0.9 ± 0.9

$$\text{Average absolute deviations} = \frac{\sum_i^n \left| \left(D_{calc} - D_{expt} \right)/D_{expt} \right|_i}{n}$$

Model	Low & High	Low			High
Mathur-Thodos equations	$30\% \pm 62\%$	$17\% \pm 32\%$	A	A	$39\% \pm 72\%$
TLSM equation (known LJ values)	$48\% \pm 145\%$	$24\% \pm 37\%$	C	C	$64\% \pm 179\%$
TLSM equation (regressed LJ values)	$32\% \pm 122\%$	$20\% \pm 32\%$	A	C	$42\% \pm 159\%$
TLSM equation (known(1)-regressed(2))	$29\% \pm 50\%$	$18\% \pm 27\%$	A	A	$37\% \pm 56\%$

For $T \geq 400°C$ data, average absolute deviations

Model	Low & High	Low			High
Mathur-Thodos equations	$18\% \pm 39\%$	$16\% \pm 32\%$	A	A	$62\% \pm 72\%$
TLSM equation (known LJ values)	$23\% \pm 36\%$	$23\% \pm 36\%$	C	C	$7\% \pm 9\%$
TLSM equation (regressed LJ values)	$19\% \pm 25\%$	$19\% \pm 25\%$	A	C	No data
TLSM equation (known(1)-regressed(2))	$19\% \pm 30\%$	$18\% \pm 28\%$	A	A	$47\% \pm 38\%$

For supercritical data, average absolute deviations

Model	Low & High	Low			High
Mathur-Thodos equations	$18\% \pm 41\%$	$15\% \pm 33\%$	A	A	$53\% \pm 63\%$
TLSM equation (known LJ values)	$23\% \pm 37\%$	$24\% \pm 38\%$	C	C	$8\% \pm 13\%$
TLSM equation (regressed LJ values)	$18\% \pm 22\%$	$18\% \pm 22\%$	A	C	No data
TLSM equation (known(1)-regressed(2))	$20\% \pm 31\%$	$18\% \pm 27\%$	A	A	$41\% \pm 43\%$

independent of density are contained in the second column of Table 63 and are helpful when comparing overall model performance.

At high densities, the Mathur-Thodos model has several predictions entering the caution zone and according to Table 63, has larger variability than the TLSM model. For densities greater than 1 g/cm^3, mutual-diffusivity ratios for both models are likely to increase exponentially and become unreasonable, but this operating regime is unlikely for typical supercritical-water applications. Diffusivity ratios for the simulated oxygen and methane datasets are nearly identical in both models, but the Mathur-Thodos scatter is less. Mathur-Thodos self-diffusivities are slightly overestimated at low densities and are underestimated at high densities. At high densities, the self-diffusivity predictions of both models cannot match the precision observed with the Reddy-Doraiswamy model, but low temperature self-diffusivities are slightly more accurate. One key modified-TLSM-model benefit is the superior accuracy of low density tracer diffusivities. There are zero excursions into the caution zone in the low density region where most supercritical-water systems operate, and the modified-TLSM AAD is 17% ± 27%$_{95\%}$ versus 19% ± 26%$_{95\%}$ for the Mathur-Thodos. Based on this analysis and combined-density statistics in Table 63 (column two), the modified TLSM model is the recommended approach for predicting diffusivities of sub- and supercritical water systems. The Mathur-Thodos approach comes in a close second, but is recommended as a backup model that can be used to verify TLSM results or in place of TLSM results if solute Lennard-Jones values are not available.

A final issue to be discussed involves the accuracy of the experimental data that are used in the analysis figures. As mentioned earlier, plotted diffusivity ratios may be skewed by experimental-data inaccuracies in every figure, but these errors have been neglected during the preliminary analysis since they do not change from one plot to another. Now that the Mathur-Thodos and the modified TLSM approaches have been recognized as the leading candidates for sub- and supercritical water systems, an analysis of errors is needed.

Experimental uncertainities can be incorporated into the analysis by merely adding it to the analysis plots. Uncertainty errors for the experimental data used in this analysis are provided by most authors and can be easily incorporated into the analysis plots. Individual experimental

uncertainties with 95% confidence intervals have been added to the Mathur-Thodos and modified TLSM plots in Figure 205 and Figure 206, respectively.

The uncertainty clouds generated by the clustered data and their respective experimental errors remain, for the most part, in the acceptable prediction-ratio range. At low densities, the Mathur-Thodos cloud in Figure 205 occupies the caution zone because the predictions are slightly less accurate and closer to the center-zone boundary. The modified TLSM cloud is slightly smaller in Figure 206, because the diffusivity ratios are scattered less and the uncertainty errors remain the same. Since nearly all of experimental error remain in the acceptable range, previous model recommendations remain unchanged.

Another potential source of error could be the property terms that are used in the prediction models. Although property constants and variables such as density are assumed to be well-known, all will have uncertainties. These errors can be ignored in this analysis for several reasons. First, the current analysis attempts to mimic the calculation approaches that are generally used. Parameters used in most diffusivity calculations are not usually subjected to an error analysis as long as their source is credible and the values are reasonable. The values used in this analysis fall within this classification. Furthermore, the calculated errors are small compared to the experimental errors, and thus, they do not play a major role in this analysis.
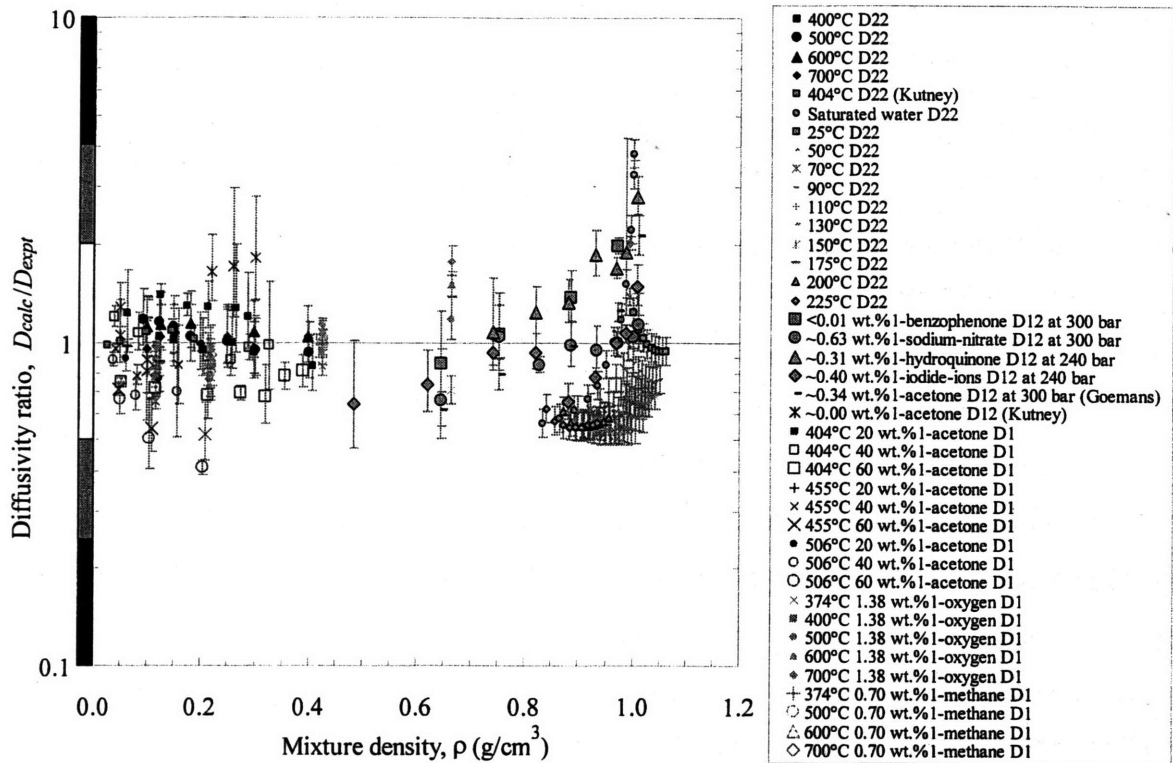
Figure 205. Mathur-Thodos D_{22}, D_{12}, and D_1 predictions with the experimental uncertainties shown (95% confidence intervals).
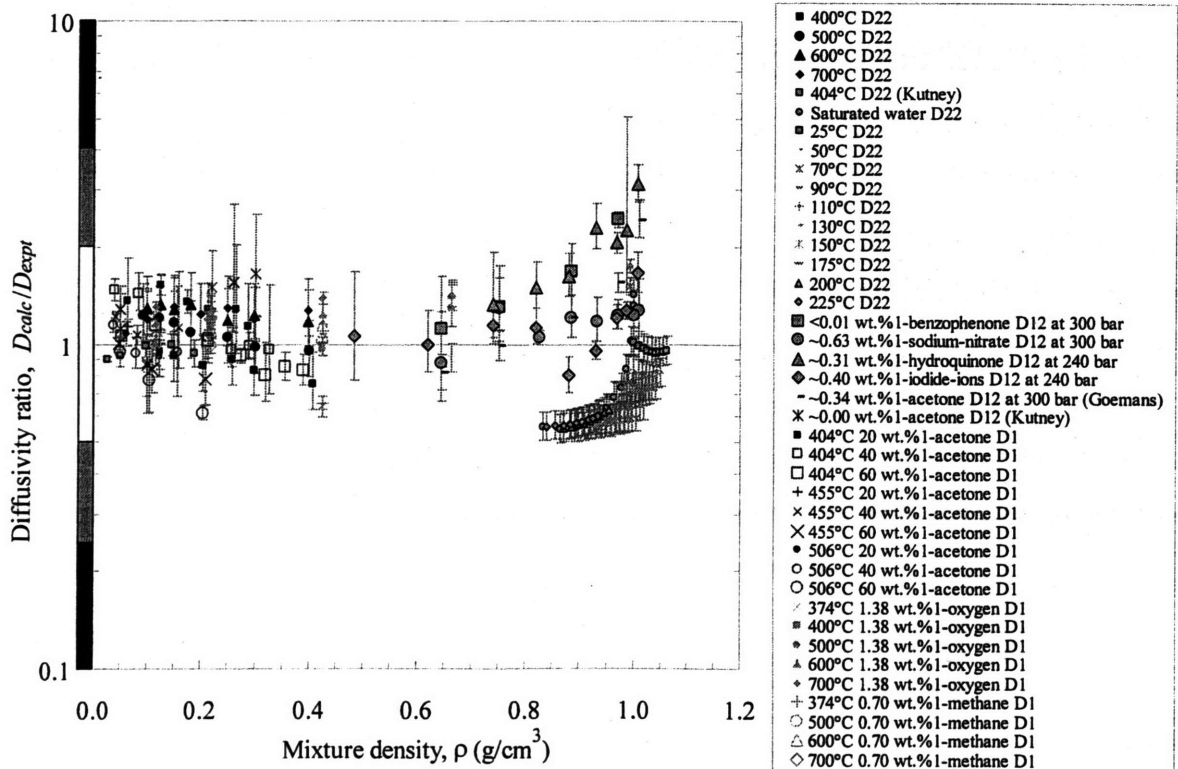
Figure 206. TLSM D_{22}, D_{12}, and D_1 predictions with the experimental uncertainties shown (95% confidence intervals).

II.5.4 Conclusions

Based on the analysis performed with a wide range of experimental and simulated data, two models are capable of providing reliable diffusivity predictions. The modified TLSM model is the primary recommended model for sub- and supercritical water predictions. The governing equations are Eqs. (145), (146), (202), (203), and (204) and known Lennard-Jones values should be used for the solute species. Lennard-Jones values for the solvent water are fit to experimental self-diffusivities in order to improve the model accuracy and are listed in Table 60. Compared to the other models analyzed, it is accurate at low densities where most supercritical-system modeling will occur. High density predictions are bimodal with self-diffusivities underestimated, while mutual diffusivities are overestimated. The modified TLSM model is not recommended for densities above one.

The second model recommended is developed by Mathur and Thodos (1965). Defined by Eqs. (132), (133), and (134), the Mathur-Thodos approach can be extended to mixtures using linear mole-fraction-weighted terms for the required critical constants and reduced variables. Lennard-Jones constants are not needed. The Mathur-Thodos approach is slightly more accurate than the modified-TLSM model at low densities, but is less accurate at high densities and has a larger overall uncertainty compared to the modified-TLSM model as seen in Table 63. The Mathur-Thodos model is also not recommended for densities above one. Both models are capable of providing reasonably accurate diffusivities as demonstrated for the systems in this analysis. When doubts are raised about predictions from either of these models, it is recommended to calculate diffusivities with the other model in order to validate the predictions and minimize suspicion.

II.5.5 References

Atkins, P.W. (1990) *Physical Chemistry*, W.H. Freeman and Co., 4th ed., New York, NY.

Ben-Amotz, D. and Herschbach, D.R. (1990) "Estimation of effective diameters for molecular fluids." *J. Phys. Chem.*, **94 (3)**, 1038–1047.

Braker, W. and Mossman, A.L. (1980) *Matheson Gas Data Book*, 6th ed., Lyndurst, NJ.

Brokaw, R.S. (1969) "Predicting transport properties of dilute gases." *Ind. Eng. Chem. Proc. Des. Dev.*, **8 (2)**, 240–253.

Chung, H.S. (1966) "On the Macedo—Litovitz hybrid equation for liquid viscosity." *J. Chem. Phys.*, **44 (4)**, 1362–1364.

Dawson, R., Khoury, F., and Kobayashi, R. (1970) "Self-diffusion measurements in methane by pulsed nuclear magnetic resonance." *AIChE J.*, **16 (5)**, 725–729.

Douglass, D.C., McCall, D.W., and Anderson, E.W. (1961) "Self-diffusion of nearly spherical molecules. neopentane and tetramethyl silane." *J. Chem. Phys.*, **34 (1)**, 152–156.

Eaton, A.P. and Akgerman, A. (1997) "Infinite-dilution diffusion coefficients in supercritical fluids." *AIChE J.*, **36**, 923–931.

Goemans, M.G.E. (1996) "Molecular diffusion and mass transfer in subcritical and supercritical water." *University of Texas at Austin*, Doctoral dissertation, Austin, TX.

He, C.H. (1997) "Prediction of binary diffusion coefficient of solutes in supercritical solvents." *AIChE J.*, **43 (11)**, 2944–2947.

He, C.H. and Yu, Y.S. (1998) "New equation for infinite-dilution diffusion coefficients in supercritical and high-temperature liquid solvents." *Ind. Eng. Chem. Res.*, **37**, 3793–3798.

Knovel (2004) Knovel Corporation database, Norwich, NY.

Lamb, W.J., Hoffman, G.A., and Jonas, J. (1981) "Self-diffusion in compressed supercritical water." *J. Chem. Phys.*, **74 (12)**, 6875–6880.

Lienhard, J.H. and Lienhard, J.H. (2002) *A Heat Transfer Textbook*, 3rd ed., Phlogiston Press, Cambridge, MA.

Liu, H. and Macedo, E.A. (1995) "Accurate correlations for the self-diffusion coefficients of CO_2, CH_4, C_2H_4, H_2O, and D_2O over wide ranges of temperature and pressure." *J. Supercritical Fluids*, **8**, 310–317.

Liu, H., Silva, C.M., and Macedo, E.A. (1998) "Unified approach to the self-diffusion coefficients of dense fluids over wide ranges of temperature and pressure-hard-sphere, square-well, Lennard-Jones and real substances." *Chem. Eng. Sci.*, **53 (13)**, 2403–2422.

Mathur, G.P. and Thodos, G. (1965) "The self-diffusivity of substances in the gaseous and liquid state." *AIChE J.*, **11 (4)**, 613–616.

NIST (1996) NIST standard reference database 10–steam tables, Boulder, CO.

NIST (2004) NIST Chemistry WebBook, Gaithersburg, MD.

Ohmori, T. and Kimura, Y. (2003) "Translational diffusion of hydrophobic solutes in supercritical water studied by molecular dynamics simulations." *J. Chem. Phys.*, **119 (14)**, 7328–7334.

Perry, R.H., Green, D.W. and Maloney, J.O. (1984) *Perry's chemical engineering handbook*, McGraw-Hill, 6th ed., New York, NY.

Poling, B.E., Prausnitz, J.M., and O'Connell, J.P. (2001) " *The Properties of Gases and Liquids*,McGraw-Hill, 5th ed., New York, NY.

Reddy, K.A. and Doraiswamy, L.K. (1967) "Estimating liquid diffusivity." *Ind. Eng. Chem. Fundam.*, **6 (1)**, 77–79.

Rogers, P.S.Z. and Pitzer, K.S. (1982) "Volumetric properties of aqueous sodium chloride solutions." *J. Phys. Chem. Ref. Data*, **11 (1)**, 15–81.

Sato, H., Watanabe, K., Levelt Sengers, J.M.H., Gallagher, J.S., Hill, P.G., Straub, J. and Wagner, W. (1991) "Sixteen thousand evaluated experimental thermodynamic property data for water and steam." *J. Phy. Chem. Ref. Data*, **20**, 1023–1044.

Silva, C.M., Liu, H., and Macedo, E.A. (1998) "Models for self-diffusion coefficients of dense fluids, including hydrogen-bonding substances." *Chem. Eng. Sci.*, **53 (13)**, 2423–2429.

Sun, C.K.J. and Chen, S.H. (1985) "Tracer diffusion of aromatic hydrocarbons in *n*-hexane up to the supercritical region." *Chem. Eng. Sci.*, **40 (12)**, 2217–2224.

Takahashi, S. (1974) "Preparation of a generalized chart for the diffusion coefficients of gases at high pressures." *J. Chem. Eng. Jpn.*, **7 (6)**, 417–420.

Walas, S.M. (1985) *Phase Equilibria in Chemical Engineering*, Butterworth-Heinemann, Stoneham, MA.

Wilhelm, E. (1973) "On the temperature dependence of the effective hard sphere diameter." *J. Chem. Phys.*, **58 (9)**, 3558–3560.

Wilke, C.R. and Lee, C.Y. (1955) "Estimation of diffusion coefficients for gases and vapors." *Ind. Eng. Chem.*, **47 (6)**, 1253–1257.

3. Conclusions and Recommendations

This thesis focuses on the development of accurate thermodynamic and diffusivity transport-property models for use at typical SCWO operating conditions, namely $25°C \leq T \leq 650°C$ and 1 bar $\leq P \leq 300$ bar, along with the measurement of molecular diffusivity using a novel high pressure, high temperature flow system.

Thermodynamic-property research:

A hard-sphere, volume-translated van der Waals equation of state for pure components

A hard-sphere, volume-translated van der Waals equation of state has been developed for use in SCWO *PVT* modeling and is comprised of the semi-theoretical Carnahan-Starling expression that properly represents the molecular interactions between hard spheres and a simple van der Waals attraction term. It also utilizes volume translation to further improve high density predictions. The translation constant is determined by a fit to liquid and vapor coexistence density data, while the Carnahan-Starling and van der Waals parameters are determined from widely available critical point data. For each pure component i, the critical temperature T_{ci} and pressure P_{ci} are required for determining a_{ci} and b_i. The volume translation requires the experimental critical volume V_{ci} and a parameter t_i which is correlated with the liquid or vapor–liquid coexistence density. Two more parameters (α_{Ai} and α_{Bi}) are used to provide temperature dependence and are fit to coexistence vapor-pressure data.

The analysis indicates that the new hard-sphere volume-translated equation of state (HSVTvdW EOS) can be used for accurate predictions of densities and thermodynamic properties over a wide range of temperatures and pressures for pure materials such as carbon dioxide, methane and water. Ammonia, ethylene, nitrogen and oxygen have also been accurately modeled with the HSVTvdW EOS. Densities and residual properties are predicted in a thermodynamically consistent manner with average errors of 5% and 7%, respectively, and within 13% and 32%, respectively, over temperatures and pressures ranging from ambient to 500°C and 400 bar. Pure component liquid-density HSVTvdW EOS predictions have been shown to be more accurate than other EOSs currently used in SCWO thermodynamic modeling, along with other water properties including enthalpy and entropy.

A hard-sphere, volume-translated van der Waals equation of state for mixtures

Another important feature of a successful equation of state is its ability to simulate thermodynamic properties of mixtures, and for supercritical-water systems, these mixtures would most likely contain low concentrations of gases and hydrocarbons. The HSVTvdW EOS has been extended to model mixtures by using a theoretically correct mixture form for hard-sphere interactions. Simple mixing and combining rules and a simple binary parameter have been employed.

Binary phase diagrams for several mixtures have been calculated using the HSVTvdW EOS and confirm that the HSVTvdW EOS can be used for mixture modeling with sufficient accuracy. While the HSVTvdW EOS has not been thoroughly tested with a wide variety of mixtures, the limited results indicate that this EOS will be suitable for modeling SCWO properties and process streams which typically have more than 85% water content. Although simple mixing and combining rules have been employed, there are no significant obstacles to using more complex rules in order to further increase the accuracy of the HSVTvdW EOS.

Since the HSVTvdW EOS has been originally formulated for more accurate density predictions, a complete analysis including density comparisons of the mixture phases should be completed. As already stated, an investigation of additional mixtures relevant to SCWO process modeling should be also performed. Those systems studied should include ones that are well characterized such as aqueous mixtures of:

simple feed waste, *e.g.*, methanol, ethanol, ammonia,

oxidant, *e.g.*, oxygen,

simple products, *e.g.*, nitrogen.

Once more systems are studied and compared and the performance of the HSVTvdW EOS is completely analyzed, it can then be determined if the HSVTvdW EOS is a worthwhile addition to a SCWO process modeler's simulation toolbox.

The behavior of the "Zeno" ($Z = PV/RT = 1$) line has been examined in a collaborative project in order to investigate this recently rediscovered empirical regularity of fluids and to determine if such a regularity can be utilized to improve EOSs and their predictions. For a wide range of pure fluids, this contour of unit compressibility factor in the temperature-density plane has been empirically observed to be nearly linear (and arrow-like, thus "Zeno") from the Boyle temperature of the low density vapor to near the triple point in the liquid region. Although quantitative agreement between Zeno EOS predictions and experimental data is not exact, the general trends suggest that these EOS models adequately capture the dynamic balance that exists between repulsive and attractive forces along the Zeno line. Accurate Zeno-line predictions indicate EOS robustness over a larger domain of PVT space. Molecular simulations of Zeno behavior using SPC, SPC/E, and Lennard-Jones models for pure water match experimental behavior over a wide range of density, thereby confirming that these models can make water property predictions as accurate as pure component EOS predictions.

The generic linearity of the $Z = 1$ contour in the T-ρ plane provides a quantitative criterion to evaluate and refine both macroscopic and molecular equations of state. By using critical-point scaling, species-dependent $Z = 1$ data can be partially generalized in a Corresponding-States framework and can be used to fundamentally improve cubic equations of state. The predictions of the Peng-Robinson EOS and other cubic EOSs are reasonably close to the experimental Zeno behavior with the regressed parameter, α, which captures attractive interactions and is normally fit to vapor-liquid equilibrium data well outside the Zeno region. Modified PR EOSs with alternative α parameters show improvements over the original PR EOS. In particular, the PR EOS with the Twu *et al.* α model shows excellent agreement with the Zeno conditions for water, implying that sensitivity to the magnitude and functional form of α may have a more fundamental connection to the density-dependent interactions.

These comparisons and others indicate that, one should examine the $Z = 1$ contour to test for the observed universal linearity when developing an EOS. This Zeno criterion provides a species-independent check of the EOS robustness. When used effectively, new EOSs can be quickly compared to these observations and modified to increase accuracy.

Transport-property research:

Molecular-diffusivity measurement

Self-diffusivities of pure supercritical water has been previously measured and published for a limited range of conditions, but accurate SCW binary-diffusivity data are extremely limited. SCW binary-diffusivity data are scarce and difficult to obtain due to the limited ability to make diffusivity measurements at harsh SCWO process conditions. In this dissertation, diffusivities of pure supercritical water and supercritical-water mixtures have been measured by using NMR. Tracer diffusivities of aqueous acetone mixtures were measured at three different concentrations at typical SCWO operating conditions with a novel, first-of-a-kind SCW/NMR flow system and the NMR spin-echo technique. Water self-diffusivity measurements are comparable with previously published values and validate the apparatus performance and the measurement capacity.

Molecular-diffusivity modeling

Binary-diffusivity models used for SCWO-diffusivity predictions have only recently been evaluated. Due to the lack of experimental data, such evaluations have not been performed in great detail. With newly available data measured in this dissertation, kinetic-gas and hydrodynamic models were reexamined. Based on the analysis performed with a wide range of experimental and simulated data, two models are capable of providing reliable diffusivity predictions.

For SCWO operating conditions, the Tracer Liu-Silva-Macedo (TLSM) and Mathur-Thodos correlations were found to provide the most accurate diffusivity predictions over a wide density range (0.01–1.0 g/cm^3). The Mathur-Thodos correlation requires only critical constants and molecular weights and has an average absolute deviation (AAD) of 18% for supercritical-water self-diffusivities and supercritical tracer & infinitely dilute mutual diffusivities above 400°C. The Mathur-Thodos approach can be extended to mixtures using simple mole-fraction-weighted terms for the required critical constants and reduced variables. Similar results were obtained with the TLSM model (23% AAD for data above 400°C) which requires only molecular weights and two Lennard-Jones parameters for each pure component. Further improvement was made when mole-fraction-weighted experimental-solute and LSM-regressed-

water Lennard-Jones parameters were used (20% AAD). This modified-TLSM method is the recommended approach because higher density supercritical predictions have a 41% AAD versus the Mathur-Thodos 53% AAD and has a smaller overall uncertainty compared to the Mathur-Thodos model. Neither model is recommended for densities above one.

Both models are capable of providing reasonably accurate diffusivities as demonstrated for the systems in this analysis. When doubts are raised about predictions from either of these models, it is recommended to calculate diffusivities with the other model in order to validate the predictions and minimize suspicion. With the modified Tracer Liu-Silva-Macedo and the Mathur-Thodos correlations recommended for use in sub- and supercritical-water diffusivity modeling based on datasets used in this dissertation analysis, additional investigations should be performed. Validation work should continue with commonly used supercritical solvents, *e.g.*, carbon dioxide, and for other water-based systems when additional data become available. Alternative mixing rules should also be evaluated since accuracy is sensitive to the form of model mixture terms.

As a result of the improved thermodynamic- and transport-property modeling capabilities along with the collection of additional aqueous supercritical diffusivities contained in this thesis, the SCWO community now has additional thermodynamic- and transport-property knowledge that leads to a greater understanding of key issues that impact the design and operation of SCWO technology.

4. Appendices

PGSE SPECTROMETER PULSE PROGRAM

```
;  2xPulse-Gradient-Spin-Echo - incr gradient method
;  hard90 - hard 180 - hard 180 rf - k space
;  AMX2 version
;  modified to include presaturation (if needed)
;  MK.pgsevg2

        d0=d4/10-p31*(1+1/10)
        0.5s ze          ; zero data block and initialize
;   START DUMMY SCANS
5       d1 thi           ; T1 delay
        p1 ph1           ; 90 degree hard pulse
        d2               ; stabilization delay
        d4               ; first k pulse delta
        d2               ; stabilization delay
        d5               ; delay for big DELTA
        p2 ph2           ; 180 degree hard pulse
        d2               ; stabilization delay
        d4               ; second k pulse delta
        d2               ; stabilization delay
        d5               ; delay for big DELTA
;START DOUBLE PGSE PART OF DUMMY SCANS
        d6
        d2               ; stabilization delay
        d4               ; third k pulse delta
        d2               ; stabilization delay
        d5               ; delay for big DELTA
        p2 ph2           ; 180 degree hard pulse
        d2               ; stabilization delay
        d4               ; fourth k pulse delta
        d2               ; stabilization delay
        d5               ; delay for big DELTA
        d6
        d5* 1.5          ; something close to ak time
        lo to 5 times l1 ; 11 dummy scans
;start first pgse part
10      d1
        p1 ph1           ; 90 degree hard pulse
        d2               ; stabilization delay
100     p31:ngrad        ; k gradient on
        d0               ; first k pulse delta
        lo to 100 times 10 ; shaped pulse loop
        p31:ngrad        ; k gradient off
        d2
        d5
        p2 ph2
```

```
          d2
200       p31:ngrad         ; k gradient on
          d0                ; second k pulse delta
          lo to 200 times 10 ; shaped pulse loop
          p31:ngrad         ; k gradient off
          d2                ; stabilization delay
          d5                ; delay for big DELTA
;START DOUBLE PGSE PART
          d6
          d2
300       p31:ngrad         ; k gradient on
          d0                ; third k pulse delta
          lo to 300 times 10 ; shaped pulse loop
          p31:ngrad         ; k gradient off
          d2
          d5
          p2 ph2
          d2
400       p31:ngrad         ; k gradient on
          d0                ; fourth k pulse delta
          lo to 400 times 10 ; shaped pulse loop
          p31:ngrad         ; k gradient off
          d2                ; stabilization delay
          d5                ; delay for big DELTA
          d6
;ACQUIRE
          5u ph3 adc
          aq
          rcyc=10 ph0
          30m wr #0 if #0 zd
          lo to 10 times td1 ; number of k-scans
          30m rf #0

          ip0               ; phase cycle
          ip0
          ip1
          ip1
          lo to 10 times 12 ; number of signal averaging scans
          exit
ph0 = 0                     ; initial phase of receiver
ph1 = 0                     ; initial phase of pulse 1
ph2 = 1                     ; initial phase of pulse 2
ph3 = 0                     ; initial phase of pulse 3
```

PGSE SPECTROMETER GRADIENT PROGRAM

In the gradient program, a half-period sine wave is divided into 1,000 intervals and used in order to generate the gradient shape file that is partially shown below. Only eleven of the increment lines are shown in order to save space. The combination of multipliers, cnstX, allow the operator to change the gradient minimum, maximum for each gradient (x, y, and z) according to the following table:

Axis	$\%G_{min}$	$\%G_{max}$
x	cnst11	cnst14
y	cnst12	cnst15
z	cnst13	cnst16

Cnst0 is ±1 depending on if the operator wants the k-scans to start with a maximum gradient (−1) or minimum gradient (+1). Before the first "|", the calculation gives the spectrometer the correct middle (mean) x-gradient value to use followed by the x-gradient required to move from maximum-to-middle and minimum-to-middle (the Δ from the mean). Before the second "|" is the y-gradient calculation and before the "|" is the z-gradient calculation. Each complete "{}" set is a new line for the next shaped pulse increment. For all of the experiments performed here, all x- and y- constants were set to zero and cnst0 was left at −1.

```
loop td1 <2D>
{
    {(0.0000*(cnst14+cnst11)/2), r2d(0.0000*cnst0*(cnst14-cnst11)/2)  |
(0.0000*(cnst15+cnst12)/2), r2d(0.0000*cnst0*(cnst15-cnst12)/2)  |
(0.0000*(cnst16+cnst13)/2), r2d(0.0000*cnst0*(cnst16-cnst13)/2)}
    {(0.0126*(cnst14+cnst11)/2), r2d(0.0126*cnst0*(cnst14-cnst11)/2)  |
(0.0126*(cnst15+cnst12)/2), r2d(0.0126*cnst0*(cnst15-cnst12)/2)  |
(0.0126*(cnst16+cnst13)/2), r2d(0.0126*cnst0*(cnst16-cnst13)/2)}
    {(0.0251*(cnst14+cnst11)/2), r2d(0.0251*cnst0*(cnst14-cnst11)/2)  |
(0.0251*(cnst15+cnst12)/2), r2d(0.0251*cnst0*(cnst15-cnst12)/2)  |
(0.0251*(cnst16+cnst13)/2), r2d(0.0251*cnst0*(cnst16-cnst13)/2)}
    {(0.0377*(cnst14+cnst11)/2), r2d(0.0377*cnst0*(cnst14-cnst11)/2)  |
(0.0377*(cnst15+cnst12)/2), r2d(0.0377*cnst0*(cnst15-cnst12)/2)  |
(0.0377*(cnst16+cnst13)/2), r2d(0.0377*cnst0*(cnst16-cnst13)/2)}
    {(0.0502*(cnst14+cnst11)/2), r2d(0.0502*cnst0*(cnst14-cnst11)/2)  |
(0.0502*(cnst15+cnst12)/2), r2d(0.0502*cnst0*(cnst15-cnst12)/2)  |
(0.0502*(cnst16+cnst13)/2), r2d(0.0502*cnst0*(cnst16-cnst13)/2)}
    {(0.0628*(cnst14+cnst11)/2), r2d(0.0628*cnst0*(cnst14-cnst11)/2)  |
(0.0628*(cnst15+cnst12)/2), r2d(0.0628*cnst0*(cnst15-cnst12)/2)  |
(0.0628*(cnst16+cnst13)/2), r2d(0.0628*cnst0*(cnst16-cnst13)/2)}
```

```
   {(0.0753*(cnst14+cnst11)/2), r2d(0.0753*cnst0*(cnst14-cnst11)/2)   |
(0.0753*(cnst15+cnst12)/2), r2d(0.0753*cnst0*(cnst15-cnst12)/2)   |
(0.0753*(cnst16+cnst13)/2), r2d(0.0753*cnst0*(cnst16-cnst13)/2)}
   {(0.0879*(cnst14+cnst11)/2), r2d(0.0879*cnst0*(cnst14-cnst11)/2)   |
(0.0879*(cnst15+cnst12)/2), r2d(0.0879*cnst0*(cnst15-cnst12)/2)   |
(0.0879*(cnst16+cnst13)/2), r2d(0.0879*cnst0*(cnst16-cnst13)/2)}


   .
   .
   .


   {(0.0251*(cnst14+cnst11)/2), r2d(0.0251*cnst0*(cnst14-cnst11)/2)   |
(0.0251*(cnst15+cnst12)/2), r2d(0.0251*cnst0*(cnst15-cnst12)/2)   |
(0.0251*(cnst16+cnst13)/2), r2d(0.0251*cnst0*(cnst16-cnst13)/2)}
   {(0.0126*(cnst14+cnst11)/2), r2d(0.0126*cnst0*(cnst14-cnst11)/2)   |
(0.0126*(cnst15+cnst12)/2), r2d(0.0126*cnst0*(cnst15-cnst12)/2)   |
(0.0126*(cnst16+cnst13)/2), r2d(0.0126*cnst0*(cnst16-cnst13)/2)}
   {(0.0000*(cnst14+cnst11)/2), r2d(0.0000*cnst0*(cnst14-cnst11)/2)   |
(0.0000*(cnst15+cnst12)/2), r2d(0.0000*cnst0*(cnst15-cnst12)/2)   |
(0.0000*(cnst16+cnst13)/2), r2d(0.0000*cnst0*(cnst16-cnst13)/2)}

}
```